

UNIVERSITY OF THESSALY

DEPARTMENT OF MECHANICAL ENGINEERING

**ADVANCED DETERMINISTIC AND STOCHASTIC
KINETIC MODELING OF GASEOUS MICROSCALE
TRANSPORT PHENOMENA**

Giorgos Tatsios

M.Sc., Mechanical Engineer
Department of Mechanical Engineering
University of Thessaly

A Dissertation Submitted for the Partial Fulfillment of the
Requirements of the Degree of
Doctor of Philosophy

2019

© 2019 Giorgos Tatsios

The approval of the current dissertation by the Department of Mechanical Engineering of the University of Thessaly does not imply acceptance of the author's opinions (Law 5343/32 number 202 paragraph 2). Also, the views and opinions expressed herein do not necessarily reflect those of the European Commission.

Certified by the members of the Dissertation Committee:

- | | |
|--|---|
| 1 st member
(Supervisor) | Prof. Dimitris Valougeorgis
Professor in the Department of Mechanical Engineering
University of Thessaly |
| 2 nd member | Prof. Vasilis Bontozoglou
Professor in the Department of Mechanical Engineering
University of Thessaly |
| 3 rd member | Prof. Nikolaos Pelekasis
Professor in the Department of Mechanical Engineering
University of Thessaly |
| 4 th member | Prof. Theodoros Karakasidis
Professor in the Department of Civil Engineering
University of Thessaly |
| 5 th member | Prof. Stéphane Colin
Professor in the Institut Clément Ader
Université de Toulouse, CNRS, INSA, ISAE-SUPAERO, Mines-Albi, UPS |
| 6 th member | Prof. Aldo Frezzotti
Professor in the Dipartimento di Scienze & Tecnologie Aerospaziali
Politecnico di Milano |
| 7 th member | Prof. Stefan Stefanov
Professor in the Institute of Mechanics
Bulgarian Academy of Sciences |

Dedicated to my family

Acknowledgements

First and foremost, I would like to express my deep and sincere gratitude to my supervisor, Prof. Dimitris Valougeorgis, for his teaching, inspiration and motivation provided to me in order to move ahead with my research and most importantly for his understanding and patience he showed towards me during our collaboration. I honestly cannot imagine having a better mentor.

I also want to express my gratitude to Prof. Stefan Stefanov for his guidance and collaboration during my postgraduate studies and for introducing me to the concept of the DSMC decomposition. In addition, I am sincerely thankful to Prof. Stéphane Colin, Assoc. Prof. Lucien Baldas and Asst. Prof. Marcos Rojas-Cárdenas for inviting me to the Institut Clément Ader, INSA Toulouse and giving me the opportunity to get acquainted with experimental techniques in rarefied gas dynamics, collaborate with the members of INSA team and participate in measurements.

I would like to deeply thank all the members of my dissertation committee for finding the time to review my dissertation and provide their valuable input. Ευχαριστώ πολύ, merci beaucoup, grazie mille, Благодаря ви много Professors Vasilis Bontozoglou, Nikolaos Pelekasis, Theodoros Karakasidis, Stéphane Colin, Aldo Frezzotti and Stefan Stefanov.

I am indebted to all my friends, collaborators and former Ph.D. students in our lab. Many thanks to Dr. Stergios Naris, Dr. John Lihnaripoulos, Dr. Christos Tantos and Makis Misdanitis for all their assistance and interesting discussions we had and to Dr. Sarantis Pantazis for giving me the opportunity to work in extensions of his general purpose DSMC solver. Special thanks to my fellow Ph.D. students, Alexandros Tsimpoukis, Nikos Vasileiadis and Guillermo Lopez-Quesada for sharing this experience with me and for all the unforgettable moments we shared. I am also obliged to Mrs. Zoe Zoupi for all the administrative support concerning my research appointment as a Ph.D. student.

I want to thank Anna Papageorgiou for her endless patience, encouragement and all the happy moments we had during these years. Finally, I am grateful to my parents

Thanasis and Maria and to my sister Natasa, for their continuous and unconditional support.

This work has been supported by the European Community under the contract of association EUROfusion-Hellenic Republic 2014-2018 (Grant Agreement No 633053, WP EDU). Partial support for conference mobility expenses has been received from the European Union's Framework Programme for Research and Innovation Horizon 2020 (2014-2020) under the Marie Skłodowska-Curie Grant Agreement No. 643095.

ADVANCED DETERMINISTIC AND STOCHASTIC KINETIC MODELING OF GASEOUS MICROSCALE TRANSPORT PHENOMENA

Giorgos Tatsios

University of Thessaly, January 2019

Supervisor: Prof. D. Valougeorgis

The theoretical and computational investigation of non-equilibrium transport phenomena in rarefied gases is one of the most interesting and challenging fields in engineering and physics. In recent years, this topic is gaining constantly increasing attention mainly due to its implementation in a wide range of technological applications, ranging from small scale devices like accelerometers and micro gas analyzers up to large scale gas distribution systems in fusion reactors and particle accelerators. The behavior of gasses in rarefied conditions cannot be captured by conventional fluid dynamic approaches, based on the Navier-Stokes-Fourier equations, due to the limited number of intermolecular collisions leading to a departure from local equilibrium. Modeling must be based on kinetic theory of gases on the basis of the Boltzmann equation, which unavoidably is associated with increased complexity and computational cost.

In the present work, advanced kinetic modeling is conducted using the well-established deterministic Discrete Velocity (DVM) and stochastic Direct Simulation Monte Carlo (DSMC) methods. Novel numerical additions are developed for both methodologies and their validity and effectiveness is demonstrated by solving prototype problems in rarefied gas dynamics. Then, these new approaches are implemented to investigate and understand the underlying physics of unexpected transport phenomena observed in gas flows and heat transfer configurations far from local equilibrium. Furthermore, based on computationally efficient and advanced modeling, certain flow and heat transfer configurations, encountered in the design of various devices with miniaturized sizes and/or operating under low pressure conditions, are simulated.

The computational advancements in conjunction with the Discrete Velocity Method include the development and implementation of a) a semi-analytical-numerical methodology based on the method of characteristics to simulate kinetic equations with external force terms, b) a marching DVM algorithm on unstructured meshes approximating complex geometries and c) a half-range synthetic acceleration scheme to speed-up

the convergence rate of the DVM including the bulk quantities at the boundaries. The computational advancement in conjunction with the DSMC method includes the decomposition of the solution into its ballistic and collision parts, by accordingly tagging the simulation particles. The four advancements are briefly analyzed.

In the majority of kinetic simulations, external forces can be neglected and numerical schemes able to treat the external force term in a deterministic manner have not gained considerable attention. The extension of deterministic kinetic modeling of rarefied flows, subject to external fields is an open issue. Here, a suitable semi-analytical-numerical scheme, based on the method of characteristics, is developed. Upon introducing the characteristic variables, the force term is eliminated from the streaming part of the kinetic equation and it is included in the collision term and in the integral expressions of the macroscopic quantities. The accuracy of the proposed algorithm is demonstrated simulating a force driven one-dimensional nonlinear fully developed flow and successful comparisons with existing results are performed.

Following the discretization of the kinetic equations in the phase space (molecular velocity and physical spaces) via the DVM leads to linear algebraic systems with a huge number of equations requiring high computational cost. The so-called marching schemes provide an alternative approach, since they do not require the solution of algebraic systems, but they are limited to simple geometries and structured meshes. Here, a marching DVM algorithm on unstructured meshes is developed using two different approaches. The first one is the typical backtracking methodology, which is robust but computationally expensive and the second novel one, is based on simple generic geometrical arguments and it is computationally efficient, but it may fail when obtuse triangular grid elements exist in the mesh. In the present implementation both methodologies are used, with the geometrical method always being the first choice and introducing the backtracking algorithm as the second choice only when the geometrical approach fails. The developed marching DVM code on unstructured meshes is successfully benchmarked in several two-dimensional rarefied gas flows and heat transfer configurations in convex and non-convex domains using both linear and nonlinear kinetic models.

The typical iteration map of the DVM suffers from slow convergence in the slip and hydrodynamic regimes. Advanced synthetic type acceleration schemes, based on the full-range Hermite polynomials, has been previously developed speeding-up the slow convergence rate, with spectacular results. Their application is limited to fully developed flows through long capillaries, due to their inability to accelerate the

boundary nodes. It is computationally demonstrated that accelerating the boundary nodes is crucial in the general case, where the boundary conditions are part of the solution. The proposed synthetic acceleration methodology is based on half-range Hermite polynomials and the derived system of half-range moment equations are accelerating the macroscopic quantities in the interior as well as in the boundary nodes of the physical domain. The developed half-range synthetic acceleration scheme is applied to one-dimensional linear flow and heat transfer configurations clearly indicating their computational efficiency. In addition, solving the half-range moment equations decoupled from the kinetic equations provides accurate results in a range of the Knudsen number, much wider than expected. This is attributed to the ability of the half-range moments to incorporate the discontinuity of the distribution function.

In rarefied conditions, where intermolecular collisions are scarce, particles can travel long distances without interacting with other particles. Particles emitted from the boundaries may reach locations well into the flow domain carrying the boundary information that may be very different from the local conditions leading to a number of interesting not always expected non-equilibrium phenomena. Therefore, it is interesting therefore to distinguish between particles with and without intermolecular collisions. In the framework of the DSMC method, the solution is decomposed into its ballistic and collision parts and the contribution of each part to the macroscopic quantities is computed, providing insight information about the microstructure of the flow and aiding physical understanding.

Continuing with the implementation of the above computational methodologies to investigate unresolved phenomena, the novel DSMC decomposition has been applied to interpret non-equilibrium phenomena arising in thermally induced flow and heat transfer configurations in enclosures. More specifically, in cavities, with temperature gradients in the lateral walls, an unexpected flow from hot to cold regions, opposite to the well-known thermal creep flow, has been observed. The formation of this counter flow is explained using physical arguments obtained by the decomposition methodology. Furthermore, computing the heat transfer in a square cavity, where the bottom wall is in a high temperature and all other three walls are maintained in the same lower temperature, it has been found that the heat flux departing from the heated wall does not have a monotonic behavior with respect to the temperature ratio but exhibits a maximum value at some particular value of the temperature ratio. Based on the DSMC decomposition methodology, a physical explanation to this counter intuitive observation has been provided.

The DSMC decomposition methodology has been also applied to pressure driven fully developed flows through long capillaries providing a complete quantitative justification of the celebrated Knudsen minimum. The minimum value of the dimensionless flow rate in the transition regime is explained in a simple manner by computing the corresponding contributions of the ballistic and collision parts.

Applying the DVM semi-analytical-numerical scheme to force driven flow it has been observed that the distribution function is strongly non-equilibrium, and multimodal with long tails. It is believed that this is due to the fact that in addition to collisions other external forces are also acting on the gas molecules.

Next, topics concerning the application of kinetic theory and modeling in the design process of devices operating under rarefied conditions are addressed. The range of validity of the so-called implicit boundary conditions in pressure driven flows with respect to the flow parameters is specified. Also, a detailed parametric investigation is conducted for various geometrical configurations encountered in thermally driven micropumps. Finally, an uncertainty propagation analysis is performed for typical gas flow and heat transfer configurations.

Pressure driven flows through capillaries are common in gas vacuum system and processes as well as in micro electromechanical systems. The literature on this subject is extensive. In flows through capillaries with relatively small length driven by large pressure gradients, proper kinetic modeling is computationally very demanding, since large upstream and downstream regions should be included in the computational domain. Recently, the so-called implicit boundary conditions have been reported, claiming the ability to eliminate the need of the inlet and outlet regions and therefore, significantly decrease the involved computational effort. Here, a systematic and detailed computational investigation of the accuracy of the implicit boundary conditions in the transition and slip regimes for capillaries of small and moderate lengths in a wide range of all involved parameters is performed. It has been computationally found that the assumptions of these boundary conditions are questionable in rarefied conditions and should be implemented with care only in capillaries with dimensionless length larger than ten. Furthermore, it is advised to always couple the implicit boundary conditions with the end effect theory in order to significantly increase their applicability range and associated accuracy.

In recent years an effort is underway for the miniaturization of devices and processes, which are considered to be, compared to their normal sized counterparts, more reliable and efficient with faster response and less expensive. There is a clear need for micro

pumping with the varying specifications, in terms of flow rate and pressure difference, depending upon the application. Knudsen type thermally driven pumps with no moving parts are of particular interest. Here, a parametric analysis of different configurations that can potentially be incorporated into the design of these pumps is performed. The examined configurations include channels with saw tooth surfaces, combination of straight and curved channels and assemblies of tapered channels. The characteristics of each configuration are identified and guidelines for the design of thermally driven micropumps are given, focusing on the tapered configuration, where the pump performance curves are also provided.

Uncertainty analysis is a critical issue in several fields of engineering and science including rarefied gas dynamics. The propagation of the uncertainty of the input parameters to the simulation results in rarefied gas dynamics configurations is examined. Three benchmark configurations are considered, namely pressure and temperature driven flows through long tubes and heat transfer between two parallel plates. The analysis is based on the Monte Carlo Method, which is reliable and applicable for the uncertainty propagation in the investigated setups, which is performed in the whole range of gas rarefaction and various values of the input quantities and their associated uncertainties (pressure, temperature, geometry, pipe roughness, etc). The effect that each input parameter has on the uncertainty of the main output quantity of interest is found. This information can facilitate comparisons and aid in the design procedure of systems operating in rarefied conditions.

It is hoped that the present work, providing certain advancements in kinetic modeling and computing, in physical understanding of non-equilibrium phenomena and in technological issues concerning the design of devices and apparatus, will prove to be useful, at some extend, to the scientific communities in rarefied gas dynamics, vacuum science and technology and gaseous microfluidics.

ΠΡΟΧΩΡΗΜΕΝΗ ΝΤΕΤΕΡΜΙΝΙΣΤΙΚΗ ΚΑΙ ΣΤΟΧΑΣΤΙΚΗ ΜΟΝΤΕΛΟΠΟΙΗΣΗ ΦΑΙΝΟΜΕΝΩΝ ΜΕΤΑΦΟΡΑΣ ΑΕΡΙΩΝ ΣΤΗ ΜΙΚΡΟΚΛΙΜΑΚΑ

Γιώργος Τατσιος

Πανεπιστήμιο Θεσσαλίας, Ιανουάριος 2019

Επιβλέπων Καθηγητής: Δ. Βαλουγεώργης

Η θεωρητική και υπολογιστική μελέτη φαινομένων μεταφοράς μακριά από τη θερμοδυναμική ισορροπία σε καταστάσεις υψηλής αραιοποίησης είναι ένας από τους πιο ενδιαφέροντες και απαιτητικούς κλάδους της μηχανικής και της φυσικής. Αυτό το πεδίο έρευνας αποκτά όλο και περισσότερη προσοχή τα τελευταία χρόνια, καθώς τέτοιες καταστάσεις απαντώνται σε ένα μεγάλο εύρος εφαρμογών, από μικροδιατάξεις όπως επιταχυνσιόμετρα και μικρό χρωματογράφους έως μεγάλης κλίμακας δίκτυα μεταφοράς αερίων σε αντιδραστήρες σύντηξης και επιταχυντές σωματιδίων. Η συμπεριφορά των αερίων σε καταστάσεις υψηλής αραιοποίησης δεν μπορεί να περιγραφεί από τις συμβατικές προσεγγίσεις της ρευστοδυναμικής που βασίζονται στις εξισώσεις Navier-Stokes-Fourier λόγω του περιορισμένου αριθμού των συγκρούσεων μεταξύ των μορίων του αερίου που οδηγεί σε μεγάλες αποκλίσεις από την θερμοδυναμική ισορροπία. Η μοντελοποίηση φαινομένων σε τέτοιες συνθήκες βασίζεται στην κινητική θεωρία των αερίων μέσω της εξίσωσης Boltzmann. Αυτό αυξάνει σημαντικά την πολυπλοκότητα και το υπολογιστικό κόστος αυτών των προσομοιώσεων.

Στην παρούσα διατριβή, οι κινητικές προσομοιώσεις γίνονται χρησιμοποιώντας τις, πλέον καθιερωμένες ντετερμινιστικές και στοχαστικές μεθόδους, αυτές των διακριτών ταχυτήτων (DVM) και της απευθείας προσομοίωσης Monte Carlo (DSMC). Καινοτόμες επεκτάσεις εισάγονται και για τις δύο αυτές μεθοδολογίες και η ακρίβεια και αποδοτικότητα τους παρουσιάζονται λύνοντας κάποια πρότυπα προβλήματα του κλάδου της αραιοποιημένης θερμορευστοδυναμικής. Στη συνέχεια οι προσεγγίσεις αυτές εφαρμόζονται για την μελέτη και κατανόηση της φυσικής πίσω από κάποια απρόσμενα και παράδοξα φαινόμενα που παρατηρούνται σε διατάξεις ροής και μεταφοράς θερμότητας σε καταστάσεις υψηλής αραιοποίησης. Επιπλέον, κάνοντας χρήση αποδοτικών και πρωτοπόρων υπολογιστικών προσεγγίσεων γίνεται υπολογιστική μελέτη ροής και μεταφοράς θερμότητας σε διατάξεις που απαντώνται σε μικροηλεκτρομηχανολογικά εξαρτήματα και σε συσκευές που λειτουργούν σε περιβάλλον χαμηλής πίεσης.

Οι καινοτομίες στις αριθμητικές μεθοδολογίες που χρησιμοποιούνται σε συνδυασμό με τη μέθοδο διακριτών ταχυτήτων περιλαμβάνουν την ανάπτυξη και εφαρμογή α) ενός ημι-αναλυτικού αριθμητικού σχήματος που βασίζεται στην μέθοδο των χαρακτηριστικών για την επίλυση των κινητικών εξισώσεων υπό την επίδραση εξωτερικών πεδίων δυνάμεων, β) ενός σχήματος προέλασης για την επίλυση των κινητικών εξισώσεων σε αδόμητα πλέγματα και περίπλοκες γεωμετρίες, γ) και ενός αριθμητικού σχήματος επιτάχυνσης της σύγκλισης της μεθόδου διακριτών ταχυτήτων που επιδρά και στους οριακούς κόμβους και βασίζεται σε ημιάπειρες ροπές. Η καινοτομία σε συνδυασμό με την μέθοδο απευθείας προσομοίωσης Monte Carlo περιλαμβάνει τη διάσπαση της λύσης σε δύο επιμέρους τμήματα που αντιστοιχούν στα σωματίδια που φτάνουν σε κάποιο σημείο του πεδίου με και χωρίς ενδομοριακές αλληλεπιδράσεις. Οι συνολικά τέσσερις αυτές καινοτομίες παρουσιάζονται συνοπτικά.

Στην πλειοψηφία των προσομοιώσεων μέσω κινητικής θεωρίας, δεν υπάρχουν εξωτερικά πεδία δυνάμεων που επιδρούν στα σωματίδια, είτε αυτά είναι αμελητέας σημασίας όπως η βαρύτητα. Για το λόγο αυτό αριθμητικά σχήματα ικανά να λάβουν υπ' όψιν τους τον όρο των εξωτερικών δυνάμεων δεν έχουν λάβει προσοχή και η ανάπτυξη τέτοιων νεότερων αριθμητικών σχημάτων είναι ένα ανοιχτό ζήτημα. Στα πλαίσια της διατριβής, αναπτύχθηκε ένα κατάλληλο ημι-αναλυτικό σχήμα βασισμένο στην μέθοδο των χαρακτηριστικών. Με την εισαγωγή των μεταβλητών που περιγράφουν τις χαρακτηριστικές καμπύλες, ο όρος της εξωτερικής δύναμης μεταφέρεται από το τμήμα της ελεύθερης κίνησης στο τμήμα των συγκρούσεων των κινητικών εξισώσεων και στις ροπές που δίνουν τις μακροσκοπικές ποσότητες. Η ακρίβεια του σχήματος παρουσιάζεται με την επίλυση μίας μη-γραμμικής πλήρως ανεπτυγμένης ροής τύπου Poiseuille λόγω εξωτερικής δύναμης ανάμεσα σε δύο πλάκες και τα αποτελέσματα συγκρίνονται με αντίστοιχα αποτελέσματα διαθέσιμα στην βιβλιογραφία.

Η διακριτοποίηση της εξίσωσης Boltzmann και των εξισώσεων των κινητικών μοντέλων με τη μέθοδο των διακριτών ταχυτήτων στον φασικό χώρο (χώρος μοριακών ταχυτήτων και φυσικός χώρος) οδηγεί σε μεγάλα γραμμικά συστήματα αλγεβρικών εξισώσεων, η επίλυση των οποίων είναι υπολογιστικά ακριβή. Μία εναλλακτική προσέγγιση είναι τα λεγόμενα σχήματα προέλασης, που δεν απαιτούν την επίλυση μεγάλων συστημάτων αλγεβρικών εξισώσεων. Η εφαρμογή τους όμως έχει περιοριστεί σε δομημένα πλέγματα και απλές γεωμετρίες. Στην παρούσα διατριβή αναπτύσσεται ένα σχήμα προέλασης εφαρμόσιμο σε αδόμητα πλέγματα βασισμένο σε δύο διαφορετικές προσεγγίσεις. Η πρώτη προσέγγιση που στηρίζεται σε έναν τυπικό backtracking αλγόριθμο, παρέχει πάντα σωστά αποτελέσματα αλλά είναι υπολογιστικά απαιτητική. Η δεύτερη προσέγγιση

είναι μία καθαρά γεωμετρική μέθοδος η οποία απαιτεί μικρότερο υπολογιστικό φορτίο αλλά αποτυγχάνει όταν υπάρχουν στοιχεία με αμβλείες γωνίες στο πλέγμα. Στην παρούσα υλοποίηση και οι δύο μεθοδολογίες χρησιμοποιούνται. Η γεωμετρική μέθοδος εφαρμόζεται πρώτα και ύστερα ο αλγόριθμος backtracking εφαρμόζεται μόνο στις περιπτώσεις που η γεωμετρική μέθοδος αποτυγχάνει να δώσει μία έγκυρη λύση. Η μεθοδολογία προέλασης σε αδόμητα πλέγματα που αναπτύχθηκε, εφαρμόστηκε με επιτυχία σε διάφορες πρότυπες δισδιάστατες διατάξεις ροής και μεταφοράς θερμότητας σε συνθήκες αραιοποίησης, σε κυρτά και μη-κυρτά χωρία χρησιμοποιώντας γραμμικά και μη-γραμμικά κινητικά μοντέλα.

Ο τυπικός επαναληπτικός χάρτης της μεθόδου διακριτών ταχυτήτων παρουσιάζει πολύ αργή σύγκλιση στην περιοχή ολίσθησης και κοντά στη συνεχή περιοχή. Αριθμητικά σχήματα επιτάχυνσης που βασίζονται στα τυπικά πολυώνυμα Hermite, έχουν εφαρμοστεί στο παρελθόν επιταχύνοντας την επίλυση με εκπληκτικά αποτελέσματα. Η εφαρμογή τους όμως περιορίστηκε σε πλήρως ανεπτυγμένες ροές σε αγωγούς μεγάλου μήκους καθώς τα σχήματα που έχουν αναπτυχθεί εφαρμόζονται μόνο στους εσωτερικούς κόμβους. Αποδεικνύεται υπολογιστικά πως η επιτάχυνση των οριακών κόμβων είναι καίριας σημασίας στη γενική περίπτωση, όπου οι οριακές συνθήκες είναι μέρος της λύσης. Σχήματα επιτάχυνσης της λύσης ικανά να επιταχύνουν τους εσωτερικούς καθώς και τους οριακούς κόμβους αναπτύχθηκαν για τις γραμμικές κινητικές εξισώσεις. Τα σχήματα αυτά βασίζονται σε ημιάπειρες ροπές και κατασκευάζονται χρησιμοποιώντας πολυώνυμα Hermite που είναι ορθογώνια σε ημιάπειρα διαστήματα και όχι σε όλο το εύρος των πραγματικών αριθμών. Η αποδοτικότητα των σχημάτων που αναπτύχθηκαν, παρουσιάζεται με την εφαρμογή τους σε μονοδιάστατη ροή λόγω διαφοράς πίεσης και σε μεταφορά θερμότητας μεταξύ δύο επιφανειών. Επιπλέον, τα συστήματα εξισώσεων ροπών που κατασκευάζονται επιλύονται ανεξάρτητα της κινητικής εξίσωσης χρησιμοποιώντας μία τυπική μεθοδολογία για το κλείσιμο των συστημάτων αυτών, παρέχοντας ακριβή αποτελέσματα σε ένα μεγαλύτερο από το αναμενόμενο εύρος του αριθμού Knudsen. Αυτό αποδίδεται στην ικανότητα αυτών των σχημάτων να αντιμετωπίσουν την ασυνέχεια της συνάρτησης κατανομής.

Σε συνθήκες υψηλής αραιοποίησης όπου οι συγκρούσεις μεταξύ σωματιδίων είναι σπάνιες, τα σωματίδια ταξιδεύουν μεγάλες αποστάσεις χωρίς να συγκρουστούν με άλλα σωματίδια. Τα σωματίδια που φεύγουν από τα τοιχώματα φτάνουν σε περιοχές του ροϊκού πεδίου μακριά από τα τοιχώματα μεταφέροντας την πληροφορία του τοιχώματος η οποία μπορεί να διαφέρει σημαντικά από τις τοπικές συνθήκες. Αυτός ο μηχανισμός οδηγεί σε ενδιαφέροντα και απρόσμενα φαινόμενα, λόγω της μεγάλης απόκλισης από τη θερμοδυναμική ισορροπία. Είναι λοιπόν ενδιαφέρον να γίνει ένας διαχωρισμός των

σωματιδίων που φτάνουν σε κάποιο σημείο του ροϊκού πεδίο μετά από συγκρούσεις και αυτών που δεν έχουν αλληλεπιδράσει με άλλα σωματίδια. Αναπτύσσεται μία μεθοδολογία, στα πλαίσια της μεθόδου DSMC που διασπά την λύση σε αυτά τα δύο τμήματα και υπολογίζει την συνεισφορά του καθενός στις μακροσκοπικές ποσότητες, παρέχοντας έτσι πληροφορία για την δομή της ροής και βοηθώντας την φυσική κατανόηση των φαινομένων που παρατηρούνται.

Συνεχίζοντας με την εφαρμογή των παραπάνω υπολογιστικών καινοτομιών σε απρόσμενα θερμορευστοδυναμικά φαινόμενα, η μεθοδολογία διάσπασης της λύσης που αναπτύχθηκε εφαρμόζεται για την καλύτερη κατανόηση φαινομένων που παρατηρούνται στη ροή και μεταφορά θερμότητας σε κοιλότητες με μη-ισοθερμοκρασιακά τοιχώματα. Πιο συγκεκριμένα, σε κοιλότητες με κλίσεις θερμοκρασίας στα κάθετα τοιχώματα παρατηρείται μία μη αναμενόμενη ροή με κατεύθυνση αντίθετη της κλίσης θερμοκρασίας, αντίθετα δηλαδή από την αναμενόμενη ροή λόγω θερμικού ερπυσμού. Ο σχηματισμός αυτής της ροής εξηγείται μέσω της μεθοδολογίας διάσπασης της λύσης. Στην μεταφορά θερμότητας μέσω αερίου σε κοιλότητα με ένα θερμαινόμενο τοίχωμα, ο ρυθμός μεταφοράς θερμότητας δεν συμπεριφέρεται μονότονα σε σχέση με τον λόγο θερμοκρασίας, αλλά παρουσιάζει μέγιστο σε κάποια κρίσιμη τιμή του. Με βάση την μεθοδολογία διάσπασης της λύσης, παρέχεται μία φυσική εξήγηση αυτού του φαινομένου. Η μεθοδολογία διάσπασης της λύσης, εφαρμόστηκε επίσης σε πλήρως ανεπτυγμένες ροές λόγω κλίσης πίεσης σε αγωγούς μεγάλου μήκους παρέχοντας μία ποσοτική εξήγηση του γνωστού παράδοξου του Knudsen. Το ελάχιστο που παρατηρείται στην αδιάστατη μαζική παροχή ερμηνεύεται με βάση την διάσπαση στα δύο τμήματα της λύσης υπολογίζοντας την επίδραση του καθενός στην συνολική μαζική παροχή.

Στη συνέχεια, γίνεται εφαρμογή της κινητικής θεωρίας στον σχεδιασμό συσκευών και διατάξεων που λειτουργούν σε συνθήκες υψηλής αραιοποίησης. Βρίσκεται το εύρος εφαρμογής, σε σχέση με τις παραμέτρους της ροής, των λεγόμενων πεπλεγμένων οριακών συνθηκών σε ροές λόγω κλίσης πίεσης. Γίνεται, επίσης, μία λεπτομερής παραμετρική ανάλυση διαφόρων διατάξεων που απαντώνται στον σχεδιασμό μικρο-αντλιών χωρίς κινούμενα μέρη. Τέλος, γίνεται ανάλυση αβεβαιότητας σε τυπικές διατάξεις ροής και μεταφοράς θερμότητας. Ροές αερίων λόγω κλίσης πίεσης συναντώνται συχνά σε συστήματα κενού και μικρο ηλεκτρομηχανολογικά συστήματα. Η βιβλιογραφία σχετικά με αυτές τις ροές είναι εκτενής. Στην περίπτωση που ο αγωγός είναι σχετικά μικρού μήκους και η βαθμίδα πίεσης μεγάλη, μεγάλες περιοχές ανάντι και κατάντι του αγωγού πρέπει να ληφθούν υπ' όψιν και το υπολογιστικό κόστος αυξάνει σημαντικά. Πρόσφατα, οι πεπλεγμένες οριακές συνθήκες έχουν προταθεί που εφαρμόζονται στα άκρα του αγωγού

εξαλείφοντας την ανάγκη για τις μεγάλες αυτές περιοχές. Μία συστηματική μελέτη της εγκυρότητάς τους στην μεταβατική περιοχή και περιοχή ολίσθησης πραγματοποιείται για αγωγούς μικρού και μέσου μήκους και για ένα μεγάλο εύρος των παραμέτρων της ροής. Αποδεικνύεται πως οι υποθέσεις πίσω από αυτές τις οριακές συνθήκες είναι αμφισβητήσιμες σε συνθήκες υψηλής αραιοποίησης και πως η εφαρμογή τους πρέπει να γίνεται με προσοχή και μόνο σε αγωγούς μεγάλου μήκους. Επιπλέον συνιστάται η εφαρμογή αυτών των οριακών συνθηκών με ταυτόχρονη εφαρμογή της θεωρίας των φαινομένων εισόδου και εξόδου κάτι που μπορεί να αυξήσει σημαντικά το εύρος εφαρμογής τους.

Τα τελευταία χρόνια υπάρχει μία έντονη τάση για σμίχρυνση συσκευών, καθώς τυπικά αυτές οι συσκευές έχουν χαμηλότερο κόστος, μεγαλύτερη αξιοπιστία και αποδοτικότητα καθώς και καλύτερη απόκριση από τις αντίστοιχες κανονικού μεγέθους. Σε αυτές τις διατάξεις υπάρχει ανάγκη για μικρο-αντλίες καθώς συχνά είναι απαραίτητη μία μαζική παροχή ή διαφορά πίεσης. Οι αντλίες τύπου Knudsen που δεν έχουν κινούμενα μέρη, αλλά η αρχή λειτουργίας των οποίων βασίζεται σε κλίσεις θερμοκρασίας, παρουσιάζουν ιδιαίτερο ενδιαφέρον. Στην παρούσα διατριβή γίνεται μία παραμετρική μελέτη διαφόρων διατάξεων που θα μπορούσαν δειντητικά να χρησιμοποιηθούν στον σχεδιασμό τέτοιων αντλιών. Οι διατάξεις που μελετήθηκαν περιλαμβάνουν κανάλια με προιονωτά τοιχώματα, συνδυασμό ευθέων και κυρτών καναλιών και διατάξεις από συγκλίνοντα και αποκλίνοντα κανάλια. Τα χαρακτηριστικά κάθε διάταξης παρουσιάζονται και διατυπώνονται κατευθυντήριες γραμμές για των σχεδιασμό τέτοιων αντλιών. Η μελέτη εστιάζεται κυρίως στην περίπτωση των συγκλινόντων και αποκλινόντων αγωγών όπου δίνονται και οι χαρακτηριστικές καμπύλες των αντλιών. Η μελέτη της αβεβαιότητας είναι υψηλής σημασίας σε διάφορες περιοχές της μηχανικής και της επιστήμης, συμπεριλαμβανομένης και της αεροδυναμικής χαμηλών πυκνοτήτων. Η διάδοση της αβεβαιότητας των παραμέτρων εισόδου στα αποτελέσματα των προσομοιώσεων μέσω κινητικής θεωρίας εξετάζεται. Συγκεκριμένα μελετώνται τρία πρότυπα προβλήματα, η ροή λόγω κλίσης πίεσης και θερμοκρασίας σε αγωγούς μεγάλου μήκους και η μεταφορά θερμότητας μεταξύ δύο πλακών. Για την διάδοση της αβεβαιότητας εφαρμόζεται η στοχαστική μεθοδολογία Monte Carlo, που είναι αξιόπιστη και ικανή να εφαρμοστεί στις συγκεκριμένες περιπτώσεις. Η ανάλυση γίνεται σε ένα μεγάλο εύρος της αραιοποίησης και για διάφορες τιμές των παραμέτρων εισόδου (πίεση, θερμοκρασία, γεωμετρικά μεγέθη, τραχύτητα επιφανειών κτλ) και των αβεβαιότητων τους. Βρίσκεται η επίδραση που έχει κάθε παράμετρος εισόδου στην αβεβαιότητα των αποτελεσμάτων. Αυτή η πληροφορία μπορεί να βοηθήσει συγκρίσεις μεταξύ πειραματικών μετρήσεων και υπολογιστικών αποτελεσμάτων καθώς και να χρησιμοποιηθεί στον σχεδιασμό συστημάτων που λειτουργούν σε καταστάσεις κενού.

Ελπίζεται πως η παρούσα διατριβή που περιλαμβάνει διάφορες καινοτομίες στην υπολογιστική εφαρμογή της κινητικής θεωρίας, στην υπολογιστική επίλυση των κινητικών εξισώσεων, στην πληρέστερη κατανόηση των φαινομένων μακριά από τη θερμοδυναμική ισορροπία καθώς και σε διάφορα θέματα που αφορούν τον σχεδιασμό συσκευών θα φανεί χρήσιμη στις επιστημονικές κοινότητες της αραιοποιημένης αεροδυναμικής, της τεχνολογίας κενού και των μικροηλεκτρομηχανολογικών εξαρτημάτων.

Contents

List of Figures	xxv
List of Tables	xxxiii
1 Introduction	1
1.1 General concepts	1
1.2 Dissertation structure and contents	2
1.3 Novelty and scientific contributions	5
2 Literature review	7
2.1 Brief historical overview and fundamental principles of kinetic theory .	7
2.2 The Knudsen number and flow regimes	10
2.3 Kinetic model equations and boundary conditions	12
2.4 Numerical methods	15
2.5 Pressure and temperature driven flows	17
2.6 Uncertainty propagation	21
3 Pressure driven rarefied gas flows through capillaries	23
3.1 Introduction	23
3.2 Nonlinear fully developed rarefied gas flow between parallel plates due to external force	25
3.2.1 Governing equations with external force term	25
3.2.2 Solution methodology based on the method of characteristics . .	30
3.2.3 Mass and heat flow rates along with macroscopic distributions .	34
3.2.4 Molecular velocity distribution function	36
3.3 Implicit boundary conditions	37
3.3.1 Flow configuration and governing equations	37

3.3.2	Inlet and outlet boundary conditions in the typical flow configuration	41
3.3.3	Inlet and outlet boundary conditions in the implicit formulation	42
3.3.4	Comparison between the flow rates of the typical and the implicit boundary conditions formulations	45
3.3.5	Comparison between the flow rates of the typical and the implicit boundary conditions plus the end effect correction formulations	47
3.4	Concluding remarks	49
4	Marching DVM algorithm on unstructured meshes	65
4.1	Introduction	65
4.2	Unstructured mesh geometry and discretization scheme	67
4.3	Identification of the marching path in unstructured grids	70
4.3.1	Backtracking algorithm	71
4.3.2	Geometrical algorithm	72
4.3.3	Comparison between the backtracking and geometrical algorithms	76
4.4	Structure of the marching DVM algorithm	76
4.5	Test case I: Fully developed flows in channels with circular, ellipsoidal and Sierpinski carpet cross sections	78
4.6	Test case II: Linear lid driven cavity flow	80
4.7	Test case III: Nonlinear thermally driven cavity flow	81
4.8	Concluding remarks	82
5	Pumping due to thermal transpiration in channels of various configurations	99
5.1	Introduction	99
5.2	Saw tooth surface channels	102
5.2.1	Flow configuration and modeling	102
5.2.2	Parametric analysis of the mass flow rate	103
5.2.3	Velocity and temperature fields	104
5.3	Tapered channels	105
5.3.1	Geometry and flow configuration	105
5.3.2	Modeling of mass flow rate and pressure difference	108
5.3.3	Zero net mass flow rate (Flow scenario A)	110
5.3.4	Equal inlet and outlet pressures (Flow scenario B)	112

5.3.5	Nonzero mass flow rate and unequal inlet and outlet pressures (Flow scenario C)	114
5.3.6	Cascades of tapered channels	115
5.4	Curved channels	116
5.4.1	Formulation	116
5.4.2	Kinetic coefficients	120
5.4.3	Simulation of thermally driven flows through curved channels .	121
5.4.4	Zero net mass flow rate	123
5.4.5	Equal inlet and outlet pressures	123
5.5	Concluding remarks	124

6 Decomposition of the DSMC solution into ballistic and collision parts and its implementation in non-equilibrium phenomena in cavities and capillaries 151

6.1	Introduction	151
6.2	Rarefied gas flow in cavities due to non-isothermal lateral walls	155
6.2.1	Flow configuration and parameters definition	155
6.2.2	Deterministic kinetic modeling	157
6.2.3	Stochastic DSMC modeling	161
6.2.4	DSMC decomposition methodology into ballistic and collision parts	163
6.2.5	Macroscopic distributions in the flow domain	168
6.2.6	Macroscopic distributions adjacent to the non-isothermal cavity walls	171
6.2.7	Ballistic and collision contributions	174
6.3	Non-equilibrium heat transfer in cavities due to uniformly heated walls	177
6.3.1	Flow configuration	177
6.3.2	Deterministic and stochastic modeling	177
6.3.3	Flow field and macroscopic quantities	178
6.3.4	Ballistic, collision and total heat fluxes	179
6.4	Prediction of the Knudsen minimum in long capillaries	180
6.4.1	Flow configuration	180
6.4.2	Stochastic modeling and decomposition	182
6.4.3	Explanation of the Knudsen minimum	183
6.5	Concluding remarks	185

7	Uncertainty propagation in rarefied gas flows and heat transfer	211
7.1	Introduction	211
7.2	General notation and the sensitivity derivatives method	213
7.3	The Monte Carlo Method	214
7.4	Pressure and temperature driven flows through long tubes	216
7.4.1	Formulation	216
7.4.2	Uncertainty of kinetic coefficients in Poiseuille and thermal creep flows	218
7.4.3	Uncertainty of mass flow rate in Poiseuille flow	219
7.4.4	Uncertainty of pressure difference in thermomolecular pressure difference	220
7.4.5	Uncertainty of mass flow rate in thermal creep flow	222
7.5	Nonlinear heat transfer between parallel plates	223
7.5.1	Formulation	223
7.5.2	Uncertainty of heat flux in heat transfer between parallel plates	227
7.6	Concluding remarks	228
8	Synthetic acceleration schemes of the discrete velocity algorithm	245
8.1	Introduction	245
8.2	Synthetic acceleration based on full-range Hermite polynomials	247
8.3	Definition of the half-range Hermite polynomials	252
8.4	Synthetic acceleration based on the half-range Hermite polynomials: Fully developed flow between parallel plates	254
8.5	Synthetic acceleration based on the half-range Hermite polynomials: Heat transfer between parallel plates	256
8.6	Computational efficiency and accuracy of the developed half-range schemes	260
8.7	Concluding remarks	263
9	Concluding remarks	269
9.1	Summary and contributions	269
9.2	Future work	274
Appendix A Formulation of the implicit boundary conditions		277
Appendix B Formulation of fully developed, linear and non-linear flows solved based on the marching DVM algorithm on unstructured meshes		279

B.1 Fully developed flows	279
B.2 Linear flows	280
B.3 Nonlinear flows	284
Appendix C Nonlinear thermally driven flow through short tapered channels	289
C.1 Zero net mass flow rate (Flow scenario A)	290
C.2 Equal inlet and outlet pressures (Flow scenario B)	291
Appendix D Computation of the kinetic coefficients used in the modeling of tapered channels	297
Appendix E Tables of coefficients used for half-range acceleration schemes	299
References	305

List of Figures

3.1	Distributions of density (top), temperature (middle) and velocity (bottom) for $\overline{F} = 0.05$ (left) and $\overline{F} = 0.5$ (right).	56
3.2	Reduced distribution function φ at five locations along the distance between the plates, with a tail region detail at the center of the flow domain (bottom right subfigure) for $\overline{F} = 0.5$ and $Kn_0 = 1$	57
3.3	Reduced distribution function φ at three locations along the distance between the plates, for $\overline{F} = 0.5$ and $Kn_0 = 1$ and 10.	58
3.4	Reduced distribution function φ at three locations along the distance between the plates for $\overline{F} = 0.05$ and $Kn_0 = 0.1, 1$	59
3.5	Reduced distribution function φ at the center of the distance between the plates for $F = 0.5$ and $Kn_0 = 10$ in terms of s_2 , for various values of ζ_x	60
3.6	3D plot of the reduced distribution function φ at $s_1 = -1/2$ for $\overline{F} = 0.5$ and $Kn_0 = 1$	61
3.7	View of the computational domains with the coordinate system and its origin for the typical flow configuration (regions (A), (B) and (C)) and the one with the implicit boundary conditions (only region (A)), with $\alpha = H/2$ or R for the channel and tube respectively.	62
3.8	Relative difference (error) of the flow rates between the typical approach and the one with implicit boundary conditions in terms of $\delta_{in}(\chi/L)(\Delta P/P_{in})$ for the channel (left) and tube (right) flows.	63
3.9	Relative difference (error) of the flow rates between the typical approach and the one with implicit boundary conditions plus the end effect correction in terms of $\delta_{in}(\chi/L)(\Delta P/P_{in})$ for the channel (left) and tube (right) flows.	63

4.1	Detail of the unstructured mesh with some elements having a common node (i) and a molecular velocity vector ξ with its origin at node i . . .	86
4.2	Flowchart of the backtracking algorithm for the solution sequence. . . .	87
4.3	Arbitrary computational domain, along with a bounding circle and a tangent line.	88
4.4	Acute triangular element with the characteristic line and a line normal to the molecular velocity vector.	88
4.5	Boundary element along with the line sweeping through the flow domain.	89
4.6	Obtuse triangular element with the characteristic line and a line normal to the molecular velocity vector.	89
4.7	Flow chart of the main steps of the marching DVM algorithm.	90
4.8	Flow chart of the initialization step in a marching DVM algorithm. . .	90
4.9	Velocity streamlines for a flow around the letters UTH based on the marching DVM algorithm on unstructured meshes.	91
4.10	Section of the unstructured mesh around the lower part of the letter U.	91
4.11	Computational domain of Sierpinski carpets of levels 0, 1, 2, 3.	92
4.12	Section of unstructured mesh in the fully developed flow through an elliptical tube.	93
4.13	Section of unstructured mesh in the fully developed flow through a circular tube.	93
4.14	Sections of unstructured meshes in fully developed flow through Sierpinski carpets.	94
4.15	Reduced flow rate G_P in terms of δ for the pressure driven fully developed flow through capillaries of Sierpinski carpet cross sections.	95
4.16	Section of unstructured mesh in the lid driven flow.	96
4.17	Section of unstructured mesh in the thermally driven flow in a cavity. .	96
4.18	Streamlines and vertical velocity contours for a lid driven flow in a cavity in terms of δ	97
5.1	One stage of the saw-tooth channel along with the dimensions.	129
5.2	Section of typical mesh used for the simulation of the saw tooth surface channel.	129
5.3	Mass flow rate for a saw-tooth channel in terms of pressure for $P_0 \in [10^2, 10^5]$ Pa (left) and $P_0 \in [10^2, 10^4]$ Pa (right).	130

5.4	Mass flow rate for a saw-tooth channel in terms of stage length L for $P_0 = 7451\text{Pa}$ (left) and $P_0 = 37255\text{Pa}$ (right).	130
5.5	Mass flow rate for a saw-tooth channel in terms of ΔT for $P_0 = 7451\text{Pa}$	131
5.6	Streamlines and temperature contours for a saw-tooth channel for various values of P_0	132
5.7	Temperature gradient along the inclined walls of a saw-tooth channel with $P_0 = 7451\text{Pa}$	133
5.8	Temperature gradient along the vertical walls of a saw-tooth channel with $P_0 = 7451\text{Pa}$	133
5.9	View of a pumping stage of a tapered Knudsen-type cascade pump with T_C and T_H denoting the cold and hot reservoir temperature, respectively.	134
5.10	Diverging (left) and converging (right) channels with inclination ratio $\alpha_{con} = \alpha_{div} = \alpha$	134
5.11	Pressure difference $\Delta P = P_{out} - P_{in}$ in terms of P_{in} for various values of α in a closed system with zero net mass flow rate and $H_m = 10\mu\text{m}$	135
5.12	Pressure diodicity coefficient E_P in terms of P_{in} for various values α in a closed system with zero net mass flow rate and $H_m = 10\mu\text{m}$	135
5.13	Pressure difference $\Delta P = P_{out} - P_{in}$ in terms of P_{in} for various values α in a closed system with zero net mass flow rate and $H_m = 20\mu\text{m}$	136
5.14	Pressure diodicity coefficient E_P in terms of P_{in} for various values of α in a closed system with zero net mass flow rate and $H_m = 20\mu\text{m}$	136
5.15	Mass flow rate \dot{m} in terms of P_{in} for $L/H_m = 20, 50$ with $H_m = 10\mu\text{m}$ and various values of α in an open system with zero pressure difference.	137
5.16	Mass diodicity coefficient $E_{\dot{m}}$ in terms of P_{in} for $L/H_m = 20, 50$ with $H_m = 10\mu\text{m}$ and various values of α in an open system with zero pressure difference.	138
5.17	Pressure and gas rarefaction parameter distributions along a converging channel with $L/H_m = 20, 50$, $H_m = 10\mu\text{m}$, $P_{in} = 10^3, 0.5 \times 10^5\text{Pa}$ and $\alpha = 2, 3, 4$ in an open system with zero pressure difference.	139
5.18	Pressure and gas rarefaction parameter distributions along a diverging channel with $L/H_m = 20, 50$, $H_m = 10\mu\text{m}$, $P_{in} = 10^3, 0.5 \times 10^5\text{Pa}$ and $\alpha = 2, 3, 4$ in an open system with zero pressure difference.	140
5.19	Pressure difference $\Delta P = P_{out} - P_{in}$ in terms of the mass flow rate \dot{m} in a converging channel with $L/H_m = 20, 50$, $H_m = 10\mu\text{m}$, $P_{in} = 10^3, 10^4, 10^5\text{Pa}$ and $\alpha = 2, 3, 4, 5, 6$	141

5.20	Pressure difference $\Delta P = P_{out} - P_{in}$ in terms of the mass flow rate \dot{m} in a diverging channel with $L/H_m = 20, 50, H_m = 10\mu\text{m}, P_{in} = 10^3, 10^4, 10^5\text{Pa}$ and $\alpha = 2, 3, 4, 5, 6$	142
5.21	Pressure diodicity coefficient for a given mass flow rate in terms of the mass flow rate with $L/H_m = 20, 50, H_m = 10\mu\text{m}, P_{in} = 10^3, 10^4, 10^5\text{Pa}$ and $\alpha = 2, 3, 4, 5, 6$	143
5.22	Typical cascade along with the temperature variation (red line).	144
5.23	Pressure difference ΔP in terms of the number of stages of multistage tapered channel assembly for various values of α and P_{in}	145
5.24	Pressure distribution along a multistage tapered channel assembly with $\alpha = 6$ for various values of P_{in}	146
5.25	View of a serpentine channel consisting of straight and curved segments (left) and a curved channel along with the median curve (dashed line) with the Cartesian and curvilinear coordinate systems (right).	147
5.26	An arch of $\pi/6$ radians of curved channels with different curvatures.	147
5.27	Pressure difference ΔP (left) and pressure ratio R_p (right) for straight and curved channels with $L_C/D = L_S/D = 20$ in terms of inlet pressure.	148
5.28	Pressure difference ΔP (left) and pressure ratio R_p (right) for straight channel with $L_S/D = 20$ and curved channels with $L_C/D = \pi/\kappa$, in terms of inlet pressure.	148
5.29	Mass flow rate \dot{m} (left) and mass flow rate ratio $R_{\dot{m}}$ (right) for straight and curved channels with $L_C/D = L_S/D = 20$ in terms of inlet pressure.	149
5.30	Mass flow rate \dot{m} (left) and mass flow rate ratio $R_{\dot{m}}$ (right) for straight channel with $L_S/D = 20$ and curved channels with $L_C/D = \pi/\kappa$, in terms of inlet pressure.	149
6.1	View of the non-isothermal wall enclosure and flow pattern with (a) Vortex-type I and (b) with Vortex-types I and II	192
6.2	Streamlines and temperature contours in a square enclosure for $T_C/T_H = 0.1$ and various Kn_0	193
6.3	Streamlines and temperature contours in a square enclosure for various Kn_0 and T_C/T_H	194

6.4	Distributions of the (a) y and (b) x components of the velocity on vertical and horizontal planes respectively, passing through the centers of the two Vortex-type I for a square enclosure with $T_C/T_H = 0.1$ and Kn_0	195
6.5	Streamlines and temperature contours in rectangular enclosures of (a) $H/W = 0.5$ and (b) $H/W = 2$, for $T_C/T_H = 0.1$ and $Kn_0 = 1$	195
6.6	Streamlines and temperature contours in a square enclosure with (a) $Kn_0 = 0.1$ and (b) $Kn_0 = 1$ for Maxwell molecules ($\omega = 1$).	196
6.7	Tangential velocity u_y along the lateral walls of a square enclosure for $T_C/T_H = 0.1$ and various Kn_0 computed by the present kinetic approach and by Eq. (6.51) based on the R13 approach.	196
6.8	Distributions of the tangential (a) velocity u_y and (b) heat flux q_y along the lateral walls of rectangular enclosures with various aspect ratios for $T_C/T_H = 0.1$ and $Kn_0 = 1$	197
6.9	Streamlines and vertical velocity contours of the ballistic and collision parts as well as of the overall solution in a square enclosure for $Kn_0 = 0.05, 2$, with $T_C/T_H = 0.1$	198
6.10	Tangential velocity and density of the ballistic and collision parts as well as of the overall solution along the lateral walls of a square enclosure for $Kn_0 = 0.05, 2$ with $T_C/T_H = 0.1$	199
6.11	View of the square microcavity with the flow pattern of vortices I and II.	200
6.12	Streamlines and temperature contours for $T_C/T_H = 0.1$ (left) and $T_C/T_H = 0.9$ (right) and various Kn_0	201
6.13	Streamlines and temperature contours for $Kn_0 = 1$ and $T_C/T_H = 0.1$ obtained by the DSMC method.	202
6.14	Temperature distribution along the axis $x = 0$ for various Kn_0 and T_C/T_H obtained by the DSMC method (open symbols) and the Shakhov kinetic model (filled symbols).	202
6.15	Distribution of the tangential velocity $u_y (\pm 1/2, y)$ along the lateral walls of the cavity for various T_C/T_H and Kn_0	203
6.16	Typical contours of the Mach number in the flow field for $Kn_0 = 1$ and $T_C/T_H = 0.1, 0.9$	204
6.17	Average heat flux q_{ave} departing from the hot plate of the cavity in terms of Kn_0 for various T_C/T_H	204

6.18	Average heat flux q_{ave} departing from the hot plate of the cavity in terms of T_C/T_H for various Kn_0	205
6.19	Average heat flux q_{ave} along with its ballistic and collision parts $q_{ave}^{(b)}$ and $q_{ave}^{(c)}$, respectively, departing from the hot plate of the cavity in terms of T_C/T_H for $Kn_0 = 0.1, 1, 10$	206
6.20	Average heat flux Q_{ave} (W/m^2) departing from the hot plate of the cavity in terms of the reference pressure P_0 for various T_C/T_H	207
6.21	Ballistic, collision, and overall reduced flow rates in terms of δ for (a) channel flow, (b) duct flow ($H/W = 0.1$), (c) duct flow ($H/W = 1$), and (d) tube flow.	208
6.22	Derivatives with respect to δ of the ballistic, collision, and overall reduced flow rates in terms of δ for (a) channel flow, (b) duct flow ($H/W = 0.1$), (c) duct flow ($H/W = 1$), and (d) tube flow.	209
6.23	Velocity (left) and number density (right) distributions for channel flow and various values of δ	210
7.1	Relative uncertainty of G_P in terms of δ for uncertainty in δ (left) and α (right) for $\alpha_n = 1$	234
7.2	Relative uncertainty of G_T in terms of δ for uncertainty in δ (left) and α (right) for $\alpha_n = 1$	234
7.3	Relative uncertainty of mass flow rate in the Poiseuille flow, in terms of δ_{in} for relative uncertainty of each input parameter equal to 0.1%, 1%, 2% and 5%.	235
7.4	Relative uncertainty of mass flow rate in the Poiseuille flow, in terms of δ_{in} for various values $u(P)/P$ and $P_{out,n}/P_{in,n} = 0.3, 0.5, 0.7$ and 0.9	236
7.5	Relative uncertainty of mass flow rate in the Poiseuille flow, in terms of δ_{in} for various values $u(\alpha)/\alpha$ and $\alpha_n = 0.7, 0.8, 0.9$ and 1	237
7.6	Relative uncertainty of the pressure difference in the thermomolecular pressure difference case, in terms of δ_{in} for relative uncertainty of each input parameter equal to 0.1%, 1%, 2% and 5%.	238
7.7	Relative uncertainty of the pressure difference in the thermomolecular pressure difference case, in terms of δ_{in} for various values $u(T)/T$ and $T_{h,n}/T_{c,n} = 1.2, 1.3, 1.5$ and 2	239

7.8	Relative uncertainty of mass flow rate in the thermal creep flow, in terms of δ_{in} for relative uncertainty of each input parameter equal to 0.1%, 1%, 2% and 5%.	240
7.9	Relative uncertainty of mass flow rate in the thermal creep flow, in terms of δ_{in} for various values $u(T)/T$ and $T_{H,n}/T_{C,n} = 1.2, 1.3, 1.5$ and 2. .	241
7.10	Relative uncertainty of heat flux in terms of δ for relative uncertainty of each input parameter equal to 0.1%, 1%, 2% and 5%.	242
7.11	Relative uncertainty of heat flux in terms of δ for various values $u(T)/T$ and $T_{C,n}/T_{H,n} = 0.3, 0.5, 0.7$ and 0.9.	243
C.1	Density (left) and temperature (right) distributions, at various cross sections along a converging channel with $\alpha = 4$ for $\delta = 0.1, 1, 20$	294
C.2	Density (left) and temperature (right) distributions, at various cross sections along a diverging channel with $\alpha = 4$ for $\delta = 0.1, 1, 20$	295

List of Tables

3.1	Mass flow rate for various values of the reference Knudsen number Kn_0 and of the external force \overline{F}	51
3.2	Heat flow rate for various values of the reference Knudsen number Kn_0 and of the external force \overline{F}	51
3.3	Reduced flow rate for various values of the reference rarefaction parameter δ_0 and external force \overline{F} , for the force driven nonlinear Poiseuille flow and the infinite capillary theory.	51
3.4	Dimensionless flow rate for channel and tube flows based on the typical formulation.	52
3.5	Relative (%) difference (error) of the flow rates between the typical and the implicit boundary formulations for channel and tube flows	53
3.6	Relative (%) difference (error) of the flow rates between the typical and the implicit boundary plus the end effect correction formulations for the channel and tube flows.	54
3.7	Relative (%) difference (error) of the flow rates between the typical and the infinite capillary plus the end effect correction formulations for the channel and tube flows.	55
4.1	Time (sec) required to find the marching node path by the backtracking (BTA) and geometrical (GM) schemes for various numbers of velocity polar angles and physical nodes	84
4.2	Flow rates G_P and G_T for various values of δ for flow through an elliptical tube.	84
4.3	Flow rate G_P for various values of δ and accommodation coefficient α for flow through a circular tube.	84
4.4	Flow rate M between the center of the vortex and the moving plate of a lid driven cavity for various values of δ	85

4.5	Drag coefficient D of the moving plate of a lid driven cavity for various values of δ	85
4.6	Location of the center of the vortex y_{loc} in a lid driven cavity for various values of δ	85
4.7	Heat flux departing from the bottom plate Q_{out} of a cavity with non-isothermal walls for $T_C/T_H = 0.1, 0.5, 0.9$ and $Kn_0 = 0.1, 1, 10$	85
5.1	Kinetic coefficient M_P in terms of δ and curvature κ for pressure driven flow through curved channels.	127
5.2	Kinetic coefficient M_T in terms of δ and curvature κ for temperature driven flow through curved channels.	128
6.1	Dimensionless flow rate of Vortex-type I in a square enclosure for various Kn_0 and T_C/T_H	188
6.2	Dimensionless flow rate of Vortex-type II in a square enclosure for various Kn_0 and T_C/T_H	188
6.3	Tangential velocity u_y along the lateral walls of a square enclosure for various Kn_0 and T_C/T_H	189
6.4	Lateral wall shear stress ($-p_{xy}$) at $x = -0.5$ of a square enclosure for various Kn_0 and T_C/T_H	189
6.5	Lateral wall heat flux q_y at $x = -0.5$ of a square enclosure for various Kn_0 and T_C/T_H	190
6.6	Average heat flux q_{av} departing from the bottom plate of a square enclosure for various Kn_0 and T_C/T_H	190
6.7	Maximum value of the Mach number in the field for various Kn_0 and T_C/T_H	190
6.8	Values of δ_{min} for flows through long capillaries of various cross sections.	191
6.9	Dimensionless average wall shear stress along with the ballistic and collision parts for the channel and tube flows in terms of δ	191
7.1	Kinetic coefficient G_P in terms of the rarefaction parameter δ and accommodation coefficient α for pressure driven flow in a plane channel.	230
7.2	Kinetic coefficient G_T in terms of the rarefaction parameter δ and accommodation coefficient α for temperature driven flow in a plane channel.	231

7.3	Heat flux in terms of temperature ratio T_C/T_H and rarefaction parameter δ for $\alpha=0.1, 0.3, 0.5$ for heat transfer between parallel plates.	232
7.4	Heat flux in terms of temperature ratio T_C/T_H and rarefaction parameter δ for $\alpha=0.7, 0.8, 0.9$ for heat transfer between parallel plates.	233
8.1	Reduced flow rate, number of iterations and computational time in seconds for the Non-Accelerated (NA), Full-Range Acceleration (FRA) and Half-Range Acceleration (HRA) schemes (Poiseuille flow).	266
8.2	Number of iterations required by the (NA) and (FRA) and the respective values when the boundary condition parameters are given (NA*) and (FRA*) (heat transfer)	266
8.3	Reduced flow rate, number of iterations and computational time in seconds for the Non-Accelerated (NA), Full-Range Acceleration (FRA) and Half-Range Acceleration (HRA) schemes (Poiseuille flow).	266
8.4	Flow rate for the Non Accelerated (NA), Full-Range Moment Method (FRMM) and Half-Range Moment Method (HRMM) (Poiseuille flow). .	267
8.5	Heat flux for the Non Accelerated (NA) and Half-Range Moment Method (HRMM) (heat transfer).	267
C.1	Pressure difference and pressure diodicity coefficient (E_P) for the closed configuration ($\dot{m} = 0$).	293
C.2	Mass flow rate (kg/m/s) and mass diodicity coefficient $E_{\dot{m}}$ for the open configuration ($\Delta P = 0$)	293
D.1	Kinetic coefficients G_P and G_T in terms of the gas rarefaction parameter δ for pressure and temperature driven flows through a plane channel. .	298
E.1	Coefficients $a_{n,i}^+$ and $a_{n,i}^-$ for up to 4^{th} order.	299
E.2	Coefficients $\beta_{n,i}^+$ and $\beta_{n,i}^-$ for up to 4^{th} order.	300
E.3	Coefficients g^\pm and s^\pm for Poiseuille flow.	300
E.4	Coefficients $p^{\pm\pm}$ for Poiseuille flow.	300
E.5	Coefficients g^\pm and f^\pm for heat transfer between parallel plates.	301
E.6	Coefficients $q^{\pm\pm}$ for heat transfer between parallel plates.	301
E.7	Coefficients $p^{\pm\pm}$ for heat transfer between parallel plates.	302
E.8	Coefficients $r^{\pm\pm}$ for heat transfer between parallel plates.	302
E.9	Coefficients $s^{\pm\pm}$ for heat transfer between parallel plates.	303
E.10	Coefficients v^\pm for heat transfer between parallel plates.	303

E.11 Coefficients w^\pm and z^\pm for heat transfer between parallel plates.	303
--	-----

Chapter 1

Introduction

1.1 General concepts

The computational investigation of transport phenomena in gasses is one of the most interesting and challenging fields in engineering and physics. The macroscopic description provided by the Navier-Stokes-Fourier equations has proven to be a valid approach, able to handle the majority of physical phenomena. However, there are a significant number of applications, where the assumptions behind this macroscopic model collapse and a more fundamental modeling approach is required. This is happening when the molecular mean free path, i.e., the average distance that gas molecules travel between successive intermolecular collisions, becomes comparable with a characteristic length scale of the flow. Then, the gas is in a rarefied state and the continuum assumption along with the constitutive laws of Newton, Fourier and Fick are no longer valid. Proper modeling in these cases should take into account the molecular nature of gasses and such an approach is the well-known kinetic theory of gasses. Simulations using kinetic theory are constantly gaining attention in recent years, because kinetic modeling may be successfully applied in emerging technological fields, which cannot be treated by other approaches. In parallel, the high computational cost (time and storage), which is typically required in mesoscale approaches, such as kinetic modeling, is constantly decreased due to the advancements in scientific computing both in software and hardware resources.

Gas flows and heat transfer in rarefied conditions may occur in low density systems, where intermolecular collisions are rare, or in micro and nano scale systems, where the characteristic lengths are very small or in setups with both low densities and small sizes. In addition, rarefied flows or otherwise flows far from local equilibrium may be

present in thin layers adjacent to the boundaries or characterized by steep gradients of the macroscopic quantities such as in Knudsen layers and shock waves respectively. High altitude aerodynamics and reentry flows [1], [2] are typical examples of such flows, where due to the high speeds many interesting non-equilibrium phenomena arise [3], [4]. Similarly, flows under rough, moderate, high and ultra-high vacuum, are also considered as rarefied flows and are encountered in many applications, from vacuum packed MEMS devices [5], or thermally driven micro-pumps [6], to large scale gas distribution networks [7] that are involved in the vacuum systems of fusion reactors [8] and accelerators. Vacuum pumps and pumping is one the major technological fields, where kinetic theory and modeling is implemented [9]–[11]. Also, the design and uncertainty analysis performed in pressure sensors and flow meters [12] used in metrology devices and standards [13] are based on measurements supplemented by accurate kinetic simulations. Furthermore, rarefied gas flows appear in semiconductors, filtering, porous media, vapor and chemical deposition processes, etc.

In general, kinetic theory and modeling has been proven to be a reliable approach to tackle physical phenomena far from local equilibrium, while the availability and the constantly reduced cost of high computing resources observed worldwide, has provided new possibilities and potential. Recently, there is an increasing need for more demanding and advanced kinetic simulations in order to properly capture complex microscale phenomena in complicated geometries very close or identical to the actual ones.

The present dissertation is focused on the derivation of advanced kinetic modeling and software as well as in the implementation of these tools to simulate non-equilibrium gaseous transport phenomena. More specifically,

- a) certain advancements in deterministic and stochastic kinetic modeling are proposed,
- b) new physical findings in the field of rarefied gas dynamics and heat transfer are presented and
- c) novel microscale devices are simulated and optimized.

1.2 Dissertation structure and contents

The present dissertation handles a number of diverse topics related to kinetic theory and modeling. These topics include new numerical schemes, which are proposed in order to improve and extend the capabilities of the existing ones, the computational solution of some physical problems, which have not been solved so far and the simulation of

some configurations, which may be used in the design of micro devices. Following Chapters 1 and 2, where a brief introduction in the field and a survey of the relative literature are presented respectively, each of the investigated topics is covered in a separate chapter of the dissertation from Chapter 3 to 8 and finally, in Chapter 9 the dissertation is concluding with a brief summary and the main concluding remarks. In Chapters 3-8, where each of the investigated topics are presented, there is some repetition, mainly related to the formulation of each problem, which is considered as necessary for completeness and clarity purposes and beneficial to the reader. Next, the detailed structure of the thesis is presented.

Chapter 1 includes a short introduction in the field highlighting the main research areas of the present work, a brief description of the contents and a summary of the main novelties and contributions of the thesis.

Chapter 2 covers a detailed literature survey related to the various areas of kinetic theory and modeling covered in the present work. The review includes the basic principles of kinetic theory, the involved flow regimes, the governing kinetic model equations with the associated boundary conditions, as well as the implemented deterministic and stochastic computational methods. In addition, specific attention is paid to pressure and temperature driven flows, which are present throughout the thesis and also to methodologies related to propagation of uncertainties.

Chapter 3 refers to two pressure driven rarefied gas flows. The first one is nonlinear fully-developed flow between parallel plates with the external force term driving the flow included in the governing equations. A new methodology based on the method of characteristics is implemented to compute the flow rate and the heat flux paying specific attention to the distribution function, which is characterized by multiple modes and long tails. The second one is typical nonlinear pressure drive flow between plates and through tubes. The range of validity of validity of the so-called implicit boundary conditions is investigated in terms of the gas rarefaction parameter, the imposed pressure difference and the capillary length by comparing this approach with others having a more solid theoretical background.

Chapter 4 presents the implementation of the discrete velocity method (DVM) on unstructured grids. The proposed novel methodology keeps the marching characteristics of the typical implementation of the discrete velocity schemes on structured grids and yields the solution of the problem without requiring the solution of a system of algebraic equations. The developed unstructured DVM algorithm is validated by solving fully

developed flows through long channels with cross sections of fractal geometries, as well as linear lid driven and nonlinear temperature driven cavity flows.

Chapter 5 refers to thermally driven flows with application to the design of micropumps without rotating parts. The considered configurations include saw-tooth surface channels, tapered channels with diverging and converging parts and curved serpentine type channels. A detailed parametric investigation is performed in terms of the geometry, the operating conditions and the number of stages. The simulation of the saw-tooth surface channels is based on the unstructured grid approach presented in Chapter 4. The diode effect in the case of tapered channels is investigated in detail. The advantages and drawbacks of each design are considered and discussed, indicating the pumping performance of each flow configuration.

Chapter 6 describes, in detail, a novel decomposition technique of the Direct Simulation Monte Carlo (DSMC) method. The particle distribution function is decomposed into ballistic and collision parts. The first one includes particles arriving directly from the boundaries without interacting with other particles and the latter one particles arriving after an arbitrary number of collisions. The decomposition technique is implemented to cavity flows driven by non-uniform temperature distributions in the lateral walls and by a heat flux in the bottom wall, as well as to the classical Poiseuille flow in capillaries. In all cases, based on the decomposition of the distribution function, very interesting physical findings of the observed non-equilibrium transport phenomena, including the famous Knudsen minimum, are interpreted.

Chapter 7 examines the propagation of uncertainties, which may be present in the input data through the numerical solution to the computed results of the thermo-fluid setup. The introduced uncertainties may be due to measurements defining the geometrical data and operational conditions, as well as due to modeling assumptions and simplifications. The proposed approach is based on the Monte Carlo Method (MCM), which is considered as the most suitable for the present work and relies on a large number of trials. The total uncertainty of fully-developed pressure and temperature driven flows, including the thermomolecular pressure difference phenomenon, as well as of the heat transfer flow between parallel plates are obtained. In each case the most important input parameters, the uncertainty of which, mostly affect the total uncertainty of the results, are identified.

Chapter 8 deals with synthetic acceleration schemes of the DVM iteration map. An extension of the existing synthetic algorithms is provided to speed-up the slow convergence of the classical iteration scheme in the slip and continuum regimes, even in

flow configurations where the boundary incoming distributions are not explicitly given but they are part of the solution. This is achieved by coupling the kinetic equations with half-range moments of the distribution functions resulting to the acceleration of the convergence of the macroscopic quantities even at the boundary nodes. This new acceleration strategy is validated by solving the one-dimensional Poiseuille flow and then, it is successfully implemented to the solution of the heat transfer flow between parallel plates.

Chapter 9 concludes the dissertation by providing a brief summary of the work included in Chapters 3-8 pointing out the main theoretical and computational observations and findings. Also, tentative extensions of the present work in the short future are proposed.

1.3 Novelty and scientific contributions

The novelties of the present dissertation include both theoretical and computational scientific contributions. They may be briefly highlighted as follows:

- a) Development and implementation of a computational methodology solving kinetic equations with external force terms, based on the method of characteristics, in order to model complicated rarefied gas flows of charged particles in the presence of electric and magnetic fields (Chapter 3).
- b) Specification of the range of validity of the so-called implicit boundary conditions in rarefied gas flows in terms of the geometrical and operational parameters in order to support decision making about their proper implementation in an effort to reduce computational resources (Chapter 3).
- c) Development and implementation of a computationally efficient DVM algorithm on unstructured meshes, capable to simulate complex geometries with boundary fitted grids (Chapter 4).
- d) Detailed parametric investigation of the thermal transpiration pumping performance in various geometrical configurations to provide useful guidelines in the design, optimization and fabrication of micro Knudsen type pumps (Chapter 5).
- e) Physical explanation and quantitative justification of unexpected non-equilibrium transport phenomena appearing in boundary heated cavities, based on the

decomposition of the DSMC computational particles into ballistic and collision particles (Chapter 6).

- f) Physical explanation and quantitative justification of the presence of the famous Knudsen minimum in rarefied gas flows, based on the DSMC decomposition (Chapter 6).
- g) Development and implementation of a computational methodology estimating the total uncertainty of the output quantities, based on the input uncertainties of the geometrical and operational data, as well as of the modeling assumptions and errors, via a large number of MC trials (Chapter 7).
- h) Development and implementation of a generalized accelerated DVM solver, coupling the kinetic equations with half-range moments, to speed up the slow convergence of the iteration map not only for fully-developed flows but also for a much wider class of linear problems, where the incoming distributions at the boundaries are part of the solution (Chapter 8).

Chapter 2

Literature review

2.1 Brief historical overview and fundamental principles of kinetic theory

The nature of matter itself has been a topic of long debates and arguments among philosophers and scientists since ancient times. Although philosophers as Leucippus, Democritus and Epicurus [14] had speculated that matter consists of tiny indivisible parts, before 1900 classical Newtonian mechanics considering matter as a continuum, was the prototype of a successful physical theory. In contrast to this view were Maxwell and Boltzmann, considering matter as composed of small tiny bits of matter with empty spaces between them [15]. As time and science advanced these two approaches were able to produce similar results and explain observations, as well as to generate interesting paradoxes, which were understood by statistical arguments breaking the classical prejudice that fundamental laws of physics have to be strictly deterministic. In gasses, the kinetic theory, which is a part of statistical mechanics, has provided solid answers to many open topics [16].

Kinetic theory of gases was first originated in 1738, when Daniel Bernoulli stated in his book “Hydrodynamica” [17] that gasses consist of large amounts of molecules traveling in all directions, while pressure is the force applied by these molecules to a surface during collisions and heat is the kinetic energy of the traveling molecules. The next great advance in kinetic theory was made much later, in 1860 by Maxwell [18], who introduced the concept of the velocity distribution function $f(t, \mathbf{r}, \boldsymbol{\xi})$, indicating the probability of finding a molecule around the location \mathbf{r} , with velocity $\boldsymbol{\xi}$ at time t . The distribution function proposed by Maxwell, although corrected few years later by

Boltzmann, bears his name and it is known as the Maxwell (or Maxwell-Boltzmann) distribution function. It is given by

$$f^M(t, \mathbf{r}, \boldsymbol{\xi}) = n(t, \mathbf{r}) \left[\frac{m}{2\pi k_B T(t, \mathbf{r})} \right]^{3/2} \exp \left[-\frac{m(\boldsymbol{\xi} - \mathbf{u}(t, \mathbf{r}))^2}{2k_B T(t, \mathbf{r})} \right] \quad (2.1)$$

where n , T and \mathbf{u} denote the local density, temperature and velocity vector, m is the molecular mass and k_B is the Boltzmann constant. There is no doubt that Maxwell's work laid the road for a statistical description of gases, which was followed and well established by Boltzmann. Furthermore, Maxwell came very close in extracting a transport equation for the distribution function, which was finally derived by Boltzmann in 1870 [19]. The evolution equation of the distribution function is the well-celebrated Boltzmann equation and may be written as [20]

$$\frac{\partial f}{\partial t} + \boldsymbol{\xi} \cdot \frac{\partial f}{\partial \mathbf{x}} + \mathbf{F} \cdot \frac{\partial f}{\partial \boldsymbol{\xi}} = Q(f, f'). \quad (2.2)$$

In Eq. (2.2), the left hand side describes the evolution of the distribution function with time as the particles move in space according to their molecular velocities and as they are accelerated due to an external force field with acceleration \mathbf{F} . The intermolecular collisions are considered by the right hand side term, which is given in terms of the so-called collision integral

$$Q(f, f') = \int \int (f' f'_* - f f_*) g \sigma d\Omega d\boldsymbol{\xi}_* \quad (2.3)$$

where $g = |\boldsymbol{\xi} - \boldsymbol{\xi}_*|$ is the relative velocity, σ is the collision cross section and Ω is the solid angle within a molecule is deflected to after the collision [16], [20]. The collision integral calculates the effect of collisions on the distribution of particles with velocity $\boldsymbol{\xi}$, investigating possible collisions with particles having all other velocities $\boldsymbol{\xi}_*$. It consists of a gain and a loss terms. The first term in the parenthesis corresponds to the gain part and refers to particles that, after a collision, obtain a velocity around $\boldsymbol{\xi}$. The second term in the parenthesis corresponds to the loss part and refers to particles that had a velocity around $\boldsymbol{\xi}$ and after a collision they obtain a different velocity. The collision cross section σ and the differential solid angle $d\Omega$ are provided by a molecular interaction potential or model (e.g., Hard Sphere, Inverse Power Law, Maxwell, Variable Hard Sphere, Variable Soft Sphere, Generalized Hard Sphere and Generalized Soft Sphere) [20]. It is noted that the Maxwellian distribution is a solution

of the Boltzmann equation for a gas in equilibrium, i.e., when the first three terms at the left hand side of Eq. (2.2) vanish.

In the derivation of the Boltzmann equation, two main assumptions are made. The first one is that only binary collisions are assumed, limiting its application to dilute gases, where the distance between molecules is at least one order of magnitude larger than the molecular diameter. The second assumption is the so-call molecular chaos assumption or as called by Boltzmann the “Stosszahlansatz”, stating that the velocities of colliding molecules are uncorrelated.

The distribution function contains the information of the location and velocity of the particles and all macroscopic quantities can be expressed as moments of the distribution function as follows:

- Number density

$$n = \int f d\boldsymbol{\xi} \quad (2.4)$$

- Velocity vector

$$\mathbf{u} = \frac{1}{n} \int \boldsymbol{\xi} f d\boldsymbol{\xi} \quad (2.5)$$

- Pressure

$$P = \frac{m}{3} \int (\boldsymbol{\xi} - \mathbf{u})^2 f d\boldsymbol{\xi} \quad (2.6)$$

- Stress tensor

$$P_{ij} = m \int (\xi_i - u_i) (\xi_j - u_j) f d\boldsymbol{\xi} \quad (2.7)$$

- Temperature

$$T = \frac{m}{3k_B n} \int (\boldsymbol{\xi} - \mathbf{u})^2 f d\boldsymbol{\xi} \quad (2.8)$$

- Heat flux vector

$$\mathbf{q} = \frac{m}{2} \int (\boldsymbol{\xi} - \mathbf{u})^2 (\boldsymbol{\xi} - \mathbf{u}) f d\boldsymbol{\xi} \quad (2.9)$$

It can readily be seen that combining Eqs. (2.6) and (2.8) yields the ideal gas law

$$P = nk_B T. \quad (2.10)$$

Another very significant advancement made by Boltzmann is his famous *H*-Theorem, stating that the average value of the *H* function, defined as

$$H = \int f \log f d\boldsymbol{\xi}, \quad (2.11)$$

is a non-increasing function of time [16], [17]. The special case of $dH/dt = 0$ corresponds to the Maxwellian distribution. It is well known that this principle is directly related to the entropy increase and to the second law of thermodynamics. This inequality $dH/dt \leq 0$ shows the tendency of the gas to minimize the H function, that is to obtain the distribution with the highest number of microstates that correspond to the macroscopic state of the system, and this distribution is the Maxwellian distribution. This fact shows an inherent irreversibility of macroscopic processes, although the interaction itself between particles is time-reversible.

2.2 The Knudsen number and flow regimes

The mean free path, introduced by Clausius in 1738 [19], is the average distance that particles travel between successive collisions. For hard sphere molecules it is provided in a closed form expression as

$$\lambda = \frac{1}{\sqrt{2}\pi d^2 n}, \quad (2.12)$$

where d is the molecular diameter, or in terms of macroscopic quantities as

$$\lambda = \frac{\sqrt{\pi}}{2} \frac{\mu v_0}{P}, \quad (2.13)$$

where μ is the dynamic viscosity at temperature T , P is the pressure and v_0 is the most probable molecular speed defined as

$$v_0 = \sqrt{\frac{2k_B T}{m}}. \quad (2.14)$$

One of the most important parameters in the field of kinetic theory and rarefied gas dynamics, is the ratio of the mean free path λ over a characteristic length scale L , known as the Knudsen number [20]

$$Kn = \frac{\lambda}{L}. \quad (2.15)$$

In cases where the typical length scales are orders of magnitude larger than the mean free path, the Knudsen number is small and becomes important only in rarefied conditions (moderate and large mean free paths) or in very small dimensions (small

characteristic length scales). The characteristic length scale L may be a geometrical or a physical length scale defined as $L = \varphi / (\partial\varphi/\partial x)$, where φ is a macroscopic flow quantity. The latter definition of L is commonly used when stiff gradients of the macroscopic quantities, such as in shock waves, are present.

The Knudsen number can be written in terms of the Mach and Reynolds numbers as

$$Kn = \sqrt{\frac{\gamma\pi}{2}} \frac{Ma}{Re}. \quad (2.16)$$

where γ is the ratio of the specific heats of the gas ($\gamma = 5/3$ for a monatomic gas). A quantity frequently utilized, instead of the Knudsen number, is the gas rarefaction parameter [23]

$$\delta = \frac{LP}{\mu v_0}, \quad (2.17)$$

which is related to the Knudsen number through

$$\delta = \frac{\sqrt{\pi}}{2Kn}. \quad (2.18)$$

The definition of the gas rarefaction parameter does not involve the mean free path, which is not readily defined and it is based on an equivalent mean free path, which may be estimated from measurable macroscopic quantities and therefore, it is commonly used, instead of the Knudsen number, to define the degree of gas rarefaction.

In terms of the Knudsen number or the gas rarefaction parameter, the following flow regimes can be distinguished [24]:

- $Kn \leq 10^{-3}$ ($\delta \geq 10^{-3}$): The gas is in the hydrodynamic regime. The gas is considered as a continuum media and deviations from the local equilibrium distribution are small. Modeling with typical CFD is valid.
- $10^{-3} < Kn \leq 10^{-1}$ ($10 < \delta < 10^3$): The gas is in the slip regime. Gas rarefaction effects start to manifest close to the boundaries. CFD modeling is still valid with the appropriate velocity slip and temperature jump boundary conditions.
- $10^{-1} < Kn < 10$ ($0.1 < \delta < 10$): The gas is in the transition regime. The effects of rarefaction are significant and the number of intermolecular collisions has been reduced. The constitutive equations used in CFD fail and a kinetic description is mandatory.

- $Kn > 10$ ($\delta \leq 0.1$): The gas is in the free molecular regime. The molecules undergo ballistic motion and intermolecular collisions are negligible.

It should be noted, that the limits of each flow regime defined above, depending on the flow setup, may slightly vary and therefore, they are commonly considered as indicative providing an order of magnitude estimation. Modeling based on kinetic theory is valid in the whole range of the Knudsen number. However, since kinetic modeling is computationally intensive compared to the CFD approaches, it is mainly used in the early slip, transition and free molecular regimes, as well as under non-equilibrium conditions, where the continuum approaches fail.

The hydrodynamic regime is dominated by intermolecular collisions and collisions between molecules and the wall boundaries. As the flow is entering in the slip regime the collisions of the molecules with the boundaries start to decrease. The Navier-Stokes-Fourier equations are still valid, while the no slip boundary conditions are not and therefore, the velocity slip and temperature jump boundary conditions are introduced [25]. In the transition regime, intermolecular collisions are also decreased, leading to particles traveling large distances between collisions. For this reason, the state of the flow field at some location is not only affected by its close neighborhood, but also from distant regions. This provides a clear physical explanation of the failure of the Navier-Stokes-Fourier equations, as they only consider local interaction. Researchers have tried to extend the range of application of the hydrodynamic equations, introducing the so-call high order hydrodynamic schemes, such as the Burnett and the super Burnett equations or the moments methods, such as the Grad moment method [26]. However, all these approaches are facing various problems including the definition of proper boundary conditions for the higher moments and in all cases are limited to some finite value of the Knudsen number. Over the years, kinetic theory and modeling, which are based on solid fundamental principles, have proven to be the most reliable modeling approach in the free molecular, transition and the early part of the slip regime.

2.3 Kinetic model equations and boundary conditions

In general, the computational solution of the Boltzmann equation is a formidable task and this is due to the five-fold collision integral, limiting significantly the potential of implementing kinetic modeling in engineering problems. In order to circumvent

this pitfall, relaxation models replacing the complicated collision integral have been proposed. The so-called kinetic models sacrifice some of the physics resolution for a greatly decreased computational load. A kinetic model is considered as acceptable, provided that it fulfills the main properties of the Boltzmann collision integral, i.e., it satisfies conservation of the collision invariants, fulfills the H -Theorem and provides correct transport coefficients. Unfortunately only few models satisfy all these conditions.

One of the first proposed models for monatomic gases is the BGK model [27], [28], that replaces the collision integral with the simple expression

$$Q = \nu (f^M - f), \quad (2.19)$$

where $\nu = P/\mu$ is the collision frequency, assumed to be the local pressure over viscosity. It is the simplest model and has been extensively used due to its unexpected effectiveness. The collision frequency is independent of the molecular velocity and the model assumes that particle velocities after one collision follow the local Maxwellian distribution. The BGK model has provided results very close to the corresponding ones obtained by the Boltzmann equation in the whole range of gas rarefaction [23]. However, it does not provide correct expressions for the viscosity and the thermal conductivity simultaneously (for an ideal monatomic gas the Prandlt number is one instead of 2/3) and therefore, it should not be used in configurations with coupled flow and heat transfer phenomena.

The Shakhov model [29] is a generalization of the BGK model and its collision term is given by

$$Q = \nu \left\{ f^M \left[1 + \frac{2(1 - \text{Pr})}{5} \frac{m}{n(k_B T)^2} \mathbf{q} \cdot (\boldsymbol{\xi} - \mathbf{u}) \left(\frac{m(\boldsymbol{\xi} - \mathbf{u})^2}{2k_B T} - \frac{5}{2} \right) \right] - f \right\}. \quad (2.20)$$

The Prandlt number is an input parameter and can be accordingly fixed. By setting $\text{Pr} = 1$, the BGK model is retrieved. The Shakhov model has proved to be a reliable approach in simulating pressure and thermally driven flows. However, since the gain term is a polynomial function of the molecular velocities and not purely exponential, as in the BGK model, it can provide negative values of the distribution function, which is obviously unphysical. In addition, there is no proof that satisfies the H -Theorem. Despite these drawbacks, it has been proven to be very reliable and accurate, providing physically justified results for the macroscopic quantities.

The BGK and Shakhov models are applied throughout the present dissertation. One model that has been derived in a similar manner as the BGK and Shakhov models and should be also mentioned is the Ellipsoidal-Statistical (ES) model [30]. The equilibrium distribution function for the ES model has an ellipsoidal base and it produces the correct Prandtl number, without however suffering the drawbacks of the Shakhov model. It is not implemented in this work because it is not considered as necessary for the investigated problems. The above mentioned models are constructed for single monatomic gases. Several other models have been proposed for polyatomic gases [30]–[37] and for gas mixtures [38]–[41].

The computational solution of the Boltzmann equation or of suitable kinetic model equations require the formulation of the associated boundary conditions, which in most cases are part of the solution. The main objective is to correlate the distribution of molecules (f^-) arriving to the boundary with the distribution of molecules (f^+) departing from the boundary. Denoting as \mathbf{n} the unit normal to the boundary vector with direction towards the flow field, a general expression for the boundary conditions can be written as [16]

$$f^+(\boldsymbol{\xi}) = - \int_{\boldsymbol{\xi}' \cdot \mathbf{n} < 0} \frac{\boldsymbol{\xi}' \cdot \mathbf{n}}{\boldsymbol{\xi} \cdot \mathbf{n}} W(\boldsymbol{\xi}' \rightarrow \boldsymbol{\xi}) f^-(\boldsymbol{\xi}') d\boldsymbol{\xi}'. \quad (2.21)$$

Here, $W(\boldsymbol{\xi}' \rightarrow \boldsymbol{\xi})$ is the scattering kernel, which presents the probability that a molecule arriving at the boundary with a velocity $\boldsymbol{\xi}'$ will depart from the boundary with a velocity $\boldsymbol{\xi}$.

The most extensively used boundary conditions are the ones by Maxwell, combining diffuse and specular reflection [42], [43]. In the diffuse reflection the gas molecules are assumed to follow a Maxwellian distribution with parameters the wall temperature T_W and velocity \mathbf{u}_W . The diffuse scattering kernel is given by

$$W_D(\boldsymbol{\xi}' \rightarrow \boldsymbol{\xi}) = \frac{1}{2\pi} \boldsymbol{\xi} \cdot \mathbf{n} \left(\frac{m}{k_B T_W} \right)^2 \exp \left[-\frac{m(\boldsymbol{\xi} - \mathbf{u}_W)^2}{2k_B T_W} \right]. \quad (2.22)$$

In the specular reflection only the velocity component normal to the wall is altered during a collision with the boundary and more specifically, its sign is changed, while its magnitude remains the same. The specular scattering kernel is given by

$$W_S(\boldsymbol{\xi}' \rightarrow \boldsymbol{\xi}) = \delta[\boldsymbol{\xi}' - \boldsymbol{\xi} + 2(\boldsymbol{\xi} \cdot \mathbf{n})\mathbf{n}]. \quad (2.23)$$

Combining the diffuse and specular scattering kernels, the so-called Maxwell (diffuse-specular) scattering kernel is obtained and may be written as

$$W_{DS}(\boldsymbol{\xi}' \rightarrow \boldsymbol{\xi}) = \alpha W_D(\boldsymbol{\xi}' \rightarrow \boldsymbol{\xi}) + (1 - \alpha) W_S(\boldsymbol{\xi}' \rightarrow \boldsymbol{\xi}), \quad (2.24)$$

where α and $(1 - \alpha)$ are the portions of molecules undergoing diffuse and specular reflection respectively. The quantity α is known as the tangential momentum accommodation coefficient.

In the present work the Maxwell diffuse-specular boundary conditions are applied. The scattering kernel in this type of boundary conditions, is independent of the molecule velocity magnitude and direction. The Epstein scattering kernel overcomes this drawback. However, it involves empirically chosen coefficients [44]. The Cercignani-Lampis scattering kernel [45] and its extensions introduced by Lord [46], [47], distinguish between the accommodation in the normal and tangential to the boundary directions and are able to consider back-scattering. Both the Epstein and the Cercignani-Lampis boundary conditions are physically superior to the Maxwellian boundary conditions but computationally more demanding and they are applied only for specific purposes. In general, the gas-surface interaction is a complicated task and its detailed investigation requires the involvement of molecular dynamics, as well as comparison with measurements [48]–[52].

2.4 Numerical methods

Several methods have been developed for the numerical solution of the Boltzmann equation and of the kinetic model equations [53], [54]. The most reliable and widely used ones are the discrete velocity and the direct simulation Monte Carlo methods. The first one is deterministic and the second one is stochastic or probabilistic. These are the two methods which are implemented and advanced in the present work and therefore, the literature survey is focused only on these two approaches.

The discrete velocity method (DVM) [53] is probably the most prevailing deterministic methodology for the solution of the Boltzmann or other kinetic equations. According to this method, the continuous molecular velocity space is discretized and a discrete set of molecular velocities is considered. The moments of the distribution function are accurately computed by numerical integration using the values of the distribution at the discrete velocity points.

By applying the DVM the kinetic integrodifferential equations are reduced to a system of differential equations, one for each discrete molecular velocity. These ordinary or partial differential equations are solved using finite element or finite volume approaches leading to large linear algebraic systems, which are solved using typical schemes. To avoid implementing time-consuming algebraic system solvers, the so-called marching schemes may be applied [55]. In these schemes, the solution propagates in the physical space in the direction of the molecular velocity by considering the nodes in the physical space in a particular order, which may differ for the different molecular velocities. For this reason these marching schemes have been limited so far to simple geometries, where the marching node sequence is easily obtained from the node indexing. In the present work this limitation is circumvented by introducing unstructured meshes and a methodology which still permits the marching approach through the mesh to be applied. The detailed description of the development and implementation of this methodology is presented in Chapter 4.

In most cases the source term driving the flow is in the boundary conditions and the kinetic equation is homogeneous. There are rarefied gas flows however, such as flows of charged particles in the presence of electric and magnetic fields, where the external force term must be included in the kinetic equation. The computational solution of kinetic equations with an external force term is not a trivial task because the source term includes a derivative of the distribution function with respect to the molecular velocity and its discretization is rather complicated. In [56], the external term is initially included in the kinetic equation but it is next eliminated using a projection procedure. An interesting approach is introduced in [57] for the lattice Boltzmann method, where the external force term is incorporated in the equilibrium distribution in the form of a sum of an infinite series. In the present work a numerical method, based on the method of characteristics, is developed and implemented to solve kinetic model equations with the force term included in the equation. This topic is covered in the first part of Chapter 3.

It is well known that the typical iteration map of the DVM exhibits a slow convergence rate in the slip and continuum regimes, limiting the application of kinetic theory to moderate and large values of the Knudsen number. In order to overcome this problem advanced synthetic iteration acceleration schemes have been developed and successfully applied in linearized kinetic model equations [58]–[60] and in the linearized Boltzmann equation [61] solving fully developed flows through capillaries. The speed-up of the convergence rate is achieved by coupling the kinetic equations with

a system of moment equations. Typically, these moment equations are constructed using full-range orthogonal polynomials, where the orthogonality conditions are defined in the whole range of the real numbers. However, these schemes accelerate the solution only in the interior spatial nodes and therefore, they are successfully applied only in fully developed flows, where there is no need to accelerate the quantities at the boundary nodes. In the present work a more generalized synthetic type acceleration approach is proposed, based on half-range polynomials. These acceleration schemes, considered in Chapter 8, are able to speed-up the iterative solution even in flows where the boundary conditions are part of the solution.

In the field of rarefied gas dynamics, particle methods and more specifically, stochastic or probabilistic ones, have received great attention, with the most prevailing one being the Direct Simulation Monte Carlo (DSMC) method. It was introduced by Bird [62] and early contributions were made by Belotserkovsky and Yanitsky [63]–[65]. The DSMC method was initially utilized for high altitude aerodynamics and re-entry flows. In this method, the large number of real particles is represented by a number of discrete simulation particles and their evolution in time is considered in discrete time steps. The free motion and collision of particles is decomposed at each time step, with the free motion treated in a determinist manner and the collisions in a stochastic manner. All macroscopic quantities are taken as sums of the microscopic properties of the simulation particles. It has been proven, that as the number of computational particles is increased, this method tends to the solution of the Boltzmann equation [66]. In Chapter 6, a solution decomposition technique is introduced to the DSMC method, in order to provide a physical insight and explanation in some interesting non-equilibrium phenomena arising in rarefied gas flows, which have not been resolved.

2.5 Pressure and temperature driven flows

Rarefied gas flows through capillaries of arbitrary length driven by pressure and/or temperature gradients are repeatedly considered in the present dissertation either as prototype flows in order to benchmark, verify and demonstrate the validity and effectiveness of introduced numerical schemes or either to investigate physical phenomena and to simulate microscale devices. Over the years, both flow configurations have been extensively explored resulting to a huge number of references, and therefore, the presented literature survey is mostly focused on research work related to the present

developments. The pressure driven flows are covered first, followed by the temperature driven ones.

Pressure driven flows through capillaries of arbitrary length, in the whole range of gas rarefaction are encountered in a number of technological fields, from small scale devices in microfluidics [67], [68] up to large gas distribution systems operated under vacuum conditions [7], [69]–[71] in fusion reactors and accelerators. Several researchers have worked on this topic, both numerically and experimentally. In terms of numerical calculations, both deterministic [23], [72]–[79] and stochastic approaches [80]–[82] have been used to obtain the flow rate in terms of the involved parameters.

When the capillary is sufficiently long and the flow can be considered as fully developed, the infinite capillary theory [23] may be applied. It is computationally the most efficient approach yielding the so-called dimensionless kinetic coefficients, which depend only on the local rarefaction parameter, the accommodation coefficient and the cross section geometry. The kinetic coefficients have been calculated in the whole range of the Knudsen number for a number of different cross-sections and they are used in order to recover the mass flow rate and the pressure distribution along the capillary by solving an ordinary differential equation derived from mass conservation principals [23].

The infinite capillary theory may be also implemented to capillaries of moderate length by introducing the so-called end effect correction [83]–[85]. According to the end effect theory, the length of the capillary is corrected to some equivalent length to take into account the inlet and outlet effects. The length increments depend on the cross-section geometry and the local gas rarefaction parameter, while they are independent of the capillary length, which makes this approach very useful.

When the capillary length is further reduced, then modeling should be based on the non-linear kinetic equations or the DSMC method. Efficiently large regions upstream and downstream of the capillary should be included in the computational domain to properly recover the flow properties and characteristics. The size of these regions is about one to two orders of magnitude larger than the capillary length [72], [86] in order to correctly imply inlet Maxwellian distributions at the open boundaries, These Maxwellians are given in terms of the local temperature and pressure (or density) with zero bulk velocity (the gas is assumed to be at rest adequately far from the capillary ends). The proper implementation of the inlet conditions at the open boundaries drastically increases the computational domain and the corresponding computational effort.

Recently, the so-called implicit boundary conditions have been proposed in [87]–[91], providing expressions for the distributions directly at the capillary inlet and outlet in terms of the local values of the macroscopic quantities and the corresponding imposed pressure and temperature. It is evident that the computational effort is drastically decreased, as the vessels upstream and downstream of the channel are eliminated. Although the implicit boundary conditions have been applied in flows well into the transition regime [87]–[90], their accuracy has only been investigated, so far, in the slip regime [90], [92]. Moreover, their formulation is based on the characteristic form of the Euler equations and the validity of the assumptions made is questionable. For this reason, a systematic investigation of the range of validity of the implicit boundary conditions is performed in the second part of Chapter 3.

Temperature driven gas flows in the rarefied regime can be induced even in the absence of gravity. A thorough description of the various types of thermal flows can be found in [93]. Here, a relatively short survey on thermal creep and thermal stress slip flows, as well as on thermally driven micropumps is discussed since these topics are all covered in the present work.

Thermal creep is one of the cross effects arising in non-equilibrium flows and it is due to the momentum transfer observed in the presence of a temperature gradient. When a temperature gradient is imposed along a boundary, momentum is transferred to the gas in a direction opposite to that of the temperature gradient, leading to a flow from cold-to-hot. It is more easily observed in the absence of gravity, or when gravitational forces are negligible (e.g. in rarefied flows), while in the continuum regime it still exists but it becomes of secondary importance due to other more prevailing effects.

The underlying mechanism that results to thermal creep flow is the following [93]. Assume a boundary with a temperature gradient and a differential area of this boundary. Particles arriving to this wall area from the hot side have large thermal velocities and after colliding with the surface their energy and consequently their thermal velocity is decreased. On the contrary, particles arriving from the cold side are accelerated and their energy is increased. Thus the molecules arriving to the boundary, exert a net force to the boundary from hot-to-cold and simultaneously, the boundary acts on them with a force from cold-to-hot. In the case of diffuse reflection on a stationary boundary, the outgoing particles have no net momentum in the tangential direction. It is concluded that a net momentum transfer from cold-to-hot is generated near a boundary with a temperature gradient.

Another type of thermally driven flow, considered here, is the thermal stress slip flow [93]–[95]. When the temperature gradient of the gas, normal to the wall is not uniform, the temperature isothermal is not parallel to the boundary and thermal stress flow is induced. More specifically, when the temperature of the boundary is higher than that of the adjacent gas, the flow is in the direction that the isothermal lines are converging and in the opposite direction when the temperature of the boundary is lower [96], [97]. Consider a differential element of the gas. The integral of the thermal stress along the element boundaries vanishes and the gas is stationary, while if one side of the element coincides with the boundary, then the balance is broken and a flow is induced. A thorough explanation is provided in [93].

The Crooke's radiometer presented in 1875 [98] was one of the first devices where such flows were observed and for many years the nature of these flows was a topic of scientific debate [99], [100]. Recently, temperature driven flows have been brought again in the attention of the scientific community mainly due to the design of temperature driven micro-pumps or micro-compressors. The main idea was introduced by Knudsen [101], [102]. A cold and a hot reservoir are connected by a straight and constant cross section tube with a temperature gradient along the wall and a thermal creep flow is generated without imposing any external pressure gradients. Alternative designs utilizing other phenomena, such as the thermal edge flow [103] and the thermal stress slip flow [104] have been also proposed.

One of the main obstacles of the original design is the fact that the pump performance, which is directly linked to the temperature gradient, is limited by the temperature that materials can withstand. In order to overcome this problem, multi-stage cascade-type designs with periodic temperature gradients have been introduced [105], [106]. In these designs, each stage consists of two elements having opposite temperature gradients. One is in the desired flow direction and the other one in the opposite direction, providing however, a net effect in the desired direction. The undesirable backflow may be reduced in various ways and several designs, such as curved channels [107]–[110] or capillaries with changing cross section areas [111], [112] have been proposed. However, mainly due to micro manufacturing constraints, only recently, prototypes have been manufactured and tested with considerable success [6], [113], [114]. In Chapter 5 an alternative design for the limitation of the backflow is investigated by utilizing the diode effect created by the combination of diverging and converging channels.

2.6 Uncertainty propagation

Uncertainties are very common in experimental work due to various sources including the uncertainty of the measurement instruments, the changing environmental conditions, the flaws in the experimental setup, the definition of the measured quantity which may involve certain approximations and therefore variations may be observed in repeated measurements. Obviously, the introduced uncertainties reflect to the output experimental results which are usually reported with the associated total uncertainties. In addition, the detailed investigation of the effect that the introduced uncertainties may have to the main measured quantities of interest may be very important in the proper design of an experimental setup [115]–[117]. More specifically, this study will clarify if an acceptable level of uncertainty is achieved and furthermore, it will indicate the preferable conditions or corrected actions which must be taken in order to more clearly observe the measured quantities. Uncertainties are also present in the input data, parameters and models used in simulations and they certainly propagate through the computational process to the final output quantities.

Several methodologies have been developed for the uncertainty propagation [118], [119]. The most well-known ones include the interval analysis [120], the sensitivity derivatives [121], the moment methods [122], the polynomial chaos [123] and the Monte Carlo (MC) method [124]. Each one has its own benefits and drawbacks. The interval analysis is easily implemented but is not very accurate, while the sensitivity derivatives approach is accurate but not general enough. The moment methods are computationally efficient, but they are limited to small input uncertainties and cannot be applied when significant nonlinearities exist. The polynomial chaos method is, in general, quite complicated to implement. Finally, the Monte Carlo method is computationally demanding, providing however very accurate results without any assumptions. It is widely used when the needed computer resources are available. According to the MC method, a large number of trials is conducted, sampling the values of the input quantities from their respective distributions and calculating the quantity whose uncertainty is being extracted. Upon completing the large number of trials, the distribution function of the quantity of interest is reconstructed and the uncertainty is calculated from the constructed distribution.

Uncertainty propagation is important in many engineering fields. In metrology, uncertainty is one of the main quantities of interest [13] since many times the accuracy required is far beyond the one in typical applications [125]. Recently, the calculation of

the uncertainty of the involved quantities has been reported in computational fluid dynamics studies [123], [126], [127] and in some cases in rarefied gas dynamics simulations [128]–[130]. In Chapter 7, the MC method is used to introduce a methodology finding the uncertainty of the main quantity of interest in terms of the input uncertainties in rarefied gas flows.

Chapter 3

Pressure driven rarefied gas flows through capillaries

3.1 Introduction

Pressure driven rarefied gas flows through capillaries in the whole range of the Knudsen number are very common in various technological fields [68], [131], [7], [69]–[71] and several simulation methodologies, depending on the capillary length, have been developed. In linear fully developed flows, the computationally efficient infinite capillary theory [23] is implemented. In capillaries of moderate length, the end effect methodology may be introduced [83]–[85] to successfully extend the range of validity of the infinite capillary theory. In short capillaries as well as nonlinear flows the infinity capillary theory even coupled with the end effect methodology fails and modeling is based on nonlinear kinetic model equations [72]–[78], [86] or on the DSMC method [80]–[82]. The computational domain must include the capillary along with inlet and outlet regions in order to properly impose at the kinetic level the incoming distributions at the open boundaries. The two added computational domains, which are one to two orders of magnitude larger than the volume of the capillary, yields very computationally intensive simulations [72], [73], [82], [86], [74]–[81], which are required however, in order to properly close the problem formulation.

In the first part of this chapter, a force driven nonlinear fully developed flow between parallel plates is considered. The external force is introduced in the governing nonlinear kinetic equation in the form of a pressure gradient term. Since the flow is fully developed kinetic simulations are implemented in a single cross section of the capillary. This flow setup has been studied in [56] on the basis of the nonlinear

BGK model. The treatment of the external force term involves a suitable projection procedure that eliminates the derivative with respect to the molecular velocity. The formulation of this method is relatively simple and the involved computational cost is not very high. However, it has a limited range of applicability, since a suitable projection may not exist when the external force depends on the molecular velocity. In the lattice Boltzmann method, a methodology has been introduced in [57] that incorporates the external force term in the equilibrium distribution through an infinite series sum in terms of Hermite polynomials. This methodology has been applied to some problems [132]–[134], always in the framework of the lattice Boltzmann method and extension to kinetic modeling has not been reported.

In the DSMC method, taking into account external force fields is relatively straightforward, due to the intuitive nature of the method. This is performed by accordingly modifying the particle velocities at each time step [135]–[137]. The corresponding work with force driven rarefied gas flows on the basis of deterministic modeling is limited since the treatment of the external force term is not straightforward.

In Section 3.2, a numerical scheme is introduced, able to solve the kinetic equations with the external force term included, in a deterministic manner. The proposed approach is based on the method of characteristics and incorporates the external force in the introduced variables that describe the characteristic curve. The methodology is presented by solving the prototype problem of force driven nonlinear Poiseuille flow, which has been also considered in [56]. The kinetic formulation is presented in Section 3.2.1 and the novel numerical scheme is developed in Section 3.2.2. A comparison with corresponding results in [56] is performed in Section 3.2.3, demonstrating the effectiveness and accuracy of the present approach. The anomalous form of the particle distribution function due to the presence of the force term is discussed in Section 3.2.4.

Next, in the second part of this chapter, the so-called implicit boundary conditions [87]–[91] are considered. This recently proposed boundary condition formulation provides boundary expressions for the incoming distribution directly at the capillary inlet and outlet, eliminating the need for large inlet and outlet vessels and significantly reducing the computational effort. These boundary conditions have been extensively studied in continuum computational fluid dynamics (CFD) in order to provide artificial boundary conditions at the far field in unbounded flow domains [138]–[140]. Their formulation assumes the flow to be locally one-dimensional, inviscid and adiabatic, although modifications to take into account viscous effects have been also proposed

[141]. They have been implemented with considerable success in various cases, such as flows around objects [142].

The implicit boundary conditions have been also applied in rarefied gas flows in the transition regime [87]–[91]. There has been however, no detailed investigation about their range of validity in terms of the involved geometric and flow parameters, as well as of the associated numerical error due to the elimination of the capillary inlet (upstream) and outlet (downstream) regions. Some validation studies have been performed only in the slip regime [90], [92] and the solution has been compared with analytical slip solutions based on the hydrodynamic equations. In addition, since the implicit boundary conditions are derived from the Euler equations describing inviscid flow their successful implementation in rarefied flows, which in general are characterized by low and moderate Reynolds numbers, must be carefully examined.

In Section 3.3, the range of validity of the implicit boundary conditions in nonlinear pressure driven rarefied gas flows between parallel plates and through circular tubes of arbitrary length is investigated. The formulation of the kinetic equations along with the boundary conditions applied at the solid walls and the symmetry axis are presented in Section 3.3.1. The boundary conditions at the open boundaries for the typical flow setup (the one with the inlet and outlet regions) and the implicit boundary conditions are given in Sections 3.3.2 and 3.3.3 respectively. The computed flow rates based on the implicit boundary conditions formulation are compared with the corresponding ones of the typical formulation, in a wide range of the gas rarefaction parameter for flows through capillaries (parallel plates and tubes) of various lengths driven by small, moderate and large pressure differences, in Section 3.3.4. Furthermore, the concept of coupling the implicit boundary conditions with the end effect methodology [83]–[85] in order to extend the applicability range of the implicit boundary conditions is investigated in Section 3.3.5.

3.2 Nonlinear fully developed rarefied gas flow between parallel plates due to external force

3.2.1 Governing equations with external force term

Consider a rarefied monatomic gas confined between two infinite parallel plates kept at distance H . The gas is in thermal equilibrium with the walls and a constant external force is acting on the gas molecules in a direction parallel to the plates (y

direction). Due to this external force a flow is induced in the y direction, with the macroscopic velocity in the other two directions vanishing. The coordinate system origin is located in the middle of the distance between the two plates and the direction normal to the plates is the x direction.

The one dimensional nonlinear BGK equation with a constant external force in the y direction is

$$\xi_x \frac{\partial f}{\partial x'} + \frac{F_y}{m} \frac{\partial f}{\partial \xi_y} = \frac{P}{\mu} (f^M - f), \quad (3.1)$$

where f is the distribution function, F_y denotes the external force magnitude, m is the molecular mass and $\boldsymbol{\xi}$ is the molecular velocity vector. The local Maxwellian distribution, denoted as f^M , is defined as

$$f^M = \frac{N}{(2\pi R_g T)^{3/2}} \exp \left[-\frac{\xi_x^2 + (\xi_y - U_y)^2 + \xi_z^2}{2R_g T} \right], \quad (3.2)$$

with R_g being the specific gas constant, N and T denote the local density and temperature and U_y the local velocity. The macroscopic quantities of interest are expressed as moments of the distribution function f by the following expressions:

- Number density

$$N = \int_{R^3} f d\xi_x d\xi_y d\xi_z \quad (3.3)$$

- Velocity

$$U_y = \frac{1}{N} \int_{R^3} \xi_y f d\xi_x d\xi_y d\xi_z \quad (3.4)$$

- Temperature

$$T = \frac{1}{3RN} \int_{R^3} [\xi_x^2 + (\xi_y - U_y)^2 + \xi_z^2] f d\xi_x d\xi_y d\xi_z \quad (3.5)$$

- Shear stress

$$P'_{xy} = m \int_{R^3} \xi_x (\xi_y - U_y) f d\xi_x d\xi_y d\xi_z \quad (3.6)$$

- Heat flux vector

$$Q_i = \frac{m}{2} \int_{R^3} (\xi_i - U_i) [\xi_x^2 + (\xi_y - U_y)^2 + \xi_z^2] f d\xi_x d\xi_y d\xi_z, i = x', y' \quad (3.7)$$

Diffuse boundary conditions are assumed at both plates, with the outgoing distribution given by

$$f^+ = \frac{N_w}{(2\pi R_g T_w)^{3/2}} \exp \left[-\frac{\xi_x^2 + \xi_y^2 + \xi_z^2}{2R_g T_w} \right], \quad (3.8)$$

for the bottom boundary at $x' = -H/2$ with $\xi_x > 0$ and the top boundary at $x' = H/2$ with $\xi_x < 0$. In Eq. (3.8), T_w is the wall temperature and N_w is a parameter used to satisfy the impermeability condition, given in terms of the incoming distribution by

$$N_W(\pm H/2) = \mp \left(\frac{2\pi}{R_g T_2} \right)^{1/2} \int_{\pm \xi_x} \xi_x f^- d\xi_x d\xi_y d\xi_z. \quad (3.9)$$

The following dimensionless quantities are defined:

$$x = \frac{x'}{H}, \zeta_i = \frac{\xi_i}{v_0}, g = f \frac{v_0^3}{N_0}, \rho = \frac{N}{N_0}, u_y = \frac{U_y}{v_0}, \tau = \frac{T}{T_0}, p_{xy} = \frac{P'_{xy}}{P_0}, q_i = \frac{Q_i}{v_0 P_0} \quad (3.10)$$

Here, $v_0 = \sqrt{2R_g T_0}$ is the most probable molecular velocity at reference temperature $T_0 = T_w$, P_0 is the reference pressure and N_0 the number density at reference conditions. Introducing the dimensionless quantities of Eq. (3.10) into Eqs. (3.1)-(3.9), the kinetic equation for the dimensionless distribution function g is

$$\zeta_x \frac{\partial g}{\partial x} + \bar{F} \frac{\partial g}{\partial \zeta_y} = \delta_0 \rho \tau^{1-\omega} (g^M - g), \quad (3.11)$$

where $\bar{F} = \frac{1}{Fr^2} = \frac{F_y H}{v_0^2}$ is the inverse of the square of the Froude number (Fr) and $\delta_0 = \frac{P_0 H}{\mu_0 v_0}$ is the gas rarefaction parameter at reference conditions, with μ_0 being the viscosity at T_0 . In the derivation of Eq. (3.11) the expression $\mu = \mu_0 (T/T_0)^\omega$ for the viscosity is used, with $\omega \in [0.5, 1]$ and the limiting values of $\omega = 0.5$ and 1 correspond to hard sphere and Maxwell molecules respectively. The dimensionless Maxwellian distribution is given by

$$g^M = \frac{\rho}{(\pi\tau)^{3/2}} \exp \left[-\frac{\zeta_x^2 + (\zeta_y - u_y)^2 + \zeta_z^2}{\tau} \right]. \quad (3.12)$$

The dimensionless macroscopic quantities are provided by the following expressions:

- Number density

$$\rho = \int_{R^3} g d\zeta_x d\zeta_y d\zeta_z \quad (3.13)$$

- Velocity

$$u_y = \frac{1}{n} \int_{R^3} \zeta_y g d\zeta_x d\zeta_y d\zeta_z \quad (3.14)$$

- Temperature

$$\tau = \frac{2}{3\rho} \int_{R^3} [\zeta_x^2 + (\zeta_y - u_y)^2 + \zeta_z^2] g d\zeta_x d\zeta_y d\zeta_z \quad (3.15)$$

- Shear stress

$$p_{xy} = 2 \int_{R^3} \zeta_x (\zeta_y - u_y) g d\zeta_x d\zeta_y d\zeta_z \quad (3.16)$$

- Heat flux vector

$$q_i = \int_{R^3} (\zeta_i - u_i) [\zeta_x^2 + (\zeta_y - u_y)^2 + \zeta_z^2] g d\zeta_x d\zeta_y d\zeta_z \quad (3.17)$$

The boundary conditions for the dimensionless distribution function g are

$$g^+ = \frac{\rho_w}{\pi^{3/2}} \exp \left[-(\zeta_x^2 + \zeta_y^2 + \zeta_z^2) \right] \quad (3.18)$$

for the bottom boundary at $x = -1/2$ with $\zeta_x > 0$ and the top boundary at $x = 1/2$ with $\zeta_x < 0$. The parameters ρ_w are given by

$$\rho_w = 2\pi^{1/2} \int_{\zeta_x > 0} \zeta_x g^- d\zeta_x d\zeta_y d\zeta_z, \quad (3.19)$$

and

$$\rho_w = -2\pi^{1/2} \int_{\zeta_x < 0} \zeta_x g^- d\zeta_x d\zeta_y d\zeta_z \quad (3.20)$$

for the top and bottom walls respectively.

At this point, the projection procedure in the y and z directions may be applied to decrease the dimensionality of the problem in the molecular velocity space along with the computational load. This projection approach, well explained in [56], eliminates the derivative with respect to the molecular velocity. Since the aim is to develop a numerical scheme able to tackle this term, a different projection approach is utilized here and only the z component of the molecular velocity is projected. The following reduced distribution functions are defined:

$$\varphi = \int_{-\infty}^{\infty} g d\zeta_z \quad (3.21)$$

$$\psi = \int_{-\infty}^{\infty} \zeta_z^2 g d\zeta_z \quad (3.22)$$

The integral operators $\int_{-\infty}^{\infty} (\cdot) d\zeta_z$ and $\int_{-\infty}^{\infty} \zeta_z^2 (\cdot) d\zeta_z$ are applied to Eq. (3.11) resulting in a system of two coupled integrodifferential equations for the two reduced distribution functions:

$$\zeta_x \frac{\partial \varphi}{\partial x} + \bar{F} \frac{\partial \varphi}{\partial \zeta_y} = \delta_0 \rho \tau^{1-\omega} (\varphi^M - \varphi), \quad (3.23)$$

$$\zeta_x \frac{\partial \psi}{\partial x} + \bar{F} \frac{\partial \psi}{\partial \zeta_y} = \delta_0 \rho \tau^{1-\omega} (\psi^M - \psi). \quad (3.24)$$

The respective reduced Maxwellian distributions are given by

$$\varphi^M = \frac{\rho}{\pi \tau} \exp \left[-\frac{\zeta_x^2 + (\zeta_y - u_y)^2}{\tau} \right], \quad (3.25)$$

$$\psi^M = \frac{\rho}{2\pi} \exp \left[-\frac{\zeta_x^2 + (\zeta_y - u_y)^2}{\tau} \right] \quad (3.26)$$

and the macroscopic quantities are given by the following expressions as moments of the reduced distribution functions:

- Number density

$$\rho = \int_{R^2} \varphi d\zeta_x d\zeta_y \quad (3.27)$$

- Velocity

$$u_y = \frac{1}{n} \int_{R^2} \zeta_y \varphi d\zeta_x d\zeta_y \quad (3.28)$$

- Temperature

$$\tau = \frac{2}{3\rho} \int_{R^2} \left([\zeta_x^2 + (\zeta_y - u_y)^2] \varphi + \psi \right) d\zeta_x d\zeta_y \quad (3.29)$$

- Shear stress

$$p_{xy} = 2 \int_{R^2} \zeta_x (\zeta_y - u_y) \varphi d\zeta_x d\zeta_y \quad (3.30)$$

- Heat flux vector

$$q_i = \int_{R^2} \left((\zeta_i - u_i) [\zeta_x^2 + (\zeta_y - u_y)^2] \right) \varphi + \psi d\zeta_x d\zeta_y, i = x, y \quad (3.31)$$

The boundary conditions for the reduced distribution functions are given by

$$\varphi^+ = \frac{\rho_w}{\pi} \exp \left[-(\zeta_x^2 + \zeta_y^2) \right], \quad (3.32)$$

$$\psi^+ = \frac{\rho_w}{2\pi} \exp \left[-(\zeta_x^2 + \zeta_y^2) \right] \quad (3.33)$$

for the bottom boundary with at $x = -1/2$ with $\zeta_x > 0$ and the top boundary at $x = 1/2$ with $\zeta_x < 0$. The parameters ρ_w are given by

$$\rho_w = 2\pi^{1/2} \int_0^{+\infty} \int_{-\infty}^{+\infty} \zeta_x \varphi^- d\zeta_y d\zeta_x \quad (3.34)$$

and

$$\rho_w = -2\pi^{1/2} \int_{-\infty}^0 \int_{-\infty}^{+\infty} \zeta_x \varphi^- d\zeta_y d\zeta_x \quad (3.35)$$

for the top and bottom walls respectively.

3.2.2 Solution methodology based on the method of characteristics

The system of kinetic equations (3.23) and (3.24) along with the moments (3.26)-(3.31) and the associated boundary conditions (3.32)-(3.35) can be solved to provide the values of the macroscopic quantities for different values of the reference rarefaction parameter δ_0 and the dimensionless external force magnitude \bar{F} . The naive approach for treating the external force term is to move it to the right hand side of the equation and use the values of the distribution function of the previous iteration to calculate the derivative with respect to the molecular velocity. This explicit approach works only for small values of \bar{F} , while the numerical scheme becomes unstable for large values of \bar{F} due to the explicit treatment of the force term.

In order to circumvent this pitfall a characteristic based method is introduced. More specifically, Eqs. (3.23) and (3.24) are written as

$$\frac{\partial \varphi}{\partial x} + \frac{\bar{F}}{\zeta_x} \frac{\partial \varphi}{\partial \zeta_y} = \frac{\delta_0 \rho \tau^{1-\omega}}{\zeta_x} (\varphi^M - \varphi), \quad (3.36)$$

$$\frac{\partial \psi}{\partial x} + \frac{\bar{F}}{\zeta_x} \frac{\partial \psi}{\partial \zeta_y} = \frac{\delta_0 \rho \tau^{1-\omega}}{\zeta_x} (\psi^M - \psi) \quad (3.37)$$

and the following two cases are distinguished, depending on the sign of ζ_x .

- Propagation from top to bottom ($\zeta_x < 0$):

The boundary condition is applied at the top wall and the solution is propagating from the top to the bottom wall. Two independent variables are introduced, s_1 and s_2 that are connected to x and ζ_y through the following ordinary differential equations

$$\frac{dx}{ds_1} = 1, \quad x(1/2, s_2) = 1/2, \quad (3.38)$$

$$\frac{d\zeta_y}{ds_1} = \frac{\bar{F}}{\zeta_x}, \quad \zeta_y(1/2, s_2) = s_2. \quad (3.39)$$

Solving Eqs (3.38) and (3.39), the characteristic line is found in terms of the two introduced variables as

$$s_1 = x, \quad (3.40)$$

$$s_2 = \zeta_y - \frac{\bar{F}}{\zeta_x} (s_1 - 1/2). \quad (3.41)$$

Using the chain rule, the derivative with respect to s_1 can be written as

$$\frac{d}{ds_1} = \frac{d}{dx} \frac{dx}{ds_1} + \frac{d}{d\zeta_y} \frac{d\zeta_y}{ds_1} = \frac{d}{dx} + \frac{\bar{F}}{\zeta_x} \frac{d}{d\zeta_y} \quad (3.42)$$

and the kinetic equations become

$$\frac{\partial \varphi}{\partial s_1} = \frac{\delta_0 \rho \tau^{1-\omega}}{\zeta_x} (\varphi^M - \varphi), \quad (3.43)$$

$$\frac{\partial \psi}{\partial s_1} = \frac{\delta_0 \rho \tau^{1-\omega}}{\zeta_x} (\psi^M - \psi), \quad (3.44)$$

with

$$\varphi^M = \frac{\rho}{\pi \tau} \exp \left[-\frac{\zeta_x^2 + ((s_1 - 1/2) \bar{F}/\zeta_x + s_2 - u_y)^2}{\tau} \right], \quad (3.45)$$

$$\psi^M = \frac{\rho}{2\pi} \exp \left[-\frac{\zeta_x^2 + ((s_1 - 1/2) \bar{F}/\zeta_x + s_2 - u_y)^2}{\tau} \right]. \quad (3.46)$$

- Propagation from bottom to top ($\zeta_x > 0$):

The boundary condition is applied at the bottom wall and the solution is propagating from bottom towards the top wall. The ordinary differential equations for the two introduced variables now become

$$\frac{dx}{ds_1} = 1, \quad x(-1/2, s_2) = -1/2, \quad (3.47)$$

$$\frac{d\zeta_y}{ds_1} = \frac{\bar{F}}{\zeta_x}, \quad \zeta_y(-1/2, s_2) = s_2. \quad (3.48)$$

Solving Eqs. (3.47) and (3.48), the characteristic line is found in terms of the two introduced variables

$$s_1 = x, \quad (3.49)$$

$$s_2 = \zeta_y - \frac{\bar{F}}{\zeta_x} (s_1 + 1/2). \quad (3.50)$$

Using the chain rule, the kinetic equations now become

$$\frac{\partial \varphi}{\partial s_1} = \frac{\delta_0 \rho \tau^{1-\omega}}{\zeta_x} (\varphi^M - \varphi), \quad (3.51)$$

$$\frac{\partial \psi}{\partial s_1} = \frac{\delta_0 \rho \tau^{1-\omega}}{\zeta_x} (\psi^M - \psi), \quad (3.52)$$

with

$$\varphi^M = \frac{\rho}{\pi \tau} \exp \left[-\frac{\zeta_x^2 + \left((s_1 + 1/2) \bar{F} / \zeta_x + s_2 - u_y \right)^2}{\tau} \right], \quad (3.53)$$

$$\psi^M = \frac{\rho}{2\pi} \exp \left[-\frac{\zeta_x^2 + \left((s_1 + 1/2) \bar{F} / \zeta_x + s_2 - u_y \right)^2}{\tau} \right]. \quad (3.54)$$

The macroscopic quantities now read as follows:

- Number density

$$\rho = \int_{-\infty}^0 \int_{-\infty}^{+\infty} \varphi ds_2 d\zeta_x + \int_0^{+\infty} \int_{-\infty}^{+\infty} \varphi ds_2 d\zeta_x \quad (3.55)$$

- Velocity

$$\begin{aligned} u_y &= \frac{1}{\rho} \int_{-\infty}^0 \int_{-\infty}^{+\infty} \left[\frac{\bar{F}}{\zeta_x} (s_1 - 1/2) + s_2 \right] \varphi ds_2 d\zeta_x + \\ &\quad \frac{1}{\rho} \int_0^{+\infty} \int_{-\infty}^{+\infty} \left[\frac{\bar{F}}{\zeta_x} (s_1 + 1/2) + s_2 \right] \varphi ds_2 d\zeta_x \end{aligned} \quad (3.56)$$

- Temperature

$$\begin{aligned} \tau &= \frac{2}{3\rho} \int_{-\infty}^0 \int_{-\infty}^{+\infty} \left[\zeta_x^2 + \left(\frac{\bar{F}}{\zeta_x} (s_1 - 1/2) + s_2 - u_y \right)^2 \right] \varphi + \psi \, ds_2 d\zeta_x + \\ &\quad \frac{2}{3\rho} \int_0^{+\infty} \int_{-\infty}^{+\infty} \left[\zeta_x^2 + \left(\frac{\bar{F}}{\zeta_x} (s_1 + 1/2) + s_2 - u_y \right)^2 \right] \varphi + \psi \, ds_2 d\zeta_x \end{aligned} \quad (3.57)$$

- Shear stress

$$\begin{aligned} p_{xy} &= 2 \int_{-\infty}^0 \int_{-\infty}^{+\infty} \zeta_x \left[\frac{\bar{F}}{\zeta_x} (s_1 - 1/2) + s_2 \right] \varphi ds_2 d\zeta_x + \\ &\quad 2 \int_0^{+\infty} \int_{-\infty}^{+\infty} \zeta_x \left[\frac{\bar{F}}{\zeta_x} (s_1 + 1/2) + s_2 \right] \varphi ds_2 d\zeta_x \end{aligned} \quad (3.58)$$

- Heat flux

$$q_x = \int_{-\infty}^0 \int_{-\infty}^{+\infty} \zeta_x \left[\left[\zeta_x^2 + \left(\frac{\bar{F}}{\zeta_x} (s_1 - 1/2) + s_2 - u_y \right)^2 \right] \varphi + \psi \right] \zeta_x ds_2 d\zeta_x +$$

$$\int_0^{+\infty} \int_{-\infty}^{+\infty} \zeta_x \left[\left[\zeta_x^2 + \left(\frac{\bar{F}}{\zeta_x} (s_1 + 1/2) + s_2 - u_y \right)^2 \right] \varphi + \psi \right] \varphi ds_2 d\zeta_x \quad (3.59)$$

$$q_y = \int_{-\infty}^0 \int_{-\infty}^{+\infty} \left[\frac{\bar{F}}{\zeta_x} (s_1 - 1/2) + s_2 \right] \left[\left[\zeta_x^2 + \left(\frac{\bar{F}}{\zeta_x} (s_1 - 1/2) + s_2 - u_y \right)^2 \right] \varphi + \psi \right] \zeta_x ds_2 d\zeta_x +$$

$$\int_0^{+\infty} \int_{-\infty}^{+\infty} \left[\frac{\bar{F}}{\zeta_x} (s_1 + 1/2) + s_2 \right] \left[\left[\zeta_x^2 + \left(\frac{\bar{F}}{\zeta_x} (s_1 + 1/2) + s_2 - u_y \right)^2 \right] \varphi + \psi \right] \varphi ds_2 d\zeta_x \quad (3.60)$$

The boundary conditions for the top wall ($s_1 = 1/2$ with $\zeta_x < 0$) and the bottom wall ($s_1 = -1/2$ with $\zeta_x > 0$) become

$$\varphi^+ = \frac{\rho_w}{\pi} \exp \left[- \left(\zeta_x^2 + s_2^2 \right) \right], \quad (3.61)$$

$$\psi^+ = \frac{\rho_w}{2\pi} \exp \left[- \left(\zeta_x^2 + s_2^2 \right) \right] \quad (3.62)$$

with the ρ_w parameters given by

$$\rho_w = 2\pi^{1/2} \int_0^{+\infty} \int_{-\infty}^{\infty} \zeta_x \varphi^- ds_2 d\zeta_x \quad (3.63)$$

and

$$\rho_w = -2\pi^{1/2} \int_{-\infty}^0 \int_{-\infty}^{\infty} \zeta_x \varphi^- ds_2 d\zeta_x \quad (3.64)$$

for the top and bottom walls respectively.

The system of kinetic equations (3.43), (3.44), (3.51) and (3.52) along with the equilibrium distributions (3.45), (3.46), (3.53) and (3.54), the moments for the macroscopic quantities (3.55)-(3.60) and the boundary conditions (3.61)-(3.64) is solved using the discrete velocity method.

The physical space is discretized into N_E equidistant intervals. Special care is taken for the discretization of ζ_x and s_2 . The outgoing distributions at the boundaries are unimodal distributions and more specifically, Maxwellians with a peak at $\zeta_x = s_2 = 0$. The equilibrium distributions are also Maxwellians, however the peak location in the s_2 direction depends on the external force, the position in the physical space, the value

of ζ_x and the local bulk velocity. These Maxwellian distributions can extend to large values of s_2 , making a discretization based on the roots of orthogonal polynomials not suitable. For this reason a uniform grid is used in the ζ_x and s_2 directions. The bounds of this grid should also be carefully chosen in order to capture the whole distribution function. Actually, very large values of the bounds in the s_2 direction are needed when the external force is also large. The discretization of ζ_x is first performed. Then, based on the discrete values of ζ_x and the values of the quantities appearing in the exponents of the equilibrium distributions, given by Eqs. (3.45), (3.46), (3.53) and (3.54), an appropriate set of discrete values of s_2 is selected to spread along the whole distribution function. For the simulations conducted here, the molecular velocity space bounds are chosen to be $\zeta_x \in [-20, 20]$ and $s_2 \in [-200, 20]$. The benefit of the proposed scheme is that the discontinuity of the distribution function with respect to the molecular velocity in the direction normal to the two plates is inherently treated as the solution propagates along the characteristic and no differentiation of the discontinuous distribution function with respect to the molecular velocity across the discontinuity is required.

The applicability and effectiveness of the proposed approach is connected to the analytical solution of Eqs. (3.38), (3.39), (3.47) and (3.48) describing the characteristic curves. In cases where the force field is a complex function of the molecular velocity, such analytical solutions may not exist. Then, the implementation of the developed approach becomes complicated since the corresponding ordinary differential equations should be solved numerically to compute the characteristic curve as the distribution propagates. The methodology becomes a kind of a deterministic Particle-In-Cell (PIC) method, which actually has been used to accurately model rarefied gas flows [143].

3.2.3 Mass and heat flow rates along with macroscopic distributions

Simulations are conducted for two values of the dimensionless external force, namely $\bar{F} = 0.05$ and 0.5 , corresponding to small and large values of the external force magnitude respectively. Since a comparison with the results presented in [56] is performed, Maxwell molecules with $\omega = 1$ are assumed and the reference Knudsen number defined as

$$Kn_0 = \frac{2}{\sqrt{\pi}\delta_0}, \quad (3.65)$$

is used, in order to be consistent with the notation used in [56]. The comparison is performed in terms of the dimensionless mass and heat flow rates, defined as

$$\dot{M} = \int_0^{1/2} \rho u_y dx \quad (3.66)$$

and

$$\dot{Q} = \int_0^{1/2} q_y dx. \quad (3.67)$$

The mass flow rate is given in Table 3.1 for $\bar{F} = 0.05, 0.5$ and $Kn_0 = 0.1, 1, 10$. The relative deviation between the current results and the results presented in [56] is less than 0.14%. The corresponding comparison for the heat flow rate is shown in Table 3.2, where the deviations are less than 1.5%.

Figure 3.1 presents the distributions of number density, temperature and velocity, for three values of the reference Knudsen number ($Kn_0 = 0.1, 1, 10$) and for two values of the external force ($\bar{F} = 0.05, 0.5$). For $\bar{F} = 0.05$, the flow velocity is relatively small, compared to the most probable molecular speed and the density and temperature deviations with respect to the reference values are relatively small. For $\bar{F} = 0.5$ the external force is increased and the flow velocity can exceed the dimensionless speed of sound which is $\sqrt{5/6}$ and the temperature and density profiles have high deviations compared to the reference values. For both values of the external force and for high values of Kn_0 , the temperature profile exhibits a well-known behavior, having a minimum in the center of the flow field [144]. It is also noted, that the distributions shown in Figure 3.1 are in good agreement with the respective ones in [56]. The very good agreement between the present results (mass and heat flow rates, as well macroscopic distributions) with the corresponding ones in [56], proves, at certain extend, the accuracy of the developed numerical scheme.

It is interesting to compare the present results obtained for the fully developed flow with the non-linear form of the BGK model, with the corresponding ones of the infinite capillary theory. The results for the reduced flow rate G_P obtained by the solution of the linearized BGK model, provided in [23] are compared to the present results, for three values of the external force $\bar{F} = 0.01, 0.05, 0.5$. The comparison is performed on the basis of the reduced flow rate, which for the nonlinear case under the current notation is calculated as

$$G_P = \frac{1}{\bar{F}} \int_{-1/2}^{1/2} \rho u_y ds_1. \quad (3.68)$$

Hard sphere molecules are assumed ($\omega = 1/2$), in order to be consistent with the results presented in [23] and the values of the rarefaction parameter are $\delta_0 = 0.01, 0.1, 1, 5, 10$. The comparison is shown in Table 3.3. It is seen that for $\bar{F} = 0.01$ the infinite capillary and the present approach are in excellent agreement, with relative deviations less than or close to 0.3%, while for $\bar{F} = 0.05$ the deviations are increased up to 2.8%. Finally, for $\bar{F} = 0.5$ the discrepancies are significantly increased up to 25%, indicating that the infinite capillary theory fails to correctly model this nonlinear flow.

3.2.4 Molecular velocity distribution function

A detailed description of the molecular velocity distribution function is provided. In all cases the distribution function is presented in terms of ζ_x and the introduced variable s_2 , which surely poses some difficulty in the intuitive understanding of the distribution form. The particles leaving the boundary follow a Maxwellian distribution around $s_2 = 0$, traveling either without or with intermolecular collisions. The former ones will keep the Maxwellian distribution originated at the boundary, while the latter ones relax to Maxwellian distributions, whose peaks can be in large values of s_2 . In terms of ζ_y , the outgoing distribution from the boundary follow a Maxwellian that for particles traveling without collisions (ballistic motion) is conveyed to high values of ζ_y , while for particles experiencing collisions is relaxed to a Maxwellian distribution around the local velocity. Combining the effects between particle collisions and particle acceleration due to the external force leads to bimodal or multimodal distribution functions with long tails. It is pointed out that far from the boundaries distributions close to a Maxwellian in terms of s_2 is characterized by long tails in terms of ζ_y , while distributions with long tails in terms of s_2 is close to a Maxwellian distribution in terms of ζ_y .

Qualitative contours of the reduced distribution function φ are shown in Figure 3.2, for $\bar{F} = 0.5$ and $Kn_0 = 1$, at five locations along the distance between the parallel plates and more specifically at $s_1 = 0, \pm 1/4$ and $\pm 1/2$, in terms of the two molecular velocity variables ζ_x and s_2 . The distribution function has a discontinuity at $\zeta_x = 0$, separating the distribution coming from the bottom wall ($s_1 = -1/2$ with $\zeta_x > 0$) and the one coming from the top wall ($s_1 = 1/2$ with $\zeta_x < 0$). At the bottom and top walls the outgoing distributions are Maxwellians, while the incoming ones have long tails extending to large absolute values of s_2 . Moving away from the boundaries, the distribution has tails in the same direction for both positive and negative values of ζ_x . In the center of the flow domain ($s_1 = 0$), the distribution is, as expected, symmetrical

with respect to ζ_x . Furthermore, there is a mirror symmetry in the physical space, where the distribution at s_1 for ζ_x is the same as the one at $-s_1$ for $-\zeta_x$ and therefore in the following description only half of the flow domain is considered. A detail of the tails of the distribution function at the center of the flow domain is shown in Figure 3.2 (see bottom-right subfigure) for $\bar{F} = 0.5$ and $Kn_0 = 1$. It is clearly seen that as the value of ζ_x becomes smaller, the distribution extends to larger values of s_2 , which is clearly contributed to the expression of the relaxation distribution and more specifically to the fact that the quantity $\left((s_1 + 1/2)\bar{F}/\zeta_x + s_2 - u_y\right)^2$ in the exponent increases as ζ_x decreases.

Figure 3.3 presents the distribution function φ for $\bar{F} = 0.5$ and $Kn_0 = 0.1, 10$. For the small value of the Knudsen number, where collisions are important, the distribution function is far from the Maxwellian. On the contrary, for the large value of the Knudsen number, where collisions are rare, the distribution function retains the shape of the outgoing distributions and is close to a Maxwellian with weak tails. The corresponding results for $\bar{F} = 0.05$ and $Kn_0 = 0.1, 10$ are shown in Figure 3.4. It is clearly seen that due to the smaller magnitude of the external force, the tails of the distribution function are much weaker.

In Figure 3.5, the reduced distribution function φ in terms of s_2 , at $s_1 = 0$ for $\bar{F} = 0.5$ and $Kn_0 = 10$ and for progressively decreasing, in magnitude, values of ζ_x , is presented. For $\zeta_x = 0.08$, the distribution has a peak close to zero, while its shape is close to a Maxwellian. As the value of ζ_x decreases, a tail starts to form. At $\zeta_x = 0.04$ the distribution becomes bimodal while for $\zeta_x = 0.025$ the tail has the maximum value of the distribution. It is also noted, that as ζ_x decreases and strongly non-equilibrium forms of the distribution function appear, the value of the distribution function decreases. Finally, In Figure 3.6 a three-dimensional plot of the distribution function φ at $s_1 = -1/2$ for $\bar{F} = 0.5$ and $Kn_0 = 1$ is shown, providing a more clear view of the discontinuity and the extension of the tails.

3.3 Implicit boundary conditions

3.3.1 Flow configuration and governing equations

Consider the pressure driven rarefied gas flow between two parallel plates separated by distance H or through a tube of radius R . In both cases the length of the capillary is L . The capillary walls are assumed to be isothermal at reference temperature T_0 .

The flow is characterized by three dimensionless parameters [80], [85], namely the ratio of the outlet over the inlet pressures P_{out}/P_{in} , the length over the characteristic dimension L/χ , where $\chi = H, R$ for the channel and the tube respectively and the reference gas rarefaction parameter defined at the inlet conditions, as

$$\delta_{in} = \frac{P_{in}\chi}{\mu_0 v_0}. \quad (3.69)$$

In Eq. (3.69), μ_0 is the viscosity at reference temperature T_0 and $v_0 = \sqrt{2R_g T_0}$ is the most probable molecular speed, with R_g denoting the gas constant. The flow is in the z' -direction, while the lateral directions are denoted by y' for the channel flow and r' for the tube flow. The macroscopic quantities to be computed include the two-component velocity vector $U(i, z')$, as well as the number density $N(i, z')$, pressure $P(i, z')$ and temperature $T(i, z')$ distributions, with $i = y', r'$. The main quantities of practical interest are the mass flows rates \dot{M}_c and \dot{M}_t for the channel and tube flows respectively.

The kinetic formulation of the channel and tube flow problems are well described in [79], [81], [82] and therefore, here, only the key issues related to the scope of the present work are provided. The following dimensionless quantities are defined:

$$y = y'/\chi, r = r'/\chi, z = z'/\chi, \mathbf{u} = \mathbf{U}/v_0, n = N/N_{in}, p = P/P_{in}, \tau = T/T_0. \quad (3.70)$$

Here, (y, z) and (r, z) are the physical space coordinates for the channel and the tube respectively (z denotes the flow direction), $\mathbf{u}(i, z) = [u_i(i, z), u_z(i, z)]$, $n(i, z)$, $p(i, z)$ and $\tau(i, z)$ are the dimensionless macroscopic velocity, number density, pressure and temperature respectively, with $i = y, r$, while $N_{in} = P_{in}/(k_B T_0)$ is the number density at inlet conditions with k_B being the Boltzmann constant.

The computational domains with the coordinate system and its origin for the typical flow configuration and the one with the implicit boundary conditions are shown in Figure 3.7. In the former one the computational domain includes the capillary region (A) plus the inlet and outlet regions denoted by (B) and (C) respectively. The inlet and outlet boundary conditions are imposed far from the capillary ends along the dotted lines. In the latter one the computational domain includes only the capillary region (A) and the boundary conditions are imposed at the capillary ends along the dashed lines. The detailed formulation and description of the conditions at the open boundaries is given in Sections 3.3.2 and 3.3.3.

In both flow configurations (with and without the inlet and outlet regions) the governing equations are identical. The BGK kinetic model is applied since in spite of its simplicity it has been proven to be accurate in the case of pressure driven flows [72], [73], [75], [78]. The gas is assumed to be monatomic going through hard sphere collisions with the viscosity varying as $\mu = \mu_0 \sqrt{T/T_0}$. Simulations are independent of the molecular mass and apply for any monatomic gas.

The channel flow is described by the coupled set of integrodifferential equations [75]

$$\zeta_y \frac{\partial \varphi}{\partial y} + \zeta_z \frac{\partial \varphi}{\partial z} = \delta_{in} n \sqrt{\tau} (\varphi^M - \varphi), \quad (3.71)$$

$$\zeta_y \frac{\partial \psi}{\partial y} + \zeta_z \frac{\partial \psi}{\partial z} = \delta_{in} n \sqrt{\tau} (\psi^M - \psi), \quad (3.72)$$

where $\varphi = \varphi(y, z, \zeta_y, \zeta_z)$ and $\psi = \psi(y, z, \zeta_y, \zeta_z)$ are the unknown reduced distribution functions, with (ζ_y, ζ_z) denoting the two components of the molecular velocity vector, while

$$\varphi^M = \frac{n}{\pi \tau} \exp \left[- \left((\zeta_y - u_y)^2 + (\zeta_z - u_z)^2 \right) / \tau \right], \quad (3.73)$$

$$\psi^M = \frac{n}{2\pi} \exp \left[- \left((\zeta_y - u_y)^2 + (\zeta_z - u_z)^2 \right) / \tau \right] \quad (3.74)$$

are the equilibrium distribution functions. The macroscopic quantities are given by the following moments of the reduced distribution functions:

$$n(y, z) = \int_{R^2} \varphi d\zeta_y d\zeta_z \quad (3.75)$$

$$u_y(y, z) = \frac{1}{n} \int_{R^2} \zeta_y \varphi d\zeta_y d\zeta_z \quad (3.76)$$

$$u_z(y, z) = \frac{1}{n} \int_{R^2} \zeta_z \varphi d\zeta_y d\zeta_z \quad (3.77)$$

$$\tau(y, z) = \frac{2}{3n} \int_{R^2} \left[(\zeta_y^2 + \zeta_z^2) \varphi + \psi \right] d\zeta_y d\zeta_z - \frac{2}{3} (u_y^2 + u_z^2) \quad (3.78)$$

The pressure is taken from the equation of state $p(y, z) = n(y, z) \tau(y, z)$.

The tube flow is described by the integrodifferential equation [75]

$$\zeta_p \cos \theta \frac{\partial g}{\partial r} - \frac{\zeta_p \sin \theta}{r} \frac{\partial g}{\partial \theta} + \zeta_z \frac{\partial g}{\partial z} = \delta_{in} n \sqrt{\tau} (g^M - g), \quad (3.79)$$

where $g = g(r, z, \zeta_p, \theta, \zeta_z)$ is the unknown distribution function, with $(\zeta_p, \theta, \zeta_z)$ denoting the three components of the molecular velocity vector in cylindrical coordinates, while

$$g^M = \frac{n}{(\pi\tau)^{3/2}} \exp \left[- \left((\zeta_p \cos \theta - u_r)^2 + (\zeta_p \sin \theta)^2 + (\zeta_z - u_z)^2 \right) / \tau \right] \quad (3.80)$$

is the equilibrium distribution. The macroscopic quantities are given by the moments of the distribution as

$$n(r, z) = \int_{R^3} g \zeta_p d\zeta_p d\theta d\zeta_z \quad (3.81)$$

$$u_r(r, z) = \frac{1}{n} \int_{R^3} \zeta_p^2 \cos \theta g d\zeta_p d\theta d\zeta_z \quad (3.82)$$

$$u_z(r, z) = \frac{1}{n} \int_{R^3} \zeta_z g \zeta_p d\zeta_p d\theta d\zeta_z \quad (3.83)$$

$$\tau(r, z) = \frac{2}{3n} \int_{R^3} (\zeta_p^2 + \zeta_z^2) g \zeta_p d\zeta_p d\theta d\zeta_z - \frac{2}{3} (u_r^2 + u_z^2) \quad (3.84)$$

$$p(r, z) = n(r, z) \tau(r, z) \quad (3.85)$$

Once the macroscopic distributions are computed, the dimensionless flow rates for the channel and the tube flow problems can be calculated as

$$W_c = \frac{\dot{M}_c}{2H^2 P_{in}/v_0} = 2 \int_0^{1/2} n u_z dy \quad (3.86)$$

and

$$W_t = \frac{\dot{M}_t}{\sqrt{\pi} R^2 P_{in}/v_0} = 4\sqrt{\pi} \int_0^1 n u_z r dr \quad (3.87)$$

respectively. The flow rates remain constant at any cross section along the capillary. Here, the computation is made at the capillary center ($z = 0$). The dimensionless flow rate is used as the main quantity in order to estimate the deviation of the implicit boundary formulation from the typical formulation and judge the accuracy of the former one. The relative difference (error) is defined as

$$e_i^{implicit} = \frac{W_i^{implicit} - W_i^{typical}}{W_i^{typical}} \times 100\%, \quad (3.88)$$

where $W_i^{typical}$ and $W_i^{implicit}$ are the dimensionless flow rates of the typical and implicit boundary formulations respectively, with $i = c$ for the channel and $i = t$ for the tube flows.

Proper closing of the channel and tube flow problems in both the typical formulation and the one with the implicit boundaries, require imposing boundary conditions a) along the symmetry axis, b) at the wall boundaries and c) at the open boundaries.

Specular boundary conditions are applied, due to symmetry, at the axes ($y' = 0$; $r' = 0$) and diffuse boundary conditions at the capillary walls ($y' = H/2$; $r' = R$). Also, the typical formulation includes diffuse boundary conditions at the lateral vessel walls next to the capillary ends ($z' = -L/2$ with $y', r' \in [\alpha, L_{in}]$ and $z' = L/2$ with $y', r' \in [\alpha, L_{out}]$). The specular and diffuse wall boundary conditions are well known and described in previous works [75], [80]–[82].

Finally, the open boundary conditions, which are of major importance in the present work are provided for the typical flow configuration with the inlet and outlet regions, as well as for the flow configuration with the implicit boundary conditions imposed at the capillary ends in Sections 3.3.2 and 3.3.3 respectively.

3.3.2 Inlet and outlet boundary conditions in the typical flow configuration

The computational domain in the typical flow configuration, as shown in Figure 3.7, consists of the capillary region (A) and the inlet and outlet regions (B) and (C) respectively. Therefore, the incoming distributions along the dotted lines must be defined. Following common practice, it is assumed that the incoming distributions are Maxwellians with zero bulk velocity [75], [80]–[82] characterized by the given inlet and outlet pressure and reference temperature. This is theoretically justified by taking the size of the inlet and outlet vessels adequately large and applying the open boundary conditions in a region where the gas is at rest far enough from the capillary ends. In the present work these conditions are fulfilled by taking $L_{in}/H = L_{out}/H = 20$ for the channel and $L_{in}/R = L_{out}/R = 15$ for the tube flow configurations. Then, the boundary conditions at the fictional boundaries of the inlet and outlet vessels in the typical flow setup become as follows [75]:

- Channel flow:

Upstream vessel

$$\varphi_u^+ = \frac{1}{\pi} \exp[-\zeta_y^2 - \zeta_z^2], \quad (3.89)$$

$$\psi_u^+ = \frac{1}{2\pi} \exp[-\zeta_y^2 - \zeta_z^2] \quad (3.90)$$

Downstream vessel

$$\varphi_d^+ = \frac{P_{out}/P_{in}}{\pi} \exp[-\zeta_y^2 - \zeta_z^2], \quad (3.91)$$

$$\psi_d^+ = \frac{P_{out}/P_{in}}{2\pi} \exp[-\zeta_y^2 - \zeta_z^2] \quad (3.92)$$

- Tube flow:

Upstream vessel

$$g_u^+ = \frac{1}{\pi^{3/2}} \exp[-\zeta_p^2 - \zeta_z^2] \quad (3.93)$$

Downstream vessel

$$g_d^+ = \frac{P_{out}/P_{in}}{\pi^{3/2}} \exp[-\zeta_p^2 - \zeta_z^2] \quad (3.94)$$

The subscripts (u) and (d) refer to the boundary conditions at the upstream and downstream vessels respectively, while the superscript (+) always refers to the incoming distributions.

The governing equations (3.71)-(3.78) with the boundary conditions (3.89)-(3.92) are numerically solved to compute the flow rate $W_c^{typical}$ for the channel flow. Similarly, the governing equations (3.79)-(3.85) with the boundary conditions (3.93), (3.94) are numerically solved to compute the flow rate $W_t^{typical}$ for the tube flow. The solution of the integrodifferential equations is performed by the well-known discrete velocity method. It is noted that the channel flow problem is four-dimensional (2D in the physical space plus 2D in the velocity space), while the tube flow problem is five-dimensional (2D in the physical space and 3D in the velocity space) and therefore, the latter one is much more computational demanding. Since these typical flow set ups are used as benchmarks, the flow rates are recalculated and tabulated in Table 3.4 for various pressure ratios P_{out}/P_{in} and capillary length L/χ , with $\chi = H, R$, in a wide range of the reference gas rarefaction parameter δ_{in} .

3.3.3 Inlet and outlet boundary conditions in the implicit formulation

The computational domain in the flow configuration with implicit boundary conditions, as shown in Figure 3.7, consists only of the capillary region (A). Now, the incoming distributions at the capillary ends, located at $z = \pm L/(2\chi) = \pm l$ along the dashed lines, must be defined. It is assumed that the incoming distributions are local Maxwellians, where the parameters of the Maxwellian distributions are obtained following the characteristic theory, which has been implemented in classical CFD

simulations in unbounded flow domains [138]–[140] assuming locally one-dimensional, inviscid and adiabatic flow. More specifically, the incoming distributions at the inlet and outlet of the channel and the tube are as follows:

- Channel flow:

$$\varphi_{in}^+(-l, y, \zeta_z, \zeta_y) = \frac{n_{in}(y)}{\pi\tau_{in}(y)} \exp \left[- \left((\zeta_y - u_{y,in}(y))^2 + (\zeta_z - u_{z,in}(y))^2 \right) / \tau_{in}(y) \right], \quad (3.95)$$

$$\psi_{in}^+(-l, y, \zeta_z, \zeta_y) = \frac{n_{in}(y)}{2\pi} \exp \left[- \left((\zeta_y - u_{y,in}(y))^2 + (\zeta_z - u_{z,in}(y))^2 \right) / \tau_{in}(y) \right], \quad (3.96)$$

$$\varphi_{out}^+(l, y, \zeta_z, \zeta_y) = \frac{n_{out}(y)}{\pi\tau_{out}(y)} \exp \left[- \left((\zeta_y - u_{y,out}(y))^2 + (\zeta_z - u_{z,out}(y))^2 \right) / \tau_{out}(y) \right], \quad (3.97)$$

$$\psi_{out}^+(l, y, \zeta_z, \zeta_y) = \frac{n_{out}(y)}{2\pi} \exp \left[- \left((\zeta_y - u_{y,out}(y))^2 + (\zeta_z - u_{z,out}(y))^2 \right) / \tau_{out}(y) \right], \quad (3.98)$$

with the following parameters [89]

$$n_{in}(y) = 1, \quad (3.99)$$

$$\tau_{in}(y) = 1, \quad (3.100)$$

$$u_{z,in}(y) = u_z(-l, y) + \frac{1 - p(-l, y)}{n(-l, y) \sqrt{2\gamma\tau(-l, y)}}, \quad (3.101)$$

$$u_{y,in}(y) = u_y(-l, y), \quad (3.102)$$

$$n_{out}(y) = n(l, y) + \frac{P_{out}/P_{in} - p(l, y)}{\gamma\tau(l, y)}, \quad (3.103)$$

$$\tau_{out}(y) = \frac{P_{out}/P_{in}}{n_{out}(y)}, \quad (3.104)$$

$$u_{z,out}(y) = u_z(l, y) + \frac{p(l, y) - P_{out}/P_{in}}{n(l, y) \sqrt{2\gamma\tau(l, y)}}, \quad (3.105)$$

$$u_{y,out}(y) = u_y(l, y) \quad (3.106)$$

- Tube flow:

$$g_{in}^+(r, -l, \zeta_p, \theta, \zeta_z) = \frac{n_{in}(r)}{(\pi\tau_{in}(r))^{3/2}} \exp \left[- \left((\zeta_p \cos \theta - u_{r,in}(r))^2 + (\zeta_p \sin \theta)^2 + (\zeta_z - u_{z,in}(r))^2 \right) / \tau_{in}(r) \right], \quad (3.107)$$

$$g_{out}^+(r, l, \zeta_p, \theta, \zeta_z) = \frac{n_{out}(r)}{(\pi\tau_{out}(r))^{3/2}} \exp \left[- \left((\zeta_p \cos \theta - u_{r,out}(r))^2 + (\zeta_p \cos \theta)^2 + (\zeta_z - u_{z,out}(r))^2 \right) / \tau_{out}(r) \right], \quad (3.108)$$

with the following parameters [89]

$$n_{in}(r) = 1, \quad (3.109)$$

$$\tau_{in}(r) = 1, \quad (3.110)$$

$$u_{z,in}(r) = u_z(r, -l) + \frac{1 - p(r, -l)}{n(r, -l) \sqrt{2\gamma\tau(r, -l)}}, \quad (3.111)$$

$$u_{r,in}(r) = u_r(r, -l) \quad (3.112)$$

$$n_{out}(r) = n(r, l) + \frac{P_{out}/P_{in} - p(r, l)}{\gamma\tau(r, l)}, \quad (3.113)$$

$$\tau_{out}(r) = \frac{P_{out}/P_{in}}{n_{out}(r)}, \quad (3.114)$$

$$u_{z,out}(r) = u_z(r, l) + \frac{p(r, l) - P_{out}/P_{in}}{n(r, l) \sqrt{2\gamma\tau(r, l)}}, \quad (3.115)$$

$$u_{r,out}(r) = u_r(r, l). \quad (3.116)$$

Again, the superscript (+) always refers to incoming distributions, while γ is denoting the ratio of specific heats that is equal to 5/3 for a monatomic gas. The macroscopic quantities of velocity, density, pressure and temperature at the right hand side of Eqs. (3.99)-(3.106) and (3.109)-(3.116) are calculated via the moments of the reduced distribution functions of the previous iteration at each boundary node according to Eqs. (3.75)-(3.78) and (3.81)-(3.85). Therefore, the input parameters in the Maxwellian expressions, Eqs. (3.95)-(3.98) and (3.107), (3.108), differ at each boundary node and are calculated in each iteration. The detailed derivation of the expressions for all parameters is given in Appendix A.

The governing equations (3.71)-(3.78) with the boundary conditions (3.95)-(3.106) and the governing equations (3.79)-(3.85) with the boundary conditions (3.107)-(3.116) are numerically solved to compute the flow rate $W_c^{implicit}$ for the channel flow and $W_t^{implicit}$ for the tube flow. As in the typical configuration, a DVM scheme is used for the solution of the involved equations. It is obvious, due to the small size of the computational domain, that the computational effort is greatly decreased compared to the corresponding one for the typical flow configuration. For example, in a channel with $L/H = 20$ the dimensionless computational area when the implicit boundary conditions are introduced is equal to 10 (considering the symmetry condition). On the contrary, for the same channel when the typical approach is applied the dimensionless computational area is $2(10 \times 20) + 10 = 410$ (inlet plus outlet vessels plus channel). Therefore, in the former compared to the latter case, the CPU time reduction is at least one order of magnitude. However, the implementation of the implicit boundary conditions is not theoretically justified, since the assumptions that the flow at the capillary ends may be approximated by local Maxwellians as well as that the parameters of the Maxwellians are estimated based on Euler equations describing inviscid and adiabatic flow are, in general, not valid. In the next section a comparison between the flow rates obtained by the typical flow configuration and the one with the implicit boundary conditions is presented.

3.3.4 Comparison between the flow rates of the typical and the implicit boundary conditions formulations

The validity of the implicit boundary conditions is computationally investigated by comparing the computed flow rates for the channel and tube flow problems with the corresponding ones obtained by the typical formulation.

The values of the three parameters characterizing the flow, considered in the computational investigation, are as follows:

- Channel flow: $P_{out}/P_{in} = [0.1, 0.3, 0.5, 0.7, 0.9]$, $\delta_{in} = [1, 5, 10]$, $L/H = [1, 2, 5, 10, 20]$
- Tube flow: $P_{out}/P_{in} = [0.1, 0.5, 0.9]$, $\delta_{in} = [1, 2, 5, 10]$, $L/R = [1, 5, 10, 20]$

These input values allow a complete comparison for flows in the transition and slip regimes through short up to long capillaries driven by small, moderate and large pressure differences.

The relative difference $e_i^{implicit}$, defined by Eq. (3.88), between the flow rate of the typical formulation and the corresponding one of the formulation with the implicit boundary conditions are tabulated in Table 3.5 for both channel ($i = c$) and tube ($i = t$) flows with $P_{out}/P_{in} = [0.1, 0.5, 0.9]$, $\delta_{in} = [1, 5, 10]$, $L/\chi = [1, 5, 10, 20]$, $\chi = H, R$. The relative difference (error) depends strongly on the dimensionless length L/χ , which is the most important parameter affecting the error. It is clearly observed that as L/χ is increased the error is decreased. It is also seen that the relative errors of the flow rates based on the formulation with the implicit boundary conditions for $L/\chi = 1$ are larger than 40% (even up to 100% and 200%), for $L/\chi = 5$ from 20-40%, for $L/\chi = 10$ from 10-20% and for $L/\chi = 20$ less or about 10%. The pressure ratio P_{out}/P_{in} has a strong effect on the error in capillaries with $L/\chi \leq 5$, while it becomes less significant in long capillaries. For short capillaries, the error generally increases as the pressure ratio increases. For longer capillaries, where the pressure ratio effect quickly diminishes, the error can either increase or decrease with the pressure ratio. Finally, the error weakly depends on the reference rarefaction parameter δ_{in} . At any dimensionless length it is decreased as δ_{in} is increased. The error behavior in terms of all three parameters is easily justified since as L/χ and δ_{in} are increased and P_{out}/P_{in} is decreased, end effects are not as pronounced, while the flow is characterized by larger Reynolds numbers, which are in accordance to the theoretical basis of the implicit boundary conditions. Based on the above, it may be stated that considering as acceptable an error of $\leq 20\%$, the formulation with the implicit boundary conditions may be implemented only to capillaries with $L/\chi \geq 10$. Furthermore, since the difference is positive in all cases it is deduced that the formulation with the implicit boundary conditions always overestimates the flow rate compared to the typical one.

A more compact picture of the error dependency on all parameters is provided in Figure 3.8, where the relative error $e_{c,t}^{implicit}$ is plotted in terms of the quantity $Z = \delta_{in} (\chi/L) (\Delta P/P_{in})$, where $\Delta P = P_{in} - P_{out}$. It is observed that for $L/\chi = 20$ the dependency of the error on the quantity Z remains almost constant, while as L/χ is reduced the error starts gradually to decrease as Z is increased. This trend simply indicates that as L/χ is reduced the effect of δ_{in} and ΔP on the error becomes more important, which is in accordance to the tabulated results in Table 3.5. Overall, it may be stated that the performance of the implicit boundary condition approach in rarefied gas flows is not as good as the one observed in continuum [138]–[141] and slip [87]–[91] gas flows.

3.3.5 Comparison between the flow rates of the typical and the implicit boundary conditions plus the end effect correction formulations

Based on the effective length concept, an end effect correction methodology has been recently proposed to extend the range of validity of the infinite capillary theory describing fully developed flows through long capillaries to capillaries of moderate length [83]–[85]. The actual length L/χ of the capillary is increased at its two ends by the length increments $\Delta L_{in}/\chi$ and $\Delta L_{out}/\chi$, which are independent of the capillary length and solely depend on the inlet and outlet gas rarefaction parameters δ_{in} and δ_{out} respectively, with $\delta_{out} = \delta_{in} P_{out}/P_{in}$. The length increments $\Delta L/\chi$ have been tabulated in terms of the gas rarefaction parameter δ for channel flow in [84] and for tube flow in [83], and they are as follows:

δ	0.1	0.2	0.4	0.6	0.8	1	2	4	6	8	10
$\Delta L/H$	2.45	2.15	1.55			1.05	0.827	0.654		0.574	0.556
$\Delta L/R$	1.52	1.33	1.16	1.07	1.01	0.964	0.841	0.735	0.704	0.688	0.682

In general, the length increment decreases as δ increases approaching a constant value as $\delta \rightarrow \infty$. At the other end, as $\delta \rightarrow 0$ the length increment $\Delta L/\chi \rightarrow \infty$. This methodology has been applied to fully developed flows with remarkable success even for relatively short capillaries ($\Delta L/\chi = 5$) and the interested reader may refer for all the details in [83]–[85].

Here, it is proposed to implement the implicit boundary conditions coupled with the end effect methodology. The computational domain, the governing equations and the boundary conditions remain the same as described in Sections 3.3.1 and 3.3.3 for the formulation with the implicit boundary conditions and the only difference is the length of the capillary which now is extended by adding to its actual length $\Delta L/\chi$ the two increments $\Delta L_{in}/\chi$ and $\Delta L_{out}/\chi$, obtained from the end correction theory based on the corresponding values of δ_{in} and δ_{out} .

The relative difference between the flow rates of the proposed methodology (implicit boundaries plus end effect) and the corresponding ones of the typical formulation, defined as

$$e_i^{implicit+EE} = \frac{|W_i^{implicit+EE} - W_i^{typical}|}{W_i^{typical}} \times 100\%, \quad (3.117)$$

is tabulated in Table 3.6, for both channel ($i = c$) and tube ($i = t$) flows with $P_{out}/P_{in} = [0.1, 0.5, 0.9]$, $\delta_{in} = [1, 5, 10]$ and $L/\chi = [1, 5, 10, 20]$, $\chi = H, R$. It is clearly observed that, compared to Table 3.5, the introduced error has been significantly reduced in all cases. Now, the relative error of the flow rates based on the formulation with the implicit boundary conditions plus the end effect correction are for $L/\chi = 1, 5, 10$ and 20 less or about 40%, 20%, 10% and 5% respectively. The error trend with regard to L/χ remains the same, i.e., it is always decreased as L/χ is increased. With regard to δ_{in} and P_{out}/P_{in} , when either of these quantities is small (i.e. $\delta_{in} = 1$ or $P_{out}/P_{in} = 0.1$) the error is steadily decreased as the other quantity is increased. For moderate and large values of δ_{in} and P_{out}/P_{in} (i.e. $\delta_{in} > 1$ and $P_{out}/P_{in} > 0.1$) the error takes small values (less than 5%) and in that case, as these quantities are increased the error does not have a monotonic behavior. Although not shown in Table 3.6, where the absolute values are tabulated, it is noted that the error without the absolute value, in most cases, is negative, while for large δ_{in} and P_{out}/P_{in} becomes positive. The behavior with respect to P_{out}/P_{in} is attributed to the end effect correction that is formulated based on small pressure gradients.

The relative difference (error) $e_i^{implicit+EE}$, $i = c, t$, is also plotted in Figure 3.9 in terms of the quantity $Z = \delta_{in} (\chi/L) (\Delta P/P_{in})$. It is observed that the relative errors are much smaller compared to the formulation with the implicit boundary conditions without the end effect correction (Figure 3.8). In fact now the error remains $< 15\%$ for almost all cases with $L/\chi = 5, 10$ and 20 .

The corresponding results comparing the typical and the infinite capillary theory [23] with end correction are shown in Table 3.7, where the relative deviation is defined as

$$e_{c,t}^{fd+ee} = \frac{|W_{c,t}^{FD+EE} - W_{c,t}^{typical}|}{W_{c,t}^{typical}} \times 100\%. \quad (3.118)$$

It is seen that the deviations for this case are smaller compared to the respective deviations for the implicit boundary plus end correction approach (Figure 3.9 and Table 3.6). In fact, in the range of parameters where the implicit boundary with end correction provides accurate values for the mass flow rate, the infinite capillary theory with end correction is also able to accurately estimate the flow rate, with a much lower computational effort.

Based on the above it is seen that adding the end effect correction to the formulation with the implicit boundary conditions greatly increases the range of its applicability with regard to the three parameters governing the pressure driven rarefied gas flow

through channels and tubes. It should be stated however, that this improvement is mainly contributed to the effectiveness of the end effect theory. It is noted that, in general, in the same range of parameters, the accuracy of the mass flow rate results obtained by the implicit boundary conditions plus the end correction approach is very close to the one obtained by the infinite capillary theory with the end effect correction [85]. The implementation of the former approach compared to the latter one is much more computationally demanding. However, it may be applied in flow configurations, where the assumptions of the infinite capillary theory are not valid, i.e. in non fully developed and non-isothermal flows.

3.4 Concluding remarks

Pressure driven flows through capillaries are of major importance and therefore have been extensively investigated. However, due to the complexity of the kinetic equations and of the associated computational schemes, there are still open issues, which must be resolved in an efficient manner. Such issues include the treatment of the external force term, which may be present in the kinetic equations, as well as the implementation of proper inlet and outlet conditions at the capillary ends. In this chapter both issues are tackled.

A force driven nonlinear fully developed Poiseuille flow is simulated based on the non-linear BGK equation with the external force term retained in the equation. A numerical scheme is developed, using the method of characteristics, obtaining the numerical solution of the kinetic equation in a deterministic manner. In particular, upon introducing the variables describing the characteristic curve, the derivative with respect to the molecular velocity vanishes and the external force term is incorporated into the equilibrium distribution and the expressions for the macroscopic quantities. The results include the mass and the heat flow rates, as well all macroscopic distributions of practical interest and they are in excellent agreement with corresponding published results for this flow configuration [56]. In addition, the form of the distribution function is of specific interest, as the external force acting on the gas molecules can give rise to interesting multimodal distribution functions. It is believed that the methodology presented here can be utilized for more complicated flows under external field forces, such as the flows of charged particles in the presence of electric and magnetic fields.

The range of validity of the so-called implicit boundary conditions [87]–[91] has been computationally investigated by simulating the pressure driven rarefied gas flow through

capillaries. More specifically, the nonlinear rarefied gas flow through a plane channel and a tube has been solved in a wide range of the three parameters characterizing the flow, namely the ratio of the outlet over the inlet pressure P_{out}/P_{in} , the dimensionless length L/χ and the reference gas rarefaction parameter at the inlet δ_{in} , by imposing the implicit boundary conditions for the incoming distributions at the capillary ends.

The computed flow rates have been compared to the corresponding ones obtained based on the so-called typical formulation, i.e., by including in the computational domain adequately large inlet and outlet regions and properly imposing the boundary conditions far from the capillary ends. It is evident that the motivation of the implicit boundary conditions formulation is to significantly reduce the computational effort due to the reduced size of the computational domain which includes only the capillary. It has been found however, that the implicit boundary formulation may introduce significant discrepancies. In general, the introduced error is increased as L/χ and δ_{in} are decreased since end effects become more important, as well as P_{out}/P_{in} is increased (ΔP is decreased) and the flow speed is reduced. The dimensionless length is the most important parameter affecting the error. The introduced relative error for $L/\chi = 20$ and 10 is less or about 10% and 20% respectively, while for $L/\chi < 10$ becomes unacceptably large. These findings are justified by the fact that the derivation of the implicit boundary conditions is based on the method of characteristics assuming one-dimensional, inviscid and adiabatic flow.

The range of validity of the implicit boundary conditions is extended by introducing in the formulation the end effect theory [83]–[85], where the actual capillary length has been increased to include the correction due to the end effects at the two capillary ends. This way the computational domain does not require the computationally costly addition of the inlet and outlet regions and the computational cost remains small, while the introduced error in the flow rates is less than 15% for $L/\chi \geq 5$. This improvement is due to the effectiveness of the end effect theory, which as it has been demonstrated performs exceptionally well even in flows through short capillaries. When the infinite capillary and the implicit boundary condition approaches are both coupled with the end effect theory, they are valid approximately in the same range of parameters, with the latter one requiring more computational time but being able to simulate phenomena beyond the fully developed flow limit. It is hoped that the present work may serve as a guideline in the implementation of the implicit boundary conditions formulation, which must be always performed with caution, considering the effect on the accuracy of the results.

Table 3.1 Mass flow rate for various values of the reference Knudsen number Kn_0 and of the external force \bar{F} .

Kn_0	$\bar{F} = 0.05$		$\bar{F} = 0.5$	
	Current	Ref. [53]	Current	Ref. [53]
0.1	7.384(-2)	7.374(-2)	5.286(-1)	5.280(-1)
1	3.842(-2)	3.841(-2)	3.492(-1)	3.492(-1)
10	4.960(-2)	4.961(-2)	4.400(-1)	4.400(-1)

Table 3.2 Heat flow rate for various values of the reference Knudsen number Kn_0 and of the external force \bar{F} .

Kn_0	$\bar{F} = 0.05$		$\bar{F} = 0.5$	
	Current	Ref. [53]	Current	Ref. [53]
0.1	-1.444(-3)	-1.445(-3)	6.702(-3)	6.680(-3)
1	-6.865(-3)	-6.875(-3)	1.188(-2)	1.206(-2)
10	-9.335(-3)	-9.317(-3)	5.483	5.509

Table 3.3 Reduced flow rate for various values of the reference rarefaction parameter δ_0 and external force \bar{F} , for the force driven nonlinear Poiseuille flow and the infinite capillary theory.

δ_0	G_P			
	$\bar{F} = 0.5$	$\bar{F} = 0.05$	$\bar{F} = 0.01$	Ref. [21]
0.01	2.260	2.963	3.039	3.049
0.1	1.697	2.019	2.028	2.031
1	1.394	1.533	1.535	1.539
5	1.708	1.981	1.986	1.988
10	2.160	2.748	2.761	2.764

Table 3.4 Dimensionless flow rate for channel and tube flows based on the typical formulation.

$W_c^{typical}$				$W_t^{typical}$				
$L/H = 1$				$L/R = 1$				
$\frac{P_{out}}{P_{in}}$	δ_{in}			$\frac{P_{out}}{P_{in}}$	δ_{in}			
	1	5	10		1	2	5	10
0.1	0.202	0.258	0.292	0.1	0.713	0.788	0.931	1.06
0.5	0.121	0.184	0.239	0.5	0.428	0.505	0.692	0.888
0.9	0.0254	0.0431	0.0633	0.9	0.0908	0.112	0.170	0.264
$L/H = 5$				$L/R = 5$				
$\frac{P_{out}}{P_{in}}$	δ_{in}			$\frac{P_{out}}{P_{in}}$	δ_{in}			
	1	5	10		1	2	5	10
0.1	0.0926	0.111	0.1359	0.1	0.312	0.341	0.423	0.537
0.5	0.0529	0.0708	0.0945	0.5	0.182	0.207	0.280	0.398
0.9	0.0108	0.0156	0.0220	0.9	0.0378	0.0444	0.0641	0.0976
$L/H = 10$				$L/R = 10$				
$\frac{P_{out}}{P_{in}}$	δ_{in}			$\frac{P_{out}}{P_{in}}$	δ_{in}			
	1	5	10		1	2	5	10
0.1	0.0562	0.0646	0.0798	0.1	0.185	0.200	0.249	0.328
0.5	0.0315	0.0398	0.0528	0.5	0.106	0.119	0.160	0.229
0.9	0.00635	0.00870	0.0121	0.9	0.0219	0.0253	0.0359	0.0543
$L/H = 20$				$L/R = 20$				
$\frac{P_{out}}{P_{in}}$	δ_{in}			$\frac{P_{out}}{P_{in}}$	δ_{in}			
	1	5	10		1	2	5	10
0.1	0.0317	0.0351	0.0433	0.1	0.0999	0.107	0.134	0.181
0.5	0.0174	0.0212	0.0280	0.5	0.0569	0.0632	0.0844	0.122
0.9	0.00348	0.00460	0.00637	0.9	0.0117	0.0134	0.0189	0.0286

Table 3.5 Relative (%) difference (error) of the flow rates between the typical and the implicit boundary formulations for channel and tube flows

$e_c^{implicit}$				$e_t^{implicit}$				
$L/H = 1$				$L/R = 1$				
$\frac{P_{out}}{P_{in}}$	δ_{in}			$\frac{P_{out}}{P_{in}}$	δ_{in}			
	1	5	10		1	2	5	10
0.1	77.78	50.43	42.38	0.1	90.94	77.27	58.14	46.12
0.5	149.31	86.62	59.48	0.5	171.20	140.98	91.82	61.17
0.9	194.80	138.58	115.78	0.9	232.48	205.58	167.12	124.99
$L/H = 5$				$L/R = 5$				
$\frac{P_{out}}{P_{in}}$	δ_{in}			$\frac{P_{out}}{P_{in}}$	δ_{in}			
	1	5	10		1	2	5	10
0.1	27.70	18.12	14.89	0.1	27.09	23.93	19.69	17.77
0.5	40.09	26.65	22.02	0.5	38.17	34.03	29.11	24.27
0.9	39.84	26.83	23.69	0.9	38.61	34.18	29.92	27.53
$L/H = 10$				$L/R = 10$				
$\frac{P_{out}}{P_{in}}$	δ_{in}			$\frac{P_{out}}{P_{in}}$	δ_{in}			
	1	5	10		1	2	5	10
0.1	17.65	11.92	9.70	0.1	15.17	13.58	11.46	10.53
0.5	21.09	14.07	12.09	0.5	18.69	16.37	14.11	13.12
0.9	20.19	13.16	11.97	0.9	18.11	15.80	14.14	13.31
$L/H = 20$				$L/R = 20$				
$\frac{P_{out}}{P_{in}}$	δ_{in}			$\frac{P_{out}}{P_{in}}$	δ_{in}			
	1	5	10		1	2	5	10
0.1	10.60	7.33	6.09	0.1	10.10	8.97	7.52	6.66
0.5	10.84	7.21	6.29	0.5	10.61	9.34	8.07	7.19
0.9	10.11	6.73	6.09	0.9	10.00	8.78	7.57	6.92

Table 3.6 Relative (%) difference (error) of the flow rates between the typical and the implicit boundary plus the end effect correction formulations for the channel and tube flows.

$e_c^{implicit+EE}$				$e_t^{implicit+EE}$				
$L/H = 1$				$L/R = 1$				
$\frac{P_{out}}{P_{in}}$	δ_{in}			$\frac{P_{out}}{P_{in}}$	δ_{in}			
	1	5	10		1	2	5	10
0.1	36.02	25.87	14.53	0.1	25.13	22.59	15.43	8.39
0.5	14.16	4.01	1.72	0.5	5.75	2.90	1.38	1.08
0.9	6.56	2.96	2.77	0.9	2.07	1.24	5.14	0.66
$L/H = 5$				$L/R = 5$				
$\frac{P_{out}}{P_{in}}$	δ_{in}			$\frac{P_{out}}{P_{in}}$	δ_{in}			
	1	5	10		1	2	5	10
0.1	17.56	11.92	8.04	0.1	11.06	9.97	7.54	4.69
0.5	4.90	0.48	0.10	0.5	2.62	1.45	0.02	0.54
0.9	1.93	0.92	0.95	0.9	1.71	0.70	0.85	0.77
$L/H = 10$				$L/R = 10$				
$\frac{P_{out}}{P_{in}}$	δ_{in}			$\frac{P_{out}}{P_{in}}$	δ_{in}			
	1	5	10		1	2	5	10
0.1	10.08	6.05	4.10	0.1	6.64	5.81	4.34	2.98
0.5	2.8	0.01	0.28	0.5	1.93	1.46	0.77	0.45
0.9	1.09	0.30	0.56	0.9	1.78	1.29	0.10	0.88
$L/H = 20$				$L/R = 20$				
$\frac{P_{out}}{P_{in}}$	δ_{in}			$\frac{P_{out}}{P_{in}}$	δ_{in}			
	1	5	10		1	2	5	10
0.1	5.01	2.53	1.53	0.1	1.79	1.55	1.10	0.87
0.5	1.44	0.08	0.21	0.5	0.15	0.32	0.53	0.22
0.9	0.71	0.24	0.31	0.9	0.01	0.26	0.51	0.10

Table 3.7 Relative (%) difference (error) of the flow rates between the typical and the infinite capillary plus the end effect correction formulations for the channel and tube flows.

e_c^{FD+EE}				e_t^{FD+EE}				
$L/H = 1$				$L/R = 1$				
$\frac{P_{out}}{P_{in}}$	δ_{in}			$\frac{P_{out}}{P_{in}}$	δ_{in}			
	1	5	10	$\frac{P_{out}}{P_{in}}$	1	2	5	10
0.1	18.24	2.78	24.42	0.1	9.83	4.95	11.03	41.10
0.5	7.24	2.75	1.72	0.5	4.49	2.67	3.96	22.78
0.9	3.69	0.38	0.55	0.9	4.08	4.30	2.45	2.37
$L/H = 5$				$L/R = 5$				
$\frac{P_{out}}{P_{in}}$	δ_{in}			$\frac{P_{out}}{P_{in}}$	δ_{in}			
	1	5	10	$\frac{P_{out}}{P_{in}}$	1	2	5	10
0.1	5.53	1.72	5.39	0.1	4.07	2.87	1.35	10.89
0.5	1.17	0.78	2.09	0.5	2.30	2.13	0.36	2.77
0.9	0.02	0.45	0.30	0.9	2.18	2.57	1.81	1.83
$L/H = 10$				$L/R = 10$				
$\frac{P_{out}}{P_{in}}$	δ_{in}			$\frac{P_{out}}{P_{in}}$	δ_{in}			
	1	5	10	$\frac{P_{out}}{P_{in}}$	1	2	5	10
0.1	2.01	0.64	2.19	0.1	3.01	2.43	0.57	3.60
0.5	0.16	0.75	1.04	0.5	1.69	1.86	1.22	0.28
0.9	0.46	0.36	0.36	0.9	1.80	2.05	1.26	1.16
$L/H = 20$				$L/R = 20$				
$\frac{P_{out}}{P_{in}}$	δ_{in}			$\frac{P_{out}}{P_{in}}$	δ_{in}			
	1	5	10	$\frac{P_{out}}{P_{in}}$	1	2	5	10
0.1	0.04	0.15	1.04	0.1	0.28	0.28	0.14	1.24
0.5	0.35	0.76	0.64	0.5	0.19	0.06	0.30	0.28
0.9	0.60	0.62	0.40	0.9	0.07	0.03	0.11	0.18

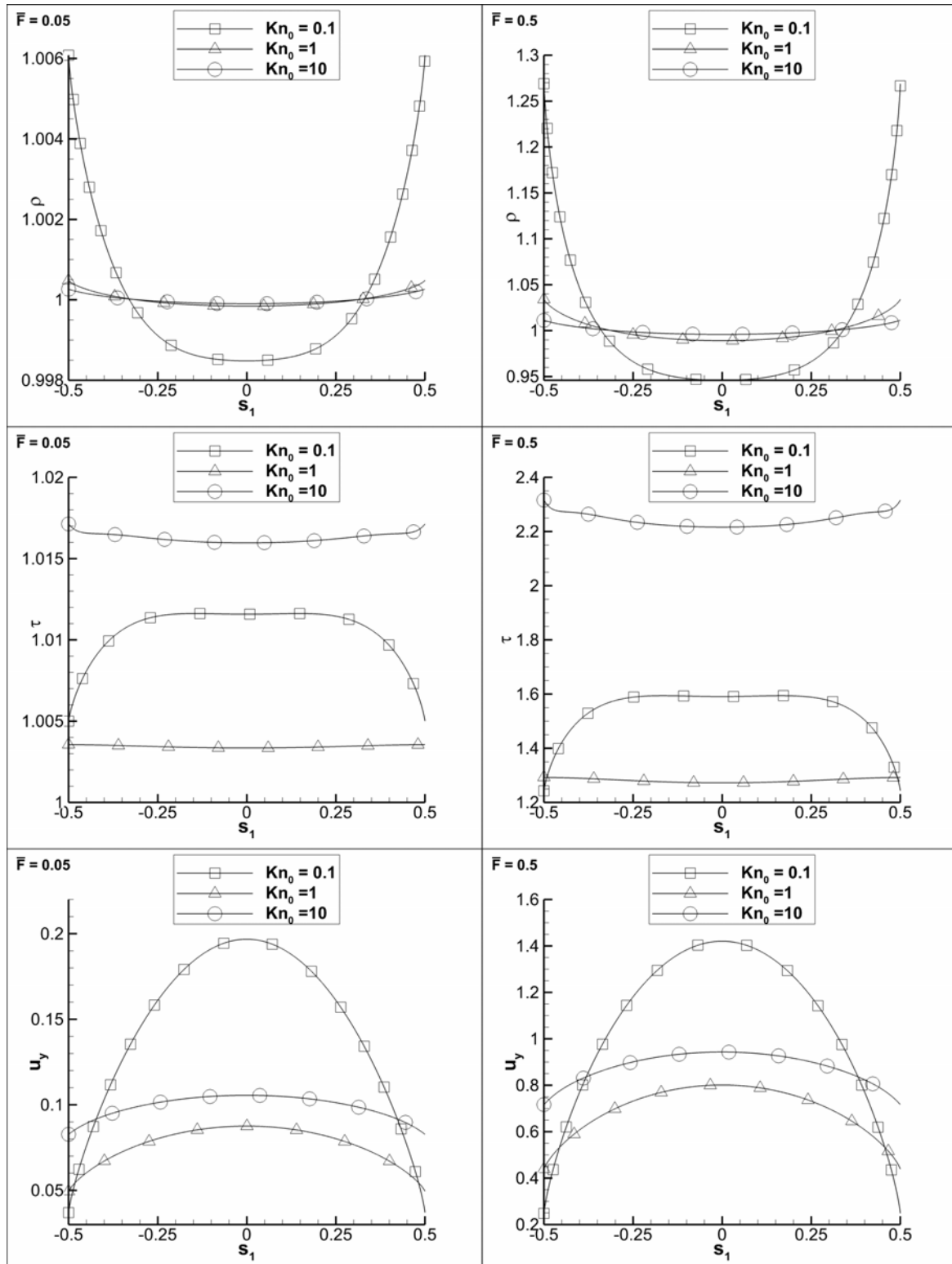


Figure 3.1 Distributions of density (top), temperature (middle) and velocity (bottom) for $\bar{F} = 0.05$ (left) and $\bar{F} = 0.5$ (right).

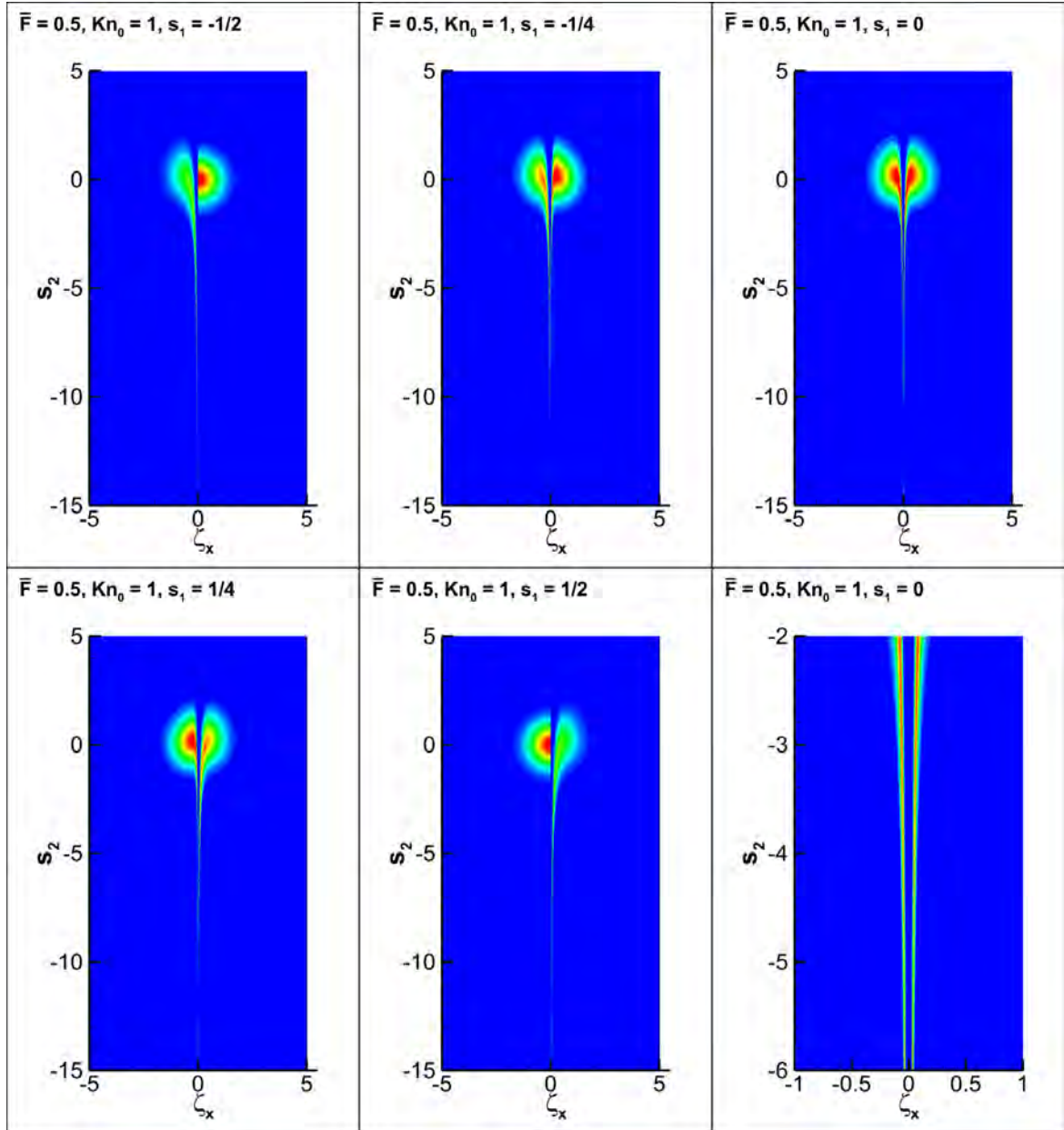


Figure 3.2 Reduced distribution function φ at five locations along the distance between the plates, with a tail region detail at the center of the flow domain (bottom right subfigure) for $\bar{F} = 0.5$ and $Kn_0 = 1$.

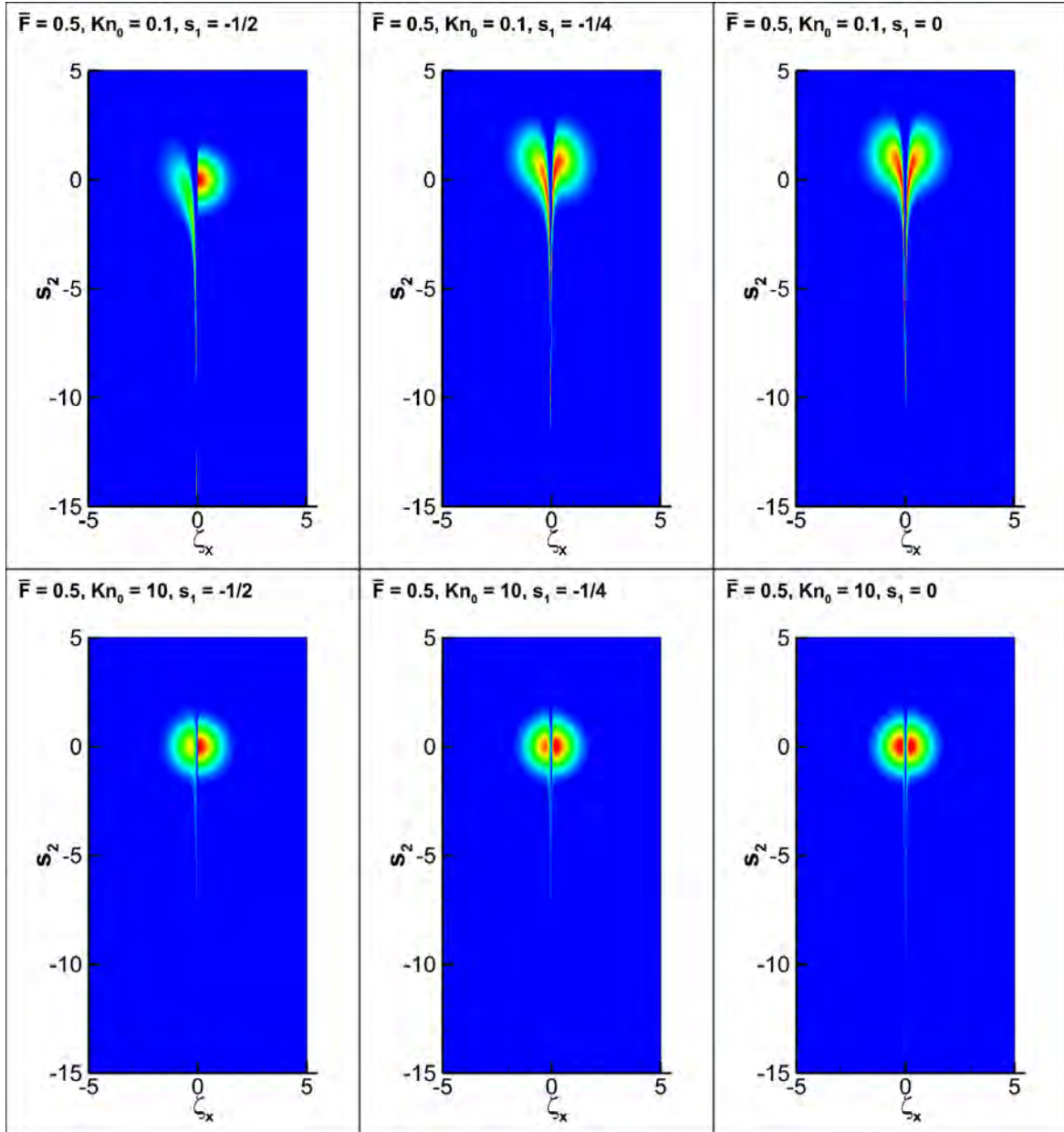


Figure 3.3 Reduced distribution function φ at three locations along the distance between the plates, for $\bar{F} = 0.5$ and $Kn_0 = 1$ and 10.

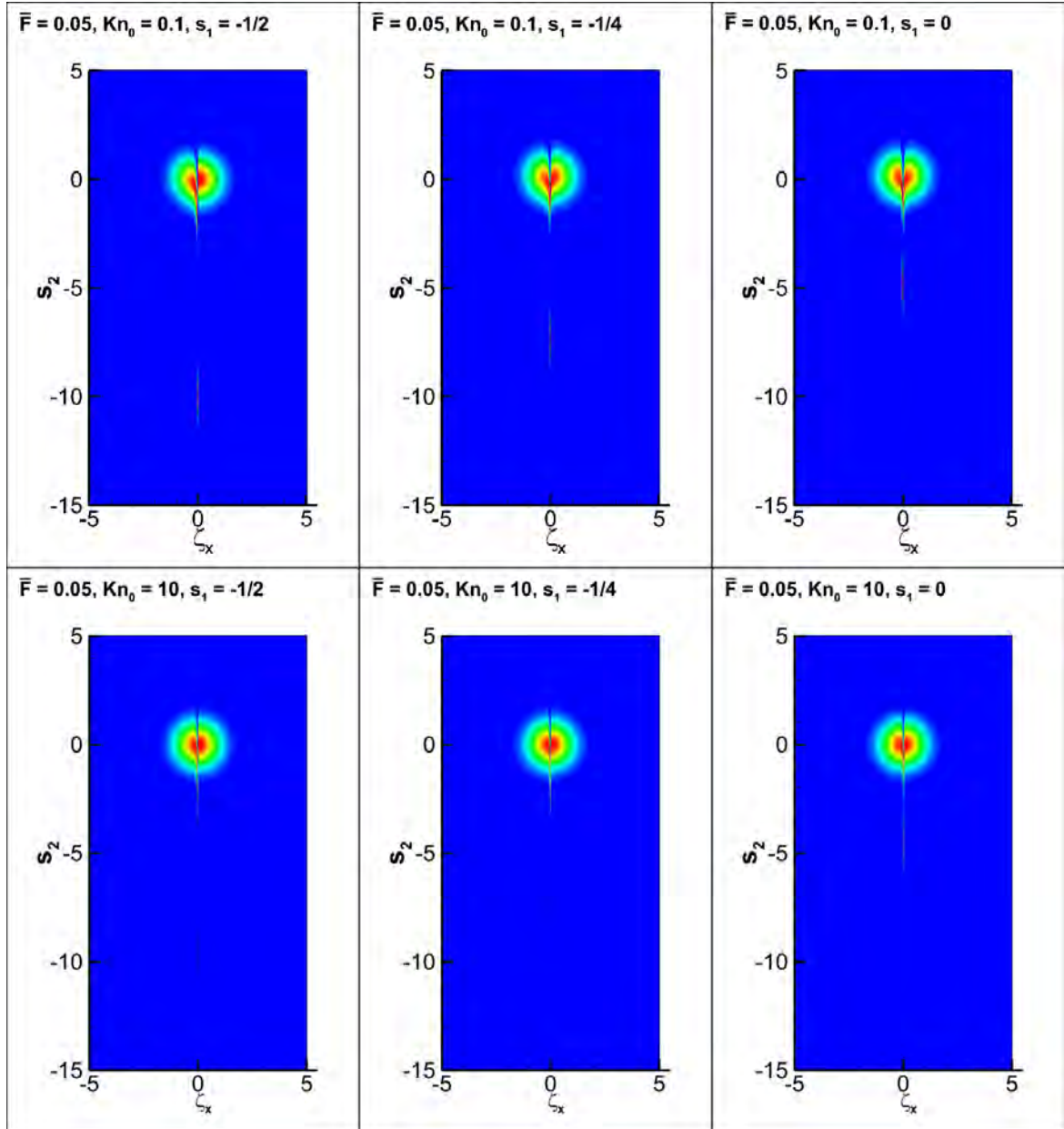


Figure 3.4 Reduced distribution function φ at three locations along the distance between the plates for $\bar{F} = 0.05$ and $Kn_0 = 0.1, 1$.

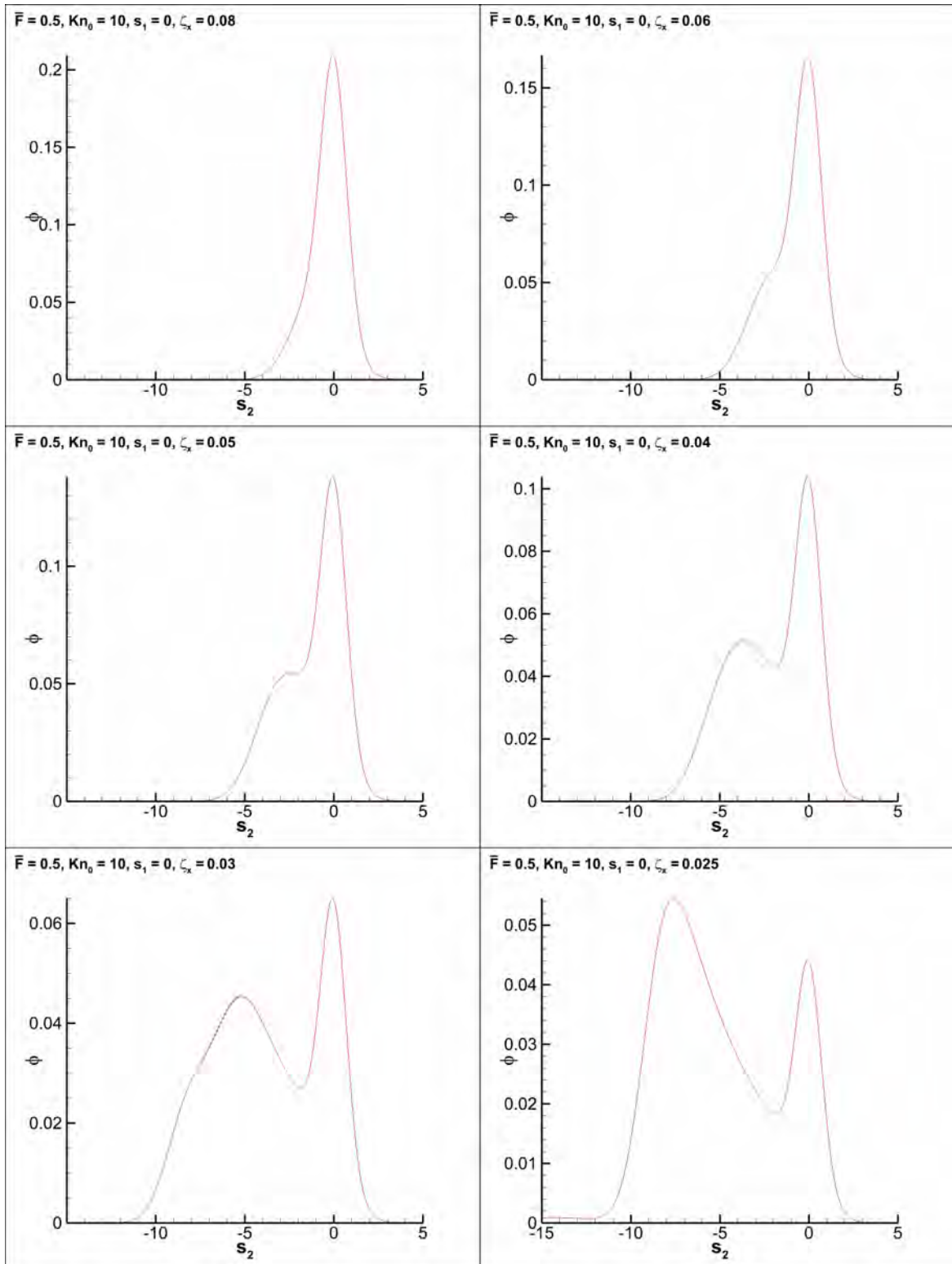


Figure 3.5 Reduced distribution function φ at the center of the distance between the plates for $F = 0.5$ and $Kn_0 = 10$ in terms of s_2 , for various values of ζ_x .

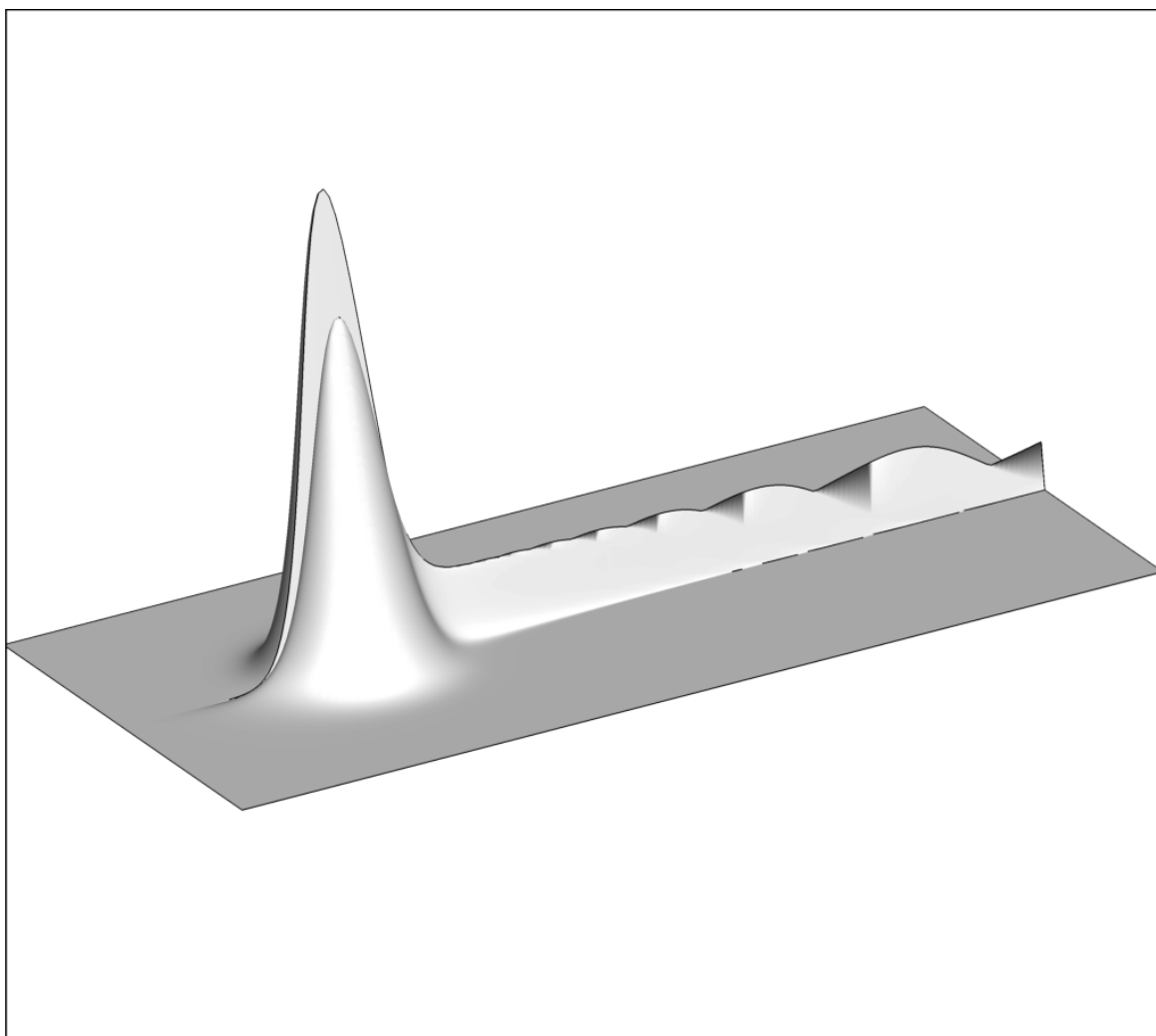


Figure 3.6 3D plot of the reduced distribution function φ at $s_1 = -1/2$ for $\bar{F} = 0.5$ and $Kn_0 = 1$.

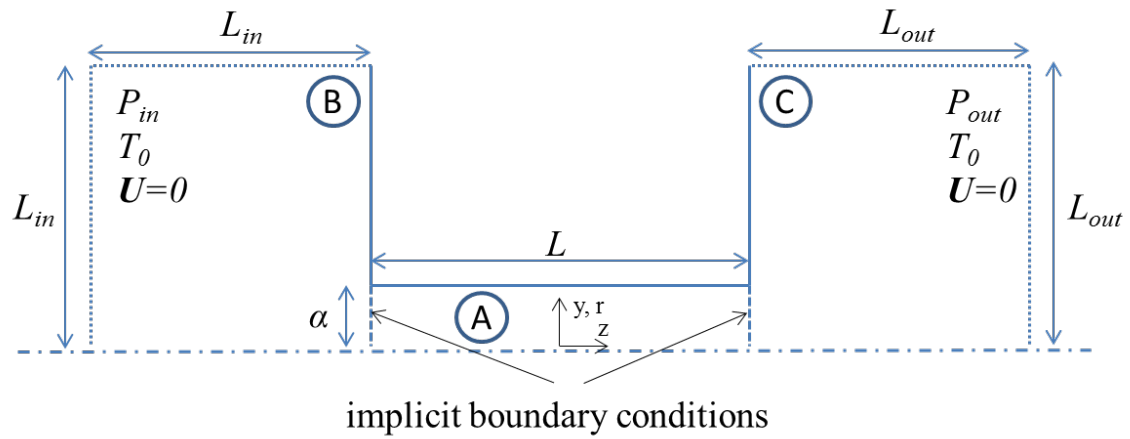


Figure 3.7 View of the computational domains with the coordinate system and its origin for the typical flow configuration (regions (A), (B) and (C)) and the one with the implicit boundary conditions (only region (A)), with $\alpha = H/2$ or R for the channel and tube respectively.

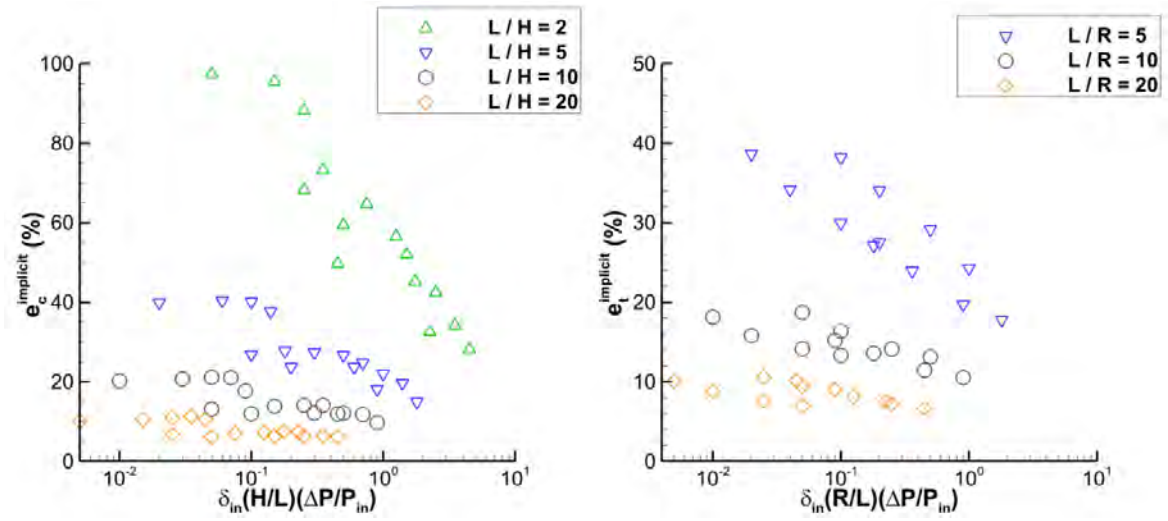


Figure 3.8 Relative difference (error) of the flow rates between the typical approach and the one with implicit boundary conditions in terms of $\delta_{in} (\chi/L) (\Delta P/P_{in})$ for the channel (left) and tube (right) flows.

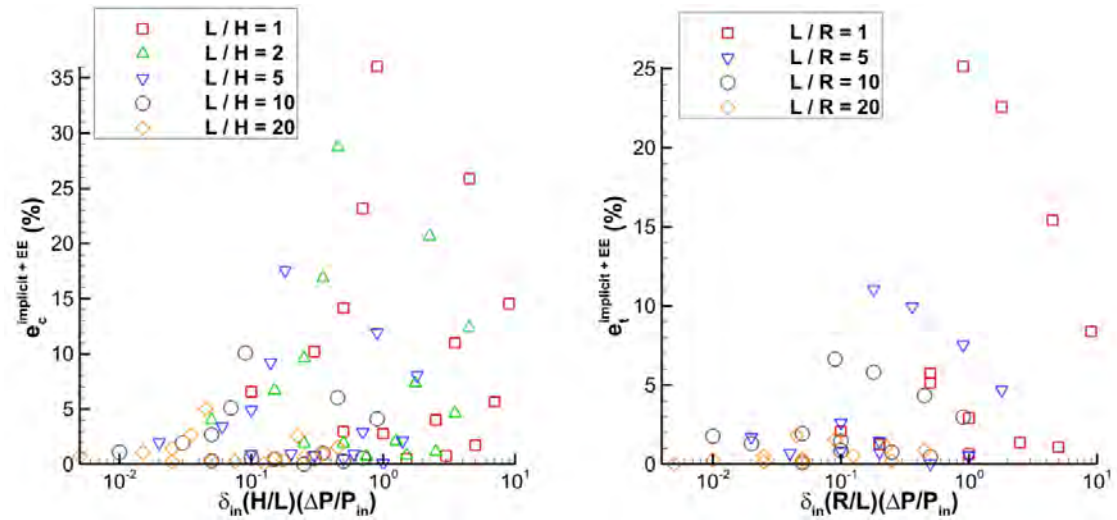


Figure 3.9 Relative difference (error) of the flow rates between the typical approach and the one with implicit boundary conditions plus the end effect correction in terms of $\delta_{in} (\chi/L) (\Delta P/P_{in})$ for the channel (left) and tube (right) flows.

Chapter 4

Marching DVM algorithm on unstructured meshes

4.1 Introduction

The Discrete Velocity Method (DVM) is probably the most prevailing deterministic computational methodology for the solution of the Boltzmann and kinetic model equations [53], [54]. In discrete velocity algorithms the continuous molecular velocity spectrum is replaced by a set of discrete velocities. The choice of the discrete velocities depends on the peculiarities and characteristics of each problem, although general rules can be developed. In steady-state flows an iteration scheme between the solution of the kinetic equations and the computed moments of the distribution function is introduced, until convergence is reached. Once the kinetic equations are discretized in the velocity space they are reduced to ordinary or partial differential equations, which are solved by finite difference or volume schemes, while the moments are obtained by numerical integration. The values of the distribution function in each iteration may be obtained either by solving a system of linear algebraic equations or alternatively using a marching scheme through the physical space for each discrete velocity. The latter methodology, compared to the former one, provides considerable computational benefits in both CPU time and memory requirements. However, so far, marching schemes have been adopted only on structured grids, where the proper marching from node to node may be easily specified via the node indexation.

In recent years several methodologies have been proposed in order to solve the kinetic equations on arbitrary geometries. In [145], a parallel solver for rarefied gas flows through porous media is developed, able to simulate geometries of arbitrary

complexity using a marching scheme. The grid however, is structured and the solution sequence is obtained directly from the node indexing. Flows with moving boundaries have been simulated using the DVM with Cartesian grids and the cut cell method has been applied to capture the irregularities of the boundaries [146]. Both approaches in [145] and [146] result in a “staircase” representation of the boundary when it is fitted to the grid lines. Furthermore, the recently introduced Unified Gas Kinetic scheme [147] and the open source `dugksFoam` code [148] available on the OpenFOAM platform, may be run on unstructured meshes. In addition, finite element approaches using the discontinuous Galerkin method have been applied [149]–[151] and three dimensional DVM solvers based on finite volume approaches, able to simulate geometries of arbitrary complexity with boundary fitted meshes [152]–[154], have been developed. In all cited works [147]–[154] however, the solution of large linear systems in each iteration is needed. It is clear that the extension of the DVM to arbitrary geometries is an active area of research.

Based on the above, in the present chapter of the dissertation, a marching DVM algorithm on unstructured grids is developed and implemented. The main concern is the identification of the proper marching path through the unstructured grid in order to properly compute for each discrete velocity the distribution function at some node in terms of the already computed distributions at the adjacent nodes. Obviously, following an erroneous path will result to the collapse of the algorithm. Furthermore, the proper path for each discrete molecular velocity may be different. Here, the calculation of the node sequence is achieved in two different ways. The first one is a backtracking algorithm, which may be considered as a special case of exhaustive (or brute force) algorithms [155]. This algorithm is robust but computationally intensive. The second one is based on purely geometrical arguments. It is computationally efficient but, as it will be shown, is not always conclusive. Overall, it is proposed to implement the geometrical methodology and only when it fails, to be replaced for the specific velocity by the backtracking algorithm. It is important to point out that always the marching path through the proper node sequence is obtained for each discrete velocity only once before the iterative procedure starts and remains the same during the iterative solution. Thus, the additional computational effort is small compared to the overall computational effort. In order to demonstrate the ability of the developed marching DVM algorithm on unstructured meshes to accurately solve the kinetic model equations, some two-dimensional rarefied gas flows are solved and the results are compared to corresponding ones available in the literature. The considered test

cases include fully developed flows and boundary driven configurations modeled using linear and non-linear kinetic model equations. Unstructured meshes are used in all cases, even if a structured mesh can be used.

The unstructured mesh geometry and the implemented numerical scheme to discretize the kinetic equation on unstructured grids are described in Section 4.2. The two methodologies, namely the backtracking and geometric algorithms, identifying the proper marching path through the mesh for each discrete velocity, along with a comparison between the two methodologies, are presented in Section 4.3. The structure of the developed marching DVM algorithm is given in Section 4.4. To demonstrate the validity and the effectiveness of the algorithm, benchmark results are obtained for fully developed flows, linear boundary driven flow in a cavity and nonlinear temperature driven flow in a cavity in Sections 4.5, 4.6 and 4.7 respectively. Finally, some concluding remarks are made in Section 4.8.

4.2 Unstructured mesh geometry and discretization scheme

Any steady nonlinear two-dimensional kinetic model equation, in the absence of external forces, may be written in a general form as

$$\xi_x \frac{\partial f}{\partial x} + \xi_y \frac{\partial f}{\partial y} = \frac{(f^{eq} - f)}{\tau}, \quad (4.1)$$

where (x, y) are the physical coordinates, (ξ_x, ξ_y) are the two-components of the molecular velocity vector, $f = f(x, y, \xi_x, \xi_y)$ is the velocity distribution function, f^{eq} is the equilibrium distribution function of the kinetic model and τ is the corresponding relaxation time. The kinetic equation is coupled with the moment of f providing the macroscopic quantities, which are present in the expression of f^{eq} . The solution of f is obtained in an iterative manner between the kinetic equation and the moment of f and is concluded when the macroscopic quantities are converged. Here, the aim is to discretize Eq.(4.1) in a way to be solvable by a marching DVM algorithm on an unstructured grid.

The molecular velocity space is transformed from Cartesian to polar coordinates, according to $\xi_x = \xi \cos \theta$ and $\xi_y = \xi \sin \theta$, where ξ is the magnitude and θ is the polar angle of the molecular velocity vector. Equation (4.1) is rewritten in the more

convenient form

$$\boldsymbol{\xi} \cdot \frac{\partial f}{\partial \mathbf{s}} = \frac{(f^{eq} - f)}{\tau}, \quad (4.2)$$

where $s = s(x, y, \theta)$ denotes the characteristic, passing from some point node (x, y) with polar angle θ .

Then, the molecular velocity space is discretized. The discrete values of the magnitude ξ_m , $m = 1, \dots, M$, are taken as the roots of a polynomial, usually the Legendre polynomial, accordingly mapped from $(-1, 1)$ to $(0, +\infty)$, while the discrete values of the polar angle θ_k , $k = 1, \dots, K$, are uniformly distributed in $[0, 2\pi]$. The polar representation of the molecular velocity space, as it will be shown, decreases the memory requirements and the computational overhead of the developed method. Also, using the roots of an orthogonal polynomial as the discrete values of the molecular velocity magnitude allows the application of Gaussian quadrature for the numerical calculation of the moments of the distribution function increasing numerical accuracy. For the integration with respect to the polar angle the trapezoidal rule is used.

The physical space is discretized by an unstructured mesh with $j = 1, \dots, N_E$ elements and $i = 1, \dots, N_N$ nodes with coordinates (x_i, y_i) . The nodes are divided into two sets, namely the interior nodes I and the boundary nodes B . Elements of any number of nodes may be introduced. For simplicity purposes, the methodology is presented assuming triangular grid elements. Extension to more complex elements is straightforward since any element can be represented using triangles and only a brief discussion for more complex elements is made in a later stage.

To clearly demonstrate the discretization process, consider, as shown in Figure 4.1, a tiny detail of the unstructured mesh consisting of some node i and all triangular elements having a common vertex, which happens to be the node i , as well as some molecular velocity vector $\xi = (\xi_m, \theta_k)$ having its origin at node i . The trace of $\boldsymbol{\xi}$, i.e., the half line that has the same slope θ_k as the molecular velocity vector and spans in the direction opposite to that of the molecular velocity vector, defines the characteristic along which information is propagated through the mesh to reach node i . The characteristic is indicated in Figure 4.1 with the dashed line. The triangular element in which the characteristic lies in, is the one between all elements having the common vertex i , which should be involved in the computation of the distribution function at node i with discrete molecular velocity $\xi = (\xi_m, \theta_k)$ based on the values of the corresponding distributions at the other two vertexes of this element. Obviously, different elements may be used, depending on the specific node $i = 1, \dots, N_N$ and polar angle $k = 1, \dots, K$ and they are specified as $E_{i,k}$, with the first and second indexes

referring to the node and the polar angle respectively. Similarly, the two vertexes of the each element defining the edge which is crossed by the characteristic, denoted by n_1 and n_2 in Figure 4.1, are also specified as $n_{1,i,k}$ and $n_{2,i,k}$. In addition, the distances between the crossing point C and the vertexes n_1 , n_2 and i , denoted by l_1 , l_2 and Δs in Figure 4.1, shall also be needed and they are specified in the general case with the same indexes, characterizing a specific node and polar angle, as $l_{1,i,k}$, $l_{2,i,k}$ and $\Delta s_{i,k}$. It is important to note that the nodes and elements which correspond to $n_{1,i,k}$, $n_{2,i,k}$ and $E_{i,k}$, as well as the distances which correspond to $l_{1,i,k}$, $l_{2,i,k}$ and $\Delta s_{i,k}$, are found only once well before the initiation of the iterative map and they are introduced as input data, which do not alter throughout the algorithm. Furthermore, the fact that these quantities depend only on the polar angle and not on the magnitude of the molecular velocity is the main reason of choosing a polar representation of the velocity space. Obviously, they should be specified in a proper way allowing the implementation of the marching DVM algorithm. This important issue is addressed in the next section, while now the discretization scheme is described.

Equation (4.2) is discretized in the molecular velocity space and the resulting system of ordinary differential equations is approximated by finite differencing at the midpoint of the characteristic line segment inside the element. In Figure 4.1, the midpoint is denoted by D and the discrete form of the equation is

$$\xi_m \frac{f_{i,m,k} - f_{C,m,k}}{\Delta s_{i,k}} = \frac{f_{D,m,k}^{eq} - f_{D,m,k}}{\tau_{D,m,k}}, \quad (4.3)$$

with $i = 1, \dots, N_N$, $m = 1, \dots, M$ and $k = 1, \dots, K$. The discretized distributions $f_{D,m,k}$ and $f_{D,m,k}^{eq}$, as well as the discrete relaxation time $\tau_{D,m,k}$, all at point D, are averaged using the corresponding values at adjacent grid point i and point C as

$$f_{D,m,k}^{eq} = (f_{i,m,k}^{eq} + f_{C,m,k}^{eq}) / 2, \quad (4.4)$$

$$f_{D,m,k} = (f_{i,m,k} + f_{C,m,k}) / 2 \quad (4.5)$$

and

$$\tau_{D,m,k} = (\tau_{i,m,k} + \tau_{C,m,k}) / 2. \quad (4.6)$$

Substituting Eqs. (4.4), (4.5) and (4.6) into Eq. (4.3), yields

$$f_{i,m,k} = \frac{f_{i,m,k}^{eq} + f_{C,m,k}^{eq} + f_{C,m,k} \left(-1 + \frac{\xi_m}{\Delta s_{i,k}} (\tau_{i,m,k} + \tau_{C,m,k}) \right)}{1 + \frac{\xi_m}{\Delta s_{i,k}} (\tau_{i,m,k} + \tau_{C,m,k})}, \quad (4.7)$$

where the distribution functions and the relaxation time at point C are obtained as a linear interpolation of the corresponding values at nodes n_1 and n_2 according to

$$f_{C,m,k} = (f_{n_1,m,k}l_{2,i,k} + f_{n_2,m,k}l_{1,i,k}) / (l_{1,i,k} + l_{2,i,k}), \quad (4.8)$$

$$f_{C,m,k}^{eq} = (f_{n_1,m,k}^{eq}l_{2,i,k} + f_{n_2,m,k}^{eq}l_{1,i,k}) / (l_{1,i,k} + l_{2,i,k}) \quad (4.9)$$

and

$$\tau_{C,m,k} = (\tau_{n_1,m,k}l_{2,i,k} + \tau_{n_2,m,k}l_{1,i,k}) / (l_{1,i,k} + l_{2,i,k}). \quad (4.10)$$

Equation (4.7) with the associated expressions (4.8), (4.9) and (4.10) may be used in each iteration to march through the mesh and compute the discrete distribution function $f_{i,m,k}$, provided that the corresponding distributions $f_{n_1,m,k}$ and $f_{n_2,m,k}$ have already been computed, the equilibrium distributions are known from the previous iteration and of course all distances have been estimated.

The key issue is the prompt computation of $f_{n_1,m,k}$ and $f_{n_2,m,k}$, which must be available in order to realize the marching expression (4.7) and this is achieved by identifying the proper node path. The sequence, according to which the nodes must be considered, depends on the polar angle of the molecular velocity and is independent of the molecular velocity magnitude. Two methodologies are proposed in the next section. The discretization scheme presented here for the nonlinear form of kinetic model equations, is applicable in a straightforward manner to linearized kinetic equations simulating linear and fully developed flows. This is easily seen since in all cases the streaming part of the kinetic equations remains the same.

4.3 Identification of the marching path in unstructured grids

Two methodologies are proposed in order to identify the correct marching path through unstructured meshes. The first one is called the backtracking approach and it is an exhaustive type algorithm. The second one is called the geometrical approach and it is a generic and intuitive approach based on simple geometrical arguments.

In both methodologies some information about the boundary nodes group, denoted as B , is needed. For each polar angle θ_k , the boundary nodes group is divided into two subgroups. One subgroup includes only the boundary nodes with outgoing distributions and the other group the remaining boundary nodes with purely incoming distributions.

If e_i is the unit normal vector on some boundary node i , facing towards the inside of the computational domain, while e_k is the unit normal vector in the direction of the molecular velocity for polar angle θ_k , then the group of boundary nodes with outgoing distributions is $B_k^+ : [i \in B \cap e_i \cdot e_k > 0]$, while the group with incoming distributions is $B_k^- : [i \in B \cap e_i \cdot e_k < 0]$. The identification of the two groups of boundary nodes for each polar angle θ_k is done before the initialization of the iterative map. Next, the two developed methodologies able to obtain the proper solution sequence are described. This sequence is denoted as $O_k(n)$ indicating the n -th node to be considered for the polar angle θ_k .

4.3.1 Backtracking algorithm

The backtracking algorithms are considered as a special case of the exhaustive or brute force algorithms. An exhaustive algorithm will identify the desired one by going through the whole set of possible solutions. When the solution must satisfy a criterion and it is possible to check if the criterion is violated without obtaining the whole solution, then backtracking algorithms can be applied. A backtracking algorithm, incrementally builds candidates to the solution and will abandon a candidate (backtrack), if the candidate in question, will give a solution violating the criterion.

The reasoning behind these algorithms can be explained using the famous puzzle with the eight queens. The objective of this puzzle is to place eight chess queen pieces on a chessboard so that no queen threatens any other. If an exhaustive algorithm is used, all the possible arrangements, which are 4.426.165.368, are identified one by one, until a solution satisfying the imposed criterion is obtained. A backtracking algorithm, at some stage of the solution, will place a queen at an empty square and if this queen threatens any other, i.e., violates the criterion, it will be removed from this square (backtracking) and will be placed on a different square. The criterion is checked again and the procedure is repeated until a valid solution is obtained.

A backtracking algorithm is used in order to find the solution sequence $O_k(n)$. A flowchart of this method is shown in Figure 4.2. The N_k^{BC} nodes that belong to B_k^+ are placed in the first N_k^{BC} positions of the O_k array. The rest $(N_N - N_k^{BC})$ nodes of the computational grid that are unsorted and have not been yet added in O_k , are placed into an array (AN). The number of sorted nodes is initialized as $NS = N_k^{BC}$ and then, the next node ($NS = NS + 1$) to be placed in the next empty position of the solution sequence array $O_k(NS)$ is sought. In order to find this node, all the nodes of the unsorted nodes array (AN) are examined until a node i is found that is connected to

the two nodes needed to propagate the distribution, namely the $n_{1,i,k}$ and $n_{2,i,k}$ nodes, which already have been placed in the O_k array. Once such a node is found, it is placed in the solution sequence array ($O_k(NS) = i$) and is removed from the AN array. It is noted that a lookup table is constructed indicating if a node had been already placed in the O_k array and this table is used when checking if a node is already in the array. The procedure is repeated until all the N_N positions of O_k are filled and of course it is applied for each discrete angle θ_k . The number of operations required by this method scales quadratically with the number of physical nodes and linearly with the number of discrete angles.

The backtracking algorithm is robust and will always provide a correct solution sequence, even when the mesh is of bad quality. Also, since the method is not directly affected by the mesh geometry, elements of any kind are handled in the same manner. Its only drawback is that it is computationally intensive.

4.3.2 Geometrical algorithm

Consider the coordinate system (x, y) with its origin O , a two dimensional arbitrary computational domain Ω and a circle with its center in O , enclosing the whole computational domain Ω , as shown in Figure 4.3. The unstructured mesh of Ω consists of acute triangular elements. Consider next, some molecular velocity vector ξ with arbitrary polar angle θ_k . A line ε normal to the molecular velocity vector and tangent to the circle is drawn. There are two such lines. The one which is sweeping through the computational domain Ω , as it is moving in the direction of the molecular velocity direction, is chosen. Both the velocity vector ξ and the line ε are also shown in Figure 4.3.

It is argued that as line ε is sweeping the computational domain and reaching at some arbitrary node i , the propagation of the distribution function with polar angle θ_k to this node, based on the marching expression (4.7), is feasible and may be realized. This implies that line ε has already scanned nodes $n_{1,i,k}$, $n_{2,i,k}$ and the corresponding distributions at these two nodes have been computed. Therefore, the n -th node encountered by line ε , will be the n -th node to be solved for the current value of θ_k . To further demonstrate and prove that based on this methodology a node path allowing the consistent propagation of the distribution function through the mesh for each polar angle may be identified, the following arguments are made:

1. Line ε sweeps through the mesh, in the direction of some velocity ξ with arbitrary polar angle θ_k and reaches an arbitrary node i .
2. All nodes behind the line, in the direction opposite of the molecular velocity, have been scanned and have known distributions.
3. The distribution functions with polar angle θ_k at node i are computed based on the known corresponding distributions at two nodes which are behind line ε .
4. The first two nodes swept by line ε belong in the boundary subgroup of nodes B_k^+ and their outgoing distributions with polar angle θ_k are known.

Argument 1, simply refers to the position of line ε with regard to node i . Arguments 2-3 ensure the proper computation sequence of the distribution function through the mesh following a compatible node path. Finally, argument 4 ensures the proper initialization via the given outgoing distributions at the boundaries.

To prove arguments 2 and 3 consider, in Figure 4.4, an acute triangular element with vertices i , n_1 and n_2 , containing the characteristic (dashed) line of molecular velocity $\xi = (\xi_m, \theta_k)$ and the line ε normal to ξ passing through node i . The objective is to prove that both n_1 and n_2 are behind line ε . Obviously, since the characteristic has the same slope as ξ , it is also normal to line ε sweeping the mesh. The characteristic divides the space into two half spaces, with each of the nodes n_1 and n_2 being at different half spaces. If both were at the same half space the characteristic would be outside the element. Furthermore, for the same reasoning, at least one of the two nodes has to be behind line ε . Without loss of generality it is assumed that n_2 is behind line ε , while n_1 can be in either side of it. The angle α at node i is divided into two angles α_1 and α_2 , as shown in Figure 4.4. Since the characteristic and line ε are normal to each other, in order of n_1 to be in front of line ε , angle α_1 should be obtuse ($\alpha_1 > \pi/2$), which is not, since a triangle with acute angles is considered. As a result both n_1 and n_2 are behind line ε .

To prove argument 4 consider, in Figure 4.5, the acute triangular element ABC . Without loss of generality it is assumed that nodes A and B belong in the group of boundary nodes B , with A being the first boundary node swept by line ε , which always is normal to ξ and moves in its direction. The objectives are to prove that A and B belong in the subgroup of boundary nodes with outgoing distributions (B_k^+) and that B is swept by line ε before C . The unit vector e_i at node A pointing towards the flow domain has the same direction with ξ , because there is no flow domain behind

line ε and therefore, $\boldsymbol{\xi} \cdot \mathbf{n}_1 > 0$, which is the condition proving that a boundary node belongs in the subgroup B_k^+ . Similarly, it is proven that B also belongs in B_k^+ . Then, it is shown that since angle $ACB < \pi/2$, line ε reaches B before reaching C , i.e., that the distance $d_{BB'}$ of node B from ε is smaller than the corresponding distance $d_{CC'}$ ($d_{BB'} < d_{CC'}$). In order to be the other way around, i.e., $d_{CC'} < d_{BB'}$, node C should be located between lines ε and ε' , where ε' is parallel to ε and goes through node B . In the limiting case $d_{CC'} = d_{BB'}$, the node C is on line ε' and this auxiliary node is denoted as C_1 . The quadrangle $C_1' C_1 B B'$ is a rectangle with its angle $C_1' C_1 B = \pi/2$. Two cases are distinguished: a) Node A is not between points C_1' and B' (shown in Figure 4.5). Then, angle $AC_1 B > \pi/2$, which cannot happen since the triangle is acute; b) Node A is between points C_1' and B' . Then, $C_1 C_1'$, which is the characteristic going through C_1 lies outside of the triangular element and another element should be considered. Thus, node C_1 cannot be on line ε' . Also, if node C_1 is moved closer to AB' , then it follows from simple trigonometry that the angle $AC_1 B$ will be further increased. In conclusion, the distance of node C_1 is smaller than the distance of B from line ε , only when the triangle is obtuse, which is not. As a result node B will be swept before C .

Based on the above it is shown that the proposed methodology based on purely geometrical principles may constitute a suitable node path to march through the unstructured mesh. The methodology of finding a consistent node marching through the mesh has been presented for some molecular velocity vector $\boldsymbol{\xi}$ with arbitrary polar angle θ_k and it may be generalized to any polar angle. To implement the methodology the following simple steps for each value of θ_k are taken:

1. Define line ε .
2. Calculate the distance of each node from line ε .
3. Sort the nodes in ascending order with regard to their distance from line ε .

Sorting the nodes based on their distance from line ε is equivalent to considering the solution sequence $O_k(n)$ according to which line ε sweeps the nodes as it moves through the mesh. This is much more practical in the application of the algorithm. Of course sorting can be a time consuming process, especially when the number of items to be sorted is large. In the present approach the number of items to be sorted is equal to the number of nodes. Furthermore, sorting is required for each discrete polar angle. Since consecutive values of discrete polar angle θ_k are very close to each

other, the solution sequence for some polar angle θ_k is expected to be close to that of the next angle θ_{k+1} . For this reason the sorting starts placing the distances for θ_{k+1} according to the sequence $O_k(n)$ of θ_k . This way the array is nearly sorted with only few elements out of order and the computational cost of sorting is drastically decreased. Using the modified Bubble sort algorithm for a nearly sorted array, the number of operations required scales linearly with the number of items to be sorted. In the current case the number of operations is a linear function of the number of nodes $O(N_N)$. For the first polar angle θ_1 where the distances are roughly in random order, a more efficient algorithm, such as the Quick sort can be used. Although in the current implementation the modified Bubble sort is applied even for the first angle. In any case as it is shown in the next subsection increasing the number of discrete angles does not have a considerable effect on the computational time required by this method.

The main restriction of the proposed geometrical methodology is the assumption of acute triangular mesh elements. In case of obtuse triangles the geometrical approach may fail to identify the proper node path. Consider an obtuse triangular element, as shown in Figure 4.6, along with the characteristic (dashed) line and the line normal to the molecular velocity vector crossing node i . It is readily seen that when $\alpha > \pi/2$, while both nodes n_1 and n_2 must be behind line ε , it happens that only n_2 is behind line ε . This situation may only arise if obtuse elements exist and even then, it will not always be the case, but it may occur. In practice, a triangular mesh is considered of high quality when the elements are equilateral. Having obtuse triangles is undesirable and thus in most mesh generators they are omitted or limited in a very small number of elements compared to the total one. In any case the proper way to implement the geometrical approach is to check for obtuse elements and if needed use for this specific polar angle θ_k the backtracking algorithm.

All arguments made above consider triangular elements. Extension to more general elements is straightforward, as always two nodes will be used for the distribution propagation, resulting to the same arguments. In cases where more general elements are used however, obtuse angles are much more commonly present and the backtracking algorithm can be proved superior.

4.3.3 Comparison between the backtracking and geometrical algorithms

The two developed methodologies are compared in terms of the computational time required to find the solution sequence. The CPU times are shown in Table 4.1 for various values of the number of discrete angles and number of physical nodes. For both methodologies the required computational time scales with the square of the number of physical nodes. However, the computational time with respect to the number of discrete polar angles scales linearly for the backtracking algorithm, while it is almost unaffected for the geometrical method. This big advantage which makes the geometrical method much faster, particularly, in dense velocity grids, is contributed to the sorting approach, where the sequence array is initialized as nearly sorted for all angles after the first one.

It is noted that the comparison between the two algorithms is based on acute triangular elements. This is an advantage for the purely geometrical method since there has been no need to look up for the combined approach, which would increase the time required for the geometrical method. Finally, it is worth mentioning that the computational time required for the calculation of the solution sequence, even for the backtracking algorithm, is relatively small compared to the total simulation time to solve the kinetic equations.

In general, it is proposed to define the node marching path based on the geometrical method and apply the backtracking algorithm only when the former one provides an erroneous sequence.

4.4 Structure of the marching DVM algorithm

The main structure of the code is presented, in a flow chart, in Figure 4.7. Following the initialization step, an iterative scheme is used for the solution of the kinetic equations. More specifically, the old values of the macroscopic quantities are stored and the solution procedure is carried out for each value of the molecular velocity in order to update the values of the distribution function. Then, the updated distribution is integrated in order to update the values of the macroscopic quantities and boundary condition parameters for the next iteration. These steps are repeated upon convergence of the macroscopic quantities.

As it is seen the overall methodology remains the same as in the case of structured grids. The main difference exists in the initiation step where the detailed geometry of the unstructured grid along with the marching node path are specified. The proposed marching DVM algorithm is realized using an object oriented programming (OOP) approach in Fortran 2008. The mesh information is consisting of the node coordinates, the element information and more specifically the number and ID of the nodes that form each element, as well as the group of nodes that form the boundary of the computational domain. They are all provided as input to the code through an I-DEAS Universal file (UNV file). These files are plain text files and are supported by a variety of mesh generators. In all cases where the developed code is used in the present dissertation, the SALOME mesh tool is used. A view of the initialization step is given in the flowchart shown in Figure 4.8.

Thus, in the initialization step the mesh information and simulation parameters provided to the code and the data structure storing the mesh information are also formed. The data required for the solution procedure, such as the boundary nodes B_k^\pm , the nodes $n_{1,i,k}$, $n_{2,i,k}$, the lengths $l_{1,i,k}$, $l_{2,i,k}$ and $\Delta s_{i,k}$ including the consistent marching path through the unstructured mesh for each node and polar angle are all specified. Furthermore, in order to decrease the computational load of each iteration, any weighting factors or parameters used throughout the simulation are also pre-calculated and stored. At each iteration, the solution starts by applying the boundary conditions to all nodes belonging in B_k^+ and the equilibrium distributions are calculated. Then, following the solution sequence obtained during the initialization step, the distribution is propagated to each node based on Eq. (4.7) using all pre-calculated geometric and mesh parameters.

These calculations in the initialization step obviously pose a computational overhead to the overall computational effort, which does not exist in tailor made codes for specific geometries, where most of the introduced data, including the marching path, are trivially found through the node indexing. However, this extra effort is done only once and the involved computational time is small compared to the computational time required for all kinetic simulations, which are needed in order to completely investigate the flow problem under consideration, in terms of all involved geometrical and operational parameters.

To demonstrate the effectiveness of the marching DVM algorithm in unstructured grids, the pressure driven flow around UTH (initials of University of Thessaly) is simulated and velocity streamlines are plotted in Figure 4.9. A block structured

quadrilateral mesh has been used, with some triangular elements utilized to connect the different blocks. A detail of the mesh around the lower part of the letter U is shown in Figure 4.10.

4.5 Test case I: Fully developed flows in channels with circular, ellipsoidal and Sierpinski carpet cross sections

Fully developed flows through long capillaries are considered based on the proposed algorithm and the computed results are compared with existing ones. Three different configurations are examined, namely a) the pressure and temperature driven flow through a tube of elliptical cross section, b) the pressure driven flow through a circular tube with partial wall accommodation and c) the pressure driven flow through capillaries of Sierpinski carpet cross sections of various levels. The kinetic formulation of fully developed flows, which is implemented in the present test cases, is given for completeness purposes in Appendix B1.

The fully developed ellipsoidal tube configuration is examined in [156] and modeling is based on the linear Shakhov model. In [156] several ellipses are considered. Here, the comparison is performed for one geometry, more specifically for an ellipse of aspect ratio equal to 2 and for values of the gas rarefaction parameter $\delta \in [0, 20]$.

The fully developed circular tube flow configuration is based on the linear BGK model and results are reported in [23]. For this case three values of the accommodation coefficient are considered, namely $\alpha = 0.8, 0.9$ and 1 and for values of the gas rarefaction parameter $\delta \in [10^{-2}, 10]$.

The fully developed flow through capillaries of Sierpinski carpets cross sections is considered in [61] on the basis of the linearized Boltzmann equation. Here, the linearized BGK model is used. Concerning the Sierpinski carpet, the first three levels along with the degenerate level 0 are shown in Figure 4.11. Starting from a square (or level 0), the domain is divided into 9 squares using a 3×3 grid and the central square is removed in order to obtain the level 1. For each subsequent level, the remaining squares of the grid constructed in the previous level are divided each with a 3×3 grid and again each central square is removed. The levels 0-3 are considered for values of the gas rarefaction parameter $\delta \in [0, 150]$.

In all cases the rarefaction parameter is defined as

$$\delta = \frac{PL}{\mu v_0}, \quad (4.11)$$

with P , μ and v_0 denoting the pressure, viscosity and most probable molecular speed at reference conditions. The reference length L for the circular tube is the radius, for the ellipsoidal tube is the length of the semi-minor axis and for the Sierpinski carpets the side length of the largest square. Unstructured mesh consisting of triangular elements is always used. Parts of the meshes of the cross sections of the ellipsoidal tube, the circular tube and the Sierpinski carpets tube are shown in Figures 4.12, 4.13 and 4.14 respectively.

The comparison is based on the calculated reduced flow rates for the pressure (G_P) and temperature (G_T) driven flows defined as

$$G_P = -\frac{1}{A} \int_{R^2} u_{z,P} dA \quad (4.12)$$

and

$$G_T = \frac{1}{A} \int_{R^2} u_{z,T} dA, \quad (4.13)$$

where A is the dimensionless cross section area. This comparison is presented in Table 4.2 for the elliptical tube and in Table 4.3 for the circular tube. The relative difference is less than or close to 1% for all cases considered. The comparison between the present results and the results of [61] for the flows through Sierpinski carpets is shown in Figure 4.15. The results are in good agreement, with some discrepancies at large values of δ for the level 0 carpet, that are attributed to the mesh size.

In Figure 4.15 the results obtained from the solution of the Stokes equation with slip boundary conditions are also shown. The solution is performed on the same mesh, using a recently developed in-house unstructured finite volume code. It is interesting that for the level zero carpet the slip solution is close to the kinetic one for $\delta > 50$, while for levels 1, 2 and 3 the slip solution becomes valid for much larger values of δ . This is because δ is defined using the length of the largest side, but for the levels different than 0, the flow has smaller scales due to the smaller squares inside the flow domain. This fact should be carefully considered when simulating fractal geometries and porous media and indicates that a kinetic approach should be preferred, even at relatively high values of the reference rarefaction parameter.

4.6 Test case II: Linear lid driven cavity flow

The linear lid driven cavity flow is next considered. A monatomic rarefied gas is confined in a square enclosure with three stationary walls and one wall moving along its axis with velocity $U_W \ll v_0$. The linear BGK model is used and the small parameter for the linearization is defined as $\varepsilon = U_W/v_0$. This configuration has been studied in [157]. Due to the wall motion a main vortex is formed with its center along the vertical centerline of the cavity. A part of the mesh used is shown in Figure 4.16. The rarefaction parameter is defined using the side length of the cavity as a reference length.

A comparison is performed for values of the rarefaction parameter $\delta \in [10^{-3}, 10]$, based on three quantities of interest, mainly the drag coefficient of the moving wall, the location of the center of the vortex along the vertical axis and the flow rate between the center of the vortex and the moving wall. All quantities are reported in [157]. The flow rate between the center of the main vortex and the top wall is given by

$$M = 2 \int_{y_{loc}}^1 u_x(1/2, y) dy, \quad (4.14)$$

where y_{loc} is the location along the vertical axis of the center of the main vortex and the drag coefficient of the moving wall is given by

$$D = -2 \int_0^1 p_{xy}(x, 1) dx. \quad (4.15)$$

The values of the flow rate between the center of the vortex and the moving wall, for the different values of the rarefaction parameter are shown in Table 4.4. The mass flow rate is almost constant for small values of δ and is steadily increased as δ increases beyond the transition regime. The drag coefficient in terms of the rarefaction parameter is shown in Table 4.5, with its values decreasing as δ increases. Table 4.6 shows the location along the vertical axis of the center of the main vortex, which is squeezed towards the moving wall as δ increases. The present results are in very good agreement with corresponding one in [157].

Velocity streamlines and vertical velocity contours are shown in Figure 4.18 for $\delta = 0.1, 1, 5$ and 10 . The characteristics of the flow are in good agreement with the ones shown in [157]. The vertical velocity component is anti-symmetrical with respect to the centerline of the cavity and although the number of physical nodes used is

around 16000, the contours are smooth and no ray effect from the discontinuity of the boundary conditions is produced. It is noted, that for the values of the rarefaction parameter considered only the main vortex is formed, and secondary vortices will appear at the bottom corners moving further into the slip regime.

4.7 Test case III: Nonlinear thermally driven cavity flow

The thermally driven flow in a cavity with the bottom and top walls kept at different but constant temperatures and a linear temperature distribution imposed along the lateral walls is considered. This setup is studied in Section 6.2 of the present dissertation [158], where the detailed kinetic formulation and solution are presented. Here, only a comparison between the present results obtained with an unstructured mesh with the corresponding ones in Section 6.2 obtained with a structured grid is made.

The nonlinear Shakhov kinetic model is applied, assuming hard sphere molecules and purely diffuse boundary conditions. The configuration is characterized by the reference Knudsen number

$$Kn_0 = \frac{\sqrt{\pi}\mu v_0}{2P_0H} \quad (4.16)$$

and the ratio of the hot over the cold wall temperatures, T_C/T_H . A comparison is performed for reference Knudsen number $Kn_0 = 0.1, 1$ and 10 and temperature ratio $T_C/T_H = 0.1, 0.5$ and 0.9 . A part of the mesh used is shown in Figure 4.17. The heat flux departing from the bottom (heated) wall of the cavity is used for the comparison, which is defined as

$$Q_{out} = \int_0^1 q_y(x, 0) dx. \quad (4.17)$$

The values of the heat flux in terms of the reference Knudsen number and the temperature ratio are presented in Table 4.7 and they are in very good agreement with the ones in [158].

Velocity streamlines and temperature contours have been also computed for $Kn_0 = 0.1, 1, 10$ and $T_C/T_H = 0.1, 0.5, 0.9$. The temperature distribution is relatively simple, with a stratified temperature profile observed in all cases, while the flow structure however is more complicated. There is always an excellent agreement with

the corresponding contours presented and further analyzed in Chapter 6 (see Figures 6.2 and 6.3) [158].

4.8 Concluding remarks

The DVM has been proven to be, over the years, the most general and reliable deterministic numerical method for the solution of the Boltzmann and kinetic model equations. It has been applied with considerable success in both structured and unstructured meshes. However, in most available solvers the implementation of the method requires the solution of large algebraic systems. It is stressed out that in kinetic modeling, discretization is performed in the physical and molecular velocity spaces.

An alternative computationally efficient methodology has been applied to compute the distribution function via a marching scheme without requiring the implementation of time consuming solvers of huge linear algebraic systems. However, this scheme has been limited so far only on structured meshes, while there is a demand for unstructured meshes in order to simulate devices and apparatus with complex geometries.

Here, two methodologies are developed to solve kinetic equations based on the marching approach on unstructured meshes. Always the key issue is the specification of a consistent marching node path through the mesh allowing the computation of the distribution function in the direction of each discrete velocity. One methodology is the backtracking approach, which it is an exhaustive type algorithm and the other one is the geometrical approach, which is a generic and intuitive approach based on simple geometrical arguments. The latter one is computationally very efficient but in some cases, when the mesh in the physical space contains elements with obtuse angles, may deduce an erroneous marching path. The former one is robust but computationally more intensive.

It is proposed to use both approaches starting with the geometrical method and apply the backtracking approach, only when the former one fails. A marching DVM code on unstructured meshes has been developed to implement the proposed algorithm and it has been successfully benchmarked in several rarefied gas flows and heat transfer configurations in convex and non-convex computational domains. The test cases include fully developed flows through capillaries of circular, ellipsoidal and fractal geometry cross sections, as well as linear and nonlinear lid driven and temperature driven flows in cavities.

The developed marching DVM algorithm on unstructured meshes has a lot of potential and opens new possibilities of deterministic kinetic modeling in complex geometries. Future work includes the extension of the code to three dimensional flows as well as the application of higher order schemes for the solution propagation in the physical space to allow accurate simulations with a smaller number of nodes.

Table 4.1 Time (sec) required to find the marching node path by the backtracking (BTA) and geometrical (GM) schemes for various numbers of velocity polar angles and physical nodes

Number of physical nodes	Number of polar angles									
	40		80		120		160		200	
	BTA	GM	BTA	GM	BTA	GM	BTA	GM	BTA	GM
8140	3.88	3.34	9.03	3.38	15.14	3.40	20.8	3.42	27.21	3.43
16128	14.14	13.18	37.35	13.39	68.86	13.42	95.09	13.48	126.4	13.48
32283	68.16	52.5	157.1	53.12	261.0	53.34	361.2	54.57	468.7	55.94
65576	352.4	216.7	733.8	219.1	1248	220.0	1689	220.3	2293	220.7

Table 4.2 Flow rates G_P and G_T for various values of δ for flow through an elliptical tube.

δ	G_P		G_T	
	Ref. [156]	Present	Ref. [156]	Present
0	2.0655	2.0612	1.0327	1.0306
0.01	2.016	2.0110	0.9770	0.974
0.1	1.9015	1.8978	0.8081	0.8066
1	2.0323	2.0273	0.4676	0.4667
5	3.4901	3.4619	0.1856	0.1848
10	5.4423	5.4060	0.1044	0.1044
20	9.41	9.2961	0.05528	0.05500

Table 4.3 Flow rate G_P for various values of δ and accommodation coefficient α for flow through a circular tube.

δ	$\alpha = 0.8$		$\alpha = 0.9$		$\alpha = 1$	
	Ref. [23]	Present	Ref. [23]	Present	Ref. [23]	Present
0.01	2.187	2.171	1.791	1.788	1.477	1.474
0.1	1.992	1.987	1.668	1.667	1.404	1.399
1	1.93	1.924	1.668	1.664	1.459	1.454
5	2.803	2.787	2.548	2.536	2.358	2.333
10	4.019	3.981	3.761	3.731	3.582	3.547

Table 4.4 Flow rate M between the center of the vortex and the moving plate of a lid driven cavity for various values of δ .

δ	0.001	0.01	0.1	1	5	10
Ref. [157]	9.7(-2)	9.7(-2)	9.7(-2)	1.0(-1)	1.3(-1)	1.4(-1)
Present	9.6(-2)	9.6(-2)	9.7(-2)	1.0(-1)	1.3(-1)	1.4(-1)

Table 4.5 Drag coefficient D of the moving plate of a lid driven cavity for various values of δ .

δ	0.001	0.01	0.1	1	5	10
Ref. [157]	0.69	0.68	0.68	0.63	0.51	0.42
Present	0.68	0.68	0.67	0.63	0.50	0.41

Table 4.6 Location of the center of the vortex y_{loc} in a lid driven cavity for various values of δ .

δ	0.001	0.01	0.1	1	5	10
Ref. [157]	0.69	0.69	0.69	0.7	0.73	0.74
Present	0.68	0.68	0.68	0.7	0.73	0.74

Table 4.7 Heat flux departing from the bottom plate Q_{out} of a cavity with non-isothermal walls for $T_C/T_H = 0.1, 0.5, 0.9$ and $Kn_0 = 0.1, 1, 10$.

Kn_0	$T_C/T_H = 0.1$		$T_C/T_H = 0.5$		$T_C/T_H = 0.9$	
	Ref. [158]	Present	Ref. [158]	Present	Ref. [158]	Present
0.1	7.20(-2)	6.98(-2)	5.18(-2)	5.16(-2)	1.19(-2)	1.19(-2)
1	1.47(-1)	1.47(-1)	1.23(-1)	1.23(-1)	2.88(-2)	2.87(-2)
10	1.78(-1)	1.78(-1)	1.50(-1)	1.49(-1)	3.47(-2)	3.46(-2)

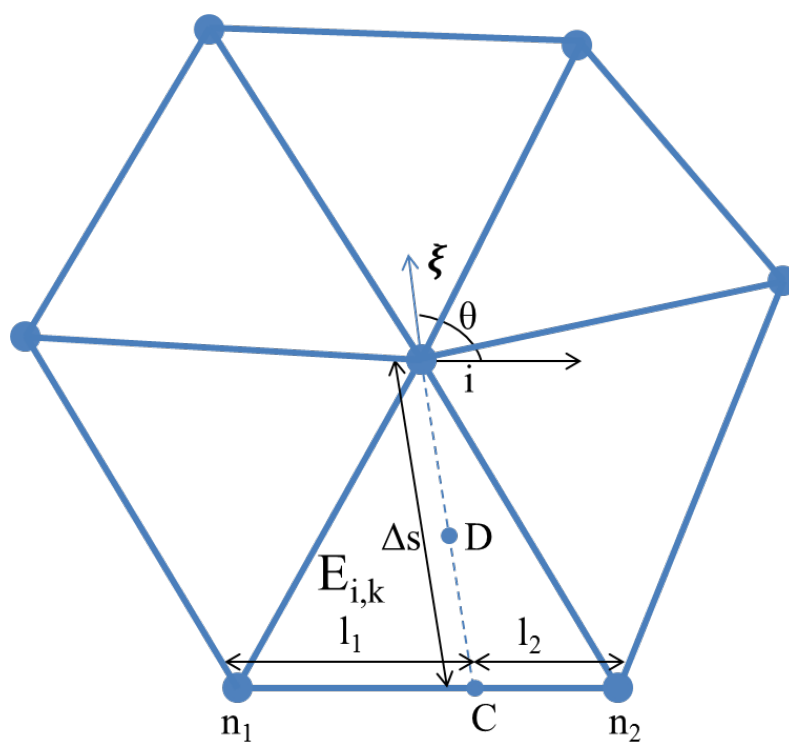


Figure 4.1 Detail of the unstructured mesh with some elements having a common node (i) and a molecular velocity vector ξ with its origin at node i .

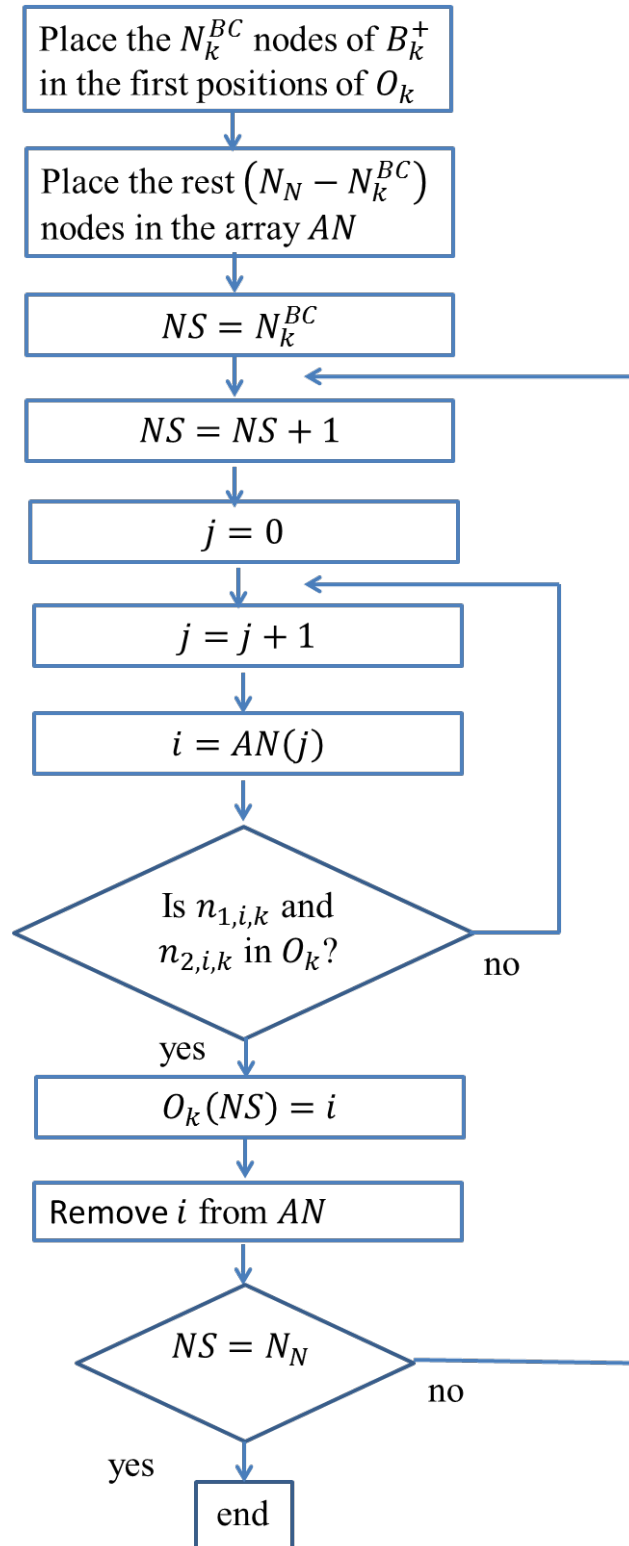


Figure 4.2 Flowchart of the backtracking algorithm for the solution sequence.

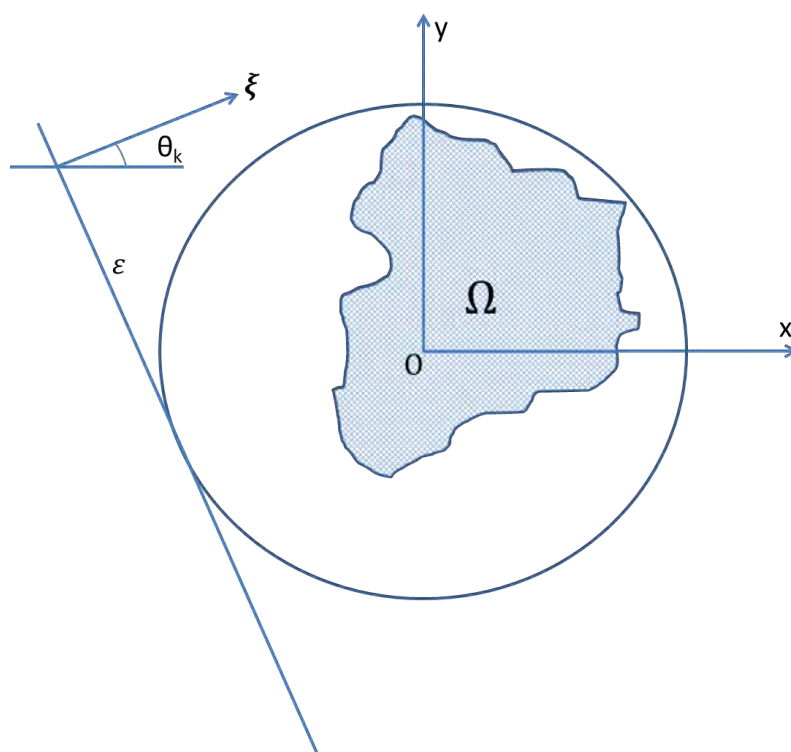


Figure 4.3 Arbitrary computational domain, along with a bounding circle and a tangent line.

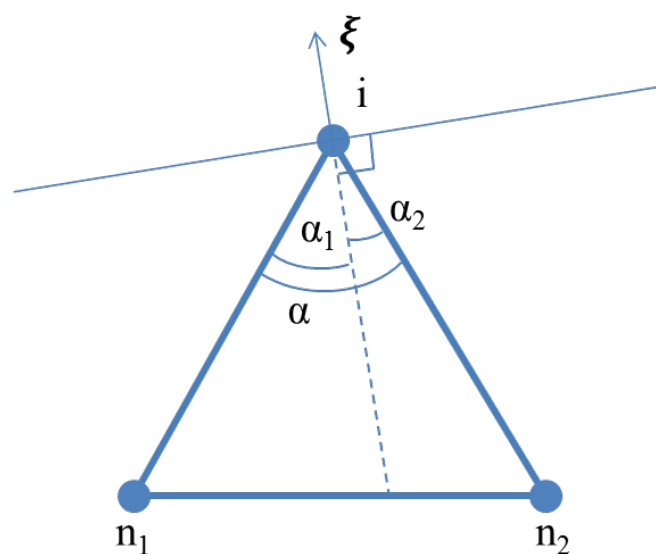
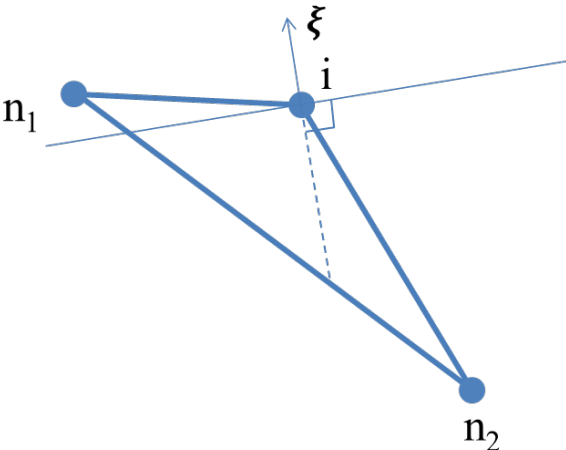
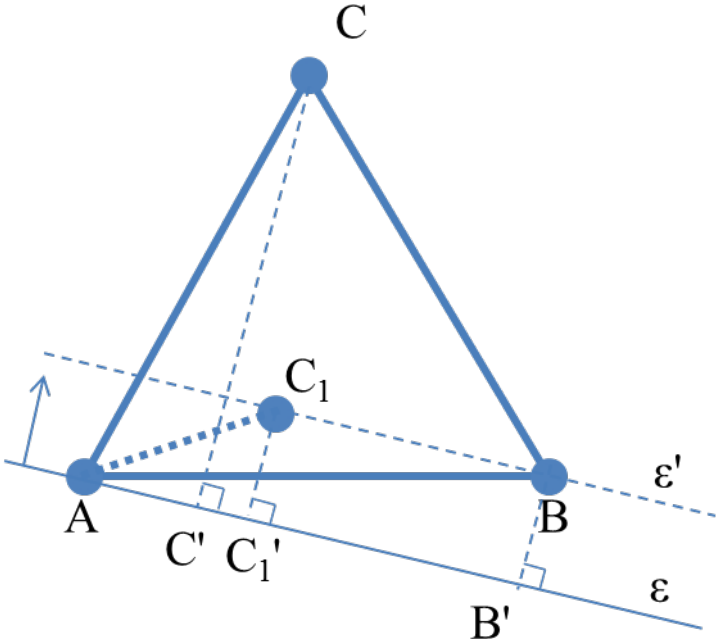


Figure 4.4 Acute triangular element with the characteristic line and a line normal to the molecular velocity vector.



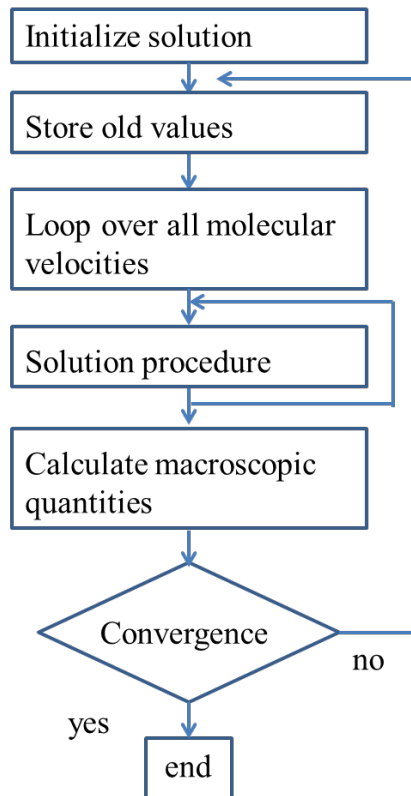


Figure 4.7 Flow chart of the main steps of the marching DVM algorithm.

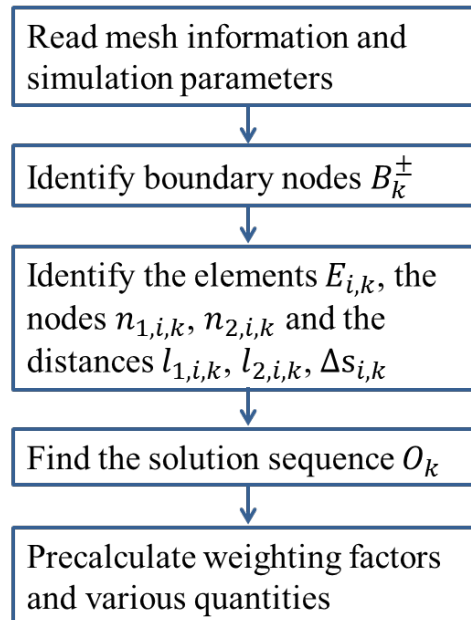


Figure 4.8 Flow chart of the initialization step in a marching DVM algorithm.

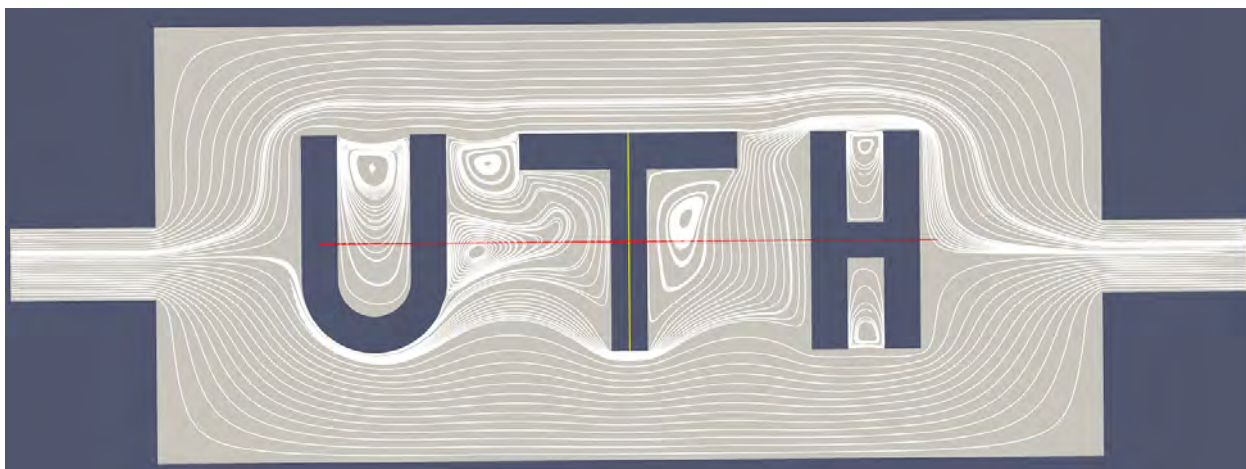


Figure 4.9 Velocity streamlines for a flow around the letters UTH based on the marching DVM algorithm on unstructured meshes.

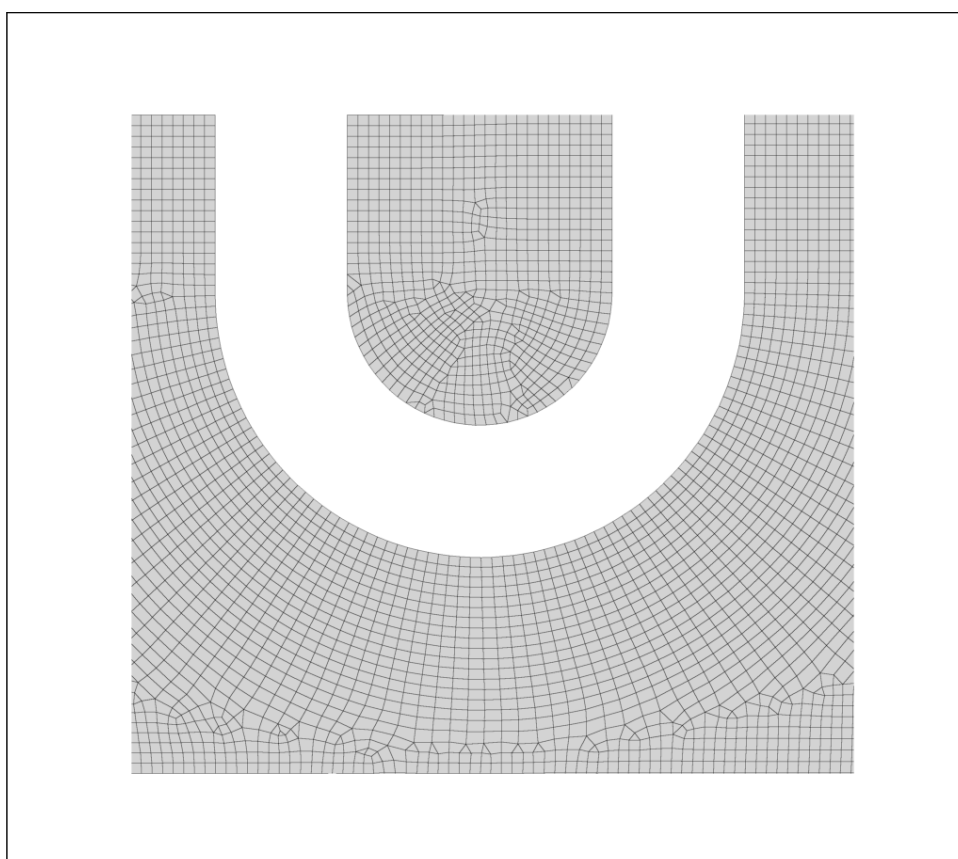


Figure 4.10 Section of the unstructured mesh around the lower part of the letter U.

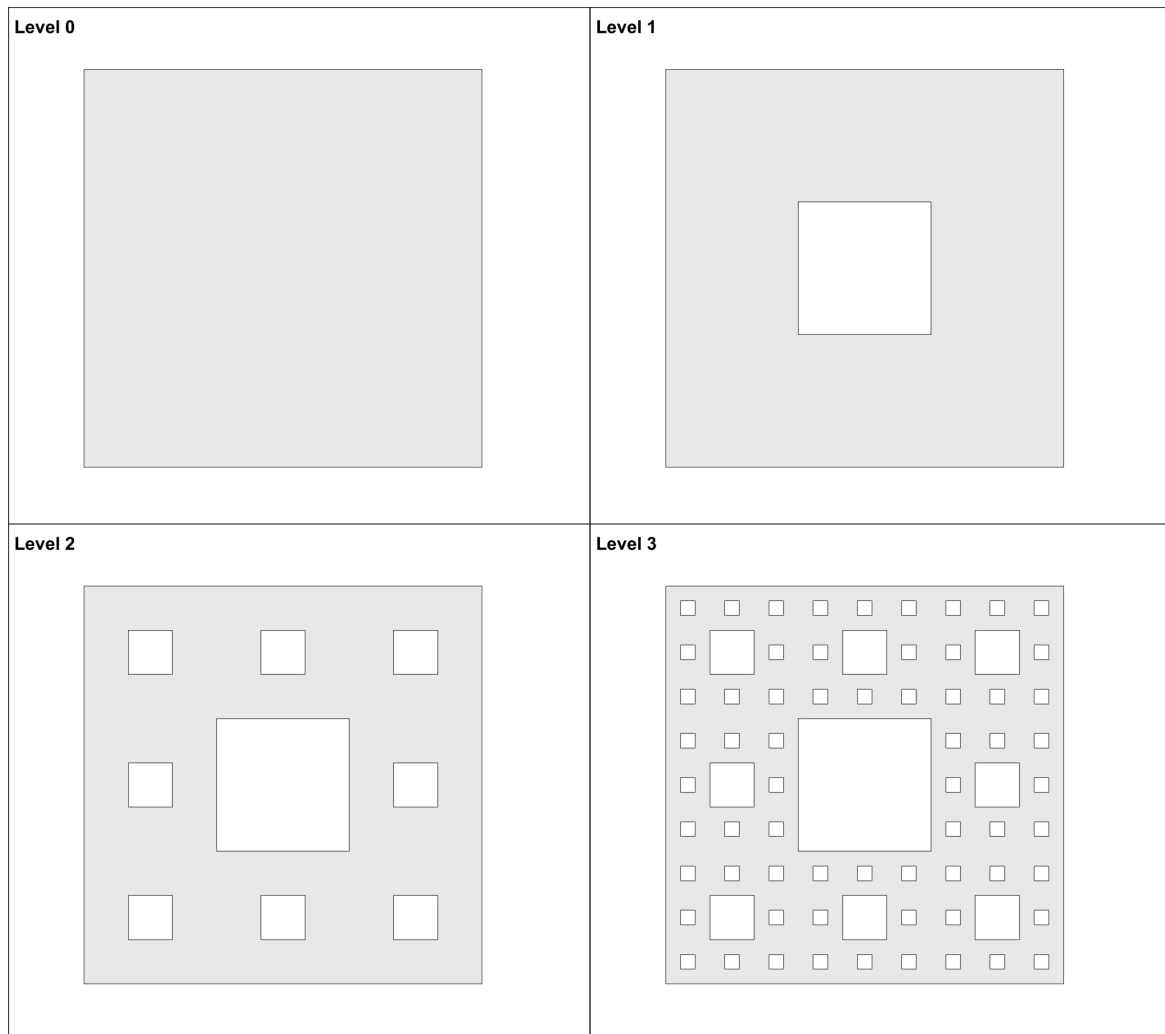


Figure 4.11 Computational domain of Sierpinski carpets of levels 0, 1, 2, 3.

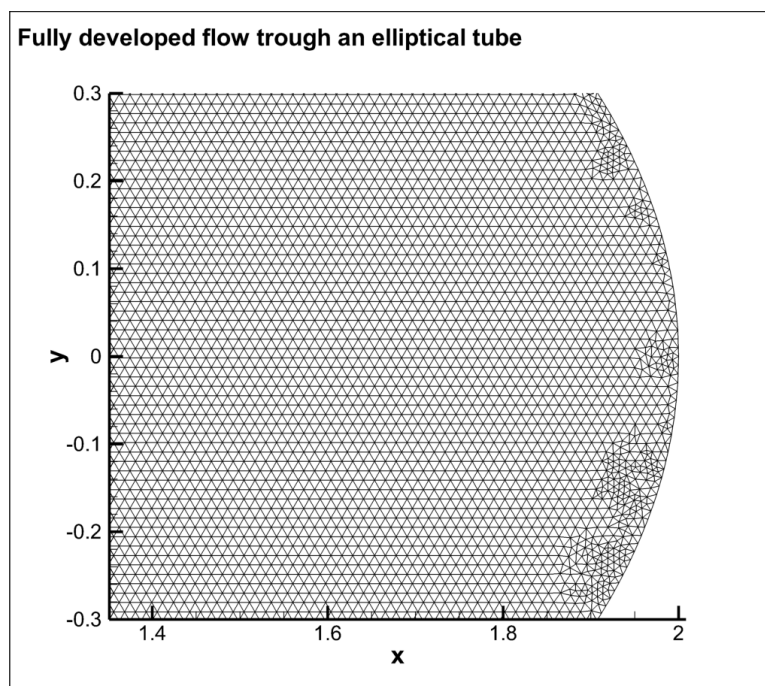


Figure 4.12 Section of unstructured mesh in the fully developed flow through an elliptical tube.

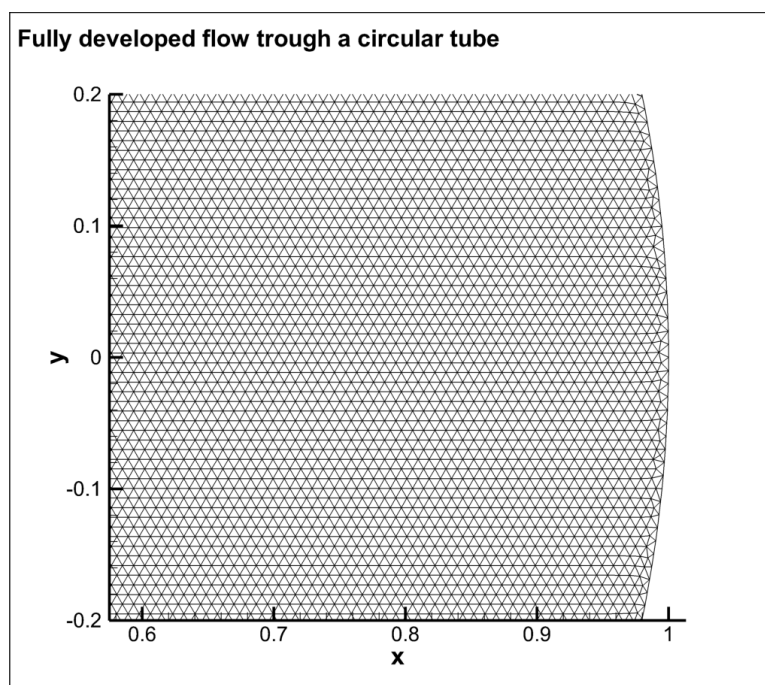


Figure 4.13 Section of unstructured mesh in the fully developed flow through a circular tube.

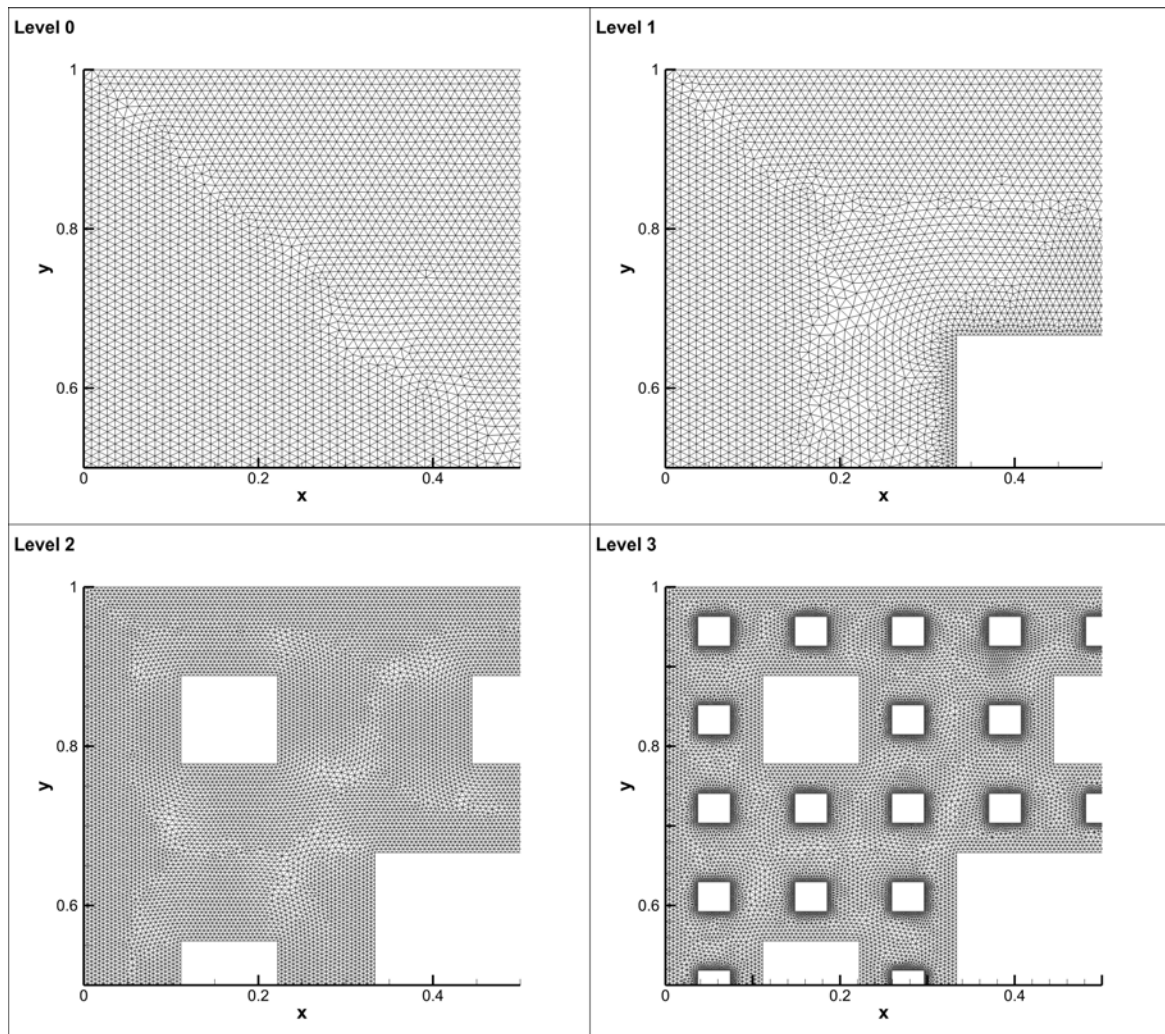


Figure 4.14 Sections of unstructured meshes in fully developed flow through Sierpinski carpets.

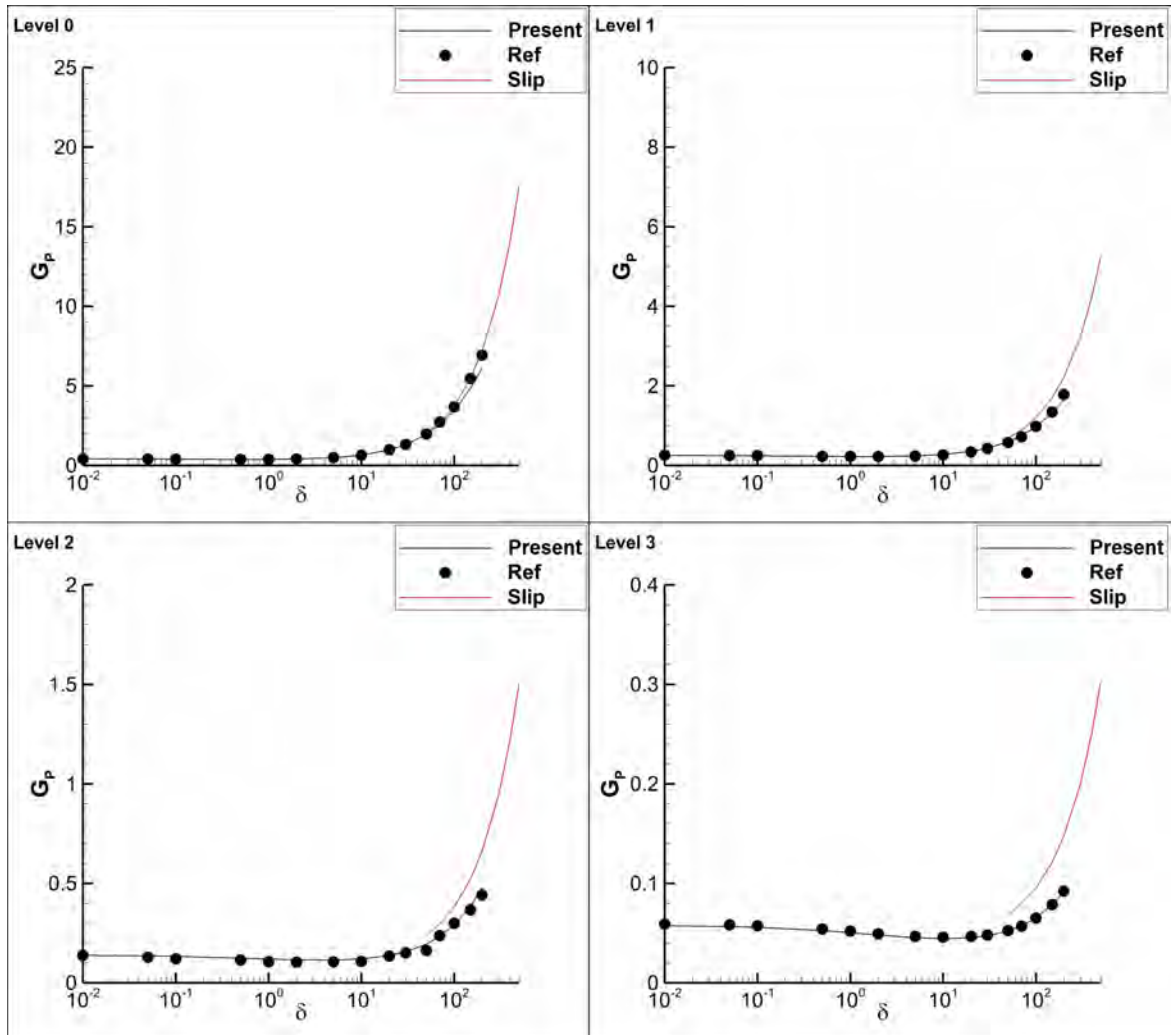


Figure 4.15 Reduced flow rate G_P in terms of δ for the pressure driven fully developed flow through capillaries of Shirpinski carpet cross sections.

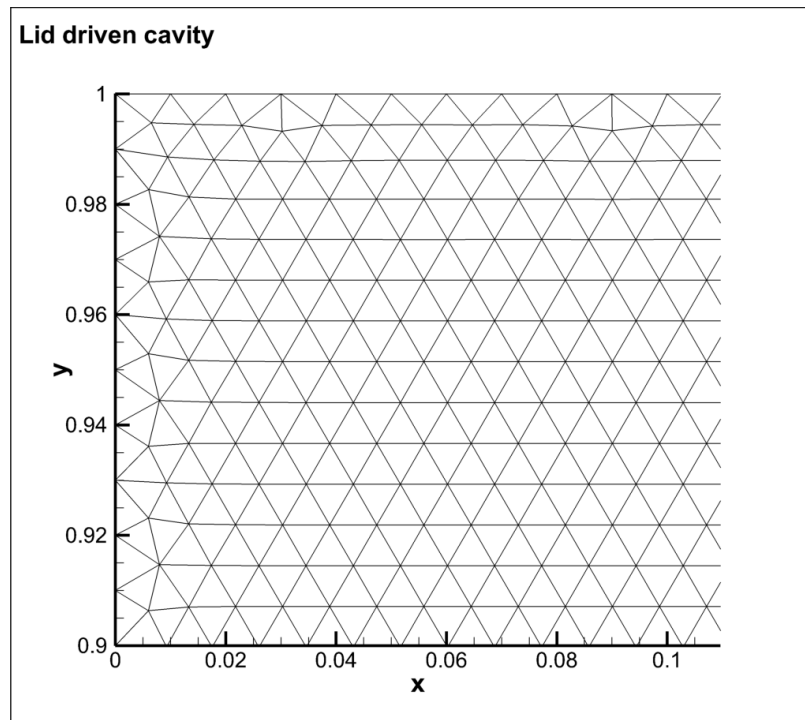


Figure 4.16 Section of unstructured mesh in the lid driven flow.

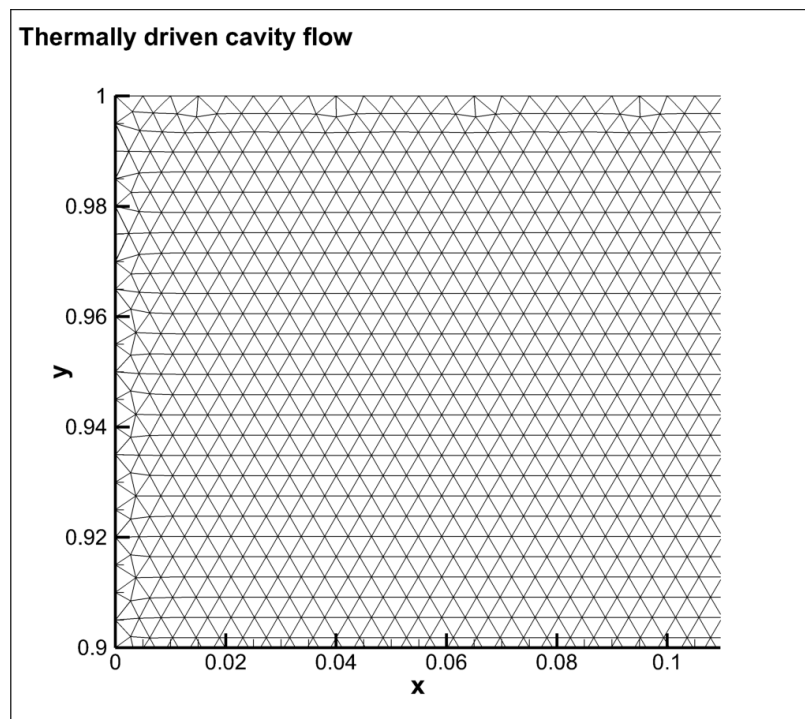


Figure 4.17 Section of unstructured mesh in the thermally driven flow in a cavity.

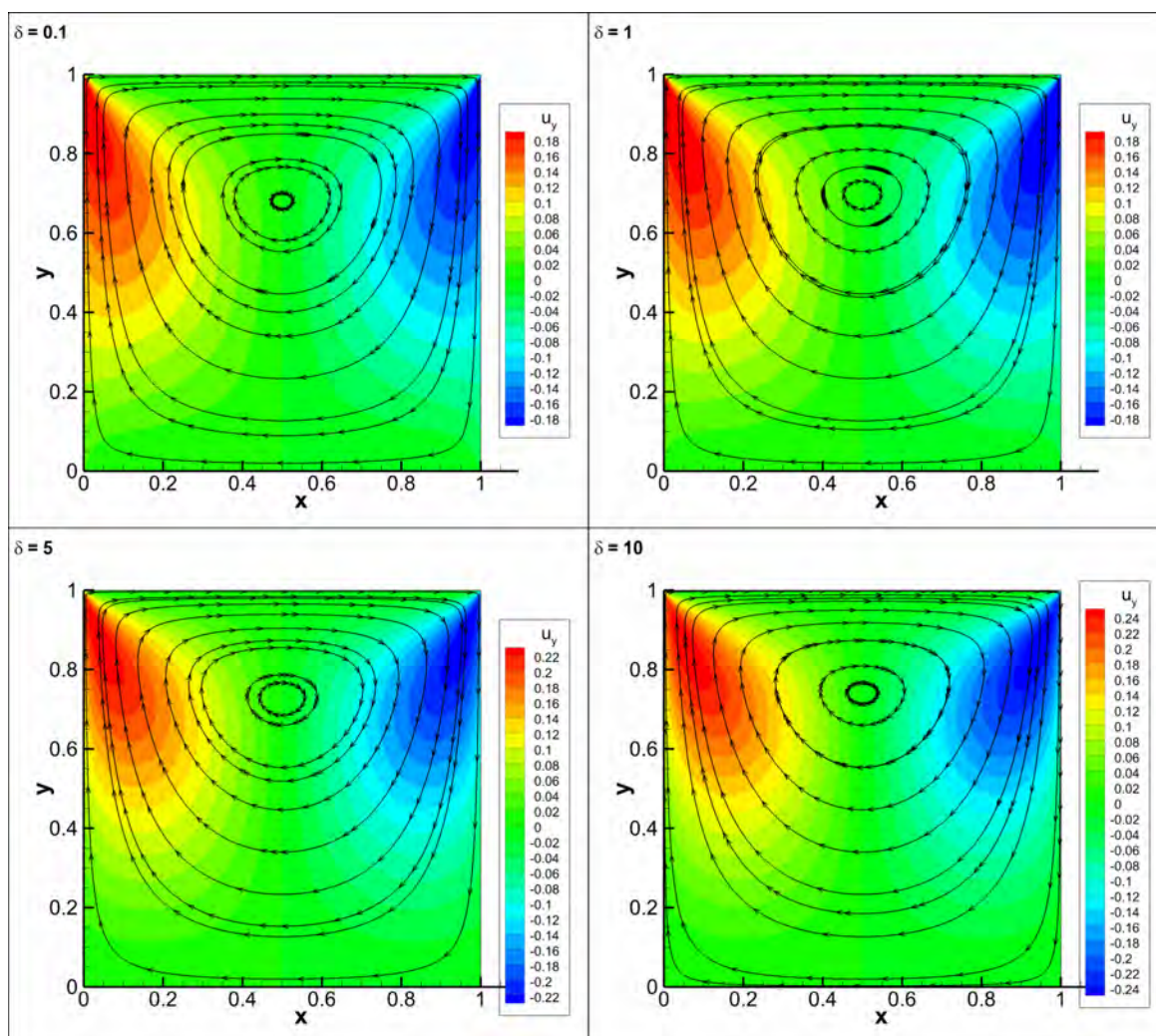


Figure 4.18 Streamlines and vertical velocity contours for a lid driven flow in a cavity in terms of δ .

Chapter 5

Pumping due to thermal transpiration in channels of various configurations

5.1 Introduction

Thermally driven flows are recently gaining attention due to their implementation in thermally driven micro pumps (i.e., pumps without moving parts), which operate based on various non-equilibrium thermally induced phenomena. Most of the proposed thermally driven pumps follow the desirable characteristics of the original design by Knudsen [101], [102], where a cold and a hot reservoir are connected by a straight constant cross section tube with a temperature gradient along the tube wall. Pumps based on other phenomena, such as the thermal edge flow [103] and the thermal stress slip flow [104] have also been proposed.

One of the main obstacles in the original Knudsen pump design is that the large temperature differences needed to enhance the flow are limited by the maximum temperature that the tube material can withstand. To circumvent this pitfall, multistage cascade-type designs with periodic temperature differences have been proposed and the effective operation conditions have been specified by carrying out the associated cascade mechanism analysis [105], [106]. Each pumping stage contains two channels: the first one, having a positive temperature gradient along its wall, connects a cold and a hot reservoir and the second one, with a negative temperature gradient, connects the hot and the next cold reservoir. The second channel is much wider than the first one in order to reduce the reverse undesirable thermal creep flow and achieve nonzero net mass flow rates. However, mainly due to manufacturing constraints, only recently,

prototypes have been manufactured and tested with considerable success [6], [113], [114].

More recent alternative multistage pump designs include the replacement of the narrow channels by curved channels [106]–[110], as well as setups with periodic ratchet-type walls [104]. However, all designs suffer certain constraints either related to microfabrication issues (combination of narrow/wide channels) or to wall temperature control limitations (straight/curved and ratchet channels). In this chapter different configurations are examined, identifying the advantages and limitations of each one, in an effort to provide some general guidelines for the design of thermally driven micropumps.

The first configuration to be examined is pumping through a saw tooth like channel utilizing the thermal stress slip flow to generate gas motion. In this setup the temperature gradient is normal to the wall and no temperature gradient needs to be maintained along the boundaries, which is an advantage since controlling temperature variation along the boundary is not trivial. The saw tooth design has been recently considered in [159] using a continuum approach and in [104] using the DSMC method. In the present chapter this formulation is reconsidered utilizing the general purpose deterministic kinetic solver developed in Chapter 4 to solve the nonlinear Shakhov kinetic model equation. Rarefied temperature driven gas flows are characterized by high Knudsen numbers and very low Mach numbers. The former renders continuum approaches unable to accurately model such flows, while the latter makes the DSMC an unsuitable choice as it leads to a low signal to noise ratio requiring a large number of samples to decrease statistical scattering and long computational times. On the contrary, deterministic methods are more suitable for such flows.

The second configuration considered here, is related to pumping through tapered channels. The pressure driven flow of a rarefied gas through channels of converging or diverging cross sections has recently been an active area of research, mainly due to its presence in various technological applications including vacuum technology and pumping [10], [160], leak detection [161], lubrication [162] and gas microfluidics [163]. Based on experimental [164], [165] and computational [67], [166], [167] investigations, it has been confirmed, that for the same inlet and outlet pressure, the mass flow rate is larger when the flow is in the converging direction compared to the corresponding one in the diverging direction [164]. This interesting phenomenon, known as the diode effect, has been phenomenologically justified [165] and may be useful in the development of novel micro devices.

The corresponding work in temperature driven rarefied gas flows through channels of converging or diverging cross sections, due to the well-known thermal transpiration (or thermal creep) phenomenon [93], [168], is very limited. The only available works are related to the computation of the dimensionless flow rates through variable cross section tubes [160] and rectangular ducts [169], without however, providing a parametrization study, addressing the diode effect and exploring the pumping potential in terms of the involved geometrical and operational data. Of course, thermal creep flows through channels of constant cross section have been extensively studied. Computational results have been reported for flows between parallel plates [23], [170], through long and short circular and elliptic tubes [69], [156], [171], [172], as well as through long rectangular, triangular and trapezoidal ducts [173], [174]. The latter ones are of main practical interest as they are easily built by standard microfabrication techniques. Experimental measurements have been also reported in [175]–[177] providing good agreement with computations.

The possibility of replacing, at each pumping stage, the narrow and wide channels that are typically used by tapered channels, i.e., channels whose width varies linearly with their length, is investigated. The channels are identical, while the flow, depending on the positive or negative temperature gradient, may be in the diverging or the converging direction respectively. Although the magnitude of the temperature gradient is the same, the flow conditions between the diverging and converging flows vary and therefore a net mass flow rate with the associated pressure difference may be obtained. This is the so-called diode effect and it could make, from a theoretical point of view, a Knudsen-type cascade pump feasible. This multistage tapered design does not suffer certain fabrication and temperature control constraints, since reservoirs and channels have dimensions of the same order and the reservoir temperatures (either hot or cold) are uniform.

The third (and final) configuration studied in this chapter includes a combination of straight and curved channels. Utilizing curved channels for this purpose has been previously investigated [107], [108], [110], [178]. In [107] the concept of a serpentine channel with straight and curved segments is analyzed and in [108] is further investigated using typical CFD methods with the appropriate boundary conditions. The serpentine channel is also considered, conducting detailed simulations via a kinetic approach and the concept of varying channel width is examined [110]. The potential of using curved channels for the flow in the desired direction and the backflow stage is considered with the channels in the two stages having different curvatures [178].

This design has been studied in depth and it is included here for completeness and comparison purposes. Simulations are based on linear kinetic theory, as in the case of long tapered channels. The formulation of the auxiliary problems for the extraction of the kinetic coefficients is not trivial and has only been shown in [107] and therefore, is presented here in detail. Upon obtaining the kinetic coefficients, simulations are conducted only for the limiting cases of zero net mass flow rate and zero pressure difference comparing the performance of the curved channels to straight channels.

The following of the chapter is structured as follows. In Section 5.2 the saw tooth surface channel is considered, and parametric analysis of the obtained mass flow rate is performed. The potential of utilizing tapered channel in the design of a thermally driven micropump is examined in Section 5.3. The investigation considers single converging and diverging channels and a parametric analysis is performed examining their performance including typical cascades of channels. In Section 5.4 the curved channel design is presented and its performance is analyzed. The concluding remarks of the chapter are made in Section 5.5.

5.2 Saw tooth surface channels

5.2.1 Flow configuration and modeling

The flow configuration consists of a monatomic gas confined between two surfaces with a saw-tooth like periodic pattern, kept at different but uniform and constant temperatures. One stage of the channel is shown in Figure 5.1. Due to the saw tooth pattern and the misalignment of the pattern on the two opposing surfaces, a temperature profile is formed when the temperature contours are not parallel to the boundaries. This leads to the formation of a macroscopic velocity in the gas side due to the thermal stress slip flow [179]. The advantage of this design is that it does not rely on the thermal creep phenomenon and temperature gradients are not needed along the boundaries, which are kept at constant temperatures.

Due to the periodic pattern only one stage of the configuration is simulated. It is shown, along with the geometric parameters characterizing the flow, in Figure 5.1. The geometrical parameters are the step height d , the channel height h_0 , the stage length L and the misalignment distance L_m . The physical parameters characterizing the flow are the cold and hot wall temperatures T_C and T_H respectively, as well as the reference pressure P_0 . The working gas is considered to be argon with gas constant

$R_g = 208\text{J/kg/K}$. The values of the geometric parameters for the considered case are as follows:

d	h_0	L	L_m
$1\mu\text{m}$	$1.5\mu\text{m}$	$4\mu\text{m}$	$2\mu\text{m}$

The cold and hot wall temperatures are chosen to be 225K and 375K respectively. Purely diffuse boundary conditions are assumed at the two surfaces, while a periodic boundary condition is applied at the lateral walls of the stage. The rarefaction parameter characterizing the flow regime is defined as

$$\delta = \frac{P_0 d}{\mu \sqrt{2R_g T_C}}. \quad (5.1)$$

The simulations are carried out using the deterministic DVM solver on unstructured meshes developed in Chapter 4 to solve the nonlinear Shakhov model equation. The need for nonlinear simulations arises as the temperature difference is not small and the main driving force (i.e. thermal stress slip flow) is a second order phenomenon, as well as other phenomena such as the nonlinear thermal stress flow [179], can be captured only by nonlinear modeling since they are beyond the range of linear kinetic theory. An unstructured triangular mesh is generated with around 300.000 and 600.000 elements for the small and large values of pressure, respectively, while 40 discrete velocity magnitudes and 100 polar angles are used. Part of a typical mesh is shown in Figure 5.2.

5.2.2 Parametric analysis of the mass flow rate

The induced mass flow rate is of major importance. It is noted that no pressure difference exists between the inlet and outlet of each stage. Moreover the effect that the stage length and temperature difference have on the mass flow rate is analyzed. Results are presented for various values of the reference pressure, covering the early slip, transition and free molecular flow regimes.

Figure 5.3 (left) shows the mass flow rate for $P_0 \in [10^2, 10^5]\text{ Pa}$. For small values of P_0 the mass flow rate takes very small values, while its magnitude increases moving to higher values of P_0 . In Figure 5.3 (right), a more detailed view of the mass flow rate for small values of P_0 is given. It is observed that the mass flow rate is initially negative, indicating a right to left net mass flow rate and becomes positive for higher values of P_0 indicating a left to right net flow.

Figure 5.4 presents the behavior of the mass flow rate when the stage length L changes, for $P_0 = 7451\text{Pa}$ (left) and 37255Pa (right), corresponding to the transition and early slip regimes respectively. All other geometrical parameters remain the same, except of the misalignment length that is kept at a constant ratio with respect to the stage length ($L_m = L/2$). In the first case, as the stage length is increased the mass flow rate increases, maintaining however the small magnitudes that appear in this regime. The situation is changed in the early slip regime, where an increase in the stage length results to a decrease of the net mass flow rate.

In Figure 5.5, the effect of the temperature difference to the mass flow rate is shown for $P_0 = 7451\text{Pa}$. The cold wall temperature is maintained at $T_C = 225\text{K}$, while the hot wall temperature is changed to produce the desired temperature difference. The mass flow rate has a linear behavior with respect to the temperature difference, in the range of temperature differences examined.

5.2.3 Velocity and temperature fields

Figure 5.6 shows the temperature profile and streamline patterns for various values of the reference pressure. The temperature profile is relatively simple and is qualitatively similar for all cases considered. The velocity profile is more complicated. In all cases, two counter rotating vortices are formed, one close to each boundary. Apart from the two vortices, a net mass flow rate exists, from the one vertical boundary to the other. The path that the net mass flow rate follows, is shown with a red line in Figure 5.6. For small values of pressure, when the flow is in the early transition regime (Figure 5.6 a and b) the net mass flow rate follows a path from the right vertical boundary, around the top vortex, close to the cold wall, through the region between the two vortices and then, around the bottom vortex, close to the hot wall and exiting from the left vertical boundary. In these cases the net mass flow rate is from right to left. When the pressure is increased and the flow is in the late transition or early slip regimes, the net mass flow rate enters from the left wall, follows the wavy pattern shown in Figure 5.6d between the two vortices and exits from the right wall.

In the design and manufacturing of such devices, the surface temperature is important. An analysis of the temperature gradients on the surfaces of the walls is given here. The temperature gradients along the inclined walls of the stage, in the directions shown by the arrows in the sketch and along the vertical walls are plotted in Figures 5.7 and 5.8 respectively. In both cases the temperature gradients take very large values, of the order of 10^7 and 10^8K/m for the inclined and vertical walls respectively. This

leads to very large heat fluxes from the gas side along the walls and imposes a major design restriction as materials with thermal properties able to maintain a constant temperature under those conditions should be utilized.

It is concluded that although this design is able to produce a mass flow rate, it has several drawbacks. The direction of the mass flow rate changes depending on the gas rarefaction and the geometrical parameters affect the mass flow rate in a different way in different rarefaction regimes. More important, the heat flux on the gas side, in the vicinity of the channel walls takes very large values, making the temperature control a very difficult task. For this reason multistage assemblies of this type are not considered and alternative designs are investigated.

5.3 Tapered channels

5.3.1 Geometry and flow configuration

Multistage thermally driven pumps consisting of tapered channels are next considered. One pumping stage is shown in Figure 5.9. The channels are connected to reservoirs with alternating hot and cold temperatures. The temperature gradient has the same magnitude for both converging and diverging channels, however due to the diodicity effect a net flow is induced. The investigation is mainly focused on single channels and a brief discussion on multistage systems is later made.

Consider the thermal creep flow of a rarefied monatomic hard sphere gas between two reservoirs maintained at temperatures T_{in} and T_{out} , with $T_{in} < T_{out}$, connected by a long converging or diverging channel of length L . The channels consists of two inclined plates and the distance $H(z)$ between the plates (z denotes the flow direction), varies linearly along the tapered-shape channel between the inlet and outlet distances H_{in} and H_{out} respectively. The characteristic length is defined as the average distance $H_m = 0.5(H_{in} + H_{out})$. Furthermore, it is assumed that the temperature of the plates varies linearly between the inlet T_{in} and outlet T_{out} temperatures. The pressures at the cold and hot reservoirs are denoted by P_{in} and P_{out} respectively. A view of the channel geometry along with the inlet and outlet conditions is shown in Figure 5.10.

In addition, a very important input parameter for the purposes of the present work is the inclination of the channel walls, which is always defined, independently of the flow direction, as the ratio α of the largest over the smallest distance between the plates. The corresponding inclination ratios are as follows:

Converging channels:

$$\alpha_{con} = H_{in}/H_{out} \quad (5.2)$$

Diverging channels:

$$\alpha_{div} = H_{out}/H_{in} \quad (5.3)$$

The definition of α in this manner, where always $\alpha \geq 1$, facilitates, as it is later seen, the direct comparison between corresponding converging and diverging flows in channels having the same inclination ratio, i.e., $\alpha_{con} = \alpha_{div} = \alpha$. Obviously the case of $\alpha = 1$ corresponds to thermal creep flow between parallel plates.

In general, the maintained temperature difference between the two reservoirs results in a temperature driven flow from the cold towards the hot reservoir, while the increased pressure in the hot reservoir results in a pressure driven flow in the opposite direction. To have a comprehensive and complete description, the following three flow setups are considered:

The investigation is initially focused on single tapered (converging and diverging) channels, where the flow is engendered by the imposed temperature difference between the inlet and outlet reservoirs. The following two limit flow configurations may be considered [23], [160], [169]:

- A maximum pressure difference is created for an imposed temperature gradient when the net mass flow rate at every section of the channel is equal to zero. In this flow setup the pressure at the hot side is higher than the pressure at the cold side and the thermal transpiration flow is counterbalanced by a Poiseuille flow engendered by the pressure difference obtained by the imposed temperature gradient itself.
- A maximum net mass flow rate is obtained for an imposed temperature gradient when the inlet and outlet pressures are equal. In this flow setup the temperature driven flow creates a non-uniform pressure distribution along the channel, which should be taken into account in order to properly estimate the thermally driven flow.

Both limit scenarios, as well as all intermediate flow setups with the associated characteristic curves, are numerically considered in this section. The formulation is based on kinetic modeling in order to have a reliable solution in the whole range of gas rarefaction. A detailed investigation and parametrization of the pumping process, in terms of all involved geometric and flow parameters, is performed. In addition, the

corresponding results between converging and diverging flows are compared to deduce the diodicity in terms of mass flow rates and pressure differences. The main incentive is the potential future implementation of tapered channels in the development of novel micro pumps utilizing the thermal creep phenomenon, and thus some typical results for cascades of converging and diverging channels are also presented.

The first flow setup, consisting of the two reservoirs and the tapered channel, is considered as closed and therefore the net mass flow rate $\dot{m} = 0$. This is the so-called thermo-molecular pressure difference (TPD) phenomenon [23], [101], [102]. The diodicity coefficient E_P is defined as the ratio of the pressure difference ΔP of the diverging channel over the converging one. The second flow set up is open and therefore there is a net flow ($\dot{m} \neq 0$), while the pressures in the two reservoirs are equal. It is noted that, although $P_{in} = P_{out}$, a pressure variation along the channel is present and, even in this case, there is a pressure driven flow due to the local pressure gradient. Now, the diodicity coefficient $E_{\dot{m}}$ is defined as the ratio of the mass flow rate \dot{m} of the diverging channel over the converging one. Finally, in the third flow setup, the net mass flow rate is again nonzero and there is also a difference between the inlet and outlet pressures. The diodicity coefficient is defined as the ratio of the pressure difference ΔP of the diverging channel over the converging one for a given mass flow rate \dot{m} and it is denoted by $E_{P|\dot{m}}$.

Summarizing, the three flow scenarios are as follows:

A.

$$\dot{m} = 0, P_{out} > P_{in}, E_P = \frac{\Delta P^{(div)}}{\Delta P^{(con)}} \text{ (closed system)} \quad (5.4)$$

B.

$$\dot{m} \neq 0, P_{out} = P_{in}, E_m = \frac{\dot{m}^{(div)}}{\dot{m}^{(con)}} \text{ (open system)} \quad (5.5)$$

C.

$$\dot{m} \neq 0, P_{out} > P_{in}, E_{P|\dot{m}} = \left. \frac{\Delta P^{(div)}}{\Delta P^{(con)}} \right|_{\dot{m}} \text{ (open system)} \quad (5.6)$$

It is clarified that the diode effect vanishes when the prescribed inclination ratio is equal to one and it is increased as the ratio departs from one, either for values larger or smaller than one.

The objective here is to obtain the net mass flow rate \dot{m} and the associated pressure distribution $P(z)$, $z \in [0, L]$, in terms of the input parameters, which include the

channel geometry (L, H_m, α) , the inlet and outlet temperatures (T_{in}, T_{out}) and the corresponding pressures (P_{in}, P_{out}) . Furthermore, comparing the results between the corresponding converging and diverging flows, the corresponding diodicity coefficient is computed.

It is seen that the third scenario is the most general one and demonstrates the coupled pumping effect. The first and second flow setups may be considered as the limit cases of the third one, i.e., it is expected to obtain the maximum pressure difference ΔP when $\dot{m} = 0$ and to obtain the maximum mass flow rate \dot{m} when $P_{out} = P_{in}$ ($\Delta P = 0$), while all other intermediate cases are covered in the third flow setup.

5.3.2 Modeling of mass flow rate and pressure difference

The fully developed rarefied gas flow between parallel plates driven by pressure and temperature gradients is a classical problem in the field of rarefied gas dynamics and has been extensively investigated based on linearized kinetic model equations [23]. Due to linearity the pressure and temperature driven flows are solved separately to deduce the corresponding dimensionless flow rates in terms of the gas rarefaction parameter and then, the overall solution of the combined flow may be obtained by a linear superposition of the two flows. Furthermore, based on the mass conservation principle, the net mass flow rate may be obtained in a straightforward manner by accordingly combining the dimensionless flow rates providing that the channel geometry and the inlet and outlet conditions are known [23], [156], [171]. Since all above analysis is well-described in the literature it is not presented here and it is just applied in the present tapered flow configuration. Although the channels investigated are not very long, the assumptions made by the fully developed theory are met, as shown in Appendix C where the thermally driven flow through tapered channels is considered using non-linear kinetic theory.

The net mass flow rate \dot{m} of the rarefied gas flow through the tapered channel driven by the imposed temperature and pressure gradients can be computed using the following ordinary differential equation [23], [156], [171], [173], [174]:

$$\dot{m} = \frac{H(z) P(z)}{v(z)} \left[-G_P(\delta) \frac{H(z)}{P(z)} \frac{dP}{dz} + G_T(\delta) \frac{H(z)}{T(z)} \frac{dT}{dz} \right] \quad (5.7)$$

Here, $z \in [0, L]$, $v(z) = \sqrt{2RT(z)}$, with R representing the specific gas constant, is the most probable velocity, $P(z)$ and $T(z)$ are the pressure and temperature distributions

along the channel, while dP/dz and dT/dz denote the corresponding local gradients. The temperature distribution, $T(z)$, is considered as known. On the contrary, the pressure distribution $P(z)$ inside the channel, is part of the solution. Also, $G_P(\delta)$ and $G_T(\delta)$ are the dimensionless flow rates, also known as kinetic coefficients [180], for the pressure and temperature driven flows respectively and they both depend on the local gas rarefaction parameter

$$\delta(z) = \frac{P(z) H(z)}{\mu(z) v(z)} \quad (5.8)$$

with $\mu(z)$ denoting the local dynamic viscosity at temperature $T(z)$. Once δ is specified, the corresponding G_P and G_T may be obtained from a kinetic data base providing the flow rates in the whole range of the gas rarefaction parameter. It is clear that $\delta = \delta(z)$ is a function of the local pressure, temperature and height. For a hard sphere gas, the local δ along the channel may be defined in terms of the inlet rarefaction parameter δ_{in} as

$$\delta(z) = \delta_{in} \left(\frac{H(z)}{H_{in}} \right) \left(\frac{P(z)}{P_{in}} \right) \left(\frac{T_{in}}{T(z)} \right). \quad (5.9)$$

Equation (5.7) is valid at any cross section $z \in [0, L]$ with the unknown net mass flow rate \dot{m} being constant. Since both \dot{m} and $P(z)$ are unknowns, it is convenient to rewrite Eq.(5.7) in the form

$$\frac{dP}{dz} = -\frac{v(z)}{H^2(z) G_P(\delta)} \dot{m} + \frac{G_T(\delta) P(z)}{G_P(\delta) T(z)} \frac{dT}{dz} \quad (5.10)$$

with boundary conditions $P(0) = P_{in}$ and $P(L) = P_{out}$.

The problem is well posed only when two out of the three quantities, namely P_{in} , P_{out} and \dot{m} , are specified. When both P_{in} and P_{out} are specified the mass flow rate is solved using a shooting method. More specifically, an initial value for the mass flow rate is assumed and then, Eq. (5.10) is integrated with initial condition $P(0) = P_{in}$ along $z \in [0, L]$. The computed outlet pressure $P(L)$ is compared to the specified P_{out} and then, the mass flow rate is accordingly corrected depending upon the difference between the computed and specified outlet pressures. This procedure is repeated until convergence. When the mass flow rate \dot{m} with either P_{in} or P_{out} are specified, Eq. (5.10) is trivially integrated along the channel to find the unknown pressure distribution $P(z)$ including the pressure at one of the two channel ends.

The kinetic coefficients G_P and G_T , required in Eq. (5.10), are taken from the solution of the linearized Shakhov kinetic model equation for flow between parallel

plates subject to purely diffuse boundary conditions [23], [181]. These values are available in the literature, but in order to have a complete and dense kinetic data base, within the range of $\delta \in [\delta_{in}, \delta_{out}]$ needed in the present work, they are recomputed and provided for completeness purposes in Appendix D.

The methodology described is introduced to investigate all three flow scenarios defined by Eqs. (5.4), (5.5) and (5.6) in a wide range of the input parameters. More specifically, the reference distance between the plates is set at $H_m = 10\text{m}$ and 20m and the length of the channel is taken equal to $L/H_m = 20$ and 50 (the restriction of the fully developed flow is then fulfilled considering also the very small induced pressure differences [85]). The inclination ratio takes various values $\alpha \in [1, 6]$. The inlet and outlet temperatures are fixed at $T_{in} = 273\text{K}$ and $T_{in} = 546\text{K}$ ($T_{out}/T_{in} = 2$), while the inlet pressure P_{in} varies between 5×10^2 and 10^5Pa . The outlet pressure P_{out} is in the range of P_{in} depending upon the computed mass flow rate \dot{m} . It is seen that the investigation covers the effect of the channel geometry, focusing on the inclination ratio and of the inlet pressure. The effect of the temperature ratio is not considered since it is easily predictable. The values of the parameters have been chosen in a range where a conclusive description of their impact is permissible, meeting in parallel manufacturing and operational constraints. In all cases the working gas is argon ($R = 208\text{J/kg/K}$).

5.3.3 Zero net mass flow rate (Flow scenario A)

The inlet and outlet boundaries are closed and the net mass flow rate is zero ($\dot{m} = 0$). In this case Eq. (5.10) is simplified and is written as

$$\frac{dP}{dT} = \frac{G_T}{G_P} \frac{P}{T} \quad (5.11)$$

with $P = P_{in}$ at T_{in} . Then, Eq. (5.11) is readily integrated with regard to temperature to compute the pressure distribution $P(z)$ including the outlet pressure P_{out} . It is seen from Eq. (5.11) that in this flow scenario, where the net mass flow rate is set equal to zero, the outlet pressure P_{out} is independent of the channel length L [156]. This remark has been also numerically confirmed.

Figure 5.11 shows the pressure difference $\Delta P = P_{out} - P_{in}$ for converging (left) and diverging (right) channels with $H_m = 10\text{m}$, in terms of the inlet pressure P_{in} for various values of the inclination ratio α . The inlet pressure varies from $5 \times 10^2\text{Pa}$ up to 10^5Pa . In all cases, as P_{in} is increased the pressure difference $\Delta P = P_{out} - P_{in}$ is also increased up to a maximum value and then, it is decreased as P_{in} keeps increasing. The largest

values of ΔP are moving to slightly higher values of P_{in} , as α is increased, always being in the range of $P_{in} = (5 - 10) \times 10^3 \text{Pa}$. The largest values of the developed pressure differences ΔP are about $300 - 350 \text{Pa}$ and they are slightly higher in the diverging channel flow. Also, in all cases the pressure difference ΔP increases monotonically with α .

The pressure diodicity coefficient $E_P = \Delta P^{(div)} / \Delta P^{(con)}$, also defined in Eq. (5.4), is plotted in Figure 5.12, in terms of the inlet pressure P_{in} for all values of α under consideration. It is seen that for $P_{in} \in [10^4 - 2 \times 10^4] \text{Pa}$ the diode effect is negligible since $E_P \approx 1$. On the contrary, for $P_{in} < 10^4 \text{Pa}$ and $P_{in} > 2 \times 10^4 \text{Pa}$, the pressure diodicity coefficient takes values larger and smaller than unity respectively and therefore for these inlet pressures the diode effect is present. In this range of inlet pressures, which are of practical interest since $E_P \neq 1$, the diode effect is always increased with α . For $P_{in} < 10^4 \text{Pa}$ the largest value of the coefficient is around $E_P = 1.1$ and it is taken at about $P_{in} \approx 3 \times 10^3 \text{Pa}$ with $\alpha = 6$. For $P_{in} > 2 \times 10^4 \text{Pa}$, E_P is monotonically decreased from unity (i.e. the diode effect becomes stronger) as the inlet pressure is increased up to $P_{in} = 10^5$. However, in these relatively high pressures the values of the corresponding pressure differences ΔP are small.

The corresponding results for the pressure difference ΔP and the pressure diodicity coefficient E_P , for converging (left) and diverging (right) channels with $H_m = 20 \text{m}$, are shown in Figures 5.13 and 5.14 respectively. It is seen in Figure 5.13 that, as expected, the qualitative dependence of ΔP on P_{in} and α remains the same. It is also seen, however, that now the produced largest pressure differences are between $150 - 180 \text{Pa}$ and they are much smaller than the corresponding ones in channels with $H_m = 10 \text{m}$. This is justified since now the flow is less rarefied (closer to the slip regime) and the pressure driven flow becomes more dominant and therefore, the zero net mass flow rate condition is reached in a lower outlet pressure. The largest differences are occurring at about $P_{in} = (3 - 6) \times 10^3 \text{Pa}$. The results of E_P with $H_m = 20 \text{m}$, shown in Figure 5.14, are close to the ones obtained for $H_m = 10 \text{m}$ (Figure 5.12).

Based on the above it may be stated that for the systems with closed boundaries and zero net mass flow rates considered here, the optimum operation scenario is obtained with $H_m = 10 \text{m}$ at inlet pressures around $4 \times 10^3 \text{Pa}$, where both the developed pressure difference is large and the diode effect is significant. It is also noted that the results correspond to the specific temperature ratio $T_{out}/T_{in} = 2$ and obviously, as the temperature ratio is increased the pressure difference will also be increased.

5.3.4 Equal inlet and outlet pressures (Flow scenario B)

Now, the inlet and outlet boundaries are open and there is a nonzero mass flow rate ($\dot{m} \neq 0$), while the inlet pressure is set equal to the outlet pressure ($P_{in} = P_{out}$ and thus $\Delta P = 0$). Equation (5.10) is solved in an iterative manner as described above. The computed mass flow rate depends on the inlet (and outlet) pressures, the inclination ratio as well as on the length of the channel, while the diodicity coefficient is defined as the ratio of the mass flow rates of the diverging flow over the converging one.

Figure 5.15 shows the mass flow rate \dot{m} per unit width (kg/m/s) in terms of the inlet pressure P_{in} for converging (left) and diverging (right) channels with $H_m = 10\text{m}$ for $L/H_m = 20, 50$ and for various inclination ratios α . With the inlet pressure varying from $5 \times 10^2\text{Pa}$ up to 10^5Pa the mass flow rate is in the order of $10^{-6} - 10^{-7}\text{kg/m/s}$. The mass flow rates in the diverging channels are always larger than the corresponding ones in the converging channels (on the contrary, in pressure driven flows the mass flow rates in converging channels are the largest ones [165]). In both diverging and converging channels, \dot{m} increases quite rapidly with P_{in} up to about $P_{in} \approx 2 \times 10^4$ and then it keeps increasing but with a much slower pace tending to a constant value in the hydrodynamic regime [174], [175]. Also, in both cases, as the inclination α is increased, the mass flow rate \dot{m} is decreased. Thus, in this flow scenario the effect of tapering is in the opposite direction compared to the zero net mass flow scenario, where ΔP increases with α . In addition, as expected, the mass flow rate is reduced when the channel length is increased.

The mass diodicity coefficient $E_{\dot{m}} = \dot{m}^{(div)}/\dot{m}^{(con)}$, also defined in Eq.(5.5), is plotted in Figure 5.16, in terms of inlet pressure for $L/H_m = 20, 50$ and for all values of α under consideration. As P_{in} is increased, the mass diodicity coefficient $E_{\dot{m}}$ is initially increased until it reaches an absolute maximum and then it is decreased until it reaches a local minimum, tending finally in an oscillatory manner to a constant value, which is the ratio of the corresponding constant mass flow rates at the hydrodynamic limit. In all cases the largest values of mass diodicity occur at about $P_{in} \approx 1.5 \times 10^4$. As α is increased, $E_{\dot{m}}$ is monotonically increased. It is seen that although the mass flow rates depend on L/H_m , $E_{\dot{m}}$ is independent of this ratio.

In Figures 5.17 and 5.18, the distributions of pressure $P(z)$ and gas rarefaction parameter $\delta(z)$ are plotted along the channel for converging and diverging channels respectively, with $L/H_m = [20, 50]$, $H_m = 10\text{m}$, $P_{in} = [10^3, 10^4, 0.5 \times 10^5]\text{Pa}$ and $\alpha = [2, 3, 4]$. In the converging channel flow (Figure 5.17), the pressure increases along

the channel until a maximum value P_{\max} and then, decreases to match the outlet pressure $P_{out} = P_{in}$. The pressure difference $P_{\max} - P_{in}$ takes its largest value at about $P_{in} = 10^4 \text{Pa}$ and, in general, its location along the channel moves closer to the channel exit, as P_{in} and α are increased. Also, the variation of $P(z)$ along the channel is more evident as α is increased. In the diverging channel case (Figure 5.18), the pressure distribution initially decreases until a minimum value P_{\min} and then increases to match the outlet pressure. The pressure difference $P_{in} - P_{\min}$ takes its largest value again at about $P_{in} = 10^4 \text{Pa}$, while its location along the channel moves now closer to the channel inlet as P_{in} and α are increased. Overall, the maximum deviation of the pressure inside the channel from the inlet pressure is about 5 – 80Pa.

Concerning the variation of $\delta(z)$ along the channels, since the pressure variation with regard to the inlet pressure is small, it is mainly affected by the temperature and height variations, as it is seen by Eq. (5.9). Therefore, as expected for the converging flow (Figure 5.17), $\delta(z)$ is monotonically reduced along the channel, since both the height $H(z)/H_{in}$ and temperature $T_{in}/T(z)$ ratios are decreased. For the diverging case (Figure 5.18), where $H(z)/H_{in}$ is increased and $T_{in}/T(z)$ is decreased, $\delta(z)$ remains almost constant for $\alpha = 2$ (the rate of change for temperature and height cancel each other) and increases for $\alpha > 2$. Finally, the length over height ratio L/H_m does not affect qualitatively the pressure and rarefaction parameter distributions. The values of the gas rarefaction parameter, for the presented inlet pressures, vary about three orders of magnitude from 0.5 up to 100, indicating that the flow for the present setups is in the transition and slip regimes.

Corresponding results for the mass flow rate \dot{m} and the mass diodicity coefficient $E_{\dot{m}}$, for converging and diverging channels with $H_m = 20\text{m}$, have also been obtained. It turns out that now both \dot{m} and $E_{\dot{m}}$ are very close to the corresponding ones with $H_m = 10\text{m}$ shown in Figures 5.15 and 5.16 respectively. Due to this qualitative and quantitative resemblance these results are not presented.

Closing this subsection, it is stated that in systems with open boundaries and zero pressure difference the optimum operation range is at inlet pressures around $1.5 \times 10^4 \text{Pa}$, where both the mass flow rate is large and the diode effect is significant. The produced mass flow rates are expected to increase with the temperature ratio T_{out}/T_{in} .

5.3.5 Nonzero mass flow rate and unequal inlet and outlet pressures (Flow scenario C)

The more general case of flow through a channel with $\Delta P = P_{out} - P_{in} > 0$ and $\dot{m} \neq 0$ is considered. In this flow scenario, the pumping effect which may be delivered by a converging and a diverging flow is more clearly demonstrated, since a nonzero net mass flow rate is coupled with a nonzero pressure difference. This is an open system and Eq. (5.10) is solved through an iterative process as described in above and, as in the previous open system, the computed mass flow rate depends on the inlet and outlet pressures, on the inclination ratio, as well as on the length of the channel.

In Figures 5.19 and 5.20, the pressure difference $\Delta P = P_{out} - P_{in}$ is plotted in terms of the mass flow rate \dot{m} for converging and diverging channels respectively with $H_m = 10\text{m}$, $L/H = [20, 50]$, $P_{in} = [10^3, 10^4, 10^5]\text{Pa}$ and $\alpha = [2, 3, 4, 5, 6]$. As it is seen in all cases, as \dot{m} is increased, ΔP is decreased and there is a nearly linear relation between the two quantities. These lines with a negative slope provide a complete picture of the pumping effect in terms of the achieved mass flow rate and pressure difference and they may be considered as the characteristic (or performance) curves of converging and diverging channels. In the limiting cases of $\dot{m} = 0$ and $\Delta P = 0$, the corresponding flow scenarios A and B are recovered. It is also seen that the characteristic curves for the various values of α are always crossing each other at some point which depends on the flow parameters. This is easily explained by considering that at $\Delta P = 0$ larger values of α correspond to smaller mass flow rates, while at $\dot{m} = 0$ larger values of α correspond to larger pressure differences.

In Figure 5.21, the pressure diodicity coefficient $E_{P|\dot{m}} = \Delta P^{(div)} / \Delta P^{(con)}$ for a given mass flow rate \dot{m} is plotted in terms of the mass flow rate for $H_m = 10\text{m}$, $L/H = [20, 50]$, $P_{in} = [10^3, 10^4, 10^5]\text{Pa}$ and $\alpha = [2, 3, 4, 5, 6]$. The pressure diodicity coefficient is always increased as the mass flow rate is increased. The reason is that the mass flow rate in diverging channels is always larger than in the corresponding converging ones and therefore, the pressure difference in the converging channels is decreased faster than in the diverging ones. For inlet pressure $P_{in} = 10^3\text{Pa}$, $E_{P|\dot{m}}$ is always larger than unity, while for $P_{in} = 10^4$ and 10^5Pa , $E_{P|\dot{m}}$ may be larger or smaller than unity depending on the mass flow rate. Also, with respect to the inclination ratio, as α is increased, for $P_{in} = 10^3$ and 10^4Pa , $E_{P|\dot{m}}$ is monotonically increased, while for $P_{in} = 10^5\text{Pa}$ this behavior remains the same at large mass flow rates, while at small ones $E_{P|\dot{m}}$ is decreased.

It is evident that the characteristic curves along with the diodicity plots are very useful in deciding on the suitability of a channel flow to meet some provided specifications. Furthermore, these results illustrate how it would be possible to fully characterize a Knudsen pump by just investigating the flow scenarios A and B since the pump characteristic curves may be readily deduced from a linear variation between these two limit cases.

5.3.6 Cascades of tapered channels

The pressure difference generated by a cascade of converging and diverging channels is considered. A typical cascade is shown in Figure 5.22, along with a typical temperature distribution (red line). Each stage consists of a diverging followed by a converging channel, while the cascade always ends with a single diverging channel. Thus the cascade shown in Figure 5.22 consists of 3.5 stages. To demonstrate the pumping performance of such a cascade only the limiting case where $\dot{m} = 0$ is considered (closed system). The modeling approach utilized in the single channels case and described in Section 5.3.2 is used. Simulations are conducted for a temperature ratio $T_H/T_C = 2$ with $T_C = 273K$, the mean channel height is $H_m = 10m$ and the working gas is Argon. In this case, the pressure difference is independent of the channel length, as discussed in Section 5.3.3. The pressure distributions are obtained considering channels of $L/H_m = 20$.

Figure 5.23 shows the pressure difference between the two ends of the cascade in terms of the number of stages for $\alpha = 3, 4, 5$ and 6 and various values of the inlet pressure $P_{in} \in [10^3, 10^5]$. As the number of stages increases, the pressure difference also increases. Increasing the inclination parameter α leads to an increase of the pressure difference. The behavior in terms of the inlet pressure is more complicated. Depending on the inlet pressure, the pressure difference can be either positive or negative. This is to be expected, as the pressure diodicity coefficient E_P for single channels can take values either larger or smaller than 1, depending on the inlet pressure. The pressure difference takes positive values for $P_{in} < 10^4 Pa$ and becomes negative for higher values of the inlet pressure. Using 200 stages, considerable pressure difference are obtained. For $\alpha = 6$ and $P_{in} = 10^3 Pa$ the pressure difference can be up to $5 \times 10^3 Pa$.

In Figure 5.24 the pressure variation through a cascade of 100 stages, with $\alpha = 6$ is presented for various values of the inlet pressure. In all cases the pressure has an oscillating profile, as the two channels of each stage create pressure differences in opposing directions. Each stage contributes a small net pressure difference, and

using a large number of stages a considerable pressure difference is generated. This indicative simulation of a cascade of tapered channels, clearly demonstrates that a thermally driven micro-pump based on the diodicity effect created by tapered channels is possible.

5.4 Curved channels

The potential implementation of curved channels in the design of temperature driven micropumps is finally, considered. The combination of straight and curved channels, arranged as shown in Figure 5.25 (left), forming a serpentine like channel, is investigated.

5.4.1 Formulation

Consider a rarefied gas enclosed between two infinitely long curved surfaces with a constant distance between them, as shown in Figure 5.25 (right). The pressure driven flow due to a pressure gradient in the direction denoted by s and the temperature driven flow due to a temperature gradient on the walls are considered. The formulation of the pressure driven flow is shown in detail, while the temperature driven case is formulated in a similar manner. The steady 2D nonlinear BGK equation is

$$\xi_x \frac{\partial f}{\partial x'} + \xi_y \frac{\partial f}{\partial y'} = \frac{P}{\mu} (f^M - f), \quad (5.12)$$

where f is the unknown velocity distribution function, $\boldsymbol{\xi}$ is the molecular velocity vector, x', y' are the physical space coordinates, P and μ are the local values of the pressure and viscosity respectively and

$$f^M = \frac{N}{(2\pi R_g T)^{3/2}} \exp \left[-\frac{(\xi_x - U_x)^2 + (\xi_y - U_y)^2 + \xi_z^2}{2R_g T} \right] \quad (5.13)$$

is the local Maxwellian distribution, with N , T , \mathbf{U} being the local number density, temperature and macroscopic velocity vector respectively (R_g is the gas constant). The coordinate system is transformed from the Cartesian (x, y) to a curvilinear system (s, r) , where s is along the channel median curve and r is perpendicular to the channel

walls, as shown in Figure 5.25 (right). Then, Eqs. (5.12) and (5.13) become [107]:

$$\frac{1}{1 - \kappa' r'} \xi_s \frac{\partial f}{\partial s'} + \xi_r \frac{\partial f}{\partial r'} + \frac{\kappa'}{1 - \kappa' r'} \xi_r \xi_s \frac{\partial f}{\partial \xi_s} - \frac{\kappa'}{1 - \kappa' r'} \xi_s^2 \frac{\partial f}{\partial \xi_r} = \frac{P}{\mu} (f^M - f) \quad (5.14)$$

$$f^M = \frac{N}{(2\pi RT)^{3/2}} \exp \left[-\frac{(\xi_r - U_r)^2 + (\xi_s - U_s)^2 + \xi_z^2}{2R_g T} \right] \quad (5.15)$$

Here, $\kappa' = 1/r'_k$ denotes the curvature with r'_k being the radius of curvature. The dimensionless pressure gradient along the channel is $X_P = \frac{D}{P_0} \frac{dP}{ds'}$ and it is assumed that $X_P \ll 1$. Since the pressure gradient is small and assuming that the pressure distribution along the channel is linear, the distribution function can be expressed as

$$f(s', r', \boldsymbol{\xi}) = f^0 (1 + X_P h_P(r', \boldsymbol{\xi}) + X_P s'/D), \quad (5.16)$$

where $h_P(r', \boldsymbol{\xi})$ is the perturbed distribution function indicating the departure of the local distribution from the reference distribution function

$$f^0 = \frac{N_0}{(2\pi RT_0)^{3/2}} \exp \left[-\frac{\boldsymbol{\xi}^2}{2RT_0} \right]. \quad (5.17)$$

Expanding the local Maxwellian distribution f^M around the reference distribution function f^0 using Taylor series and keeping terms up to first order the following expression is obtained:

$$f^M = f^0 \left[1 + \frac{N - N_0}{N_0} + \frac{2\boldsymbol{\xi} \cdot \mathbf{U}}{2RT_0} + \left(\frac{\boldsymbol{\xi}^2}{2RT_0} - \frac{3}{2} \right) \frac{T - T_0}{T_0} \right] \quad (5.18)$$

Since the pressure distribution along the channel is assumed to be linear, it can be expressed as $P = P_0 + \frac{dP}{ds'} s'$. Rearranging the terms and using the ideal gas law $P = NkT$ the following expression is obtained:

$$\frac{N - N_0}{N_0} \frac{1}{X_P} - \frac{s'}{D} = 0 \quad (5.19)$$

The following dimensionless quantities are introduced:

$$r = r'/D, \mathbf{u} = \mathbf{U}/(v_0 X_P), \boldsymbol{\zeta} = \boldsymbol{\xi}/v_0, \kappa = \kappa' D, u_{s,P} = \frac{U_{s,P}}{v_0 X_P} \quad (5.20)$$

The quantity $v_0 = \sqrt{2R_g T_0}$ is the most probable molecular speed. Substituting Eqs. (5.18) and (5.19) along with the dimensionless quantities of Eq. (5.20) and the expression of the distribution function (5.16) into Eq. (5.14), while assuming that $U_r = 0$ and the temperature is constant, the following equation for the perturbed distribution function is derived

$$\zeta_r \frac{\partial h_P}{\partial r} + \frac{\kappa}{1 - \kappa r} \zeta_r \zeta_s \frac{\partial h_P}{\partial \zeta_s} - \frac{\kappa}{1 - \kappa r} \zeta_s^2 \frac{\partial h_P}{\partial \zeta_r} = \delta (2\zeta_s u_{s,P} - h_P) - \frac{1}{1 - \kappa r} \zeta_s, \quad (5.21)$$

where

$$\delta = \frac{PD}{\mu v_0} \quad (5.22)$$

is the gas rarefaction parameter.

In order to reduce the computational load, the projection procedure is introduced, eliminating the z -component of the molecular velocity. The reduced distribution function is defined as

$$\varphi_P = \frac{1}{\sqrt{\pi}} \int_{-\infty}^{\infty} h_P e^{-\zeta_z^2} d\zeta_z \quad (5.23)$$

and the integral operator $\frac{1}{\sqrt{\pi}} \int_{-\infty}^{\infty} (\cdot) e^{-\zeta_z^2} d\zeta_z$ is applied to Eq. (5.21) to yield

$$\zeta_r \frac{\partial \varphi_P}{\partial r} + \frac{\kappa}{1 - \kappa r} \zeta_r \zeta_s \frac{\partial \varphi_P}{\partial \zeta_s} - \frac{\kappa}{1 - \kappa r} \zeta_s^2 \frac{\partial \varphi_P}{\partial \zeta_r} = \delta (2\zeta_s u_{s,P} - \varphi_P) - \frac{1}{1 - \kappa r} \zeta_s. \quad (5.24)$$

It is convenient to transform the molecular velocity space from Cartesian to a polar coordinate system according to $\zeta_r = \zeta \cos \theta$ and $\zeta_s = \zeta \sin \theta$, where ζ is the magnitude and θ is the polar angle. The derivatives of the distribution with respect to the molecular velocity then become:

$$\frac{\partial \varphi_P}{\partial \zeta_s} = \sin \theta \frac{\partial \varphi_P}{\partial \zeta} + \frac{\cos \theta}{\zeta} \frac{\partial \varphi_P}{\partial \theta} \quad (5.25)$$

$$\frac{\partial \varphi_P}{\partial \zeta_r} = \cos \theta \frac{\partial \varphi_P}{\partial \zeta} - \frac{\sin \theta}{\zeta} \frac{\partial \varphi_P}{\partial \theta} \quad (5.26)$$

Introducing this transformation to Eq. (5.24) yields:

$$\zeta \cos \theta \frac{\partial \varphi_P}{\partial r} + \frac{\kappa}{1 - \kappa r} \zeta \sin \theta \frac{\partial \varphi_P}{\partial \theta} + \delta \varphi_P = 2\delta \zeta \sin \theta u_{s,P} - \frac{1}{1 - \kappa r} \zeta \sin \theta \quad (5.27)$$

The velocity in the flow direction is defined as

$$U_s = \frac{1}{N} \int_{R^3} \xi_s f d\boldsymbol{\xi}. \quad (5.28)$$

Expanding the term $1/N$ around the reference value $1/N_0$, using Taylor series, while keeping terms up to first order and utilizing Eq. (5.19) results to

$$\frac{N_0}{N} = 1 - X_P \frac{s'}{D} \quad (5.29)$$

Expression (5.29) along with the linearization of Eq. (5.16) and the projection (5.23) are introduced into Eq. (5.28) and neglecting second order terms of X_P , since $X_P \ll 1$, the following expression for the velocity in the flow direction is obtained:

$$u_{s,P} = \frac{U_{s,P}}{v_0 X_P} = \frac{1}{\pi} \int_0^{2\pi} \int_0^\infty \zeta \sin \theta \varphi_P e^{-\zeta^2} \zeta d\zeta d\theta \quad (5.30)$$

When the temperature driven flow is considered, the formulation follows the same steps, as for the pressure driven case, with small adjustments that are briefly discussed below. The dimensionless temperature gradient along the channel walls is $X_T = \frac{D}{T_0} \frac{dT}{ds'}$ with $X_T \ll 1$. Since the temperature gradient is small the distribution function can be expressed as

$$f(s', r', \boldsymbol{\xi}) = f^0 \left(1 + X_T h_T(r', \boldsymbol{\xi}) + (\zeta^2 - 5/2) X_T s'/D \right). \quad (5.31)$$

Working in the same manner as in the pressure driven case, based on the expression (5.31) for the linearization of the distribution function and assuming constant density and temperature at each cross section the kinetic equation for the temperature driven flow becomes

$$\zeta \cos \theta \frac{\partial \varphi_T}{\partial r} + \frac{\kappa}{1 - \kappa r} \zeta \sin \theta \frac{\partial \varphi_T}{\partial \theta} + \delta \varphi_T = 2\delta \zeta \sin \theta u_{s,T} - \frac{1}{1 - \kappa r} \zeta \sin \theta (\zeta^2 - 2), \quad (5.32)$$

where

$$u_{s,T} = \frac{U_{s,T}}{v_0 X_T} = \frac{1}{\pi} \int_0^{2\pi} \int_0^\infty \zeta \sin \theta \varphi_T e^{-\zeta^2} \zeta d\zeta d\theta. \quad (5.33)$$

In both pressure and temperature driven flows, utilizing the impermeability condition, the following boundary conditions are obtained [182]:

Outer wall ($r = 1/2$) with $\cos \theta < 0$:

$$\varphi_i^+ = \frac{2}{\sqrt{\pi}} \int_0^\infty \int_{\cos\theta>0} \varphi_i^- \zeta \cos\theta e^{-\zeta^2} \zeta d\theta d\zeta \quad (5.34)$$

Inner wall ($r = 1/2$) with $\cos\theta > 0$:

$$\varphi_i^+ = -\frac{2}{\sqrt{\pi}} \int_0^\infty \int_{\cos\theta<0} \varphi_i^- \zeta \cos\theta e^{-\zeta^2} \zeta d\theta d\zeta \quad (5.35)$$

Here, $i = P, T$ refers to the pressure and temperature driven flow.

For the pressure driven flow Eq. (5.27) is solved subject to boundary conditions (5.34) and (5.35), using Eq. (5.30) for the macroscopic velocity. For the temperature driven flow Eq. (5.32) is solved, subject to the same boundary conditions (5.34) and (5.35), using Eq. (5.33) for the macroscopic velocity.

5.4.2 Kinetic coefficients

Upon solving the kinetic equations, the reduced flow rates or kinetic coefficients are obtained in terms of the rarefaction parameter δ and curvature κ . The kinetic coefficient for the pressure driven flow is given by

$$M_P(\delta, \kappa) = -2 \int_{-1/2}^{1/2} u_{s,P} dr \quad (5.36)$$

and for the temperature driven flow by

$$M_T(\delta, \kappa) = 2 \int_{-1/2}^{1/2} u_{s,T} dr. \quad (5.37)$$

The kinetic coefficients are tabulated in Tables 5.1 and 5.2 for the pressure and temperature driven flows respectively, in a wide range of the rarefaction parameter $\delta \in [10^{-2}, 10^2]$ and for various values of the curvature $\kappa = 0.2, 0.5, 0.8, 1$ and 1.2 . The respective results for the straight channel ($\kappa = 0$) are also included for comparison purposes. It is noted, that under the current notation the limiting value of the curvature is $\kappa = 2$, where the inner wall coincides with the center of curvature and the channel is reduced to a circle.

For the pressure driven flow, when $\delta \geq 5$ increasing the curvature leads to small changes in the kinetic coefficient and the curvature becomes significant for $\kappa > 0.8$.

The curvature has a greater effect in highly rarefied flows where even small values of curvature have a significant effect on M_P . When the channel is straight, as δ is decreased M_P is constantly increased, while for curved channels it reaches a constant value as $\delta \rightarrow 0$. As the curvature increases, the Knudsen minimum moves to smaller values of δ and finally, for $\kappa \geq 0.5$ vanishes. The reason is that the channel curvature provides a geometrical limit to the long trajectories of ballistic particles, resulting to a smoother decrease of the ballistic flow rate as δ increases, while the rate of increase of the collision part of the flow rate is only slightly altered. The rate of increase of the collision part is always larger in magnitude than the rate of decrease of the ballistic part, so the Knudsen minimum does not appear. It is also interesting that increasing the curvature, leads to a decrease of the flow rate for small δ , while for $\delta \geq 50$ it initially decreases until a minimum is reached and then is increased as the curvature is further increased.

The behavior of the kinetic coefficient for the temperature driven flow (M_T) with respect to the rarefaction parameter (δ) is relatively simple, with M_T decreasing monotonically when δ increases. For $\delta \leq 0.2$ increasing the curvature leads to a decrease of M_T until it reaches a minimum and then increases again, while for large values of δ increasing the curvature always increases M_T .

5.4.3 Simulation of thermally driven flows through curved channels

Upon obtaining the databases for the kinetic coefficients, the following ordinary differential equation is solved

$$\frac{dP}{ds} = -\frac{v(s)}{D^2 M_P(\delta, \kappa)} \dot{m} + \frac{M_T(\delta, \kappa)}{M_P(\delta, \kappa)} \frac{P(s)}{T(s)} \frac{dT}{ds}. \quad (5.38)$$

This equation is equivalent to Eq. (5.10) for straight channels. However, now the kinetic coefficients are also a function of the local channel curvature. In order to solve Eq. (5.38) the temperature $T(s)$ and curvature $\kappa(s)$ profiles should be specified along with the inlet and outlet pressure or alternatively, the mass flow rate with one of the end pressures. When one end pressure and the mass flow rate are specified, Eq. (5.38) is trivially integrated to give the pressure distribution along the channel, while when the two pressures are given then a shooting method is used to solve Eq. (5.38) and obtain the pressure distribution and mass flow rate.

Following the analysis of tapered channels, two limiting cases are considered, that of a closed channel ($\dot{m} = 0$) and that of equal inlet and outlet pressures ($P_{in} = P_{out}$). In the former case the induced pressure difference is of interest and it is compared to that of the straight channel, based on the ratio

$$R_P = \frac{\Delta P^{curved}}{\Delta P^{straight}}. \quad (5.39)$$

In the latter case the mass flow rate is of interest and it is compared to that of the straight channel, based on the ratio

$$R_{\dot{m}} = \frac{\dot{m}^{curved}}{\dot{m}^{straight}}. \quad (5.40)$$

It is expected that all intermediate cases can be derived from the two limiting ones, as shown for the tapered channels. The two ratios correspond to the diodicity coefficients used in tapered channels.

Simulations are conducted for single straight and curved channels with width $D = 10\mu m$. The length of the straight channel is set to $L_S/D = 20$. Concerning the curved channel length, two cases are considered. In the first one, the curved channel has the same length as the straight one ($L_C/D = L_S/D = 20$) and it is used to compare straight and curved channels on the same basis. In the second one, the curved channel length is connected to the construction of a serpentine like pump and therefore it is restricted as it should cover an arch of π radians and it is taken to be $L_C/D = \pi/\kappa$. The dimensionless length of the curved channel covering π radians for the different values of curvature examined is given the table below.

κ	0.2	0.5	0.8	1	1.2
$L_S/D = \pi/\kappa$	15.70796	6.28319	3.92699	3.14159	2.61799

The temperature distribution along the channel walls is assumed to be linear and the inlet and outlet temperatures are $T_{in} = 273K$ and $T_{out} = 546K$. The curvatures for the examined curved channels examined are $\kappa = 0.2, 0.5, 0.8, 1$ and 1.2 . The inlet pressure is in a wide range as $P_{in} \in [20, 0.4 \times 10^5]Pa$. Segments of the curved channels of various curvatures are plotted in Figure 5.26 to help understanding the corresponding serpentine shapes (in all cases an arch of $\pi/6$ radians is shown).

5.4.4 Zero net mass flow rate

In the limiting case of zero net mass flow rate the two ends of the channel are assumed to be closed and the net mass flow rate vanishes. Due to the temperature gradient a pressure difference is generated between the two ends of the channel. In Figure 5.27 (left), the pressure difference is shown in terms of the inlet pressure for the straight channel, as well as for the curved channels with different values of curvature and length equal to the straight channel ($L_C = L_S$). It is observed that the curved channels generate a higher pressure difference than the straight channel and the pressure difference increases as the curvature is increased. As the inlet pressure initially increases, the pressure difference generated is increased until a maximum value is reached around $P_{in} \approx 4 \times 10^3 \text{Pa}$ and increasing the inlet pressure further, leads to a decrease of the pressure difference. The maximum pressure difference ranges from 240Pa for the straight channel up to 360Pa for a channel with $\kappa = 1.2$. It is noted that the results for the straight channel are not identical as the respective results given in the tapered channel investigation as the BGK model is used here, instead of the Shakhov.

The pressure difference ratio R_P , as shown in Figure 5.27 (right), is always larger than one, as the pressure difference of the curved channels is always larger than the straight one. In the tapered channels the pressure diodicity could take values either larger or smaller than one and certainly this an advantage of the tapered design. The pressure difference ratio is close to one for small values of the inlet pressure, then, it increases and can reach up to 1.6 for $\kappa = 1.2$ and finally, decreases again. The pressure difference ratio is also increased as the curvature is increased. The optimum range of the inlet pressure for this design is $P_{in} \approx 2 - 5 \times 10^3 \text{Pa}$, where both the pressure difference and the pressure difference ratio take high values.

In Figure 5.28 the respective results are provided, with the length of the curved channel now being restricted by the serpentine channel design. The results are identical with the ones for equal lengths, as in the thermo-molecular pressure difference phenomenon the generated pressure difference is independent of the channel length.

5.4.5 Equal inlet and outlet pressures

In the limiting case of zero pressure difference the inlet and outlet pressures are equal. Although the overall pressure difference is zero, local pressure gradients exist inside the channel so Poiseuille type flow cannot be neglected. In Figure 5.29 (left) the

mass flow rate per unit depth is shown for the straight and the curved channels with $L_S = L_C$. The straight channel has a larger mass flow rate compared to the curved channels for $P_{in} < 10^3 \text{Pa}$, while the situation is reversed for larger values of P_{in} .

The mass flow rate ratio R_m is shown in Figure 5.29 (right) for $L_S = L_C$. Following the mass flow rate behavior, the mass flow rate ratio may take values either smaller or larger than one for small and large values of P_{in} respectively. In the tapered channels the mass diodicity coefficient was always larger than one.

It is more interesting to consider the case where the length of the curved channel is $L_C = \pi D/\kappa$, following the design restrictions. The mass flow rate and mass flow rate ratio R_m are shown in Figure 5.30. In this case the curved channels produce larger mass flow rates than the straight one (with the exception of $\kappa = 0.2$ and $P_{in} \leq 50 \text{Pa}$). This is due to the length of channel which has a strong effect in the mass flow rate generated. Thus the mass flow rate ratio takes quite high values, up to 9 for $\kappa = 1.2$, since higher curvature means shorter curved channel.

5.5 Concluding remarks

Three thermally driven flow configurations have been examined and the design of the corresponding thermally driven micropumps has been considered. The first configuration consists of a channel with saw tooth surfaces, which are kept at constant but different temperatures and the flow is driven by the thermal stress slip flow mechanism. The other two configurations are based on thermal transpiration. The concepts of creating multistage assemblies of tapered channels, as well as serpentine type channels, are investigated. In all cases, the main advantages or drawbacks of each configuration are discussed and guidelines on their implementation are provided.

The flow configuration in a saw tooth surface channel is first considered. Since the temperature along the channel walls remain constant, temperature control becomes simpler. Simulations are conducted on unstructured meshes built via the geometrical approach by solving the nonlinear Shakhov kinetic model equation. The ability of this configuration to create a mass flow rate is demonstrated and the effect of the pressure, temperature and of the main geometrical parameters on the mass flow rate is examined. The mass flow rate is very sensitive to the different parameters characterizing the flow and can even change direction depending on the value of the reference pressure. The temperature gradients close to the channel walls have been computed and found to be very high, imposing certain restrictions on the materials utilized. Thus, although

the constant wall temperature is appealing, maintaining such high temperatures and ensuring proper thermal insulation raise serious drawbacks in the realization of such devices.

Next, the thermally driven flow along with the associated pressure difference obtained through long converging and diverging channels has been computationally investigated. The analysis is performed by accordingly integrating the dimensionless flow rate obtained by the linear kinetic modeling into a simple algorithm based on the mass conservation principle. The computed net mass flow rate through the tapered channel from the low toward the high temperature reservoir and the associated pressure differences are computed and parametrized, in terms of the channel geometry focusing on the channel inclination ratio and on the inlet pressure covering a wide range of gas rarefaction. By comparing the corresponding converging and diverging flows, the diode effect is also examined.

In systems with closed boundaries (zero net mass flow rate), the optimum operation scenario is obtained at inlet pressures around $4 \times 10^3 \text{Pa}$, where both the developed pressure difference is large and the diode effect is significant. The pressure difference is always increased with the inclination ratio, and depending on the inlet pressure, it may be larger for either the diverging or converging channel. In systems with open boundaries (nonzero net mass flow rate) and zero pressure difference (inlet pressure equal to outlet pressure), the optimum operation range is at inlet pressures around $1.5 \times 10^4 \text{Pa}$ where both the mass flow rate is large and the diode effect is significant. The mass flow rate is always decreased with the inclination ratio and it is always larger for the diverging channel. In open systems with nonzero net mass flow rate and pressure difference, the computed performance curves show that in all cases the pressure difference decreases almost linearly as the mass flow rate increases and provides a complete picture of the pumping effect in converging and diverging channels. The negative slope of these lines depends strongly on the inlet pressure and the inclination ratio.

In order to fully demonstrate the ability of multistage designs based on tapered channels, indicative results are presented for cascades of diverging and converging channels with up to 200 stages. The pressure can either increase or decrease along the cascade, depending on the inlet pressure, as the pressure diodicity coefficient can be either smaller or larger than one.

Finally, a combination of straight and curved channels is also considered, and the simulation of this case is performed in a similar manner as in the tapered channels.

It is deduced that the combination of curved and straight channels can indeed be used for the design of thermally driven pumps based on the thermal transpiration phenomenon. The curved channels always produce larger pressure differences than the straight channel when the mass flow rate is zero. Furthermore, the pressure difference ratio takes relatively high values in the same range of pressures where the pressure difference is also large ($P_{in} \approx 2 - 5 \times 10^3 \text{Pa}$ for the present geometry). In terms of the mass flow rate, although the effect of the curvature alone can be either beneficial or detrimental, if the different lengths are taken into account, the curved channels produce much higher mass flow rates compared to the straight ones. It is believed that this design could potentially be implemented, if associated manufacturing and temperature control issues are overcome.

In recent years, there have been targeted attempts to build thermally driven pumping devices, without moving parts, in gaseous microfluidics based on various configurations. In this context the results presented in this chapter may be very useful in deciding on the suitability of a tentative design for developing Knudsen type pumps.

Table 5.1 Kinetic coefficient M_P in terms of δ and curvature κ for pressure driven flow through curved channels.

δ	κ					
	0	0.2	0.5	0.8	1	1.2
0.01	3.05	1.44	1.17	1.05	1.00	9.80(-1)
0.02	2.71	1.44	1.17	1.05	1.00	9.82(-1)
0.05	2.30	1.43	1.18	1.05	1.01	9.85(-1)
0.08	2.12	1.43	1.18	1.06	1.01	9.89(-1)
0.1	2.03	1.43	1.18	1.06	1.01	9.92(-1)
0.2	1.81	1.43	1.20	1.08	1.03	1.01
0.5	1.60	1.43	1.24	1.13	1.08	1.05
0.8	1.55	1.45	1.29	1.18	1.13	1.10
1	1.54	1.47	1.32	1.21	1.16	1.13
2	1.60	1.57	1.49	1.39	1.34	1.30
5	1.99	1.99	1.96	1.90	1.86	1.83
8	2.45	2.45	2.43	2.40	2.38	2.35
10	2.77	2.77	2.76	2.73	2.71	2.69
20	4.40	4.40	4.39	4.39	4.38	4.38
50	9.36	9.35	9.35	9.35	9.36	9.39
80	1.44(+1)	1.22(+1)	1.22(+1)	1.22(+1)	1.22(+1)	1.22(+1)
100	1.77(+1)	1.77(+1)	1.77(+1)	1.78(+1)	1.78(+1)	1.78(+1)

Table 5.2 Kinetic coefficient M_T in terms of δ and curvature κ for temperature driven flow through curved channels.

δ	κ					
	0	0.2	0.5	0.8	1	1.2
0.01	1.24	7.09(-1)	5.80(-1)	5.19(-1)	4.97(-1)	4.87(-1)
0.02	1.06	6.98(-1)	5.74(-1)	5.16(-1)	4.94(-1)	4.84(-1)
0.05	8.45(-1)	6.67(-1)	5.59(-1)	5.05(-1)	4.85(-1)	4.76(-1)
0.08	7.42(-1)	6.40(-1)	5.44(-1)	4.95(-1)	4.76(-1)	4.68(-1)
0.1	6.95(-1)	6.23(-1)	5.35(-1)	4.88(-1)	4.71(-1)	4.63(-1)
0.2	5.58(-1)	5.54(-1)	4.95(-1)	4.59(-1)	4.46(-1)	4.40(-1)
0.5	3.99(-1)	4.22(-1)	4.09(-1)	3.93(-1)	3.87(-1)	3.86(-1)
0.8	3.27(-1)	3.46(-1)	3.49(-1)	3.45(-1)	3.43(-1)	3.45(-1)
1	2.95(-1)	3.10(-1)	3.19(-1)	3.19(-1)	3.20(-1)	3.23(-1)
2	2.06(-1)	2.11(-1)	2.23(-1)	2.31(-1)	2.37(-1)	2.43(-1)
5	1.14(-1)	1.15(-1)	1.19(-1)	1.25(-1)	1.30(-1)	1.35(-1)
8	7.95(-2)	7.98(-2)	8.15(-2)	8.48(-2)	8.78(-2)	9.14(-2)
10	6.61(-2)	6.63(-2)	6.74(-2)	6.98(-2)	7.20(-2)	7.48(-2)
20	3.57(-2)	3.57(-2)	3.61(-2)	3.69(-2)	3.77(-2)	3.86(-2)
50	1.49(-2)	1.49(-2)	1.50(-2)	1.52(-2)	1.54(-2)	1.56(-2)
80	9.41(-3)	9.26(-3)	9.33(-3)	9.47(-3)	9.58(-3)	9.68(-3)
100	7.55(-3)	7.31(-3)	7.61(-3)	7.71(-3)	7.79(-3)	7.64(-3)

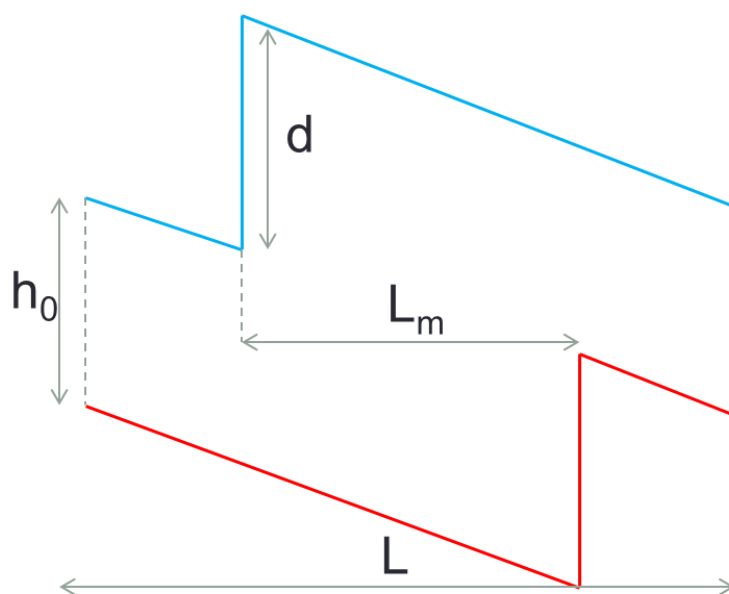


Figure 5.1 One stage of the saw-tooth channel along with the dimensions.

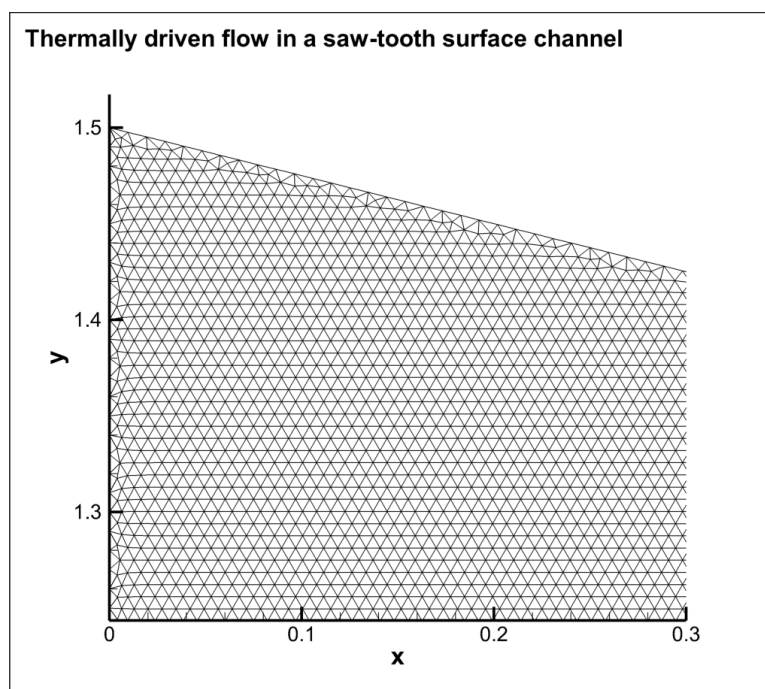


Figure 5.2 Section of typical mesh used for the simulation of the saw tooth surface channel.

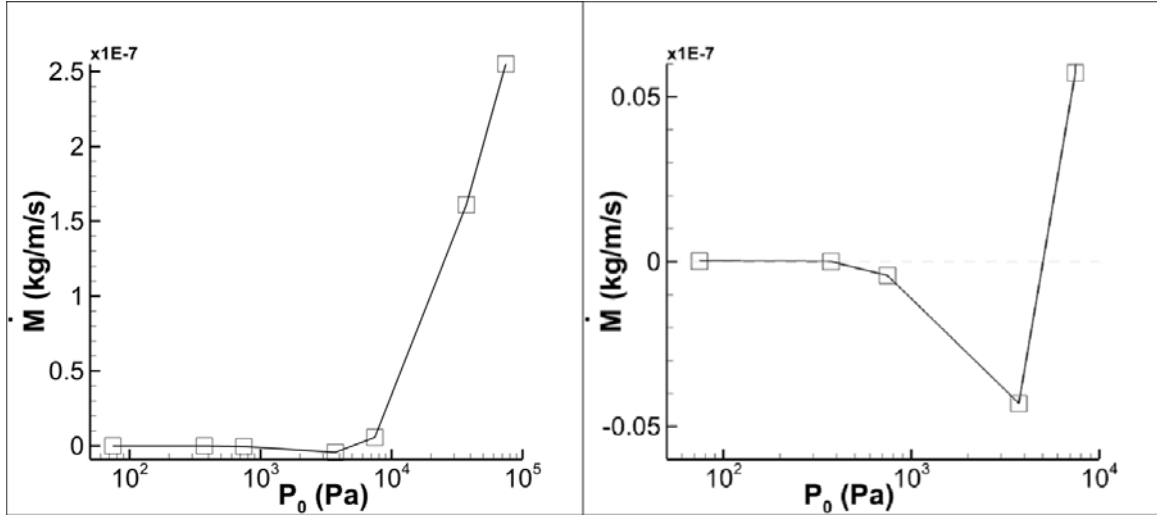


Figure 5.3 Mass flow rate for a saw-tooth channel in terms of pressure for $P_0 \in [10^2, 10^5]$ Pa (left) and $P_0 \in [10^2, 10^4]$ Pa (right).

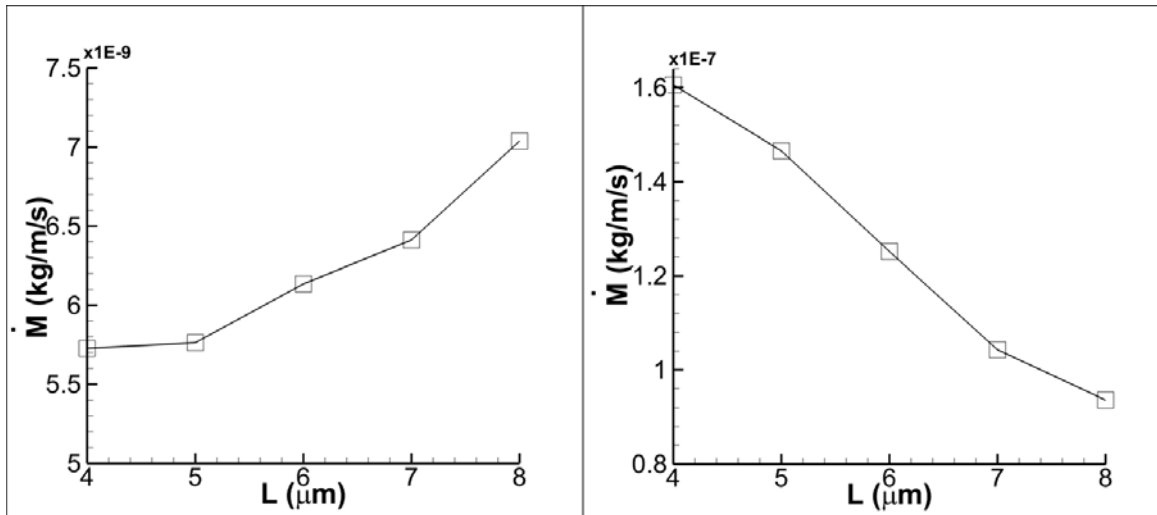


Figure 5.4 Mass flow rate for a saw-tooth channel in terms of stage length L for $P_0 = 7451$ Pa (left) and $P_0 = 37255$ Pa (right).

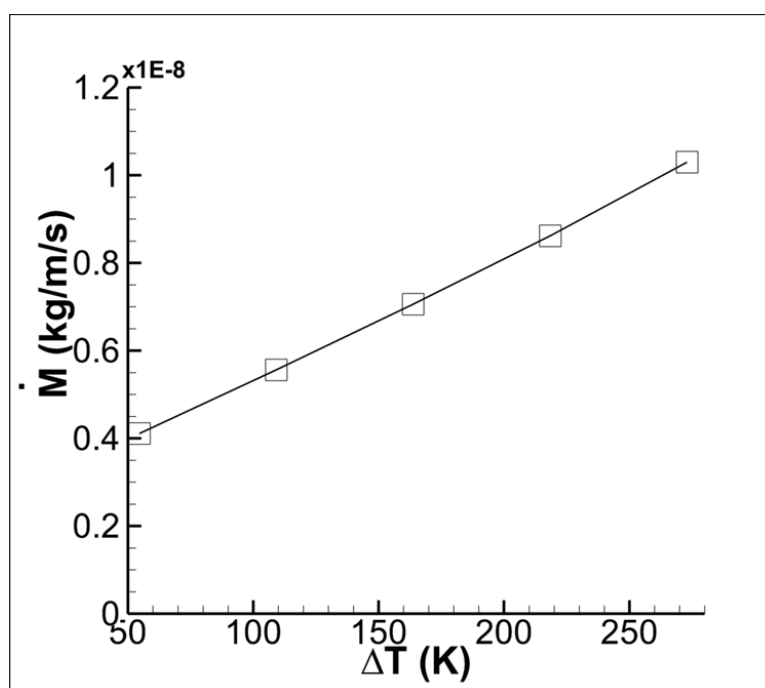


Figure 5.5 Mass flow rate for a saw-tooth channel in terms of ΔT for $P_0 = 7451\text{Pa}$.

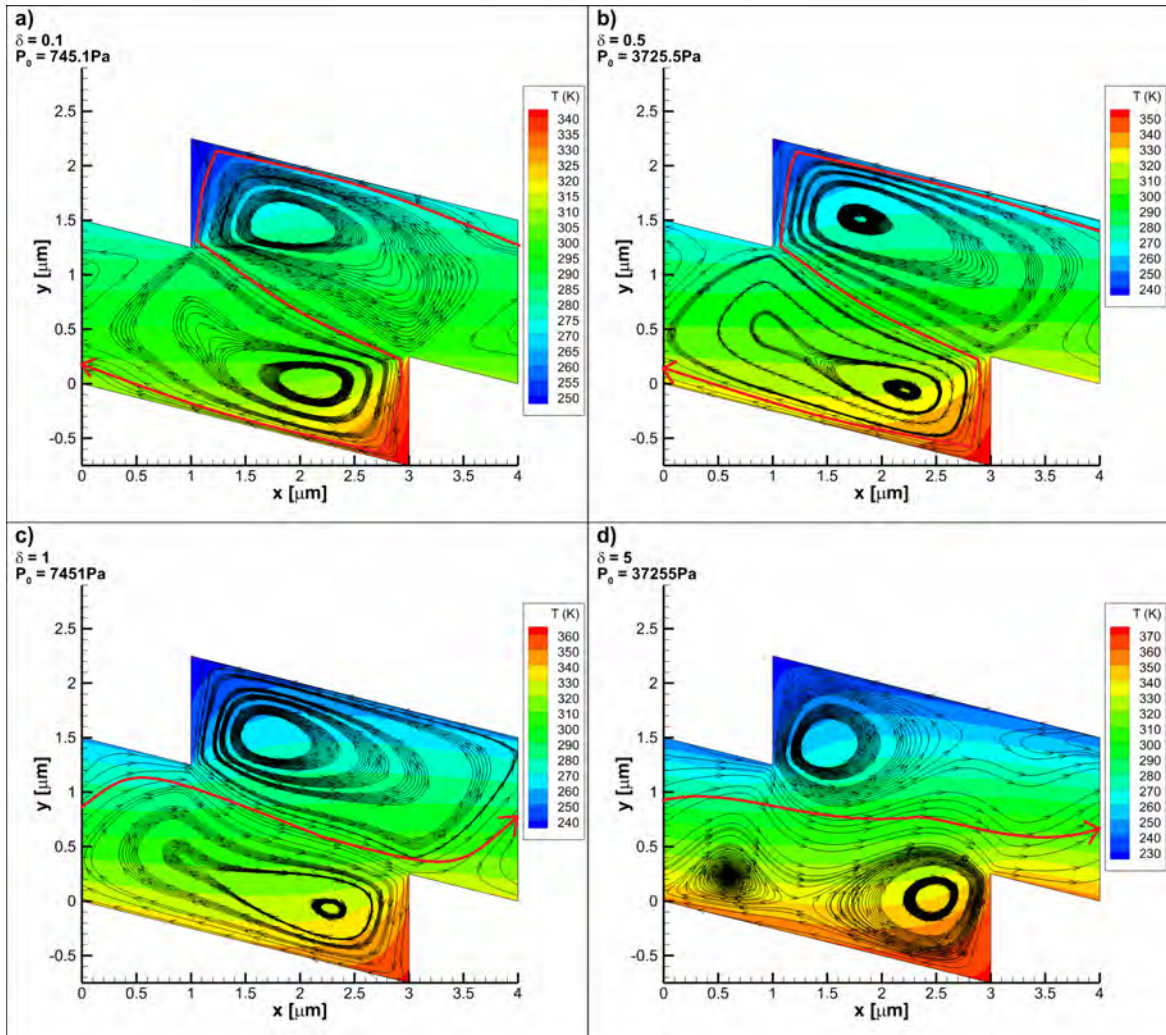


Figure 5.6 Streamlines and temperature contours for a saw-tooth channel for various values of P_0 .

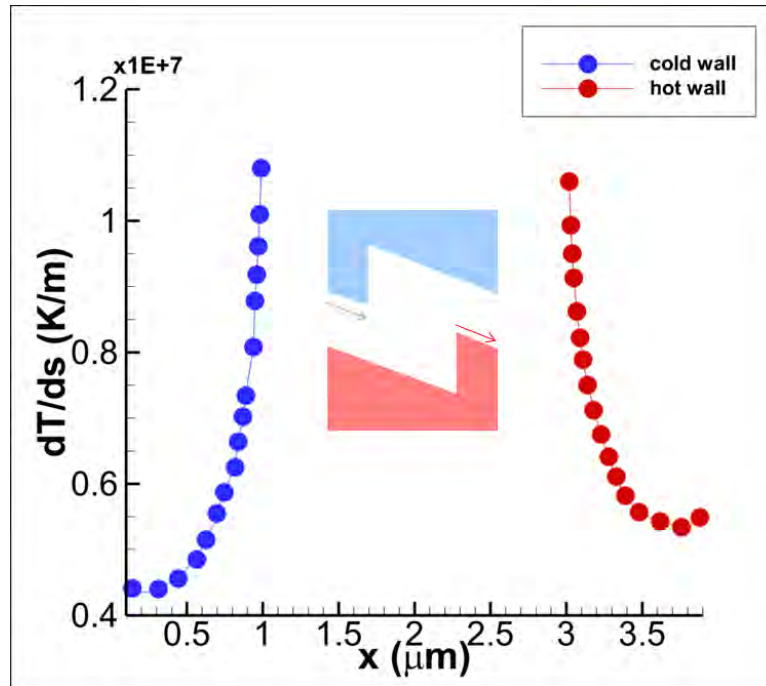


Figure 5.7 Temperature gradient along the inclined walls of a saw-tooth channel with $P_0 = 7451\text{Pa}$.

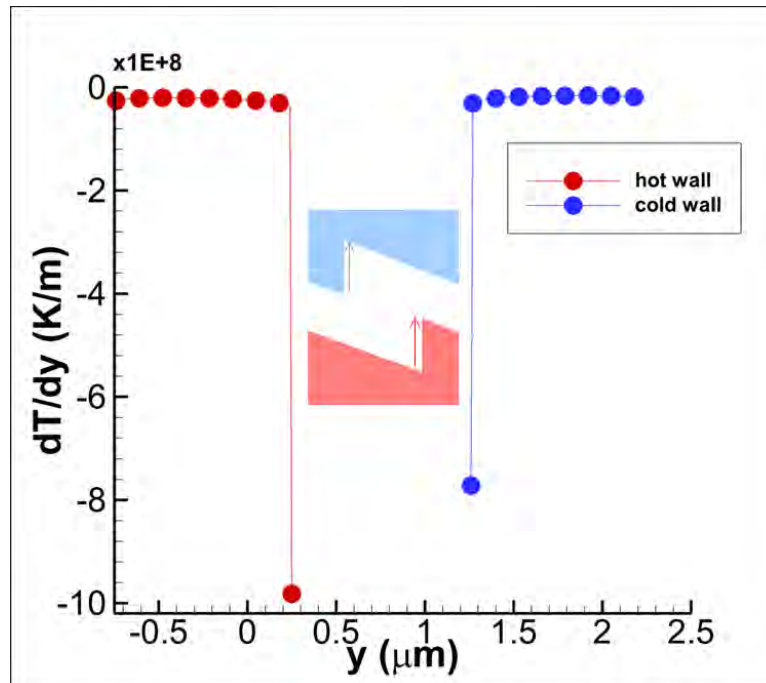


Figure 5.8 Temperature gradient along the vertical walls of a saw-tooth channel with $P_0 = 7451\text{Pa}$.

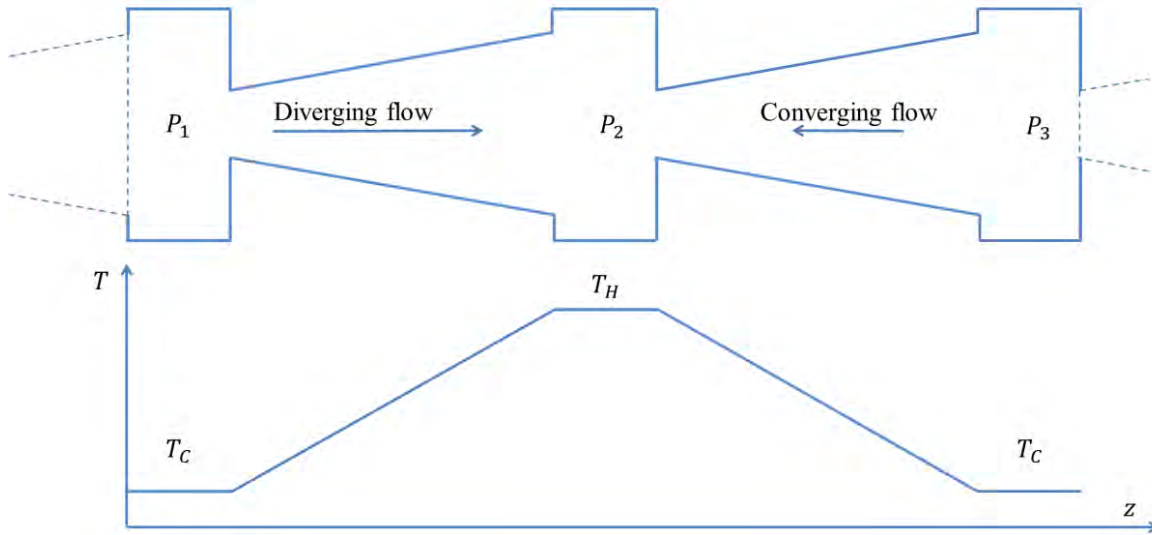


Figure 5.9 View of a pumping stage of a tapered Knudsen-type cascade pump with T_C and T_H denoting the cold and hot reservoir temperature, respectively.

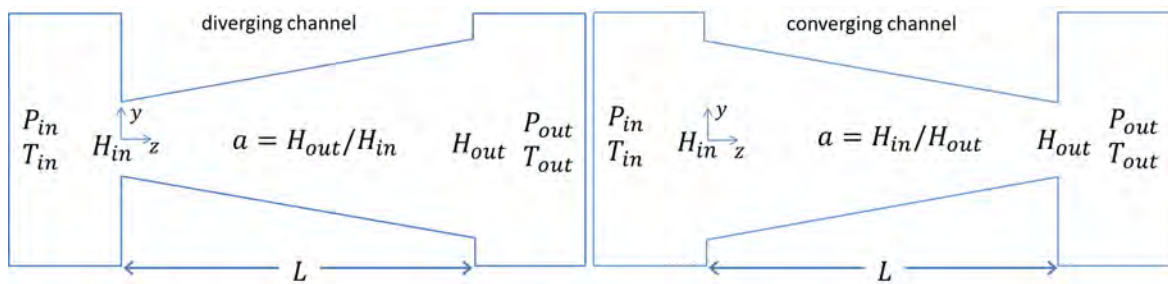


Figure 5.10 Diverging (left) and converging (right) channels with inclination ratio $\alpha_{con} = \alpha_{div} = \alpha$.

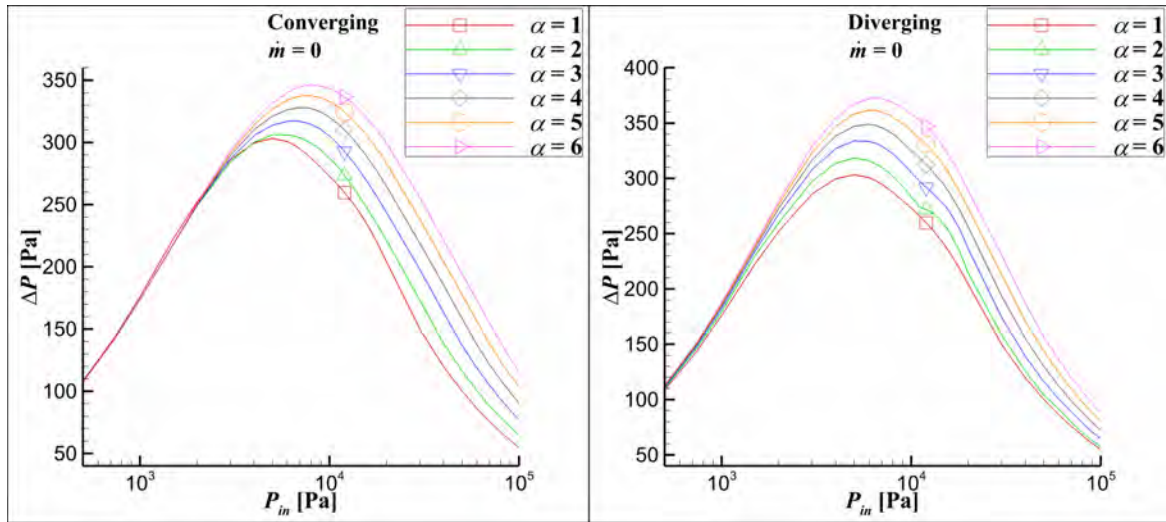


Figure 5.11 Pressure difference $\Delta P = P_{out} - P_{in}$ in terms of P_{in} for various values of α in a closed system with zero net mass flow rate and $H_m = 10\mu\text{m}$.

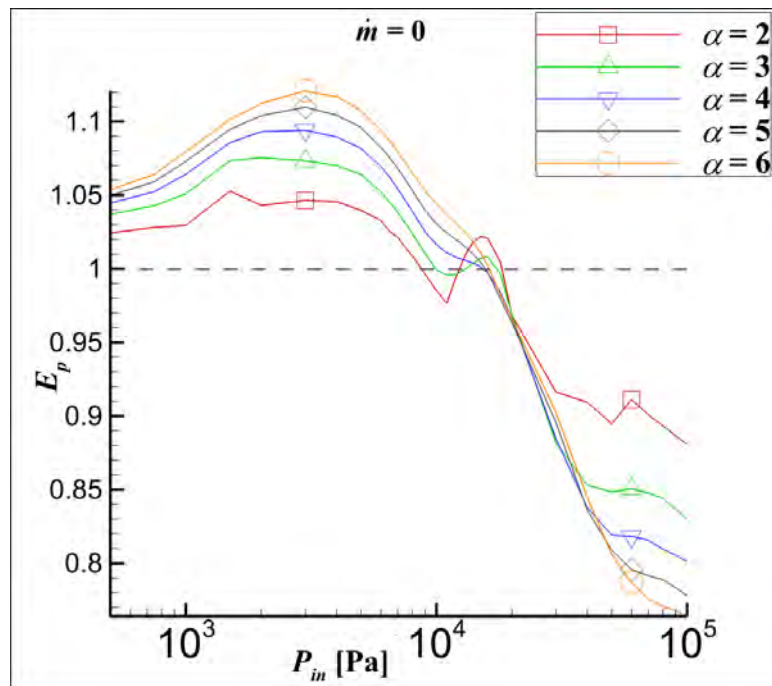


Figure 5.12 Pressure diodicity coefficient E_P in terms of P_{in} for various values α in a closed system with zero net mass flow rate and $H_m = 10\mu\text{m}$.

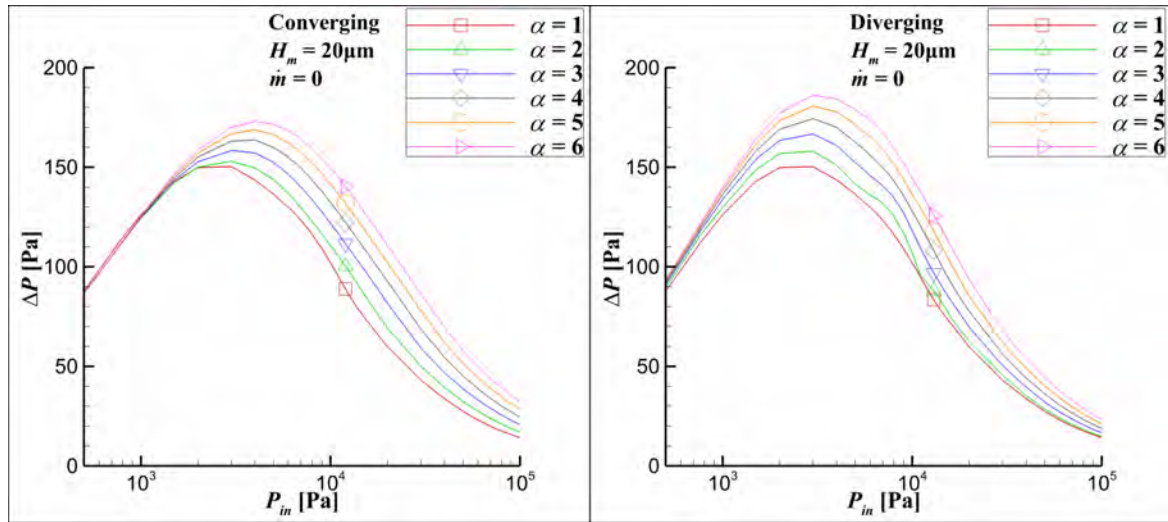


Figure 5.13 Pressure difference $\Delta P = P_{out} - P_{in}$ in terms of P_{in} for various values α in a closed system with zero net mass flow rate and $H_m = 20\mu\text{m}$.

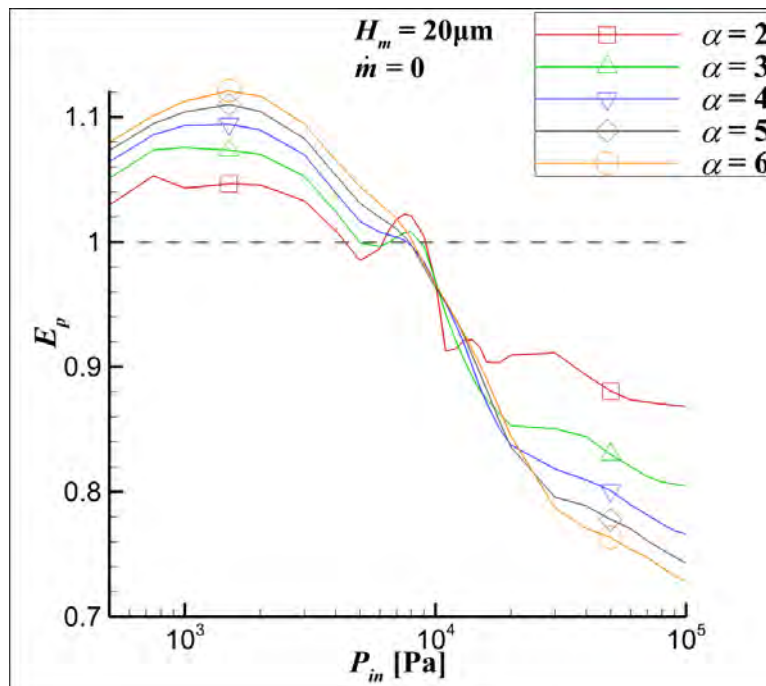


Figure 5.14 Pressure diodicity coefficient E_P in terms of P_{in} for various values of α in a closed system with zero net mass flow rate and $H_m = 20\mu\text{m}$.

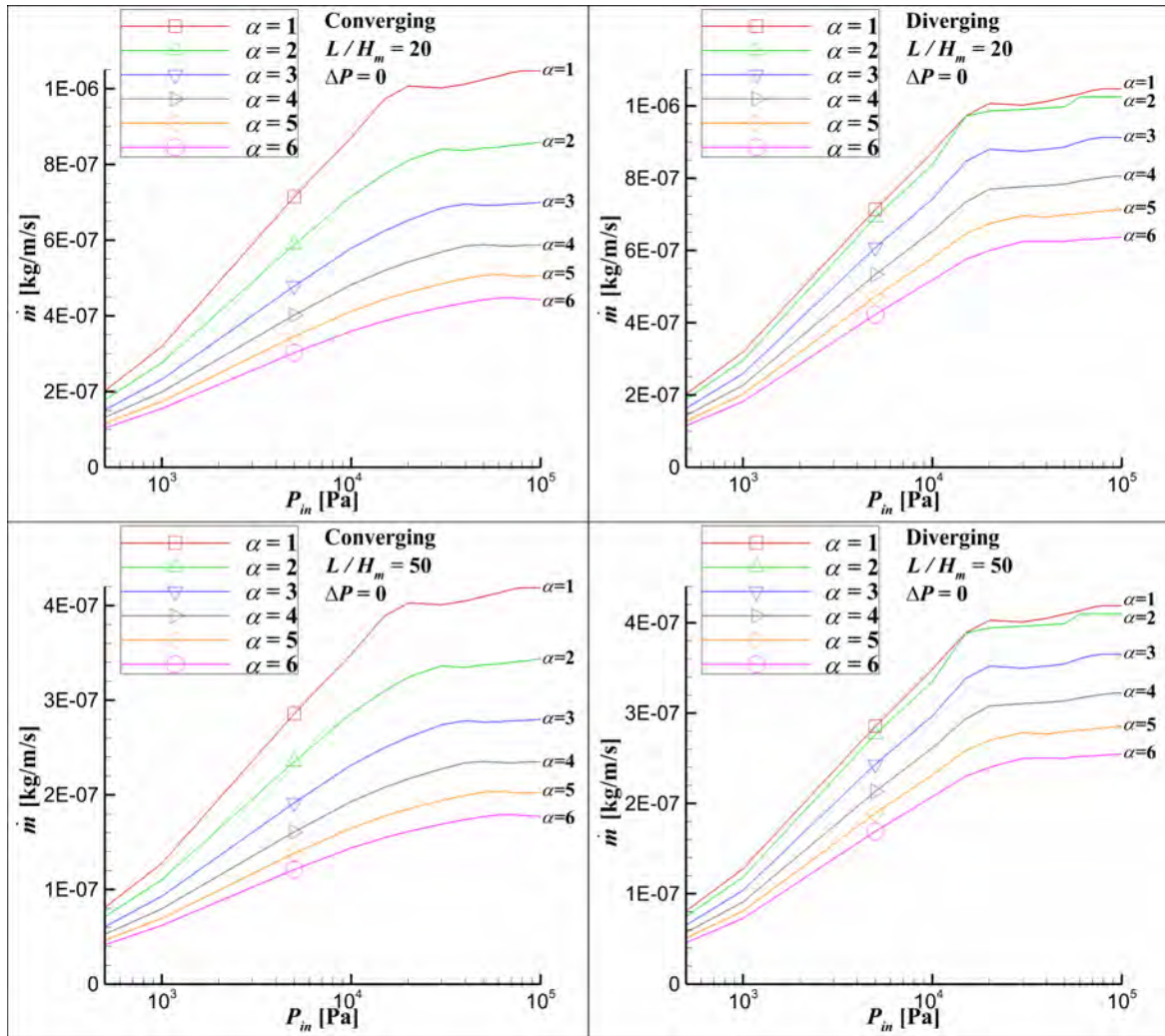


Figure 5.15 Mass flow rate \dot{m} in terms of P_{in} for $L/H_m = 20, 50$ with $H_m = 10\mu\text{m}$ and various values of α in an open system with zero pressure difference.

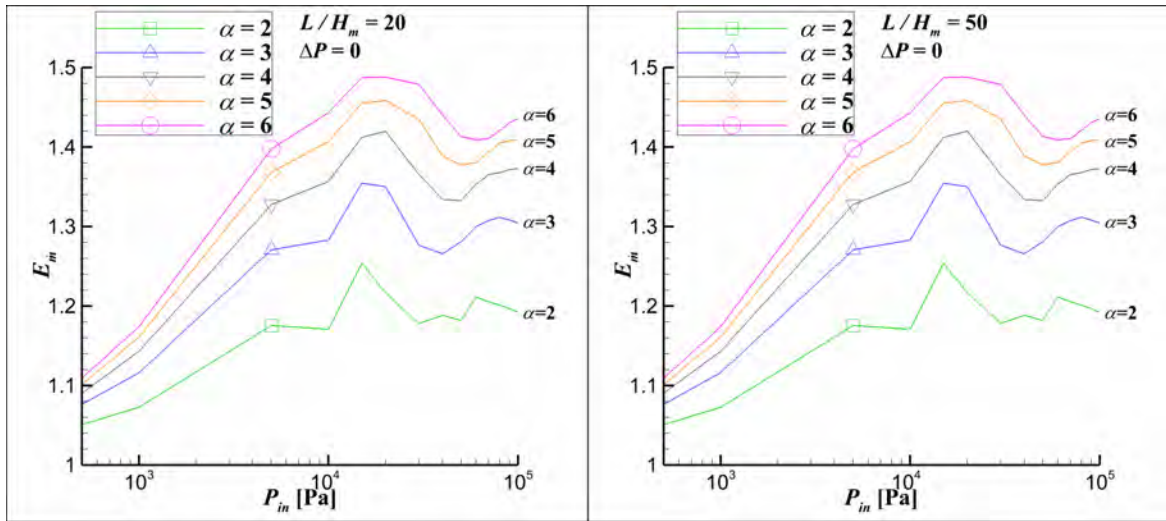


Figure 5.16 Mass diodicity coefficient E_m in terms of P_{in} for $L/H_m = 20, 50$ with $H_m = 10\mu\text{m}$ and various values of α in an open system with zero pressure difference.

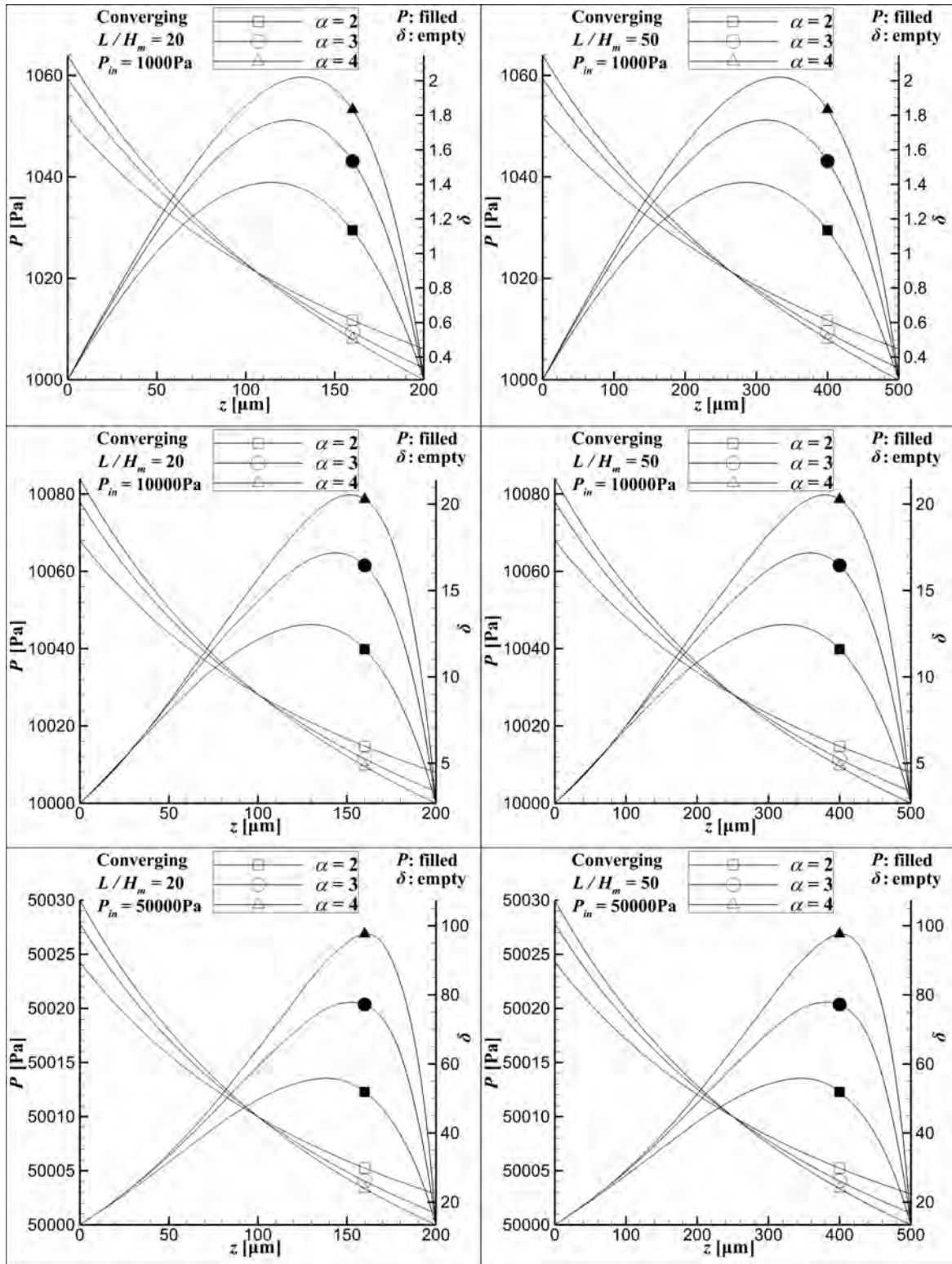


Figure 5.17 Pressure and gas rarefaction parameter distributions along a converging channel with $L/H_m = 20, 50$, $H_m = 10 \mu\text{m}$, $P_{in} = 10^3, 0.5 \times 10^5 \text{ Pa}$ and $\alpha = 2, 3, 4$ in an open system with zero pressure difference.

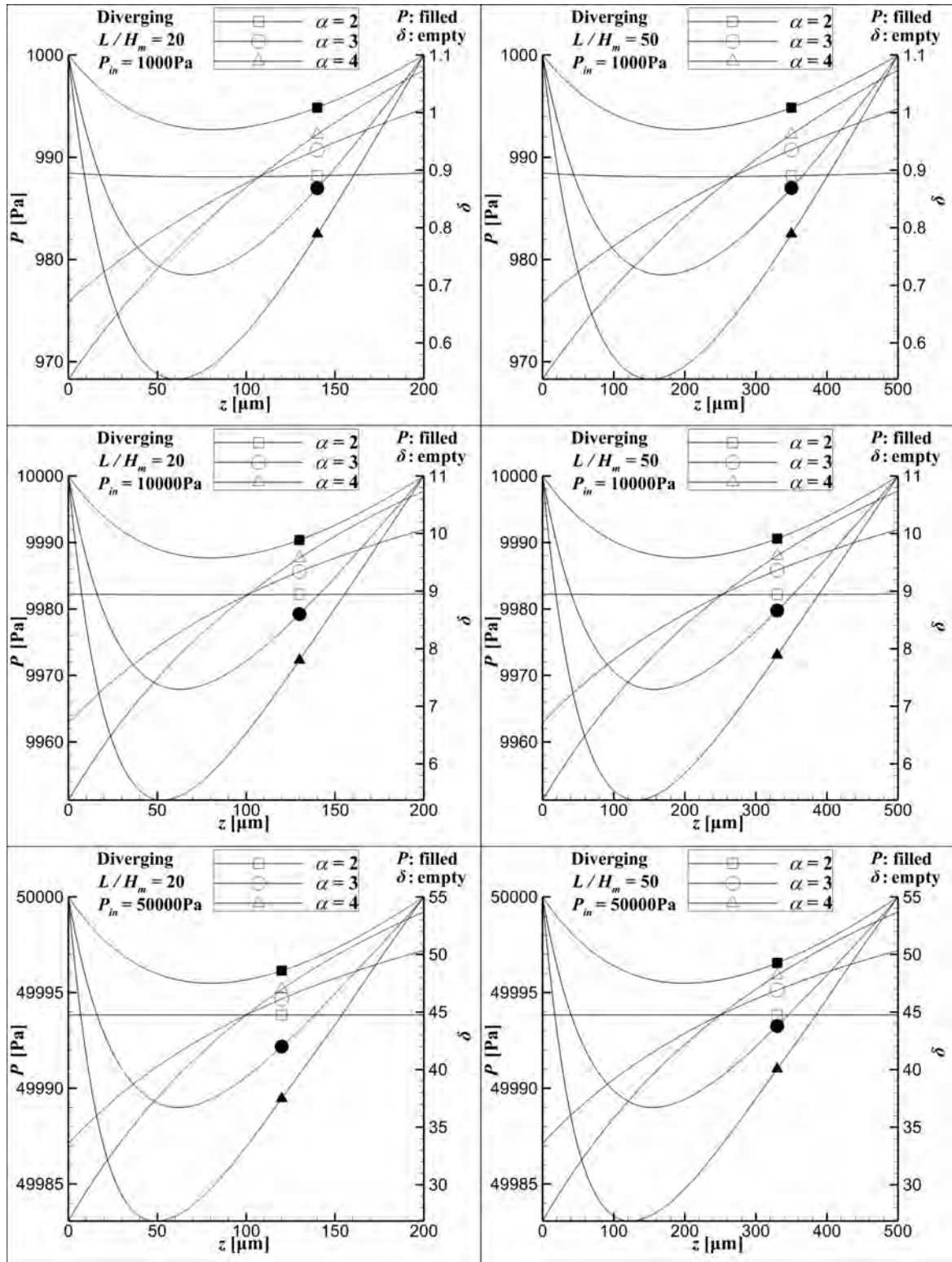


Figure 5.18 Pressure and gas rarefaction parameter distributions along a diverging channel with $L/H_m = 20, 50$, $H_m = 10 \mu\text{m}$, $P_{in} = 10^3, 0.5 \times 10^5 \text{ Pa}$ and $\alpha = 2, 3, 4$ in an open system with zero pressure difference.

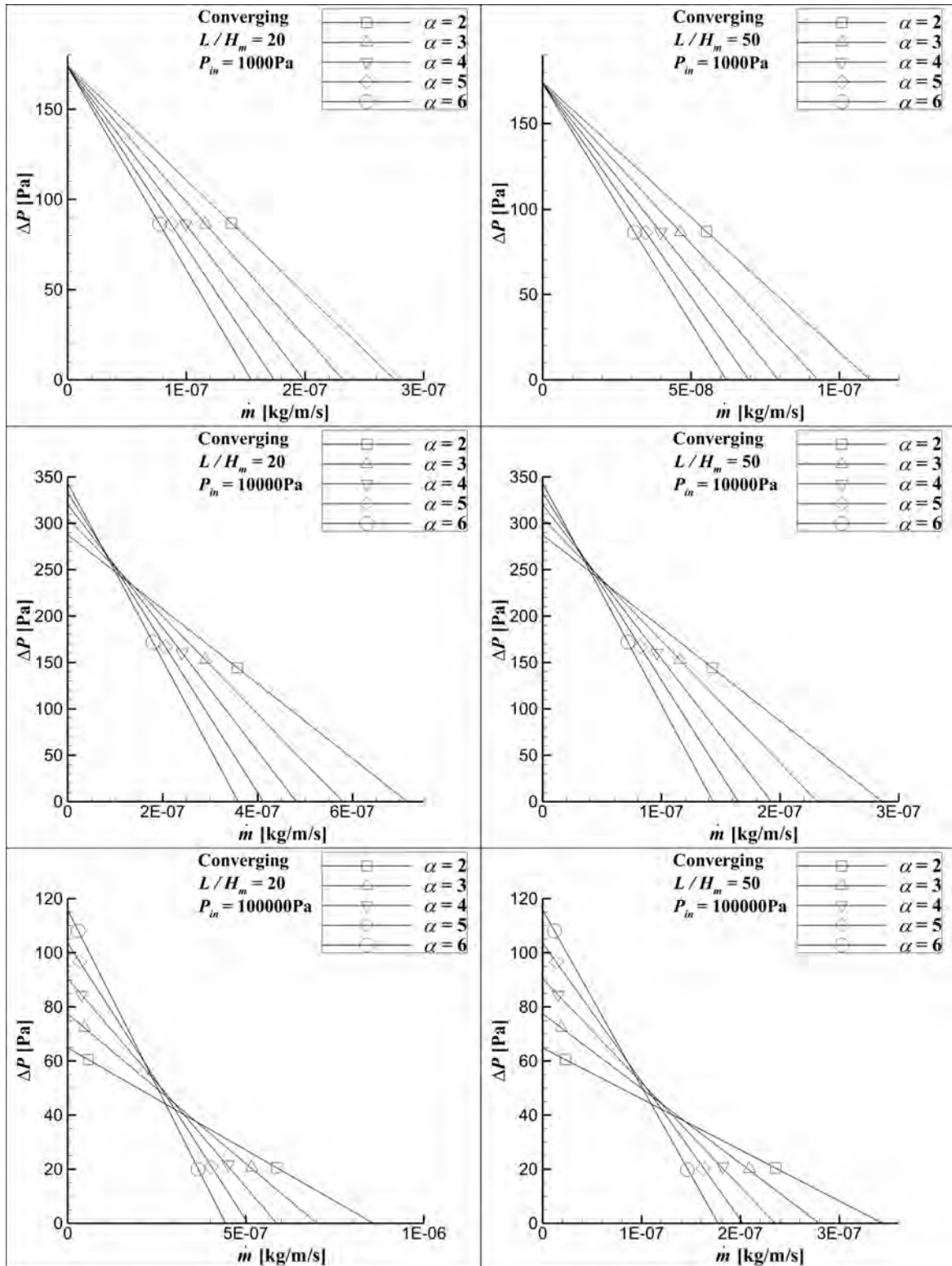


Figure 5.19 Pressure difference $\Delta P = P_{out} - P_{in}$ in terms of the mass flow rate \dot{m} in a converging channel with $L/H_m = 20, 50$, $H_m = 10 \mu\text{m}$, $P_{in} = 10^3, 10^4, 10^5 \text{ Pa}$ and $\alpha = 2, 3, 4, 5, 6$.

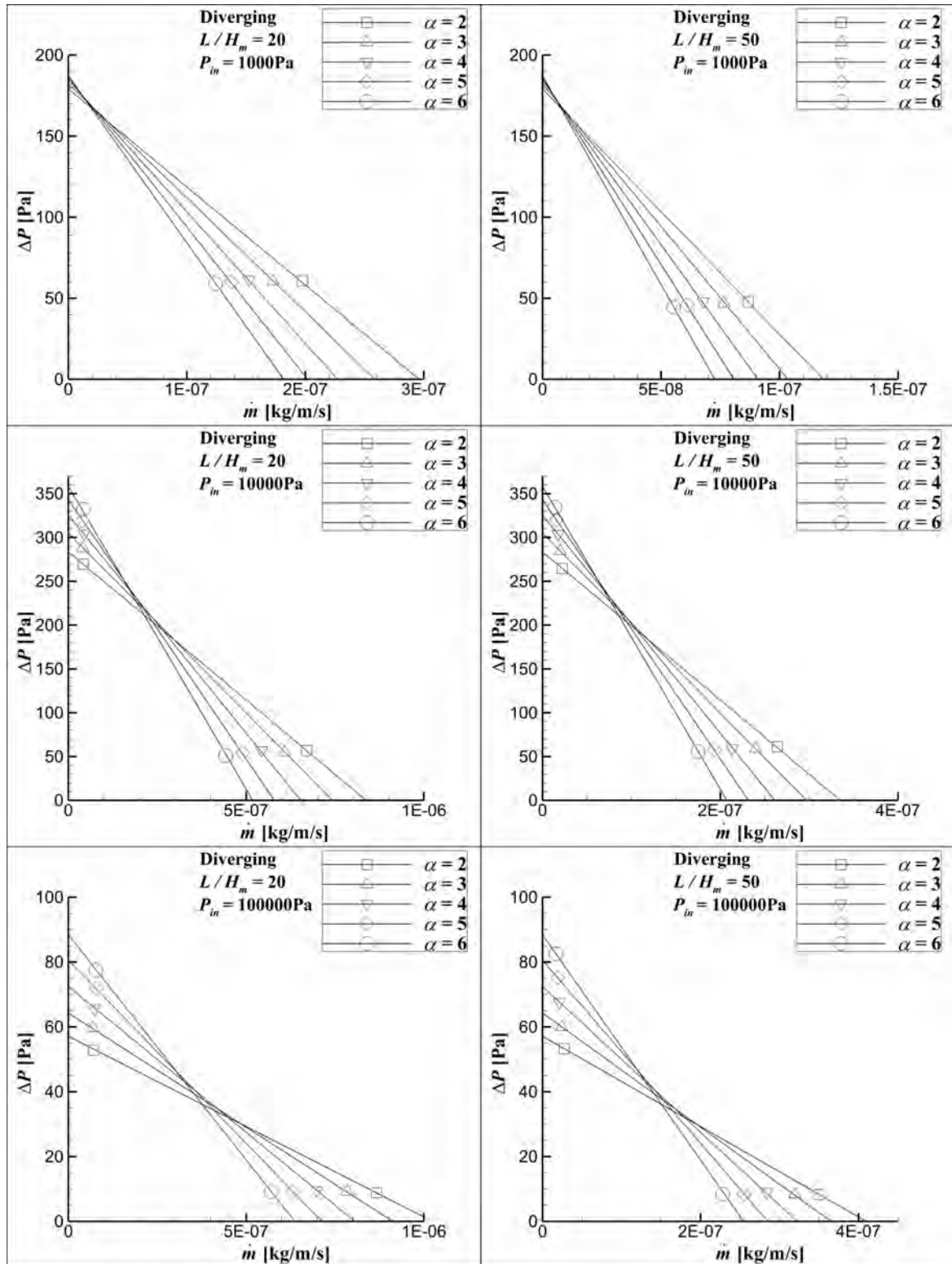


Figure 5.20 Pressure difference $\Delta P = P_{out} - P_{in}$ in terms of the mass flow rate \dot{m} in a diverging channel with $L/H_m = 20, 50$, $H_m = 10 \mu\text{m}$, $P_{in} = 10^3, 10^4, 10^5 \text{ Pa}$ and $\alpha = 2, 3, 4, 5, 6$.

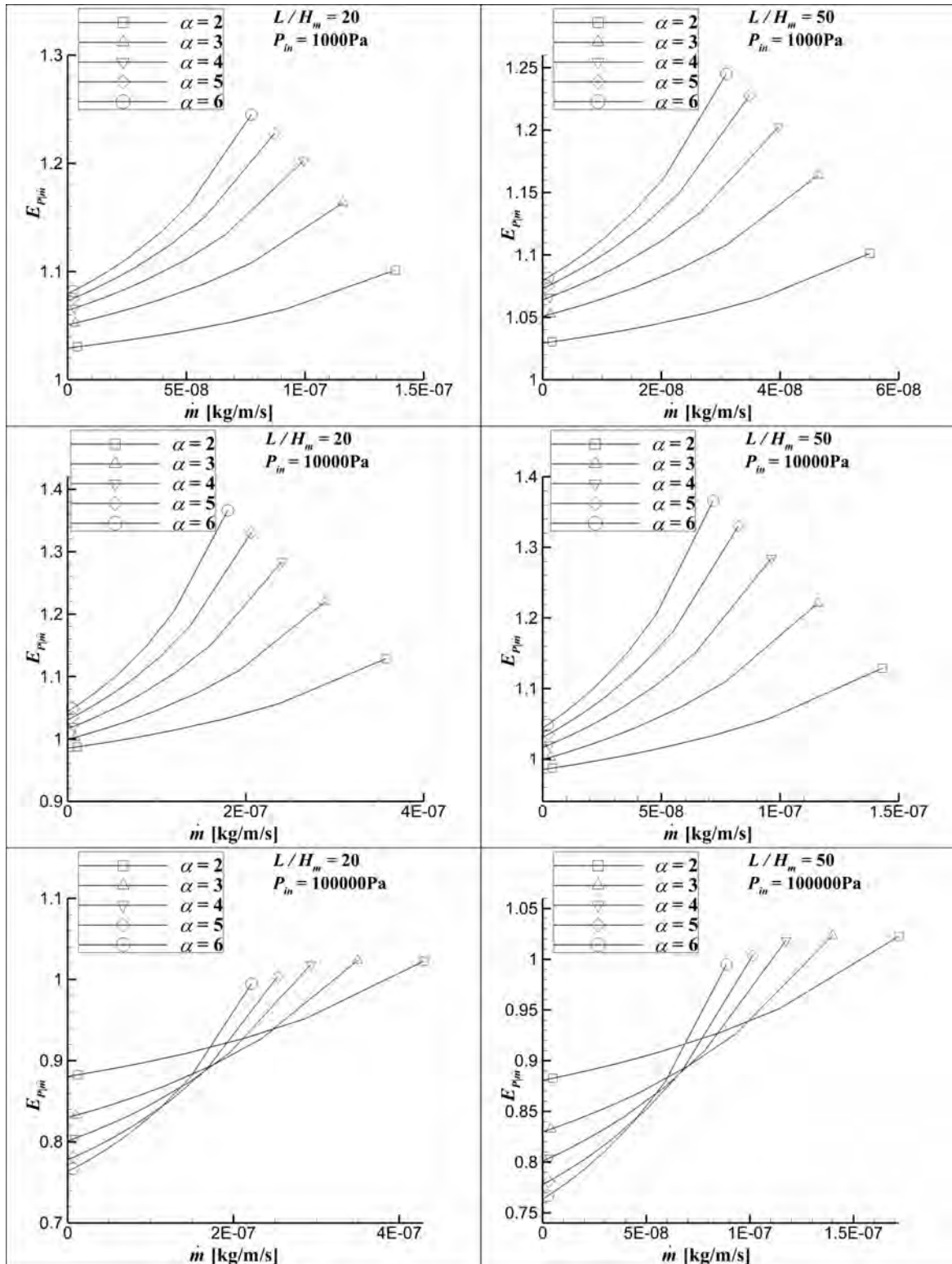


Figure 5.21 Pressure diodicity coefficient for a given mass flow rate in terms of the mass flow rate with $L/H_m = 20, 50$, $H_m = 10\mu\text{m}$, $P_{in} = 10^3, 10^4, 10^5\text{Pa}$ and $\alpha = 2, 3, 4, 5, 6$.

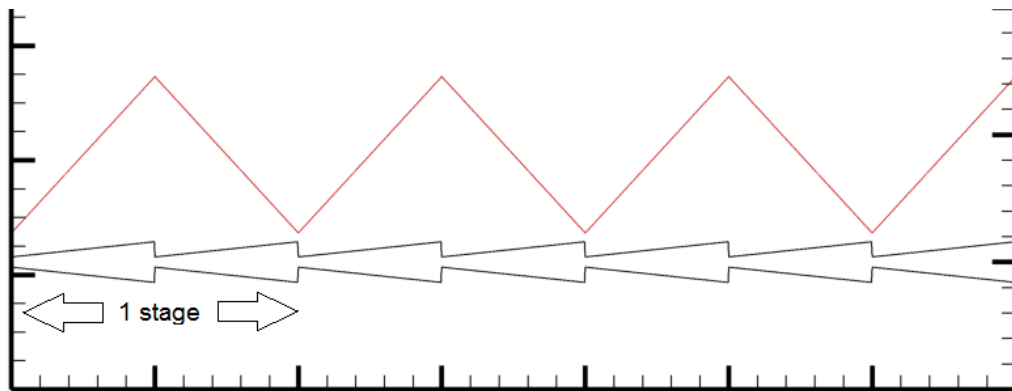


Figure 5.22 Typical cascade along with the temperature variation (red line).

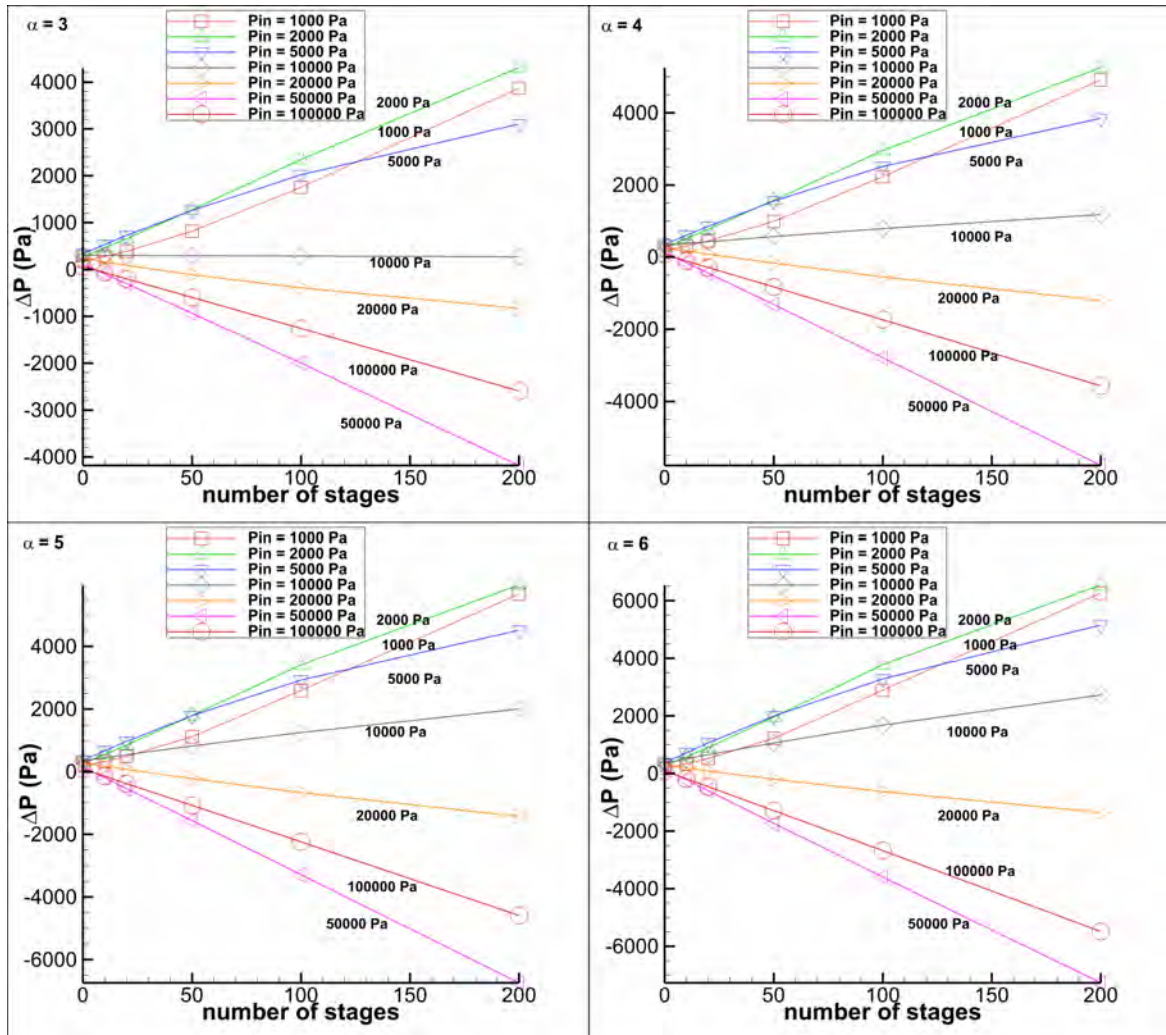


Figure 5.23 Pressure difference ΔP in terms of the number of stages of multistage tapered channel assembly for various values of α and P_{in} .

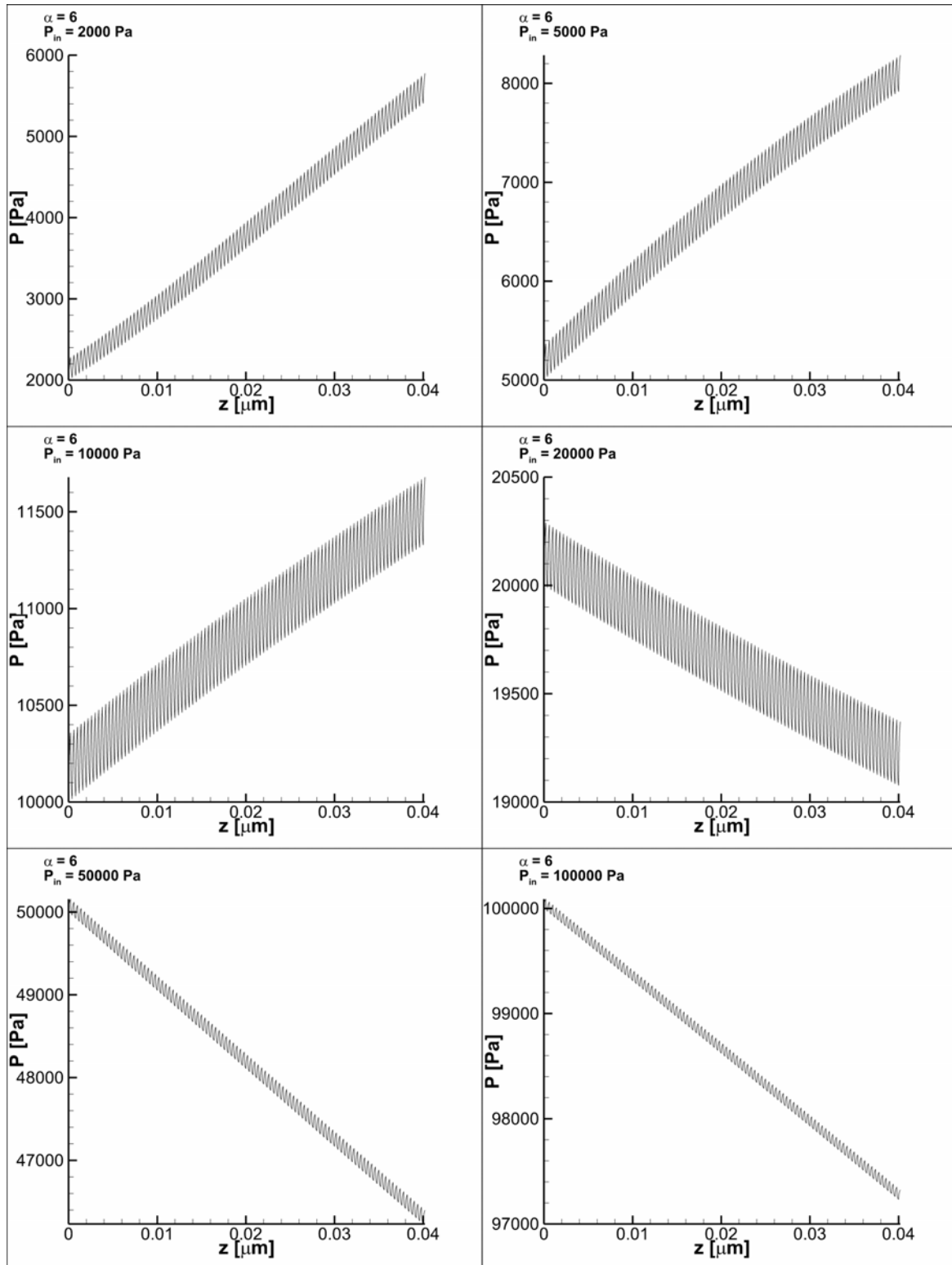


Figure 5.24 Pressure distribution along a multistage tapered channel assembly with $\alpha = 6$ for various values of P_{in} .

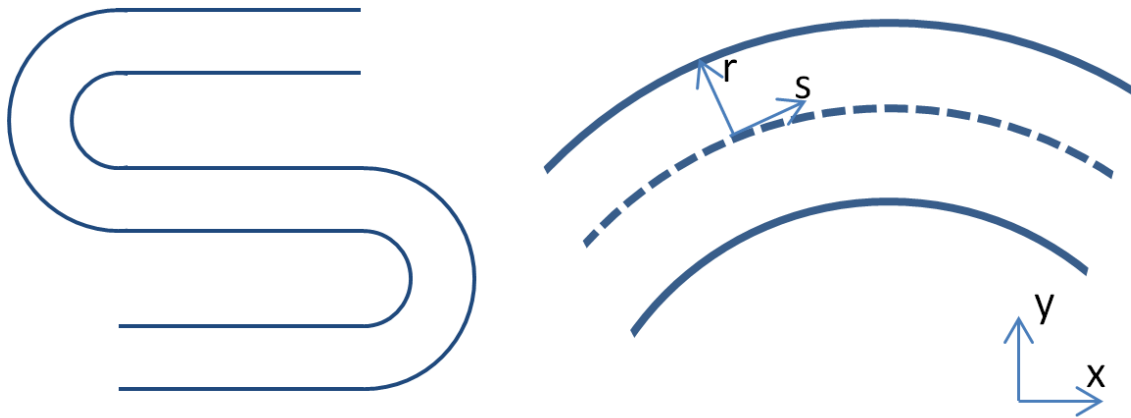


Figure 5.25 View of a serpentine channel consisting of straight and curved segments (left) and a curved channel along with the median curve (dashed line) with the Cartesian and curvilinear coordinate systems (right).

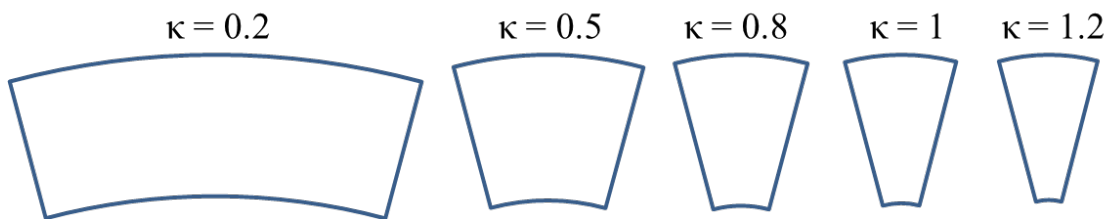


Figure 5.26 An arch of $\pi/6$ radians of curved channels with different curvatures.

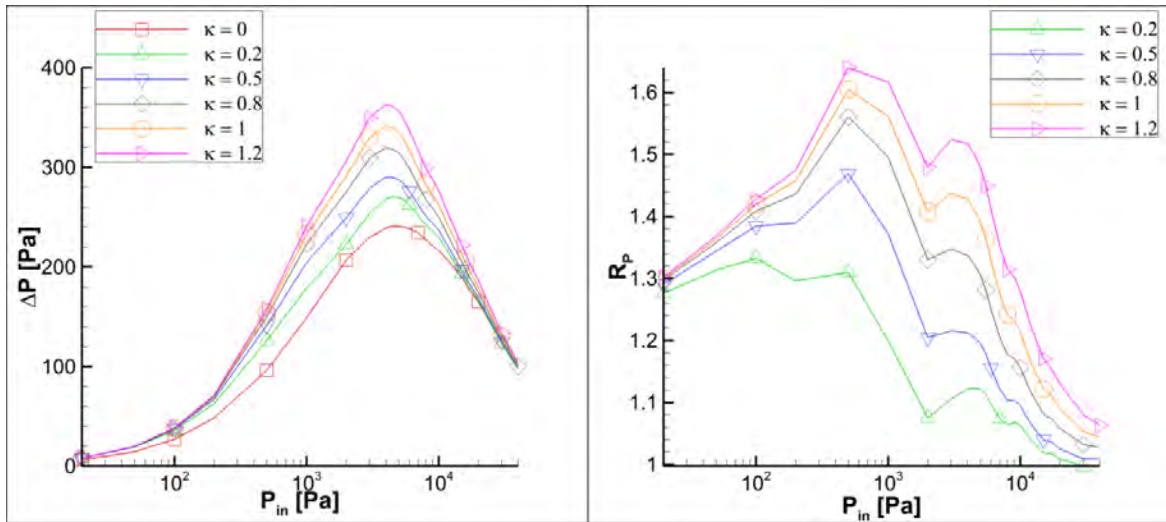


Figure 5.27 Pressure difference ΔP (left) and pressure ratio R_p (right) for straight and curved channels with $L_C/D = L_S/D = 20$ in terms of inlet pressure.

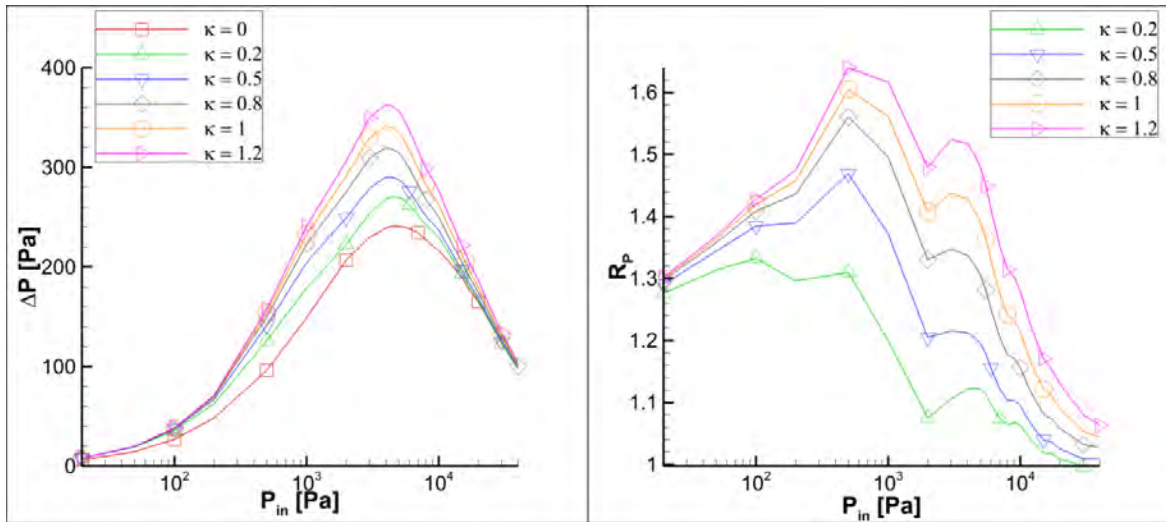


Figure 5.28 Pressure difference ΔP (left) and pressure ratio R_p (right) for straight channel with $L_S/D = 20$ and curved channels with $L_C/D = \pi/\kappa$, in terms of inlet pressure.

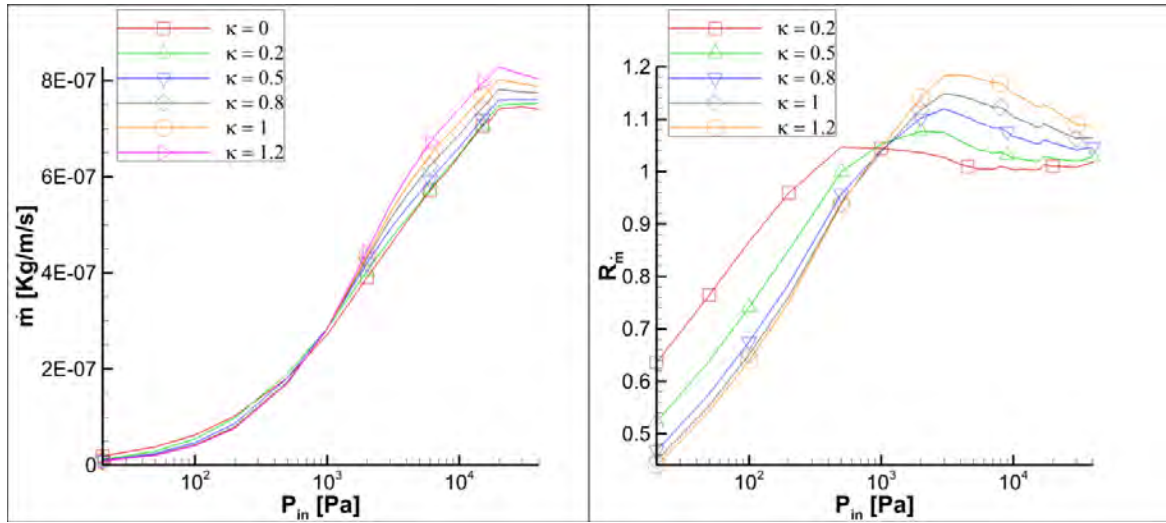


Figure 5.29 Mass flow rate \dot{m} (left) and mass flow rate ratio $R_{\dot{m}}$ (right) for straight and curved channels with $L_C/D = L_S/D = 20$ in terms of inlet pressure.

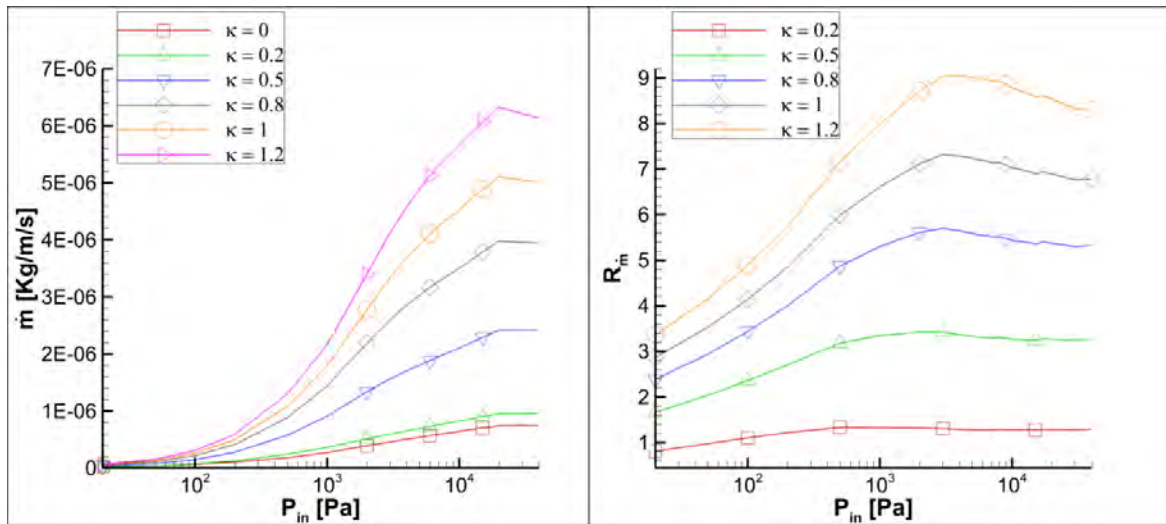


Figure 5.30 Mass flow rate \dot{m} (left) and mass flow rate ratio $R_{\dot{m}}$ (right) for straight channel with $L_S/D = 20$ and curved channels with $L_C/D = \pi/\kappa$, in terms of inlet pressure.

Chapter 6

Decomposition of the DSMC solution into ballistic and collision parts and its implementation in non-equilibrium phenomena in cavities and capillaries

6.1 Introduction

Rarefied gas flows are characterized by long mean free paths, compared to the problem characteristic length, leading to moderate and high Knudsen numbers. Due to the long mean free paths, the particle distribution function at some location in the flow domain is composed of particles arriving directly from the boundaries without interacting with other particles and of particles arriving after an arbitrary number of collisions. Decomposing the distribution into those two parts namely the ballistic and collision parts and computing the corresponding parts of the solution may provide physical information, interpretation and justification of appearing non-equilibrium phenomena. The DSMC method, as a particle method, may be used in introducing the concept of decomposing the distribution function into its ballistic and collision parts and investigate separately the contribution of each part.

In this chapter a methodology is developed for the decomposition of the DSMC method by introducing a tag on each particle indicating whether it belongs to the ballistic or collision part and adjusting accordingly the sampling procedure. In addition, this methodology is implemented to investigate some interesting non-equilibrium flow and heat transfer phenomena in cavities and capillaries. More specifically, two cavity thermally driven flows are considered. In the first one the flow is due to a temperature

distribution imposed along the lateral walls and in the second one due a uniformly heated wall. In addition, the well-known Knudsen paradox in capillaries of various cross sections is investigated.

Thermally induced non-equilibrium gas flows in cavities have received considerable attention and, at some extent, this is due to their implementation in the emerging field of microfluidics [183] and more specifically, in vacuum packaged MEMS [5], [184], micropumps [105], [172] and microactuators/microsensors [185], [186]. In addition, temperature driven flows in cavities have been commonly applied in rarefied gas dynamics to investigate theoretically interesting physical phenomena [137], [187]–[190], as well as to benchmark and validate novel numerical schemes [191]–[193]. The literature survey on rarefied gas flows driven by temperature differences on the basis of kinetic theory is very extensive. A thorough description of various types of thermal flows, including thermal creep flow, thermal stress slip flow, and nonlinear thermal stress flow in various configurations may be found in the book by Sone [93]. In this chapter, the investigation is focused on rarefied gas flows in enclosures driven by non-isothermal walls with no synergetic contributions from external force fields.

The flow generated by thermal creep in a rectangular enclosure for zero-gravity conditions was investigated by the Direct Simulation Monte Carlo (DSMC) method in [194]. The top and bottom walls were kept at different temperatures and along the side walls a linear temperature profile was assumed. Two main counter-rotating vortices have been observed with mass flow, as expected, from cold to hot in the vicinity of the side walls. The gas flow in a square container, where the left and right halves of the container wall were maintained at uniform but different temperature, has been also considered [187] by numerically solving the BGK equation. In this discontinuous wall temperature setup, the basic flow mechanism is the same as in the thermal creep flow but this flow in the continuum limit, contrary to the thermal creep flow, vanishes in a non-uniform manner. A more recent study on the importance of the imposed boundary conditions in steady highly rarefied gas flows induced by non-uniform wall temperature has been recently carried out based on the Boltzmann equation and the DSMC method [195]. It has been deduced that by applying the Cercignani-Lampis (CL) gas-surface interaction model [196] a steady flow is induced even in the free molecular limit, while as it is known from earlier theoretical investigations in this limit and for Maxwell-type boundary conditions the flow velocity is vanishing [189]. Complimentary work with the Lord model [46] has shown that no steady flow is induced as in the case of the Maxwell model.

Next, in order to model vacuum packaged MEMS, the flow and heat transfer in an enclosure with a hot surface in the bottom has been simulated by the DSMC method in [5]. The effect of the temperature gradient and of the temperature discontinuities is examined and it is deduced that when the bottom temperature is partly uniform only close to the center of the bottom plate, the gas flow is enhanced due to thermal creep and as a result the heat transfer in the hot chip bottom surface is also enhanced. The reported rarefied flow close to the wall is according to the typical thermal creep mechanism from cold to hot [93].

Similar studies of the heat transfer through rarefied gases confined in microcavities have been reported in [192] and [193]. In [192] it has been demonstrated that the regularized-13 (R13) equations [197] result to a numerical method, which is applicable in the slip and early transition regime capturing flow characteristics and features which are well beyond the Navier-Stokes-Fourier (NSF) range. In [193] it has been shown that the unified gas-kinetic scheme [198] is indeed a reliable and accurate flow solver for low-speed non-equilibrium flows. Interestingly, in both works it has been observed that the gas flow close to the wall is not necessarily going from the cold to the hot wall region. Depending on the flow parameters the flow along the boundary may move from hot to cold regions as well. In both works this unexpected flow pattern has been also confirmed by DSMC simulations. According to [192] this flow behavior is due to the opposite contribution of the viscous and transpirational parts of the tangential velocity at the side walls, which are caused by the shear stress and the tangential heat flux, respectively.

Recently the thermally driven gas flow in a microcavity with one wall maintained at high temperature and the other three walls at the same low temperature has been investigated in [199] based on the NSF equations with slip and jump boundary conditions and the regularized 13 moment (R13) equations [200]. The results have been compared with corresponding DSMC results clearly indicating the limitations of the NSF and the R13 approaches. For this specific configuration, the former one cannot capture typical flow patterns even in the slip regime, while the latter one gives satisfying results in the transition regime but only up to $Kn \leq 0.3$.

Based on all above it is evident that thermally induced rarefied gas flows in enclosures, although geometrically are relatively simple flow configurations, they still are rich in non-equilibrium physical phenomena. Therefore, despite the work performed and the progress achieved, it still remains a topic of major theoretical, computational, and practical importance and further investigation is valuable.

The two cavity problems, considered in this chapter, are thermally induced flows and they are investigated in a wide range of the Knudsen number covering the slip and transitions regimes and for small, moderate, and large temperature differences. In the first configuration [158] the bottom and top walls were kept at constant and different temperatures while a linear temperature distribution between the top and bottom temperatures is applied to the lateral walls. It is observed that a flow near the lateral boundaries is formed, having a velocity from hot-to-cold regions, contrary to the thermal creep flow. In the second configuration three walls are kept at a constant low temperature and the other at a higher temperature [201]. A very interesting finding is that the heat flux departing from the hot wall, for some given Knudsen number had a non-monotonic behavior with respect to the temperature ratio and a maximum heat flux appeared at some intermediate ratio. It is noted that in both problems the DSMC decomposition procedure is introduced to split the solution into the ballistic and collision parts and the contribution of each part to the macroscopic quantities is studied to explain the interesting phenomena arising in these flows. Modeling is based on the numerical solution of the Shakhov kinetic model [29], [202] and the DSMC method [62]. Solving the problem both deterministically and stochastically allows a systematic comparison and verification of the results and more important the exploitation of the advantages of each approach in the numerical investigation of the flow and heat transfer patterns

Furthermore, capillary flows are also considered. Internal rarefied gas flow in a wide range of the Knudsen number was first studied experimentally and theoretically by Knudsen, who examined the dependence of the conductance at different pressure and geometrical parameters [203]. Considering a tube much longer than its radius, he developed an expression for the tube conductance and observed a conductance minimum at $Kn \approx 1$, well known as the *Knudsen minimum* or the *Knudsen paradox*. Over the years these preliminary results have been improved, extended, and generalized. The steady isothermal pressure driven gas flow through long capillaries still remains an active research topic and a subject of many investigations [10], [50], [210]–[215], [170], [185], [204]–[209]. Recently, simple closed-form expressions for the reduced flow rate in long tubes in all flow regimes were deduced in [216] and [217], based on the direct simulation Monte Carlo (DSMC) and kinetic simulations, respectively. These formulas, as the one in [203], produce the Knudsen minimum, indicating that the conductance (or the reduced flow rate) lies below the corresponding free-molecular values over a range of pressures in the transition regime.

A qualitative explanation for the conductance minimum in a long capillary has been suggested by Pollard and Present [218]. They considered two groups of molecules flowing across a differential cross section of the capillary. The first one consists of particles which arrived from the boundaries with no collisions and the second one of particles which experienced at least one collision. At zero pressure the total flow comes from particles only of the first group, while as the pressure is increased to small values the flow of the first group particles is decreased because of the obstruction of the long particle paths by the added molecules. In parallel, the flow of the second group of particles is increased through the development of a drift transport due to intermolecular collisions. The authors claim that at small pressures the rate of reduction of the first flow is larger than the rate of increase of the second one and therefore, the total flow must initially decrease with pressure. A further increase in pressure stimulates the overall drift velocity that in turn, from that point on, monotonically increases the entire flow through the tube.

The concept of decomposing the DSMC solution into two parts, is also implemented here to investigate the Knudsen paradox in a precise manner with quantitative arguments. The flow through long channels of various cross sections is simulated and through the decomposition technique an interpretation to the Knudsen minimum is obtained in a quantitative manner, confirming previous qualitative results [218].

The thermally driven flow in a cavity with a temperature gradient along the lateral walls is presented in Section 6.2, the heat transfer in a cavity with one heated wall in Section 6.3 and the Knudsen minimum appearing in long capillaries in Section 6.4. Finally, some concluding remarks are made in Section 6.5.

6.2 Rarefied gas flow in cavities due to non-isothermal lateral walls

6.2.1 Flow configuration and parameters definition

A monatomic rarefied gas is contained in a two-dimensional enclosure with rectangular cross section $W \times H$. The orthogonal cross section of the enclosure and the origin of the coordinate system are shown in Figure 6.1. The bottom and top boundaries at $y = 0$ and $y = H$ are kept isothermal at temperatures T_H and T_C with $T_C < T_H$, while along the side boundaries at $x = \pm W/2$ a linear temperature profile is assumed according to $T_S = T_H - (T_H - T_C)y'/H$. The enclosure is considered as unbounded in

the third direction and end effects in that direction are neglected, while radiation and gravity effects are also assumed to be negligible. The gas-surface interaction is taken to be purely diffusive to all four boundaries.

In view of the above set-up, a symmetric about $x = 0$ thermal creep type flow of the rarefied gas is expected. In the vicinity of the two lateral walls at $x = \pm W/2$ there will be a mass flow in the negative y direction from cold to hot and due to mass conservation a mass flow of comparable magnitude does arise near the symmetry axis $x = 0$. The presence of the non-isothermal side walls forces the thermal creep driven gas into a circulatory motion creating two counter-rotating vortices. This flow pattern, shown in Figure 6.1(a), has been captured in [194] for a square enclosure and for small Knudsen numbers. The vortices of this flow pattern are named Vortex-type I.

Recent work [219] however, has revealed that in the same set-up, with the specific temperature ratio of $T_C/T_H = 0.1$, when the Knudsen number is adequately large additional vortices in the two bottom corners may appear and as the Knudsen number is increased they are further increased. These vortices are counter rotating to the main ones, i.e., the gas flows from hot-to-cold along the lateral walls. Now, the flow pattern, shown in Figure 6.1(b), consists of four eddies, namely, two eddies of type I, which are squeezed towards the center and the top of the cavity and two additional vortices named, Vortex-type II, which are rotating along the lateral walls in the cold-to-hot direction. It is noted that we refer to these two types of vortices as I and II, instead of using the typical terminology of primary and secondary vortices, because as it will be seen, depending upon the flow parameters may both occupy small or large regions of the flow domain and may both become important in the characterization of the flow pattern. As it has been pointed in the introduction, similar observations in enclosures with a slightly different non-isothermal wall set-up have been reported in [192] and [193].

Here, the flow configuration described above (Figure 6.1) is computationally investigated in a detailed and systematic manner based on kinetic theory principles. The macroscopic quantities of interest include the number density distribution $N(x', y')$, the two component velocity vector $\mathbf{U} = [U_x(x', y'), U_y(x', y')]$, the shear stress tensor $P_{xy}(x', y')$, the temperature distribution $T(x', y')$, and the two component heat flux vector $\mathbf{Q} = [Q_x(x', y'), Q_y(x', y')]$, while the gas pressure is given by $P = Nk_B T$.

The solution is determined by three main dimensionless parameters, namely, the reference Knudsen number defined as

$$Kn_0 = \frac{\sqrt{\pi}}{2} \frac{\mu_0 v_0}{P_0 W}, \quad (6.1)$$

the temperature ratio T_C/T_H , and the aspect ratio of the two-dimensional cavity H/W . In Eq. (6.1), P_0 is a reference pressure, W is the width of the cavity, which is taken as the characteristic length, μ_0 is the gas viscosity at reference temperature $T_0 = T_H$, and $v_0 = \sqrt{2k_B T_0/m}$, with k_B and m denoting the Boltzmann constant and the gas molecular mass, respectively, is the most probable molecular speed, which is taken as the characteristic velocity. The reference number density N_0 is related to the reference pressure and temperature according to $P_0 = N_0 k_B T_0$. Then, it is convenient to introduce the dimensionless quantities:

$$\begin{aligned} x = x'/W, y = y'/W, n = N/N_0, u_x = U_x/v_0, u_y = U_y/v_0, p = P/P_0, \\ \tau = T/T_0, q_x = Q_x/(P_0 v_0), q_y = Q_y/(P_0 v_0) \end{aligned} \quad (6.2)$$

It is noted that $x \in [-0.5, 0.5]$ and $y \in [0, H/W]$ are the space variables, $n, (u_x, u_y), p, \tau$, with $p = n \times \tau$ and (q_x, q_y) are the two-dimensional distributions of the number density, the two components of the velocity vector, the gas pressure and temperature and the two components of the heat flux vector, respectively. The Inverse Power Law (IPL) interaction, [62] is introduced yielding a viscosity of the form $\mu = \mu_0 \tau^\omega$, with the parameter $\omega \in [0.5, 1]$. The values of $\omega = 0.5$ and $\omega = 1$ correspond to the limiting cases of hard sphere and Maxwell molecules.

The solution of the problem described above is obtained in a deterministic manner by numerically solving the nonlinear Shakhov model equations and in a stochastic manner by the DSMC method presented in Sections 6.2.2 and 6.2.3, respectively.

6.2.2 Deterministic kinetic modeling

In kinetic modeling the main unknown is the distribution function, which for this flow configuration is a function of five independent variables: the two space variables (x', y') and the three components of the molecular velocity vector $\boldsymbol{\xi} = (\xi_x, \xi_y, \xi_z)$, i.e., $f = f(x', y', \boldsymbol{\xi})$. The flow is simulated by the nonlinear Shakhov kinetic model [29], [202], which has been proved to be a reliable model for non-isothermal flows [74], [77], [152], [220], [221], subject to purely diffuse boundary conditions. In the course of this work the deterministic solution has been proved always very reliable including the cases of small temperature differences and large Knudsen numbers, both characterized by very low speeds.

The nonlinear Shakhov model for the steady-state two-dimensional flow under consideration takes the form

$$\xi_x \frac{\partial f}{\partial x'} + \xi_y \frac{\partial f}{\partial y'} = \frac{P}{\mu} (f^S - f), \quad (6.3)$$

where P is the local pressure, $\mu = \mu(T)$ is the viscosity at local temperature T . The Shakhov relaxation distribution is

$$f^S = f^M \left[1 + \frac{2}{15} \frac{m}{N(k_B T)^2} [Q_x (\xi_x - U_x) + Q_y (\xi_y - U_y)] \times \left(\frac{m}{2k_B T} [(\xi_x - U_x)^2 + (\xi_y - U_y)^2 + \xi_z^2] - \frac{5}{2} \right) \right], \quad (6.4)$$

with

$$f^M = \frac{N}{(2\pi RT)^{3/2}} \exp \left[-\frac{m}{2k_B T} [(\xi_x - U_x)^2 + (\xi_y - U_y)^2 + \xi_z^2] \right] \quad (6.5)$$

being the local Maxwellian. The dimensionless distribution function $g = f v_0^3 / N_0$ and molecular velocity $\boldsymbol{\zeta} = \boldsymbol{\xi} / v_0$, along with the reference Knudsen number defined by Eq. (6.1), the dimensionless quantities defined by Eq. (6.2) and the expression for the viscosity given by the IPL molecular interaction, are introduced into Eqs. (6.3), (6.4) and (6.5) to yield after some straightforward manipulation the corresponding equations in dimensionless form:

$$\zeta_x \frac{\partial g}{\partial x} + \zeta_y \frac{\partial g}{\partial y} = \frac{1}{Kn_0} \frac{\sqrt{\pi}}{2} n \tau^{1-\omega} (g^S - g) \quad (6.6)$$

$$g^S = g^M \left[1 + \frac{4}{15} \frac{1}{n \tau^2} [q_x (\zeta_x - u_x) + q_y (\zeta_y - u_y)] \times \left[\frac{(\zeta_x - u_x)^2 + (\zeta_y - u_y)^2 + \zeta_z^2}{\tau} - \frac{5}{2} \right] \right] \quad (6.7)$$

$$g^M = \frac{n}{(\pi \tau)^{3/2}} \exp \left[-\frac{(\zeta_x - u_x)^2 + (\zeta_y - u_y)^2 + \zeta_z^2}{\tau} \right] \quad (6.8)$$

Furthermore, taking advantage of the two-dimensionality of the problem, the z component of the molecular velocity can be eliminated by introducing the reduced distribution functions $\varphi = \int_{-\infty}^{\infty} g d\zeta_z$ and $\psi = \int_{-\infty}^{\infty} \zeta_z^2 g d\zeta_z$. By operating accordingly on Eqs. (6.6), (6.7) and (6.8) the following two coupled integrodifferential equations for

the unknown reduced distribution functions $\varphi = \varphi [x, y, \zeta_x, \zeta_y]$ and $\psi = \psi [x, y, \zeta_x, \zeta_y]$ are obtained:

$$\zeta_x \frac{\partial \varphi}{\partial x} + \zeta_y \frac{\partial \varphi}{\partial y} = \frac{1}{Kn_0} \frac{\sqrt{\pi}}{2} n \sqrt{\tau} (\varphi^S - \varphi) \quad (6.9)$$

$$\zeta_x \frac{\partial \psi}{\partial x} + \zeta_y \frac{\partial \psi}{\partial y} = \frac{1}{Kn_0} \frac{\sqrt{\pi}}{2} n \sqrt{\tau} (\psi^S - \psi) \quad (6.10)$$

Here,

$$\varphi^S = \varphi^M \left(1 + \frac{4}{15} \frac{1}{n\tau^2} [q_x (\zeta_x - u_x) + q_y (\zeta_y - u_y)] \times \left[\frac{(\zeta_x - u_x)^2 + (\zeta_y - u_y)^2}{\tau} - 2 \right] \right) \quad (6.11)$$

and

$$\psi^S = \psi^M \left(1 + \frac{4}{15} \frac{1}{n\tau^2} [q_x (\zeta_x - u_x) + q_y (\zeta_y - u_y)] \times \left[\frac{(\zeta_x - u_x)^2 + (\zeta_y - u_y)^2}{\tau} - 1 \right] \right), \quad (6.12)$$

with the reduced local Maxwellians

$$\varphi^M = \frac{n}{\pi\tau} \exp \left[-\frac{(\zeta_x - u_x)^2 + (\zeta_y - u_y)^2}{\tau} \right], \quad (6.13)$$

$$\psi^M = \frac{n}{2\pi} \exp \left[-\frac{(\zeta_x - u_x)^2 + (\zeta_y - u_y)^2}{\tau} \right], \quad (6.14)$$

The macroscopic quantities in Eqs. (6.9), (6.10), (6.11), (6.12), (6.13) and (6.14) are readily deduced by applying the same nondimensionalization and projection procedures to the moments of f and finally they are expressed, in terms of φ and ψ , according to the following double integrals:

Number density:

$$n(x, y) = \int_{-\infty}^{\infty} \int_{-\infty}^{\infty} \varphi d\zeta_x d\zeta_y \quad (6.15)$$

Velocity:

$$u_x(x, y) = \frac{1}{n} \int_{-\infty}^{\infty} \int_{-\infty}^{\infty} \zeta_x \varphi d\zeta_x d\zeta_y, u_y(x, y) = \frac{1}{n} \int_{-\infty}^{\infty} \int_{-\infty}^{\infty} \zeta_y \varphi d\zeta_x d\zeta_y \quad (6.16)$$

Temperature:

$$\tau(x, y) = \frac{2}{3n} \int_{-\infty}^{\infty} \int_{-\infty}^{\infty} [(\zeta_x^2 + \zeta_y^2) \varphi + \psi] d\zeta_x d\zeta_y - \frac{2}{3} (u_x^2 + u_y^2) \quad (6.17)$$

Heat flux:

$$q_x(x, y) = \int_{-\infty}^{\infty} \int_{-\infty}^{\infty} [(\zeta_x - u_x)^2 + (\zeta_y - u_y)^2] \varphi + \psi (\zeta_x - u_x) d\zeta_x d\zeta_y \quad (6.18)$$

$$q_y(x, y) = \int_{-\infty}^{\infty} \int_{-\infty}^{\infty} [(\zeta_x - u_x)^2 + (\zeta_y - u_y)^2] \varphi + \psi (\zeta_y - u_y) d\zeta_x d\zeta_y \quad (6.19)$$

At the boundaries, the reduced distribution functions representing outgoing particles are denoted by φ^+ , ψ^+ and they are expressed by the Maxwell purely diffuse reflection as [222]

$$\varphi^+ = \frac{n_w}{\pi \tau_w} \exp \left[-(\zeta_x^2 + \zeta_y^2) / \tau_w \right] \quad (6.20)$$

$$\psi^+ = \frac{n_w}{2\pi} \exp \left[-(\zeta_x^2 + \zeta_y^2) / \tau_w \right], \quad (6.21)$$

where τ_w is the dimensionless local wall temperature and n_w is a parameter given in terms of the ingoing distributions satisfying the impermeability wall conditions.

Equations (6.9) and (6.10), subject to the boundary conditions (6.20) and (6.21) along with the associated expressions (6.11)-(6.19) provide a complete description of the problem and constitute the basic set of equations to be numerically solved.

The implemented deterministic algorithm has been repeatedly applied to solve nonlinear flows and heat transfer problems with considerable success [69], [75], [223]. A brief description is provided here mainly for completeness purposes.

The problem is solved by discretizing the molecular velocity and physical spaces. In the velocity space it is computationally efficient to present the velocity vector in polar

coordinates, according to $\zeta_x = \zeta \cos \theta$ and $\zeta_y = \zeta \sin \theta$. Then, the continuum velocity spectrum (ζ, θ) is replaced by a set of discrete velocities (ζ_m, θ_n) , where $\zeta_m \in (0, +\infty)$, $m = 1, 2, \dots, M$ and $\theta_n \in (0, 2\pi)$, $n = 1, 2, \dots, N$. The magnitudes ζ_m are taken to be the roots of the Legendre polynomial of order M accordingly mapped from $(-1, 1)$ to $(0, +\infty)$, while the polar angles are $\theta_n = \pi(2n - 1)/N$. The number of discrete velocity vectors is $M \times N$. In the physical space the flow domain is divided into $I \times J$ rectangular elements, with $i = 1, 2, \dots, I$ and $j = 1, 2, \dots, J$. The number of points in the physical space is $(I + 1) \times (J + 1)$.

The integro-differential equations (6.9) and (6.10) are first discretized in the molecular velocity space and the deduced set of partial differential equations are integrated over each space element defined by the intervals $[x_{i-1/2}, x_{i+1/2}]$ and $[y_{j-1/2}, y_{j+1/2}]$ following a typical second order control volume approach. The moments (6.15)-(6.19) are numerically integrated by applying the trapezoidal rule and Gauss-Legendre quadrature in the polar angle θ and the velocity magnitude ζ , respectively, of the molecular velocity vector. The resulting discretized equations for φ and ψ with the associated discretized moments are solved in an iterative manner which is concluded when the convergence criteria given by

$$\varepsilon^{(k)} = \max_{i,j} \left\{ \left| n_{i,j}^{(k)} - n_{i,j}^{(k-1)} \right| + \left| u_{x,i,j}^{(k)} - u_{x,i,j}^{(k-1)} \right| + \left| u_{y,i,j}^{(k)} - u_{y,i,j}^{(k-1)} \right| + \left| \tau_{i,j}^{(k)} - \tau_{i,j}^{(k-1)} \right| \right\} \leq 10^{-10} \quad (6.22)$$

is fulfilled. Here, k denotes the iteration index and $\varepsilon^{(k)}$ the error after k iterations. It is noted that upon convergence all conservation principles are accordingly fulfilled. The results presented in Sections 6.2.5 and 6.2.6 have been obtained with $M = 80$, $N = 400$, $I = 400$, and $J = 400 \times (H/W)$.

It may be useful to note that the implemented discrete velocity algorithm suffers a breakdown of the positivity of the distribution function which is inherent in the Shakhov model. However, in all cases tested the ratio of the weighted sums of the negative over the positive distributions is at least less than 10^{-4} and therefore its effect on the implementation of the algorithm and the accuracy of the results is negligible.

6.2.3 Stochastic DSMC modeling

Stochastic modeling is based on the DSMC method proposed by Bird [62]. The typical DSMC approach is implemented. The gas is represented by a discrete number of model particles, which are evolved in time to statistically mimic the behavior of real

molecules. The physical space and time domains are discretized and the real motion of the particles is split into the free motion step, where all particles are traveling a distance proportional to their velocities and the collision step, where particles are interacting, while keeping their positions unchanged. In the first step the particle motion is purely deterministic, while in the second particle collisions are carried out in a stochastic manner.

The collision technique that is employed here is the No Time Counter (NTC) scheme suggested by Bird [62]. A slight modification is introduced in the calculation of the maximum number of collisions N_C in each cell, which is estimated according to [224]

$$N_C = \frac{1}{2} \frac{N(N-1) F_N (\sigma_T c_r)_{\max} \Delta t}{V_C}, \quad (6.23)$$

where N is the actual number of particles in cell, F_N is the number of real particles represented by a simulator, $(\sigma_T c_r)_{\max}$ is the maximum value of the product of the collision cross section and the relative velocity of the particles in the collision (this quantity is updated throughout the simulation), Δt is the timestep, and V_C is the volume of the cell.

The space domain has been discretized by using squared cells ($\Delta x = \Delta y = 0.01$), i.e., 100 cells have been taken in the x-direction, while the number of cells in the y-direction depends on the aspect ratio (H/W) and it is equal to $n_C = 100 \times (H/W)$. The number of particles per cell on the NTC scheme is fixed to 25 and the time step is chosen to be sufficiently smaller (about 1/3) than the cell traversal time, defined as $W/(n_C v_0)$. The macroscopic quantities, defined by Eq. (6.2), are volume based calculated by averaging the microscopic values of the particles at a given cell and are given by the following summations:

Number density:

$$n = \frac{\sum_{k=1}^S N(t_k)}{SV_C} \quad (6.24)$$

Velocity:

$$u_x = \frac{1}{N_T} \sum_{k=1}^S \sum_{i=1}^{N(t_k)} \zeta_{x,i}(t_k), u_y = \frac{1}{N_T} \sum_{k=1}^S \sum_{i=1}^{N(t_k)} \zeta_{y,i}(t_k) \quad (6.25)$$

Temperature:

$$\tau_\alpha = \frac{1}{N_T} \sum_{k=1}^S \sum_{i=1}^{N(t_k)} \zeta_{\alpha,i}^2 - \left(\frac{1}{N_T} \sum_{k=1}^S \sum_{i=1}^{N(t_k)} \zeta_{\alpha,i} \right)^2, \alpha = \{x, y, z\}, \tau = 2(\tau_x + \tau_y + \tau_z)/3 \quad (6.26)$$

Shear Stress:

$$p_{xy} = \frac{1}{N_T} \sum_{k=1}^S \sum_{i=1}^{N(t_k)} (\zeta_{x,i} \zeta_{y,i}) - u_x u_y \quad (6.27)$$

Heat flux:

$$\begin{aligned} \frac{q_x}{2} = & \frac{1}{N_T} \sum_{k=1}^S \sum_{i=1}^{N(t_k)} \zeta_{x,i} (\zeta_{x,i}^2 + \zeta_{y,i}^2 + \zeta_{z,i}^2) - 2u_x \frac{1}{N_T} \sum_{k=1}^S \sum_{i=1}^{N(t_k)} (\zeta_{x,i}^2 - u_x^2) \\ & - 2u_y \frac{1}{N_T} \sum_{k=1}^S \sum_{i=1}^{N(t_k)} (\zeta_{x,i} \zeta_{y,i} - u_x u_y) - u_x \frac{1}{N_T} \sum_{k=1}^S \sum_{i=1}^{N(t_k)} (\zeta_{x,i}^2 + \zeta_{y,i}^2 + \zeta_{z,i}^2) \end{aligned} \quad (6.28)$$

$$\begin{aligned} \frac{q_y}{2} = & \frac{1}{N_T} \sum_{k=1}^S \sum_{i=1}^{N(t_k)} \zeta_{y,i} (\zeta_{x,i}^2 + \zeta_{y,i}^2 + \zeta_{z,i}^2) - 2u_x \frac{1}{N_T} \sum_{k=1}^S \sum_{i=1}^{N(t_k)} (\zeta_{x,i} \zeta_{y,i} - u_x u_y) \\ & - 2u_y \frac{1}{N_T} \sum_{k=1}^S \sum_{i=1}^{N(t_k)} (\zeta_{y,i}^2 - u_y^2) - u_y \frac{1}{N_T} \sum_{k=1}^S \sum_{i=1}^{N(t_k)} (\zeta_{x,i}^2 + \zeta_{y,i}^2 + \zeta_{z,i}^2) \end{aligned} \quad (6.29)$$

In Eqs. (6.24)-(6.29), N_T is the total number of sampled particles, S denotes the number of samples, t_k indicates the different times over which the sampling is performed, and $N(t_k)$ is the number of particles in the cell at time t_k . It is noted that the macroscopic properties are obtained by time averaging over $S = 5 \times 10^5$ time steps after the steady-state regime has been recovered.

6.2.4 DSMC decomposition methodology into ballistic and collision parts

In general, a kinetic solution at some point in a flow domain consists of two parts, namely, the ballistic and the collision parts. The former one is due to particles arriving at this point from the boundaries with no collisions, while the latter one is due to particles arriving at this point after an arbitrary number of collisions (at least one).

The ballistic and collision parts of the solution of the thermally induced flow in the enclosure are computed separately and the contribution of each part to the overall solution is analyzed. The dimensionless distribution function $g = g(x, y, \zeta)$ at a local point (x, y) , defined in Section 6.2.2, is decomposed as

$$g(x, y, \zeta) = g^{(b)}(x, y, \zeta) + g^{(c)}(x, y, \zeta), \quad (6.30)$$

where $g^{(b)}$ and $g^{(c)}$ denote the ballistic and collision parts of the distribution function, respectively. It is noted that particles contributing to the ballistic part of the solution at point (x, y) may collide to other particles in their movement after that point. Therefore, the two parts of the solution are named ballistic and collision in order to distinguish this splitting from the typical free molecular and collisional decomposition, as well as from other decompositions of the distribution function, which have been previously introduced to treat boundary induced discontinuities [157], [225], [226].

The prescribed decomposition of the particle distribution in a given cell of the computational grid with center point (x, y) can be implemented in the basic DSMC algorithm by making some additions in the indexing stage. More specifically, all model particles $j = 1, \dots, N_T$ taking place in the simulation are tagged by introducing the indicator I_j , which has the value of 0 or 1 indicating if a particle contributes to the ballistic or the collision part of the distribution, respectively. A particle passes into the ballistic part when it is reflected from a wall and goes into the collision part when interacts with another particle. The indicator is set to 0 each time that a particle is reflected from the bounding walls of the enclosure, while in the stage of particle free motion the indicators are not changed. In the stage of binary collisions the indicators (I_j, I_k) of any pair of particles (j, k) involved in a collision are set to 1. During the simulation process the particle indicators may change their values all the time. In the sampling stage of the macroscopic properties at given time t_m all particles with indicators $I_j = 0$, are considered belonging to the ballistic part of the particle distribution and all particles with indicators $I_j = 1$ to the collision part. As a result, the total number of all particles accumulated in a cell is divided into two groups $N_T = N^{(b)} + N^{(c)}$ and the macroscopic quantities are sampled into the two corresponding parts.

In this chapter we are mainly interested to the distributions of number density, velocity and heat flux components which are decomposed according to

$$n(x, y) = n^{(b)}(x, y) + n^{(c)}(x, y), \quad (6.31)$$

$$u_x(x, y) = u_x^{(b)}(x, y) + u_x^{(c)}(x, y), \quad (6.32)$$

$$u_y(x, y) = u_y^{(b)}(x, y) + u_y^{(c)}(x, y), \quad (6.33)$$

$$q_x(x, y) = q_x^{(b)}(x, y) + q_x^{(c)}(x, y), \quad (6.34)$$

$$q_y(x, y) = q_y^{(b)}(x, y) + q_y^{(c)}(x, y), \quad (6.35)$$

where the superscripts (b) and (c) denote the ballistic and collision parts of the distributions, respectively. They are computed by accordingly integrating the distribution function. For example the ballistic and collision contributions to the horizontal part of the macroscopic velocity (u_x) can be obtained as

$$u_x(x, y) = \frac{1}{n} \int \zeta_x g d\zeta = \frac{1}{n} \int \zeta_x g^{(b)} d\zeta + \frac{1}{n} \int \zeta_x g^{(c)} d\zeta = u_x^{(b)}(x, y) + u_x^{(c)}(x, y). \quad (6.36)$$

In this notation, the distribution function, as well as its ballistic and collision parts can be written as

$$g(x, y, \zeta) = \frac{1}{SV_{Cell}} \sum_{k=1}^S \sum_{i=1}^{N(t_k)} \delta(\zeta - \zeta_i(t_k)), \quad (6.37)$$

$$g^{(b)}(x, y, \zeta) = \frac{1}{SV_{Cell}} \sum_{k=1}^S \sum_{i=1}^{N(t_k)} [1 - I_i(t_k)] \delta(\zeta - \zeta_i(t_k)), \quad (6.38)$$

$$g^{(c)}(x, y, \zeta) = \frac{1}{SV_{Cell}} \sum_{k=1}^S \sum_{i=1}^{N(t_k)} I_i(t_k) \delta(\zeta - \zeta_i(t_k)), \quad (6.39)$$

where $\delta(\zeta - \zeta_i(t_k))$ denotes the Dirac function. Thus the ballistic and collision parts of the macroscopic quantities can be calculated in the same manner as shown in (6.36) when the expressions (6.38) and (6.39) for the distribution function are substituted in the integrals. After some algebraic manipulation the following expressions are derived: Number density:

$$n^{(b)} = \frac{\sum_{k=1}^S [1 - I_i(t_k)] N(t_k)}{SV_C}, n^{(c)} = \frac{\sum_{k=1}^S I_i(t_k) N(t_k)}{SV_C} \quad (6.40)$$

Velocity:

$$u_x^{(b)} = \frac{1}{N_T} \sum_{k=1}^S \sum_{i=1}^{N(t_k)} [1 - I_i(t_k)] \zeta_{x,i}(t_k), u_x^{(c)} = \frac{1}{N_T} \sum_{k=1}^S \sum_{i=1}^{N(t_k)} I_i(t_k) \zeta_{x,i}(t_k) \quad (6.41)$$

$$u_y^{(b)} = \frac{1}{N_T} \sum_{k=1}^S \sum_{i=1}^{N(t_k)} [1 - I_i(t_k)] \zeta_{y,i}(t_k), u_y^{(c)} = \frac{1}{N_T} \sum_{k=1}^S \sum_{i=1}^{N(t_k)} I_i(t_k) \zeta_{y,i}(t_k) \quad (6.42)$$

Shear stress:

$$p_{lm}^{(b)} = \frac{1}{N_T} \sum_{k=1}^S \sum_{i=1}^{N(t_k)} [1 - I_i(t_k)] (\zeta_{l,i} \zeta_{m,i}) - u_l^{(b)} u_m - u_m^{(b)} u_l + n^{(b)} u_l u_m \quad (6.43)$$

$$p_{lm}^{(c)} = \frac{1}{N_T} \sum_{k=1}^S \sum_{i=1}^{N(t_k)} I_i(t_k) (\zeta_{l,i} \zeta_{m,i}) - u_l^{(c)} u_m - u_m^{(c)} u_l + n^{(c)} u_l u_m \quad (6.44)$$

Temperature:

$$\begin{aligned} \tau_\alpha^{(b)} &= \frac{1}{N_T} \sum_{k=1}^S \sum_{i=1}^{N(t_k)} [1 - I_i(t_k)] \zeta_{\alpha,i}^2 - 2u^{(b)} u_\alpha + n^{(b)} u_\alpha^2, \alpha = \{x, y, z\}, \\ \tau^{(b)} &= 2(\tau_x^{(b)} + \tau_y^{(b)} + \tau_z^{(b)})/3 \end{aligned} \quad (6.45)$$

$$\begin{aligned} \tau_\alpha^{(c)} &= \frac{1}{N_T} \sum_{k=1}^S \sum_{i=1}^{N(t_k)} I_i(t_k) \zeta_{\alpha,i}^2 - 2u^{(c)} u_\alpha + n^{(c)} u_\alpha^2, \alpha = \{x, y, z\}, \\ \tau^{(c)} &= 2(\tau_x^{(c)} + \tau_y^{(c)} + \tau_z^{(c)})/3 \end{aligned} \quad (6.46)$$

Heat Flux:

$$\begin{aligned}
 \frac{q_x^{(b)}}{2} = & \frac{1}{N_T} \sum_{k=1}^S \sum_{i=1}^{N(t_k)} [1 - I_i(t_k)] \zeta_{x,i} (\zeta_{x,i}^2 + \zeta_{y,i}^2 + \zeta_{z,i}^2) - u_x \left\{ \frac{1}{N_T} \sum_{k=1}^S \sum_{i=1}^{N(t_k)} [1 - I_i(t_k)] (\zeta_{x,i}^2 + \zeta_{y,i}^2 + \zeta_{z,i}^2) \right\} \\
 & - 2u_x \left\{ \frac{1}{N_T} \sum_{k=1}^S \sum_{i=1}^{N(t_k)} [1 - I_i(t_k)] \zeta_{x,i}^2 \right\} - 2u_y \left\{ \frac{1}{N_T} \sum_{k=1}^S \sum_{i=1}^{N(t_k)} [1 - I_i(t_k)] \zeta_{x,i} \zeta_{y,i} \right\} \\
 & + (u_x^2 + u_y^2 + u_z^2) (u_x^{(b)} - n^{(b)} u_x) + 2u_x (u_x u_x^{(b)} + u_y u_y^{(b)})
 \end{aligned} \tag{6.47}$$

$$\begin{aligned}
 \frac{q_x^{(c)}}{2} = & \frac{1}{N_T} \sum_{k=1}^S \sum_{i=1}^{N(t_k)} I_i(t_k) \zeta_{x,i} (\zeta_{x,i}^2 + \zeta_{y,i}^2 + \zeta_{z,i}^2) - u_x \left\{ \frac{1}{N_T} \sum_{k=1}^S \sum_{i=1}^{N(t_k)} I_i(t_k) (\zeta_{x,i}^2 + \zeta_{y,i}^2 + \zeta_{z,i}^2) \right\} \\
 & - 2u_x \left\{ \frac{1}{N_T} \sum_{k=1}^S \sum_{i=1}^{N(t_k)} I_i(t_k) \zeta_{x,i}^2 \right\} - 2u_y \left\{ \frac{1}{N_T} \sum_{k=1}^S \sum_{i=1}^{N(t_k)} I_i(t_k) \zeta_{x,i} \zeta_{y,i} \right\} \\
 & + (u_x^2 + u_y^2 + u_z^2) (u_x^{(c)} - n^{(c)} u_x) + 2u_x (u_x u_x^{(c)} + u_y u_y^{(c)})
 \end{aligned} \tag{6.48}$$

$$\begin{aligned}
 \frac{q_y^{(b)}}{2} = & \frac{1}{N_T} \sum_{k=1}^S \sum_{i=1}^{N(t_k)} [1 - I_i(t_k)] \zeta_{y,i} (\zeta_{x,i}^2 + \zeta_{y,i}^2 + \zeta_{z,i}^2) - u_y \left\{ \frac{1}{N_T} \sum_{k=1}^S \sum_{i=1}^{N(t_k)} [1 - I_i(t_k)] (\zeta_{x,i}^2 + \zeta_{y,i}^2 + \zeta_{z,i}^2) \right\} \\
 & - 2u_y \left\{ \frac{1}{N_T} \sum_{k=1}^S \sum_{i=1}^{N(t_k)} [1 - I_i(t_k)] \zeta_{y,i}^2 \right\} - 2u_x \left\{ \frac{1}{N_T} \sum_{k=1}^S \sum_{i=1}^{N(t_k)} [1 - I_i(t_k)] \zeta_{x,i} \zeta_{y,i} \right\} \\
 & + (u_x^2 + u_y^2 + u_z^2) (u_y^{(b)} - n^{(b)} u_y) + 2u_y (u_y u_y^{(b)} + u_x u_x^{(b)})
 \end{aligned} \tag{6.49}$$

$$\begin{aligned}
 \frac{q_y^{(c)}}{2} = & \frac{1}{N_T} \sum_{k=1}^S \sum_{i=1}^{N(t_k)} I_i(t_k) \zeta_{y,i} (\zeta_{x,i}^2 + \zeta_{y,i}^2 + \zeta_{z,i}^2) - u_y \left\{ \frac{1}{N_T} \sum_{k=1}^S \sum_{i=1}^{N(t_k)} I_i(t_k) (\zeta_{x,i}^2 + \zeta_{y,i}^2 + \zeta_{z,i}^2) \right\} \\
 & - 2u_y \left\{ \frac{1}{N_T} \sum_{k=1}^S \sum_{i=1}^{N(t_k)} I_i(t_k) \zeta_{y,i}^2 \right\} - 2u_x \left\{ \frac{1}{N_T} \sum_{k=1}^S \sum_{i=1}^{N(t_k)} I_i(t_k) \zeta_{x,i} \zeta_{y,i} \right\} \\
 & + (u_x^2 + u_y^2 + u_z^2) (u_y^{(c)} - n^{(c)} u_y) + 2u_y (u_y u_y^{(c)} + u_x u_x^{(c)})
 \end{aligned} \tag{6.50}$$

Based on the above description it is deduced that for the ballistic part of the particle distribution the boundaries act as a source, while the bulk flow acts as a sink. The situation is reversed for the collision part of the particle distribution, where the bulk flow acts as a distributed source and the walls as a sink.

The macroscopic description of the whole flow domain of the enclosure in terms of the flow parameters is given in Section 6.2.5 and then, in Section 6.2.6 the discussion is focused on the behavior of the macroscopic quantities along the enclosure walls. Finally, in Section 6.2.7, the solution is split into the ballistic and collision parts, based on the methodology presented, and the flow behavior along the lateral walls is explained. All results are in dimensionless form.

6.2.5 Macroscopic distributions in the flow domain

Results are provided for all macroscopic quantities of theoretical importance and practical interest in a wide range of the Knudsen number ($0.1 \leq Kn_0 \leq 10$) covering the whole transition regime as well as parts of the slip and free molecular regimes and for temperature ratios $T_C/T_H = 0.1, 0.5$, and 0.9 corresponding to large, moderate, and small temperatures differences between the top and bottom plates, respectively. Enclosures with aspect ratios $H/W = 0.5, 1, 2$ are considered. Most of the results are for hard sphere molecules ($\omega = 0.5$), while some results for Maxwell molecules ($\omega = 1$) are provided as well.

In the case of the large temperature difference $T_C/T_H = 0.1$, simulations have been performed for all Knudsen numbers and aspect ratios by both the deterministic solver of the Shakhov model equation and the DSMC solver. The agreement between the corresponding results produced by these two completely different approaches is always very good as it is indicatively demonstrated for some cases. In the cases of $T_C/T_H = 0.5$ and 0.9 simulations have been performed mainly by the deterministic solver.

The effect of the degree of the gas rarefaction on the patterns of the flow field is shown in Figure 6.2, where the velocity streamlines superimposed on the temperature contours for $Kn_0 = 0.01, 0.1, 0.2, 0.5, 1$, and 10 in a square enclosure with $T_C/T_H = 0.1$ are presented. The flow is symmetric about $x = 0$. It is seen that for $Kn_0 = 0.01$ only the two Vortex-type I are observed and the gas flows next to the lateral walls from the colder towards the hotter region (from top to bottom). At $Kn_0 = 0.1$, at the two bottom corners of the enclosure, Vortex-type II start to appear counter rotating to the other ones. As the Knudsen number is increased, they are gradually increased as well, and for $Kn_0 = 0.5, 1$, and 10 these eddies of type II are well developed and cover large

portions of the flow domain with the gas flowing along the whole length of the side walls from the hotter to the colder region (from bottom to top). The two Vortex-type I have been squeezed towards the top and the center of the cavity. The temperature contours indicate that the flow domain is thermally stratified and as expected, the temperature jump at the walls becomes larger as the Knudsen number is increased. In general, as the flow becomes more rarefied the hot-to-cold motion next to the lateral walls is enhanced and the structure of the flow pattern becomes more complex. Of course as the Knudsen number tends to infinity the gas velocity vanishes.

It may be interesting to note that while in the classical lid driven cavity problem as we are approaching the hydrodynamic regime (i.e., as the Knudsen number is decreased) the flow becomes more complex with secondary vortices added to the main ones, here on the contrary, the interesting flow patterns with the Vortex-type II eddies, start to appear as we are moving into the transition regime (i.e., as the Knudsen number is increased). Overall, the degree of gas rarefaction significantly influences the thermally driven flow in the enclosure.

Figure 6.3 shows also streamlines and temperature contours in a square cavity for the cases of moderate and small temperature differences, namely, $T_C/T_H = 0.5$ and 0.9 , respectively, and for the typical values of $Kn_0 = 0.1, 1$, and 10 . These results along with the corresponding ones in Figure 6.2 are helpful to describe the effect of the temperature ratio on the flow pattern. In general, for the same Kn_0 , as the temperature difference between the bottom and top plates, as well as the temperature gradient along the lateral walls, are decreased, the Vortex-type II with the hot-to-cold flow in the vicinity of the walls become thinner covering a smaller portion of the flow domain. For the small temperature difference of $T_C/T_H = 0.9$ at $Kn_0 = 1$ these eddies are very thin but still cover the whole length of the non-isothermal side walls and then as the temperature difference is increased they are grown pushing the Vortex-type I towards the center.

A more quantitative description of the flow is provided in Figure 6.4, where the x and y components of the macroscopic velocity on vertical and horizontal planes, respectively, passing through the centers of the Vortex-type I are plotted. The results are for a square enclosure with $T_C/T_H = 0.1$ with $Kn_0 = 0.01, 0.1$, and 1 . The u_y profiles are plotted versus $x \in [-0.5, 0.5]$ and the u_x profiles are plotted versus $y \in [0, 1]$. Both deterministic and stochastic results are shown and it is seen that the agreement is always very good. The distributions of u_y are symmetric about $x = 0$ and the points where u_y changes sign correspond to the x coordinate of the center of the two eddies of

type I. The distributions of u_x are changing sign in the case of $Kn_0 = 0.01$ and 0.1 only once, which implies that only the two Vortex-type I are present (actually for $Kn_0 = 0.1$ the Vortex-type II has been created but it is not extended up to horizontal axis passing through the centers of the Vortex-type I). In the case of $Kn_0 = 1$ the distributions of u_x are changing sign several times, which indicates that both Vortex-type I and II are present. These observations are in accordance to the flow patterns shown in Figure 6.2 for the corresponding Knudsen numbers. In all cases the maximum absolute value of the velocities is small, approximately in the order of 10^{-2} or even less (the local Mach is about 10% higher than the reported velocity magnitudes), which is typical in rarefied thermally driven flows. Comparing between the absolute values of the velocity for various Knudsen numbers it is seen that the maximum values are at $Kn_0 = 0.1$. Also, as the Knudsen number is increased the magnitude of the velocities u_x related to Vortex-type II, in Figure 6.4(b), is increased and may become even larger than that of Vortex-type I.

These latter remarks are confirmed by the dimensionless flow rates of the Vortex-type I and II presented in Tables 6.1 and 6.2 respectively, for various temperature ratios and reference Knudsen numbers. The former ones are computed by integrating the dimensionless flux nu_x in the y direction from the center of the Vortex-type I to the top wall and the latter ones by integrating the flux nu_y in the x direction from the center of Vortex-type II to the side wall. The tabulated results have been obtained by the deterministic solution of the Shakhov model equation. Also, flow rates have been obtained by the DSMC approach for the case of $T_C/T_H = 0.1$ and they are in very good agreement with the corresponding tabulated ones. It is seen in Table 6.1 that starting from $Kn_0 = 0.01$ as the Knudsen number is increased and for the same temperature ratio, the flow rate of Vortex-type I is increased obtaining a maximum value around $Kn_0 = 0.07$ and then is constantly decreased as the Knudsen number keeps increasing. This is valid for all three temperature ratios. The corresponding flow rates of Vortex-type II, shown in Table 6.2, indicate a maximum flow rate around $Kn_0 = 1.2$. The exact physical reasoning for these maximum flow rates with regard to the reference Knudsen number is contributed to the number of collisions between particles and between particles and boundaries as the gas rarefaction is changing. In addition, while for $Kn_0 < 0.1$ the flow rate of Vortex-type II is several orders of magnitudes smaller compared to the corresponding ones of Vortex-type I, as the Knudsen number is increased the two flow rates become of the same order and in some

cases the former ones are even larger. Also, for the same Knudsen number as the temperature difference is increased the flow rate, as expected, is also increased.

The effect of the lateral walls on the flow pattern may be seen in Figure 6.5, where the streamlines and temperature contours for two rectangular enclosures, namely, $H/W = 0.5$ and 2 for the specific case of $T_C/T_H = 0.1$ and $Kn_0 = 1$ are plotted. Observing these flow fields along with the corresponding one for a square cavity ($H/W = 1$) in Figure 6.2, it is seen that as the aspect ratio is increased the presence of the Vortex-type II becomes more dominant covering a larger part of the flow domain. Obviously, as the aspect ratio is increased, i.e., as the depth prevails over the width of the cavity, the importance of the non-isothermal side walls compared to the bottom and top walls is also increased. The computed dimensionless flow rates of the Vortex type I and II are also changing significantly with the aspect ratio. It is concluded that the aspect ratio is a very important factor in this flow configuration.

Since this is a thermally induced flow it is reasonable to investigate the effect of the intermolecular collision model and this is done by including in Figure 6.6, some results for Maxwell molecules for the specific cases of $T_C/T_H = 0.1$, with $Kn_0 = 0.1$ and 1. Comparing the plotted streamlines and temperature contours with the corresponding ones for hard spheres in Figure 6.2, it is observed that for $Kn_0 = 0.1$ there is actually no effect, while for $Kn_0 = 1$ there are differences. This remark is also confirmed by the computed dimensionless flow rates of Vortex type I and II. It may be stated that as the intermolecular interaction becomes softer the region occupied by the Vortex-type II is reduced and the cold-to-hot flow becomes less intensive. However, again the hot-to-cold motion appears as the Knudsen number is increased.

6.2.6 Macroscopic distributions adjacent to the non-isothermal cavity walls

Here, a more thorough description of the macroscopic quantities in the vicinity of the boundaries of the enclosure is provided. This includes the y components of the velocity and heat flux as well as the shear stress along the lateral walls and the average heat flux from the bottom wall. Some comments on the range of validity of the mechanism explaining the formation of Vortex-type II, as described in [192], are included.

In Table 6.3, the tangential velocity u_y along the lateral walls of a square enclosure for small, moderate, and large temperature differences in a wide range of the reference

Knudsen number are provided. Due to symmetry these results correspond to $x = \pm 0.5$. When $u_y < 0$, the flow is from the top to bottom and corresponds to the expected thermal type flow as described by the Vortex-type I pattern, while when $u_y > 0$ the flow is the other way around and corresponds to the unexpected flow pattern as described by Vortex-type II. It is observed that when $Kn_0 = 0.01$ the values of u_y are negative and only very close to $y = 0$ and 1 very small positive values may appear. The Vortex-type I flow covers the whole flow domain. When $Kn_0 = 1$ and 10 the values of u_y are always positive, which implies that the Vortex-type II flow covers the whole length of the lateral walls. Finally, for $Kn_0 = 0.1$ both positive and negative values of u_y are observed. The positive values are close to the two ends and the negative values in the middle part of the wall. That implies that although the Vortex-type I flow still covers most of the whole flow field, counter rotating vortices at the bottom and top corners have been created, which, as the Knudsen number is increased, grow and merge into a Vortex-type II along the whole length of the side wall. These observations qualitatively hold for all three temperature ratios. Combining these results with the previous ones in Section 6.2.5 it is concluded that in small Knudsen numbers the expected thermal creep flow prevails and then for $Kn_0 \geq 0.5$ the importance of the unexpected hot-to-cold flow is gradually increased and its presence significantly effects both qualitatively and quantitatively the flow configuration.

According to the R13 approach in [192], the formation of the Vortex-type II is explained by the opposite contribution of the two different terms of the tangential velocity at the wall, which in the present notation, is written as

$$u_y^{R13} = -\frac{1}{(\tau n + 0.5p_{yy})} \left(\frac{\sqrt{\pi\tau}}{2} p_{xy} + \frac{1}{5} q_y \right). \quad (6.51)$$

The superscript R13 has been added here, in order to distinguish in our discussion the tangential velocity obtained by Eq. (6.51) from the one (u_y) obtained by the kinetic solution. The first term in the parenthesis corresponds to the viscous part of the tangential wall velocity and the second one to the transpirational part, caused by the shear stress and the tangential heat flux, respectively. The respective magnitude of these terms determines the sign of the tangential velocity and the local direction of the flow along the side walls. In order to examine the validity of this theory, the kinetic results of p_{xy} and q_y are introduced to compute, according to Eq. (6.51), the viscous and transpirational parts of the wall tangential velocity and the whole velocity as well.

The shear stress p_{xy} and the tangential heat flux q_y along the lateral wall at $x = -1/2$ of a square enclosure for various Knudsen numbers and temperature ratios are provided in Tables 6.4 and 6.5, respectively. It is seen that always $p_{xy} < 0$ and $q_y > 0$, i.e., they indeed have an opposite contribution to the tangential velocity. Since, however, as the Knudsen number is increased, both the values of the heat flux and the absolute values of the shear stresses are increased, it is necessary to further compute the contribution of each part separately.

In Figure 6.7, the tangential velocities obtained by kinetic theory and according to Eq. (6.51) denoted by u_y and u_y^{R13} , respectively, for $Kn_0 = 0.01, 0.05, 0.1$, and 1 , are plotted. When the velocity distributions are negative the transpirational part of the solution dominates and the flow along the lateral walls is from cold-to-hot (Vortex-type I), while when they are positive the viscous part dominates and the flow is from hot-to-cold (Vortex-type II). The agreement between the kinetic and R13 theory in small Knudsen numbers is very good and then, as the flow becomes more rarefied, the discrepancies, as expected, are increased. In general, the good qualitative agreement for $Kn_0 \leq 0.1$ indicates that the theory developed in [192] in order to explain the formation of the hot-to-cold flow in the vicinity of the walls is valid in the slip regime and fails as the Knudsen number is increased. In Section 6.2.7 a reasonable explanation for this type of flow in the whole range of the Knudsen number is provided.

It has been pointed in the introduction that the aspect ratio of the enclosure effects significantly the flow configuration and quantities. To further demonstrate the effect of the lateral walls, the tangential velocity and heat flux along the lateral walls of enclosures with $H/W = 0.5, 1, 2$ for $T_C/T_H = 0.1$ and $Kn_0 = 1$ are plotted in Figure 6.8. For the specific Knudsen number and temperature ratio the velocities are positive for all three aspect ratios and approximately of the same magnitude resulting to stiffer velocity gradients as H/W is decreased. The tangential heat flux is significantly increased as H/W is decreased, i.e., as the effect of the side walls is decreased.

Closing this subsection the average dimensionless heat flux directed from the bottom plate into the enclosure is estimated by integrating the heat flux $q_y(x, 0)$ over the distance $x \in [-0.5, 0.5]$. In Table 6.6, the average dimensionless heat flux, denoted by q_{av} is given in terms of the reference Knudsen number Kn_0 for $T_C/T_H = 0.1, 0.5$, and 0.9 . The corresponding results obtained by the DSMC method, using 400 cells in each direction and 100 particles per cell, are also included for comparison purposes. The agreement between the corresponding Shakhov and the DSMC results is excellent. As it is seen when the temperature difference between the top and bottom plates

is increased the average heat flux for the same Kn_0 , as expected, is also increased. Although not shown in the table it is noted that as H/W is increased the average heat flux is decreased, e.g., the computed values of q_{av} in the case of $T_C/T_H = 0.1$ for $H/W = 0.5, 1$, and 2 are $0.35, 0.14$, and 0.057 , respectively. Concerning the effect of the collision parameter ω on q_{av} it turns out that it is small since the values of the computed average heat fluxes for hard sphere and Maxwell molecules are close.

6.2.7 Ballistic and collision contributions

The decomposition of the DSMC solution into the ballistic and collision parts, as described in Section 6.2.4, is applied in a square enclosure for $Kn_0 = 0.05, 2$, with $T_C/T_H = 0.1$. The two values of the reference Knudsen numbers have been chosen as representatives to demonstrate the contribution of the ballistic and collision parts to the overall solution in the slip and transition regimes. In addition, the corresponding results are typical for analyzing the thermal effects on the flow configuration in small and large Knudsen numbers.

The streamlines and the contours of the vertical velocities of the ballistic and collision parts of the solutions, denoted by $u_y^{(b)}$ and $u_y^{(c)}$, respectively, as well as the overall solutions are given for $Kn_0 = 0.05$ and 2 in Figure 6.9. More specifically, Figure 6.9(a) and (b) show the ballistic parts and Figure 6.9(c) and (d) the collision parts, while the overall solutions which are the summation of the two corresponding parts are shown in Figure 6.9(e) and (f). It is seen that the streamlines of the ballistic parts (Figure 6.9(a) and (b)) are directed from the boundaries toward the interior of the bulk flow, while the streamlines of the collision parts (Figure 6.9(c) and (d)) are directed from the interior of the bulk flow toward the walls. These qualitative observations are well expected from the physical point of view since as it has been pointed before, in the ballistic part the walls act as source and the bulk flow as sink, while it is the other way around in the collision part. The streamlines along with the vertical velocities contours clearly indicate when the flow is in the positive or negative direction corresponding to hot-to-cold and cold-to-hot flow, respectively. The summation of these flow fields deduce the overall solutions shown in Figure 6.9(e) and (f), which are in excellent agreement with the corresponding deterministic ones. It is seen that for $Kn_0 = 0.05$ only the Vortex-type I are present, while for $Kn_0 = 2$ the Vortex-type II are also well developed, with the gas flowing along the lateral walls in the first case from cold-to-hot and in the second one from hot-to-cold.

The streamlines in Figure 6.9 may be further analyzed. Starting with $Kn_0 = 2$, where the flow patterns are simpler, the streamlines of the ballistic and collision parts are directed to and originated from single points, with total velocity equal to zero. The slight displacement between the two focal points and the small differences in the velocity magnitudes of the collision and ballistic parts, lead to the creation of Vortex-type II, shown in Figure 6.9(f). Continuing with $Kn_0 = 0.05$ it is seen that the streamline patterns of the ballistic and collision parts are quite different. The ballistic part has some resemblance with the corresponding one for $Kn_0 = 2$, showing one single point towards which the streamlines are directed. The collision part however is different indicating two single points from which the streamlines are originated. These points are symmetrically located about $x = 0$ and are centers of two symmetric spiral swirls caused by flow vorticity at this low Knudsen number. Also, at some extent streamlines are concentrated along a curve where the vertical velocities are zero. In addition, there is one point along $x = 0$ where the total velocity is zero and this point is transformed to a saddle point separating the streamline patterns into two branches directed to the hot and cold walls. The slope of the streamlines with respect to the vertical walls is another important element in the present analysis. It is seen that at $Kn_0 = 0.05$ the negative slope of the streamlines of the collision part is larger than the positive slope of the streamlines of the ballistic part and this is a clear sign for a cold-to-hot gas motion along the vertical walls. At $Kn_0 = 2$ the two slopes are about the same with the ballistic one appearing to be larger, which is an indication for a hot-to-cold gas motion.

A more detailed view of the flow along the lateral walls is presented in Figure 6.10, where the tangential velocities and number densities are presented. In Figure 6.10(a) the tangential velocities of the ballistic and collision parts, $u_y^{(b)}$ and $u_y^{(c)}$, respectively, are plotted along $y \in [0, 1]$ for $Kn_0 = 0.05$ and 2, while the corresponding overall tangential velocities u_y are given in Figure 6.10(b). It is seen in Figure 6.10(a), that for $Kn_0 = 0.05$, the tangential velocities $u_y^{(b)}$ and $u_y^{(c)}$ are positive and negative, respectively, along almost the whole length of the side walls and only very close to the top corners ($y = 1$) their signs are interchanged. In parallel, the overall tangential velocity u_y , in Figure 6.10(b), is negative.

In the case of $Kn_0 = 2$, the tangential velocities $u_y^{(b)}$ and $u_y^{(c)}$ in Figure 6.10(a), are positive and negative, respectively, up to about $y = 0.65$ and then their signs are interchanged. The overall velocity u_y , in Figure 6.10(b), is positive up to about $y = 0.7$ and then its value becomes negative taking very small values close to zero. From the

above it is deduced that the negative or positive values of u_y , corresponding to cold-to-hot or hot-to-cold flow along the walls depends on which part of the solution, either the ballistic or the collision part prevails with respect to the other. At $Kn_0 = 0.05$ the contribution of the collision part is more significant and only the Vortex-type I flow is observed, while at $Kn_0 = 2$ the magnitude of the ballistic part has been increased and becomes respectively more significant and therefore the Vortex-type II flow shows up.

These arguments are also supported by the ballistic and collision number density profiles denoted by $n^{(b)}$ and $n^{(c)}$, in Figure 6.10(c). It is seen that along the walls for $Kn_0 = 0.05$, $n^{(b)} < n^{(c)}$ and for $Kn_0 = 2$, $n^{(b)} > n^{(c)}$, which also indicate that in the overall solution the contribution of the collision part dominates at small Knudsen numbers, while at large Knudsen numbers the contribution of the ballistic part becomes more significant. In Figure 6.10(d) the overall density profiles n , computed as the summations of the two parts are provided for $Kn_0 = 0.05$ and 2.

Based on both Figures 6.9 and 6.10 and the previous discussion some more general comments on the ballistic and collision contributions in the overall solution may be stated. In the free molecular limit, the flow is perfectly balanced by pressure and temperature distributions and both collision and ballistic velocities are equal to zero. Increasing the gas density and respectively decreasing the Knudsen number, collisions between molecules destroy this balance and from thermodynamic viewpoint, the gas reaction is a weak motion in the enclosure with streamline patterns depending on the Knudsen number, the wall temperature distribution, and the enclosure geometry. At very large Knudsen numbers, the ballistic part is dominating. At moderate values there is interplay between the ballistic and collision parts and the behavior of the overall solution is very subtle particularly in the transition regime. Finally, at very small Knudsen numbers the collision part is dominating. In this latter case, the classic thermal creep theory works and predicts correctly the cold-to-hot direction of the streamlines along the vertical walls. As the Knudsen number increases the impact of the ballistic part also increases and the convective vortices start to rotate in the hot-to-cold direction along the lateral walls.

6.3 Non-equilibrium heat transfer in cavities due to uniformly heated walls

6.3.1 Flow configuration

The flow configuration is identical as the one presented in Section 6.2, while the boundary conditions are slightly altered. One wall, namely the bottom one, without loss of generality, is at temperature T_H , while the other three walls are kept at temperature T_C , with $T_C < T_H$. To avoid discontinuities at the two bottom corners, the temperature of the hot wall close to the two corners (5% of the total length W) is linearly decreased from T_H to match the temperature of the side walls T_C .

Due to thermal creep a flow is expected near the side walls directed from cold-to-hot regions and to ensure mass conservation a flow near the symmetry axis ($x' = 0$) is expected in the opposite direction. This would create two counter rotating vortices in the enclosure. Due to the same mechanism described in Section 6.2, in addition to these vortices, even at small Knudsen numbers, two more vortices appear in the upper part of the enclosure, with a flow along the lateral walls from hot-to-cold regions [158], [192], [199]. All four vortices are shown in Figure 6.11, with the former ones denoted by the symbol I and the latter unexpected ones by II. The detailed flow pattern depends on the gas rarefaction and the temperature ratio of the cold over the hot walls.

Another parameter of the flow field of practical interest is the local Mach number defined as $Ma = |U/c_0|$, where $U = \sqrt{U_x^2 + U_y^2}$ is the magnitude of the bulk velocity and $c_0 = \sqrt{\gamma k_B T_0 / m}$, with $\gamma = 5/3$ being the ratio of the specific heats of monatomic gases, is the speed of sound. It is readily shown that the local Mach number in terms of the dimensionless bulk velocity is given by $Ma = |u| \sqrt{6/5}$.

6.3.2 Deterministic and stochastic modeling

The problem is solved both in a deterministic and stochastic manner. The deterministic modeling is based on the direct solution of the nonlinear Shakhov kinetic model and the stochastic modeling on the DSMC method. Modeling of this flow configuration is identical as the one presented in Section 6.2 and thus a detailed description is omitted here. Furthermore, the solution of the thermally induced flow in the enclosure is decomposed into the ballistic and collision parts, focusing however on the heat flux departing from the hot wall, instead of the velocity field.

6.3.3 Flow field and macroscopic quantities

The flow in the square cavity was simulated in a wide range of the Knudsen number, namely for $0.1 \leq Kn_0 \leq 10^2$ and various temperature ratios $0.05 \leq T_C/T_H \leq 0.9$. Simulations have been conducted both by the deterministic and stochastic methods, and a very good agreement between corresponding results has been obtained.

In Figure 6.12 a view of the flow field in terms of the involved parameters is provided. The streamlines and the temperature contours are plotted for $Kn_0 = [0.1, 1, 10]$ and $T_C/T_H = [0.1, 0.9]$. At $Kn_0 = 0.1$ and for both temperature ratios the largest part of the cavity is covered by the typical thermal creep type vortices I and vortices II are restricted near the side walls of the cavity. As the gas rarefaction is increased vortices II start to expand squeezing the vortices I towards the bottom part of the cavity. As it is seen at $Kn_0 = 1$, vortices II are already well developed covering large areas of the square cavity. The flow configuration is similar at $Kn_0 = 10$, with vortices I further squeezed towards the bottom of the cavity. These observations are valid for both temperature ratios $T_C/T_H = 0.1$ and 0.9 corresponding to large and small temperature differences respectively, while in general at the same Kn_0 the dependency of the flow pattern on the temperature ratio T_C/T_H is qualitatively weak. In all the cases tested, the vertical velocity along the lateral walls is positive for the biggest part of the wall, leading to a flow directed from hot-to-cold regions.

The agreement between the Shakhov and corresponding DSMC results is very good and this is demonstrated in Figures 6.13 and 6.14. In Figure 6.13, DSMC streamlines and temperature contours are plotted for $Kn_0 = 1$ and $T_C/T_H = 0.1$. In addition, in Figure 6.14 the computed temperatures based on the DSMC method and the Shakhov kinetic model along the axis $x = 0$ are plotted for various values of Kn_0 and T_C/T_H . It is seen that in all cases very good agreement is achieved.

The y component of the velocity distribution along the lateral walls $u_y(\mp 1/2, y)$ is shown in Figure 6.15. Due to symmetry these results correspond to $x = \mp 1/2$. Results are provided $T_C/T_H = [0.1, 0.5, 0.9]$ corresponding to large, moderate and small temperature differences and in each case for $Kn_0 = [0.1, 1, 10]$. The negative values of the velocity are related to the well-known thermal creep flow from cold-to-hot, whereas the positive ones to a non-equilibrium flow from hot-to-cold. We observe that even for small Knudsen numbers, and for all temperature ratios, in the biggest part of the two vertical walls the velocity is positive, leading to a mass flow rate from

hot-to-cold. This is in accordance with the results presented in Section 6.2.5 and the same explanation given in Section 6.2.7 holds.

The local Mach number may be calculated based on the relation $Ma = |u| \sqrt{6/5}$, defined in Section 6.3.1. To have some information of the velocity field the maximum Mach number is tabulated in Table 6.7. It is seen that it is increased as the reference Knudsen number is decreased and the temperature difference between the hot and cold plates is increased. Also, in Figure 6.16, typical contours of the Mach number are plotted for $Kn_0 = 1$ and $T_C/T_H = [0.1, 0.9]$. In general, as expected for flows induced by temperature differences the Mach number is very small.

6.3.4 Ballistic, collision and total heat fluxes

An overall quantity of great practical interest for this specific heat flow configuration is the average dimensionless heat flux q_{ave} departing from the hot plate, which is estimated by integrating the heat flux $q_y(x, 0)$ over $x \in [-0.5, 0.5]$. This quantity is plotted in Figure 6.17 in terms of Kn_0 for various temperature ratios $T_C/T_H = [0.05, 0.1, 0.3, 0.5, 0.9]$. Results obtained both by the kinetic modeling and the DSMC approaches are provided for comparison purposes. As it is seen the agreement is excellent in all cases. For all temperature ratios the average dimensionless heat flux increases as Kn_0 increases from 0.1 to 1 and then for $T_C/T_H = [0.3, 0.5, 0.9]$ keeps slowly increasing, while for $T_C/T_H = [0.05, 0.1]$ is slightly decreasing. In all cases as $Kn_0 \rightarrow \infty$, q_{ave} tends to an asymptotic value. A very interesting result is the variation of q_{ave} in terms of T_C/T_H at a given Kn_0 . It is clearly seen, that q_{ave} is not steadily increased as the temperature difference between the hot and cold plates becomes greater, i.e. as T_C/T_H is decreased. For example at $Kn_0 = 1$, as the temperature ratio T_C/T_H is decreased from 0.9 to 0.3 the average heat flux is, as expected, increased, while as T_C/T_H is further decreased from 0.3 to 0.05 the average heat flux is decreased. The behavior of q_{ave} can be seen more clearly in Figure 6.18 where it is given in terms of the temperature ratio for various values of the Knudsen number. This observation is valid in a whole range of the reference Knudsen number tested and it is found that the maximum average heat flux emitted from the hot wall occurs at about $T_C/T_H = 0.3$. This behavior has been captured individually by both modeling approaches.

To further investigate this finding in Figure 6.19, the ballistic and collision parts of the average heat flux at the hot wall, denoted as $q_{ave}^{(b)}$ and $q_{ave}^{(c)}$ respectively are plotted in terms of the temperature ratio T_C/T_H for $Kn_0 = 0.1, 1$ and 10 . The total average heat flux $q_{ave} = q_{ave}^{(b)} + q_{ave}^{(c)}$ is plotted as well. The ballistic and collision parts of the

heat flux are opposed with $q_{ave}^{(b)} > 0$ and $q_{ave}^{(c)} < 0$, while their summation, i.e., the total average heat flux, is always, as expected, larger than zero ($q_{ave} > 0$). It is seen that as T_C/T_H is increasing, initially $q_{ave}^{(b)}$ is increasing with a pace which is faster than the one that $q_{ave}^{(c)}$ is decreasing and therefore the total heat flux q_{ave} is initially increasing with T_C/T_H . Then, as T_C/T_H is further increasing $q_{ave}^{(b)}$ is increasing with a slower pace and finally for large values of T_C/T_H and $Kn_0 \geq 1$ is even decreasing, while in parallel $q_{ave}^{(c)}$ always keeps decreasing and therefore after some critical value of T_C/T_H the total heat flux q_{ave} is decreasing. Consequently, the non-monotonic behavior and the maximum q_{ave} at $T_C/T_H = 0.3$ may be explained by analyzing the overall solution to its ballistic and collision parts. Also, as $T_C/T_H \rightarrow 1$ the ballistic and collision parts have the same magnitude and due to their opposite sign the total heat flux q_{ave} vanishes.

Some indicative dimensional results are shown in Figure 6.20, where the dimensional average heat flux $Q_{ave}[\text{W/m}^2]$ is plotted in terms of the reference pressure $P_0[\text{Pa}]$ for various values of $T_C/T_H = [0.05, 0.1, 0.3, 0.5, 0.9]$. The results are for a square cavity with a side length of $W = 50\mu\text{m}$ and the hot wall temperature equal to $T_H = 10^3\text{K}$ filled with Argon ($m = 39.95\text{kg}/\text{kmol}$). The corresponding Kn_0 is also shown in Figure 6.20. It is seen that Q_{ave} is steadily increased as P_0 is increased, i.e. as the gas becomes less rarefied. It is also seen that for the same P_0 , as T_C/T_H is decreased from 0.9 to 0.3, Q_{ave} is increased and then as T_C/T_H is further decreased to 0.1, Q_{ave} is decreased. Thus, as in the dimensionless results, there is a maximum value of Q_{ave} at $T_C/T_H = 0.3$. It may be stated that in order to maximize cooling a temperature ratio close to 0.3 is to be used, while to optimize operation stability (and probably efficiency) a temperature ratio close to 0.1 – 0.4, depending on Kn_0 , can be used.

6.4 Prediction of the Knudsen minimum in long capillaries

6.4.1 Flow configuration

Consider the classical pressure driven isothermal flow of a rarefied gas at a reference temperature T_0 through a capillary of length L with the pressure at the inlet and outlet of the capillary maintained at P_1 and P_2 , respectively ($P_1 > P_2$). The area and the perimeter of the capillary cross section are denoted by A' and Γ' , respectively. The z' axis is taken along the capillary and the cross section is on the (x, y) plane. The characteristic length of the cross section, denoted by H , is assumed to be much smaller

than its length ($H/L \ll 1$). In this case, as rigorously proved in [106], the pressure (and density) is constant on each cross section and varies only along the capillary in the flow direction, i.e., $P = P(z') \in [P_1, P_2]$ and the flow is considered as fully developed in the z' direction.

The basic flow parameter is the Knudsen number (Kn) or alternatively the rarefaction parameter (δ), defined as

$$\delta = \frac{HP_0}{\mu_0 v_0} \frac{1}{Kn} = \frac{\lambda}{H}, \quad (6.52)$$

where $P_0 = (P_1 + P_2)/2$ is the reference pressure, H is the characteristic length, μ_0 is the gas viscosity at T_0 , $v_0 = \sqrt{2k_B T_0/m}$ is the most probable molecular velocity (k_B is the Boltzmann constant and m the molecular mass), and λ denotes the mean free path. It is convenient to introduce the dimensionless variables $x = x'/H$, $y = y'/H$, $z = z'/H$, the dimensionless cross section $A = A'/H^2$ and perimeter $\Gamma = \Gamma'/H$, as well as the dimensionless bulk velocity in the z' direction $u(x, y) = u'(x', y') / (v_0 X_P)$ (the other two velocity components are zero) and shear stresses $\tau_{\alpha z}(x, y) = \tau'_{\alpha z}(x', y') / (2X_P P_0)$, $\alpha = x, y$, where $X_P = (dP/dz) / P_0$ is the local pressure gradient.

A quantity of major importance is the kinetic coefficient (or reduced flow rate) G , which is defined according to

$$G = \frac{2}{A} \int_A u(x, y) dA. \quad (6.53)$$

The variation of G in terms of δ for gas flows through long capillaries of various cross sections has been a focal point of investigation and tabulated results are available in the literature [23], [170], [204], [206], [207], [209], [227]–[229]. The Knudsen minimum always appears in the transition regime and the exact value of δ where the minimum occurs depends on the capillary cross section and the gas-surface accommodation coefficient.

The average shear stress at the wall is also introduced to be later used for benchmarking purposes. Since the flow is fully developed and there is no net momentum flux in the flow direction. The net pressure and the wall shear stress are equated to yield $\bar{\tau}'_w = (A'/\Gamma') (dP/dz')$, which may be nondimensionalized to find $\bar{\tau}_w = \bar{\tau}'_w / (2P_0 X_P) = A / (2\Gamma) = 0.25$ [208], [229]. This result is always valid independent of the channel cross section and the rarefaction parameter δ and it may be used as a benchmark to test the accuracy of the DSMC calculations.

6.4.2 Stochastic modeling and decomposition

The flow is simulated based on the Boltzmann equation which is solved via the DSMC method subject to the no time counter (NTC) scheme proposed by Bird [62]. The flow is simulated only on the capillary cross section pushed by a uniform force in the flow direction resulting in a dimensionless acceleration equal to X_P acting on each gas molecule. It is noted that X_P is a constant taking sufficiently small values to ensure the linearity of the flow.

As described in Section 6.2.4 an index $I_i(t_k)$ is attached to each particle $i = 1, \dots, N(t_k)$ indicated whether it belongs to the ballistic ($I_i(t_k) = 0$) or collision ($I_i(t_k) = 1$) part of the distribution. The total number of all particles accumulated in a cell is divided into the ballistic and collision groups as $N_T = N_T^{(b)} + N_T^{(c)}$. The macroscopic quantities are decomposed into the ballistic and collision parts as:

Number density:

$$n^{(b)}(x, y) = \frac{N_T^{(b)}}{SV_{Cell}} \quad (6.54)$$

$$n^{(c)}(x, y) = \frac{N_T^{(c)}}{SV_{Cell}} \quad (6.55)$$

Velocity:

$$u^{(b)} = \frac{1}{X_P N_T} \sum_{k=1}^S \sum_{i=1}^{N(t_k)} [1 - I_i(t_k)] \zeta_{z,i}(t_k) \quad (6.56)$$

$$u^{(c)} = \frac{1}{X_P N_T} \sum_{k=1}^S \sum_{i=1}^{N(t_k)} I_i(t_k) \zeta_{z,i}(t_k) \quad (6.57)$$

Shear stress:

$$\tau_{\alpha z}^{(b)} = \frac{1}{X_P N_T} \sum_{k=1}^S \sum_{i=1}^{N(t_k)} [1 - I_i(t_k)] \zeta_{\alpha,i}(t_k) \zeta_{z,i}(t_k) - u_{\alpha}^{(b)} u_z \quad (6.58)$$

$$\tau_{\alpha z}^{(c)} = \frac{1}{X_P N_T} \sum_{k=1}^S \sum_{i=1}^{N(t_k)} I_i(t_k) \zeta_{\alpha,i}(t_k) \zeta_{z,i}(t_k) - u_{\alpha}^{(c)} u_z \quad (6.59)$$

Similarly the reduced flow rate is decomposed as $G = G^{(b)} + G^{(c)}$ where $G^{(b)}$ and $G^{(c)}$ are the reduced ballistic and collision flow rates, respectively.

Applying this methodology, four rarefied gas flows through long capillaries, namely the flow between parallel plates (channel flow), through orthogonal ducts with two aspect ratios $H/W = 0.1$ and 1 (duct flow), and through long circular tubes (tube flow) are explored. Purely diffuse boundary conditions are considered and the hard sphere model was used. The physical space domain is discretized using 100 cells per unit length with about 1000 simulator particles per cell. Such a large number of simulator particles is utilized as the acceleration acting on each particle takes very small values. The time step is chosen close to $1/3$ of the cell transversal time, defined as $\Delta x'/v_0$. The macroscopic quantities are obtained by time averaging over more than $S = 10^7$ time steps after the steady state has been recovered. By setting the acceleration parameter $X_P/2 = 0.01$ the deduced DSMC solution has the well-known linear characteristics (i.e., the solution is directly proportional to the source term) and nonlinear phenomena are absent. The results presented here are accurate up to at least two significant figures which is adequate for the objectives of the present work.

6.4.3 Explanation of the Knudsen minimum

The flow rates $G^{(b)}$, $G^{(c)}$, and G are plotted in terms of δ in Figure 6.21 for the channel, the duct ($H/W = 0.1$ and 1), and the tube flows. The well-known behavior of G with a minimum in the transition regime is observed [23], [170], [207], [227]. The values of δ where the Knudsen minimum occurs, denoted by δ_{\min} , are indicated in Figure 6.21 and in tabulated form in Table 6.8.

For the channel flow, a detailed comparison between the results in Figure 6.21(a) with the corresponding ones in Table V of [170] has been performed. To achieve that δ has been related to the parameter k of [170] according to $\delta = 1/(\alpha k)$ with $\alpha = 5/4$ and also the present flow rates have been divided by 2. For all values of $\delta \in [0.1, 10]$ the agreement is excellent with the relative error being less than 0.5%. Based on this comparison and on the previously described formulation it is quantitatively verified that the present “linear” DSMC solution corresponds to the one obtained by solving the same flow configurations based on the linear Boltzmann equation for hard sphere molecules.

In Figure 6.21, the ballistic and collision flow rates always have a monotonous behavior with respect to δ . As δ is increased $G^{(b)}$ constantly decreases and finally diminishes as $\delta \rightarrow \infty$, while $G^{(c)}$ initially at $\delta = 0$ is zero and then constantly increases. Thus, at $\delta = 0$ and $\delta \rightarrow \infty$ the overall flow rate is $G = G^{(b)}$ and $G = G^{(c)}$ respectively.

In the free-molecular and early transition regimes the reduction rate of $G^{(b)}$ is larger than the increase rate of $G^{(c)}$ resulting to the Knudsen minimum of the overall flow G .

To further elaborate on this issue, in Figure 6.22, the derivatives $dG^{(b)}/d\delta$, $dG^{(c)}/d\delta$, and $dG/d\delta$ are plotted in terms of δ . They are computed numerically based on the results of $G^{(b)}$ and $G^{(c)}$. It is seen that $dG^{(b)}/d\delta$ is always negative and as δ is increased it tends to zero since $G^{(b)}$ itself is zero. Actually, for $\delta > 5$ there is no contribution of $G^{(b)}$ to G . In parallel $dG^{(c)}/d\delta$ is always positive and as $\delta \rightarrow \infty$, the $\lim_{\delta \rightarrow \infty} (dG^{(c)}/d\delta) = \lim_{\delta \rightarrow \infty} (dG/d\delta) = c$. In the hydrodynamic limit, solving the Stokes equation (with or without slip boundary conditions) it is readily deduced that $c = 1/6$ in the channel flow and $c = 0.25$ in the tube flow [23]. The corresponding values in Figure 6.22 at $\delta = 10$ are very close to these ones. Furthermore, it is computationally confirmed that

$$\left| \frac{dG^{(b)}}{d\delta} \right| \geq \frac{dG^{(c)}}{d\delta} \text{ for } \delta \leq \delta_{\min}. \quad (6.60)$$

Clearly, this behavior of the derivatives of the two parts leads to a single root of the derivative of the overall reduced flow rate, which is crossing the δ -axis from negative to positive values, indicating the existence of a minimum. Obviously, the value of $\delta = \delta_{\min}$ where $dG/d\delta = 0$ is where the Knudsen minimum occurs. This description quantitatively explains the appearance of the Knudsen minimum and verifies the qualitative physical arguments presented in [218].

In Figure 6.21 only the case of purely diffuse accommodation is presented. The DSMC decomposition may also be applied in the case of Maxwell boundary conditions. In this latter case the indicator of the particles following a specular reflection at the wall is not set equal to 0 (as is done with the diffuse reflection) and on the contrary remains the same as before the specular reflection. Beyond that the methodology is identical and the values of δ where the Knudsen minimum occurs for $\alpha < 1$ are accordingly obtained and justified.

The behavior of the ballistic and collision velocity distributions, shown for the channel case in Figure 6.23 (left), is according to the corresponding flow rate results, i.e., as δ is increased, $u^{(b)}$ is decreased, while $u^{(c)}$ is increased. It is noted that at $\delta = 0.1$, $u^{(b)}(x)$ is larger than $u^{(c)}(x)$, then at $\delta = 1$ is smaller but remains large enough compared to $u^{(c)}$, while at $\delta = 5$ becomes negligibly small.

More interesting is the partition of the number density into its ballistic and collision segments which are plotted, scaled to the average sampled initial density, in Figure

6.23 (right) for channel flow with $\delta = [0.1, 1, 5]$. The overall number density $n(x) = n^{(b)} + n^{(c)} = 1$ is always constant. The ballistic number density $n^{(b)}(x)$ for all δ has its largest values at the walls ($x = 0$ and $x = 1$) and it decreases moving towards the center of the channel, taking its lowest values at $x = 0.5$. The collision number density $n^{(c)}(x) = 1 - n^{(b)}$ behaves in an exactly opposite manner. For the ballistic particle distribution the boundaries act as a source, while the bulk flow acts as a sink and the situation is reversed for the collision particle distribution, where the bulk flow acts as a distributed source and the walls as a sink. The overall behavior of the ballistic and collision number densities in terms of δ is similar to the one of the velocities. Note that even at $\delta = 5$, although at the center of the channel $n^{(b)}$ is negligible small compared to $n^{(c)}$, close to the boundaries is lower but still close to $n^{(c)}$. The region next to the boundaries where $n^{(b)}$ is nonzero corresponds to the Knudsen layer.

Tabulated results of the dimensionless average wall shear stress and the associated ballistic and collision parts are given in Table 6.9 for the channel and tube flows. The overall stresses $\bar{\tau}_{\alpha z}$ are independent of δ and they are slightly lower than the analytical result of 0.25, since they are calculated, as all macroscopic quantities, at the center of each cell. Once again, as δ is increased $\bar{\tau}_{\alpha z}^{(b)}$ decreases and $\bar{\tau}_{\alpha z}^{(c)}$ increases, with $\bar{\tau}_{\alpha z}^{(b)}$ remaining important as a wall quantity even at $\delta = 5$, i.e., even close to the slip regime. It is noted that the contribution of $\bar{\tau}_{\alpha z}^{(b)}$ to $\bar{\tau}_{\alpha z}$ far from the wall at large values of δ rapidly vanishes.

6.5 Concluding remarks

A stochastic solution decomposition methodology has been developed, decomposing the distribution function into its ballistic and collision parts. The ballistic part is composed of particles that have not collided with other particles after they were emitted from the boundaries, while the collision part is composed of particles that have undergone an arbitrary number of collisions. This decomposition technique has been implemented to the typical DSMC algorithm and applied in two thermally driven flows in cavities and in pressure driven fully developed flows in capillaries. In all cases, the contributions of the ballistic and collision parts of the distribution function have been separately computed, providing a thorough understanding of non-equilibrium interesting phenomena appearing in these flows.

The thermally induced rarefied gas flow in a rectangular enclosure, with different temperatures at the bottom and top walls and linear temperature distributions at

the two lateral walls, has been simulated. The solution is given in terms of the three parameters characterizing the flow, namely, the reference Knudsen number, the temperature ratio of the top over the bottom plates, and the aspect ratio of the enclosure. Both deterministic and stochastic simulations have been performed based on the numerical solution of the Shakhov kinetic equation and the DSMC method, respectively. Results have been obtained for enclosures with various aspect ratios in the whole range of the Knudsen number and for small, moderate, and large temperature differences.

Confirming previous results in similar non-isothermal set-ups, it has been found that in the vicinity of the lateral walls the gas is not necessarily going from cold-to-hot. Actually, even for relatively small Knudsen numbers in the slip or early transition regime a hot-to-cold flow along the non-isothermal side walls is observed, which is enhanced as the Knudsen number and the temperature difference are increased. The cavity aspect ratio is also an important factor and the hot-to-cold flow is becoming more dominant as the depth compared to the width of the cavity is increased. The effect of these parameters on the flow configuration and bulk quantities has been thoroughly examined. Furthermore, the introduced novel decomposition of the DSMC solution into the ballistic and collision parts illuminates, at the particle level, important details of the flow. It has been found that at small Knudsen numbers the collision part dominates and the classic thermal creep theory works, while at large Knudsen numbers the ballistic part prevails and then the gas along the wall flows from hot-to-cold.

The non-equilibrium gas flow and heat transfer in a two-dimensional square cavity with one wall maintained at high temperature and the other three at low temperature has been numerically investigated. Simulations have been conducted for the two parameters characterizing the problem namely the temperature ratio and the reference Knudsen number based on the Shakhov kinetic model and the DSMC method deducing excellent agreement between the two methodologies.

It has been found that the flow along the lateral walls is directed from hot-to-cold even for small temperature differences and small Knudsen numbers, confirming previous findings in similar set-ups [192], [199]. As the temperature difference and the Knudsen number are increased this non-equilibrium flow pattern becomes more dominant. Also, the average heat flux departing from the hot plate exhibits a non-monotonic dependency with regard to the temperature ratio in a wide range of the Knudsen number. More specifically, a maximum dimensionless heat flux occurs at $T_C/T_H = 0.3$. This behavior

is explained by computing the ballistic and collision parts of the total heat flux and by investigating the contribution of each part to the overall solution.

The well-known Knudsen paradox has been also investigated by decomposing the particle distribution function into its ballistic and collision parts and examining the effect of each part to the overall solution. Fully developed flows through long capillaries of various cross sections have been considered. It has been shown in a precise quantitative manner that the difference in the rate of change of the corresponding ballistic and collision flow rates with respect to the rarefaction parameter yields the Knudsen minimum of the overall reduced flow rate or conductance.

The stochastic solution decomposition technique has provided physical arguments and justifications to three interesting non-equilibrium phenomena. It is believed that this methodology can be further applied to a broader range of configurations in order to increase our understanding of the flow microstructure and provide physical intuition on the mechanism behind a number of phenomena.

Table 6.1 Dimensionless flow rate of Vortex-type I in a square enclosure for various Kn_0 and T_C/T_H .

T_C/T_H	Kn_0						
	0.01	0.06	0.07	0.08	0.1	1	10
0.1	6.34(-4)	1.70(-3)	1.72(-3)	1.71(-3)	1.67(-3)	2.89(-4)	2.76(-5)
0.5	2.87(-4)	7.51(-4)	7.53(-4)	7.44(-4)	7.08(-4)	8.60(-5)	6.38(-6)
0.9	5.07(-5)	1.31(-4)	1.31(-4)	1.30(-4)	1.23(-4)	1.21(-5)	6.99(-7)

Table 6.2 Dimensionless flow rate of Vortex-type II in a square enclosure for various Kn_0 and T_C/T_H .

T_C/T_H	Kn_0					
	0.1	1	1.1	1.2	1.3	10
0.1	2.55(-6)	1.18(-4)	1.198(-4)	1.204(-4)	1.202(-4)	3.99(-5)
0.5	6.98(-7)	2.46(-5)	2.504(-5)	2.513(-5)	2.512(-5)	8.70(-6)
0.9	8.41(-8)	2.85(-6)	2.902(-6)	2.936(-6)	2.942(-6)	1.08(-6)

Table 6.3 Tangential velocity u_y along the lateral walls of a square enclosure for various Kn_0 and T_C/T_H .

$\frac{T_C}{T_H}$	Kn_0	y									
		0.05	0.15	0.25	0.35	0.45	0.55	0.65	0.75	0.85	0.95
0.1	0.01	-5.1(-4)	-1.5(-3)	-1.9(-3)	-2.0(-3)	-2.0(-3)	-1.9(-3)	-1.8(-3)	-1.6(-3)	-1.3(-3)	-8.4(-4)
	0.1	1.7(-3)	8.8(-4)	-1.5(-4)	-1.1(-3)	-1.8(-3)	-2.5(-3)	-2.8(-3)	-2.8(-3)	-2.0(-3)	-5.9(-5)
	1	5.4(-3)	5.8(-3)	5.6(-3)	5.0(-3)	4.4(-3)	3.6(-3)	2.8(-3)	1.9(-3)	1.2(-3)	7.7(-4)
	10	1.3(-3)	1.3(-3)	1.2(-3)	1.1(-3)	9.2(-4)	7.4(-4)	5.7(-4)	3.9(-4)	2.5(-4)	1.3(-4)
0.5	0.01	-2.8(-4)	-6.5(-4)	-7.7(-4)	-8.0(-4)	-8.1(-4)	-7.9(-4)	-7.6(-4)	-7.1(-4)	-6.1(-4)	-3.5(-4)
	0.1	5.6(-4)	-2.2(-5)	-5.2(-4)	-8.6(-4)	-1.1(-3)	-1.2(-3)	-1.1(-3)	-9.1(-4)	-4.4(-4)	3.2(-4)
	1	1.5(-3)	1.6(-3)	1.5(-3)	1.4(-3)	1.2(-3)	1.1(-3)	1.0(-3)	9.4(-4)	9.2(-4)	8.7(-4)
	10	3.4(-4)	3.5(-4)	3.2(-4)	2.9(-4)	2.6(-4)	2.3(-4)	2.2(-4)	2.0(-4)	1.9(-4)	1.8(-4)
0.9	0.01	-5.5(-5)	-1.1(-4)	-1.3(-4)	-1.4(-4)	-1.4(-4)	-1.4(-4)	-1.4(-4)	-1.3(-4)	-1.1(-4)	-5.7(-5)
	0.1	8.2(-5)	-3.5(-5)	-1.2(-4)	-1.7(-4)	-2.0(-4)	-2.0(-4)	-1.8(-4)	-1.3(-4)	-4.6(-5)	7.6(-5)
	1	2.2(-4)	2.3(-4)	2.1(-4)	2.0(-4)	1.9(-4)	1.9(-4)	1.9(-4)	2.0(-4)	2.1(-4)	2.0(-4)
	10	4.6(-5)	4.8(-5)	4.6(-5)	4.3(-5)	4.2(-5)	4.1(-5)	4.1(-5)	4.3(-5)	4.4(-5)	4.2(-5)

Table 6.4 Lateral wall shear stress ($-p_{xy}$) at $x = -0.5$ of a square enclosure for various Kn_0 and T_C/T_H .

$\frac{T_C}{T_H}$	Kn_0	y					
		0	0.2	0.4	0.6	0.8	1.0
0.1	0.01	1.4(-3)	7.7(-4)	5.1(-4)	4.1(-4)	4.3(-4)	2.1(-3)
	0.1	1.0(-2)	1.2(-2)	1.3(-2)	1.3(-2)	1.5(-2)	2.1(-2)
	1	3.1(-2)	3.8(-2)	4.3(-2)	4.5(-2)	4.6(-2)	4.5(-2)
	10	4.3(-2)	4.9(-2)	5.3(-2)	5.5(-2)	5.4(-2)	5.0(-2)
0.5	0.01	9.1(-4)	3.5(-4)	2.4(-4)	2.2(-4)	2.8(-4)	1.0(-3)
	0.1	7.0(-3)	7.5(-3)	7.5(-3)	7.6(-3)	8.1(-3)	8.7(-3)
	1	2.2(-2)	2.6(-2)	2.8(-2)	2.8(-2)	2.8(-2)	2.5(-2)
	10	2.9(-2)	3.3(-2)	3.5(-2)	3.5(-2)	3.4(-2)	3.1(-2)
0.9	0.01	1.9(-4)	6.4(-5)	4.5(-5)	4.4(-5)	6.2(-5)	2.0(-4)
	0.1	1.5(-3)	1.6(-3)	1.5(-3)	1.5(-3)	1.6(-3)	1.6(-3)
	1	4.7(-3)	5.4(-3)	5.7(-3)	5.7(-3)	5.4(-3)	4.8(-3)
	10	6.0(-3)	6.7(-3)	7.1(-3)	7.1(-3)	6.8(-3)	6.1(-3)

Table 6.5 Lateral wall heat flux q_y at $x = -0.5$ of a square enclosure for various Kn_0 and T_C/T_H .

$\frac{T_C}{T_H}$	Kn_0	y					
		0	0.2	0.4	0.6	0.8	1.0
0.1	0.01	5.5(-3)	7.2(-3)	6.7(-3)	5.8(-3)	4.6(-3)	2.1(-3)
	0.1	3.5(-2)	4.1(-2)	4.5(-2)	4.5(-2)	4.2(-2)	3.3(-2)
	1	8.9(-2)	9.9(-2)	1.1(-1)	1.1(-1)	1.1(-1)	1.0(-1)
	10	1.2(-1)	1.3(-1)	1.3(-1)	1.3(-1)	1.3(-1)	1.2(-1)
0.5	0.01	3.2(-3)	4.4(-3)	4.2(-3)	3.9(-3)	3.7(-3)	2.4(-3)
	0.1	2.5(-2)	3.0(-2)	3.2(-2)	3.2(-2)	3.0(-2)	2.4(-2)
	1	7.7(-2)	8.3(-2)	8.7(-2)	8.8(-2)	8.6(-2)	8.0(-2)
	10	1.0(-1)	1.1(-1)	1.1(-1)	1.1(-1)	1.1(-1)	1.0(-1)
0.9	0.01	6.5(-4)	9.2(-3)	9.1(-4)	9.1(-4)	8.9(-4)	6.2(-4)
	0.1	5.7(-3)	6.9(-3)	7.3(-3)	7.3(-3)	6.9(-3)	5.6(-3)
	1	1.8(-2)	2.0(-2)	2.0(-2)	2.0(-2)	2.0(-2)	1.8(-2)
	10	2.3(-2)	2.5(-2)	2.6(-2)	2.6(-2)	2.5(-2)	2.3(-2)

Table 6.6 Average heat flux q_{av} departing from the bottom plate of a square enclosure for various Kn_0 and T_C/T_H .

Kn_0	$T_C/T_H = 0.1$		$T_C/T_H = 0.5$		$T_C/T_H = 0.9$	
	Shakhov	DSMC	Shakhov	DSMC	Shakhov	DSMC
0.01	1.33(-2)	1.38(-2)	8.55(-3)	8.60(-3)	1.87(-3)	1.80(-3)
0.1	7.20(-2)	7.16(-2)	5.18(-2)	5.32(-2)	1.19(-2)	1.22(-2)
1	1.48(-1)	1.49(-1)	1.23(-1)	1.27(-1)	2.88(-2)	2.94(-2)
10	1.78(-1)	1.79(-1)	1.50(-1)	1.51(-1)	3.47(-2)	3.50(-2)

Table 6.7 Maximum value of the Mach number in the field for various Kn_0 and T_C/T_H .

$\frac{T_C}{T_H}$	Kn_0		
	0.1	1	10
0.1	9.19(-3)	3.99(-3)	9.21(-4)
0.5	3.69(-3)	2.45(-3)	4.62(-4)
0.9	7.21(-4)	4.83(-4)	9.54(-5)

Table 6.8 Values of δ_{\min} for flows through long capillaries of various cross sections.

Capillary	Channel ($H/W \rightarrow 0$)	Duct ($H/W \rightarrow 0.1$)	Duct ($H/W \rightarrow 1$)	Tube
δ_{\min}	1.1	0.93	0.61	0.31

Table 6.9 Dimensionless average wall shear stress along with the ballistic and collision parts for the channel and tube flows in terms of δ .

δ	Channel			Tube		
	$\bar{\tau}_{xz}$	$\bar{\tau}_{xz}^{(b)}$	$\bar{\tau}_{xz}^{(c)}$	$\bar{\tau}_{rz}$	$\bar{\tau}_{rz}^{(b)}$	$\bar{\tau}_{rz}^{(c)}$
0.01	2.47(-1)	2.40(-1)	7.00(-3)	2.49(-1)	2.45(-1)	4.83(-3)
0.1	2.48(-1)	2.13(-1)	3.48(-2)	2.49(-1)	2.13(-1)	3.71(-2)
1	2.47(-1)	1.45(-1)	1.03(-1)	2.49(-1)	1.25(-1)	1.25(-1)
5	2.47(-1)	1.13(-1)	1.34(-1)	2.48(-1)	1.06(-1)	1.42(-1)
10	2.46(-1)	1.08(-1)	1.39(-1)	2.48(-1)	1.03(-1)	1.42(-1)

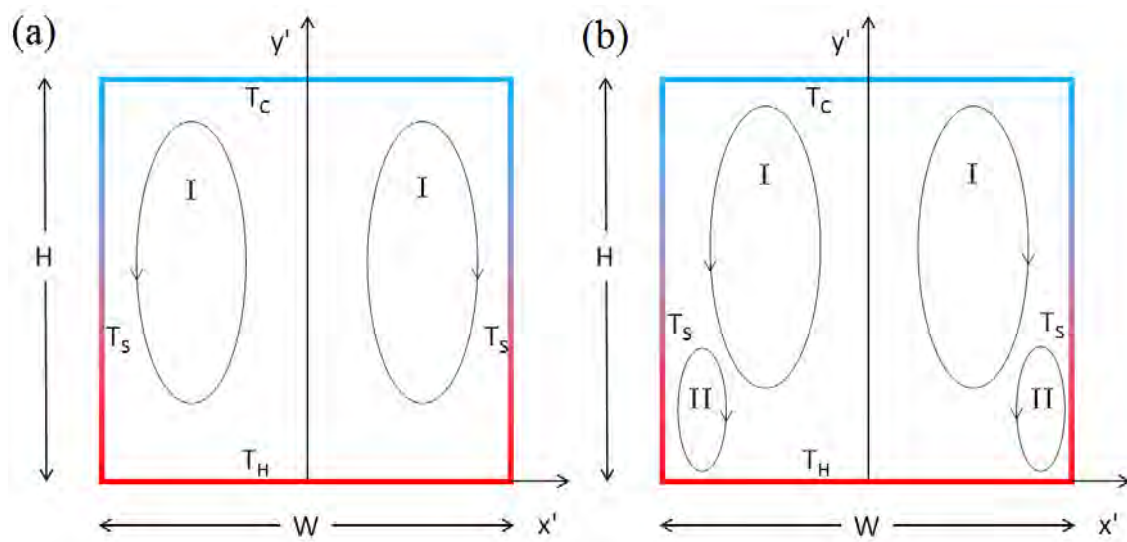


Figure 6.1 View of the non-isothermal wall enclosure and flow pattern with (a) Vortex-type I and (b) with Vortex-types I and II

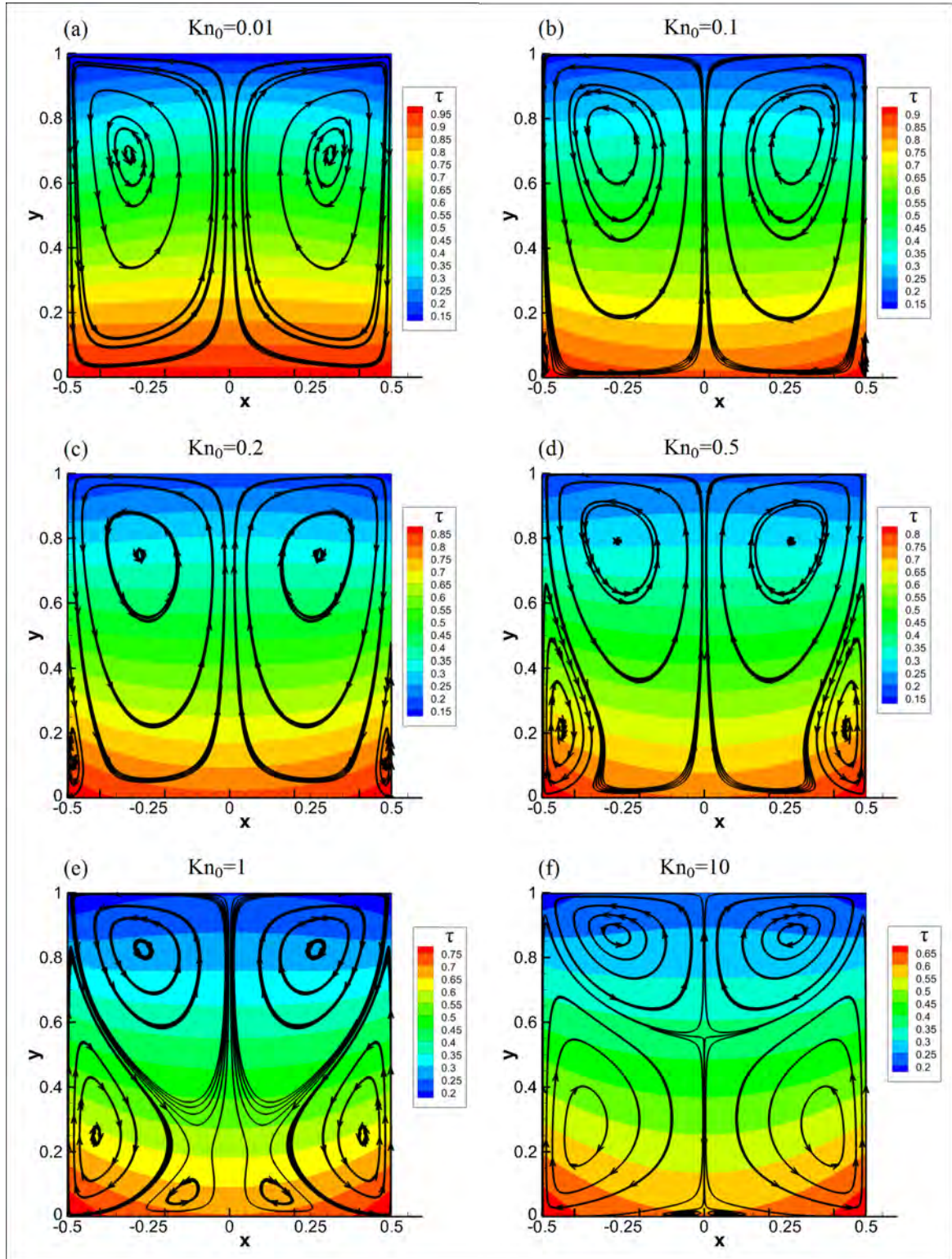


Figure 6.2 Streamlines and temperature contours in a square enclosure for $T_C/T_H = 0.1$ and various Kn_0 .

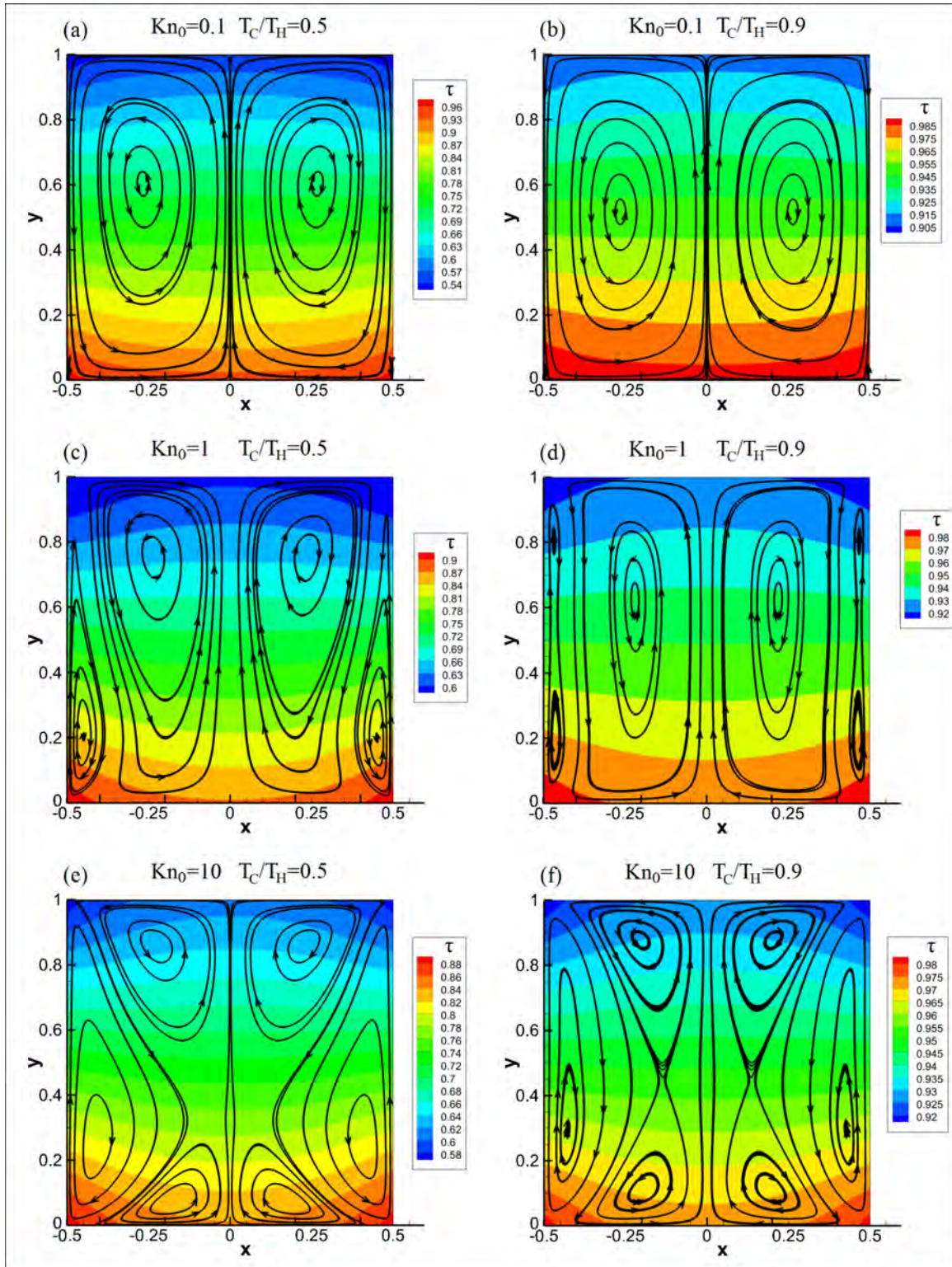


Figure 6.3 Streamlines and temperature contours in a square enclosure for various Kn_0 and T_C/T_H .

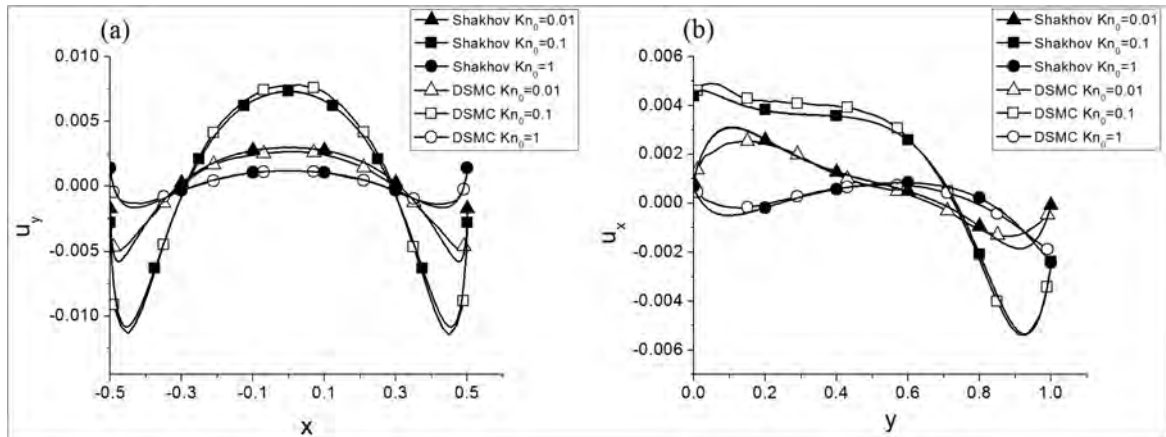


Figure 6.4 Distributions of the (a) y and (b) x components of the velocity on vertical and horizontal planes respectively, passing through the centers of the two Vortex-type I for a square enclosure with $T_C/T_H = 0.1$ and Kn_0 .

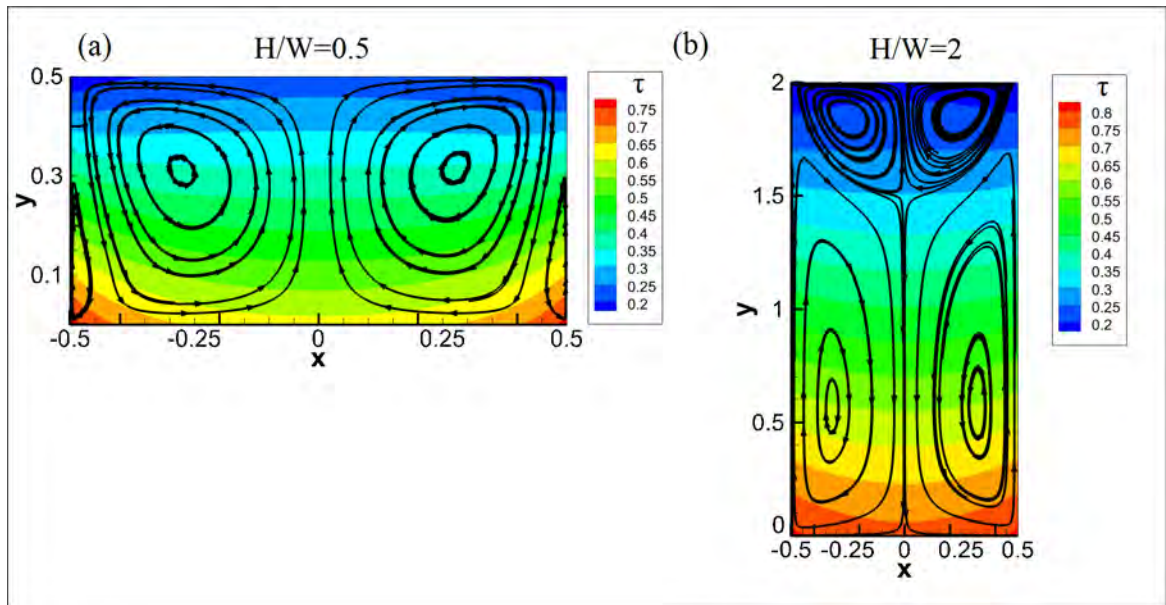


Figure 6.5 Streamlines and temperature contours in rectangular enclosures of (a) $H/W = 0.5$ and (b) $H/W = 2$, for $T_C/T_H = 0.1$ and $Kn_0 = 1$.

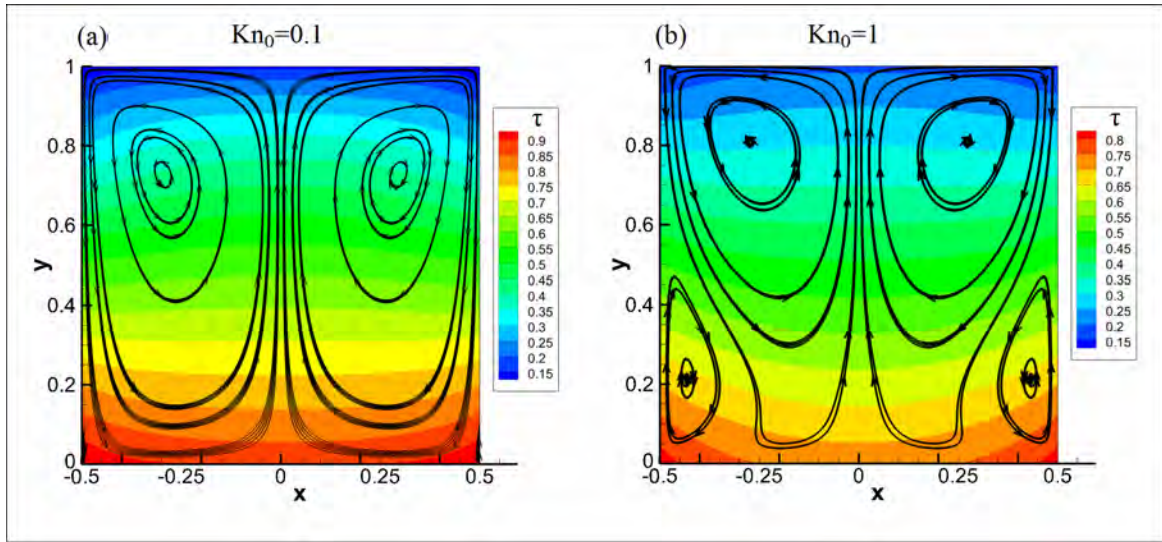


Figure 6.6 Streamlines and temperature contours in a square enclosure with (a) $Kn_0 = 0.1$ and (b) $Kn_0 = 1$ for Maxwell molecules ($\omega = 1$).

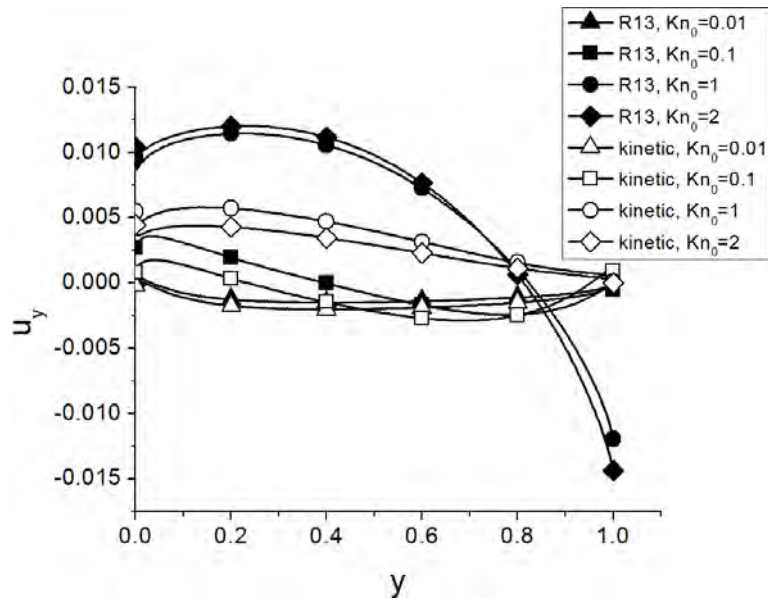


Figure 6.7 Tangential velocity u_y along the lateral walls of a square enclosure for $T_C/T_H = 0.1$ and various Kn_0 computed by the present kinetic approach and by Eq. (6.51) based on the R13 approach.

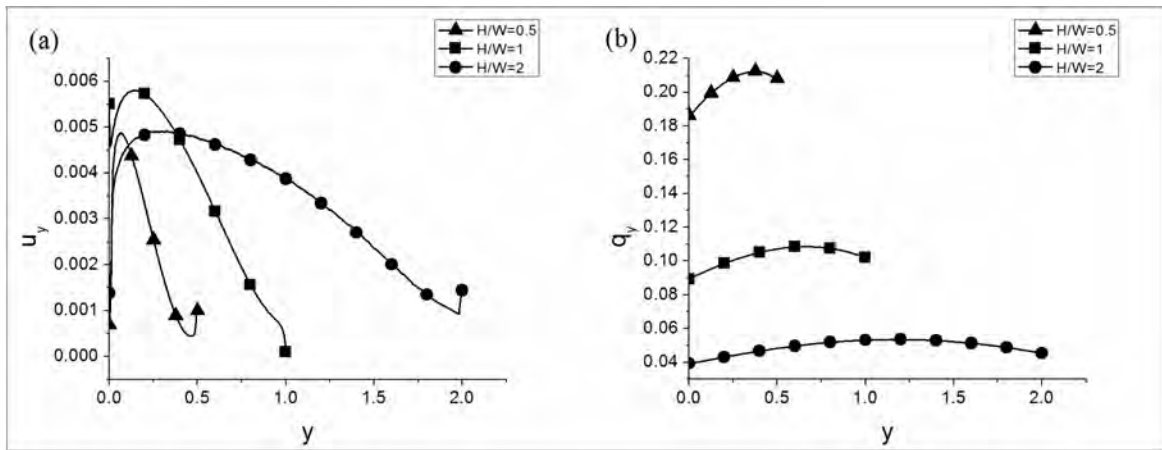


Figure 6.8 Distributions of the tangential (a) velocity u_y and (b) heat flux q_y along the lateral walls of rectangular enclosures with various aspect ratios for $T_C/T_H = 0.1$ and $Kn_0 = 1$.

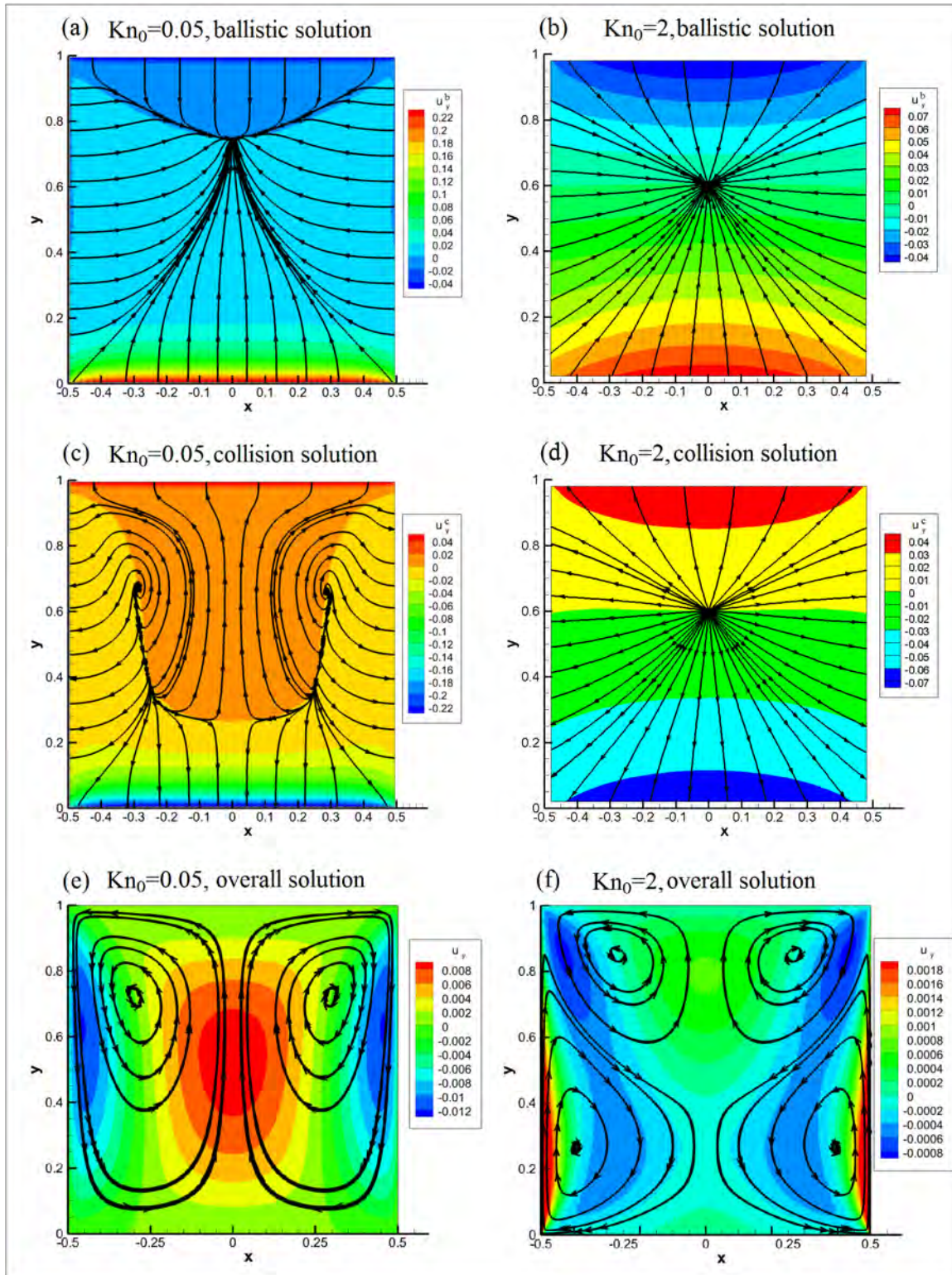


Figure 6.9 Streamlines and vertical velocity contours of the ballistic and collision parts as well as of the overall solution in a square enclosure for $Kn_0 = 0.05, 2$, with $T_C/T_H = 0.1$.

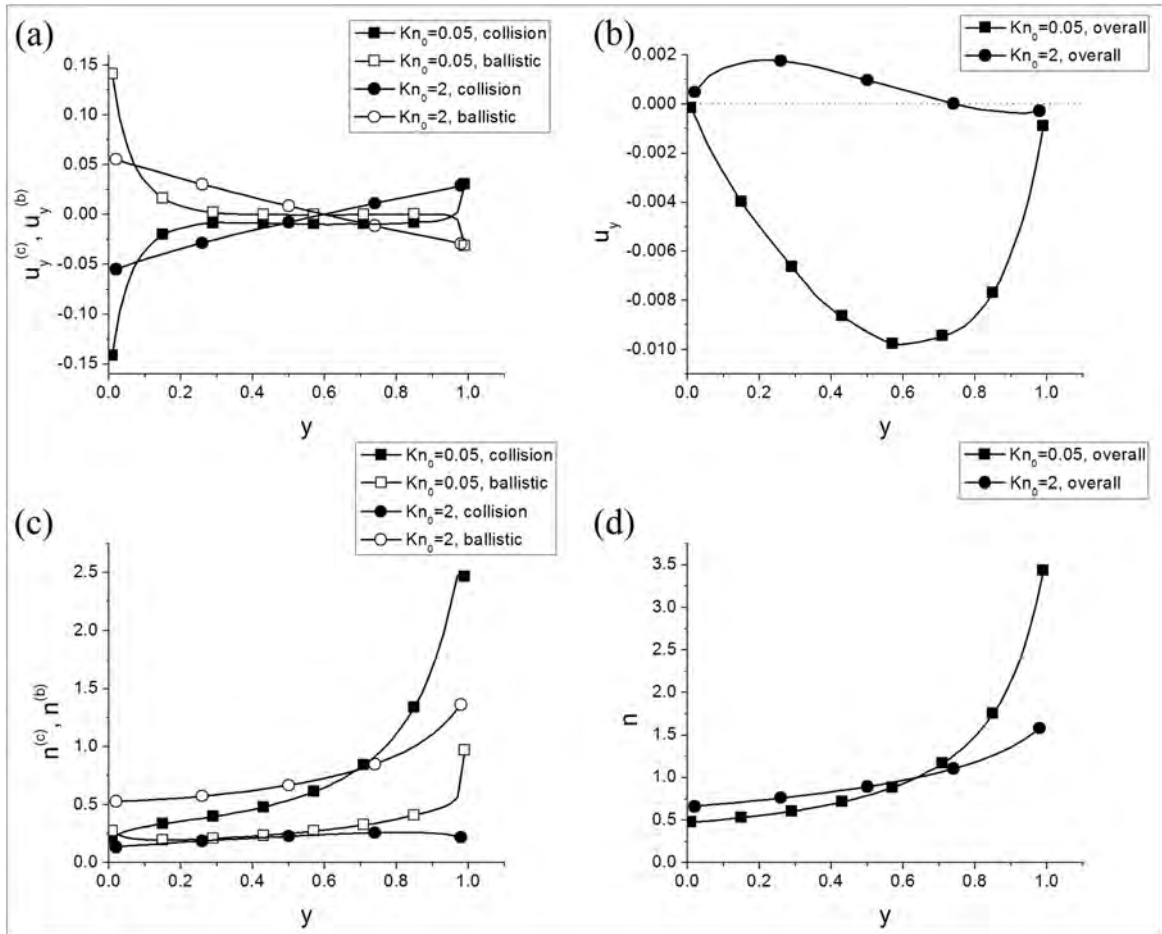


Figure 6.10 Tangential velocity and density of the ballistic and collision parts as well as of the overall solution along the lateral walls of a square enclosure for $Kn_0 = 0.05, 2$ with $T_C/T_H = 0.1$.

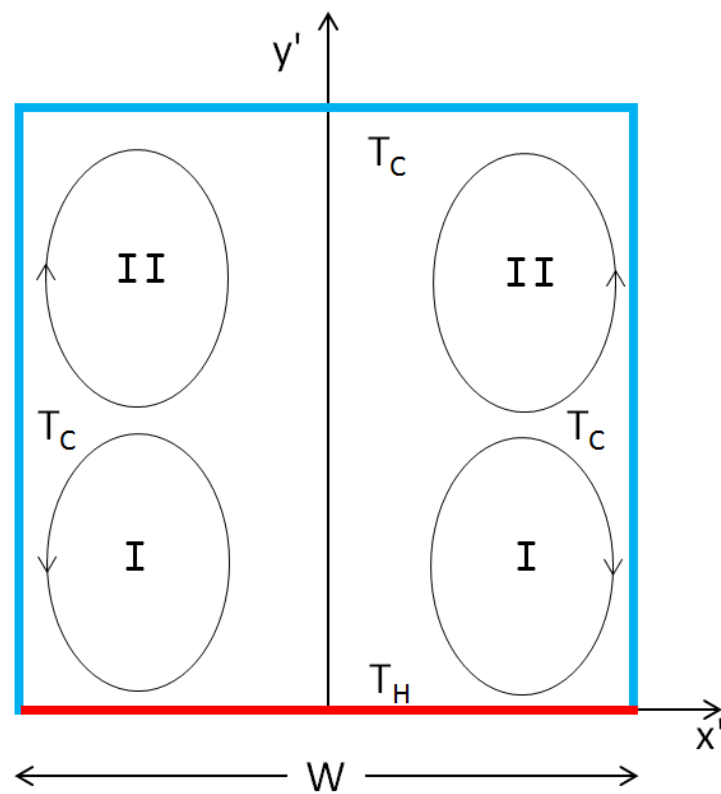


Figure 6.11 View of the square microcavity with the flow pattern of vortices I and II.

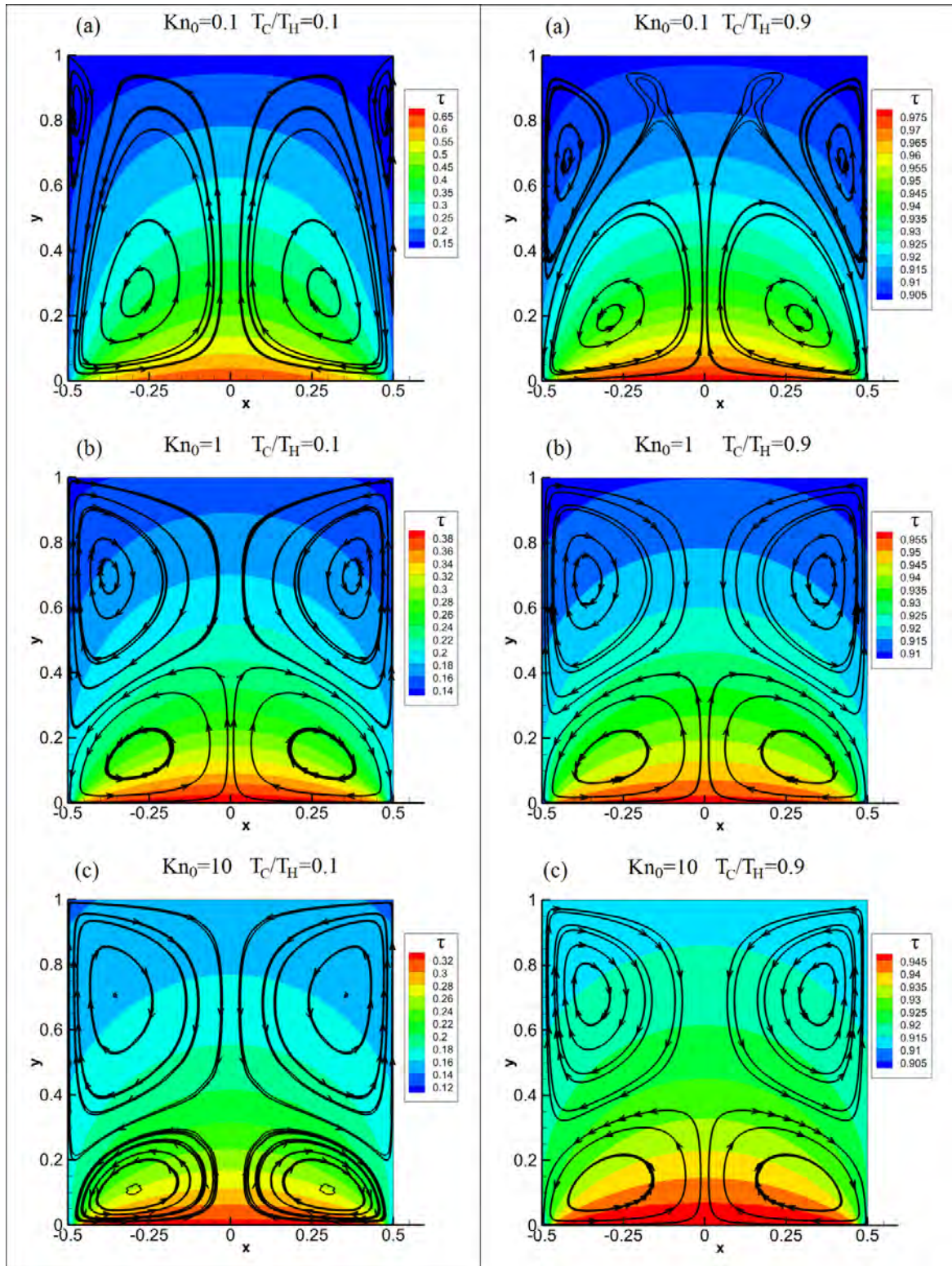


Figure 6.12 Streamlines and temperature contours for $T_C/T_H = 0.1$ (left) and $T_C/T_H = 0.9$ (right) and various Kn_0 .

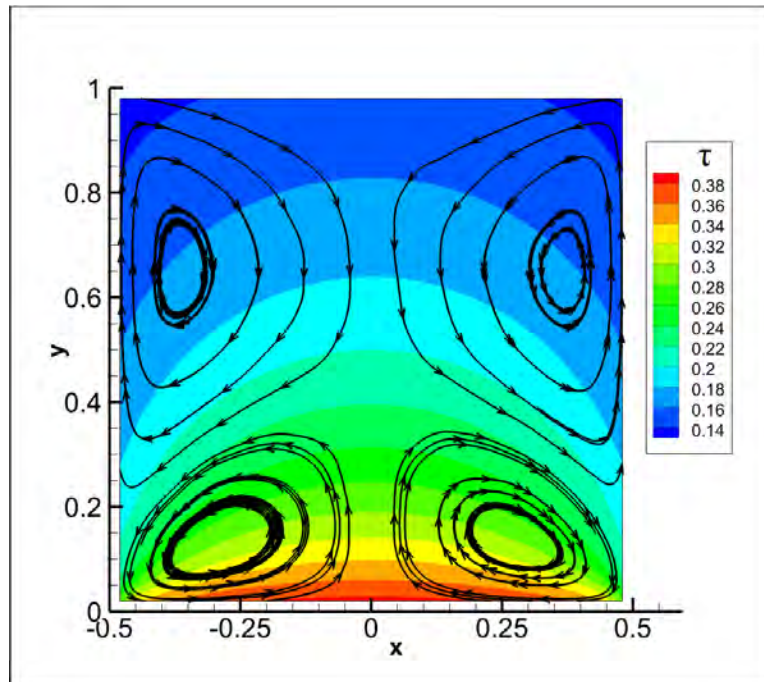


Figure 6.13 Streamlines and temperature contours for $Kn_0 = 1$ and $T_C/T_H = 0.1$ obtained by the DSMC method.

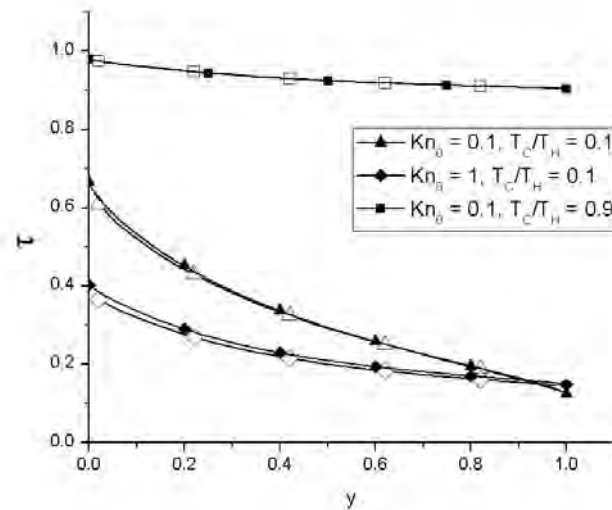


Figure 6.14 Temperature distribution along the axis $x = 0$ for various Kn_0 and T_C/T_H obtained by the DSMC method (open symbols) and the Shakhov kinetic model (filled symbols).

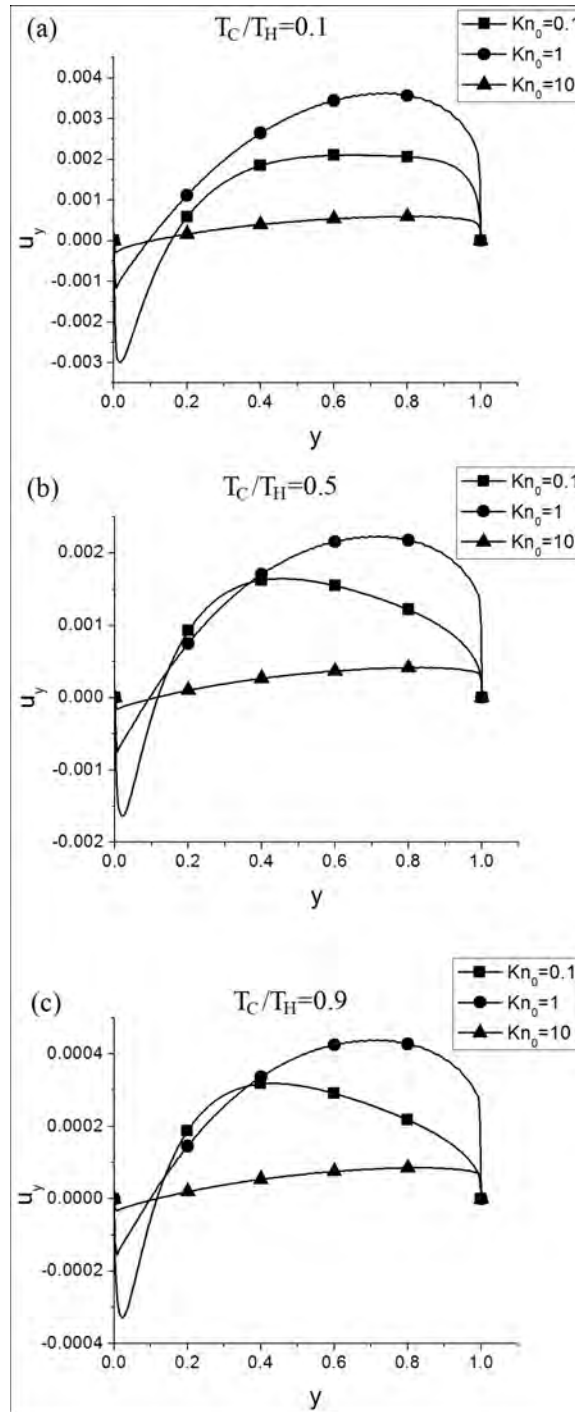


Figure 6.15 Distribution of the tangential velocity $u_y (\pm 1/2, y)$ along the lateral walls of the cavity for various T_C/T_H and Kn_0 .

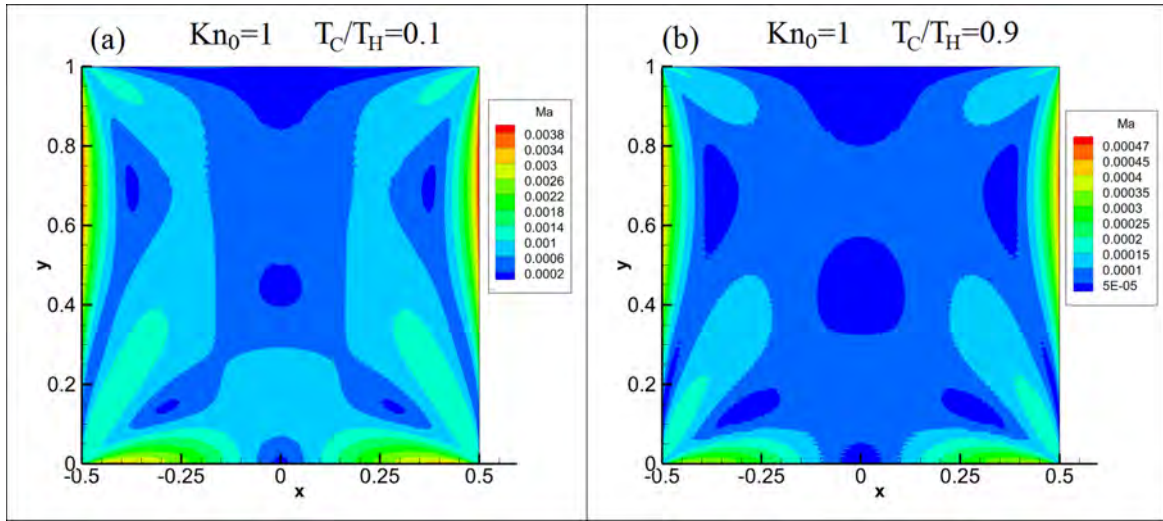


Figure 6.16 Typical contours of the Mach number in the flow field for $Kn_0 = 1$ and $T_C/T_H = 0.1, 0.9$.

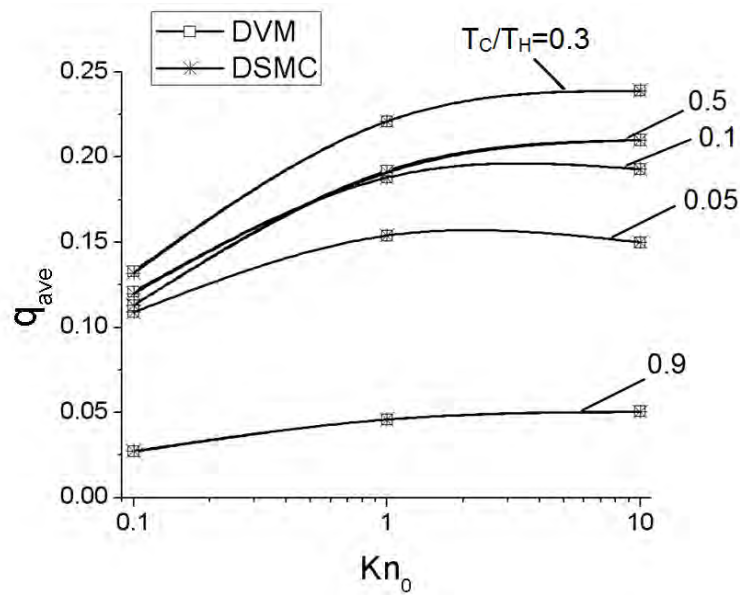


Figure 6.17 Average heat flux q_{ave} departing from the hot plate of the cavity in terms of Kn_0 for various T_C/T_H .

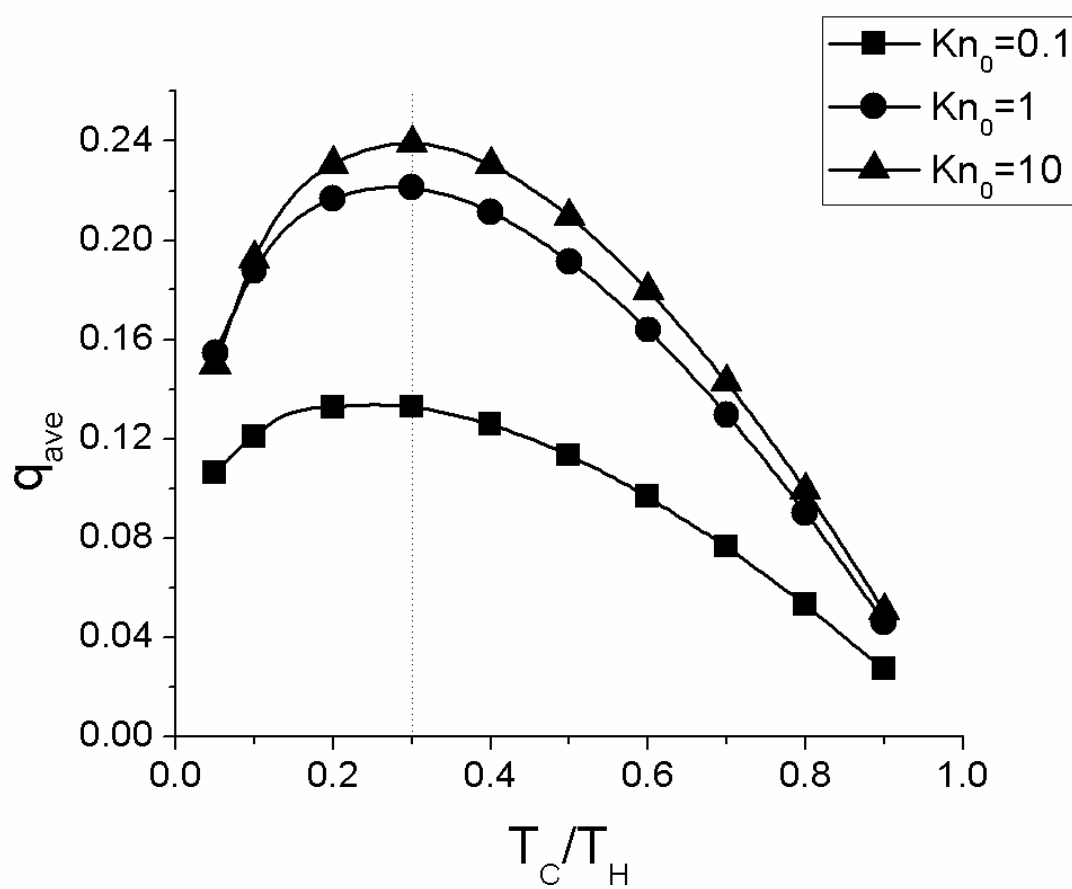


Figure 6.18 Average heat flux q_{ave} departing from the hot plate of the cavity in terms of T_C/T_H for various Kn_0 .

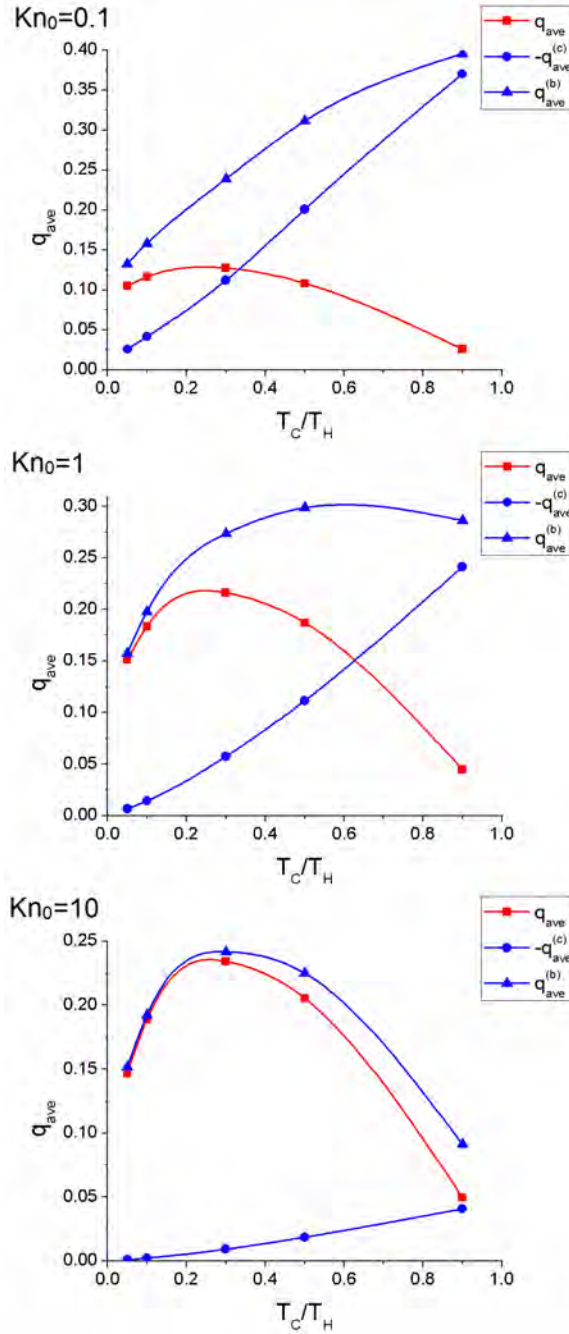


Figure 6.19 Average heat flux q_{ave} along with its ballistic and collision parts $q_{ave}^{(b)}$ and $q_{ave}^{(c)}$, respectively, departing from the hot plate of the cavity in terms of T_C/T_H for $Kn_0 = 0.1, 1, 10$.

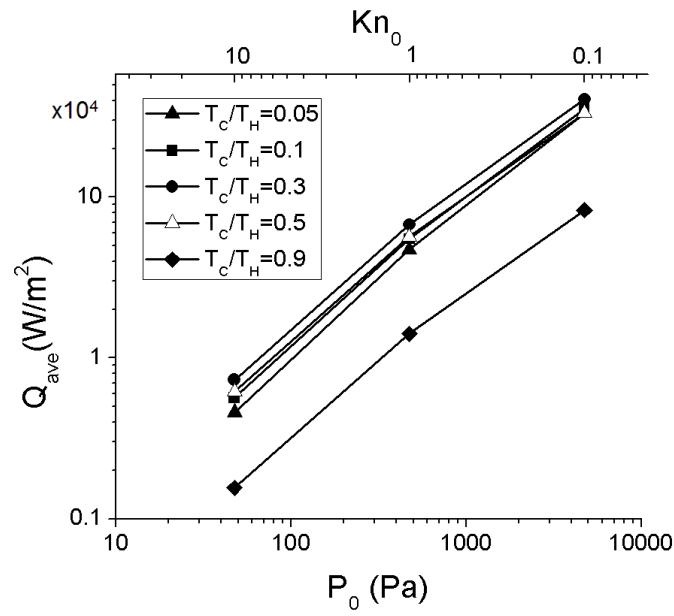


Figure 6.20 Average heat flux Q_{ave} (W/m^2) departing from the hot plate of the cavity in terms of the reference pressure P_0 for various T_C/T_H .

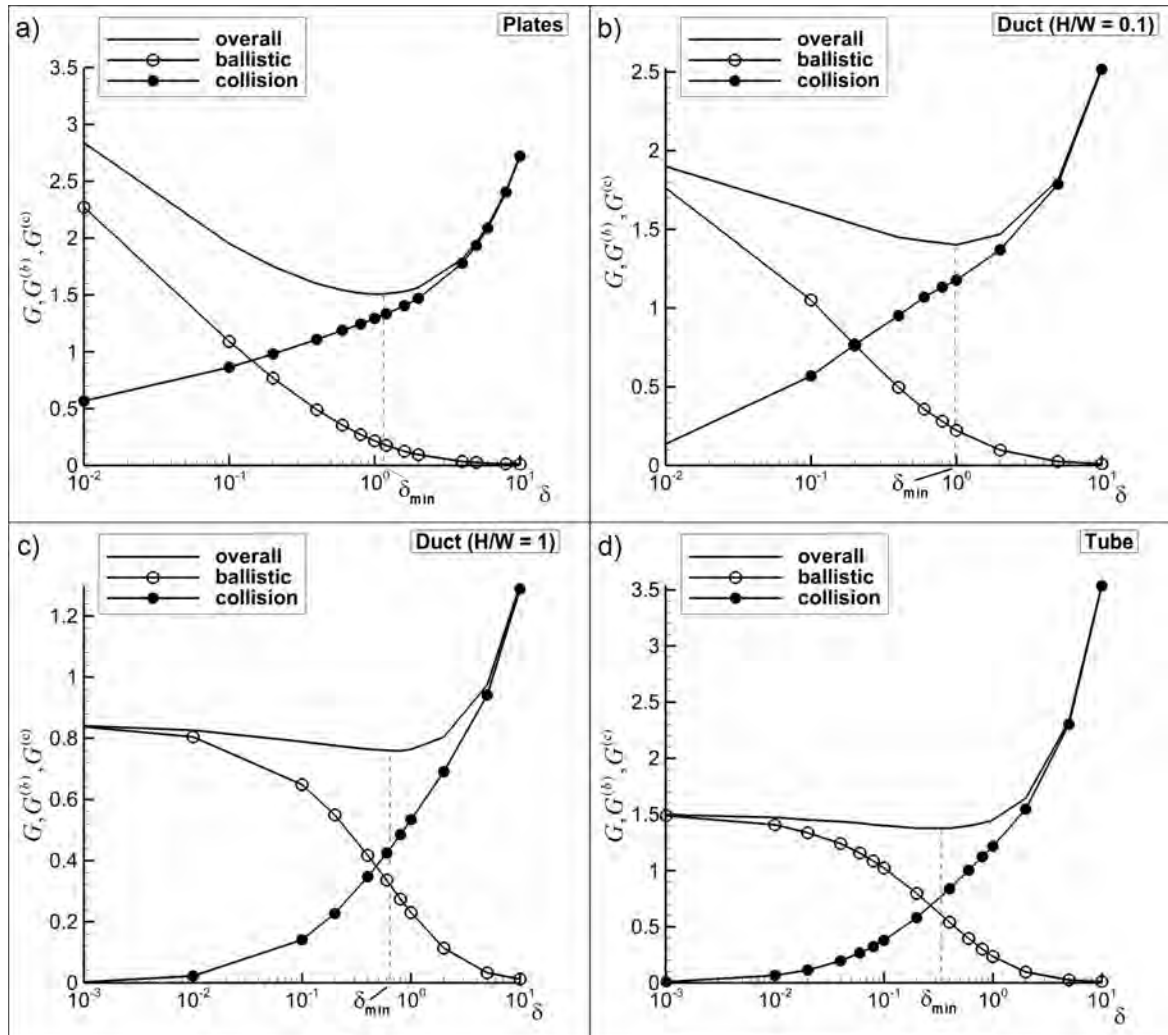


Figure 6.21 Ballistic, collision, and overall reduced flow rates in terms of δ for (a) channel flow, (b) duct flow ($H/W = 0.1$), (c) duct flow ($H/W = 1$), and (d) tube flow.

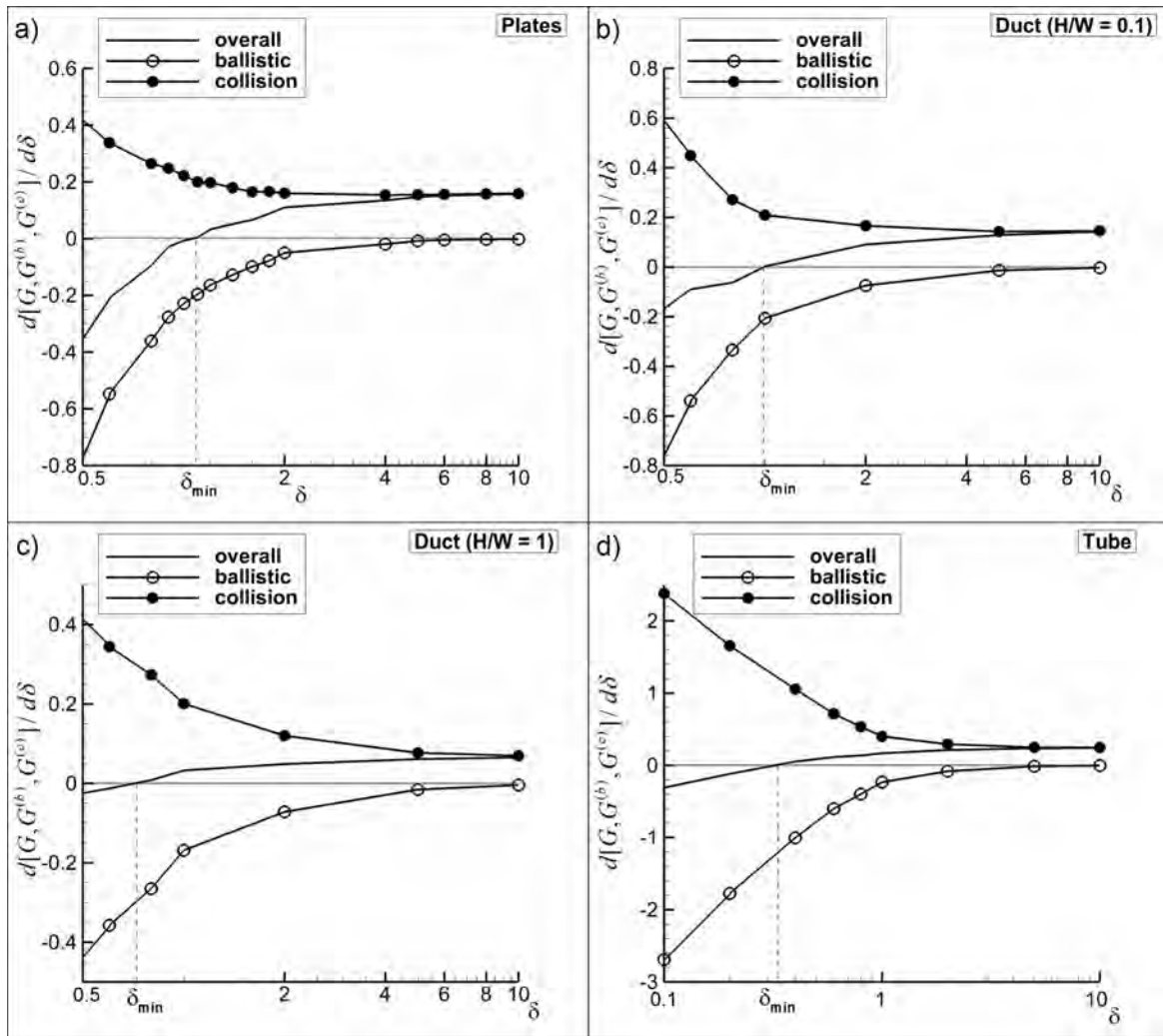


Figure 6.22 Derivatives with respect to δ of the ballistic, collision, and overall reduced flow rates in terms of δ for (a) channel flow, (b) duct flow ($H/W = 0.1$), (c) duct flow ($H/W = 1$), and (d) tube flow.

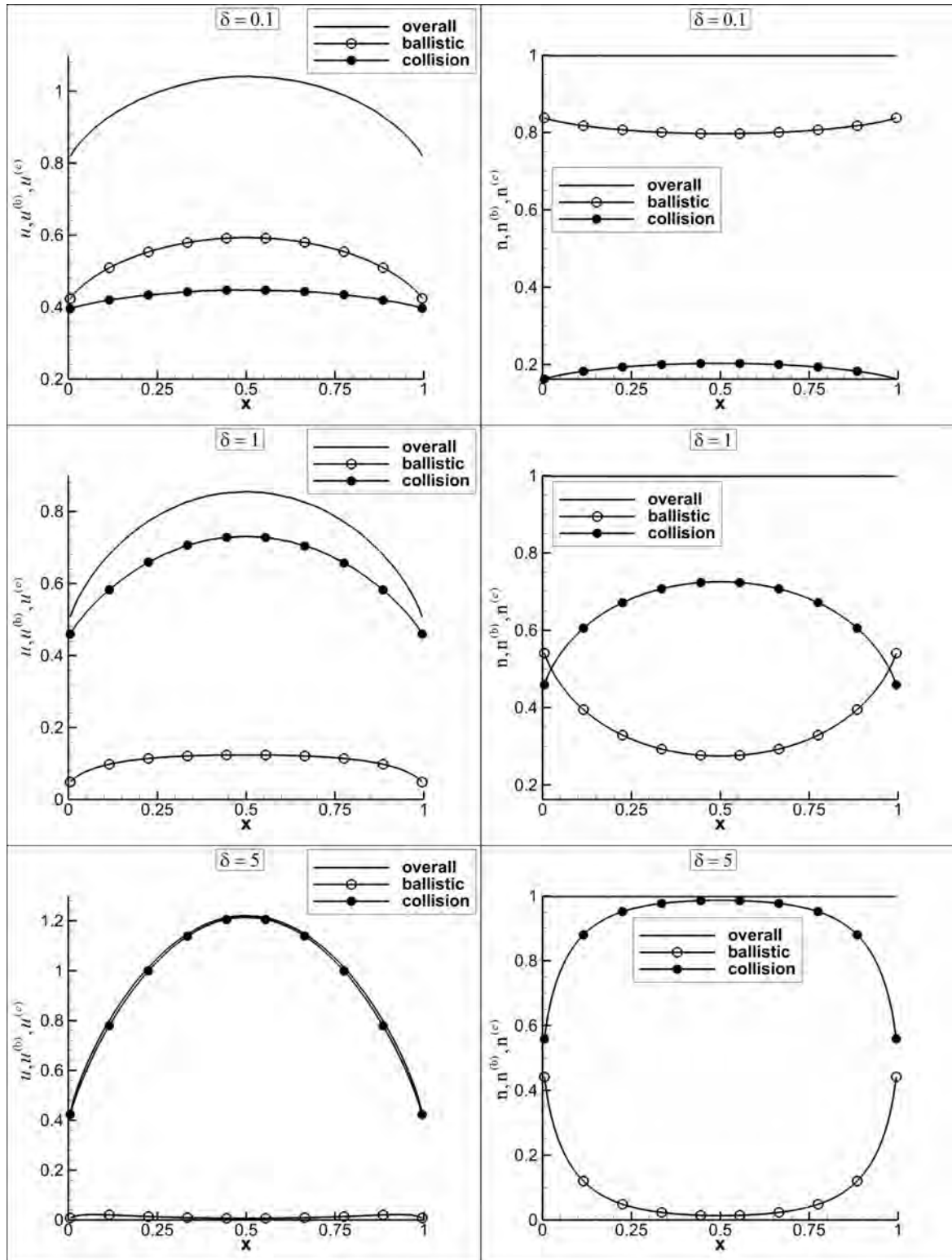


Figure 6.23 Velocity (left) and number density (right) distributions for channel flow and various values of δ .

Chapter 7

Uncertainty propagation in rarefied gas flows and heat transfer

7.1 Introduction

Uncertainties are always present both in experimental and computational work. They may be introduced through the input data or generated during the development of the task. Commonly, they propagate along the implemented process reaching finally the output. In experimental work, they are introduced due to various sources, such as the uncertainty of the measurement instruments, the changing environmental conditions, the definition of the measured quantities which may involve approximations, the flaws in the experimental setup and measurements, resulting to significant variations in repeated measurements. Monitoring and reporting the uncertainty of the output measured quantities is very valuable in order to judge their expected validity and accuracy. In addition, the information of the expected uncertainty of the output quantities in terms of the uncertainties of the involved input parameters can be crucial for the proper design of the experimental setup [115]–[117]. Estimating the overall uncertainty will clarify if the output results are acceptable and it will indicate the preferable conditions for the measurements. In computational work, uncertainties are introduced due to the assumptions and simplifications in the physical and mathematical modeling, the discretization of the problem, the boundary conditions, the floating point operations and others. Concerning modeling and simulations in rarefied gas dynamics, uncertainties are introduced due to all above causes, as well as due to a simplified geometrical representation to measurement uncertainties defining the geometry and to gas surface interaction modeling. In general, the effect of the uncertainties of the input

quantities or of the uncertainties generated during the task implementation, on the uncertainty of the output quantity is called uncertainty propagation.

Uncertainties and uncertainty propagation is important in several engineering and technological fields. In metrology, the very accurate estimation of uncertainty in measurements and in the associated computations supporting the experimental results is of major importance in order to classify measurement devices and processes [13], [125]. The calculation of the uncertainty of the involved quantities has been also reported in computational fluid dynamics studies [123], [126], [127] and in some cases in rarefied gas dynamics simulations [128]–[130].

In the literature several methods have been reported for uncertainty propagation [118], [119]. Interval analysis [120] accounts for the overall uncertainty by calculating the output of the simulation for the values bounding the domain of the input quantities. It is a relatively simple method, with small computational requirements and no sophisticated algorithms. It has however, several drawbacks as it can only provide a range for the output quantities, without any more statistical information. Sensitivity derivatives [121] can also be used and since they are of some interest in the present work, they will be briefly discussed in Section 7.2. In this method the model through which the uncertainty propagates should be analytical and differentiable. A computationally efficient method frequently utilized is the Moment methods [122], which is based on expanding all input quantities with uncertainty around the mean value using Taylor series. This methodology is subject to certain approximations and it is limited to small values of input uncertainties. It is not applicable when significant nonlinearities exist. The Polynomial Chaos decomposition [123] is a spectral method, where each quantity with uncertainty is decomposed into a product of deterministic and stochastic basis functions. Finally, a very accurate method, that can be utilized almost universally and can propagate the uncertainty through complicated models is the Monte Carlo Method (MCM) [118], [124]. It is a stochastic methodology and the basic scheme involves a large number of trials. In each trial the values of the input parameters are sampled from their respective distributions and the distribution function of the model output is constructed. This methodology has a board range of application with no assumptions on the model and is able to simulate cases where the model involves the solution of differential equations. It is a general, robust and accurate approach, requiring however high computational cost.

In this chapter, the MCM is implemented to develop and implement a methodology to investigate the uncertainty propagation in the numerical solution of some benchmark

problems of rarefied gas dynamics. In Sections 7.2 and 7.3, the description of the sensitivity derivatives method and the MCM, are presented. In Section 7.4, pressure and temperature driven flows through tubes are considered, where the uncertainty of the mass flow rate in pressure and temperature driven flows, as well as the uncertainty of the pressure difference in the thermomolecular pressure difference flow are calculated. In Section 7.5, the corresponding work is performed for the uncertainty of the heat flux in the heat transfer flow between parallel plates. The concluding remarks are stated in Section 7.6. In all cases, the uncertainty of the main quantity of interest is calculated in terms of the uncertainties of the main parameters characterizing the configuration. The notation and methodologies used in this chapter are according to the GUM [230], which is a standard adopted by the majority of measurement institutes, according to the ISO/IEC 17025.

7.2 General notation and the sensitivity derivatives method

In the current framework, the nominal value of some input quantity x_i is denoted by the subscript n as $x_{i,n}$, while the uncertainty associated with this parameter is denoted as $u(x_i)$. Thus, any quantity can be presented as $x_i = x_{i,n} \pm u(x_i)$. The distribution of some input quantity x_i is denoted as g_{x_i} , while the output quantity $y = f(x_1, x_2, \dots, x_N)$ is given as a function of the input quantities x_i and follows a distribution g_y . The aim is to estimate how the uncertainties of the input quantities x_i propagate through the model $f(x_1, x_2, \dots, x_N)$ to the output quantity y .

When the model is linear or the non-linearity of the model is not significant the uncertainty of the output $u_{x_i}(y)$ due to the uncertainty of some input quantity x_i can be calculated using the sensitivity derivatives [121], [230] by the following expression:

$$u_{x_i}(y) = \frac{\partial f}{\partial x_i} u(x_i) \quad (7.1)$$

The derivative in Eq. (7.1) is often called sensitivity coefficient $c_i = \partial f / \partial x_i$. The combined uncertainty $u_c(y)$ due to the uncertainties of all the input quantities when these input quantities are uncorrelated can be calculated as

$$u_c^2(y) = \sum_{i=1}^N (c_i u(x_i))^2 = \sum_{i=1}^N (u_{x_i}(y))^2. \quad (7.2)$$

When the input quantities are correlated, the covariance $u(x_i, x_j)$ should be taken into account and the combined uncertainty becomes

$$u_c^2(y) = \sum_{i=1}^N (c_i u(x_i))^2 + 2 \sum_{i=1}^{N-1} \sum_{j=i+1}^N c_i c_j u(x_i, x_j). \quad (7.3)$$

The sensitivity derivatives method is limited to small values of the input uncertainty in non-linear models or marginally to models with no significant nonlinearities. In addition, the method depends on the ability of calculating the sensitivity coefficients. When the model requires the solution of differential equations an estimation of the sensitivity coefficients is not always possible and more advanced methodologies must be applied.

7.3 The Monte Carlo Method

One methodology that overcomes the limitations of the sensitivity derivatives and is implemented in a straightforward manner is the Monte Carlo Method (MCM) [231]. The MCM is a stochastic method, according to which a large number of trials (N_t) is carried out. For each trial, the values of the input quantities are sampled from their respective distributions and a value for the output quantity is found. After the required number of trials is carried out, the distribution function of the output quantity is reconstructed and the uncertainty associated with it can be calculated.

In this framework, the uncertainty of the output quantity is usually defined as the 95% or 99% coverage interval. When a sufficient amount of trials ($N_t \geq 10^6$) is carried out, it is possible to use the discrete form of the output quantity distribution function in order to find the uncertainty. In this case, the uncertainty is simply the shortest interval covering the required percentile of the distribution. In other cases however, when the calculation of the output quantity through the model $y = f(x_1, x_2, \dots, x_N)$ requires the solution of differential equations such a large number of trials is prohibitively expensive. Then, the uncertainty can be estimated using the standard deviation of the output quantity distribution function. The output quantity is given as the mean value along with the uncertainty

$$y = \bar{y} \pm u(y), \quad (7.4)$$

where the mean value is

$$\bar{y} = \frac{1}{N_t} \sum_{i=1}^{N_t} y_i, \quad (7.5)$$

with y_i denoting the output of the i -th trial. Also, the associated uncertainty is

$$u(y) = k\sigma_y, \quad (7.6)$$

with the standard deviation given by

$$\sigma_y = \sqrt{\frac{1}{N_t - 1} \sum_{i=1}^{N_t} (y_i - \bar{y})^2}. \quad (7.7)$$

The coefficient k in Eq. (7.6) is the coverage factor and common values are $k = 2$ and $k = 3$ for the 95% and 99% coverage intervals respectively. These values are used when a sufficient number of trials is performed (e.g., $N_t > 10^3$), while for smaller number of trials the coefficient k is taken from the Student distribution with N_t degrees of freedom. It is noted that using Eq. (7.6) along with the aforementioned values of k is a conservative approach that slightly overestimates the output uncertainty compared to finding the uncertainty from the discrete form of the output cumulative distribution function. This is done in order to account for the relatively small number of trials conducted.

The input quantities are usually reported along with their uncertainty as $x_i = x_{i,n} \pm u(x_i)$, but the distribution of the input quantities is not always known. In cases where the form of the distribution is known, the value of x_i for each trial is sampled from this distribution. In the general case, where this distribution is not known, according to the supplement 1 of the GUM, a uniform distribution is assumed $x_i \in [x_{i,n} - u(x_i), x_{i,n} + u(x_i)]$ and the value of each trial is sampled from this distribution as $x_i = x_{i,n} + u(x_i)(1 - 2R_f)$, where R_f is a random number between 0 and 1. In this chapter, all input quantities are assumed to follow a uniform distribution. Also, all uncertainties are reported as relative uncertainties defined as

$$\frac{u(x)}{x} \times 100. \quad (7.8)$$

The above described methodology is applied to the pressure and temperature driven flows through long tubes, as well as to the heat transfer flow between parallel plates. The formulation of the pressure and temperature driven flows is presented in Section 7.4.1 and the associated uncertainties of the kinetic coefficients are analyzed in Section 7.4.2. The results concerning the pressure driven flow are given in Section 7.4.3 and the temperature driven flows in Sections 7.4.4 and 7.4.5. The formulation for the heat

transfer flow is given in Section 7.5.1, followed by the analysis and discussion of the results in Section 7.5.2. The concluding remarks are presented in Section 7.6.

7.4 Pressure and temperature driven flows through long tubes

7.4.1 Formulation

Consider a long tube connecting two vessels kept, in the general case, at different pressures and temperatures. A linear temperature distribution, defined between the temperatures of the two vessels, is applied along the tube wall. The ODE describing the pressure distribution along the tube is [23], [156], [171], [174], [227]

$$\frac{dP(z)}{dz} = -\frac{v_0}{\pi R^3 G_P(\delta, \alpha)} \dot{m} + \frac{P}{T} \frac{G_T(\delta, \alpha)}{G_P(\delta, \alpha)} \frac{dT(z)}{dz}, \quad (7.9)$$

where $P(z)$, $T(z)$ are the pressure and temperature distributions with z being the axial tube direction, R is the tube radius, \dot{m} the mass flow rate and $v_0 = \sqrt{2R_g T}$ is the most probably molecular speed at temperature T with R_g denoting the gas constant. The reduced flow rates G_P for the pressure driven flow and G_T for the temperature driven one are taken from the solution of the linearized Shakhov model equation [23] and are tabulated in Tables 7.1 and 7.2 respectively. The rarefaction parameter is defined as

$$\delta = \frac{PR}{\mu v_0}, \quad (7.10)$$

with μ denoting the viscosity and is given in terms of the inlet rarefaction parameter as

$$\delta(z) = \delta_{in} \frac{P(z)}{P_{in}} \frac{T_{in}}{T(z)}. \quad (7.11)$$

Diffuse-specular Maxwell boundary conditions are applied with the accommodation coefficient $\alpha \in [0, 1]$ denoting the percentage of particles undergoing diffuse reflection. The limiting values of $\alpha = 0$ and $\alpha = 1$, correspond to specular and purely diffuse reflection respectively.

Three different cases are considered, namely Poiseuille flow, thermomolecular pressure difference flow and purely thermal creep flow. For the Poiseuille flow, the tube walls are assumed to be isothermal ($T(z) = T_{in}$) and the pressure gradient drives

the flow. In this flow the second term in the right hand side of Eq. (7.9) vanishes and the inlet and outlet pressures are specified in order to calculate the mass flow rate. The main output of the simulation is the mass flow rate (\dot{m}) and its uncertainty is calculated.

When a temperature gradient is applied on the tube walls and the two ends of the tube are closed ($\dot{m} = 0$), a pressure difference is obtained. This phenomenon is well known as thermomolecular pressure difference. In the thermomolecular pressure difference the inlet pressure, as well as the vanishing mass flow rate, are specified. The main output is the pressure difference ($\Delta P = P(L) - P(0)$) and its uncertainty is calculated.

In the thermal creep flow, the temperature gradient along the tube is imposed, while the inlet and outlet pressure are kept constant ($P_{in} = P_{out}$). In this flow the uncertainty of the mass flow rate is the main quantity of interest and its uncertainty is calculated. The temperature driven flows (thermomolecular pressure difference and thermal creep) are considered as the limiting cases of temperature driven flows and the characteristics of the intermediate cases, where neither the mass flow rate, nor the pressure difference are zero, can be obtained through them [232].

When the inlet and outlet pressures (P_{in}, P_{out}) are given, Eq. (7.9) is solved using a shooting method in order to find the pressure distribution and the mass flow rate. When the mass flow rate \dot{m} and one of the two pressures is provided Eq. (7.9) is integrated in a straightforward manner to obtain the pressure distribution.

In all cases the uncertainties of the main quantity of interest due to uncertainties in pressure $u(P)$, temperature $u(T)$, radius $u(R)$ and accommodation coefficient $u(\alpha)$ are considered. The uncertainty of the rarefaction parameter due to uncertainties in pressure ($u_P(\delta)$), temperature ($u_T(\delta)$) and radius ($u_R(\delta)$) can be obtained using Eq. (7.1) and they are expressed in terms of the corresponding quantity uncertainty by the following expressions

$$\frac{u_R(\delta)}{\delta} = \frac{u(R)}{R}, \frac{u_P(\delta)}{\delta} = \frac{u(P)}{P}, \frac{u_T(\delta)}{\delta} = \frac{u(T)}{T}. \quad (7.12)$$

The uncertainties due to pressure, temperature and radius are introduced to Eq. (7.9) directly, as those quantities appear in the equation. Furthermore, the uncertainties of these quantities are also introduced through the boundary conditions and the kinetic coefficients, while the uncertainty of the accommodation coefficient is introduced only through the kinetic coefficients.

7.4.2 Uncertainty of kinetic coefficients in Poiseuille and thermal creep flows

The uncertainty of the kinetic coefficients due to the uncertainties in the rarefaction parameter δ and accommodation coefficient α are calculated using the MCM. For each simulation $N_t = 10^6$ trials are conducted. More specifically, a database of kinetic coefficients is constructed and then for each trial an interpolation is used to find the kinetic coefficient for the required values.

Figure 7.1 shows the uncertainty of G_P in terms of the rarefaction parameter δ for uncertainties in the rarefaction parameter and accommodation coefficient for purely diffuse reflection. In both cases the values of the input relative uncertainty are $u(x)/x = 0.1, 1, 2$ and 5% . The uncertainty of δ has a small effect on G_P for small values of δ , while it increases after the transition regime. This is easily explained since in the free molecular up to the early transition regimes, G_P has an almost constant value and starts increasing after $\delta \approx 1$. The situation is reversed for uncertainties in the accommodation coefficient. In this case the uncertainty of the accommodation coefficient has a large effect on G_P when the flow is in the free molecular regime and constantly decreases as δ increases taking very small values in the slip and hydrodynamic regimes.

The corresponding results for G_T are given in Figure 7.2, where the behavior for the relative uncertainty of G_T for uncertainties in the rarefaction parameter δ is qualitatively similar as in G_P . The uncertainties are small for small values of δ and are increased as δ is increased. In this case however, the uncertainty decreases for very large δ . This is happening because in this region G_T approaches zero. The situation is different when uncertainties in the accommodation coefficient are considered. Again the uncertainty of the accommodation coefficient is important for small values of δ and its significance is decreased as δ is initially increased. It reaches a minimum around $\delta = 5$ and then, increases again, while decreasing for very large values of δ . The reason for the minimum is the behavior of G_T with respect to α . For $\delta < 5$ increasing α decreases G_T , while for $\delta \geq 5$ G_T increases as α is increased. This change of behavior means that $dG_T/d\alpha = 0$ for some value of $\delta [2, 5]$, leading to this minimum. For very large value of δ , the uncertainty decreases, because G_T approaches zero.

In both kinetic coefficients the output uncertainty is close to or lower than the input uncertainty, concluding that the uncertainties are not magnified. Of course the kinetic coefficients are not the only source of uncertainty, since the input quantities

also appear in Eq. (7.9) meaning that the simulation of each specific case is required in order to perform the uncertainty propagation.

7.4.3 Uncertainty of mass flow rate in Poiseuille flow

The purely pressure driven Poiseuille flow is here considered. Simulations are conducted for various values of the inlet rarefaction parameter δ_{in} ranging from the free molecular up to the continuum regime. The effect of the uncertainties in pressure, temperature, radius and accommodation coefficient on the uncertainty of the mass flow rate is analyzed. Furthermore, the effect of the pressure ratio and of specular wall reflection on the mass flow uncertainties is analyzed. For each case $N_t = 10^3$ trials are conducted.

In this purely pressure driven flow, Eq. (7.9) is rewritten as

$$\frac{dP(z)}{dz} = -\frac{v_0}{\pi R^3 G_P(\delta, \alpha)} \dot{m}. \quad (7.13)$$

Considering Eq. (7.13) and utilizing the sensitivity derivatives approach, the following expression for the uncertainty of the mass flow rate for uncertainties in the length is obtained:

$$\frac{u(\dot{m})}{\dot{m}} = \frac{u(L)}{L} \quad (7.14)$$

In long channels however, the length measurement is associated with relatively very small uncertainties.

Figure 7.3 presents the relative uncertainty of the mass flow rate in terms of δ_{in} for four values of the input relative uncertainty, namely 0.1, 1, 2 and 5%, in pressure, temperature, radius and accommodating coefficient, for a tube with $L/R_n = 20$, pressure ratio $P_{out,n}/P_{in,n} = 0.5$ and accommodation coefficient $\alpha_n = 1$. As expected, in all cases, larger input uncertainties lead to larger output uncertainties. The radius, temperature and pressure uncertainties are important for all values of δ_{in} and have a slight increase at large values of δ_{in} . The accommodation coefficient uncertainty is important for small values of δ_{in} and its effect becomes negligible in the continuum regime. The behavior with respect to the accommodation coefficient, closely resembles the effect that the accommodation coefficient has on G_P , since it is introduced only by the kinetic coefficient. The effect of pressure, temperature and radius is qualitatively similar with the effect of δ on G_P . Quantitatively however, the uncertainties are enlarged, because these quantities, apart from affecting G_P through δ , also appear

in Eq. (7.9). For all values of the input uncertainty, the qualitative behavior of the output uncertainty is the same. In all flow regimes, the radius uncertainty is the most important one. The pressure and temperature uncertainties are of equal importance but less important than the radius. It is interesting to note that the accommodation coefficient uncertainty, when $\alpha_n = 1$, has a smaller effect compared to all other ones in all flow regimes.

In Figure 7.4 the effect of the pressure uncertainty is plotted for different values of the pressure ratio, namely $P_{out,n}/P_{in,n} = 0.3, 0.5, 0.7$ and 0.9 , while keeping the length $L/R_n = 20$ and accommodation coefficient $\alpha_n = 1$. As the pressure ratio increases (pressure difference decreases) the uncertainty of the mass flow rate due to the uncertainty of the pressure is increased. In fact for very small pressure differences the pressure uncertainty becomes the major factor of the output uncertainty. Also, as the pressure ratio increases, the uncertainty due to the pressure uncertainty becomes independent of δ .

In Figure 7.5 results are presented for different values of the accommodation coefficient, namely $\alpha_n = 0.7, 0.8, 0.9$ and 1 , for the same pressure ratio and length as in Figure 7.3. When $\alpha_n < 1$ the output uncertainties are roughly doubled compared to the corresponding ones for $\alpha_n = 1$. This is expected, as for the case of purely diffuse accommodation, where $\alpha = 1 \pm u(\alpha)$, the uncertainty is de facto decreased, since α cannot be larger than one. This is a common feature in all cases examined and for this reason this discussion is omitted in the rest of the result sections.

7.4.4 Uncertainty of pressure difference in thermomolecular pressure difference

The thermomolecular pressure difference phenomenon is considered in this subsection. Simulations are conducted for various values of the inlet rarefaction parameter δ_{in} ranging from the free molecular up to the continuum regime. The pressure difference generated is independent of the tube length and Eq. (7.9) can be written as

$$\frac{dP}{dT} = \frac{P}{T} \frac{G_T(\delta, \alpha)}{G_P(\delta, \alpha)}. \quad (7.15)$$

The effect of the uncertainties in pressure, temperature, radius and accommodation coefficient on the uncertainty of the generated pressure difference (ΔP) is analyzed. Also, the effect that the temperature ratio and of specular wall reflection on the pressure

difference uncertainties is analyzed. For each case $N_t = 10^3$ trials are conducted. In this case the uncertainties of the input quantities are introduced directly in the differential equations and through the two kinetic coefficients. Since both kinetic coefficients are introduced, the behavior of the pressure difference is more complicated.

Figure 7.6 presents the relative uncertainty of the generated pressure difference in terms of δ_{in} for four values of the input relative uncertainty of each parameter, namely 0.1, 1, 2 and 5% for a temperature ratio $T_{h,n}/T_{c,n} = 1.5$ and accommodation coefficient $\alpha_n = 1$. Now, contrary to the previous results, the accommodation coefficient uncertainty is not important for small values of δ_{in} and its effect increases as δ_{in} increases, reaching some maximum and then decreasing again. This behavior is attributed to the fact, that although for small values of δ_{in} the accommodation coefficient has a large effect on G_P and G_T individually, their ratio remains almost constant. The effect for large δ_{in} is expected as in this regime the uncertainty of the kinetic coefficients becomes small. For intermediate cases, the accommodation coefficient has a different effect on the kinetic coefficients, leading to an increased uncertainty in this regime. The uncertainty due to pressure uncertainty initially decreases as δ_{in} increases, reaching a minimum, then, increases again to a maximum and finally, decreases again for very large values of δ_{in} . This complicated behavior is due to the different effect that the pressure has on the rarefaction parameter that is introduced to the kinetic coefficients and to Eq. (7.15). Its magnitude however, does not change considerably for the different values of δ_{in} . The effect of the radius uncertainty increases as δ_{in} increases, reaching some maximum and then decreases as δ_{in} is going towards the hydrodynamic regime where this phenomenon vanishes. Temperature uncertainties are very important for this temperature driven flow and the effect of this uncertainty is important for all values of δ_{in} . For all values of the input uncertainty the qualitative behavior of the output uncertainty is the same. In all flow regimes, the temperature uncertainty is the most important one. For small δ_{in} the pressure uncertainty is second in importance, while for large δ_{in} it is overtaken by the radius uncertainty. It is interesting to note that the accommodation coefficient uncertainty, when $\alpha_n = 1$, has a smaller effect compared to all others in all flow regimes.

In Figure 7.7 the effect of the temperature uncertainty is plotted for different values of the temperature ratio, namely $T_{h,n}/T_{c,n} = 1.2, 1.3, 1.5$ and 2. As the temperature ratio decreases (temperature difference decreases) the uncertainty of the pressure difference due to the temperature uncertainty is increased. The uncertainty of the pressure difference can take values as high as 85%, 48%, 28%, 15% for $T_{h,n}/T_{c,n} = 1.2, 1.3, 1.5$

and 2 respectively for an input uncertainty of the temperature of 5%. Furthermore, as the temperature ratio decreases, the uncertainty due to the temperature uncertainty becomes independent of δ .

In the case of $\alpha_n < 1$, the uncertainty of the pressure difference due to accommodation coefficient uncertainty will be roughly double than that in Figure 7.6, as discussed before for the pressure driven flow.

7.4.5 Uncertainty of mass flow rate in thermal creep flow

The thermally driven flow through a tube connecting two vessels kept at the same pressure is considered and corresponding results are presented. Simulations are conducted for various values of the inlet parameter $\delta_{in} = \delta_{out}$ ranging from the free molecular up to the continuum regime. In this flow the Eq. (7.9) is solved using a shooting method in order to provide the mass flow rate. The same way as in pressure driven flow, using sensitivity derivatives in Eq. (7.9), the uncertainty of the mass flow rate due to length uncertainty can be readily obtained as

$$\frac{u(\dot{m})}{\dot{m}} = \frac{u(L)}{L}. \quad (7.16)$$

The effect of the uncertainties in pressure, temperature, radius and accommodation coefficient on the uncertainty of the mass flow rate is analyzed. The effect that the temperature ratio and specular wall reflection on the uncertainties is analyzed. For each case $N_t = 10^3$ trials are conducted. The uncertainties of the input quantities are introduced directly in the differential equations and through the two kinetic coefficients. As in the thermomolecular pressure difference flow, both kinetic coefficients are introduced and the behavior of the mass flow rate uncertainty may be complicated.

Figure 7.8 shows the relative uncertainty of the mass flow rate in terms of δ_{in} for four values of the input relative uncertainty of each parameter, namely 0.1, 1, 2 and 5% for a tube with $L/R_n = 20$, with a temperature ratio $T_{h,n}/T_{c,n} = 1.5$ and accommodation coefficient $\alpha_n = 1$. The uncertainty of the mass flow rate due to uncertainty of the accommodation coefficient closely resembles the behavior of $u(G_T)/G_T$ for uncertainties in the accommodation coefficient. The accommodation coefficient uncertainty is important only at small values of δ_{in} . As δ_{in} is increased, the uncertainty due to the accommodation coefficient decreases, reaching a minimum and then increases again to a maximum. Finally, it decreases again tending to zero for very large δ_{in} , since the effect of the accommodation coefficient diminishes when the flow is close to the

hydrodynamic regime. The effect of the pressure uncertainty on the mass flow rate is qualitatively similar to its effect on the pressure difference in the thermomolecular pressure difference flow. The effect of the radius uncertainty is important in this case in the whole range of δ_{in} , with the uncertainty of the mass flow rate taking values between 10% and 17% for radius uncertainty 5%. Temperature uncertainties are very important for temperature driven flows and the effect of this uncertainty is important for all values of δ_{in} . For all values of the input uncertainty the qualitative behavior of the output uncertainty is the same. In all flow regimes, the temperature uncertainty is the most important one, followed by the radius uncertainty. The uncertainties due to pressure and accommodation coefficient ($\alpha_n = 1$) are of lesser importance.

In Figure 7.9 the effect of the temperature uncertainty is plotted for different values of the temperature ratio, namely $T_{h,n}/T_{c,n} = 1.2, 1.3, 1.5$ and 2 . As the temperature ratio decreases (temperature difference decreases) the uncertainty of the mass flow rate due to the uncertainty of the temperature is increased. In fact, for a 5% temperature uncertainty the mass flow rate uncertainty takes values close to 85%, 47%, 26% and 14% for $T_{h,n}/T_{c,n} = 1.2, 1.3, 1.5$ and 2 , respectively.

7.5 Nonlinear heat transfer between parallel plates

7.5.1 Formulation

The heat transfer flow between parallel plates is considered. The effect of the input uncertainty of pressure, temperature and thermal accommodation coefficient on the output uncertainty of the heat flux is considered. A monatomic gas is confined between two parallel plates that are at a distance H and kept at different temperatures T_H and T_C for the bottom and top plates respectively with $T_H > T_C$.

Kinetic modeling is based on the nonlinear Shakhov kinetic model equation. The following dimensionless parameters are introduced

$$y = y'/H, \zeta_y = \xi_y/v_0, g = f v_0^3/N_0, \rho = N/N_0, \tau = T/T_0, q = Q/(P_0 v_0) \quad (7.17)$$

where y is the physical space coordinate normal to the plates, ζ_y the molecular velocity in the y direction, g denotes the distribution function, while ρ , τ and q are the dimensionless density, temperature and heat flux respectively. The reference value of the temperature is $T_0 = T_H$, while the reference number density N_0 is taken from the

equation of state $P_0 = N_0 k_B T_0$ with k_B denoting the Boltzmann constant and the most probable molecular speed is defined as $v_0 = \sqrt{2R_g T_0}$ with R_g being the gas constant.

The following reduced distribution functions are introduced:

$$\varphi = \int_{-\infty}^{+\infty} \int_{-\infty}^{+\infty} g e^{-\zeta_x^2 - \zeta_z^2} d\zeta_x d\zeta_z \quad (7.18)$$

$$\psi = \int_{-\infty}^{+\infty} \int_{-\infty}^{+\infty} (\zeta_x^2 + \zeta_z^2) g d\zeta_x d\zeta_z \quad (7.19)$$

The projection procedure is applied and the governing set of coupled integro-differential equations is derived as

$$\zeta_y \frac{\partial \varphi}{\partial y} = \delta \rho \tau^{1-\omega} (\varphi^S - \varphi), \quad (7.20)$$

$$\zeta_y \frac{\partial \psi}{\partial y} = \delta \rho \tau^{1-\omega} (\psi^S - \psi), \quad (7.21)$$

where

$$\varphi^S = \varphi^M \left[1 + \frac{4}{15 \rho \tau^2} q \zeta \left(\frac{\zeta_y^2}{\tau} - \frac{3}{2} \right) \right], \quad (7.22)$$

$$\psi^S = \psi^M \left[1 + \frac{4}{15 \rho \tau^2} q \zeta \left(\frac{\zeta_y^2}{\tau} - \frac{1}{2} \right) \right], \quad (7.23)$$

with

$$\varphi^M = \frac{\rho}{\sqrt{\pi \tau}} \exp \left[-\zeta_y^2 / \tau \right], \quad (7.24)$$

$$\psi^M = \frac{\rho}{\sqrt{\pi / \tau}} \exp \left[-\zeta_y^2 / \tau \right]. \quad (7.25)$$

In the above expressions, φ , ψ are the reduced distribution functions, φ^M , ψ^M are the corresponding Maxwellian distributions while φ^S , ψ^S are the Shakhov equilibrium distributions. The rarefaction parameter is defined as

$$\delta = \frac{P_0 H}{\mu_0 v_0}, \quad (7.26)$$

where μ_0 is the viscosity at reference temperature. It is noted that in Eq. (7.20) and (7.21) the expression $\mu = \mu_0(T/T_0)^\omega$ is used for the viscosity, where $\omega \in [0.5, 1]$ with the limiting values corresponding to hard sphere and Maxwell molecules respectively. In the present section hard sphere gas has been assumed.

The boundary conditions for the bottom wall are

$$\varphi^+ = \frac{\rho_{w,b}}{\sqrt{\pi\tau_{\alpha,b}}} \exp \left[-\zeta_y^2/\tau_{\alpha,b} \right], \zeta_y > 0, \quad y = -1/2, \quad (7.27)$$

$$\psi^+ = \frac{\rho_{w,b}}{\sqrt{\pi/\tau_{\alpha,b}}} \exp \left[-\zeta_y^2/\tau_{\alpha,b} \right], \zeta_y > 0, \quad y = -1/2, \quad (7.28)$$

while for the top

$$\varphi^+ = \frac{\rho_{w,t}}{\sqrt{\pi\tau_{\alpha,t}}} \exp \left[-\zeta_y^2/\tau_{\alpha,t} \right], \zeta_y < 0, \quad y = 1/2, \quad (7.29)$$

$$\psi^+ = \frac{\rho_{w,t}}{\sqrt{\pi/\tau_{\alpha,t}}} \exp \left[-\zeta_y^2/\tau_{\alpha,t} \right], \zeta_y < 0, \quad y = 1/2. \quad (7.30)$$

In the boundary conditions the wall densities $\rho_{w,b}$ and $\rho_{w,t}$ for the bottom and top walls respectively, as well as the corresponding temperatures $\tau_{\alpha,b}$ and $\tau_{\alpha,t}$ are specified. Temperature (τ_α) is an equivalent temperature, taking into account the thermal accommodation of the wall. The boundary condition parameters for each wall are coupled and calculated using the impermeability condition along with the definition of the thermal accommodation coefficient, which is defined as [233]

$$\alpha = \frac{E'^- - E'^+}{E'^- - E'_W{}^+}. \quad (7.31)$$

In the definition of the thermal accommodation coefficient, E'^- is the incident energy flux to the wall, E'^+ is the reflected one and $E'_W{}^+$ is the reflected energy flux if the gas is fully accommodated. Combining the impermeability condition with Eq. (7.31) the following expressions for the boundary condition parameters are derived:

$$\rho_{w,b} = 2\sqrt{\frac{\pi}{\tau_{\alpha,b}}} J_b^- \quad (7.32)$$

$$\rho_{w,t} = 2\sqrt{\frac{\pi}{\tau_{\alpha,t}}} J_t^- \quad (7.33)$$

$$\tau_{\alpha,b} = \tau_b \alpha + (1 - \alpha) \frac{E_b^-}{2J_b^-} \quad (7.34)$$

$$\tau_{\alpha,t} = \tau_t \alpha + (1 - \alpha) \frac{E_t^-}{2J_t^-} \quad (7.35)$$

Here, $\tau_b = 1$ and $\tau_t = T_C/T_H$. The dimensionless energy fluxes ($E = E'/(P_0 v_0)$) and particle fluxes are [233]:

$$J_b^- = - \int_{-\infty}^0 \varphi^- \zeta_y d\zeta_y \quad (7.36)$$

$$J_t^- = \int_0^{+\infty} \varphi^- \zeta_y d\zeta_y \quad (7.37)$$

$$E_b^- = - \int_{-\infty}^0 (\varphi^- \zeta_y^2 + \psi^-) \zeta_y d\zeta_y \quad (7.38)$$

$$E_t^- = \int_0^{+\infty} (\varphi^- \zeta_y^2 + \psi^-) \zeta_y d\zeta_y \quad (7.39)$$

The macroscopic quantities are given as moments of the reduced distribution functions:
Number density

$$\rho = \int_{-\infty}^{+\infty} \varphi d\zeta_y \quad (7.40)$$

Temperature

$$\tau = \frac{2}{3\rho} \int_{-\infty}^{+\infty} (\varphi \zeta_y^2 + \psi) d\zeta_y \quad (7.41)$$

Heat flux

$$q = \int_{-\infty}^{+\infty} (\varphi \zeta_y^2 + \psi) \zeta_y d\zeta_y \quad (7.42)$$

Upon specifying the accommodation coefficient α , the rarefaction parameter δ and the temperature ratio $\tau_t = T_C/T_H$, equations (7.20) and (7.21) are solved, under boundary conditions (7.27)-(7.30), along with the expressions (7.32)-(7.39) for the boundary conditions parameters and (7.40)-(7.42) for the macroscopic quantities, using the DVM scheme. The heat computed heat flux values are tabulated and used for the uncertainty propagation.

In the heat transfer flow is not computationally efficient to solve the kinetic equations for each MCM trial. Instead, a dense database of the heat flux values in terms of the involved parameters is created and then for each trial an interpolation is performed providing the heat flux values at the random values of the input quantities. A part of this database is shown in Tables 7.3 and 7.4. The methodology described in Section 7.2 is used to find the uncertainty, performing $N_t = 10^6$ trials in each case.

7.5.2 Uncertainty of heat flux in heat transfer between parallel plates

The relative uncertainty of the heat flux is presented for a wide range of the rarefaction parameter covering the free molecular up to the slip regimes. The effect of uncertainties of the wall temperatures, gas rarefaction parameter and thermal accommodation coefficient on the uncertainty of the heat flux is investigated. It is noted that in this setup, the uncertainties of the temperature also lead to uncertainties in the rarefaction parameter. Since the uncertainty of the rarefaction parameter is used, uncertainties in pressure or distance between the plates can be translated into rarefaction parameter uncertainties using Eqs. (7.12) and (7.2).

Figure 7.10 presents the relative uncertainty of the heat flux in terms of the rarefaction parameter for different values of the uncertainty of the input quantities for a temperature ratio $T_{C,n}/T_{H,n} = 0.5$ and thermal accommodation coefficient $\alpha_n = 1$. For all four values of the input uncertainty investigated, namely 0.1, 1, 2 and 5%, the qualitative behavior is the same. The temperature uncertainty is the leading source of uncertainty in the whole range of the gas rarefaction examined. The thermal accommodation coefficient is equally important for small values of δ , while its significance decreases as δ is increased. The uncertainty associated with the rarefaction parameter is negligible for small values of δ , increases reaching a maximum around $\delta = 10$ and then decreases again.

Figure 7.11 shows the relative uncertainty of the heat flux in terms of the input uncertainty of the temperature for temperature ratio $T_{C,n}/T_{H,n} = 0.3, 0.5, 0.7$ and 0.9 . As the temperature ratio increases and the temperature difference decreases, the uncertainties associated with the temperature are increased. In fact for a relative uncertainty of the temperature ratio of 5%, the heat flux uncertainty which is of the order of 2% for $T_{C,n}/T_{H,n} = 0.3$ is increased up to 70% for $T_{C,n}/T_{H,n} = 0.9$. Also,

for large temperature ratios, the uncertainty becomes independent of the rarefaction parameter.

7.6 Concluding remarks

The uncertainty propagation in prototype flow and heat transfer configurations of rarefied gas dynamics is investigated. More specifically, the pressure and temperature driven flows through long tubes and the heat transfer between parallel plates are considered. In the Poiseuille and thermal creep flows, the effect of the uncertainties in the pressure, temperature, length, radius and accommodation coefficient on the mass flow rate is computed. In the thermomolecular pressure difference flow, the corresponding effect on the generated pressure difference is also found. Furthermore, in the heat transfer flow, the effect of the uncertainties in the rarefaction parameter, temperature ratio and thermal accommodation coefficient on the produced heat flux is computed. The uncertainty propagation is performed using the Monte Carlo Method that is applicable and accurate in all these setups.

In the Poiseuille flow, the radius uncertainty is the most important one, in most cases, while the temperature and pressure uncertainties are of lesser importance, in the whole gas rarefaction regime. The accommodation coefficient uncertainty is important for highly rarefied flows, while its effect diminishes as the flow moves to the continuum regime. Considering a 5% uncertainty in all input parameters, the typical values of the relative uncertainty of the output mass flow rate are 20% for the radius, 10% for temperature and pressure and 5% for the accommodation coefficient. The pressure uncertainty becomes the predominant factor of uncertainty for small pressure differences and the uncertainty of the mass flow rate may reach up to 40% for 5% uncertainty in pressure and pressure ratio of 0.9.

In the thermomolecular pressure difference flow, the temperature uncertainty is the most important, in most cases, while the radius and pressure uncertainties are of lesser importance, in the whole gas rarefaction regime. The accommodation coefficient uncertainty is the least important for all flow regimes when $\alpha_n = 1$ and it is interesting that its effect is negligible in the free molecular regime, increases in the transition regime and finally, decreases in the continuum regime. Typical values of the uncertainty of the pressure difference are 27% for the temperature, 10% for the radius, 5% for the pressure and 3% for the accommodation coefficient, with 5% uncertainty introduced to the corresponding quantities. The effect of the temperature uncertainty is further

magnified in small temperature differences and may result to an output uncertainty of the pressure difference up to 85% with 5% uncertainty in temperature and temperature ratio equal to 1.2.

In the thermal creep flow, the temperature uncertainty is the most important, in most cases, while it is overtaken by the radius uncertainty for large temperature differences and small values of the rarefaction parameter. The radius uncertainty is the second largest source of uncertainty, in most cases, while the accommodation coefficient and pressure uncertainties are of lesser importance. Typical values of the uncertainty of the mass flow rate, with 5% uncertainty in the respective quantities, are 25% for the temperature, 15% for the radius and less than 5% for the pressure and accommodation coefficient. The temperature uncertainty is further magnified and becomes the predominant factor of uncertainty for small temperature differences, reaching up to 80% for temperature uncertainty of 5% and temperature ratio equal to 1.2.

In the heat transfer cases, the uncertainties of the input parameters do not lead to much larger uncertainties of the heat flux when the temperature difference is relatively large. For small temperature differences however, temperature uncertainties are magnified and can lead to very large uncertainties in the heat flux, reaching up to 70% for temperature uncertainty 5% and temperature ratio 0.9.

It may be concluded that in most cases, the uncertainty of the quantity driving the phenomenon, i.e., the pressure for the Poiseuille flow and the temperature for thermally driven flows, is the most important source of uncertainty, especially for small driving forces.

The methodology for the uncertainty propagation implemented in the present work can be implemented in a straightforward manner in a broader range of rarefied gas flows. Furthermore, the implementation of more efficient methodologies is an expected future step and the results presented here can be used to judge the accuracy of these more advanced methodologies. The results presented in the present chapter for the benchmark configurations of rarefied flows through tubes and heat transfer between plates, can aid researchers and engineers engaged in the design of systems with miniaturized sizes and/or operating in low pressure conditions.

Table 7.1 Kinetic coefficient G_P in terms of the rarefaction parameter δ and accommodation coefficient α for pressure driven flow in a plane channel.

δ	G_P							
	$\alpha = 0.6$	$\alpha = 0.7$	$\alpha = 0.8$	$\alpha = 0.9$	$\alpha = 0.92$	$\alpha = 0.95$	$\alpha = 0.98$	$\alpha = 1$
0	3.51	2.79	2.26	1.84	1.77	1.66	1.57	1.50
0.001	3.48	2.77	2.24	1.83	1.76	1.66	1.56	1.50
0.01	3.34	2.68	2.18	1.79	1.72	1.63	1.53	1.48
0.1	2.95	2.41	2.00	1.67	1.61	1.53	1.45	1.40
0.2	2.82	2.31	1.93	1.63	1.57	1.50	1.43	1.38
0.5	2.70	2.24	1.89	1.61	1.56	1.49	1.43	1.39
0.8	2.69	2.24	1.91	1.64	1.59	1.53	1.46	1.43
1	2.71	2.27	1.93	1.67	1.62	1.56	1.50	1.46
2	2.88	2.45	2.12	1.86	1.82	1.76	1.70	1.66
5	3.57	3.13	2.81	2.55	2.51	2.45	2.39	2.35
8	4.30	3.86	3.54	3.28	3.24	3.17	3.11	3.07
10	4.79	4.36	4.03	3.77	3.73	3.66	3.60	3.56
20	7.27	6.84	6.51	6.25	6.21	6.14	6.08	6.04
50	1.48(+1)	1.43(+1)	1.40(+1)	1.37(+1)	1.37(+1)	1.36(+1)	1.36(+1)	1.35(+1)

Table 7.2 Kinetic coefficient G_T in terms of the rarefaction parameter δ and accommodation coefficient α for temperature driven flow in a plane channel.

δ	G_T							
	$\alpha = 0.6$	$\alpha = 0.7$	$\alpha = 0.8$	$\alpha = 0.9$	$\alpha = 0.92$	$\alpha = 0.95$	$\alpha = 0.98$	$\alpha = 1$
0	1.76	1.40	1.13	9.19(-1)	8.83(-1)	8.31(-1)	7.83(-1)	7.52(-1)
0.001	1.72	1.38	1.11	9.11(-1)	8.75(-1)	8.24(-1)	7.77(-1)	7.47(-1)
0.01	1.58	1.28	1.05	8.69(-1)	8.37(-1)	7.91(-1)	7.48(-1)	7.21(-1)
0.1	1.14	9.67(-1)	8.30(-1)	7.17(-1)	6.97(-1)	6.67(-1)	6.39(-1)	6.21(-1)
0.2	9.44(-1)	8.24(-1)	7.25(-1)	6.40(-1)	6.25(-1)	6.03(-1)	5.81(-1)	5.67(-1)
0.5	6.78(-1)	6.18(-1)	5.66(-1)	5.20(-1)	5.11(-1)	4.99(-1)	4.87(-1)	4.79(-1)
0.8	5.46(-1)	5.11(-1)	4.79(-1)	4.51(-1)	4.45(-1)	4.38(-1)	4.30(-1)	4.25(-1)
1	4.87(-1)	4.61(-1)	4.38(-1)	4.17(-1)	4.13(-1)	4.07(-1)	4.01(-1)	3.97(-1)
2	3.23(-1)	3.18(-1)	3.13(-1)	3.08(-1)	3.07(-1)	3.05(-1)	3.04(-1)	3.03(-1)
5	1.64(-1)	1.67(-1)	1.70(-1)	1.73(-1)	1.73(-1)	1.74(-1)	1.75(-1)	1.76(-1)
8	1.09(-1)	1.12(-1)	1.16(-1)	1.19(-1)	1.19(-1)	1.20(-1)	1.21(-1)	1.22(-1)
10	8.82(-2)	9.16(-2)	9.48(-2)	9.78(-2)	9.84(-2)	9.92(-2)	1.00(-1)	1.01(-1)
20	4.40(-2)	4.65(-2)	4.88(-2)	5.09(-2)	5.13(-2)	5.19(-2)	5.25(-2)	5.29(-2)
50	1.51(-2)	1.65(-2)	1.78(-2)	1.90(-2)	1.92(-2)	1.95(-2)	1.99(-2)	2.01(-2)

Table 7.3 Heat flux in terms of temperature ratio T_C/T_H and rarefaction parameter δ for $\alpha=0.1, 0.3, 0.5$ for heat transfer between parallel plates.

Q						
$\alpha=0.1$						
δ	$T_C/T_H=0.1$	$T_C/T_H=0.3$	$T_C/T_H=0.5$	$T_C/T_H=0.7$	$T_C/T_H=0.9$	$T_C/T_H=0.99$
0.01	1.98(-2)	1.67(-2)	1.29(-2)	8.21(-3)	2.89(-3)	2.96(-4)
0.1	1.97(-2)	1.67(-2)	1.28(-2)	8.19(-3)	2.89(-3)	2.95(-4)
1	1.93(-2)	1.64(-2)	1.26(-2)	8.04(-3)	2.83(-3)	2.90(-4)
5	1.80(-2)	1.53(-2)	1.18(-2)	7.54(-3)	2.66(-3)	2.72(-4)
10	1.66(-2)	1.42(-2)	1.10(-2)	7.03(-3)	2.48(-3)	2.54(-4)
15	1.54(-2)	1.33(-2)	1.03(-2)	6.58(-3)	2.32(-3)	2.38(-4)
20	1.44(-2)	1.24(-2)	9.64(-3)	6.18(-3)	2.18(-3)	2.23(-4)
$\alpha=0.3$						
δ	$T_C/T_H=0.1$	$T_C/T_H=0.3$	$T_C/T_H=0.5$	$T_C/T_H=0.7$	$T_C/T_H=0.9$	$T_C/T_H=0.99$
0.01	6.59(-2)	5.59(-2)	4.30(-2)	2.75(-2)	9.69(-3)	9.92(-4)
0.1	6.52(-2)	5.54(-2)	4.26(-2)	2.73(-2)	9.61(-3)	9.84(-4)
1	6.08(-2)	5.20(-2)	4.01(-2)	2.57(-2)	9.05(-3)	9.26(-4)
5	4.91(-2)	4.26(-2)	3.31(-2)	2.12(-2)	7.49(-3)	7.67(-4)
10	4.01(-2)	3.52(-2)	2.74(-2)	1.76(-2)	6.21(-3)	6.36(-4)
15	3.41(-2)	3.00(-2)	2.34(-2)	1.50(-2)	5.31(-3)	5.43(-4)
20	2.97(-2)	2.62(-2)	2.04(-2)	1.31(-2)	4.64(-3)	4.74(-4)
$\alpha=0.5$						
δ	$T_C/T_H=0.1$	$T_C/T_H=0.3$	$T_C/T_H=0.5$	$T_C/T_H=0.7$	$T_C/T_H=0.9$	$T_C/T_H=0.99$
0.01	1.22(-1)	1.05(-1)	8.09(-2)	5.18(-2)	1.83(-2)	1.87(-3)
0.5	1.12(-1)	9.71(-2)	7.53(-2)	4.83(-2)	1.70(-2)	1.74(-3)
1	1.05(-1)	9.16(-2)	7.11(-2)	4.57(-2)	1.61(-2)	1.65(-3)
5	7.48(-2)	6.62(-2)	5.17(-2)	3.33(-2)	1.18(-2)	1.20(-3)
10	5.62(-2)	5.00(-2)	3.91(-2)	2.52(-2)	8.89(-3)	9.10(-4)
15	4.53(-2)	4.02(-2)	3.14(-2)	2.02(-2)	7.15(-3)	7.32(-4)
20	3.80(-2)	3.37(-2)	2.63(-2)	1.69(-2)	5.98(-3)	6.12(-4)

Table 7.4 Heat flux in terms of temperature ratio T_C/T_H and rarefaction parameter δ for $\alpha=0.7, 0.8, 0.9$ for heat transfer between parallel plates.

Q						
$\alpha=0.7$						
δ	$T_C/T_H=0.1$	$T_C/T_H=0.3$	$T_C/T_H=0.5$	$T_C/T_H=0.7$	$T_C/T_H=0.9$	$T_C/T_H=0.99$
0.01	1.86(-1)	1.65(-1)	1.30(-1)	8.35(-2)	2.95(-2)	3.02(-3)
0.1	1.81(-1)	1.61(-1)	1.26(-1)	8.14(-2)	2.88(-2)	2.94(-3)
1	1.51(-1)	1.35(-1)	1.06(-1)	6.86(-2)	2.42(-2)	2.48(-3)
5	9.57(-2)	8.67(-2)	6.82(-2)	4.40(-2)	1.56(-2)	1.59(-3)
10	6.79(-2)	6.11(-2)	4.79(-2)	3.09(-2)	1.09(-2)	1.12(-3)
15	5.30(-2)	4.72(-2)	3.69(-2)	2.38(-2)	8.40(-3)	8.60(-4)
20	4.34(-2)	3.85(-2)	3.01(-2)	1.93(-2)	6.83(-3)	6.99(-4)
$\alpha=0.8$						
δ	$T_C/T_H=0.1$	$T_C/T_H=0.3$	$T_C/T_H=0.5$	$T_C/T_H=0.7$	$T_C/T_H=0.9$	$T_C/T_H=0.99$
0.01	2.45(-1)	2.39(-1)	1.93(-1)	1.26(-1)	4.47(-2)	4.58(-3)
0.1	2.37(-1)	2.31(-1)	1.86(-1)	1.21(-1)	4.31(-2)	4.41(-3)
1	1.89(-1)	1.82(-1)	1.46(-1)	9.50(-2)	3.37(-2)	3.45(-3)
5	1.13(-1)	1.05(-1)	8.29(-2)	5.36(-2)	1.90(-2)	1.94(-3)
10	7.71(-2)	6.97(-2)	5.47(-2)	3.53(-2)	1.25(-2)	1.28(-3)
15	5.86(-2)	5.23(-2)	4.09(-2)	2.63(-2)	9.30(-3)	9.52(-4)
20	4.73(-2)	4.19(-2)	3.26(-2)	2.10(-2)	7.41(-3)	7.59(-4)
$\alpha=0.9$						
δ	$T_C/T_H=0.1$	$T_C/T_H=0.3$	$T_C/T_H=0.5$	$T_C/T_H=0.7$	$T_C/T_H=0.9$	$T_C/T_H=0.99$
0.01	2.44(-1)	2.78(-1)	2.32(-1)	1.53(-1)	5.46(-2)	5.59(-3)
0.1	2.40(-1)	2.68(-1)	2.22(-1)	1.46(-1)	5.21(-2)	5.34(-3)
1	1.99(-1)	2.06(-1)	1.68(-1)	1.10(-1)	3.90(-2)	3.99(-3)
5	1.20(-1)	1.13(-1)	8.96(-2)	5.81(-2)	2.06(-2)	2.11(-3)
10	8.09(-2)	7.33(-2)	5.76(-2)	3.72(-2)	1.31(-2)	1.35(-3)
15	6.09(-2)	5.44(-2)	4.25(-2)	2.74(-2)	9.66(-3)	9.89(-4)
20	4.88(-2)	4.32(-2)	3.37(-2)	2.16(-2)	7.64(-3)	7.82(-4)

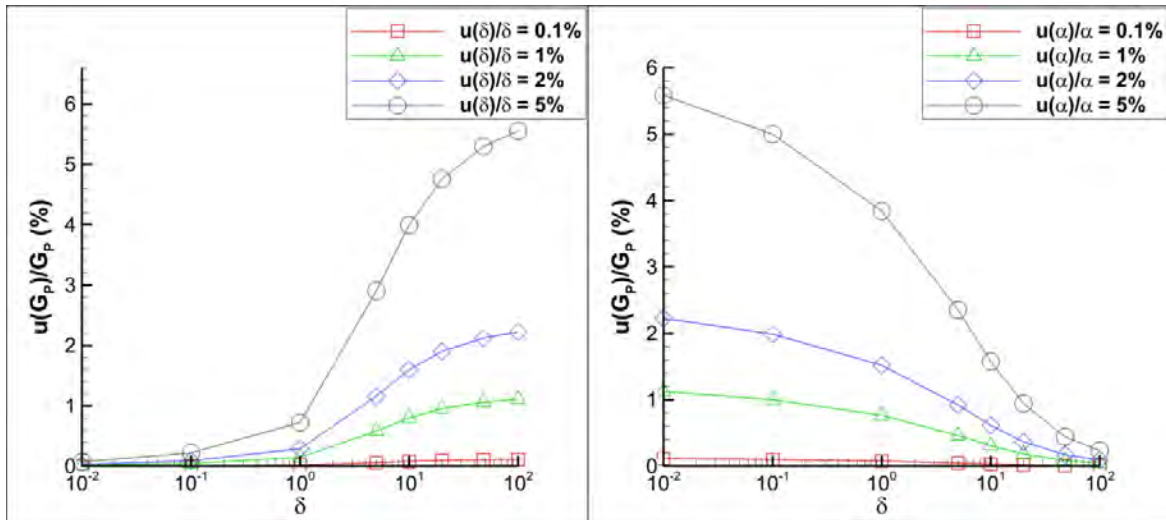


Figure 7.1 Relative uncertainty of G_P in terms of δ for uncertainty in δ (left) and α (right) for $\alpha_n = 1$.

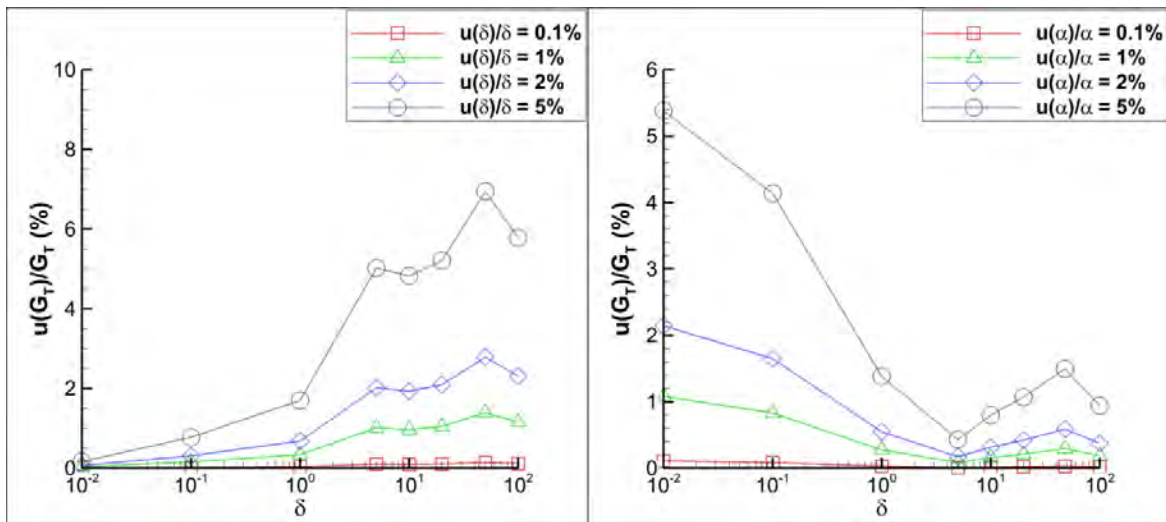


Figure 7.2 Relative uncertainty of G_T in terms of δ for uncertainty in δ (left) and α (right) for $\alpha_n = 1$.

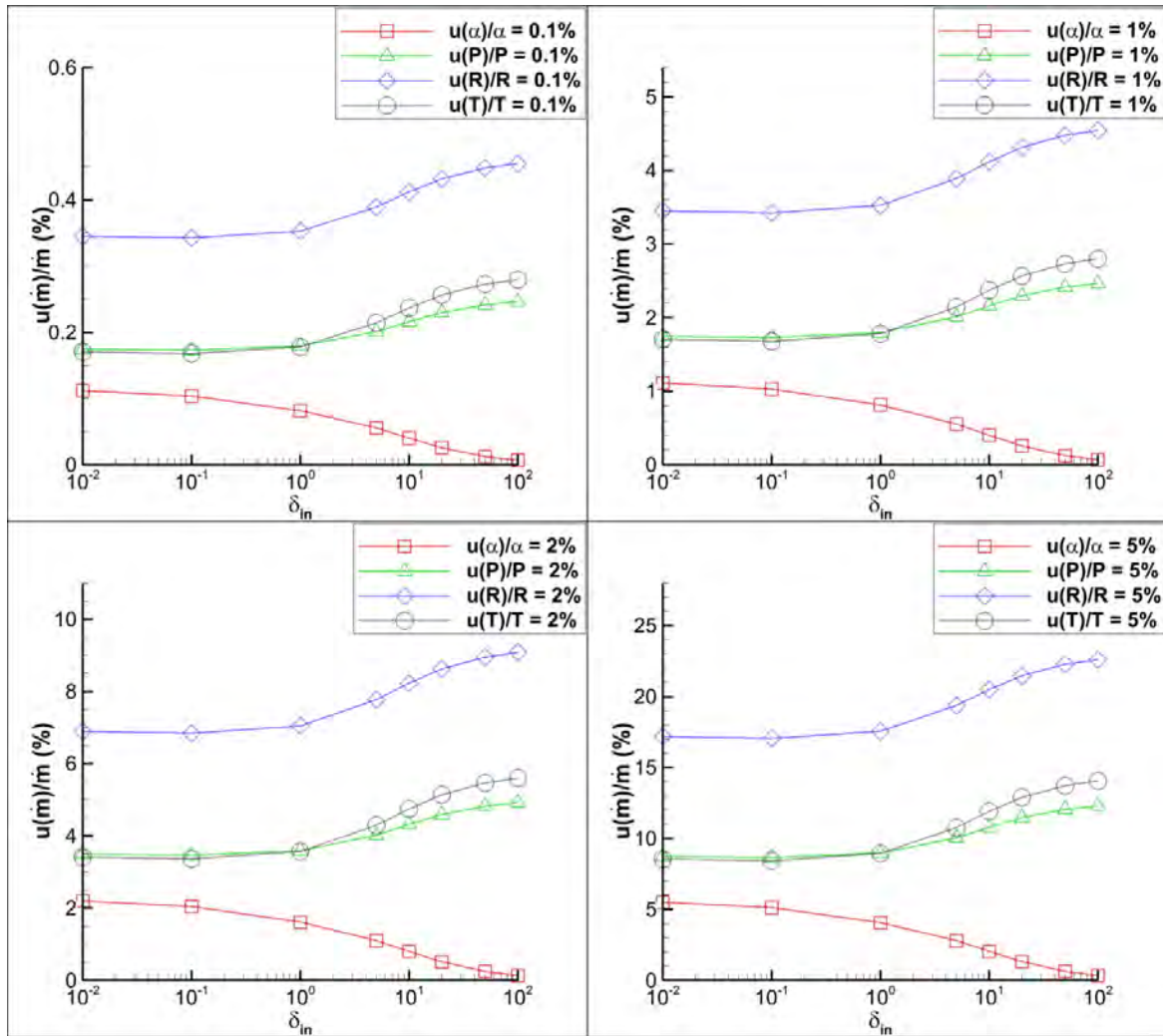


Figure 7.3 Relative uncertainty of mass flow rate in the Poiseuille flow, in terms of δ_{in} for relative uncertainty of each input parameter equal to 0.1%, 1%, 2% and 5%.

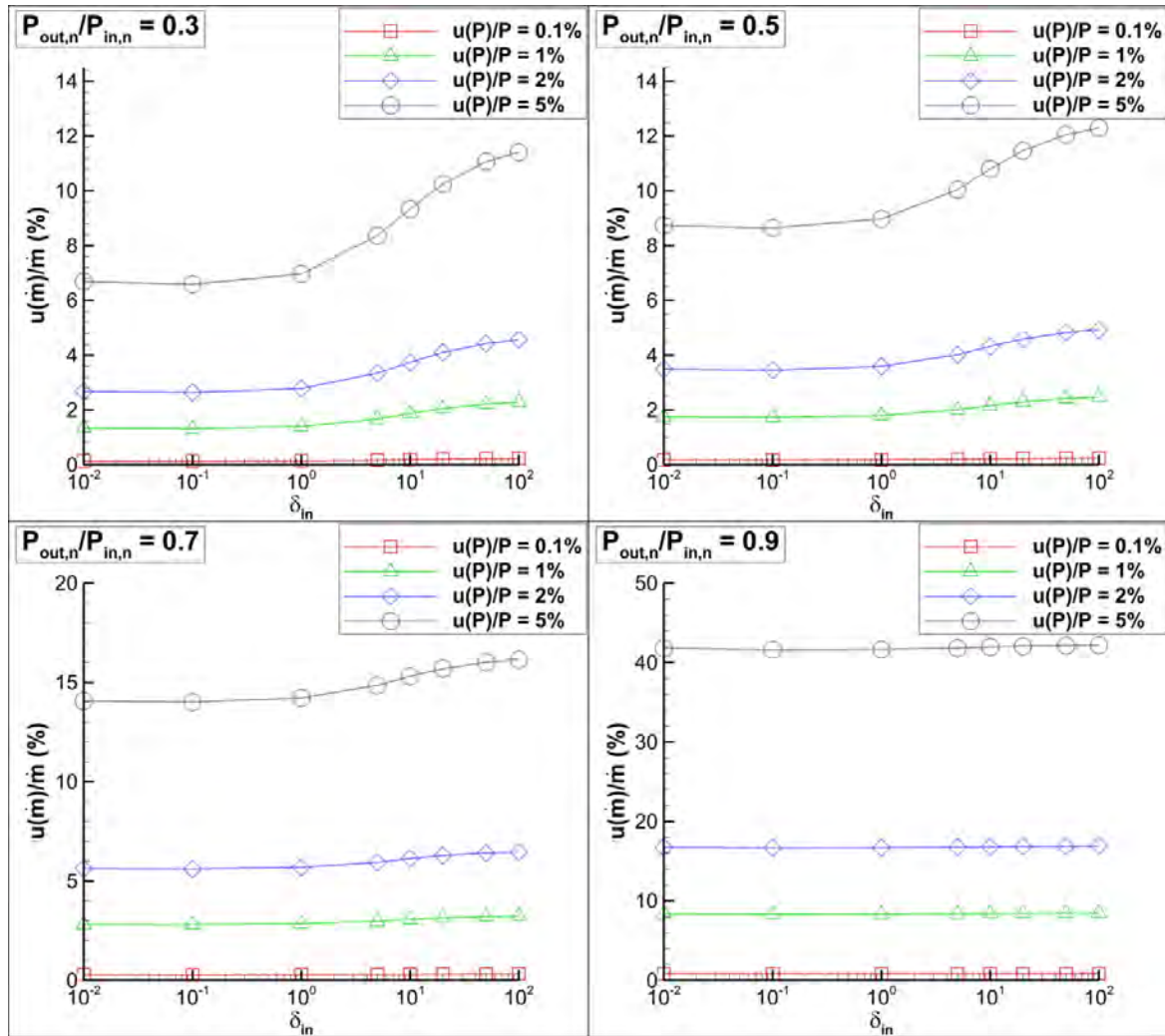


Figure 7.4 Relative uncertainty of mass flow rate in the Poiseuille flow, in terms of δ_{in} for various values $u(P)/P$ and $P_{out,n}/P_{in,n} = 0.3, 0.5, 0.7$ and 0.9 .

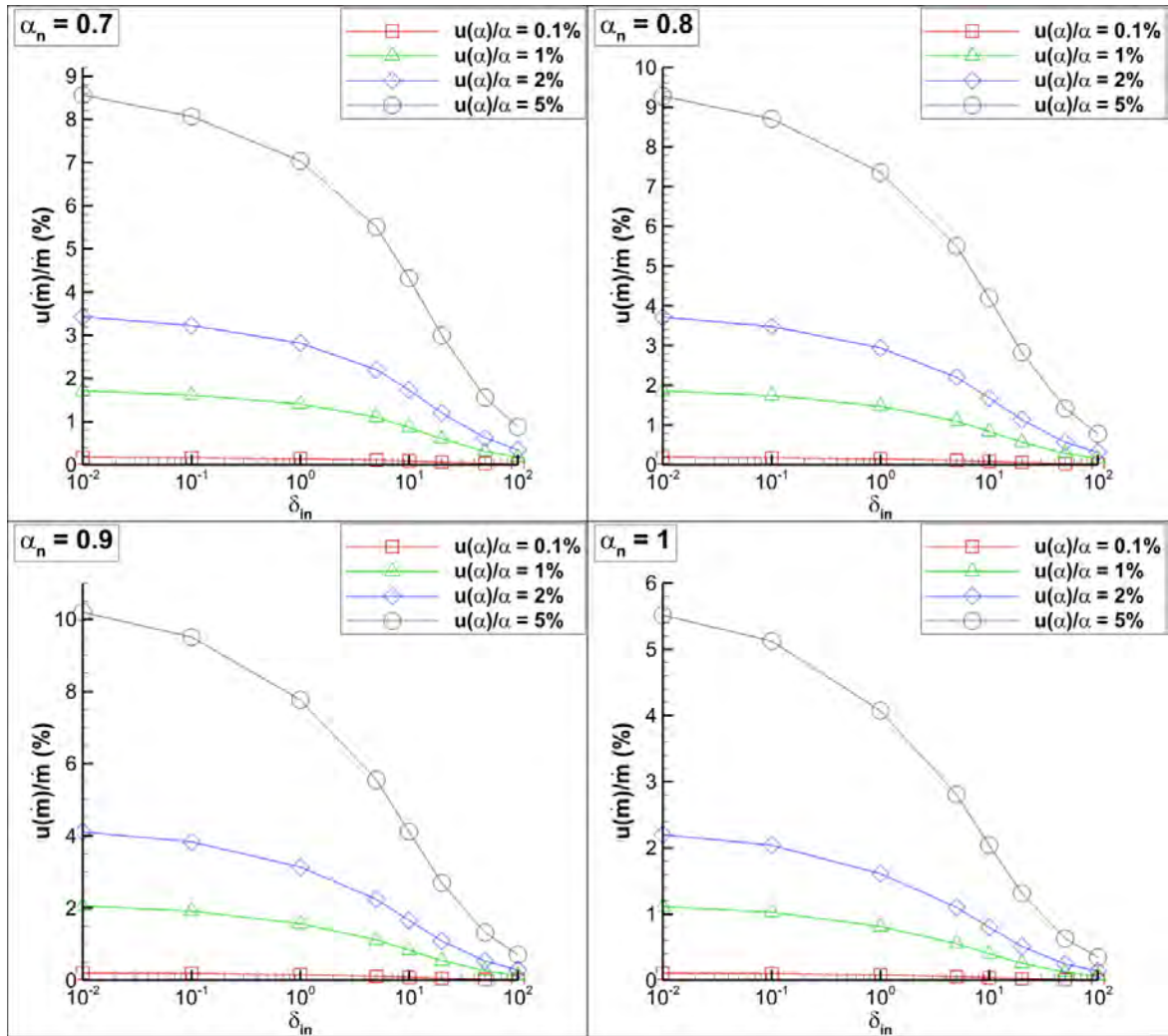


Figure 7.5 Relative uncertainty of mass flow rate in the Poiseuille flow, in terms of δ_{in} for various values $u(\alpha)/\alpha$ and $\alpha_n = 0.7, 0.8, 0.9$ and 1 .

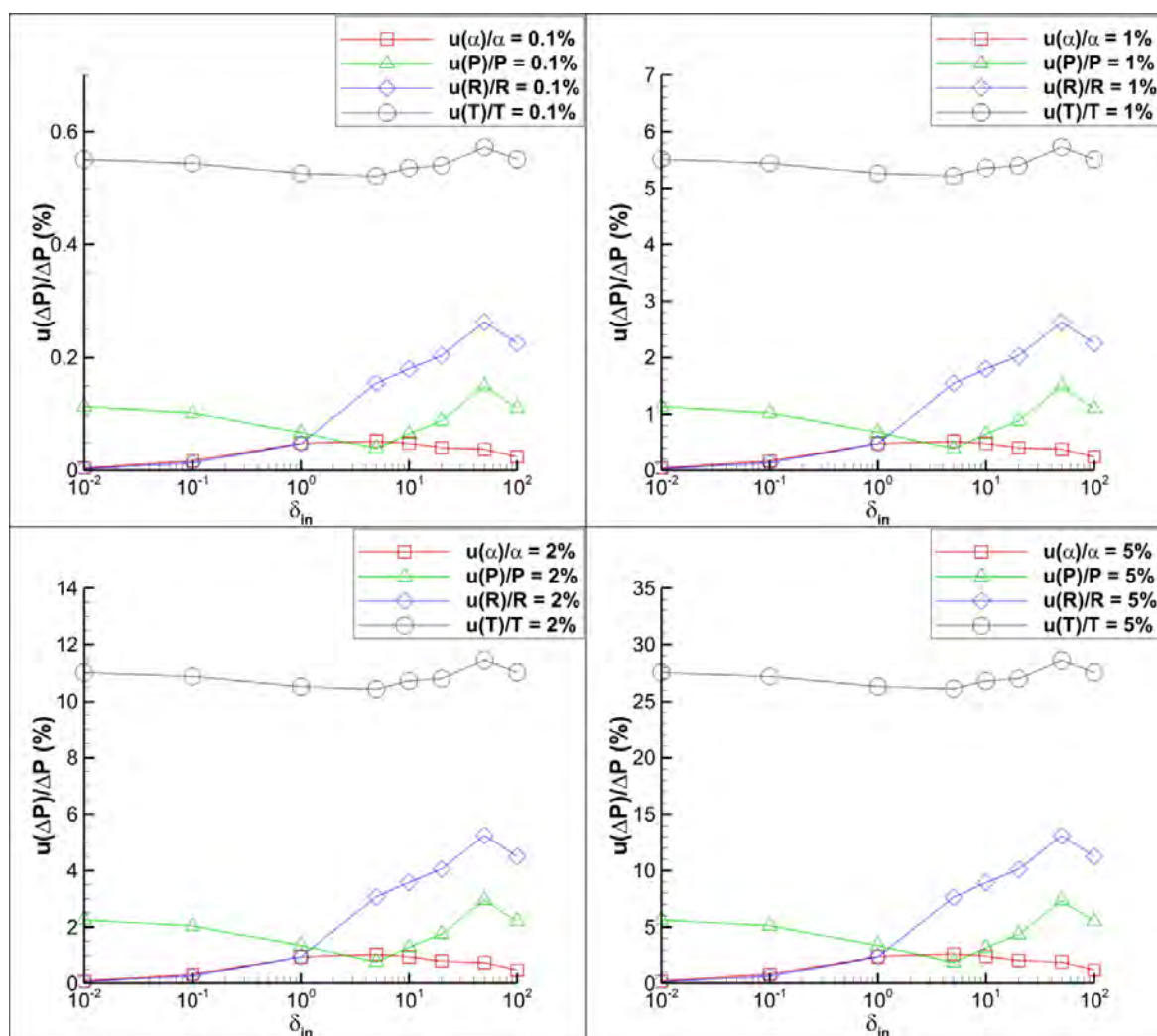


Figure 7.6 Relative uncertainty of the pressure difference in the thermomolecular pressure difference case, in terms of δ_{in} for relative uncertainty of each input parameter equal to 0.1%, 1%, 2% and 5%.

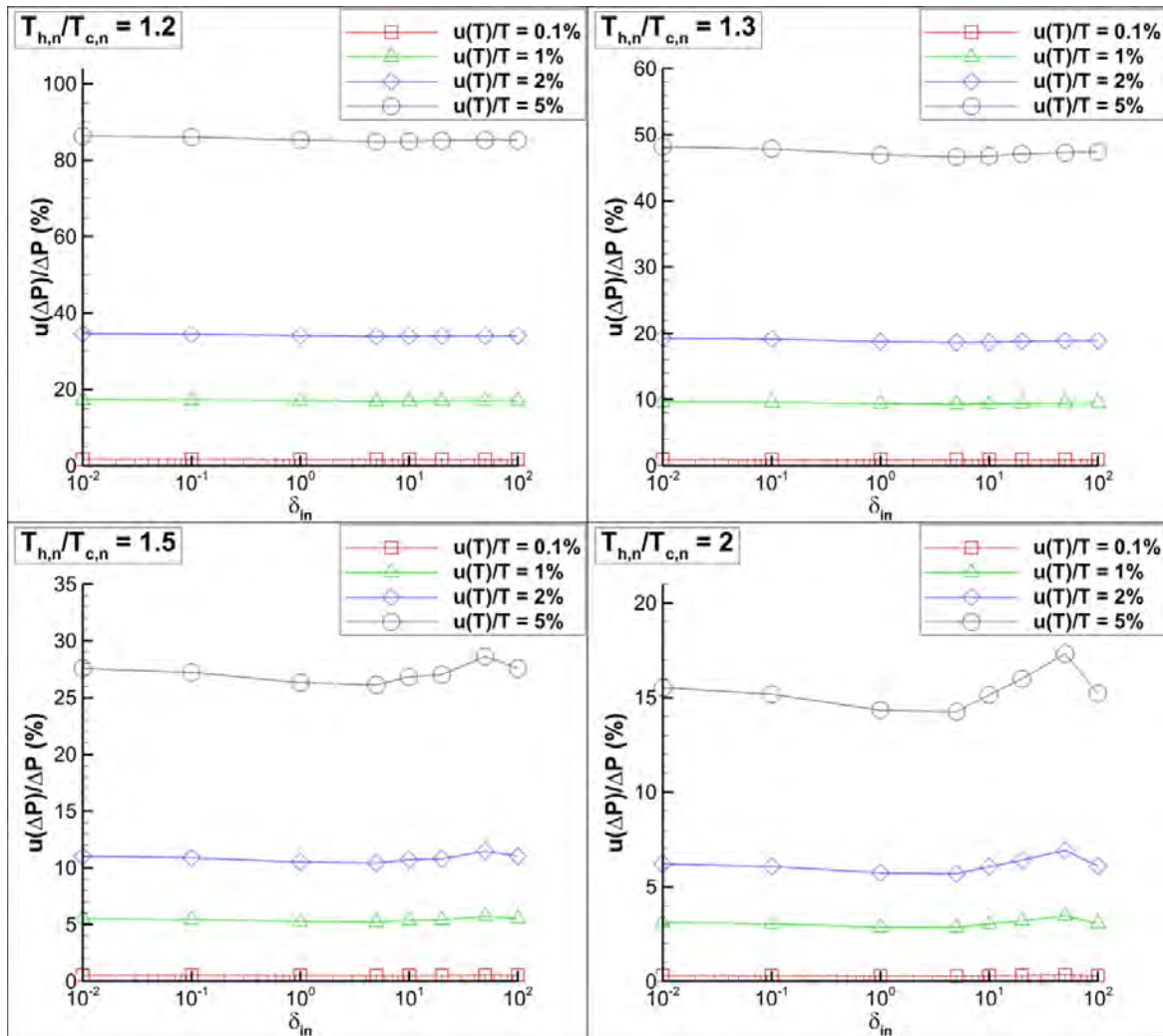


Figure 7.7 Relative uncertainty of the pressure difference in the thermomolecular pressure difference case, in terms of δ_{in} for various values $u(T)/T$ and $T_{h,n}/T_{c,n} = 1.2, 1.3, 1.5$ and 2 .

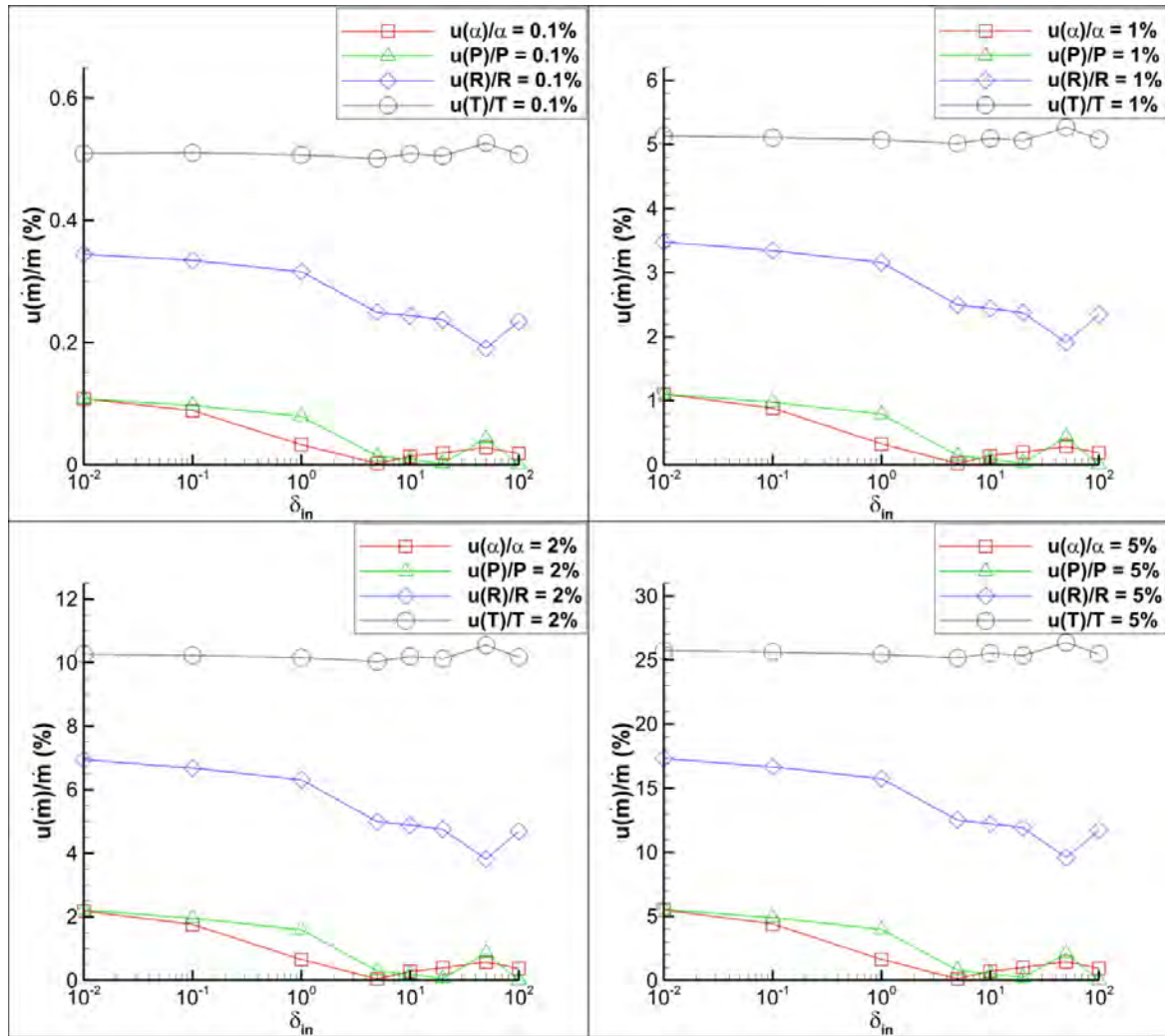


Figure 7.8 Relative uncertainty of mass flow rate in the thermal creep flow, in terms of δ_{in} for relative uncertainty of each input parameter equal to 0.1%, 1%, 2% and 5%.

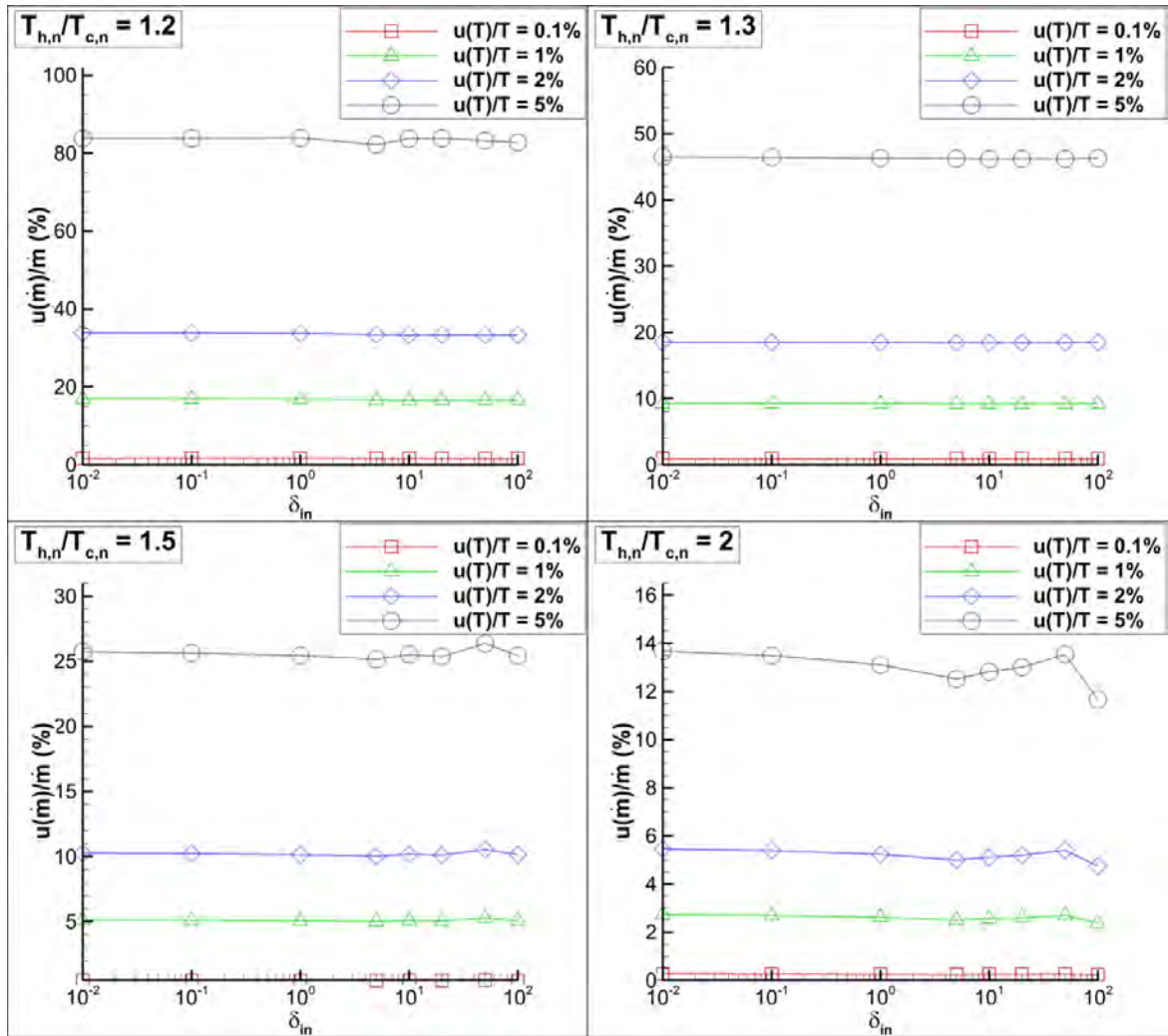


Figure 7.9 Relative uncertainty of mass flow rate in the thermal creep flow, in terms of δ_{in} for various values $u(T)/T$ and $T_{H,n}/T_{C,n} = 1.2, 1.3, 1.5$ and 2 .

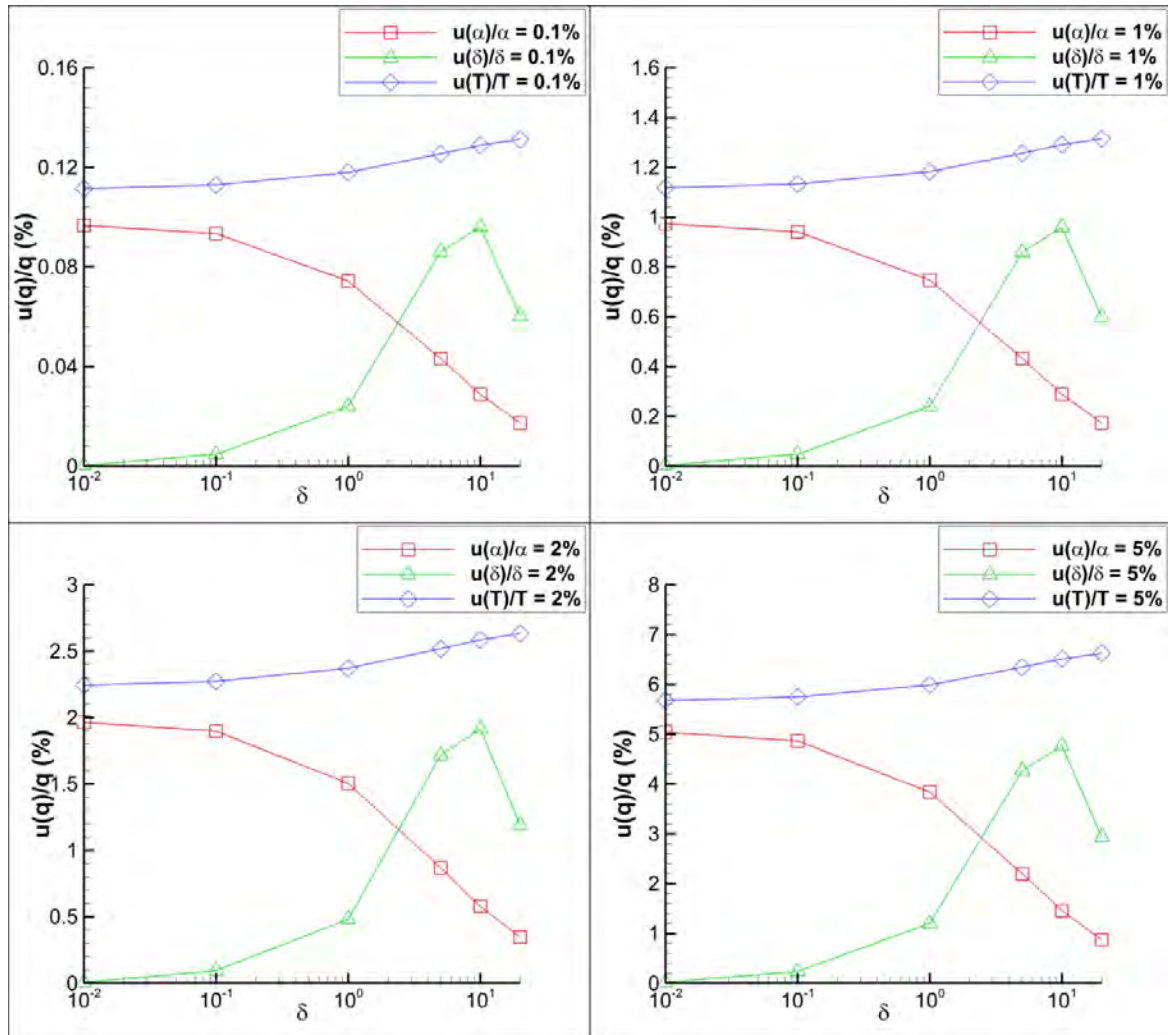


Figure 7.10 Relative uncertainty of heat flux in terms of δ for relative uncertainty of each input parameter equal to 0.1%, 1%, 2% and 5%.

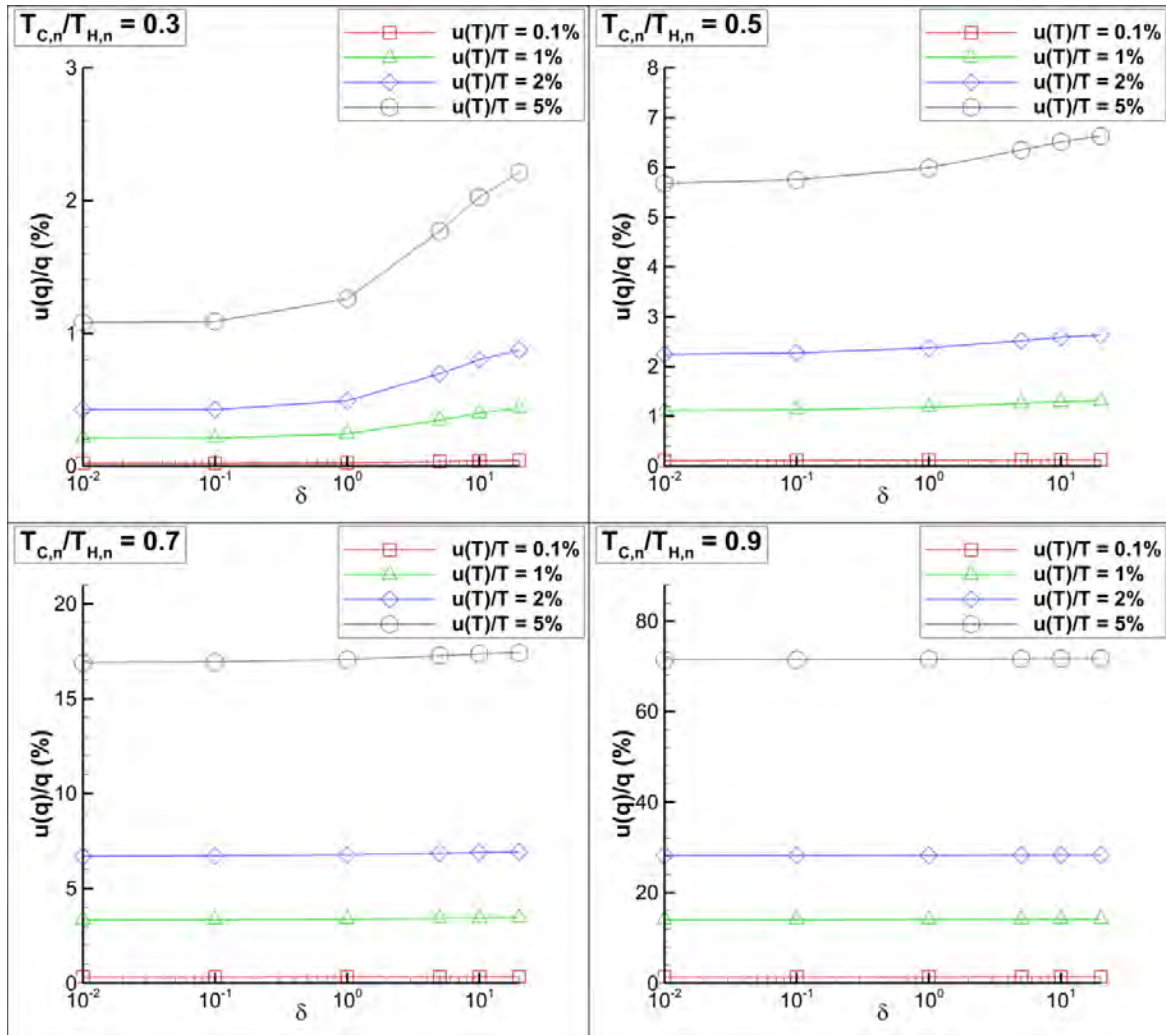


Figure 7.11 Relative uncertainty of heat flux in terms of δ for various values $u(T)/T$ and $T_{C,n}/T_{H,n} = 0.3, 0.5, 0.7$ and 0.9 .

Chapter 8

Synthetic acceleration schemes of the discrete velocity algorithm

8.1 Introduction

The deterministic solution of the Boltzmann equation or suitable kinetic model equations has been extensively applied with considerable success to solve rarefied gas flows and heat transfer problems in the whole range of the Knudsen number [54]. The molecular velocity space is discretized by a finite set of molecular velocities and the physical space by typical finite difference or control volume scheme, while the macroscopic quantities are computed by numerically integrating the moments of the distribution function. The resulting system of discretized equations is solved in an iterative manner between the kinetic equation and the moments of the distribution function. This numerical approach is widely known as the discrete velocity (or ordinates) method. Researchers implementing the Discrete Velocity Method (DVM) are well aware however, of the slow convergence rate of this simple iteration map as the flow approaches the slip and continuum regimes [58], [59]. To speed-up convergence, synthetic iteration acceleration schemes have been developed [234].

Synthetic acceleration schemes couple the kinetic equation with a system of moment equations, derived by accordingly operating on the kinetic equation. The moments needed to close the system of moment equations are taken from the calculated distribution function. The updated values of the accelerated macroscopic quantities are obtained by the solution of the moment equations and not directly as moments of the distribution function. This advanced iteration map exhibits rapid convergence especially close to the continuum regime.

Such schemes have been applied to kinetic model equations [60] and to the linearized Boltzmann equation [61] to model fully developed flows through various capillaries. The implemented acceleration schemes are applied only to the interior nodes and not to the boundary ones. This is of no great importance in fully developed flows, where the outgoing distribution function at the boundary nodes is known a priori. In more general cases however, where the outgoing distribution at the boundaries are expressed in terms of the unknown incoming distributions, not including the corresponding acceleration moment equations at the boundary nodes severely decreases the efficiency of the acceleration scheme.

In the present chapter, a synthetic iterative acceleration scheme able to accelerate the macroscopic quantities at the boundary nodes is proposed. It is constructed taking the half-range moments of the involved distribution functions, leading to a set of hyperbolic ordinary or partial differential equations involving these moments. The system of moments is closed by calculating the associated higher order moments from the distribution function. This acceleration strategy allows the acceleration of the appropriate moments at the boundary nodes and provides a considerable speedup, compared to the typical acceleration schemes, extending the applicability of the synthetic acceleration schemes to more general flows. Still however, the analysis is limited to linear kinetic equations.

The proposed methodology and the deduced convergence speed-up are demonstrated by solving the one-dimensional problems of Poiseuille flow and heat transfer between parallel plates. The former one is a fully developed flow and the outgoing distributions boundary conditions are known. Since both the full-range and the half-range acceleration schemes work fine a systematic comparison between the existing and the new speed-up schemes is performed. The latter one is more complicated and the outgoing distributions are part of the solution. It is shown that in the heat transfer configuration the performance of the full-range acceleration scheme is very low, while on the contrary the proposed acceleration scheme provides a very good speed-up of the convergence rate of the iteration map. In both problems the number of iterations required by the DVM with no acceleration (NA), the DVM with the typical full-range acceleration (FRA) and the proposed DVM with half-range acceleration (HRA), able to accelerate the proper quantities at the boundaries, are compared. The obtained results clearly demonstrate the importance of accelerating the boundary nodes in flow setups where the boundary conditions are part of the solution.

In Section 8.2, the well-known full-range acceleration scheme is reviewed. In Section 8.3 the half-range Hermite polynomials, which are used in the formulation of the half-range accelerated schemes, are constructed. The novel half-range acceleration scheme is developed in Sections 8.4 and 8.5 solving the Poiseuille flow and the heat transfer between plates problems respectively. A brief discussion on the performance of the half-range moment method is included. Finally, some concluding remarks are made in Section 8.7.

8.2 Synthetic acceleration based on full-range Hermite polynomials

The construction of the full-range acceleration scheme, although is well known, it is reviewed here for the two problems under consideration, mainly for completeness purposes.

The fully developed pressure driven flow between parallel plates is modeled by the linearized BGK model equation written as [235]

$$\zeta \frac{\partial h}{\partial y} + \delta h = \delta u - \frac{1}{2}, \quad (8.1)$$

where $\zeta \in (-\infty, +\infty)$ is the dimensionless molecular velocity, $y \in [0, 1]$ is the physical space variable in the direction normal to the plates, h is the local perturbation of the distribution function from the reference Maxwellian distribution. Also, the rarefaction parameter is defined as

$$\delta = \frac{PH}{\mu v_0}, \quad (8.2)$$

with P , H , μ denoting the pressure, the distance between the plates and the viscosity at reference temperature respectively, while $v_0 = \sqrt{2R_g T_0}$ is the most probable molecular speed at the reference temperature T_0 , with R_g denoting the specific gas constant. The macroscopic velocity is expressed as the zeroth moment of the distribution function as

$$u = \frac{1}{\sqrt{\pi}} \int_{-\infty}^{+\infty} h e^{-\zeta^2} d\zeta. \quad (8.3)$$

The purely diffuse boundary conditions are given by

$$h^+ = 0, \text{ at } y = 0 \text{ with } \zeta > 0 \text{ and at } y = 1 \text{ with } \zeta < 0. \quad (8.4)$$

In order to construct the full-range acceleration scheme, the following moments of the distribution function are defined

$$M_m = \frac{1}{\sqrt{\pi}} \int_{-\infty}^{+\infty} h H_m(\zeta) e^{-\zeta^2} d\zeta, \quad (8.5)$$

where H_m denotes the full-range Hermite polynomial of order m , satisfying the orthogonality condition

$$\int_{-\infty}^{+\infty} H_m H_n e^{-x^2} dx = \sqrt{\pi} 2^m m! \delta_{mn}, \quad (8.6)$$

where δ_{mn} is the Kronecker delta. The first five full-range Hermite polynomials are:

$$H_0 = 1, H_1 = 2x, H_2 = 4x^2 - 2, H_3 = 8x^3 - 12x, H_4 = 16x^4 - 48x^2 + 12. \quad (8.7)$$

Applying the integral operator $\frac{1}{\sqrt{\pi}} \int_{-\infty}^{+\infty} (\cdot) \zeta^n e^{-\zeta^2} d\zeta$ with $n = 0, 1$ to Eq. (8.1) and using the definition of the full-range Hermite moments (8.5), after some mathematical manipulation, the following 2nd order ordinary differential equation is derived:

$$\frac{d^2 M_0}{dy^2} = -\delta - \frac{1}{2} \frac{d^2 M_2}{dy^2} \quad (8.8)$$

The zeroth moment is the unknown macroscopic velocity ($M_0 = u$) and the high order moment is calculated directly from the distribution function using Eq. (8.5). It is interesting to note that Stokes equation for the current case, using the present notation is written as

$$\frac{d^2 u}{dy^2} = -\delta. \quad (8.9)$$

It turns out that the moment equation (8.8) is the Stokes equation with a correction term.

Using k as the iteration index, the iterative map of the DVM scheme with no acceleration (NA) is written as:

$$\zeta \frac{\partial h^{(k+1/2)}}{\partial y} + \delta h^{(k+1/2)} = \delta u^{(k)} - \frac{1}{2} \quad (8.10)$$

$$u^{(k+1)} = \frac{1}{\sqrt{\pi}} \int_{-\infty}^{+\infty} h^{(k+1/2)} e^{-\zeta^2} d\zeta \quad (8.11)$$

The iterative procedure starts with an initial guess of the macroscopic velocity $u^{(0)}$ and then, Eq. (8.10) is solved to provide the value of the distribution function. Next, Eq. (8.11) is utilized to provide an updated value of the macroscopic velocity, which is substituted back into the kinetic equation (8.10). This procedure is repeated until convergence is reached.

The iteration map of the DVM with the typical full-range acceleration (FRA) is written as:

$$\zeta \frac{\partial h^{(k+1/2)}}{\partial y} + \delta h^{(k+1/2)} = \delta u^{(k)} - \frac{1}{2} \quad (8.12)$$

$$M_2^{(k+1/2)} = \frac{1}{\sqrt{\pi}} \int_{-\infty}^{+\infty} h^{(k+1/2)} H_2 e^{-\zeta^2} d\zeta \quad (8.13)$$

$$\frac{d^2 M_0^{(k+1)}}{dy^2} = -\delta - \frac{1}{2} \frac{d^2 M_2^{(k+1/2)}}{dy^2} \quad (8.14)$$

The solution starts with an initial guess of the macroscopic velocity and then, Eq. (8.12) is solved to provide the value of the distribution function. Next, Eq. (8.13) is used to compute the 2^{nd} order moment of the distribution function, which is introduced into the moment ordinary differential equation (8.14) to compute the updated accelerated value of the macroscopic velocity $u^{(k+1)} = M_0^{(k+1)}$. This value is substituted back into the kinetic equation (8.12) to continue the iterative procedure upon convergence. It is obvious that the computational effort per iteration is increased when the acceleration scheme is used. However, due to the reduced number of iterations required, the overall computational effort is drastically reduced. In one-dimensional problems, the linear system approximating Eq. (8.14) has a banded tridiagonal coefficient matrix, which is solved very efficiently by the Thomas algorithm (so the additional computational cost per iteration is small).

To solve Eq. (8.14), boundary conditions at $y = 0$ and $y = 1$ should be supplied. The boundary values of the macroscopic velocity at the boundaries are the values given by Eq. (8.5) using the values of the distribution function of the current iteration. In the pressure driven fully developed flow, the outgoing distributions at the two boundary nodes are known (see Eq. (8.4)) and not including the boundary nodes in the

acceleration scheme, which accelerates the zeroth moment only at the interior nodes, is not very detrimental to the speed-up of the synthetic acceleration method which, as shown in the results section, works really well.

The linearized heat transfer between parallel plates is next considered, demonstrating the importance of deriving acceleration moment equations for the interior, as well as for the boundary nodes. The heat transfer flow is modeled by the linearized BGK equation written as a system of coupled integrodifferential equations [236]:

$$\zeta \frac{\partial \varphi}{\partial y} + \delta \varphi = \delta \left[\rho + \tau \left(\zeta^2 - 1/2 \right) \right] \quad (8.15)$$

$$\zeta \frac{\partial \psi}{\partial y} + \delta \psi = \delta \tau \quad (8.16)$$

The perturbations of the number density and temperature are given by

$$\rho = \frac{1}{\sqrt{\pi}} \int_{-\infty}^{+\infty} \varphi e^{-\zeta^2} d\zeta \quad (8.17)$$

and

$$\tau = \frac{2}{3\sqrt{\pi}} \int_{-\infty}^{+\infty} \left[\psi + \varphi \left(\zeta^2 - 1/2 \right) \right] e^{-\zeta^2} d\zeta \quad (8.18)$$

respectively, while the heat flux is given by

$$q = \frac{1}{\sqrt{\pi}} \int_{-\infty}^{+\infty} \left[\psi + \varphi \left(\zeta^2 - 3/2 \right) \right] \zeta e^{-\zeta^2} d\zeta. \quad (8.19)$$

The boundary conditions at the top wall ($y = 1/2$) with $\zeta < 0$ are given by

$$\varphi^+ = \frac{1 - \zeta^2}{2} + 2\rho_W^T, \quad (8.20)$$

$$\psi^+ = -\frac{1}{2} \quad (8.21)$$

and at the bottom wall ($y = -1/2$) with $\zeta > 0$ by

$$\varphi^+ = -\frac{1 - \zeta^2}{2} + 2\rho_W^B, \quad (8.22)$$

$$\psi^+ = \frac{1}{2}. \quad (8.23)$$

Here, the boundary condition parameters ρ_W^T and ρ_W^B used to satisfy the impermeability condition are given by

$$\rho_W^T = \int_0^{+\infty} \zeta \varphi e^{-\zeta^2} d\zeta, \quad (8.24)$$

$$\rho_W^B = - \int_{-\infty}^0 \zeta \varphi e^{-\zeta^2} d\zeta. \quad (8.25)$$

It is noted that the impermeability parameters are computed in each iteration using the distribution function at the boundary nodes and thus are not accelerated by the full-range acceleration scheme.

The full-range acceleration methodology is implemented. Using the Hermite polynomials, the following moments of the two reduced distribution function are defined:

$$M_m = \frac{1}{\sqrt{\pi}} \int_{-\infty}^{+\infty} H_m(\zeta) \varphi e^{-\zeta^2} d\zeta \quad (8.26)$$

$$N_m = \frac{1}{\sqrt{\pi}} \int_{-\infty}^{+\infty} H_m(\zeta) \psi e^{-\zeta^2} d\zeta \quad (8.27)$$

The macroscopic quantities involved in the kinetic equations are written in terms of these moments as

$$\rho = M_0, \quad (8.28)$$

$$\tau = \frac{2}{3} N_0 + \frac{1}{6} M_2. \quad (8.29)$$

Applying the integral operator $\frac{1}{\sqrt{\pi}} \int_{-\infty}^{+\infty} (\cdot) \zeta^n e^{-\zeta^2} d\zeta$ to the Eq. (8.15) for φ , with $n = 0, 1, 2, 3$ and to Eq. (8.16) for ψ , with $n = 0, 1$ and after some algebraic manipulation of the resulting expressions, the following system of moment equations is obtained:

$$\frac{1}{4} \frac{d^2 M_2}{dy^2} + \frac{1}{2} \frac{d^2 M_0}{dy^2} = 0 \quad (8.30)$$

$$\frac{3}{4} \frac{d^2 M_2}{dy^2} + \frac{3}{4} \frac{d^2 M_0}{dy^2} + \frac{\delta^2}{3} N_0 - \frac{\delta^2}{6} M_2 = -\frac{1}{16} \frac{d^2 M_4}{dy^2} \quad (8.31)$$

$$\frac{1}{2} \frac{d^2 N_0}{dy^2} - \frac{\delta^2}{3} N_0 + \frac{\delta^2}{6} M_2 = -\frac{1}{4} \frac{d^2 N_2}{dy^2} \quad (8.32)$$

The boundary conditions for the above system of moment equations, as well as the high order moments in the right hand side are obtained directly from the distribution function, based on the Eqs. (8.26) and (8.27). The linear system obtained discretizing the system of moment equations (8.30), (8.31) and (8.32) is solved in an iterative manner by using a static iterative method such as Gauss Seidel or SOR.

It is clearly seen that this system does not accelerate the quantities at the boundary nodes, including the impermeability parameters. The iteration map is the same as the one presented for the Poiseuille flow. At each iteration, the system of kinetic equations is solved, then the high order moments are computed directly from the distribution function are computed and finally, the low order moments (the ones which are needed in the kinetic equation) are found from the moment equations and updated in the kinetic equations to continue with the next iteration.

8.3 Definition of the half-range Hermite polynomials

The key point in the proposed synthetic acceleration methodology is the derivation of a set of half-range moment equations at the interior as well as at the boundary nodes of the physical grid. Since half-range moments are required, the utilized polynomials should be orthogonal in the corresponding half-space range where the respective moment is defined. Half-range moments and expansions in half-range polynomials have been used before in solving rarefied gas flows, based on moment methods [237], [238] and in CFD simulations, based on lattice Boltzmann schemes [239]–[241].

In the present work the half-range Hermite polynomials are applied and can be written as

$$H_n^+ = x^n + \sum_{i=0}^{n-1} a_{n,i}^+ x^i, \quad (8.33)$$

$$H_n^- = x^n + \sum_{i=0}^{n-1} a_{n,i}^- x^i, \quad (8.34)$$

with the polynomial H_n^+ and H_n^- defined for $x > 0$ for $x < 0$ respectively. The orthogonality conditions are

$$\langle H_m^+, H_n^+ \rangle^+ = \delta_{mn} c_m^+, \quad (8.35)$$

$$\langle H_m^-, H_n^- \rangle^- = \delta_{mn} c_m^-, \quad (8.36)$$

where c_m^\pm are constants, with

$$\langle f, g \rangle^+ = \int_0^\infty f g e^{-x^2} dx, \quad (8.37)$$

$$\langle f, g \rangle^- = \int_{-\infty}^0 f g e^{-x^2} dx. \quad (8.38)$$

The coefficients $a_{n,i}^\pm$ of the x^i term for the polynomial of order n are obtained using the Gram-Schmidt process and the polynomials are obtained using the recursion relations

$$H_n^+ = x^n - \sum_{i=0}^{n-1} \frac{\langle x^n, H_i^+ \rangle^+}{\langle H_i^+, H_i^+ \rangle^+} H_i^+ \quad (8.39)$$

$$H_n^- = x^n - \sum_{i=0}^{n-1} \frac{\langle x^n, H_i^- \rangle^-}{\langle H_i^-, H_i^- \rangle^-} H_i^- \quad (8.40)$$

It is also convenient to solve Eqs. (8.34) for the highest order term (x^n), resulting to

$$x^n = H_n^+ + \sum_{i=0}^{n-1} \beta_{n,i}^+ H_i^+, x > 0 \quad (8.41)$$

$$x^n = H_n^- + \sum_{i=0}^{n-1} \beta_{n,i}^- H_i^-, x < 0. \quad (8.42)$$

The coefficients $a_{n,i}^\pm$ and $\beta_{n,i}^\pm$ for polynomials up to the 4th order, are given in Appendix E. Next, using the above half-range polynomials, boundary including acceleration schemes are constructed.

8.4 Synthetic acceleration based on the half-range Hermite polynomials: Fully developed flow between parallel plates

The formulation of the fully developed flow, presented in Section 8.2, may be summarized by providing the kinetic equation

$$\zeta \frac{\partial h}{\partial y} + \delta h = \delta u - \frac{1}{2} \quad (8.43)$$

and the macroscopic velocity

$$u = \frac{1}{\sqrt{\pi}} \int_{-\infty}^{+\infty} h e^{-\zeta^2} d\zeta, \quad (8.44)$$

along with the boundary conditions at $y = 0$ with $\zeta > 0$ and at $y = 1$ with $\zeta < 0$,

$$h^+ = 0 \quad (8.45)$$

To construct the half-range acceleration scheme, the integral operators $\frac{1}{\sqrt{\pi}} \int_{-\infty}^0 (\cdot) \zeta^n e^{-\zeta^2} d\zeta$ and $\frac{1}{\sqrt{\pi}} \int_0^{+\infty} (\cdot) \zeta^n e^{-\zeta^2} d\zeta$ with $n = 0, 1$ are applied to Eq. (8.43) and the half-range moments

$$M_n^+ = \frac{1}{\sqrt{\pi}} \int_0^{+\infty} H_n^+ h e^{-\zeta^2} d\zeta, \quad (8.46)$$

$$M_n^- = \frac{1}{\sqrt{\pi}} \int_{-\infty}^0 H_n^- h e^{-\zeta^2} d\zeta \quad (8.47)$$

are defined with the macroscopic velocity given in terms of the two zeroth order half-range moments as $u = M_0^- + M_0^+$. Upon applying the integral operators to the kinetic equation and algebraically manipulating the resulting expressions, the following system is derived:

$$\frac{dM_0^+}{dy} = g_0^+ \frac{dM_2^+}{dy} + \delta p_{0,0}^{+-} M_0^- + \delta p_{0,0}^{++} M_0^+ + \delta p_{0,1}^{++} M_1^+ + s_0^+ \quad (8.48)$$

$$\frac{dM_1^+}{dy} = g_1^+ \frac{dM_2^+}{dy} + \delta p_{1,0}^{+-} M_0^- + \delta p_{1,0}^{++} M_0^+ + \delta p_{1,1}^{++} M_1^+ + s_1^+ \quad (8.49)$$

$$\frac{dM_0^-}{dy} = g_0^- \frac{dM_2^-}{dy} + \delta p_{0,0}^- M_0^- + \delta p_{0,0}^+ M_0^+ + \delta p_{0,1}^- M_1^- + s_0^- \quad (8.50)$$

$$\frac{dM_1^-}{dy} = g_1^- \frac{dM_2^-}{dy} + \delta p_{1,0}^- M_0^- + \delta p_{1,0}^+ M_0^+ + \delta p_{1,1}^- M_1^- + s_1^- \quad (8.51)$$

The coefficients g_n^+ , s_n^+ and $p_{n,i}^{\pm\pm}$, $n, i = 0, 1$ involved in the above system of ordinary differential equations (ODE) are given in Appendix E.

Furthermore, the initial conditions for this system of ODEs are obtained applying the integral operators defined above to the expressions for the boundary conditions (8.45). Then, the initial conditions are at the bottom wall ($y = 0$)

$$M_0^+ = M_1^+ = 0 \quad (8.52)$$

and at the top wall ($y = 1$)

$$M_0^- = M_1^- = 0. \quad (8.53)$$

The iteration map of the half-range acceleration scheme (HRA) consists of the solution of the kinetic equation (8.43), followed by the calculation of the high order moments based on the direct integration of the distribution function, using Eqs. (8.47). Then, the moment equations (8.48)-(8.51) are solved to yield the macroscopic velocity, which is substituted back into the kinetic equation for the next iteration.

It is noted that if the high order moments M_2^\pm are set to zero, then the system of equations (8.48)-(8.51) with boundary conditions (8.53) is a closed system of equations and can be solved by itself without any coupling with the kinetic equations. The half-range moment methodology (HRMM) is also examined.

In Section 8.6 comparative results in terms of accuracy, number of iterations and computational time are provided for solving the Poiseuille flow based on the DVM with no acceleration (NA), the DVM with the typical full-range acceleration (FRA), the DVM with the proposed half-range acceleration (HRA) and the half-range moment method (HRMM).

8.5 Synthetic acceleration based on the half-range Hermite polynomials: Heat transfer between parallel plates

The formulation of the heat transfer flow between parallel plates, presented in Section 8.2, may be summarized by providing the kinetic equations

$$\zeta \frac{\partial \varphi}{\partial y} + \delta \varphi = \delta \left[\rho + \tau \left(\zeta^2 - 1/2 \right) \right], \quad (8.54)$$

$$\zeta \frac{\partial \varphi}{\partial y} + \delta \psi = \delta \tau, \quad (8.55)$$

and the density, temperature and heat flux distributions given by

$$\rho = \frac{1}{\sqrt{\pi}} \int_{-\infty}^{+\infty} \varphi e^{-\zeta^2} d\zeta, \quad (8.56)$$

$$\tau = \frac{2}{3\sqrt{\pi}} \int_{-\infty}^{+\infty} \left[\psi + \varphi \left(\zeta^2 - 1/2 \right) \right] e^{-\zeta^2} d\zeta, \quad (8.57)$$

$$q = \frac{1}{\sqrt{\pi}} \int_{-\infty}^{+\infty} \left[\psi + \varphi \left(\zeta^2 - 3/2 \right) \right] \zeta e^{-\zeta^2} d\zeta \quad (8.58)$$

respectively, along with the boundary conditions at the top wall ($y = 1/2$) with $\zeta < 0$

$$\varphi^+ = \frac{1 - \zeta^2}{2} + 2\rho_W^T, \quad (8.59)$$

$$\psi^+ = -\frac{1}{2} \quad (8.60)$$

and at the bottom wall ($y = -1/2$) with $\zeta > 0$

$$\varphi^+ = -\frac{1 - \zeta^2}{2} + 2\rho_W^B, \quad (8.61)$$

$$\psi^+ = \frac{1}{2}, \quad (8.62)$$

where the parameters

$$\rho_W^T = \int_0^{+\infty} \zeta \varphi e^{-\zeta^2} d\zeta, \quad (8.63)$$

$$\rho_W^B = - \int_{-\infty}^0 \zeta \varphi e^{-\zeta^2} d\zeta. \quad (8.64)$$

The following half-range moments of the two reduced distribution functions, using the half-range Hermite polynomials are defined:

$$M_n^+ = \frac{1}{\sqrt{\pi}} \int_0^{\infty} H_n^+ \varphi e^{-\zeta^2} d\zeta \quad (8.65)$$

$$M_n^- = \frac{1}{\sqrt{\pi}} \int_{-\infty}^0 H_n^- \varphi e^{-\zeta^2} d\zeta \quad (8.66)$$

$$N_n^+ = \frac{1}{\sqrt{\pi}} \int_0^{\infty} H_n^+ \psi e^{-\zeta^2} d\zeta \quad (8.67)$$

$$M_n^- = \frac{1}{\sqrt{\pi}} \int_{-\infty}^0 H_n^- \psi e^{-\zeta^2} d\zeta \quad (8.68)$$

The macroscopic quantities of interest, are given in terms of the half-range moments through the following expressions:

$$\rho = M_0^- + M_0^+ \quad (8.69)$$

$$\tau = \frac{2}{3} (M_2^- + \beta_{2,1}^- M_1^- + N_0^-) + \frac{2}{3} (M_2^+ + \beta_{2,1}^+ M_1^+ + N_0^+) \quad (8.70)$$

$$\begin{aligned} q = & N_1^- + \beta_{1,0}^- N_0^- + M_3^- + \beta_{3,2}^- M_2^- + \beta_{3,1}^- M_1^- + \beta_{3,0}^- M_0^- - \frac{3}{2} (M_1^- + \beta_{1,0}^- M_0^-) + \\ & + N_1^+ + \beta_{1,0}^+ N_0^+ + M_3^+ + \beta_{3,2}^+ M_2^+ + \beta_{3,1}^+ M_1^+ + \beta_{3,0}^+ M_0^+ - \frac{3}{2} (M_1^+ + \beta_{1,0}^+ M_0^+) \end{aligned} \quad (8.71)$$

The boundary conditions are also given in terms of the half-range moments at the top wall ($y = 1/2$) with $\zeta > 0$, as

$$\varphi^+ = \frac{1 - \zeta^2}{2} + 2\sqrt{\pi} \left(M_1^+ + \beta_{1,0}^+ M_0^+ \right), \quad (8.72)$$

$$\psi^+ = -\frac{1}{2} \quad (8.73)$$

and at the bottom wall ($y = -1/2$) with $\zeta > 0$, as

$$\varphi^+ = -\frac{1 - \zeta^2}{2} - 2\sqrt{\pi} \left(M_1^- + \beta_{1,0}^- M_0^- \right), \quad (8.74)$$

$$\psi^+ = \frac{1}{2}. \quad (8.75)$$

The integral operators $\frac{1}{\sqrt{\pi}} \int_{-\infty}^0 (\cdot) \zeta^n e^{-\zeta^2} d\zeta$ and $\frac{1}{\sqrt{\pi}} \int_0^{+\infty} (\cdot) \zeta^n e^{-\zeta^2} d\zeta$ are applied to the kinetic equation (8.54) for φ with $n = 0, 1, 2, 3$ and to (8.55) for ψ with $n = 0, 1$ and after some long algebraic manipulation of the resulting expressions, the following system of ODEs is obtained:

$$\frac{dM_n^+}{dy} = g_n^+ \frac{dM_4^+}{dy} + \delta \sum_{i=0}^3 M_i^+ q_{n,i}^{++} + \delta \sum_{i=0}^3 M_i^- q_{n,i}^{+-} + \delta \sum_{i=0}^1 N_i^+ p_{n,i}^{++} + \delta \sum_{i=0}^1 N_i^- p_{n,i}^{+-} \quad (8.76)$$

$n = 0, 1, 2, 3$

$$\frac{dM_n^-}{dy} = g_n^- \frac{dM_4^-}{dy} + \delta \sum_{i=0}^3 M_i^+ q_{n,i}^{-+} + \delta \sum_{i=0}^3 M_i^- q_{n,i}^{--} + \delta \sum_{i=0}^1 N_i^+ p_{n,i}^{-+} + \delta \sum_{i=0}^1 N_i^- p_{n,i}^{--} \quad (8.77)$$

$n = 0, 1, 2, 3$

$$\frac{dN_n^+}{dy} = f_n^+ \frac{dN_2^+}{dy} + \delta \sum_{i=0}^3 M_i^+ r_{n,i}^{++} + \delta \sum_{i=0}^3 M_i^- r_{n,i}^{+-} + \delta \sum_{i=0}^1 N_i^+ s_{n,i}^{++} + \delta \sum_{i=0}^1 N_i^- s_{n,i}^{+-} \quad (8.78)$$

$n = 0, 1$

$$\frac{dN_n^-}{dy} = f_n^- \frac{dN_2^-}{dy} + \delta \sum_{i=0}^3 M_i^+ r_{n,i}^{-+} + \delta \sum_{i=0}^3 M_i^- r_{n,i}^{--} + \delta \sum_{i=0}^1 N_i^+ s_{n,i}^{-+} + \delta \sum_{i=0}^1 N_i^- s_{n,i}^{--} \quad (8.79)$$

$n = 0, 1$

This is a set of 12 initial value ODEs. The high order moments M_4^\pm and N_2^\pm are calculated integrating the distribution function. The coefficients involved in the above system are given in Appendix E. The initial conditions for this system of ODEs, are obtained by applied the integral operators defined above, to Eqs. (8.72)-(8.75) resulting to the following expressions at the top wall ($y = 1$)

$$M_n^- = v_{n,1}^- M_1^+ + v_{n,0}^- M_0^+ + w_n^-, n = 0, 1, 2, 3, \quad (8.80)$$

$$N_n^- = z_n^-, n = 0, 1 \quad (8.81)$$

and at the bottom wall ($y = 0$)

$$M_n^+ = v_{n,1}^+ M_1^- + v_{n,0}^+ M_0^- + w_n^+, n = 0, 1, 2, 3, \quad (8.82)$$

$$N_n^+ = z_n^+, n = 0, 1, \quad (8.83)$$

with the involved coefficients given in Appendix E. The initial conditions at the bottom boundary for the “positive” moments are given in terms of the values of the “negative” moments at the same point and the other way around at the top boundary.

It is noted that for the system of kinetic equations the boundary conditions at the top boundary (Eqs. (8.72) and (8.73)) are given in terms of the “positive” moments at this node and the boundary conditions for the bottom boundary (Eqs. (8.74) and (8.75)) are given in terms of the respective “negative” moments. The most important aspect of the half-range acceleration scheme is that the accelerated values of the moments are obtained solving the system of moment equations including the corresponding quantities at the boundary nodes. This is the cornerstone of the efficiency of such half-range moment equations when they are used to accelerate the iterative solution of kinetic equations.

The iteration map for this half-range acceleration (HRA) scheme consists of solving the kinetic equations, followed by the computation of the high order moments and the moments involved in the boundary conditions of the moment equations. Then, the system of moment equations is solved in an iterative manner, where the “positive” and “negative” moments are solved separately and the values of the moments in the right hand side of the ODEs are updated, repeating this process until convergence. It is noted, that when the system of moment equations is used for acceleration, the initial

conditions are not updated during the solution of the system and the values obtained from the kinetic step are used. Once the system of moment equations is solved and the macroscopic quantities are obtained they are substituted back into the kinetic equations.

If the high order moments in the right hand side of the ODEs (8.76)-(8.79) are set to zero, then a closed system of equations is obtained, under the initial conditions (8.80)-(8.83). When the system of half-range moment equations is used for the simulation, decoupled from the kinetic equation, due to the half-range nature of the involved moments, the discontinuity of the distribution in the Knudsen layers is inherently treated, increasing the range of application of such schemes, as it will be demonstrated in the next section. This is the so-called HRMM. Another benefit compared to systems of full-range moment equations is that the initial values of the moments are obtained in the same manner as the system itself, i.e., by taking the corresponding moments of the boundary conditions. Thus, although in the full-range moment method the derivation of boundary conditions corresponding to the high order moment equations is problematic, in the half-range moment scheme the initial conditions are obtained in a systematic manner.

8.6 Computational efficiency and accuracy of the developed half-range schemes

The developed half-range schemes HRA and HRMM are compared in terms of computational efficiency and accuracy to the typical DVM without acceleration (NA) and with full-range acceleration scheme (FRA) as well as to the full-range moment method (FRMM).

The computational accuracy is judged by computing for the Poiseuille flow and the heat transfer problems the reduced flow rate and heat flux given by $G = -2 \int_0^1 u dy$ and $Q = q(y) = ct$ respectively. The computational efficiency is compared in terms of the number of iterations and the computational time required for convergence by the different schemes.

Table 8.1 presents the reduced flow rate for the Poiseuille flow for various values of the rarefaction parameter, from the free molecular up to the slip regime, for the Non Accelerated (NA), Full-Range Acceleration (FRA) and Half-Range Acceleration (HRA) schemes. The results of all three approaches are in excellent agreement, which is a

clear indication of the correct implementation of the HRA scheme. The corresponding number of iterations required for convergence of each approach is also presented in Table 8.1. In the free molecular regime (small values of δ), the number of iterations required by all three numerical schemes is very small and more or less the same. As δ is increased the required number of iterations for the NA scheme is rapidly increased, which clearly indicates the very slow convergence rate of the DVM with no acceleration particularly for $\delta > 10$. On the contrary the required number of iterations of the FRA and the HRA schemes is initially increased but then for $\delta \geq 1$ it is constant and practically independent of δ . The speed-up of the convergence rate of the two acceleration schemes is significant. It is interesting to note that the HRA scheme performs better than the FRA scheme. The respective computational time required by the three approaches is also shown in Table 8.1. For small values of δ , the computational effort required by all three methods is similar. As δ is increased both the FRA and HRA schemes are much superior compared to the NA scheme. Comparing the required computational time for convergence between FRA and HRA it is about the same for $\delta < 100$ but for $\delta = 100$ the HRA requires considerable more computational time than the FRA although it requires a smaller number of iterations. This is due to the system of HRA moment equations, that becomes stiff for large values of δ and a more advanced numerical method to solve this system should be used. Overall, it may be stated that for fully developed flows, where the FRA performs really well, the implementation of the HRA does not provide any benefits. This is contributed to the numerical solution of the FRA moment equations which is obtained by the efficient Thomas algorithm and to the boundary conditions which are known a priori and therefore, the main advantage of the HRA is irrelevant for this case.

Next, moving to the heat transfer problem and before perform the comparative study between the approaches, a numerical experiment is performed in order to demonstrate the importance of accelerating the moments at the boundary points, when the outgoing distributions are part of the solution. In this task the NA and FRA schemes are used and the number of iterations required is shown in Table 8.2, along with the corresponding number of iterations required by the two schemes assuming that the boundary condition parameters are known and provided as input. These complimentary schemes are denoted by NA* and FRA*. Starting with the FRA performance, it is clearly seen that although the number of iterations required by the FRA is reduced compared to the NA is reduced, the acceleration is not as substantial as it was in the Poiseuille case. More specifically, for $\delta = 100$ in the Poiseuille flow problem the number

of iterations is reduced by three orders of magnitude, while is the heat transfer problem only by one order. Next, examining the performance of the NA* and the FRA* schemes, it is seen that even in the former one, which involves no acceleration the number of iterations are significantly reduced, while in the latter one, the number of iterations is drastically decreased and its performance is very similar to the FRA performance in the Poiseuille flow. The present numerical experiment proves the importance of accelerating the boundary nodes, which however cannot be done by a purely FRA scheme and this exactly is the motivation for the HRA schemes.

The accuracy of the FRA and HRA schemes for the heat transfer problem is demonstrated in Table 8.3, where an excellent agreement between the computed heat fluxes is observed. Concerning the number of required iterations the effectiveness of the HRA approach compared to the other two is clearly demonstrated in the whole range of δ from the free molecular up to the slip regimes. More specifically, the number of iterations required by the HRA scheme compared to the NA and FRA is reduced up to three and two orders of magnitude respectively. The superiority of the HRA scheme is due to the acceleration of the boundary parameters. The respective computational time required is also tabulated in Table 8.3. Now, the FRA computational time is always larger than that of the NA. The FRA is slower because the number of iterations has not been adequately reduced to counterbalance the increased computational time per iteration and therefore, the overall computational time for convergence of the FRA scheme is larger than that of the NA scheme. On the other hand, the HRA is faster than the NA (except for $\delta = 0$, which is of minor importance). However, the reduction in computational time is by no means comparable to the significant reduction in the number of iterations, which is clearly contributed to the increased computational time per iteration needed to solve the half-range moment system. This becomes more evident for $\delta = 100$, where an increased number of physical nodes is used for the HRA, due to the stiffness of the system. Overall, it may be stated that for the heat transfer problem, where the boundary conditions are part of the solution, the HRA proves to be more efficient than the NA and FRA schemes and it is important to develop more efficient algorithms for the solution of the system of moment equations.

It has been pointed out that the system of moment equations that are used for the acceleration of the iterative map can be solved decoupled from the kinetic equation, closing the system by setting the high order moments equal to zero. It is interesting to study the range of applicability and the accuracy of these moment methods, namely the Full-Range Moment Method (FRMM) and the Half-Range Moment Method (HRMM).

It is noted that for the HRMM the boundary conditions are constructed in a systematic manner, while for the FRMM they are imposed using the macroscopic quantity values at the boundaries. For the Poiseuille flow the boundary conditions for the FRMM are the values of the macroscopic velocity at the boundaries. For the heat transfer problem, three quantities (M_0 , M_2 , N_0) must be specified at each boundary. However, only the temperature and density are known and it is not straightforward to introduce boundary conditions for this system of moment equations.

A comparison in terms of the flow rate and between the typical non-accelerated, the FRMM and the HRMM is shown in Table 8.4. As expected, the moment methods are not accurate for small values of δ , with the FRMM getting close to the NA for $\delta = 100$, while the HRMM is accurate for $\delta > 1$. It is noted that if slip boundary conditions were used for the FRMM, the accuracy would improve. It is unexpected and rather surprising however, that the HRMM produces accurate results even in the transition regime. The comparison between the heat flux given by the NA and HRMM is shown in Table 8.5 for the heat transfer problem. Now, the HRMM turns to be accurate in the whole range of gas rarefaction, which again is not expected. The ability of half-range moment methods to simulate gas flows in the whole range of the Knudsen number observed here, has been also reported in [237] and it is field where further research is needed.

Since the half-range moment methods can be used decoupled from the kinetic equations starting from the transition regime, it is reasonable to wonder why the half-range acceleration schemes are considered. One of the reasons is that for more general cases, the half-range moment methods could prove to be less accurate, while the accuracy of the acceleration scheme is guaranteed since the kinetic equation is solved. Furthermore, the acceleration of the boundary nodes is a first step towards the acceleration of the nonlinear kinetic equations.

8.7 Concluding remarks

Synthetic acceleration schemes to speed-up the iterative solution of linearized kinetic equations have been developed in recent years based on the full-range moments of the distribution function. Such schemes have been successfully applied to fully developed flows through capillaries, providing a considerable acceleration of the convergence rate of the iteration map. However, their implementation is limited by the fact that the moments at the boundary nodes are not accelerated, which is especially detrimental

in cases where the boundary condition parameters are part of the solution. Here, the acceleration of the boundary nodes is achieved utilizing half-range moments of the distribution function and the corresponding half-range schemes are developed and implemented. Operating accordingly on the kinetic equations a system of moment equations is obtained for the interior as well as for the boundary nodes of the physical grid. The boundary conditions of the moment equations are derived in a consistent manner similar to the one for the moment equations. The iterative map includes the kinetic equations, the higher order moments computed by accordingly integrating the distribution function and the system differential equations for the accelerated moments.

The channel Poiseuille flow and the heat transfer between two plates are applied in order to indicate the computational accuracy and efficiency of the developed schemes. In the Poiseuille flow, where the boundary conditions are known a priori the half-range acceleration schemes do not provide a considerable benefit compared to the full-range ones. However, in the heat transfer problem, where the boundary conditions are part of the solution, the half-range acceleration scheme proves to be superior to the full-range one, both in terms of the number of iterations and the computational time required.

Finally, solving the half-range moment equations decoupled from the kinetic equations provides accurate results for the heat transfer case in the whole range of gas rarefaction and for the Poiseuille case from the transition up to the slip regimes. The accuracy of the half-range moment method in a range of the Knudsen number, much wider than expected, is attributed to the ability of the half-range moments to incorporate the discontinuity of the distribution function. In the Poiseuille flow the half-range moment method is not accurate from the transition down to the free molecular regimes, because the moment method does not inherit the degenerate nature of the kinetic equation for this flow, that predicts an infinite flow rate in the free molecular limit.

Accelerating the boundary nodes makes acceleration schemes applicable to a larger range of rarefied gas flow and heat transfer configurations. However, the analysis is still limited to problems where the kinetic equation can be linearized. Accelerating the boundary nodes is an important step towards acceleration schemes for the nonlinear kinetic equations although a number of obstacles towards this goal exists. As mentioned the involved system of equations for the half-range acceleration is a stiff system and a suitable numerical scheme should be introduced. A limitation of this kind of schemes is that the range of integration for the moments is directed by the configuration boundaries, so although it is straightforward to construct such schemes when the boundaries are aligned with the coordinate system axes it can be cumbersome for

arbitrary geometries. A promising next step of this work is to introduce a hybrid scheme, where half-range moments are used in the Knudsen layer and full-range ones in the rest of the flow field, and since the half-range scheme is used locally, application to arbitrary geometries would be easier to tackle.

Table 8.1 Reduced flow rate, number of iterations and computational time in seconds for the Non-Accelerated (NA), Full-Range Acceleration (FRA) and Half-Range Acceleration (HRA) schemes (Poiseuille flow).

δ	Flow Rate			Number of iterations			Computational time (s)		
	NA	FRA	HRA	NA	FRA	HRA	NA	FRA	HRA
0.01	3.0496	3.0496	3.0499	6	6	5	0.25	0.26	0.28
0.1	2.0327	2.0327	2.0332	9	9	6	0.37	0.36	0.31
1	1.5387	1.5387	1.5392	27	22	6	1.08	0.91	0.33
10	2.7686	2.7686	2.7696	342	27	6	13.5	1.12	0.55
100	17.6905	17.6933	17.7899	18498	27	6	779	1.11	8.17

Table 8.2 Number of iterations required by the (NA) and (FRA) and the respective values when the boundary condition parameters are given (NA*) and (FRA*) (heat transfer)

δ	Number of iterations			
	NA	FRA	NA*	FRA*
0.1	75	75	6	6
1	19	17	17	15
10	321	111	166	29
100	19296	888	7183	31

Table 8.3 Reduced flow rate, number of iterations and computational time in seconds for the Non-Accelerated (NA), Full-Range Acceleration (FRA) and Half-Range Acceleration (HRA) schemes (Poiseuille flow).

δ	Heat flux			Number of iterations			Computational time (s)		
	NA	FRA	HRA	NA	FRA	HRA	NA	FRA	HRA
0	0.5642	0.5642	0.5642	2	2	2	0.0007	0.03	0.015
0.01	0.5599	0.5599	0.5599	546	546	4	0.19	6.1	0.031
0.1	0.5276	0.5276	0.5276	75	75	5	0.03	0.86	0.031
1	0.3616	0.3616	0.3616	19	17	6	0.015	0.19	0.031
10	0.09918	0.09918	0.09911	321	111	6	0.12	1.26	0.031
100	0.01218	0.01218	0.01218	16296	888	10	5.44	9.81	1.83

Table 8.4 Flow rate for the Non Accelerated (NA), Full-Range Moment Method (FRMM) and Half-Range Moment Method (HRMM) (Poiseuille flow).

δ	Flow Rate		
	NA	FRMM	HRMM
0.01	3.0496	1.6667(-3)	1.3181
0.1	2.0327	1.6667(-2)	1.3488
1	1.5387	1.6667(-1)	1.5374
10	2.7686	1.6667	2.7874
100	17.6905	16.6667	17.7997

Table 8.5 Heat flux for the Non Accelerated (NA) and Half-Range Moment Method (HRMM) (heat transfer).

δ	Heat flux	
	NA	HRMM
0	0.5642	0.5642
0.01	0.5599	0.5599
0.1	0.5276	0.5259
1	0.3616	0.3588
10	0.09918	0.09912
100	0.01218	0.01218

Chapter 9

Concluding remarks

9.1 Summary and contributions

The context of this dissertation includes the development and implementation of advanced deterministic and stochastic kinetic modeling in solving non-equilibrium gaseous transport phenomena at microscale level. The proposed numerical schemes are related to certain advancements of the well-known discrete velocity (DVM) and direct simulation Monte Carlo (DSMC) methods. The effectiveness and validity of the introduced methodologies has been demonstrated by solving prototype problems in rarefied gas dynamics and then, these new approaches have been implemented to investigate and understand the underlying physics of unexpected phenomena observed in gas flows and heat transfer far from local equilibrium. In addition, based on computationally efficient and advanced modeling, various flow and heat transfer configurations, encountered in the design of various devices with miniaturized sizes and/or operating under low pressure (or density) conditions, have been simulated.

Pressure driven rarefied gas flows are modeled in Chapter 3. Kinetic equations with an acceleration term, modeling flows in the presence of an external force, are numerically solved, based on the method of characteristics. Upon introducing the characteristic variables the force term is eliminated from the streaming part of the equation and is incorporated into the collision term and in the expressions for the macroscopic quantities. This semi analytical – computational methodology is implemented in the solution of the nonlinear BGK model equation modeling the force driven fully developed Poiseuille flow between parallel plates. The obtained mass and heat flow rates, as well as the distributions of macroscopic quantities, are in very good agreement with the corresponding published results for this configuration. A comparison of the reduced

flow rate with the corresponding results provided by the infinite capillary theory is performed, finding out that the later methodology being accurate even for large values of the external force. Another interesting finding is the form of the distribution function, since the external force acting on the gas molecules may result to strongly non-equilibrium multimodal distribution functions with long tails. Next, in the same chapter, the range of validity of the so-called implicit boundary conditions has been investigated. The nonlinear BGK model is used to simulate the pressure driven flow rarefied gas flow through a plane channel and a tube using the typical configuration with the inlet and outlet regions and the one with the implicit boundary conditions omitting the two regions at the capillary ends. A comparison is performed based on the computed flow rates of the two configurations in a wide range of the parameters characterizing the flow, namely the ratio of the outlet over the inlet pressures, the dimensionless capillary length and the reference rarefaction parameter. It is found that the dimensionless length is the most important parameter affecting the error. For capillaries of small length the relative error may be unacceptable large dropping below 20% only for capillaries with dimensionless length larger than ten. The range of validity is increased introducing the end effect theory, where the actual capillary length is corrected to account for the end effects. In this case the deviation of the flow rates is less than 15% for capillaries with dimensionless length larger than five. It is concluded that the range of validity of the implicit boundary conditions is limited. Furthermore, the infinite capillary theory is valid in the same range of parameters as the implicit boundary condition formulation when they are both coupled with the end effect theory with the latter one requiring larger computational effort but being able to simulate a boarder range of phenomena.

The extension of the Discrete Velocity Method to unstructured grids is performed in Chapter 4. The proposed methodology utilizes the so-called marching schemes which are typically implemented on structured grids and yields the solution without requiring the solution of a system of algebraic equations. The main obstacle is obtaining the proper node marching sequence through the mesh, since following an erroneous path will lead to collapse of the algorithm. Two methodologies are developed able to obtain the correct marching sequence. The first one relies on generic geometrical arguments and the second one on a backtracking algorithm. The former one is more computationally efficient but in a limited number of cases may provide an erroneous sequence, while the latter one is more robust but computationally demanding. In the present implementation both methodologies are used, with the geometrical method

always being the first choice and introducing the backtracking algorithm as the second choice only when the geometrical approach fails. The developed marching DVM code on unstructured meshes is successfully benchmarked in several rarefied gas flows and heat transfer configurations in convex and non-convex domains using both linear and nonlinear kinetic models.

Thermally driven flow configurations with application in the design of micro pumps are examined in Chapter 5. The configurations include channels with saw-tooth surfaces, tapered channels and curved channels. The saw-tooth channel configuration is appealing as the walls are kept at constant temperatures and the flow is driven by the thermal stress slip flow phenomenon. Although the ability of this configuration to produce a mass flow rate is demonstrated, the mass flow rate is very sensitive to the flow parameters and can even change direction by altering the reference pressure. More importantly, the heat flux close to the boundaries in the gas side takes very large values, making temperature control a daunting task. The concept of utilizing the diodicity effect created by tapered channels in the design of a multistage assembly is next examined. Simulations are conducted for single converging and diverging channels for the limiting cases for zero pressure difference and zero net mass flow rate, as well as the intermediate cases, for a wide range of the involved parameters, providing, a detailed study for the channel inclination ratio and the working pressure parameters. In the limiting case of vanishing net mass flow rate, the pressure difference is always increased with the inclination ratio and depending on the inlet pressure it may be larger for either converging or diverging channels. In the limiting case of vanishing pressure difference, the mass flow rate is always decreased with the inclination ratio being always higher for the diverging channel. The performance characteristic curves are extracted providing a complete picture of the pumping effect of this configuration and the optimal working conditions are identified. Cascades of tapered channels are also considered and the potential implementation of such configurations in multistage assemblies is demonstrated. For completeness purposes, the potential design of pumping stages consisting of straight and curved channels is examined, considering only single channel elements. A parametric analysis is performed for the two limiting cases and the potential of this configuration is reaffirmed.

In the framework of the DSMC method, a novel methodology decomposing the DSMC solution into its ballistic and collision parts is developed, in Chapter 6, providing insight information about the microstructure of the flow. The ballistic part refers to particles arriving at some point of the flow domain directly from the boundaries with no

collisions, while the collision part refers to particles arriving after an arbitrary number of collisions with other particles. This technique is applied to interpret non-equilibrium phenomena arising in thermally induced flow and heat transfer configurations in cavities, explaining the presence of unexpected non-equilibrium flow adjacent to the non-isothermal wall. The decomposition methodology has been also applied to pressure driven fully developed flows through long capillaries to provide a complete quantitative description of the celebrated Knudsen minimum appearing in the transition regime. In all cases based on the decomposition technique a physical explanation to the interesting transport phenomena observed is provided.

The uncertainty propagation in some typical rarefied gas dynamics configurations is considered in Chapter 7. More specifically, the examined configurations include pressure and temperature driven flow through long tubes and heat transfer between parallel plates. In all problems the effect of the uncertainties of the input parameters (geometry, pressure, temperature, pipe roughness) on the uncertainty of the output quantities (flow rate, pressure difference, heat flux) is thoroughly analyzed. In pressure and thermally driven flows the analysis is focused on the produced mass flow rate and in the thermomolecular pressure difference phenomenon on the generated pressure difference. In the heat transfer flow the uncertainty analysis is focused on the heat flux. The uncertainty propagation analysis is performed using the Monte Carlo method. In general, it may be stated that in the pressure driven flow the radius uncertainty is the most important one, while in the temperature driven and heat transfer flows the temperature uncertainty is the predominant one. Furthermore, the uncertainty of the driving force (pressure or temperature difference) leads to very large values of uncertainty when the driving force takes small values.

The extension of synthetic acceleration schemes of the slow convergence of the iterative map of the DVM, is investigated in Chapter 8. So far, the available synthetic acceleration schemes are based on full-range Hermite polynomials deriving a set of moment equations accelerating the macroscopic quantities only in the interior nodes of the physical domain. It is computationally demonstrated that accelerating the boundary nodes is crucial in the general case, where the boundary conditions are part of the solution. The proposed methodology is based on half-range Hermite polynomials and the derived system of half-range moment equations are accelerating the macroscopic quantities in the interior as well as in the boundary nodes of the physical domain. The developed half-range synthetic acceleration schemes are applied to one-dimensional flow and heat transfer configurations clearly indicating their computational efficiency.

Overall, in the course of the present work both theoretical and computational advancements have been achieved. Novel numerical schemes have been developed, existing ones have been extended, interesting and counterintuitive phenomena have been analyzed in a systematic manner and flow and heat transfer configurations of interest in the design of various devices are simulated. To sum up, the most important contributions of this dissertation may be outlined as follows:

Computational advancements:

- Development and implementation of an analytical - numerical scheme simulating kinetic model equations with external force term.
- Development and implementation of a geometric type methodology enabling the extension of the efficient marching schemes in DVM algorithms to unstructured meshes.
- Development and implementation of a computational methodology decomposing the DSMC solution into ballistic and collision parts.
- Development and implementation of a half-range synthetic acceleration scheme speeding-up the slow convergence of the iterative map of the DVM algorithm.

Theoretical advancements:

- Observation of multimodal distribution functions with long tails in the presence of external force fields
- Physical explanation and quantitative justification of unexpected non-equilibrium phenomena appearing in boundary heated cavities, based on the DSMC solution decomposition methodology.
- Physical explanation and quantitative justification of the Knudsen minimum, based on the DSMC solution decomposition methodology.

Technological advancements:

- Specification of the range of validity of the so-called implicit boundary conditions with respect to the flow parameters in pressure driven flows.
- Parametric investigation of thermally driven micropumps using various geometrical configurations.

- Uncertainty propagation analysis in rarefied gas flow and heat transfer configurations based on the Monte Carlo method.

9.2 Future work

The present work covers a broad range of topics in the field of rarefied gas dynamics and non-equilibrium transport phenomena. Most of the material presented here, may be further advanced or it may be implemented to model and simulate other phenomena. Some indicative areas of future work are outlined.

In pressure driven flows the numerical – computational methodology introduced to tackle the external force term which may be present in the governing kinetic equations may be implemented to more complex configurations, such as flows of charged particles in the presence of electric and magnetic fields. It could also be interesting to investigate the implementation of relative approaches in the Lattice Boltzmann Method, in kinetic simulations based on the DVM. Furthermore, the range of applicability of the implicit boundary conditions may be investigated in pressure driven flows of polyatomic gases, as well as of mixtures of gases.

The implementation of DVM algorithms on unstructured meshes has a lot of potential and should be further investigated. Consistent higher order schemes may be introduced for the distribution propagation in the physical space. A hybrid parallelization approach (MPI+OpenMP) should be also applied in order to tackle larger domains and more complex flow configurations. The extension of the developed methodology to three dimensions in the physical space may be also considered. Another feature that is already under development is the implementation of adaptive mesh refinement in the physical space.

The design of thermally driven micropumps is a promising and emerging technological field. The present modeling which is based on parallel plates could be extended to orthogonal ducts. A larger range of configurations can be considered, with combinations of converging or diverging and uniform channels. Furthermore, configurations where the channel geometry is varying along the cascade could be investigated, so that in combination with the varying pressure, the optimal operational conditions serving the specific needs are maintained. Also, in order to increase the mass flow rate, configurations with pumping stages consisting of multiple parallel channels, could be introduced.

The decomposition of the DSMC into ballistic and collision parts is a powerful methodology capable of providing a better insight and thorough understanding of many non-equilibrium phenomena and paradoxes, such as the well-known inverted velocity profile in the cylindrical Couette flow with partial wall accommodation and the anomalous temperature profile in the Poiseuille flow. Extension of this approach to binary gas mixtures may help better understand gas separation and mixing. In addition, the implementation of this methodology to deterministic modeling remains an open and very challenging issue.

The uncertainty propagation in rarefied gas modeling is an important topic and the proposed methodology could be applied to many configurations with practical interest. It is recommended to always perform such an uncertainty analysis in comparing numerical and experimental results. A possible extension includes flow and heat transfer configurations with gas mixtures where the effect of the concentration uncertainty may play a significant role. Furthermore, the application of more advanced methodologies such as the polynomial chaos can be considered in order to apply the uncertainty propagation in problems, where the Monte Carlo method is very time consuming.

The developed half-range synthetic acceleration scheme is still in a preliminary stage. Certain steps must be taken to ensure its applicability and effectiveness in more realistic multi-dimensional problems. The main issue under future investigation should include the implementation of fast solvers of the systems on moment equations, as well as the extension of the whole approach in more complex geometries. Furthermore, full and half-range acceleration schemes could be coupled, with the half-range applied in the Knudsen layer close to the boundaries and the full-range in the rest of the flow domain. Another future challenging step is the formulation of acceleration schemes for the nonlinear kinetic equations.

Overall, it is hoped that the present work will prove useful to the scientific communities in rarefied gas dynamics, vacuum science and technology and gaseous microfluidics, as well as that the developed numerical schemes, methodologies and approaches will generate more research.

Appendix A

Formulation of the implicit boundary conditions

The one-dimensional characteristic form of the Euler equations is [242]

$$\frac{dU}{a} = \pm \frac{d\rho}{\rho}, \quad (\text{A.1})$$

where U is the velocity in the characteristic direction, ρ is the gas mass density and $a = \sqrt{\gamma RT} = \sqrt{dP/d\rho}$ is the local speed of sound, with

$$\frac{dU}{a} = \pm \frac{dP}{a^2 \rho}, \quad (\text{A.2})$$

where the definition of the speed of sound has been used. Introducing the dimensionless variables of Eq. (3.70), as well as $\rho/\rho_{in} = P/P_{in}$ into Eq. (A.2) yields

$$du = \pm \frac{dp}{n\sqrt{2\gamma\tau}}. \quad (\text{A.3})$$

In Eq. (A.3) the plus sign corresponds to a forward moving wave, i.e., a wave that moves in the positive direction along the characteristic line and the minus sign in the opposite direction. In both cases z is the characteristic direction. Thus, the plus sign denotes a wave entering from the capillary inlet at $z = -L/(2\chi)$, while the minus sign denotes a wave entering from the capillary outlet at $z = L/(2\chi)$.

For some arbitrary node j , across the two ends of the capillary, Eq. (A.3) can be written as $u_j - u_{in,j} = \frac{p_j - p_{in,j}}{n_j \sqrt{2\gamma\tau_j}}$ for the inlet and $u_{out,j} - u_j = -\frac{p_{out,j} - p_j}{n_j \sqrt{2\gamma\tau_j}}$ for the outlet. Rearranging the terms and substituting $p_{in} = 1$ and $p_{out} = P_{out}/P_{in}$ the boundary conditions for the inlet and outlet velocities are found to be

$$u_{in,j} = u_j + \frac{1 - p_j}{n_j \sqrt{2\gamma\tau_j}}, \quad (\text{A.4})$$

and

$$u_{out,j} = u_j + \frac{p_j - P_{out}/P_{in}}{n_j \sqrt{2\gamma\tau_j}} \quad (\text{A.5})$$

respectively. For the number density and temperature at the inlet, the reference values are taken

$$n_{in,j} = 1 \text{ and } \tau_{in,j} = 1. \quad (\text{A.6})$$

Furthermore, the definition of the speed of sound, using the dimensionless variables of Eq. (3.70), becomes $dn = dp/(\gamma\tau)$. Then, for some arbitrary node j at the capillary outlet it becomes $n_{out,j} - n_j = \frac{p_{out,j} - p_j}{\gamma\tau_j}$ and re-arranging the terms the boundary conditions for the number density at the capillary outlet is found to be

$$n_{out,j} = n_j + \frac{P_{out}/P_{in} - p_j}{\gamma\tau_j}. \quad (\text{A.7})$$

Finally, the temperature at the outlet is given by the equation of state

$$\tau_{out,j} = \frac{P_{out}/P_{in}}{n_{out,j}}. \quad (\text{A.8})$$

Two sets of equations are formed giving the boundary condition parameters. The set of equations (A.4) and (A.6) are applied at the inlet and Eqs. (A.5), (A.7) and (A.8) at the outlet.

Appendix B

Formulation of fully developed, linear and non-linear flows solved based on the marching DVM algorithm on unstructured meshes

Simulations conducted by the marching DVM algorithm on unstructured meshes developed in Chapter 4 are separated into three categories, fully developed flows, linear cases and non-linear cases. The formulation of the considered cases is presented here. The solution methodology remains the same for each type of simulation, even if the equations involved are different. It is also noted that simulations are performed using the dimensionless form of the equations. In all cases the dimensionless molecular velocity is defined as $\zeta = \xi/v_0$, where $v_0 = \sqrt{2R_g T_0}$ is the most probable molecular velocity, with R_g and T_0 denoting the gas constant and the reference temperature respectively.

B.1 Fully developed flows

In fully developed flows the linearized BGK kinetic model equation is written as [23], [182], [228]

$$\zeta_x \frac{\partial h_i}{\partial x} + \zeta_y \frac{\partial h_i}{\partial y} = \delta(u_{z,i} - h_i) + S_i \quad (\text{B.1})$$

where $i = P, T$ refers to the pressure and temperature driven flows, respectively and h_i is the perturbation of the distribution function. The macroscopic velocity is given by

$$u_{z,i} = \frac{u'_{z,i}}{v_0 X_i} = \int_{R^2} h_i e^{-\zeta^2} d\zeta \quad (\text{B.2})$$

where u'_z is the dimensional velocity. The dimensionless gradients are denoted as X_i and defined as $X_P = \frac{H}{P_0} \frac{dP}{dz}$ and $X_T = \frac{H}{T_0} \frac{dT}{dz}$, where H is the characteristic length of the configuration. The source terms are $S_P = -\frac{1}{2}$ and $S_T = -\frac{\zeta^2 - 1}{2}$ for the pressure and temperature driven flows respectively. The rarefaction parameter is defined as

$$\delta = \frac{P_0 H}{\mu v_0} \quad (\text{B.3})$$

where μ is the viscosity at temperature T_0 .

In fully developed flows the linearized Shakhov kinetic model equation is written as [23], [156], [174], [180]

$$\zeta_x \frac{\partial \varphi_i}{\partial x} + \zeta_y \frac{\partial \varphi_i}{\partial y} + = \delta \left[u_{z,i} + \frac{2}{15} q_{z,i} (\zeta^2 - 1) - \varphi_i \right] + S_i^h \quad (\text{B.4})$$

$$\zeta_x \frac{\partial \psi_i}{\partial x} + \zeta_y \frac{\partial \psi_i}{\partial y} + = \delta \left[\frac{3}{2} u_{z,i} + \frac{1}{5} q_{z,i} \zeta^2 - \psi_i \right] + S_i^p \quad (\text{B.5})$$

where the source terms for the pressure driven flow are $S_P^\varphi = -\frac{1}{2}$, $S_P^\psi = -\frac{3}{4}$ while for the temperature driven flow they become $S_T^\varphi = -\frac{1}{2} (\zeta^2 - 1)$, $S_T^\psi = -\frac{3}{4} \zeta^2$. The velocity and heat flux in this case are given by

$$u_{z,i} = \frac{u'_{z,i}}{v_0 X_i} = \int_{R^2} \varphi_i e^{-\zeta^2} d\zeta \quad (\text{B.6})$$

$$q_{z,i} = \frac{Q_{z,i}}{P_0 v_0 X_i} = \int_{R^2} \left[(\zeta^2 - 5/2) \varphi_i + \psi_i \right] e^{-\zeta^2} d\zeta \quad (\text{B.7})$$

The outgoing distributions for Maxwell diffuse-specular boundary conditions are for the BGK model $h_i^+ = (1 - \alpha) h_i^-$ while for the Shakhov model $\varphi_i^+ = (1 - \alpha) \varphi_i^-$ and $\psi_i^+ = (1 - \alpha) \psi_i^-$. The superscripts (+) and (−) denote the outgoing and incoming distributions respectively.

B.2 Linear flows

Linear kinetic theory can be applied in the cases where the driving force is relatively small. For example in the case of a flow driven by a moving wall or due to a temperature

difference, this small parameter can be the ratio of the wall velocity over the most probable molecular velocity $\varepsilon = U_W/\nu_0$ or the ratio of the small temperature difference over the characteristic temperature $\varepsilon = \Delta T/T_0$, respectively. The formulation of the kinetic equations is independent of the driving force and the small parameter ε , which is only used in the dimensionalization process.

An expansion of the distribution function f around a reference value f^0 using $f = f^0 (1 + \varepsilon g)$ is performed. Introducing this expansion the kinetic equation for the perturbed distribution function g is obtained and it may be written as [55], [157], [188], [243]

$$\zeta_x \frac{\partial g}{\partial x} + \zeta_y \frac{\partial g}{\partial y} = \delta [g^{eq} - g], \quad (\text{B.8})$$

where the equilibrium distributions for the BGK and Shakhov models are as follows: BGK:

$$g^{eq} = \rho + 2\boldsymbol{\zeta} \cdot \mathbf{u} + \tau \left(\zeta^2 - \frac{3}{2} \right) \quad (\text{B.9})$$

Shakhov:

$$g^{eq} = \rho + 2\boldsymbol{\zeta} \cdot \mathbf{u} + \tau \left(\zeta^2 - \frac{3}{2} \right) + \frac{4}{15} \boldsymbol{\zeta} \cdot \mathbf{q} \left(\zeta^2 - 5/2 \right) \quad (\text{B.10})$$

Upon applying the projection procedure, Eq. (B.8) results to the following system of equations:

$$\zeta_x \frac{\partial \varphi}{\partial x} + \zeta_y \frac{\partial \varphi}{\partial y} = \delta [\varphi^{eq} - \varphi] \quad (\text{B.11})$$

$$\zeta_x \frac{\partial \psi}{\partial x} + \zeta_y \frac{\partial \psi}{\partial y} = \delta [\psi^{eq} - \psi] \quad (\text{B.12})$$

The equilibrium distributions for the BGK and Shakhov models are:

$$\varphi^{eq} = \rho + 2\boldsymbol{\zeta} \cdot \mathbf{u} + \tau \left(\zeta^2 - 1 \right), \psi^{eq} = \frac{\tau}{2} \quad (\text{B.13})$$

$$\varphi^{eq} = \rho + 2\boldsymbol{\zeta} \cdot \mathbf{u} + \tau \left(\zeta^2 - 1 \right) + \frac{4}{15} \boldsymbol{\zeta} \cdot \mathbf{q} \left(\zeta^2 - 2 \right), \psi^{eq} = \frac{\tau}{2} + \frac{2}{15} \boldsymbol{\zeta} \cdot \mathbf{q} \quad (\text{B.14})$$

The reduced distribution functions are defined as

$$\varphi = \frac{1}{\sqrt{\pi}} \int_{-\infty}^{+\infty} g e^{-\zeta_z^2} d\zeta_z \quad (\text{B.15})$$

$$\psi = \frac{1}{\sqrt{\pi}} \int_{-\infty}^{+\infty} \left(\zeta_z^2 - \frac{1}{2} \right) g e^{-\zeta_z^2} d\zeta_z \quad (\text{B.16})$$

The macroscopic quantities in terms of the reduced distribution functions are given by the following expressions:

Number density:

$$\rho = \frac{N - N_0}{N_0 \varepsilon} = \frac{1}{\pi} \int_{R^2} \varphi e^{-\zeta^2} d\zeta \quad (\text{B.17})$$

Velocity vector:

$$u_i = \frac{U_i}{v_0 \varepsilon} = \frac{1}{\pi} \int_{R^2} \zeta_i \varphi e^{-\zeta^2} d\zeta \quad (\text{B.18})$$

Temperature:

$$\tau = \frac{T - T_0}{T_0 \varepsilon} = \frac{2}{3\pi} \int_{R^2} \left[(\zeta^2 - 1) \varphi + \psi \right] e^{-\zeta^2} d\zeta \quad (\text{B.19})$$

Stress tensor:

$$p_{i,j} = \frac{P_{i,j}}{2P_0 \varepsilon} = \frac{1}{\pi} \int_{R^2} \zeta_i \zeta_j \varphi e^{-\zeta^2} d\zeta, i \neq j \quad (\text{B.20})$$

Heat flux vector:

$$q_i = \frac{Q_i}{P_0 v_0 \varepsilon} = \frac{1}{\pi} \int_{R^2} \zeta_i \left[(\zeta^2 - 2) \varphi + \psi \right] e^{-\zeta^2} d\zeta \quad (\text{B.21})$$

Pressure perturbation:

$$p = \frac{P - P_0}{P_0 \varepsilon} = \rho + \tau \quad (\text{B.22})$$

The boundary conditions at some node i that belongs in B_k^+ for the polar angle θ_k and for the molecular velocity magnitude ζ_m , for the different cases, are formulated as follows:

- Diffuse:

$$\varphi_i^+ = \rho_{W,i} + 2\zeta \cdot \mathbf{u}_{W,i} + \tau_{W,i} (\zeta^2 - 1), \psi_i^+ = \tau_{W,i}/2 \quad (\text{B.23})$$

where ρ_W is a quantity used to satisfy the impermeability condition and is calculated as

$$\rho_{W,i} = - \frac{\int_{\mathbf{n}_i \cdot \boldsymbol{\zeta} < 0} (\mathbf{n}_i \cdot \boldsymbol{\zeta}) \varphi_i^- e^{-\zeta^2} d\boldsymbol{\zeta} + \int_{\mathbf{n}_i \cdot \boldsymbol{\zeta} > 0} (\mathbf{n}_i \cdot \boldsymbol{\zeta}) \left[2\boldsymbol{\zeta} \cdot \mathbf{u}_{W,i} + \tau_{W,i} (\zeta^2 - 1) \right] e^{-\zeta^2} d\boldsymbol{\zeta}}{\int_{\mathbf{n}_i \cdot \boldsymbol{\zeta} > 0} (\mathbf{n}_i \cdot \boldsymbol{\zeta}) e^{-\zeta^2} d\boldsymbol{\zeta}} \quad (\text{B.24})$$

with $\mathbf{u}_W = \mathbf{U}_W / (v_0 \varepsilon)$ and $\tau_W = (T_W - T_0) / (T_0 \varepsilon)$.

- Specular:

The outgoing distribution is given in terms of the incoming distribution as $\varphi_i^+ = \varphi_i^R$ and $\psi_i^+ = \psi_i^R$ where φ_i^R and ψ_i^R for some molecular velocity $\boldsymbol{\zeta}$ are connected to the incoming distribution through the expressions $\varphi_i^R(\boldsymbol{\zeta}) = \varphi_i^-(\boldsymbol{\zeta} - 2(\mathbf{n}_i \cdot \boldsymbol{\zeta}) \cdot \mathbf{n}_i)$ and $\varphi_i^R(\boldsymbol{\zeta}) = \varphi_i^-(\boldsymbol{\zeta} - 2(\mathbf{n}_i \cdot \boldsymbol{\zeta}) \cdot \mathbf{n}_i)$.

- Diffuse-Specular:

The outgoing distributions are:

$$\varphi_i^+ = (1 - \alpha) \varphi_i^R + \alpha \left[\rho_{W,i} + 2\boldsymbol{\zeta} \cdot \mathbf{u}_{W,i} + \tau_{W,i} (\zeta^2 - 1) \right], \psi_i^+ = (1 - \alpha) \psi_i^R + \alpha (\tau_{W,i} / 2) \quad (\text{B.25})$$

The accommodation coefficient $\alpha \in (0, 1)$ is denoting the percentage of particles undergoing purely diffusive emission and the parameter ρ_W is now given by

$$\rho_{W,i} = - \frac{1}{\alpha \int_{\mathbf{n}_i \cdot \boldsymbol{\zeta} > 0} (\mathbf{n}_i \cdot \boldsymbol{\zeta}) e^{-\zeta^2} d\boldsymbol{\zeta}} \left[\int_{\mathbf{n}_i \cdot \boldsymbol{\zeta} < 0} (\mathbf{n}_i \cdot \boldsymbol{\zeta}) \varphi_i^- e^{-\zeta^2} d\boldsymbol{\zeta} + \alpha \int_{\mathbf{n}_i \cdot \boldsymbol{\zeta} > 0} (\mathbf{n}_i \cdot \boldsymbol{\zeta}) \left[2\boldsymbol{\zeta} \cdot \mathbf{u}_{W,i} + \tau_{W,i} (\zeta^2 - 1) \right] e^{-\zeta^2} d\boldsymbol{\zeta} + (1 - \alpha) \int_{\mathbf{n}_i \cdot \boldsymbol{\zeta} > 0} (\mathbf{n}_i \cdot \boldsymbol{\zeta}) \varphi_i^R e^{-\zeta^2} d\boldsymbol{\zeta} \right] \quad (\text{B.26})$$

- Open:

In open boundaries, the incoming distributions are given by Eq. (B.23), while the quantity ρ_W is replaced by the number density perturbation of the incoming gas stream as

$$\rho_i = (N_i - N_0) / (N_0 \varepsilon) \quad (\text{B.27})$$

- Periodic:

In the case of periodic boundaries, the distribution arriving at some position of one boundary is the outgoing distribution at the corresponding point at the other boundary. When those boundaries are not parallel, the appropriate rotation of the molecular velocity is performed.

B.3 Nonlinear flows

Nonlinear kinetic modeling is the most general approach and is applied when no assumptions or simplifications can be made. The kinetic equation, on the basis of the dimensionless distribution function $g = f v_0^3 / N_0$ can be written as [75], [158], [201], [223]

$$\zeta_x \frac{\partial g}{\partial x} + \zeta_y \frac{\partial g}{\partial y} = \delta_0 n \tau^{1-\omega} [g^{eq} - g]. \quad (\text{B.28})$$

The equilibrium distribution for the BGK model is $g^{eq} = g^M$, where

$$g^M = \frac{\rho}{(\pi\tau)^{3/2}} \exp \left[-\frac{(\boldsymbol{\zeta} - \mathbf{u})^2}{\tau} \right] \quad (\text{B.29})$$

is the local Maxwellian distribution and for the Shakhov model

$$g^{eq} = g^M \left(1 + \frac{4}{15} \frac{\mathbf{q} \cdot (\boldsymbol{\zeta} - \mathbf{u})}{\rho\tau^2} \left[\frac{(\boldsymbol{\zeta} - \mathbf{u})^2}{\tau} - \frac{5}{2} \right] \right) \quad (\text{B.30})$$

Upon applying the projection procedure, Eq. (B.28) results to the following system of equations:

$$\zeta_x \frac{\partial \varphi}{\partial x} + \zeta_y \frac{\partial \varphi}{\partial y} = \delta_0 n \tau^{1-\omega} [\varphi^{eq} - \varphi] \quad (\text{B.31})$$

$$\zeta_x \frac{\partial \psi}{\partial x} + \zeta_y \frac{\partial \psi}{\partial y} = \delta_0 n \tau^{1-\omega} [\psi^{eq} - \psi] \quad (\text{B.32})$$

The equilibrium distributions for the BGK model are the respective Maxwellian distributions

$$\varphi^M = \frac{\rho}{\pi\tau} \exp \left[-\frac{(\boldsymbol{\zeta} - \mathbf{u})^2}{\tau} \right] \quad (\text{B.33})$$

$$\psi^M = \frac{\rho}{2\pi} \exp \left[-\frac{(\boldsymbol{\zeta} - \mathbf{u})^2}{\tau} \right] \quad (\text{B.34})$$

while for the Shakhov model they become

$$\varphi^{eq} = \varphi^M \left(1 + \frac{4}{15} \frac{\mathbf{q} \cdot (\boldsymbol{\zeta} - \mathbf{u})}{\rho\tau^2} \left[\frac{(\boldsymbol{\zeta} - \mathbf{u})^2}{\tau} - 2 \right] \right) \quad (\text{B.35})$$

$$\psi^{eq} = \psi^M \left(1 + \frac{4}{15} \frac{\mathbf{q} \cdot (\boldsymbol{\zeta} - \mathbf{u})}{\rho\tau^2} \left[\frac{(\boldsymbol{\zeta} - \mathbf{u})^2}{\tau} - 1 \right] \right). \quad (\text{B.36})$$

The reduced distribution functions are defined as

$$\varphi = \frac{1}{\sqrt{\pi}} \int_{-\infty}^{+\infty} g d\zeta_z \quad (\text{B.37})$$

$$\psi = \frac{1}{\sqrt{\pi}} \int_{-\infty}^{+\infty} \zeta_z^2 g d\zeta_z. \quad (\text{B.38})$$

The macroscopic quantities in terms of the reduced distribution functions are given by the following moments:

Number density:

$$\rho = \frac{N}{N_0} = \int_{R^2} \varphi d\boldsymbol{\zeta} \quad (\text{B.39})$$

Velocity vector:

$$\mathbf{u}_i = \frac{U_i}{v_0} = \frac{1}{\rho} \int_{R^2} \zeta_i \varphi d\boldsymbol{\zeta} \quad (\text{B.40})$$

Temperature:

$$\tau = \frac{T}{T_0} = \frac{2}{3\rho} \int_{R^2} [\zeta^2 \varphi + \psi] d\boldsymbol{\zeta} - \frac{2}{3} \mathbf{u}^2 \quad (\text{B.41})$$

Stress tensor:

$$p_{i,j} = \frac{P_{i,j}}{P_0} = 2 \int_{R^2} (\zeta_i - u_i) (\zeta_j - u_j) \varphi d\boldsymbol{\zeta} \quad (\text{B.42})$$

Heat flux vector:

$$q_i = \frac{Q_i}{P_0 v_0} = \int_{R^2} (\zeta_i - u_i) [(\boldsymbol{\zeta} - \mathbf{u})^2 \varphi + \psi] d\boldsymbol{\zeta} \quad (\text{B.43})$$

Pressure:

$$p = \rho\tau \quad (\text{B.44})$$

The boundary conditions at some node i that belongs in B_k^+ for the polar angle θ_k and for the molecular velocity magnitude ζ_m , for the different cases, are formulated as follows:

- Diffuse:

The outgoing distributions are

$$\varphi_i^+ = \frac{\rho_{W,i}}{\pi\tau_{W,i}} \exp \left[-\frac{(\boldsymbol{\zeta} - \mathbf{u}_{W,i})^2}{\tau_{W,i}} \right] \quad (\text{B.45})$$

$$\psi_i^+ = \frac{\rho_{W,i}}{2\pi} \exp \left[-\frac{(\boldsymbol{\zeta} - \mathbf{u}_{W,i})^2}{\tau_{W,i}} \right], \quad (\text{B.46})$$

where ρ_W is a quantity used to satisfy the impermeability condition and is calculated as

$$\rho_{W,i} = -\pi\tau_{W,i} \frac{\int_{\mathbf{n}_i \cdot \boldsymbol{\zeta} < 0} (\mathbf{n}_i \cdot \boldsymbol{\zeta}) \varphi_i^- d\boldsymbol{\zeta}}{\int_{\mathbf{n}_i \cdot \boldsymbol{\zeta} > 0} (\mathbf{n}_i \cdot \boldsymbol{\zeta}) \exp \left[-\frac{(\boldsymbol{\zeta} - \mathbf{u}_{W,i})^2}{\tau_{W,i}} \right] d\boldsymbol{\zeta}}, \quad (\text{B.47})$$

with $\mathbf{u}_W = \mathbf{U}_W/\nu_0$ and $\tau_W = T_W/T_0$.

- Specular:

The outgoing distribution is given in terms of the incoming distribution as $\varphi_i^+ = \varphi_i^R$, $\psi_i^+ = \psi_i^R$, where φ_i^R and ψ_i^R for some molecular velocity $\boldsymbol{\zeta}$ are connected to the incoming distribution through the expressions $\varphi_i^R(\boldsymbol{\zeta}) = \varphi_i^-(\boldsymbol{\zeta} - 2(\mathbf{n}_i \cdot \boldsymbol{\zeta}) \cdot \mathbf{n}_i)$ and $\psi_i^R(\boldsymbol{\zeta}) = \psi_i^-(\boldsymbol{\zeta} - 2(\mathbf{n}_i \cdot \boldsymbol{\zeta}) \cdot \mathbf{n}_i)$.

- Diffuse-Specular:

$$\varphi_i^+ = (1 - \alpha) \varphi_i^R + \alpha \frac{\rho_{W,i}}{\pi\tau_{W,i}} \exp \left[-\frac{(\boldsymbol{\zeta} - \mathbf{u}_{W,i})^2}{\tau_{W,i}} \right] \quad (\text{B.48})$$

$$\psi_i^+ = (1 - \alpha) \psi_i^R + \alpha \frac{\rho_{W,i}}{2\pi} \exp \left[-\frac{(\boldsymbol{\zeta} - \mathbf{u}_{W,i})^2}{\tau_{W,i}} \right] \quad (\text{B.49})$$

The accommodation coefficient $\alpha \in (0, 1)$ is denoting the percentage of particles undergoing purely diffusive emission and the parameter ρ_W is now given by

$$\rho_{W,i} = -\pi\tau_{W,i} \frac{\int_{\mathbf{n}_i \cdot \boldsymbol{\zeta} < 0} (\mathbf{n}_i \cdot \boldsymbol{\zeta}) \varphi_i^- d\boldsymbol{\zeta} + (1-\alpha) \int_{\mathbf{n}_i \cdot \boldsymbol{\zeta} > 0} (\mathbf{n}_i \cdot \boldsymbol{\zeta}) \varphi_i^R d\boldsymbol{\zeta}}{\alpha \int_{\mathbf{n}_i \cdot \boldsymbol{\zeta} > 0} (\mathbf{n}_i \cdot \boldsymbol{\zeta}) \exp \left[-\frac{(\boldsymbol{\zeta} - \mathbf{u}_{W,i})^2}{\tau_{W,i}} \right] d\boldsymbol{\zeta}} \quad (\text{B.50})$$

- Open:

In the case of open boundaries, the incoming distributions are given by Eqs. (B.45) and (B.46), however the quantity ρ_W is replaced by the number density of the incoming gas stream $\rho_i = N_i/N_0$.

- Periodic:

The periodic boundary conditions are treated in the same manner as for the linear cases.

Appendix C

Nonlinear thermally driven flow through short tapered channels

The thermally driven flow through short tapered channels is considered on the basis of the non-linear Shakhov model equation using the DVM algorithm on unstructured meshes developed in Chapter 4. The nonlinear simulations are conducted in order to investigate the validity of the assumptions of the the infinite capillary approach used in Section 5.3. The configuration consists of short converging/diverging channels along with upstream and downstream vessels. The two limiting cases (zero net mass flow rate and zero pressure difference) are considered, where the boundaries of the vessels are either closed or open, while purely diffusive boundary conditions are assumed at the other boundaries. In the case of open boundaries upstream and downstream of the channel the same pressure P_0 is assumed for both. The vessel boundaries are kept at different temperatures T_C and T_H with a linear temperature distribution along the channel walls. For the converging channel, the low temperature (T_C) is applied at the left vessel boundary, while the high temperature (T_H) at the right vessel boundary. In the divergent channel, those temperatures are reversed. The need for non-linear simulations arises from the fact that the channel is relatively short and the temperature differences assumed are large. The simulation parameters are given in the table bellow

T_{out}/T_{in}	T_{in}	L/H_m	L_v/H_m	H_v/H_m	$a = H_{max}/H_{min}$	H_m
2	273K	10	5	5	1, 2, 4	$10^{-5}m$

The following dimensionless quantities are introduced

$$x = x'/H_m, y = y'/H_m, \tau = T/T_{in}, \mathbf{u} = \mathbf{U}/v_0 \text{ and } \rho = N/N_0 \quad (\text{C.1})$$

where $v_0 = \sqrt{2RT_{in}}$ is the most probably molecular speed with R denoting the gas constant, $N_0 = P_0/(k_B T_{in})$ is the reference number density with k_B denoting the Boltzmann constant. In the open configuration the reference pressure (P_0) is the pressure imposed at the open boundaries while in the closed configuration N_0 is the average number density. The reference rarefaction parameter is

$$\delta = \frac{P_0 H}{\mu v_0}, \quad (C.2)$$

where μ is the viscosity at the reference temperature T_{in} . The two limiting cases are considered where either the net mass flow rate or the pressure difference is zero.

C.1 Zero net mass flow rate (Flow scenario A)

The vessel walls are assumed to be solid boundaries and the channel plus vessels configuration is closed. Due to the temperature gradient, a flow is induced from cold to hot regions. However, since the inlet and outlet are closed the net mass flow rate in every cross section necessarily vanishes. This leads to the creation of a pressure difference, with the pressure in the hot side increasing and with that of the cold side decreasing, leading to a pressure driven flow from hot to cold vessels that counteracts the thermally driven flow. More specifically the effect of the diodicity created by the tapered channels is investigated, comparing the pressure difference generated by converging and diverging channels.

Simulations are conducted for the parameters given in the table above and values of the reference rarefaction parameter $\delta = 0.1, 1, 10, 20$, for converging and diverging channels with $\alpha = 2$ and 4 as well as for straight channels. In all cases a triangular mesh is used, with approximately 2.2×10^5 triangular elements.

The dimensional values of the pressure difference are shown in Table C.1. As the reference pressure is increased, the dimensional pressure difference is also increased, however the ratio of the pressure difference to the reference pressure ($\Delta P/P_0$) is decreasing. For small values of δ , the inclination ratio α has a small effect on the pressure difference, while for larger values higher inclination ratios lead to higher pressure differences. Comparing the diverging and converging channels, for small values of δ the diverging channels produce higher pressure differences and the situation is reversed moving to larger δ . This can also be seen from the pressure diodicity

coefficient E_P , that is initially larger than one, although very close to it, and then becomes smaller.

C.2 Equal inlet and outlet pressures (Flow scenario B)

The vessel walls are assumed to be open. Both open boundaries are kept at the same pressure P_0 , but at different temperatures while the macroscopic velocity of the incoming distribution is assumed to be zero. Due to the temperature gradient a thermally driven flow is formed from cold to hot regions through the channel.

Simulations are conducted for reference rarefaction parameter $\delta \in [0.1, 20]$, for converging and diverging channels with $\alpha = 2$ and 4 as well as for straight channels. The reference pressure for each value of the rarefaction parameter examined is given in the table below.

δ	0.1	1	5	8	10	15	20
P_0 (Pa)	74.51037	745.1037	3725.519	5960.83	7451.037	11176.56	14902.07

The mass flow rate per unit length is given in Table C.2, along with the mass diodicity coefficient. The mass flow rate increases as the pressure increases, and tends to an asymptotic value when $\delta \rightarrow \infty$. Increasing the channel inclination α reduces the mass flow rate, as the constriction at the small end of the channel acts as a bottleneck to the flow. Moreover, the straight channel always has the highest mass flow rate out of all three followed by the diverging channels. The mass diodicity coefficient $E_{\dot{m}}$ increases as α is increased. For low values of pressure, $E_{\dot{m}}$ is close to unity, while it increases as the pressure is increased, reaching a maximum and then decreases with further increase of the pressure. In contrast to the pressure diodicity coefficient that takes values both smaller and larger than one, the mass diodicity coefficient for this limiting case is always larger than one.

Density and temperature distributions are shown in Figures C.1 and C.2 at three cross sections along the channel, namely $x = 5.5, 10, 14.5$, corresponding to the center and close to the two ends of the channel for converging and diverging channels with $\alpha = 4$ and $\delta = 0.1, 1, 20$. The interesting observation about those distributions is that both temperature and density are almost uniform at each cross-section for small values of δ , while they slightly deviate from uniform for $\delta = 20$. Although the height to length

ratio $H/L = 0.1$ is not very small, the infinite capillary theory can be applied, due to the uniformity of density and temperature along the cross section. The infinite capillary approach, compared to extensive 4D non-linear simulations, is very computationally efficient and allows for a far more detailed parametric analysis of this flow setup.

Table C.1 Pressure difference and pressure diodicity coefficient (E_P) for the closed configuration ($\dot{m} = 0$).

δ	P_0 (Pa)	Converging		Diverging		E_P	
		$\alpha = 2$	$\alpha = 4$	$\alpha = 2$	$\alpha = 4$	$\alpha = 2$	$\alpha = 4$
0.1	74.477	31.84	31.48	32.08	31.99	1.007	1.016
1	744.77	188.96	187.67	190.81	216.32	1.01	1.153
10	7447.7	365.61	402.03	359.35	394.58	0.983	0.981
20	14895.4	363.89	476.50	332.02	393.83	0.912	0.827

Table C.2 Mass flow rate (kg/m/s) and mass diodicity coefficient $E_{\dot{m}}$ for the open configuration ($\Delta P = 0$)

δ	P_0 (Pa)	Straight	Converging		Diverging		$E_{\dot{m}}$	
			$\alpha = 2$	$\alpha = 4$	$\alpha = 2$	$\alpha = 4$	$\alpha = 2$	$\alpha = 4$
0.1	74.51037	7.49E-08	6.59E-08	4.74E-08	6.78E-08	5.00E-08	1.03	1.06
1	745.1037	4.46E-07	3.81E-07	2.67E-07	4.15E-07	3.12E-07	1.09	1.17
5	3725.519	1.09E-06	8.94E-07	6.01E-07	1.05E-06	7.98E-07	1.17	1.33
8	5960.83	1.29E-06	1.05E-06	7.02E-07	1.25E-06	9.55E-07	1.19	1.36
10	7451.037	1.37E-06	1.12E-06	7.43E-07	1.33E-06	1.02E-06	1.19	1.37
15	11176.56	1.49E-06	1.21E-06	8.11E-07	1.44E-06	1.11E-06	1.18	1.37
20	14902.07	1.54E-06	1.26E-06	8.48E-07	1.48E-06	1.15E-06	1.17	1.36

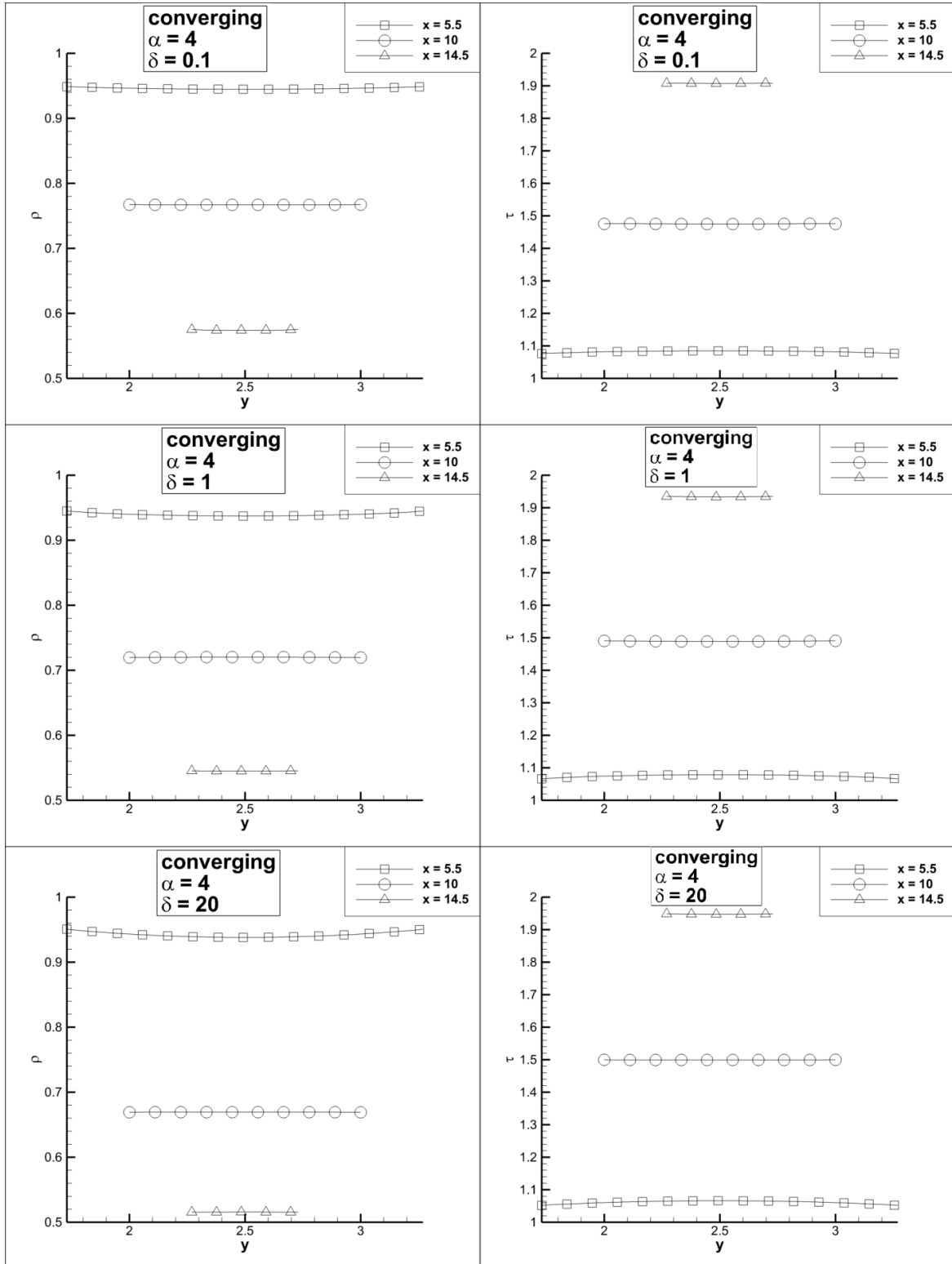


Figure C.1 Density (left) and temperature (right) distributions, at various cross sections along a converging channel with $\alpha = 4$ for $\delta = 0.1, 1, 20$.

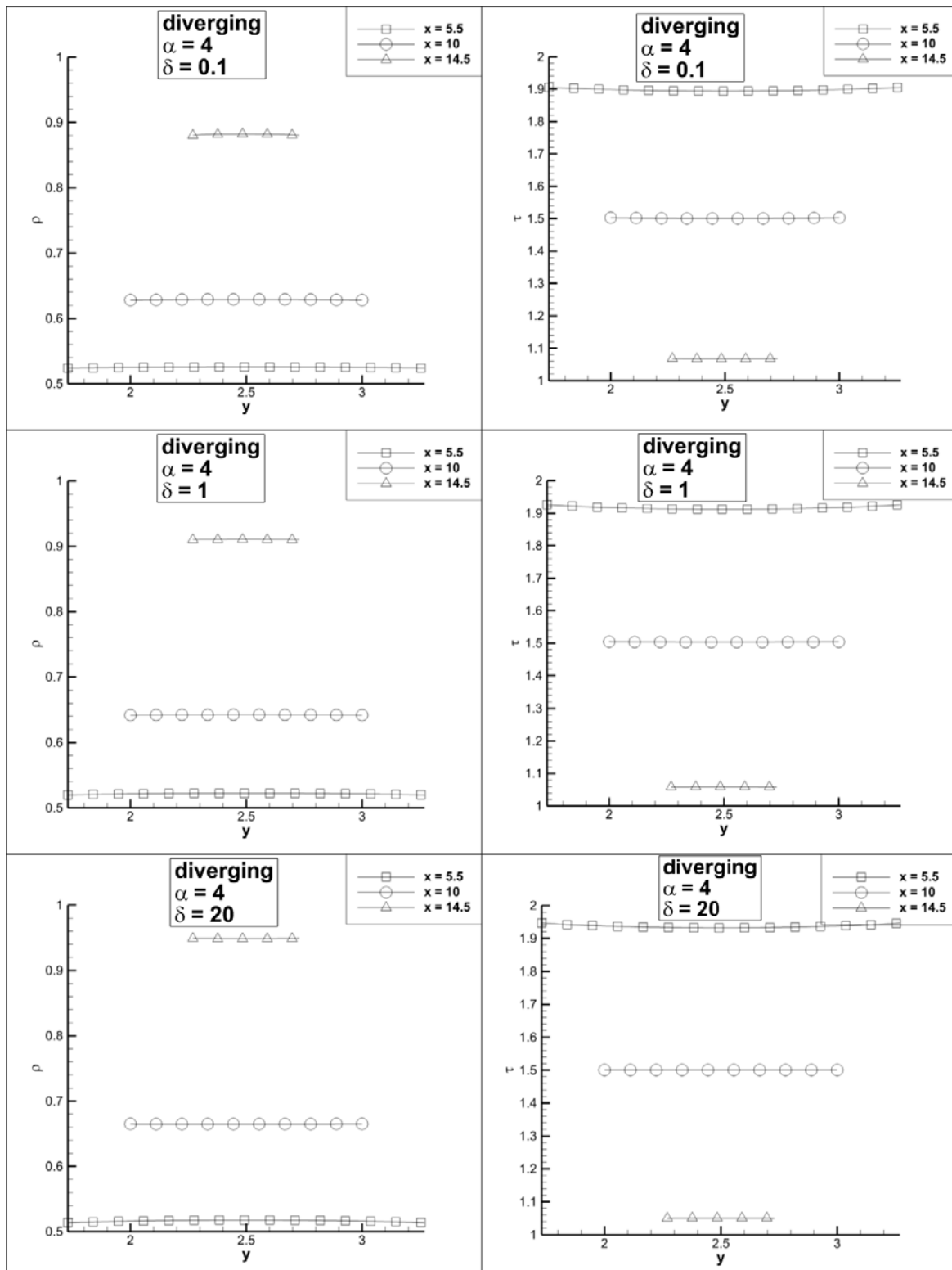


Figure C.2 Density (left) and temperature (right) distributions, at various cross sections along a diverging channel with $\alpha = 4$ for $\delta = 0.1, 1, 20$.

Appendix D

Computation of the kinetic coefficients used in the modeling of tapered channels

The kinetic coefficients presented here are used in the modeling of the tapered channel design in Section 5.3. The linearized Shakhov model equation for the pressure and temperature driven flow between two plates is given in dimensionless form by [235]:

$$c_y \frac{\partial \varphi_j}{\partial y} + \delta \varphi_j = \delta \left[u_j + \frac{2}{15} q_j \left(c_y^2 - \frac{1}{2} \right) \right] - S_j^\varphi \quad (\text{D.1})$$

$$c_y \frac{\partial \psi_j}{\partial y} + \delta \psi_j = \delta \frac{4}{15} q_j - S_j^\psi \quad (\text{D.2})$$

Here, the subscripts $j = P, T$ denote the pressure and temperature driven cases respectively, y is the space variable normal to the two plates, c_y the molecular velocity in the y -direction, $\varphi_j(y, c_y)$ and $\psi_j(y, c_y)$ are the reduced linearized distribution functions, δ the gas rarefaction parameter, u_j and q_j the axial components of the bulk velocity and heat flux given by

$$u_j = \frac{1}{\sqrt{\pi}} \int_{-\infty}^{\infty} \varphi_j e^{-c_y^2} dc_y, \quad (\text{D.3})$$

$$q_j = \frac{1}{\sqrt{\pi}} \int_{-\infty}^{\infty} \left[\psi_j + \left(c_y^2 - \frac{1}{2} \right) \varphi_j \right] e^{-c_y^2} dc_y, \quad (\text{D.4})$$

while the source terms are

$$S_P^\varphi = \frac{1}{2}, S_T^\varphi = \frac{1}{2} \left(c_y^2 - \frac{1}{2} \right), S_P^\psi = 0, S_T^\psi = 1. \quad (\text{D.5})$$

The associated boundary conditions can be written as

$$\varphi_j(1/2, c_y) = 0, c_y < 0 \text{ and } \varphi_j(-1/2, c_y) = 0, c_y > 0 \quad (\text{D.6})$$

$$\psi_j(1/2, c_y) = 0, c_y < 0 \text{ and } \psi_j(-1/2, c_y) = 0, c_y > 0 \quad (\text{D.7})$$

The system of Eqs. (D.1) and (D.2) coupled with the expressions (D.3), (D.4) and (D.5) subject to the boundary conditions (D.6) and (D.7) is solved numerically to yield the dimensionless flow rates, also known as kinetic coefficients,

$$G_P = -2 \int_{-1/2}^{1/2} u_p dy, \quad (\text{D.8})$$

$$G_T = 2 \int_{-1/2}^{1/2} u_T dy. \quad (\text{D.9})$$

Tabulated values of the flow rates G_P and G_T are provided in Table D.1 for $\delta \in [10^{-2}, 50]$ and they are used in the solution of Eq. (5.10). For values of $\delta > 50$ the analytical slip expressions $G_P^{slip} = \frac{\delta}{6} + \sigma_P$, $G_T^{slip} = \frac{\sigma_T}{\delta}$ where $\sigma_P = 1.018$ and $\sigma_T = 1.175$ are applied [23].

Table D.1 Kinetic coefficients G_P and G_T in terms of the gas rarefaction parameter δ for pressure and temperature driven flows through a plane channel.

δ	0.01	0.02	0.03	0.04	0.05	0.06	0.07	0.08
G_P	3.052	2.714	2.528	2.401	2.307	2.233	2.172	2.121
G_T	1.247	1.078	9.846(-1)	9.207(-1)	8.726(-1)	8.344(-1)	8.029(-1)	7.761(-1)
δ	0.09	0.1	0.2	0.3	0.4	0.5	0.6	0.7
G_P	2.078	2.040	1.817	1.713	1.653	1.614	1.589	1.573
G_T	7.530(-1)	7.327(-1)	6.075(-1)	5.408(-1)	4.962(-1)	4.629(-1)	4.365(-1)	4.146(-1)
δ	0.8	0.9	1	2	3	4	5	6
G_P	1.563	1.556	1.554	1.611	1.727	1.861	2.005	2.155
G_T	3.960(-1)	3.798(-1)	3.655(-1)	2.741(-1)	2.233(-1)	1.890(-1)	1.640(-1)	1.448(-1)
δ	7	8	9	10	20	30	40	50
G_P	2.308	2.464	2.621	2.779	4.406	6.053	7.710	9.363
G_T	1.295(-1)	1.171(-1)	1.068(-1)	9.814(-2)	5.386(-2)	3.697(-2)	2.814(-2)	2.269(-2)

Appendix E

Tables of coefficients used for half-range acceleration schemes

The coefficients required in the formulation of the half-range acceleration schemes developed in Chapter 8 are given in the current Appendix. More specifically, the coefficients of the half-range Hermite polynomials for order up to 4 are given in Table E.1, while in Table E.2 the corresponding coefficients multiplying the Hermite polynomials in order to obtain monomials are given. Tables E.3 and E.4 present the coefficients of the moment equations for the Poiseuille flow. Finally, for the heat transfer configuration Tables E.5 - E.9 present the coefficients of the moment equations, while Tables E.10 and E.11 coefficients of the initial conditions.

Table E.1 Coefficients $a_{n,i}^+$ and $a_{n,i}^-$ for up to 4th order.

n	$a_{n,i}^+$				
	$i = 0$	$i = 1$	$i = 2$	$i = 3$	$i = 4$
0	1	0	0	0	0
1	-0.5641895835477563	1	0	0	0
2	0.3759691969420544	-1.552614976394557	1	0	0
3	-0.2909121307837363	2.031256652965526	-2.838582595758498	1	0
4	0.2537095744566917	-2.603999687995054	5.854340551373520	-4.363303439838602	1
n	$a_{n,i}^-$				
	$i = 0$	$i = 1$	$i = 2$	$i = 3$	$i = 4$
0	1	0	0	0	0
1	0.5641895835477563	1	0	0	0
2	0.3759691969420544	1.552614976394557	1	0	0
3	0.2909121307837363	2.031256652965526	2.838582595758498	1	0
4	0.2537095744566917	2.603999687995054	5.854340551373520	4.363303439838602	1

Appendix E

Table E.2 Coefficients $\beta_{n,i}^+$ and $\beta_{n,i}^-$ for up to 4th order.

n	$\beta_{n,i}^+$				
	$i = 0$	$i = 1$	$i = 2$	$i = 3$	$i = 4$
0	1	0	0	0	0
1	0.5641895835477563	1	0	0	0
2	0.5	1.552614976394557	1	0	0
3	0.5641895835477564	2.375969196942055	2.838582595758498	1	0
4	0.75	3.881537440986388	6.531256652965524	4.363303439838602	1
n	$\beta_{n,i}^-$				
	$i = 0$	$i = 1$	$i = 2$	$i = 3$	$i = 4$
0	1	0	0	0	0
1	-0.5641895835477563	1	0	0	0
2	0.5	-1.552614976394557	1	0	0
3	-0.5641895835477564	2.375969196942055	-2.838582595758498	1	0
4	0.75	-3.881537440986388	6.531256652965524	-4.363303439838602	1

Table E.3 Coefficients g^\pm and s^\pm for Poiseuille flow.

n	g^+	g^-	s^+	s^-
0	2.65979236632549	2.65979236632549	0.657251578644048	-0.657251578644048
1	-1.50062714748068	1.50062714748068	-0.120814494441291	-0.120814494441291

Table E.4 Coefficients $p^{\pm\pm}$ for Poiseuille flow.

n	p^{++}		p^{+-}	
	$i = 0$	$i = 1$	$i = 0$	$i = 1$
0	-1.31450315728810	2.569792366325488	1.31450315728810	0
1	0.24162898882581	-1.500627147480680	-0.24162898882581	0
n	p^{-+}		p^{--}	
	$i = 0$	$i = 1$	$i = 0$	$i = 1$
0	-1.31450315728810	0	1.31450315728810	2.569792366325488
1	-0.24162898882581	0	0.24162898882581	1.500627147480680

Table E.5 Coefficients g^{\pm} and f^{\pm} for heat transfer between parallel plates.

n	g^{+}	g^{-}	f^{+}	f^{-}
0	3.94151463200184	3.94151463200184	2.65979236632549	2.65979236632549
1	-2.22376149877651	2.22376149877651	-1.50062714748068	1.50062714748068
2	1.48188809092909	1.48188809092909	-	-
3	-1.14663442011093	1.14663442011093	-	-

Table E.6 Coefficients $q^{\pm\pm}$ for heat transfer between parallel plates.

n	q^{++}			
	$i = 0$	$i = 1$	$i = 2$	$i = 3$
0	-1.81014821515383	5.09314478179876	-6.42502906052862	3.94151463200184
1	0.52126676766735	-2.87349923339147	3.62493446994188	-2.22376149877651
2	-0.18634727437408	1.06086041967950	-2.32158141895835	1.48188809092909
3	0.06171511410546	-0.35133930491015	0.76886910558464	-1.14663442011093
n	q^{+-}			
	$i = 0$	$i = 1$	$i = 2$	$i = 3$
0	1.81014821515383	0.64483134379989	-0.41531954386869	0
1	-0.52126676766735	-0.36380712731700	0.23431896049452	0
2	0.18634727437408	0.09644185633450	-0.06211575812469	0
3	-0.06171511410546	-0.03193993681001	0.02057170470182	0
n	q^{-+}			
	$i = 0$	$i = 1$	$i = 2$	$i = 3$
0	-1.81014821515383	0.64483134379989	0.41531954386869	0
1	-0.52126676766735	0.36380712731700	0.23431896049452	0
2	-0.18634727437408	0.09644185633450	0.06211575812469	0
3	-0.06171511410546	0.03193993681001	0.02057170470182	0
n	q^{--}			
	$i = 0$	$i = 1$	$i = 2$	$i = 3$
0	1.81014821515383	5.09314478179876	6.42502906052862	3.94151463200184
1	0.52126676766735	2.87349923339147	3.62493446994187	2.22376149877650
2	0.18634727437408	1.06086041967950	2.32158141895834	1.48188809092909
3	0.06171511410546	0.35133930491015	0.76886910558464	1.14663442011093

Table E.7 Coefficients $p^{\pm\pm}$ for heat transfer between parallel plates.

n	p^{++}		p^{+-}	
	$i = 0$	$i = 1$	$i = 0$	$i = 1$
0	-0.41531954386869	0	-0.41531954386869	0
1	0.23431896049452	0	0.23431896049452	0
2	-0.06211575812469	0	-0.06211575812469	0
3	0.02057170470182	0	0.02057170470182	0
n	p^{-+}		p^{--}	
	$i = 0$	$i = 1$	$i = 0$	$i = 1$
0	0.41531954386869	0	0.41531954386869	0
1	0.23431896049452	0	0.23431896049452	0
2	0.06211575812469	0	0.06211575812469	0
3	0.02057170470182	0	0.02057170470182	0

Table E.8 Coefficients $r^{\pm\pm}$ for heat transfer between parallel plates.

n	r^{++}			
	$i = 0$	$i = 1$	$i = 2$	$i = 3$
0	0	1.36061152568228	0.87633543819206	0
1	0	-0.25010452458011	-0.16108599258839	0
n	r^{+-}			
	$i = 0$	$i = 1$	$i = 2$	$i = 3$
0	0	-1.36061152568228	0.87633543819206	0
1	0	0.25010452458011	-0.16108599258839	0
n	r^{-+}			
	$i = 0$	$i = 1$	$i = 2$	$i = 3$
0	0	-1.36061152568228	-0.87633543819206	0
1	0	-0.25010452458011	-0.16108599258839	0
n	r^{--}			
	$i = 0$	$i = 1$	$i = 2$	$i = 3$
0	0	1.36061152568228	-0.87633543819206	0
1	0	0.25010452458011	-0.16108599258839	0

Appendix E

Table E.9 Coefficients $s^{\pm\pm}$ for heat transfer between parallel plates.

n	s^{++}		s^{+-}	
	$i = 0$	$i = 1$	$i = 0$	$i = 1$
0	-1.75267087638413	2.65979236632549	0.87633543819206	0
1	0.32217198517678	-1.50062714748068	-0.16108599258838	0
n	s^{-+}		s^{--}	
	$i = 0$	$i = 1$	$i = 0$	$i = 1$
0	-0.87633543819206	0	1.75267087638413	2.65979236632549
1	-0.16108599258838	0	0.32217198517678	1.50062714748068

Table E.10 Coefficients v^{\pm} for heat transfer between parallel plates.

n	v^{+}		v^{-}	
	$i = 0$	$i = 1$	$i = 0$	$i = 1$
0	1	1.77245385090552	1	-1.77245385090552
1	0	0	0	0
2	0	0	0	0
3	0	0	0	0

Table E.11 Coefficients w^{\pm} and z^{\pm} for heat transfer between parallel plates.

n	w^{+}	w^{-}	z^{+}	z^{-}
0	0.125	-0.125	-0.25	0.25
1	0.07052369794347	0.07052369794347	0	0
2	-0.01550385038224	0.01550385038224	-	-
3	0	0	-	-

References

- [1] P. A. Gnoffo, “Planetary-entry Gas Dynamics,” *Annu. Rev. Fluid Mech.*, vol. 31, no. 1, pp. 459–494, 1999.
- [2] K. Moe, M. M. Moe, and S. D. Wallace, “Improved Satellite Drag Coefficient Calculations from Orbital Measurements of Energy Accommodation,” *J. Spacecr. Rockets*, vol. 35, no. 3, pp. 266–272, 1998.
- [3] F. Sharipov, “Hypersonic flow of rarefied gas near the Brazilian satellite during its reentry into atmosphere,” *Brazilian J. Phys.*, vol. 33, no. 2, pp. 398–405, 2003.
- [4] M. S. Ivanov and S. F. Gimelshein, “Computational Hypersonic Rarefied Flows,” *Annu. Rev. Fluid Mech.*, vol. 30, no. 1, pp. 469–505, 1998.
- [5] H. Liu et al., “Monte Carlo simulations of gas flow and heat transfer in vacuum packaged MEMS devices,” *Appl. Therm. Eng.*, vol. 27, no. 2–3, pp. 323–329, 2007.
- [6] N. K. Gupta, S. An, and Y. B. Gianchandani, “A Si-micromachined 48-stage Knudsen pump for on-chip vacuum,” *J. Micromechanics Microengineering*, vol. 22, no. 10, p. 105026, 2012.
- [7] N. Vasileiadis, G. Tatsios, S. Misdanitis, and D. Valougeorgis, “Modeling of complex gas distribution systems operating under any vacuum conditions: Simulations of the ITER divertor pumping system,” *Fusion Eng. Des.*, vol. 103, pp. 125–135, 2016.
- [8] C. Day and D. Murdoch, “The ITER vacuum systems,” *J. Phys. Conf. Ser.*, vol. 114, no. 1, p. 012013, 2008.
- [9] F. Sharipov, “Numerical simulation of turbomolecular pump over a wide range of gas rarefaction,” *J. Vac. Sci. Technol. A Vacuum, Surfaces, Film.*, vol. 28, no. 6, pp. 1312–1315, 2010.
- [10] S. Naris, C. Tantos, and D. Valougeorgis, “Kinetic modeling of a tapered Holweck pump,” *Vacuum*, vol. 109, pp. 341–348, 2014.

- [11] S. Giors, L. Campagna, and E. Emelli, “New spiral molecular drag stage design for high compression ratio, compact turbomolecular-drag pumps,” *J. Vac. Sci. Technol. A Vacuum, Surfaces, Film.*, vol. 28, no. 4, pp. 931–936, 2010.
- [12] W. Jitschin and S. Ludwig, “Dynamical behaviour of the Pirani sensor,” *Vacuum*, vol. 75, no. 2, pp. 169–176, 2004.
- [13] S. Naris, N. Vasileiadis, D. Valougeorgis, A. S. Hashad, and W. Sabuga, “Computation of the effective area and associated uncertainties of non-rotating piston gauges FPG and FRS,” *Metrologia*, vol. 56, no. 1, p. 015004, 2018.
- [14] D. J. Furley, *Two studies in the Greek atomists*, vol. 2406. Princeton University Press, 2015.
- [15] D. Flamm, “Ludwig Boltzmann – A Pioneer of Modern Physics,” 1997.
- [16] J. H. Ferziger and H. . Kaper, *Mathematical Theory of Transport Processes in Gases*. Amsterdam: North-Holland, 1972.
- [17] D. Bernoulli, *Hydrodynamica*. 1738.
- [18] J. C. Maxwell, “V. Illustrations of the dynamical theory of gases.—Part I. On the motions and collisions of perfectly elastic spheres,” *London, Edinburgh, Dublin Philos. Mag. J. Sci.*, vol. 19, no. 124, pp. 19–32, 1860.
- [19] L. Boltzmann, “Weitere Studien über das Wörmegleichgewicht unter Gas-molekülen,” *Sitzungsberichte Akad. Wiss., Vienna*, part II, no. 66, pp. 275–370, 1872.
- [20] C. Shen, *Rarefied gas dynamics: fundamentals, simulations and micro flows*. Springer Science & Business Media, 2006.
- [21] R. Clausius, “On the nature of the motion which we call heat,” *London, Edinburgh, Dublin Philos. Mag. J. Sci.*, vol. 14, no. 91, pp. 108–127, 1857.
- [22] M. Knudsen, “Die molekularströmung der gase durch offnungen und die effusion,” *Ann. Phys.*, vol. 333, no. 5, pp. 999–1016, 1909.
- [23] F. Sharipov and V. Seleznev, “Data on Internal Rarefied Gas Flows,” *J. Phys. Chem. Ref. Data*, vol. 27, no. 3, p. 657, 1998.
- [24] M. Gad-el-Hak, *MEMS: introduction and fundamentals*. CRC press, 2005.
- [25] F. Sharipov, “Data on the Velocity Slip and Temperature Jump on a Gas-Solid Interface,” *J. Phys. Chem. Ref. Data*, vol. 40, no. 2, p. 023101, 2011.
- [26] H. Struchtrup, “Macroscopic transport equations for rarefied gas flows,” in *Macroscopic Transport Equations for Rarefied Gas Flows*, Springer, 2005, pp. 145–160.

- [27] P. L. Bhatnagar, E. P. Gross, and M. Krook, "A Model for Collision Processes in Gases. I. Small Amplitude Processes in Charged and Neutral One-Component Systems," *Phys. Rev.*, vol. 94, no. 3, pp. 511–525, 1954.
- [28] P. Welander, "On the temperature jump in a rarefied gas," *Ark. Fys.*, vol. 7, 1954.
- [29] E. M. Shakhov, "Generalization of the Krook kinetic relaxation equation," *Fluid Dyn.*, vol. 3, no. 5, pp. 95–96, 1972.
- [30] L. H. Holway, "New Statistical Models for Kinetic Theory: Methods of Construction," *Phys. Fluids*, vol. 9, no. 9, p. 1658, 1966.
- [31] V. A. Rykov, "A model kinetic equation for a gas with rotational degrees of freedom," *Fluid Dyn.*, vol. 10, no. 6, pp. 959–966, 1976.
- [32] P. Andries, P. Le Tallec, J.-P. Perlat, and B. Perthame, "The Gaussian-BGK model of Boltzmann equation with small Prandtl number," *Eur. J. Mech. - B/Fluids*, vol. 19, no. 6, pp. 813–830, 2000.
- [33] F. B. Hanson and T. F. Morse, "Kinetic Models for a Gas with Internal Structure," *Phys. Fluids*, vol. 10, no. 2, p. 345, 1967.
- [34] C. A. Brau, "Kinetic Theory of Polyatomic Gases: Models for the Collision Processes," *Phys. Fluids*, vol. 10, no. 1, p. 48, 1967.
- [35] W. P. Wood, "Kinetic theory analysis of light scattering in polyatomic gases," *Aust. J. Phys.*, vol. 24, p. 555, 1971.
- [36] W. Marques, "Light scattering and sound propagation in polyatomic gases with classical degrees of freedom," *Contin. Mech. Thermodyn.*, vol. 16, no. 6, pp. 517–528, 2004.
- [37] A. S. Fernandes and W. Marques, "Kinetic model analysis of time-dependent problems in polyatomic gases," *Phys. A Stat. Mech. its Appl.*, vol. 373, pp. 97–118, 2007.
- [38] T. F. Morse, "Kinetic model equations for a gas mixture," *Phys. fluids*, vol. 7, no. 12, pp. 2012–2013, 1964.
- [39] B. B. Hamel, "Kinetic Model for Binary Gas Mixtures," *Phys. Fluids*, vol. 8, no. 3, p. 418, 1965.
- [40] F. J. McCormack, "Construction of linearized kinetic models for gaseous mixtures and molecular gases," *Phys. Fluids*, vol. 16, no. 12, p. 2095, 1973.
- [41] S. Kosuge, "Model Boltzmann equation for gas mixtures: Construction and numerical comparison," *Eur. J. Mech. - B/Fluids*, vol. 28, no. 1, pp. 170–184, 2009.

- [42] P. Bassanini, C. Cercignani, and C. D. Pagani, “Influence of the accommodation coefficient on the heat transfer in a rarefied gas,” *Int. J. Heat Mass Transf.*, vol. 11, no. 9, pp. 1359–1369, 1968.
- [43] J. R. Thomas, T. S. Chang, and C. E. Siewert, “Heat transfer between parallel plates with arbitrary surface accommodation,” *Phys. Fluids*, vol. 16, no. 12, p. 2116, 1973.
- [44] M. Epstein, “A model of the wall boundary condition in kinetic theory,” *AIAA J.*, vol. 5, no. 10, pp. 1797–1800, 1967.
- [45] C. Cercignani and M. Lampis, “Kinetic models for gas-surface interactions,” *Transp. Theory Stat. Phys.*, vol. 1, no. 2, pp. 101–114, 1971.
- [46] R. G. Lord, “Some extensions to the Cercignani–Lampis gas–surface scattering kernel,” *Phys. Fluids A Fluid Dyn.*, vol. 3, no. 4, pp. 706–710, 1991.
- [47] R. G. Lord, “Some further extensions of the Cercignani–Lampis gas–surface interaction model,” *Phys. Fluids*, vol. 7, no. 5, pp. 1159–1161, 1995.
- [48] D. Bruno, M. Cacciatore, S. Longo, and M. Rutigliano, “Gas-surface scattering models for particle fluid dynamics: a comparison between analytical approximate models and molecular dynamics calculations,” *Chem. Phys. Lett.*, vol. 320, no. 3–4, pp. 245–254, 2000.
- [49] K. Yamamoto, H. Takeuchi, and T. Hyakutake, “Scattering properties and scattering kernel based on the molecular dynamics analysis of gas-wall interaction,” *Phys. Fluids*, vol. 19, no. 8, p. 087102, 2007.
- [50] J. Pitakarnnop, S. Varoutis, D. Valougeorgis, S. Geoffroy, L. Baldas, and S. Colin, “A novel experimental setup for gas microflows,” *Microfluid. Nanofluidics*, vol. 8, no. 1, pp. 57–72, 2010.
- [51] S. Colin, P. Lalonde, and R. Caen, “Validation of a Second-Order Slip Flow Model in Rectangular Microchannels,” *Heat Transf. Eng.*, vol. 25, no. 3, pp. 23–30, 2004.
- [52] S. Colin and Cé. Aubert, “High-Order Boundary Conditions for Gaseous Flows in Rectangular Microducts,” *Microscale Thermophys. Eng.*, vol. 5, no. 1, pp. 41–54, 2001.
- [53] L. Mieussens, “A survey of deterministic solvers for rarefied flows (Invited),” in *AIP Conference Proceedings*, 2014, vol. 1628, no. 1, pp. 943–951.
- [54] V. V. Aristov, *Direct methods for solving the Boltzmann equation and study of nonequilibrium flows*. Springer Science & Business Media, 2012.

- [55] S. Pantazis and D. Valougeorgis, “Rarefied gas flow through a cylindrical tube due to a small pressure difference,” *Eur. J. Mech. - B/Fluids*, vol. 38, pp. 114–127, 2013.
- [56] K. Aoki, S. Takata, and T. Nakanishi, “Poiseuille-type flow of a rarefied gas between two parallel plates driven by a uniform external force,” *Phys. Rev. E*, vol. 65, no. 2, p. 026315, 2002.
- [57] N. S. Martys, X. Shan, and H. Chen, “Evaluation of the external force term in the discrete Boltzmann equation,” *Phys. Rev. E*, vol. 58, no. 5, pp. 6855–6857, 1998.
- [58] D. Valougeorgis and S. Naris, “Acceleration Schemes of the Discrete Velocity Method: Gaseous Flows in Rectangular Microchannels,” *SIAM J. Sci. Comput.*, vol. 25, no. 2, pp. 534–552, 2003.
- [59] J. Lihnaropoulos, S. Naris, and D. Valougeorgis, “Formulation and Stability Analysis of Rapidly Convergent Iteration Schemes for the 2-D Linearized BGK Equation,” *Transp. Theory Stat. Phys.*, vol. 36, no. 4–6, pp. 513–528, 2007.
- [60] L. Szalmás and D. Valougeorgis, “A fast iterative model for discrete velocity calculations on triangular grids,” *J. Comput. Phys.*, vol. 229, no. 11, pp. 4315–4326, 2010.
- [61] L. Wu, J. Zhang, H. Liu, Y. Zhang, and J. M. Reese, “A fast iterative scheme for the linearized Boltzmann equation,” *J. Comput. Phys.*, vol. 338, pp. 431–451, 2017.
- [62] G. A. Bird, “Molecular gas dynamics and the direct simulation monte carlo of gas flows,” Clarendon, Oxford, vol. 508, p. 128, 1994.
- [63] O. M. Belotserkovskii and V. E. Yanitskii, “The statistical particles-in-cells method for solving rarefied gas dynamics problems,” *USSR Comput. Math. Math. Phys.*, vol. 15, no. 5, pp. 101–114, 1975.
- [64] O. M. Belotserkovskii and V. E. Yanitskii, “The statistical particles-in-cells method for solving rarefied gas dynamics problems,” *Zh. Vychisl. Mat. Mat. Fiz.*, vol. 15, no. 5, p. 1195–1208 (in Russian), 1975.
- [65] O. M. Belotserkovskii, “Numerical modeling in continuum mechanics,” Moscow Izd. Nauk., 1984.
- [66] W. Wagner, “A convergence proof for Bird’s direct simulation Monte Carlo method for the Boltzmann equation,” *J. Stat. Phys.*, vol. 66, no. 3–4, pp. 1011–1044, 1992.

- [67] C. Aubert, S. Colin, and R. Caen, “Unsteady gaseous flows in tapered microchannels,” in Technical proceedings of the 1998 international conference on modeling and simulation of microsystems, volume, 1998, pp. 486–491.
- [68] A. Batikh, R. Caen, S. Colin, L. Baldas, A. Kourta, and H. BOISSON, “Numerical and experimental of micro synthetic jets for flow control,” *Int. J. Heat Technol.*, vol. 26, pp. 139–145, 2008.
- [69] S. Pantazis et al., “Nonlinear vacuum gas flow through a short tube due to pressure and temperature gradients,” *Fusion Eng. Des.*, vol. 88, no. 9–10, pp. 2384–2387, 2013.
- [70] C. Gleason-González, S. Varoutis, V. Hauer, and C. Day, “Simulation of neutral gas flow in a tokamak divertor using the Direct Simulation Monte Carlo method,” *Fusion Eng. Des.*, vol. 89, no. 7–8, pp. 1042–1047, 2014.
- [71] S. Varoutis, V. Hauer, C. Day, S. Pantazis, and D. Valougeorgis, “Experimental and numerical investigation in flow configurations related to the vacuum systems of fusion reactors,” *Fusion Eng. Des.*, vol. 85, no. 10–12, pp. 1798–1802, 2010.
- [72] F. Sharipov, “Benchmark problems in rarefied gas dynamics,” *Vacuum*, vol. 86, no. 11, pp. 1697–1700, 2012.
- [73] I. Graur, A. P. Polikarpov, and F. Sharipov, “Numerical modeling of rarefied gas flow through a slit into vacuum based on the kinetic equation,” *Comput. Fluids*, vol. 49, no. 1, pp. 87–92, 2011.
- [74] V. A. Titarev, “Rarefied gas flow in a planar channel caused by arbitrary pressure and temperature drops,” *Int. J. Heat Mass Transf.*, vol. 55, no. 21–22, pp. 5916–5930, 2012.
- [75] S. Misdanitis, S. Pantazis, and D. Valougeorgis, “Pressure driven rarefied gas flow through a slit and an orifice,” *Vacuum*, vol. 86, no. 11, pp. 1701–1708, 2012.
- [76] V. A. Titarev, “Efficient Deterministic Modelling of Three-Dimensional Rarefied Gas Flows,” *Commun. Comput. Phys.*, vol. 12, no. 01, pp. 162–192, 2012.
- [77] V. A. Titarev and E. M. Shakhov, “Computational study of a rarefied gas flow through a long circular pipe into vacuum,” *Vacuum*, vol. 86, no. 11, pp. 1709–1716, 2012.
- [78] I. A. Graur, A. P. Polikarpov, and F. Sharipov, “Numerical modelling of rarefied gas flow through a slit at arbitrary pressure ratio based on the kinetic equation,” *Zeitschrift für Angew. Math. und Phys.*, vol. 63, no. 3, pp. 503–520, 2012.

- [79] O. I. Rovenskaya, A. P. Polikarpov, and I. A. Graur, "Comparison of the numerical solutions of the full Boltzmann and S-model kinetic equations for gas flow through a slit," *Comput. Fluids*, vol. 80, pp. 71–78, 2013.
- [80] S. Varoutis, D. Valougeorgis, O. Sazhin, and F. Sharipov, "Rarefied gas flow through short tubes into vacuum," *J. Vac. Sci. Technol. A Vacuum, Surfaces, Film.*, vol. 26, no. 2, pp. 228–238, 2008.
- [81] S. Varoutis, C. Day, and F. Sharipov, "Rarefied gas flow through channels of finite length at various pressure ratios," *Vacuum*, vol. 86, no. 12, pp. 1952–1959, 2012.
- [82] S. Varoutis, D. Valougeorgis, and F. Sharipov, "Simulation of gas flow through tubes of finite length over the whole range of rarefaction for various pressure drop ratios," *J. Vac. Sci. Technol. A Vacuum, Surfaces, Film.*, vol. 27, no. 6, pp. 1377–1391, 2009.
- [83] S. Pantazis, D. Valougeorgis, and F. Sharipov, "End corrections for rarefied gas flows through circular tubes of finite length," *Vacuum*, vol. 101, pp. 306–312, 2014.
- [84] S. Pantazis, D. Valougeorgis, and F. Sharipov, "End corrections for rarefied gas flows through capillaries of finite length," *Vacuum*, vol. 97, pp. 26–29, 2013.
- [85] N. Vasileiadis and V. Titarev, "Validity range of linear kinetic modeling in rarefied pressure driven single gas flows through circular capillaries," *Eur. J. Mech. - B/Fluids*, vol. 64, pp. 2–7, 2017.
- [86] F. Sharipov and D. V. Kozak, "Rarefied gas flow through a thin slit into vacuum simulated by the Monte Carlo method over the whole range of the Knudsen number," *J. Vac. Sci. Technol. A Vacuum, Surfaces, Film.*, vol. 27, no. 3, pp. 479–484, 2009.
- [87] W. W. Liou and Y. C. Fang, "Implicit boundary conditions for direct simulation Monte Carlo method in MEMS flow predictions," *In other words*, vol. 2, p. 7, 2000.
- [88] Y. Fang and W. W. Liou, "Computations of the Flow and Heat Transfer in Microdevices Using DSMC With Implicit Boundary Conditions," *J. Heat Transfer*, vol. 124, no. 2, p. 338, 2002.
- [89] M. Wang and Z. Li, "Simulations for gas flows in microgeometries using the direct simulation Monte Carlo method," *Int. J. Heat Fluid Flow*, vol. 25, no. 6, pp. 975–985, 2004.
- [90] W. W. Liou and Y. Fang, *Microfluid mechanics: principles and modeling*. 2006.

- [91] R. P. Nance, D. B. Hash, and H. A. Hassan, "Role of Boundary Conditions in Monte Carlo Simulation of Microelectromechanical Systems," *J. Thermophys. Heat Transf.*, vol. 12, no. 3, pp. 447–449, 1998.
- [92] A. A. Alexeenko, S. F. Gimelshein, and D. A. Levin, "Reconsideration of low Reynolds number flow-through constriction microchannels using the DSMC method," *J. Microelectromechanical Syst.*, vol. 14, no. 4, pp. 847–856, 2005.
- [93] Y. Sone, *Molecular Gas Dynamics*. Boston, MA: Birkhäuser Boston, 2007.
- [94] Y. Sone and S. Tanaka, "Thermal stress slip flow induced in rarefied gas between noncoaxial circular cylinders," in *Theoretical and Applied Mechanics*, 1980, pp. 405–416.
- [95] K. Aoki, Y. Sone, and T. Yano, "Numerical analysis of a flow induced in a rarefied gas between noncoaxial circular cylinders with different temperatures for the entire range of the Knudsen number," *Phys. Fluids A Fluid Dyn.*, vol. 1, no. 2, pp. 409–419, 1989.
- [96] T. Ohwada and Y. Sone, "Analysis of thermal stress slip flow and negative thermophoresis using the Boltzmann equation for hard-sphere molecules," *Eur. J. Mech. B Fluids*, vol. 11, pp. 389–414, 1992.
- [97] Y. Sone and K. Aoki, "Slightly rarefied gas flow over a specularly reflecting body," *Phys. Fluids*, vol. 20, no. 4, p. 571, 1977.
- [98] W. Crookes and others, "I. On attraction and repulsion resulting from radiation.—Part II," *Proc. R. Soc. London*, vol. 23, no. 156–163, pp. 373–378, 1875.
- [99] J. C. Maxwell, "VII. On stresses in rarefied gases arising from inequalities of temperature," *Philos. Trans. R. Soc. London*, vol. 170, pp. 231–256, 1879.
- [100] A. Einstein, "Zur theorie der radiometerkräfte," *Zeitschrift Fuer Phys.*, vol. 27, no. 1, pp. 1–6, 1924.
- [101] M. Knudsen, "Eine Revision der Gleichgewichtsbedingung der Gase. Thermische Molekularströmung," *Ann. Phys.*, vol. 336, no. 1, pp. 205–229, 1909.
- [102] M. Knudsen, "Thermischer Molekulardruck der Gase in Röhren," *Ann. Phys.*, vol. 338, no. 16, pp. 1435–1448, 1910.
- [103] H. Sugimoto and Y. Sone, "Vacuum Pump without a Moving Part Driven by Thermal Edge Flow," in *AIP Conference Proceedings*, 2005, vol. 762, no. 1, pp. 168–173.
- [104] J. Chen, S. K. Stefanov, L. Baldas, and S. Colin, "Analysis of flow induced by temperature fields in ratchet-like microchannels by Direct Simulation Monte Carlo," *Int. J. Heat Mass Transf.*, vol. 99, pp. 672–680, 2016.

- [105] Y. Sone, Y. Waniguchi, and K. Aoki, “One-way flow of a rarefied gas induced in a channel with a periodic temperature distribution,” *Phys. Fluids*, vol. 8, no. 8, p. 2227, 1998.
- [106] K. Aoki, P. Degond, S. Takata, and H. Yoshida, “Diffusion models for Knudsen compressors,” *Phys. Fluids*, vol. 19, no. 11, p. 117103, 2007.
- [107] K. Aoki, P. Degond, L. Mieussens, S. Takata, and H. Yoshida, “A Diffusion Model for Rarefied Flows in Curved Channels,” *Multiscale Model. Simul.*, vol. 6, no. 4, pp. 1281–1316, 2008.
- [108] V. Leontidis, J. Chen, L. Baldas, and S. Colin, “Numerical design of a Knudsen pump with curved channels operating in the slip flow regime,” *Heat Mass Transf.*, vol. 50, no. 8, pp. 1065–1080, 2014.
- [109] D. M. Bond, V. Wheatley, and M. Goldsworthy, “Numerical investigation into the performance of alternative Knudsen pump designs,” *Int. J. Heat Mass Transf.*, vol. 93, pp. 1038–1058, 2016.
- [110] D. M. Bond, V. Wheatley, and M. Goldsworthy, “Numerical investigation of curved channel Knudsen pump performance,” *Int. J. Heat Mass Transf.*, vol. 76, pp. 1–15, 2014.
- [111] E. P. Muntz, Y. Sone, K. Aoki, S. Vargo, and M. Young, “Performance analysis and optimization considerations for a Knudsen compressor in transitional flow,” *J. Vac. Sci. Technol. A Vacuum, Surfaces, Film.*, vol. 20, no. 1, pp. 214–224, 2002.
- [112] S. McNamara and Y. B. Gianchandani, “On-chip vacuum generated by a micro-machined Knudsen pump,” *J. Microelectromechanical Syst.*, vol. 14, no. 4, pp. 741–746, 2005.
- [113] S. An, N. K. Gupta, and Y. B. Gianchandani, “A Si-Micromachined 162-Stage Two-Part Knudsen Pump for On-Chip Vacuum,” *J. Microelectromechanical Syst.*, vol. 23, no. 2, pp. 406–416, 2014.
- [114] Y. Qin, S. An, and Y. B. Gianchandani, “Arrayed architectures for multi-stage Si-micromachined high-flow Knudsen pumps,” *J. Micromechanics Microengineering*, vol. 25, no. 11, p. 115026, 2015.
- [115] M. Lorenzini, G. L. Morini, T. Henning, and J. Brandner, “Uncertainty assessment in friction factor measurements as a tool to design experimental set-ups,” *Int. J. Therm. Sci.*, vol. 48, pp. 282–289, 2009.

- [116] G. L. Morini, M. Lorenzini, and M. Spiga, “A criterion for experimental validation of slip-flow models for incompressible rarefied gases through microchannels,” *Microfluid. Nanofluidics*, vol. 1, no. 2, pp. 190–196, 2005.
- [117] M. Lorenzini, G. L. Morini, T. Henning, and J. Brandner, “Experimental uncertainties analysis as a tool for friction factor determination in microchannels,” *Proc. Inst. Mech. Eng. Part C J. Mech. Eng. Sci.*, vol. 222, no. 5, pp. 817–827, 2008.
- [118] R. W. Walters and L. Huyse, “Uncertainty analysis for fluid mechanics with applications,” 2002.
- [119] M. G. Morgan, M. Henrion, and M. Small, *Uncertainty: a guide to dealing with uncertainty in quantitative risk and policy analysis*. Cambridge university press, 1992.
- [120] R. E. Moore, *Methods and applications of interval analysis*, vol. 2. Siam, 1979.
- [121] M. M. Putko, A. C. Taylor, P. A. Newman, and L. L. Green, “Approach for Input Uncertainty Propagation and Robust Design in CFD Using Sensitivity Derivatives,” *J. Fluids Eng.*, vol. 124, no. 1, p. 60, 2002.
- [122] L. Huyse, “Solving problems of optimization under uncertainty as statistical decision problems,” in *19th AIAA Applied Aerodynamics Conference*, 2001, p. 1519.
- [123] O. M. Knio and O. P. Le Maître, “Uncertainty propagation in CFD using polynomial chaos decomposition,” *Fluid Dyn. Res.*, vol. 38, no. 9, pp. 616–640, 2006.
- [124] J. M. Hammersley and D. C. Handscomb, “Monte Carlo Methods. Methuen’s monographs on applied probability and statistics,” Methuen, London, 1964.
- [125] T. Rosenband et al., “Frequency ratio of Al⁺ and Hg⁺ single-ion optical clocks; metrology at the 17th decimal place,” *Science (80-.)*, vol. 319, no. 5871, pp. 1808–1812, 2008.
- [126] P. J. Roache, “Quantification of Uncertainty in Computational Fluid Dynamics,” *Annu. Rev. Fluid Mech.*, vol. 29, no. 1, pp. 123–160, 1997.
- [127] K. Kume, J. Hasegawa, Y. Tsukada, J. Fujisawa, R. Fukasawa, and M. Hinatsu, “Measurements of hydrodynamic forces, surface pressure, and wake for obliquely towed tanker model and uncertainty analysis for CFD validation,” *J. Sci. Technol.*, vol. 11, no. 2, pp. 65–75, 2006.

- [128] X. Guo, J. Li, D. Xiu, and A. Alexeenko, "Uncertainty quantification models for micro-scale squeeze-film damping," *Int. J. Numer. Methods Eng.*, vol. 84, no. 10, pp. 1257–1272, 2010.
- [129] A. Alexeenko and M. Kulakhmetov, "Modeling Uncertainties in Direct Simulation Monte Carlo Calculations of Hypersonic Leading-Edge Flow," *J. Spacecr. Rockets*, vol. 49, no. 3, pp. 461–473, 2012.
- [130] M. Kulakhmetov and A. Alexeenko, "Model Uncertainties in a Sharp Leading-Edge Hypersonic Boundary," in *49th AIAA Aerospace Sciences Meeting including the New Horizons Forum and Aerospace Exposition*, 2011.
- [131] S. Colin, C. Aubert, and R. Caen, "Unsteady gaseous flows in rectangular microchannels: frequency response of one or two pneumatic lines connected in series," *Eur. J. Mech. / B Fluids*, vol. 1, no. 17, pp. 79–104, 1998.
- [132] G. Breyiannis and D. Valougeorgis, "Lattice kinetic simulations in three-dimensional magnetohydrodynamics," *Phys. Rev. E*, vol. 69, no. 6, p. 065702, 2004.
- [133] A. A. Mohamad and A. Kuzmin, "A critical evaluation of force term in lattice Boltzmann method, natural convection problem," *Int. J. Heat Mass Transf.*, vol. 53, no. 5–6, pp. 990–996, 2010.
- [134] Z. Chai and B. Shi, "Simulation of electro-osmotic flow in microchannel with lattice Boltzmann method," *Phys. Lett. A*, vol. 364, no. 3–4, pp. 183–188, 2007.
- [135] G. Tatsios, S. K. Stefanov, and D. Valougeorgis, "Predicting the Knudsen paradox in long capillaries by decomposing the flow into ballistic and collision parts," *Phys. Rev. E*, vol. 91, no. 6, p. 061001, 2015.
- [136] S. Stefanov, V. Roussinov, and C. Cercignani, "Rayleigh–Be?ard flow of a rarefied gas and its attractors. I. Convection regime," *Phys. Fluids*, vol. 14, no. 7, p. 2255, 2002.
- [137] S. Stefanov, V. Roussinov, and C. Cercignani, "Rayleigh–Be?ard flow of a rarefied gas and its attractors. II. Chaotic and periodic convective regimes," *Phys. Fluids*, vol. 14, no. 7, p. 2270, 2002.
- [138] D. Whitfield, "Three-dimensional unsteady Euler equations solution using flux vector splitting," in *17th Fluid Dynamics, Plasma Dynamics, and Lasers Conference*, 1984, p. 1552.
- [139] K. W. Thompson, "Time dependent boundary conditions for hyperbolic systems," *J. Comput. Phys.*, vol. 68, no. 1, pp. 1–24, 1987.

- [140] K. W. Thompson, “Time-dependent boundary conditions for hyperbolic systems, II,” *J. Comput. Phys.*, vol. 89, no. 2, pp. 439–461, 1990.
- [141] T. . Poinso and S. . Lele, “Boundary conditions for direct simulations of compressible viscous flows,” *J. Comput. Phys.*, vol. 101, no. 1, pp. 104–129, 1992.
- [142] S. V. Tsynkov, “Numerical solution of problems on unbounded domains. A review,” *Appl. Numer. Math.*, vol. 27, no. 4, pp. 465–532, 1998.
- [143] G. Tatsios, “Introductory study of applying Particle-In-Cell methods in deterministic rarefied gas flow simulations,” University of Thessaly, 2015.
- [144] M. Malek Mansour, F. Baras, and A. L. Garcia, “On the validity of hydrodynamics in plane Poiseuille flows,” *Phys. A Stat. Mech. its Appl.*, vol. 240, no. 1–2, pp. 255–267, 1997.
- [145] M. T. Ho et al., “A multi-level parallel solver for rarefied gas flows in porous media,” *Comput. Phys. Commun.*, vol. 234, pp. 14–25, 2019.
- [146] G. Dechristé and L. Mieussens, “A Cartesian cut cell method for rarefied flow simulations around moving obstacles,” *J. Comput. Phys.*, vol. 314, pp. 465–488, 2016.
- [147] L. Zhu, Z. Guo, and K. Xu, “Discrete unified gas kinetic scheme on unstructured meshes,” *Comput. Fluids*, vol. 127, pp. 211–225, 2016.
- [148] L. Zhu, S. Chen, and Z. Guo, “dugksFoam: An open source OpenFOAM solver for the Boltzmann model equation,” *Comput. Phys. Commun.*, vol. 213, pp. 155–164, 2017.
- [149] W. Su, P. Wang, Y. Zhang, and L. Wu, “A high-order hybridizable discontinuous Galerkin method with fast convergence to steady-state solutions of the gas kinetic equation,” *J. Comput. Phys.*, vol. 376, pp. 973–991, 2019.
- [150] S. Jaiswal, A. A. Alexeenko, and J. Hu, “A Discontinuous Galerkin Fast Spectral Method for the Full Boltzmann Equation with General Collision Kernels,” 2018.
- [151] W. Su, A. A. Alexeenko, and G. Cai, “A parallel Runge–Kutta discontinuous Galerkin solver for rarefied gas flows based on 2D Boltzmann kinetic equations,” *Comput. Fluids*, vol. 109, pp. 123–136, 2015.
- [152] V. Titarev, M. Dumbser, and S. Utyuzhnikov, “Construction and comparison of parallel implicit kinetic solvers in three spatial dimensions,” *J. Comput. Phys.*, vol. 256, pp. 17–33, 2014.

- [153] V. A. Titarev, S. V. Utyuzhnikov, and A. V. Chikitkin, “OpenMP + MPI parallel implementation of a numerical method for solving a kinetic equation,” *Comput. Math. Math. Phys.*, vol. 56, no. 11, pp. 1919–1928, 2016.
- [154] A. Chikitkin, M. Petrov, V. Titarev, and S. Utyuzhnikov, “Parallel Versions of Implicit LU-SGS Method,” *Lobachevskii J. Math.*, vol. 39, no. 4, pp. 503–512, 2018.
- [155] F. Rossi, P. Van Beek, and T. Walsh, *Handbook of constraint programming*. Elsevier, 2006.
- [156] I. Graur and F. Sharipov, “Non-isothermal flow of rarefied gas through a long pipe with elliptic cross section,” *Microfluid. Nanofluidics*, vol. 6, no. 2, pp. 267–275, 2009.
- [157] S. Naris and D. Valougeorgis, “The driven cavity flow over the whole range of the Knudsen number,” *Phys. Fluids*, vol. 17, no. 9, p. 097106, 2005.
- [158] M. Vargas, G. Tatsios, D. Valougeorgis, and S. Stefanov, “Rarefied gas flow in a rectangular enclosure induced by non-isothermal walls,” *Phys. Fluids*, vol. 26, no. 5, p. 057101, 2014.
- [159] J. Chen, L. Baldas, and S. Colin, “Numerical study of thermal creep flow between two ratchet surfaces,” *Vacuum*, vol. 109, pp. 294–301, 2014.
- [160] F. Sharipov and G. Bertoldo, “Rarefied gas flow through a long tube of variable radius,” *J. Vac. Sci. Technol. A Vacuum, Surfaces, Film.*, vol. 23, no. 3, pp. 531–533, 2005.
- [161] L. R. Silva and C. J. Deschamps, “Modeling of gas leakage through compressor valves,” *Int. J. Refrig.*, vol. 53, pp. 195–205, 2015.
- [162] N. Stevanovic and V. Djordjevic, “The exact analytical solution for the gas lubricated bearing in the slip and continuum flow regime,” *Publ. l’Institut Math.*, vol. 91, no. 105, pp. 83–93, 2012.
- [163] T. Veltzke, L. Kiewidt, and J. Thöming, “Multicomponent gas diffusion in nonuniform tubes,” *AIChE J.*, vol. 61, no. 4, pp. 1404–1412, 2015.
- [164] I. Graur, T. Veltzke, J. G. Méolans, M. T. Ho, and J. Thöming, “The gas flow diode effect: theoretical and experimental analysis of moderately rarefied gas flows through a microchannel with varying cross section,” *Microfluid. Nanofluidics*, vol. 18, no. 3, pp. 391–402, 2015.
- [165] I. Graur, J. G. Méolans, P. Perrier, J. Thöming, and T. Veltzke, “A physical explanation of the gas flow diode effect,” *Microfluid. Nanofluidics*, vol. 20, no. 10, p. 145, 2016.

- [166] V. A. Titarev, S. V. Utyuzhnikov, and E. M. Shakhov, "Rarefied gas flow through a pipe of variable square cross section into vacuum," *Comput. Math. Math. Phys.*, vol. 53, no. 8, pp. 1221–1230, 2013.
- [167] L. Szalmás, T. Veltzke, and J. Thöming, "Analysis of the diodic effect of flows of rarefied gases in tapered rectangular channels," *Vacuum*, vol. 120, pp. 147–154, 2015.
- [168] Y. Sone, "Thermal Creep in Rarefied Gas," *J. Phys. Soc. Japan*, vol. 21, no. 9, pp. 1836–1837, 1966.
- [169] I. Graur and M. T. Ho, "Rarefied gas flow through a long rectangular channel of variable cross section," *Vacuum*, vol. 101, pp. 328–332, 2014.
- [170] T. Ohwada, Y. Sone, and K. Aoki, "Numerical analysis of the Poiseuille and thermal transpiration flows between two parallel plates on the basis of the Boltzmann equation for hard-sphere molecules," *Phys. Fluids A Fluid Dyn.*, vol. 1, no. 12, pp. 2042–2049, 1989.
- [171] F. Sharipov, "Rarefied gas flow through a long tube at any temperature ratio," *J. Vac. Sci. Technol. A Vacuum, Surfaces, Film.*, vol. 14, no. 4, pp. 2627–2635, 1996.
- [172] A. A. Alexeenko, S. F. Gimelshein, E. P. Muntz, and A. D. Ketsdever, "Kinetic modeling of temperature driven flows in short microchannels," *Int. J. Therm. Sci.*, vol. 45, no. 11, pp. 1045–1051, 2006.
- [173] F. Sharipov, "Non-isothermal gas flow through rectangular microchannels," *J. Micromechanics Microengineering*, vol. 9, no. 4, pp. 394–401, 1999.
- [174] K. Ritos, Y. Lihnaropoulos, S. Naris, and D. Valougeorgis, "Pressure- and Temperature-Driven Flow Through Triangular and Trapezoidal Microchannels," *Heat Transf. Eng.*, vol. 32, no. 13–14, pp. 1101–1107, 2011.
- [175] H. Yamaguchi, M. Rojas-Cárdenas, P. Perrier, I. Graur, and T. Niimi, "Thermal transpiration flow through a single rectangular channel," *J. Fluid Mech.*, vol. 744, pp. 169–182, 2014.
- [176] M. Rojas-Cárdenas, I. Graur, P. Perrier, and J. G. Méolans, "Time-dependent experimental analysis of a thermal transpiration rarefied gas flow," *Phys. Fluids*, vol. 25, no. 7, p. 072001, 2013.
- [177] H. Yamaguchi, P. Perrier, M. T. Ho, J. G. Méolans, T. Niimi, and I. Graur, "Mass flow rate measurement of thermal creep flow from transitional to slip flow regime," *J. Fluid Mech.*, vol. 795, pp. 690–707, 2016.

- [178] K. Aoki, S. Takata, E. Tatsumi, and H. Yoshida, “Rarefied gas flows through a curved channel: Application of a diffusion-type equation,” *Phys. Fluids*, vol. 22, no. 11, p. 112001, 2010.
- [179] Y. Sone, *Kinetic Theory and Fluid Dynamics*. Boston, MA: Birkhäuser Boston, 2002.
- [180] S. Naris, D. Valougeorgis, D. Kalempa, and F. Sharipov, “Flow of gaseous mixtures through rectangular microchannels driven by pressure, temperature, and concentration gradients,” *Phys. Fluids*, vol. 17, no. 10, p. 100607, 2005.
- [181] V. G. Chernyak, V. V. Kalinin, and P. E. Suetin, “Theory of nonisothermal gas motion in a plane channel,” *J. Eng. Phys.*, vol. 36, no. 6, pp. 696–700, 1979.
- [182] S. Naris and D. Valougeorgis, “Rarefied gas flow in a triangular duct based on a boundary fitted lattice,” *Eur. J. Mech. - B/Fluids*, vol. 27, no. 6, pp. 810–822, 2008.
- [183] H. A. Stone, A. D. Stroock, and A. Ajdari, “Engineering Flows in Small Devices,” *Annu. Rev. Fluid Mech.*, vol. 36, no. 1, pp. 381–411, 2004.
- [184] H.-A. Yang, M. Wu, and W. Fang, “Localized induction heating solder bonding for wafer level MEMS packaging,” *J. Micromechanics Microengineering*, vol. 15, no. 2, pp. 394–399, 2005.
- [185] A. Ketsdever, N. Gimelshein, S. Gimelshein, and N. Selden, “Radiometric phenomena: From the 19th to the 21st century,” *Vacuum*, vol. 86, no. 11, pp. 1644–1662, 2012.
- [186] M. Vargas, M. Wüest, and S. Stefanov, “Monte Carlo analysis of thermal transpiration effects in capacitance diaphragm gauges with helicoidal baffle system,” *J. Phys. Conf. Ser.*, vol. 362, no. 1, p. 012013, 2012.
- [187] K. Aoki, S. Takata, H. Aikawa, and F. Golse, “A rarefied gas flow caused by a discontinuous wall temperature,” *Phys. Fluids*, vol. 13, no. 9, pp. 2645–2661, 2001.
- [188] S. Naris and D. Valougeorgis, “Gas Flow in a Grooved Channel Due to Pressure and Temperature Gradients,” in *ASME 4th International Conference on Nanochannels, Microchannels, and Minichannels, Parts A and B*, 2006, vol. 2006, pp. 539–546.
- [189] Y. Sone, “Comment on ‘Heat transfer in vacuum packaged microelectromechanical system devices’ [*Phys. Fluids* 20, 017103 (2008)],” *Phys. Fluids*, vol. 21, no. 11, p. 119101, 2009.

- [190] A. Mohammadzadeh, E. Roohi, H. Niazmand, S. Stefanov, and R. S. Myong, “Thermal and second-law analysis of a micro- or nanocavity using direct-simulation Monte Carlo,” *Phys. Rev. E*, vol. 85, no. 5, p. 056310, 2012.
- [191] N. D. Masters and W. Ye, “Octant flux splitting information preservation DSMC method for thermally driven flows,” *J. Comput. Phys.*, vol. 226, no. 2, pp. 2044–2062, 2007.
- [192] A. Rana, M. Torrilhon, and H. Struchtrup, “Heat transfer in micro devices packaged in partial vacuum,” *J. Phys. Conf. Ser.*, vol. 362, no. 1, p. 012034, 2012.
- [193] J.-C. Huang, K. Xu, and P. Yu, “A Unified Gas-Kinetic Scheme for Continuum and Rarefied Flows III: Microflow Simulations,” *Commun. Comput. Phys.*, vol. 14, no. 05, pp. 1147–1173, 2013.
- [194] D. H. Papadopoulos and D. E. Rosner, “Enclosure gas flows driven by non-isothermal walls,” *Phys. Fluids*, vol. 7, no. 11, pp. 2535–2537, 1995.
- [195] S. Kosuge, K. Aoki, S. Takata, R. Hattori, and D. Sakai, “Steady flows of a highly rarefied gas induced by nonuniform wall temperature,” *Phys. Fluids*, vol. 23, no. 3, p. 030603, 2011.
- [196] C. Cercignani and M. Lampis, “Kinetic models for gas-surface interactions,” *Transp. Theory Stat. Phys.*, vol. 1, no. 2, pp. 101–114, 1971.
- [197] A. Rana, M. Torrilhon, and H. Struchtrup, “A robust numerical method for the R13 equations of rarefied gas dynamics: Application to lid driven cavity,” *J. Comput. Phys.*, vol. 236, pp. 169–186, 2013.
- [198] K. Xu and J.-C. Huang, “A unified gas-kinetic scheme for continuum and rarefied flows,” *J. Comput. Phys.*, vol. 229, no. 20, pp. 7747–7764, 2010.
- [199] A. S. Rana, A. Mohammadzadeh, and H. Struchtrup, “A numerical study of the heat transfer through a rarefied gas confined in a microcavity,” *Contin. Mech. Thermodyn.*, vol. 27, no. 3, pp. 433–446, 2015.
- [200] H. Struchtrup and P. Taheri, “Macroscopic transport models for rarefied gas flows: a brief review,” *IMA J. Appl. Math.*, vol. 76, no. 5, pp. 672–697, 2011.
- [201] G. Tatsios, M. H. Vargas, S. K. Stefanov, and D. Valougeorgis, “Nonequilibrium Gas Flow and Heat Transfer in a Heated Square Microcavity,” *Heat Transf. Eng.*, vol. 37, no. 13–14, pp. 1085–1095, 2016.
- [202] E. M. Shakhov, “Kinetic model equations and numerical results,” in *Proc. 14th Int. Symp. Rarefied Gas Dynamics*, 1984, pp. 137–148.

- [203] M. Knudsen, “Die Gesetze der Molekularströmung und der inneren Reibungsströmung der Gase durch Röhren,” *Ann. Phys.*, vol. 333, no. 1, pp. 75–130, 1909.
- [204] K. Aoki, “Numerical analysis of rarefied gas flows by finite-difference method,” *Prog. Astronaut. Aeronaut.*, vol. 117, pp. 297–322, 1989.
- [205] S. Tison, “Experimental data and theoretical modeling of gas flows through metal capillary leaks,” *Vacuum*, vol. 44, no. 11–12, pp. 1171–1175, 1993.
- [206] S. K. Loyalka and S. A. Hamoodi, “Poiseuille flow of a rarefied gas in a cylindrical tube: Solution of linearized Boltzmann equation,” *Phys. Fluids A Fluid Dyn.*, vol. 2, no. 11, pp. 2061–2065, 1990.
- [207] F. M. Sharipov and V. D. Seleznev, “Rarefied gas flow through a long tube at any pressure ratio,” *J. Vac. Sci. Technol. A Vacuum, Surfaces, Film.*, vol. 12, no. 5, pp. 2933–2935, 1994.
- [208] D. Valougeorgis, “The friction factor of a rarefied gas flow in a circular tube,” *Phys. Fluids*, vol. 19, no. 9, p. 091702, 2007.
- [209] S. Varoutis, S. Naris, V. Hauer, C. Day, and D. Valougeorgis, “Computational and experimental study of gas flows through long channels of various cross sections in the whole range of the Knudsen number,” *J. Vac. Sci. Technol. A Vacuum, Surfaces, Film.*, vol. 27, no. 1, pp. 89–100, 2009.
- [210] P. Perrier, I. A. Graur, T. Ewart, and J. G. Méolans, “Mass flow rate measurements in microtubes: From hydrodynamic to near free molecular regime,” *Phys. Fluids*, vol. 23, no. 4, p. 042004, 2011.
- [211] A. Ganguly, S. L. Nail, and A. Alexeenko, “Experimental Determination of the Key Heat Transfer Mechanisms in Pharmaceutical Freeze-Drying,” *J. Pharm. Sci.*, vol. 102, no. 5, pp. 1610–1625, 2013.
- [212] S. Pantazis and K. Jousten, “Computational and experimental study of unsteady gas flow in a dynamic vacuum standard,” *Vacuum*, vol. 109, pp. 373–384, 2014.
- [213] H. Struchtrup and M. Torrilhon, “Higher-order effects in rarefied channel flows,” *Phys. Rev. E*, vol. 78, no. 4, p. 046301, 2008.
- [214] W. P. Yudistiawan, S. K. Kwak, D. V. Patil, and S. Ansumali, “Higher-order Galilean-invariant lattice Boltzmann model for microflows: Single-component gas,” *Phys. Rev. E*, vol. 82, no. 4, p. 046701, 2010.
- [215] S. K. Dadzie and H. Brenner, “Predicting enhanced mass flow rates in gas microchannels using nonkinetic models,” *Phys. Rev. E*, vol. 86, no. 3, p. 036318, 2012.

- [216] M. A. Gallis and J. R. Torczynski, “Direct simulation Monte Carlo-based expressions for the gas mass flow rate and pressure profile in a microscale tube,” *Phys. Fluids*, vol. 24, no. 1, p. 012005, 2012.
- [217] F. Sharipov and I. Graur, “General approach to transient flows of rarefied gases through long capillaries,” *Vacuum*, vol. 100, pp. 22–25, 2014.
- [218] W. G. Pollard and R. D. Present, “On Gaseous Self-Diffusion in Long Capillary Tubes,” *Phys. Rev.*, vol. 73, no. 7, pp. 762–774, 1948.
- [219] M. H. Vargas, “Modeling and simulation of heat transfer and thermal phenomena in micro gas flows,” Institute of Mechanics, Bulgarian Academy of Sciences, 2012.
- [220] I. A. Graur and A. P. Polikarpov, “Comparison of different kinetic models for the heat transfer problem,” *Heat Mass Transf.*, vol. 46, no. 2, pp. 237–244, 2009.
- [221] V. A. Titarev, E. M. Shakhov, and S. V. Utyuzhnikov, “Rarefied gas flow through a diverging conical pipe into vacuum,” *Vacuum*, vol. 101, pp. 10–17, 2014.
- [222] C. Cercignani, *The Boltzmann Equation and Its Applications*, vol. 67. New York, NY: Springer New York, 1988.
- [223] S. Pantazis and D. Valougeorgis, “Heat transfer through rarefied gases between coaxial cylindrical surfaces with arbitrary temperature difference,” *Eur. J. Mech. - B/Fluids*, vol. 29, no. 6, pp. 494–509, 2010.
- [224] S. Stefanov, P. Gospodinov, and C. Cercignani, “Monte Carlo simulation and Navier–Stokes finite difference calculation of unsteady-state rarefied gas flows,” *Phys. Fluids*, vol. 10, no. 1, p. 289, 1998.
- [225] Y. Sone and S. Takata, “Discontinuity of the velocity distribution function in a rarefied gas around a convex body and the S layer at the bottom of the Knudsen layer,” *Transp. Theory Stat. Phys.*, vol. 21, no. 4–6, pp. 501–530, 1992.
- [226] K. Aoki, C. Bardos, C. Dogbe, and F. Golse, “A Note on the Propagation of Boundary Induced Discontinuities in Kinetic Theory,” *Math. Model. Methods Appl. Sci.*, vol. 11, no. 09, pp. 1581–1595, 2001.
- [227] F. Sharipov, “Rarefied gas flow through a long rectangular channel,” *J. Vac. Sci. Technol. A Vacuum, Surfaces, Film.*, vol. 17, no. 5, p. 3062, 1999.
- [228] I. Graur and F. Sharipov, “Gas flow through an elliptical tube over the whole range of the gas rarefaction,” *Eur. J. Mech. - B/Fluids*, vol. 27, no. 3, pp. 335–345, 2008.

- [229] G. Breyiannis, S. Varoutis, and D. Valougeorgis, “Rarefied gas flow in concentric annular tube: Estimation of the Poiseuille number and the exact hydraulic diameter,” *Eur. J. Mech. - B/Fluids*, vol. 27, no. 5, pp. 609–622, 2008.
- [230] I. I. and B. OIML, “Guide to the Expression of Uncertainty in Measurement,” Geneva, Switz., 1995.
- [231] B. I. I. I. and I. ISO, “Evaluation of Measurement Data—Supplement 1 to the Guide to the Expression of Uncertainty in Measurement,” *Propagation of Distributions Using a Monte Carlo Method, Joint Committee for Guides in Metrology*, Bur. Int. des Poids Mes. JCGM, vol. 101, 2008.
- [232] G. Tatsios, G. Lopez Quesada, M. Rojas-Cardenas, L. Baldas, S. Colin, and D. Valougeorgis, “Computational investigation and parametrization of the pumping effect in temperature-driven flows through long tapered channels,” *Microfluid. Nanofluidics*, vol. 21, no. 5, p. 99, 2017.
- [233] C. Tantos, S. Naris, and D. Valougeorgis, “Gas flow towards an adsorbing planar wall subject to partial gas-surface thermal accommodation,” *Vacuum*, vol. 125, pp. 65–74, 2016.
- [234] M. L. Adams and E. W. Larsen, “Fast iterative methods for discrete-ordinates particle transport calculations,” *Prog. Nucl. Energy*, vol. 40, no. 1, pp. 3–159, 2002.
- [235] F. Sharipov, “Application of the Cercignani–Lampis scattering kernel to calculations of rarefied gas flows. I. Plane flow between two parallel plates,” *Eur. J. Mech. - B/Fluids*, vol. 21, no. 1, pp. 113–123, 2002.
- [236] G. Tatsios and D. Valougeorgis, “Accelerated discrete velocity schemes for solving thermal flow problems in rarefied gas dynamics,” in *2nd European Conference on Non-equilibrium Gas Flows*, 2015.
- [237] A. Frezzotti, L. Gibelli, and B. Franzelli, “A moment method for low speed microflows,” *Contin. Mech. Thermodyn.*, vol. 21, no. 6, pp. 495–509, 2009.
- [238] S. Lorenzani, L. Gibelli, A. Frezzotti, A. Frangi, and C. Cercignani, “Kinetic Approach to Gas Flows in Microchannels,” *Nanoscale Microscale Thermophys. Eng.*, vol. 11, no. 1–2, pp. 211–226, 2007.
- [239] G. P. Ghioldi and L. Gibelli, “A Finite-Difference Lattice Boltzmann Approach for Gas Microflows,” *Commun. Comput. Phys.*, vol. 17, no. 04, pp. 1007–1018, 2015.
- [240] V. E. Ambrus and V. Sofonea, “Lattice Boltzmann models based on half-range Gauss–Hermite quadratures,” *J. Comput. Phys.*, vol. 316, pp. 760–788, 2016.

- [241] V. E. Ambrus and V. Sofonea, “Half-range lattice Boltzmann models for the simulation of Couette flow using the Shakhov collision term,” arXiv Prepr. arXiv1702.01335, 2017.
- [242] P. L. Roe, “Characteristic-based schemes for the Euler equations,” *Annu. Rev. Fluid Mech.*, vol. 18, no. 1, pp. 337–365, 1986.
- [243] S. Naris and D. Valougeorgis, “Boundary-driven nonequilibrium gas flow in a grooved channel via kinetic theory,” *Phys. Fluids*, vol. 19, no. 6, p. 067103, 2007.